HIBALL - A Conceptual Heavy Ion Beam Driven Fusion Reactor Study

B. Badger, F. Arendt, K. Becker, K. Beckert, R. Bock, D. Böhne, I. Bozsik, J. Brezina, M. Dalle Donne, L. El-Guebaly, R. Engelstad, W. Eyrich, R. Fröhlich, N. Ghoniem, B. Goel, A. Hassanein, D. Henderson, W. Höbel, I. Hofmann, E. Hoyer, R. Keller, G. Kessler, A. Klein, R. Kreutz, G. Kulcinski, E. Larsen, K. Lee, K. Long, E. Lovell, N. Metzler, J. Meyer-ter-Vehn, U. von Möllendorff, N. Moritz, G. Moses, R. Müller, K. O'Brien, R. Peterson, K. Plute, L. Pong, R. Sanders, J. Sapp, M. Sawan, K. Schretzmann, T. Spindler, I. Sviatoslavsky, K. Symon, D. Sze, N. Tahir, W. Vogelsang, A. White, S. Witkowski, H. Wollnik

September 1981

UWFDM-450

FUSION TECHNOLOGY INSTITUTE

UNIVERSITY OF WISCONSIN

MADISON WISCONSIN

HIBALL - A Conceptual Heavy Ion Beam Driven Fusion Reactor Study

B. Badger, F. Arendt, K. Becker, K. Beckert, R. Bock, D. Böhne, I. Bozsik, J. Brezina, M. Dalle Donne, L. El-Guebaly, R. Engelstad, W. Eyrich, R. Fröhlich, N. Ghoniem, B. Goel, A. Hassanein, D. Henderson, W. Höbel, I. Hofmann, E. Hoyer, R. Keller, G. Kessler, A. Klein, R. Kreutz, G. Kulcinski, E. Larsen, K. Lee, K. Long, E. Lovell, N. Metzler, J. Meyer-ter-Vehn, U. von Möllendorff, N. Moritz, G. Moses, R. Müller, K. O'Brien, R. Peterson, K. Plute, L. Pong, R. Sanders, J. Sapp, M. Sawan, K. Schretzmann, T. Spindler, I. Sviatoslavsky, K. Symon, D. Sze, N. Tahir, W. Vogelsang, A. White, S. Witkowski, H. Wollnik

Fusion Technology Institute
University of Wisconsin
1500 Engineering Drive
Madison, WI 53706

http://fti.neep.wisc.edu

September 1981

UWFDM-450

HIBALL - A Conceptual Heavy Ion Beam Driven Fusion Reactor Study

Preliminary Report

by

B. Badger[a]
F. Arendt[b]
K. Becker[c]
K. Beckert[d]
R. Bock[d]
D. Böhne[d]
I. Bozsik[e]
J. Brezina[c]
M. Dalle Donne[f]
L. El-Guebaly[a]
R. Engelstad[a]
W. Eyrich[f]
R. Fröhlick[f]
N. Ghoniem[g]
B. Goel[f]
A. Hassanein[a]
D. Henderson[f]
W. Höbel[f]
I. Hofmann[e]
E. Hoyer[h]
R. Keller[d]
G. Kessler[f]
A. Klein[a]
R. Kreutz[i]
G. Kulcinski[a]
E. Larsen[a]
K. Lee[a]
K. Long[f]
E. Lovell[a]
N. Metzler[j]
J. Meyer-ter-Vehn[j]
U. von Möllendorff[f]
N. Moritz[f]
G. Moses[a]
R. Müller[d]
K. O'Brien[a]
R. Peterson[a]
K. Plute[a]
L. Pong[a]
R. Sanders[a]
J. Sapp[k]
M. Sawan[a]
K. Schretzmann[f]
T. Spindler[a]
I. Sviatoslavsky[a]
K. Symon[a]
D. Sze[a]
N. Tahir[f]
W. Vogelsang[a]
A. White[a]
S. Witkowski[j]
H. Wollnik[c]

June 1981

[a]UW
[b]KfK-ITP
[c]Universität Giessen
[d]GSI
[e]IPP
[f]KfK-INR
[g]UCLA
[h]LBL
[i]INTERATOM
[j]MPQ
[k]McDonnell-Douglas

UWFDM-450
KfK-3202

PREFACE

HIBALL (Heavy Ion Beams and Lithium Lead) is a conceptual reactor design study for inertial confinement fusion (ICF) with beams of heavy ions. The HIBALL study was started in January 1980 and is being jointly performed by research groups of the

University of Wisconsin, Fusion Engineering Program (UW)

Kernforschungszentrum Karlsruhe (KfK)

Gesellschaft für Schwerionenforschung, Darmstadt (GSI)

Max-Planck-Institut für Quantenoptik, Garching (MPQ)

Institut für Plasmaphysik, Garching (IPP), and

II. Physikalisches Institut, Universität Giessen.

The objectives of this study are the investigation of the system characteristics of a fusion reactor based on a heavy ion accelerator as the driver facility and the identification of problems to be investigated in the future.

The HIBALL study is part of a basic research program established by the German Federal Ministry of Research and Technology (BMFT). This program is aimed at the investigation of key problems in the fields of accelerator research, atomic physics, target physics and reactor design. Another main purpose is to examine the present conviction, generally accepted in the accelerator community, that no fundamental physics problems inhibit the use of heavy ions as a driver for ICF.

The present report, published jointly by KfK and UW, is of a preliminary nature and represents the status as of June 1981. In the text, this stage of the design will sometimes be referred to as HIBALL-I. A final report with an advanced, more complete and more consistent design (HIBALL-II) is scheduled for the end of 1982.

Acknowledgments

We wish to acknowledge R. Bangerter, A. Bell, J. Beyer, R. Burke, R. Evans, C. Hendricks, N. Hoffman, Y. Kim, G. Magelssen, D.J. Nicholas, U. Trinks and Z. Zinamon for valuable technical discussions.

The German contributions to this study have been funded by the BMFT heavy-ion fusion research program. The UW efforts were performed under a contract jointly funded by KfK (70%) and the BMFT program (30%). We express our appreciation to W. Klose for his support and to R. Rennebohm for making financial arrangements.

Finally, we gratefully acknowledge the help of the secretarial and support staff at UW -- Elizabeth Brown, Gail Herrington, Linda Kraft, and Dennis Bruggink - for their most professional efforts in typing and assembling this report.

TABLE OF CONTENTS

References are found after each subchapter (e.g., III.1) or chapter (e.g., I).

I Introduction

I.1 General Perspectives

Inertial Confinement Fusion (ICF) is considered as an alternative to Magnetic Confinement Fusion, with the goal, in both cases, of exploiting the energy released from thermonuclear fusion reactions to produce electric energy. In the case of ICF, this is accomplished by imploding targets containing DT fuel to very high densities (1000 x liquid density) with the use of intense beams of photons or charged particles. The ICF program started later (~ 1961) and with substantially less financial support than magnetic fusion. Because of this fact, as well as the emphasis on military rather than civilian applications in the United States, the ICF approach to electric power generation is not as well developed at this time as the magnetic fusion approach. However, inertial confinement fusion has many attractive features, including: the separation of the driver from the reactor cavity with its high level of radioactivity, and a relatively simple geometry (compared with tokamak reactors) and therefore greater design flexibility along with better maintenance accessibility of the reactor. On the other hand, new problems related to the pulsed release of energy (~ 10^{-8} sec) require innovative protection schemes for the first wall and the final components that focus the driver beams onto the target.

The specific design and overall economics of an ICF reactor are mainly determined by the choice of driver and the target characteristics. Heavy ion beams, from accelerator systems similar to those widely used in high energy physics, have been considered since 1975-76 as an attractive driver choice for reactors. This is because they can deliver large amounts of energy per pulse at a high repetition frequency. Different criteria might favor other drivers if an experimental proof-of-principle device for a single shot facility is

visualized. A major target physics requirement common to all drivers - whether lasers, light ions or heavy ions - is that several hundreds of terawatts of power should be delivered onto a target of a few mm radius to achieve compression and ignition with high gain. Heavy ions are the only candidate which permit essentially classical beam transport to the target and classical deposition of energy in the target ablator shell. This is due to the fact that, based on the same classical penetration depth, the energy of very heavy ions ($A > 200$) can be of the order of 10 GeV, whereas the equivalent energy of very light ions is below 10 MeV. As a consequence, the same demand for beam power has to be met with megaamperes of light ions (along with possible collective effects in both the cavity transport and the target deposition region) whereas heavy ion beam currents can remain in the kiloampere range. It is generally accepted now[1] that these requirements can be met - at least in principle - with existing accelerator technology. This technology has other significant advantages.

- A high efficiency of 20-25% is credited to high energy accelerators. This allows for "conservative" target design with allowable target gain of less than 100.
- A high repetition rate of 20 Hz is realizable for the RF accelerator based scenario. Such an accelerator can support several reactor cavities, the number of which is determined by the time needed to reestablish beam propagation conditions.
- High working reliability (70-80%) can be extrapolated from existing accelerators.
- The option of ballistic beam focusing on target - as though in vacuum - using superconducting quadrupole magnets is available. This provides an independence from plasma channel transport schemes which cannot yet be

assessed for a reactor with the present level of theoretical and experimental understanding.

On the other hand, it has become clear since the first Heavy Ion Fusion Study at Berkeley[2] in 1976 that the size and cost of a heavy ion driver can be considerable and such factors certainly have a major influence on the anticipated cost of electricity. This gives strong justification to a complete conceptual reactor design study at the present time.

I.2 Basis and Objectives of HIBALL

The specific goal of the HIBALL study is to demonstrate the compatibility of physics and engineering design in the areas of the driver (including final beam transport), target, and reactor chamber through a self-consistent conceptual reactor design. In addition, it is required that HIBALL be a DT fusion power plant that produces electricity on an economically and environmentally acceptable basis as compared to other fusion conceptual reactor designs. Before HIBALL can be built, successful operation of at least three heavy-ion driven fusion facilities will probably have to be achieved:

1) a "scientific breakeven" device ($\frac{\text{energy out}}{\text{energy in}} = 1$),
2) an Engineering Test Facility, and
3) a Demonstration Fusion Power Plant (net electricity and tritium production).

This means that HIBALL, as a reactor concept, will have the benefit from at least two or three decades of research in imploding targets.

I.2.1 Driver Scenario

The task of the driver in HIBALL is to produce high beam intensity within a six-dimensional phase space volume that is small enough to be focused onto a 3 mm radius target at the reactor stand-off distance of 8.5 m with a pulse duration of 20 nsec. This has been evaluated within the following scenario:

- A RF linear accelerator is used to achieve the final energy of 10 GeV for Bi^{+2} at a current level of 150 mA. This choice benefits from the high level of confidence in design reliability and cost estimates for RF accelerator technology.
- A large radius transfer ring and several more compact condenser and storage rings are used to raise the current by almost three orders of magnitude through a sequence of stacking and bunching procedures.

- Induction linear accelerators in the final beam lines supply a ramped voltage of several hundred MeV to achieve a final ten-fold compression on the long path (2/3 of a kilometer) of the ions to the target chamber. This raises the particle current per beamlet from 120 A to 1200 A, hence 20 beamlets per cavity will produce a power of 240 terawatts on target.

The overall scenario for HIBALL resembles the BNL RF accelerator scenario suggested several years ago. The design has benefitted also from the results of heavy ion fusion (HIF) studies performed in the past years at major U.S. high energy laboratories (ANL, BNL and LBL) and at the Rutherford Laboratory in England[1-4].

Recent experimental progress at GSI in Germany, in the development of ion sources with the required performance (50 mA of extracted ions with $A/q \approx 100$ and a normalized emittance of $\lesssim 2 \cdot 10^{-7}$ m-rad), has been incorporated in the design. Progress has also been achieved at GSI in the design of the low-velocity accelerating structures. This includes the RFQ structure (developed jointly with the University of Frankfurt) and a Wideröe-based funneling scheme to feed the current of a total of eight ion sources into the main Alvarez accelerator.

Less design effort has been dedicated to the storage rings, where a number of topics will have to be the subject of future theoretical and experimental studies. The main distinction of these storage rings from machines designed and built so far stems from the high intensity and consequently, the dominant space charge effects. The following novel issues also appear important:

- stacking under conditions of large space charge,
- beam loss at septa, and
- longitudinal microwave instabilities with a space charge dominated coupling impedance.

A detailed study will also be needed to assess the performance and cost of final compression induction modules. Significant design work in this area has been done by the HIF group at Lawrence Berkeley Laboratory, and the modules suggested here are based on their design results.

In the framework of the HIBALL study, progress has been made also in the area of final transport and focusing. Control of emittance growth and space charge effects has been achieved and the consistency of the vacuum propagation mode with cavity conditions ($\sim 10^{-5}$ Torr of Pb reestablished after each shot) has been demonstrated.

I.2.2 Target Design

The target is the central element of the reactor system on which the heavy ion beams are focused and where the fusion energy is released. High gain targets (fusion energy/input beam energy = 50-100) are required for a Heavy Ion Beam ICF power reactor. The feasibility of such targets is inferred from theoretical analysis, but we are still far from actual experimental tests of such targets. For the time being, one has to rely on parameter models and numerical simulation.

The responsibility for HIBALL target design was designated to be at MPQ and KfK. Since the target activities at MPQ and KfK had started just recently and no detailed design was available at the beginning of the HIBALL study, a set of parameters was fixed at an early stage under the guidance of the UW group, relying on unclassified target design literature from the Lawrence Livermore National Laboratory. This set has served as a "frozen" basis for the driver design and the reactor cavity analysis. The objective for the target design work then was to check the general consistency of these parameters.

The chosen working point for the HIBALL target (input beam energy, 4.8 MJ, released fusion energy, 400 MJ, and gain, 83) was well justified by a simple parameter study with reasonable assumptions concerning hydrodynamic efficiency, convergence ratio, cold fuel isentrope, ignition pressure and burn rate. The work now in progress at KfK and MPQ will connect these parameters with the ion energy of the beam and maximum beam power as well as target geometry to allow for a general optimization. The physics of heavy ion stopping in hot dense plasma has been investigated, and actual ranges and deposition profiles have been calculated for a specific target configuration. As a first attempt, a cryogenic single shell design has been chosen, closely following a Livermore design for light-ion beam fusion. The objective was to study one-dimensional implosions of this target to obtain a general insight and to identify critical issues rather than to present an optimal design which, at the moment, is beyond the capabilities of the groups involved. The spectra of X-rays and ions emerging from the burning target as well as the target neutronics have been calculated by both of the groups at the UW and KfK and their effect on the cavity design has been analyzed.

I.3 Assumptions on Level of Technology and on Utilization of HIBALL

The level of technology that has been assumed for HIBALL is what we think will be typical of the year 2000-2020 period. This means that information developed over the next 20 years on accelerator design, superconducting magnets, liquid metal handling, radiation damage, and remote maintenance will be available. The target physics is assumed to have been established on a proof-of-principle device, the delivery of the target and repetitive operation of the system will have been demonstrated in an Engineering Test Facility, and the power handling, as well as indications of economic performance will have been established in a Demonstration Power Reactor. Since the HIBALL class of reactors is designed to operate perhaps in the 2020-2030 period, the size of the electrical grids will be larger than at the present time, thus allowing larger units to be integrated into the utility without fear of overdependence on a single reactor. (The largest Light Water Reactor units have at present a power output of 1300 MWe. There are several sites already now in Europe and the USA where 4-5 units with about 5 GWe total output will be operated at one site.)

Finally, we have chosen to examine the production of electricity first because we think that is where HIF reactor systems will have the most immediate impact. Other modes of operation, e.g., production of fissile fuel, synthetic fuels, or steam could also have been considered. At the present time, the relative economics of the various options are not readily apparent so there is no way to define the optimum form in which to derive energy from HIBALL. The large capital costs of a high energy accelerator driven reactor and the finite limits to waste heat disposal or electrical grid size, may require a combination of integrative (e.g., fissile or synthetic fuel

production) and real time (e.g., electricity or process steam) systems for optimum performance.

References for Chapter I

1. Proceedings of the Heavy Ion Fusion Workshop, Argonne, September 1978, ANL 79-41.

2. ERDA Summer of Heavy Ions for Inertial Fusion Final Report, December 1976, LBL-5543.

3. Proceedings of the Heavy Ion Fusion Workshop, Brookhaven, October 1977, BNL-50769.

4. Proceedings of the Heavy Ion Fusion Workshop, Berkeley, September 1980, LBL-10301.

II Overview and Recommendations

II.1 Overview of HIBALL

The main operating parameters of the HIBALL (Heavy Ion Beams and Lithium-Lead) reactor are given in Table II.1-1. A detailed list of operating parameters is included in Appendix A. We have chosen a DT fusion power of 8000 MW from a preliminary economic consideration of the number of reactor chambers to be served by a common heavy-ion driver. This power level results in a net electrical output of 3768 MW.

HIBALL utilizes 4 reactor chambers, each fired at a repetition rate of 5 Hz. The overall plant layout is shown in Fig. II.1-1. The beam ions are Bi^{+2} at 10 GeV and the total energy of each pulse is 4.8 MJ. This energy is delivered in a reactor chamber to the target by 20 beams with a maximum electrical current of 2.5 kA/beam. The 20 beams are propagated through the gas vapor atmosphere of a reaction chamber (Fig. II.1-2) which contains no more than 10^{11} atoms of Pb vapor per cm^3 before each shot. The targets are made from Pb and PbLi surrounding a cryogenic layer of deuterium and tritium (Fig. II.1-3). The 4.8 MJ pulse of Bi^{+2} ions is assumed to give a target gain of 83 and a total DT yield of about 400 MJ. With an accelerator efficiency of 26.7%, the fusion gain (driver efficiency x target gain) is 22. This results in a recirculating power fraction of 12.3% if we assume that all of the beam hits the target and we include the power requirements of the coolant circulation pumps, vacuum system, etc.

The first metallic wall, made of HT-9 ferritic steel, is 7 meters from the target (see Fig. II.1-2). It is protected from the target X-rays, ions, and neutrons by an array of porous SiC tubes through which $Pb_{83}Li_{17}$ is flowing. These tubes, called INPORT units, for the Inhibited Flow-Porous Tube Concept, occupy a region 2 meters in front of the first wall and are arranged

Table II.1-1 HIBALL Parameters

DT power level	8000 MW
Gross thermal power	10233 MW
Gross electrical output	4298 MWe
Net electrical output	3768 MWe
Accelerator type	RF-Linac
Accelerator efficiency	26.7%
Ion	Bi^{+2}
Ion energy	10 GeV
Beam energy	4.8 MJ
Beam power	240 TW
Total pulse rate	20 Hz
Base chamber pressure, torr at RT	10^{-5} (Pb vapor)
No. of ion beams per chamber	20
Electrical current per ion beam	2.5 kA
Target	Pb-PbLi-DT
Target yield	396 MJ
Target gain	83
Target shot rate per cavity	5 Hz
Fusion gain (ηG)	22
No. of cavities	4
Breeder and coolant	$Pb_{83}Li_{17}$
Tritium breeding ratio	1.25
Tritium inventory (active)	1 kg
Structural material	HT-9
Maximum coolant temperature	500°C
F. W. protection scheme	INPORT units ($SiC/Pb_{83}Li_{17}$)
Maximum dpa rate in HT-9 first wall	2.7/FPY
Lifetime of first wall	20 FPY
Lifetime of INPORT units	2 FPY

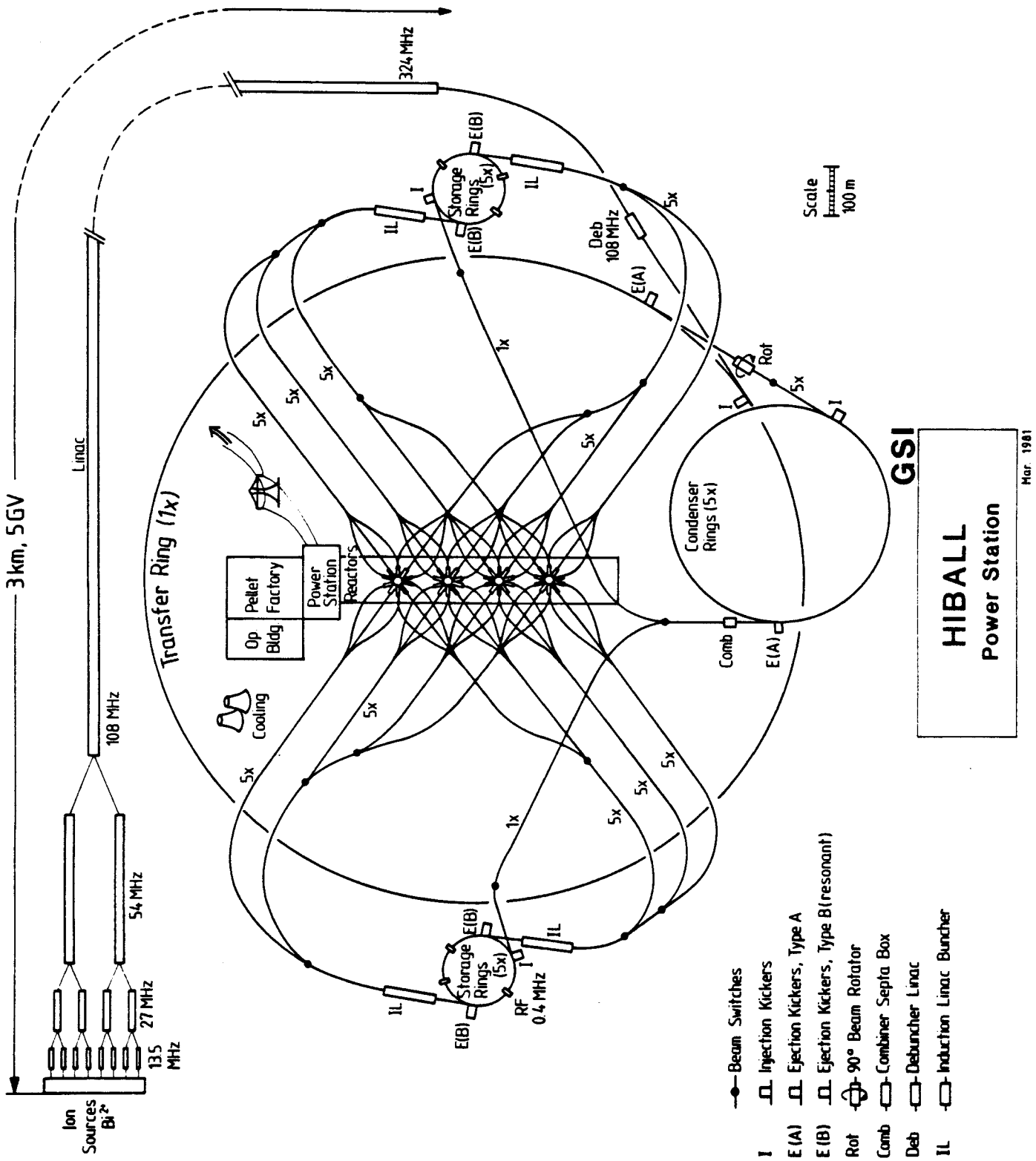
3 km, 5 GV
Linac
324 MHz
108 MHz
54 MHz
27 MHz
135 MHz
Ion Sources Bi2+
Transfer Ring (1x)
Op Bldg
Pellet Factory
Power Station Reactors
Cooling
Storage Rings (5x)
E(B)
IL
I
RF 0.4 MHz
Deb 108 MHz
E(A)
Rot
Comb
Condenser Rings (5x)
Scale 100 m
GSI
HIBALL
Power Station
Mar 1981
Beam Switches
Injection Kickers
Ejection Kickers, Type A
Ejection Kickers, Type B (resonant)
90° Beam Rotator
Combiner Septa Box
Debuncher Linac
Induction Linac Buncher

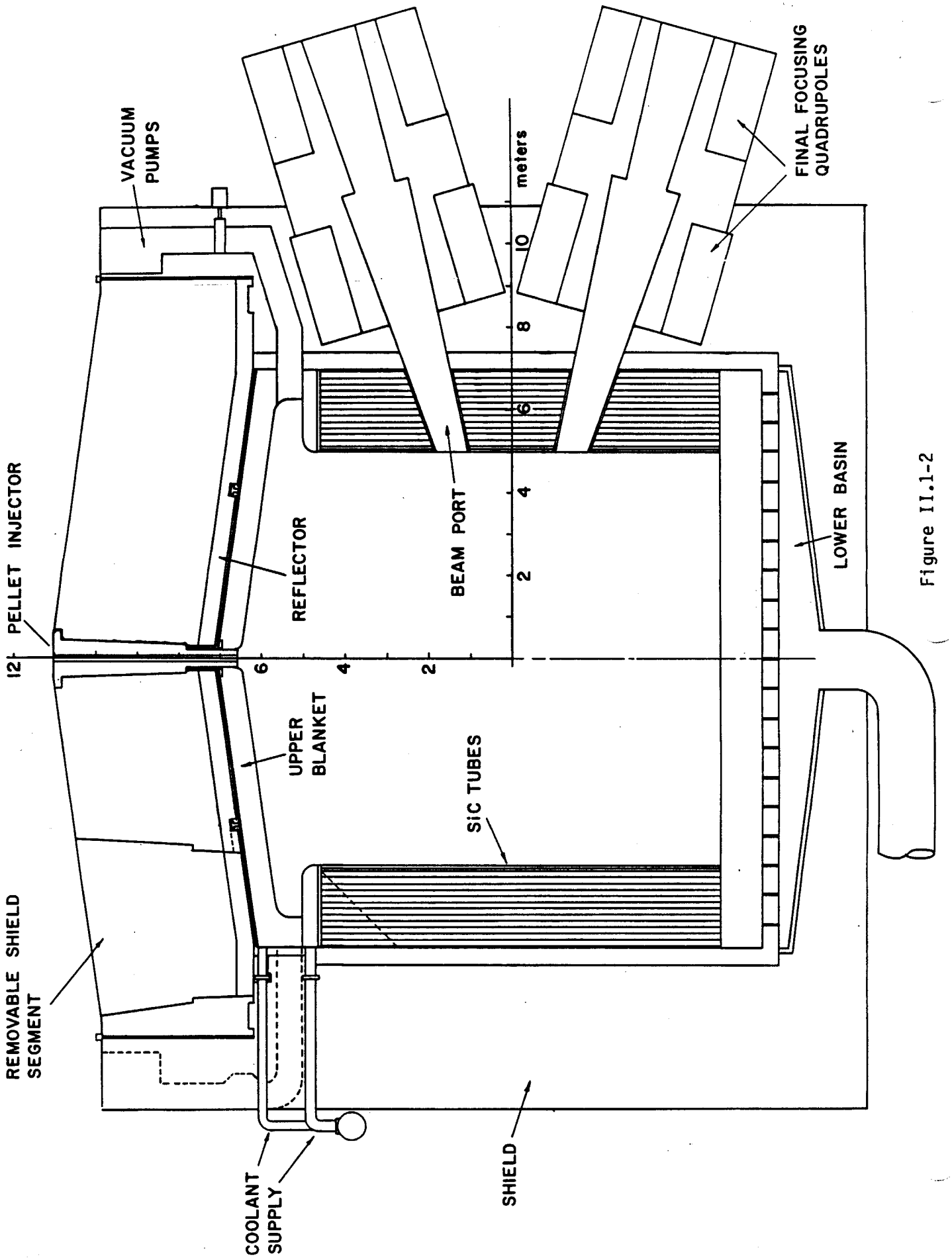
VACUUM PUMPS
FINAL FOCUSING QUADRUPOLES
meters
10
8
6
4
2
PELLET INJECTOR
12
6
4
2
REFLECTOR
BEAM PORT
LOWER BASIN
UPPER BLANKET
SiC TUBES
REMOVABLE SHIELD SEGMENT
COOLANT SUPPLY
SHIELD

Figure II.1-2

Figure II.1-3

Perspective view of the HIBALL pellet.

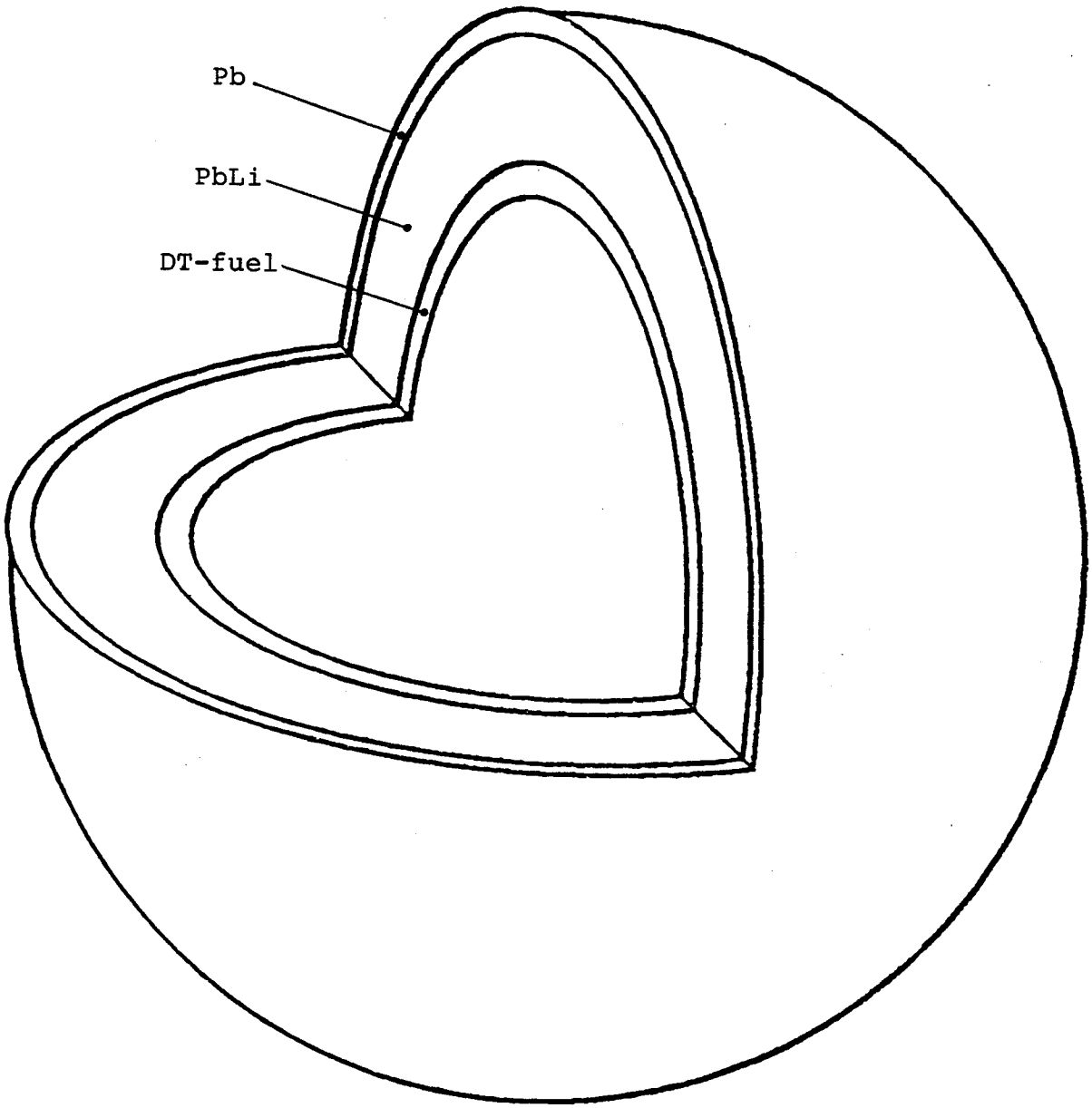

Figure II.1-4

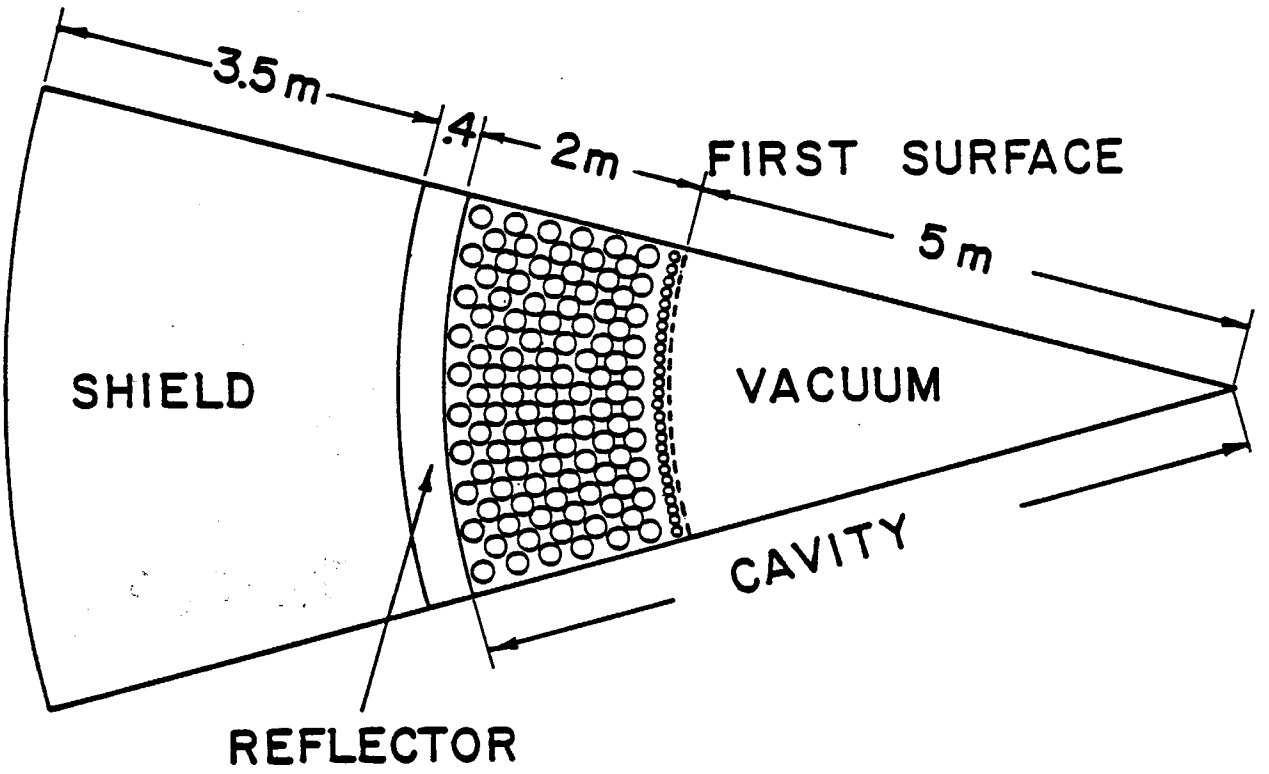

with a 33% volume fraction (Fig. II.1-4). The SiC INPORT tubes are protected from the short range X-rays and ion debris by a thin coating of $Pb_{83}Li_{17}$ flowing through the porous tube wall. This coating is partially vaporized on each shot and recondenses on the tubes in the 200 ms between shots. The maximum coolant temperature is 500°C insuring that the Pb pressure in the cavity is less than 10^{-5} torr (normalized to 0°C). The tritium breeding ratio is 1.25 and the low solubility of tritium in $Pb_{83}Li_{17}$ results in less than 100 grams of inventory in the blanket and fuel processing system. The low solubility also allows all tritium extraction to be done in the cavity itself. Hence, the bred tritium is removed through the vacuum system along with the unburned tritium from the target.

The effective 66 cm thickness of the INPORT blanket, composed of 98% $Pb_{83}Li_{17}$ and 2% SiC, reduces the radiation damage in the first structural wall to 2.7 dpa per full power year (FPY) meaning that damage equivalent to 5 MW-y/m^2 will be accumulated over 30 calendar years. Since the fusion materials community hopes to develop steels which will last more than 10 MW-y/m^2 under those conditions, we fully expect the steel chamber to last the life of the plant.

The preliminary economic analysis of HIBALL reveals that the capital cost (in 1981 dollars) is $1795 per KWe and the busbar cost of electricity is 41 mills per kWh. Such numbers are very competitive with previous tokamaks and tandem mirror reactor studies and therefore give us a good reason to pursue the HIBALL concept to an even greater level of detail.

II.2 Areas of Further Improvement

As mentioned previously, the first phase of the HIBALL design study has already pointed out several areas where more work needs to be done. The present self-consistent point design, with 10 GeV Bi^{2+} ions, should be extended to accelerator scenarios where the heavy ions have either lower (5 GeV) or higher energy (20 GeV). This will directly affect the accelerator design, the number of beam lines, the pulse energy on target as well as the target size and design. Only a parametric analysis including cost considerations can lead to an optimum set of design characteristics. The present pulse repetition rate of the HIBALL-I driver should be raised from 20 Hz to 30 Hz in order to support more reactor chambers and thereby decrease the capital costs. The induction linac section envisaged for the final fast bunch compression must be considered in more detail. The present focal spot of the Bi^{2+} beams at the center of the cavity is not consistent with the target diameter, so that an unacceptably large fraction of the ions miss the target. Additional studies are required to increase the target size but at the same time the beam focussing must be improved to yield a smaller spot. Also, from the target physics point of view, it is highly desirable to use a shaped pulse. The realization of this by superimposing pulses from different beam lines has to be investigated in detail. More refined calculations are also necessary to determine the debris and the photon spectra from the burning target. All parameters used in the current parameter list are scaled up from a 1 mg target design. Once a credible 400 MJ target is designed, it should be used to generate the target output characteristics.

In the area of reactor chamber design the last mentioned discrepancies directly affect the vaporization and condensation processes of the PbLi film at the surface of the SiC woven INPORT blanket tubes. More detailed beam

transmission calculations in Pb vapor are still needed. The solubility of tritium in PbLi must be experimentally substantiated, the tritium inventory in the target facilities should be decreased, and the tritium permeation through the barriers of the primary heat exchangers must be analyzed in more detail. Material problems like the compatibility of SiC with PbLi, the strength and fatigue lifetime of the woven tubes must be further considered. In addition, further analysis of the PbLi heat transport system, the secondary coolant systems, and the vacuum system for the reactor chamber is necessary. A more detailed assessment of costs and the design of reactor buildings with beam lines will be needed.

Finally, some areas could not be addressed at all in the first phase of the work. Among these are the assembly process of the targets and the target manufacturing costs, the reliability of the driver system and its impact on plant performance, as well as safety and environmental questions. All or most of these improvements and extensions of the present study are scheduled for HIBALL-II.

In addition to the above items, we also should investigate applications other than electricity generation for HIBALL. For example, we might investigate the use of HIBALL to produce:

1.) fissile fuel

2.) synthetic fuel

3.) process steam

Another area of interest could be the use of HIBALL to support "captive" industries, such as Al producers, which could accommodate interruptable power easier than the general public. The trade-off in economics and flexibility between using different chambers to provide energy in different forms should also be examined. For example, one scenario might be as follows:

Chamber 1 - Support captive Al plant with 800 MWe.

Chamber 2 - Provide ~ 10 tonnes ^{239}Pu per full power year.

Chamber 3 - Generate ~ 200,000 tonnes of H_2 per FPY.

Chamber 4 - Provide ~ 4×10^6 tonnes of steam at 500°C per FPY.

It is possible that the tritium breeding ratio (TBR) could be maximized or minimized in each chamber to optimize production of the end product. One could reduce the TBR in the hybrid chamber while maximizing it in the process steam chamber through the use of enriched Li for instance.

We have not determined how small the HIBALL reactor could be and still be "competitive". Such an analysis could be done in the future with the HIBALL configuration.

Finally we have investigated the RF linac driver in HIBALL but it would be interesting to see what effect an induction linac may have on the overall cost of the system. The rest of the plant could be held constant for this study.

It is clear that much work has been done, but there is much more work to do. The large size of the heavy ion beam system should be turned to an advantage through flexibility and integration into "energy park" scenarios. We have only scratched the surface of the possibilities for heavy ion fusion reactors.

III Target Design

Fusion reactor conceptual designs depend in a fundamental way on the plasma physics models and assumptions used to estimate the fusion performance. In the case of inertial confinement fusion, the plasma physics is replaced by so-called target physics which includes: driver beam-target interaction, plasma hydrodynamics, high pressure equations of state, thermonuclear burn phenomena, fluid instabilities, design creativity, etc. In this chapter we describe the parameters chosen for the HIBALL design and supporting analysis that serves as a basis for our choices. Three different groups at MPQ, KfK, and UW have contributed to these studies and the results of each group's activities are reported in different subsections of this chapter, following the discussion of the HIBALL target parameters.

This organization of Chapter III is necessitated by the chronological difficulties that we met in determining target parameters for HIBALL. A set of target parameters was required early in the study to serve as the basis for much of the reactor analysis (source neutron spectrum, X-ray and ion spectra and yields, target materials, DT fractional burnup, etc.). However, during the HIBALL study the target analysis groups at MPQ and KfK were in a developmental stage where their main emphasis was on computer code development and physical understanding of the target phenomena. Actual target design activities were premature. To solve this problem the UW group made a "best-guess" at reasonable target parameters and these were used for the HIBALL reactor analysis. Subsequent analysis by the MPQ and KfK groups showed that this crude estimate was not totally correct in detail. However, there is nothing fundamentally in error.

The independent target design contributions of the MPQ and KfK groups are reported in sections III.2 and III.3, respectively. These represent

preliminary attempts at target designs that meet the HIBALL requirements. Because this is an iterative process (and we have not yet iterated once) there are inconsistencies between the target designs reported here and the fixed set of target parameters used in HIBALL. At this early stage of target design activity, these inconsistencies are unavoidable. In the future we hope to perform the iteration between target design and driver and cavity requirements to provide a fully consistent picture of HIBALL.

III.1 Set of Target Parameters for HIBALL

The main target parameters used for the HIBALL study are given in Table III.1-1. The yield from the DT fuel is 400 MJ but the net target yield is only 396 MJ when endoergic neutron reactions are taken into account. This subtlety will be discussed later. The absorbed ion energy of 4.8 MJ therefore gives a gain of 83. This value of target gain is within the "conservative" band of the Livermore gain curves shown in Fig. III.1-1. Analysis in section III.2 shows that this gain is also consistent with the work of Bodner.[1] Details of the target design are an adaptation of a light ion beam target design reported by Bangerter[2,3] and Meeker. Some explanation of these adaptations is necessary.

No heavy ion beam target designs for reactor applications have been reported in the journal literature. Furthermore, we were not prepared to undertake a detailed target design activity during this initial HIBALL study. Consequently, we elected to use the closest available substitute target design that was available in the open literature. This was the so-called "Bangerter" design shown in Fig. III.1-2. This is a single shell design consisting of three material layers: DT fuel levitated at an aspect ratio of 10, a low density high-Z impregnated plastic (TaCOH) to serve as an ablator-pusher, and a high-Z lead layer to act as an inertial tamper. This target requires 1.3 MJ of 6.5 MeV protons in a pulse shape shown in Fig. III.1-3. The very pronounced Bragg peak in the ion range energy curve, Fig. III.1-4, is used to great advantage in this design. The protons preferentially deposit their energy in the TaCOH ablator-pusher rather than in the lead tamper. This leads to a very efficient implosion. The gain of this target is 88 giving a yield of 113 MJ.

Table III.1-1 Target Parameters for HIBALL

DT yield	400 MJ
Target yield	396 MJ
Target energy multiplication	0.99
Ion beam energy	4.8 MJ
Ion beam power	240 TW
Ion energy	10 GeV
Ion type	Bi^{+2}
Target gain	83
Target diameter	0.6 cm
Configuration (# of shells, # of layers)	1 shell, 3 layers
Composition	
D	1.6 mg
T	2.4 mg
Pb_5Li_{95}	67.1 mg
Pb	288. mg
Total target mass	359. mg
Fuel R at ignition	2 g/cm^2
Pusher R at ignition	1 g/cm^2
Fractional DT burnup	29%
Neutron yield	284.8 MJ
Average neutron energy	11.98 MeV
Neutron multiplication	1.046
Gamma yield	0.6 MJ
Average gamma energy	1.53 MeV
X-ray yield	89.5 MJ
X-ray spectrum (equivalent blackbody)	1 keV
Debris yield	21.0 MJ
Debris spectrum	0.85 keV/amu
Radioactivity production	1.2×10^6 Curies at t = 0

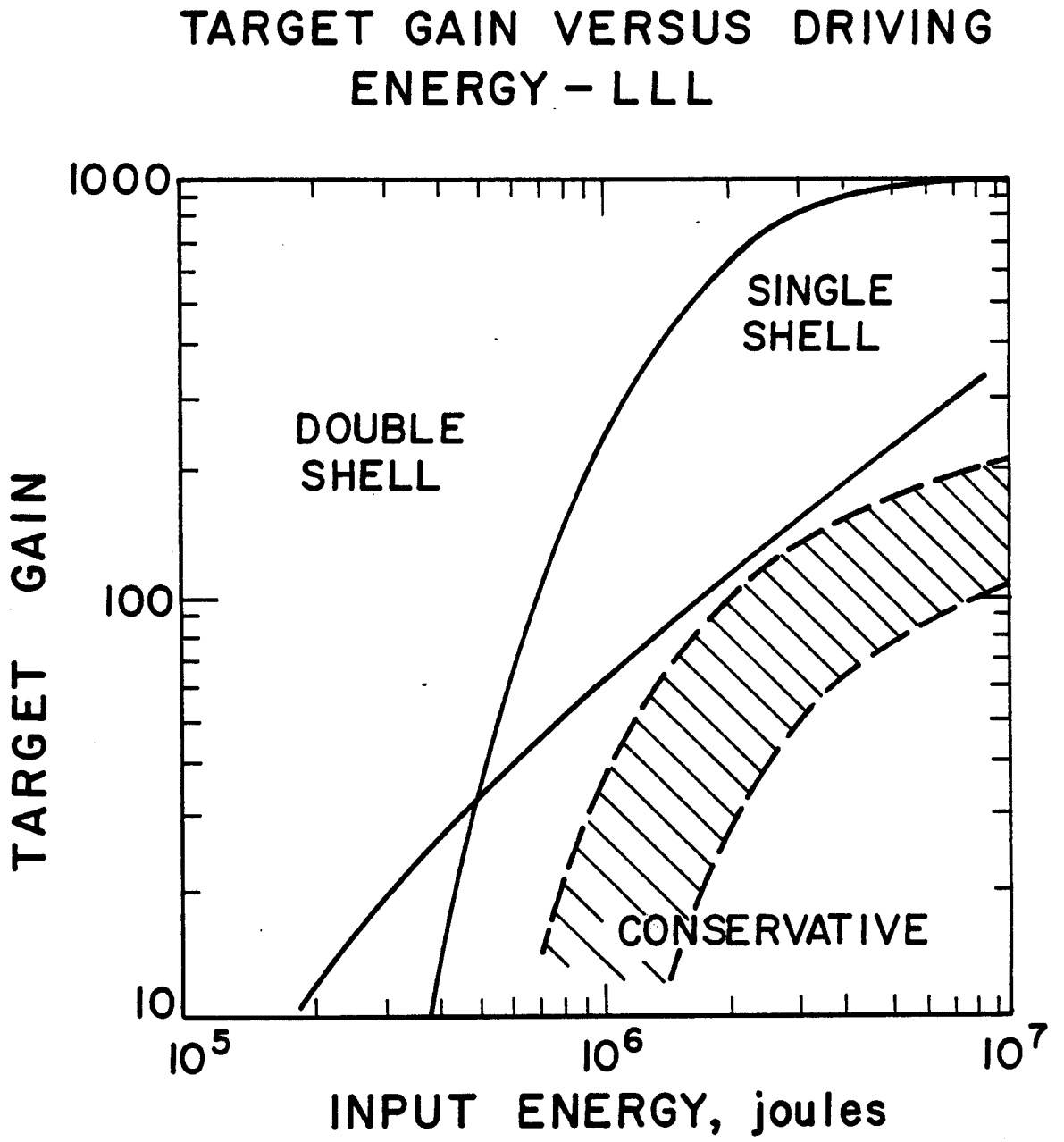
TARGET GAIN VERSUS DRIVING ENERGY - LLL
1000
100
10
TARGET GAIN
SINGLE SHELL
DOUBLE SHELL
CONSERVATIVE
10^5
10^6
10^7
INPUT ENERGY, joules

Fig. III.1-1

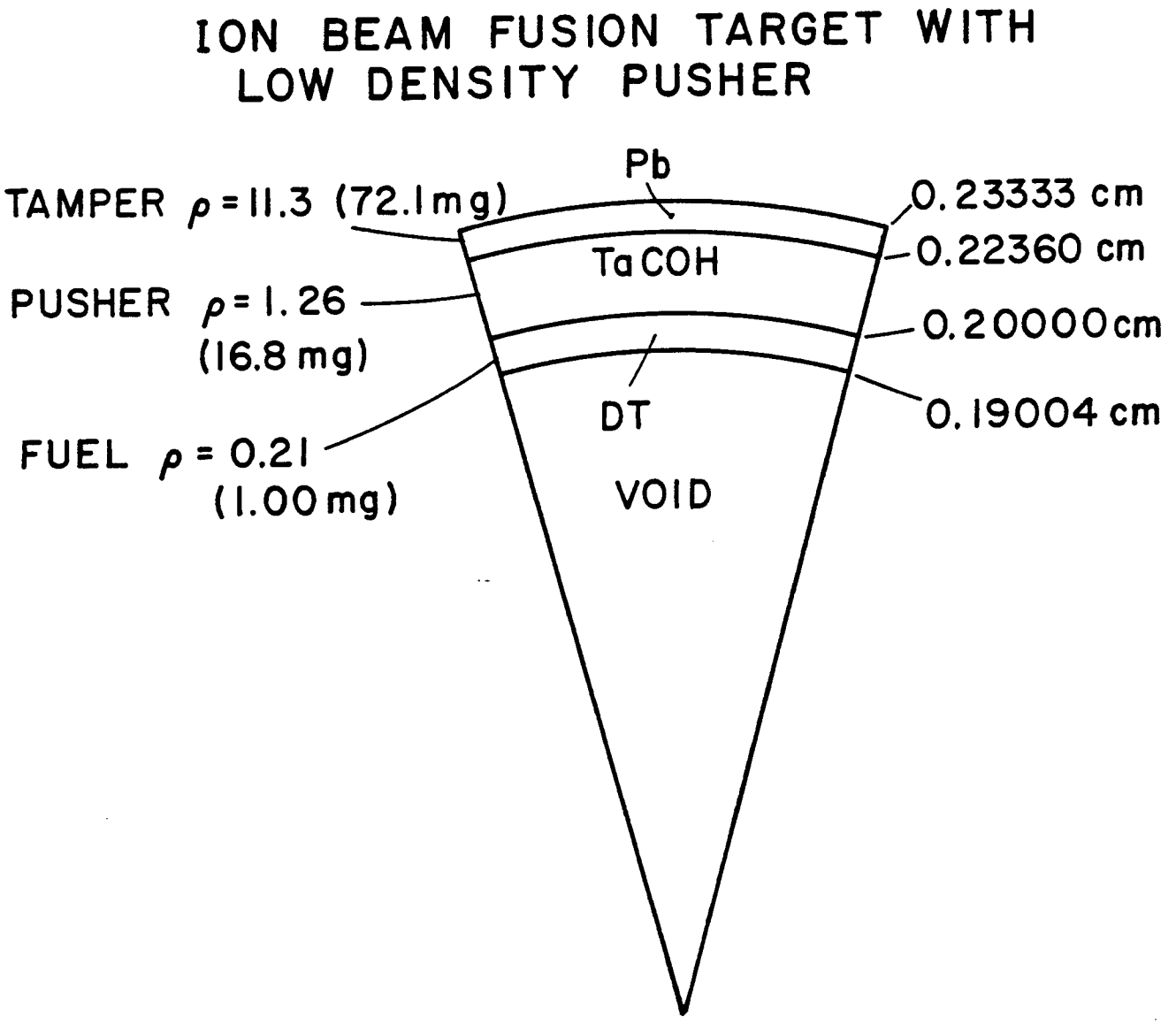
ION BEAM FUSION TARGET WITH
LOW DENSITY PUSHER
TAMPER ρ = 11.3 (72.1 mg)
PUSHER ρ = 1.26
(16.8 mg)
FUEL ρ = 0.21
(1.00 mg)
Pb
Ta COH
DT
VOID
0.23333 cm
0.22360 cm
0.20000 cm
0.19004 cm

Fig. III.1-2

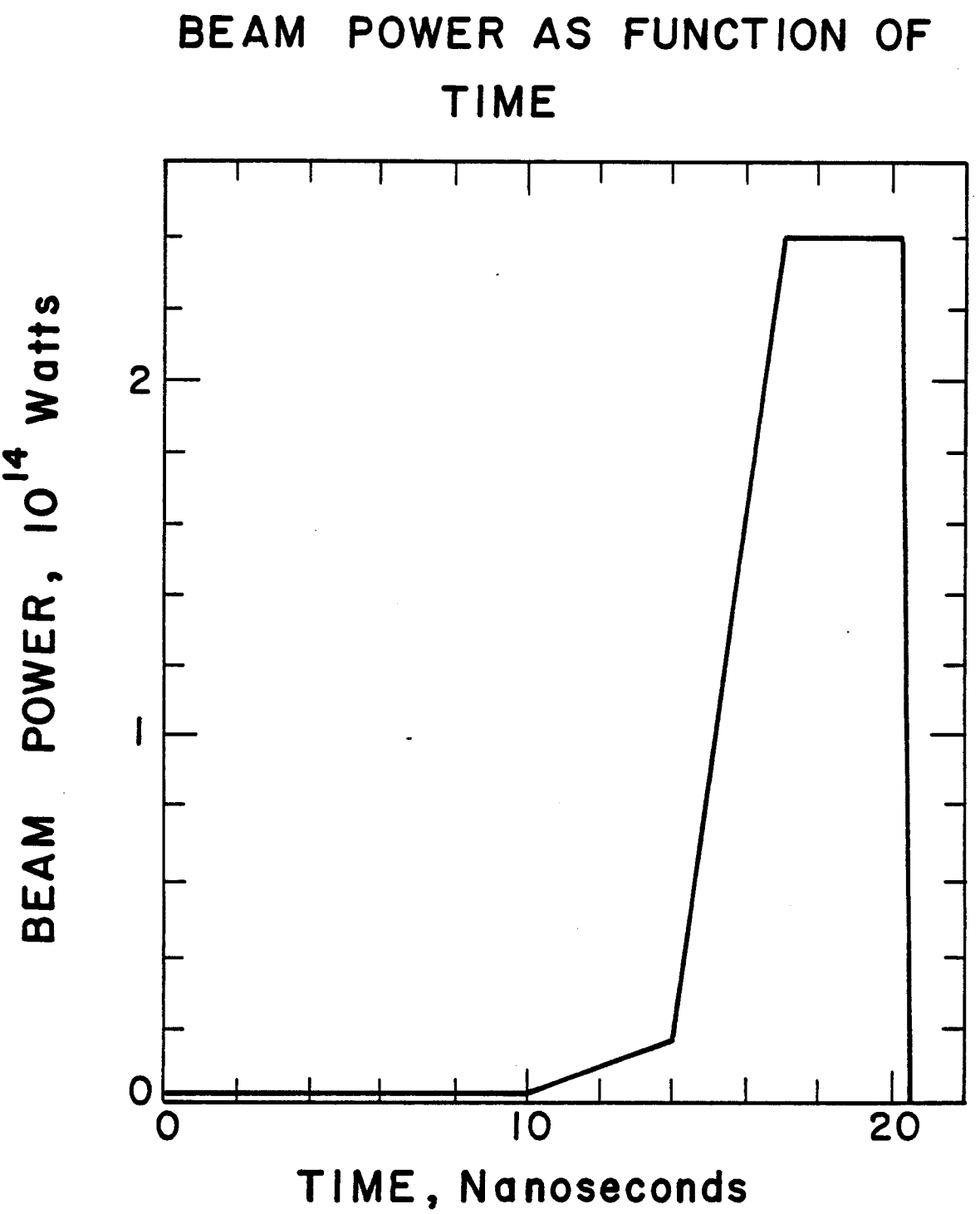
BEAM POWER AS FUNCTION OF TIME
BEAM POWER, 10^{14} Watts
2
1
0
0
10
20
TIME, Nanoseconds

Fig. III.1-3

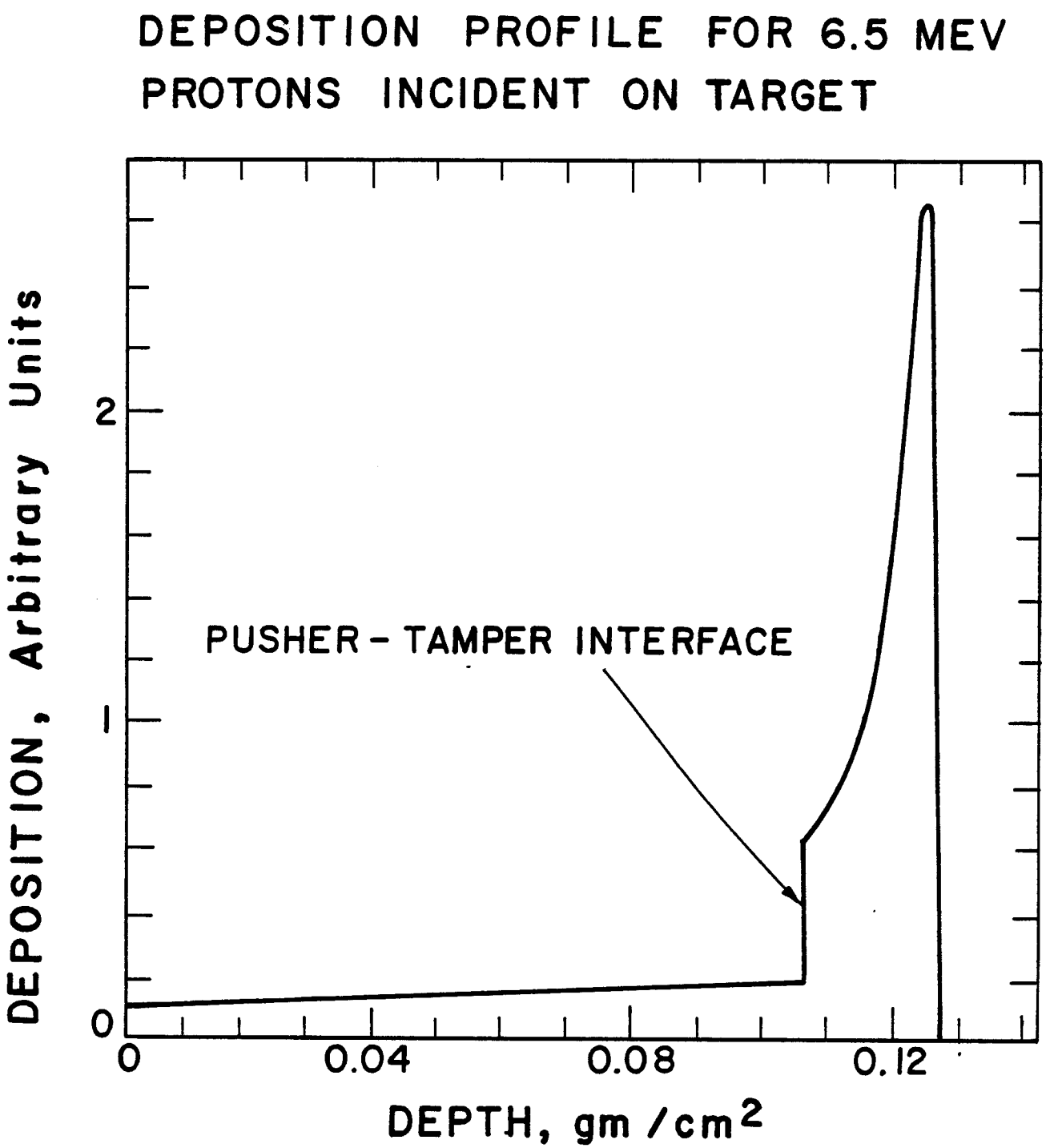
DEPOSITION PROFILE FOR 6.5 MEV PROTONS INCIDENT ON TARGET
DEPOSITION, Arbitrary Units
0
1
2
PUSHER - TAMPER INTERFACE
0
0.04
0.08
0.12
DEPTH, gm /cm2

Fig. III.1-4

This target design is modified in several ways for the HIBALL study. The TaCOH ablator-pusher is replaced with a Pb-Li mixture that gives the same mass density, 1.26 g/cm^3, as in the Bangerter design. This will not greatly perturb the implosion dynamics. It has a very beneficial effect on the target material recovery problem because now the target materials are the same as the PbLi coolant. Thus the materials separation problem is eliminated. The HIBALL target must produce a yield of 400 MJ, hence there must be more than the 1 mg of fuel used in the Bangerter design. This is straightforwardly solved by multiplying all target masses used in the Bangerter design by a factor of four. This allows us to do all of our calculations using the 1 mg target. Intrinsic quantities such as neutron, X-ray and ion spectra are assumed to be the same for the two targets while absolute quantities such as neutron, X-ray and ion yield are all scaled by a factor of four. This is admittedly a crude approximation. However, there are equally serious questions about the details of such a target design for heavy ions. For instance the heavy ions, with a flatter range-energy relation, will not deposit such a large amount of energy at the inner surface of the LiPb absorber. A total reoptimization of the design is required for applications to heavy ions. With all of these shortcomings we believe that this design will provide us with representative values for neutron, X-ray, and ion spectra and yields for heavy ion targets.

The target design used for the HIBALL analysis is shown in Fig. III.1-5 in both its initial configuration and its configuration at the time of ignition. This second configuration was not obtained from an implosion calculation but was derived from the gain reported by Bangerter and a previous knowledge of conditions required for ignition and propagating burn.[4] It is

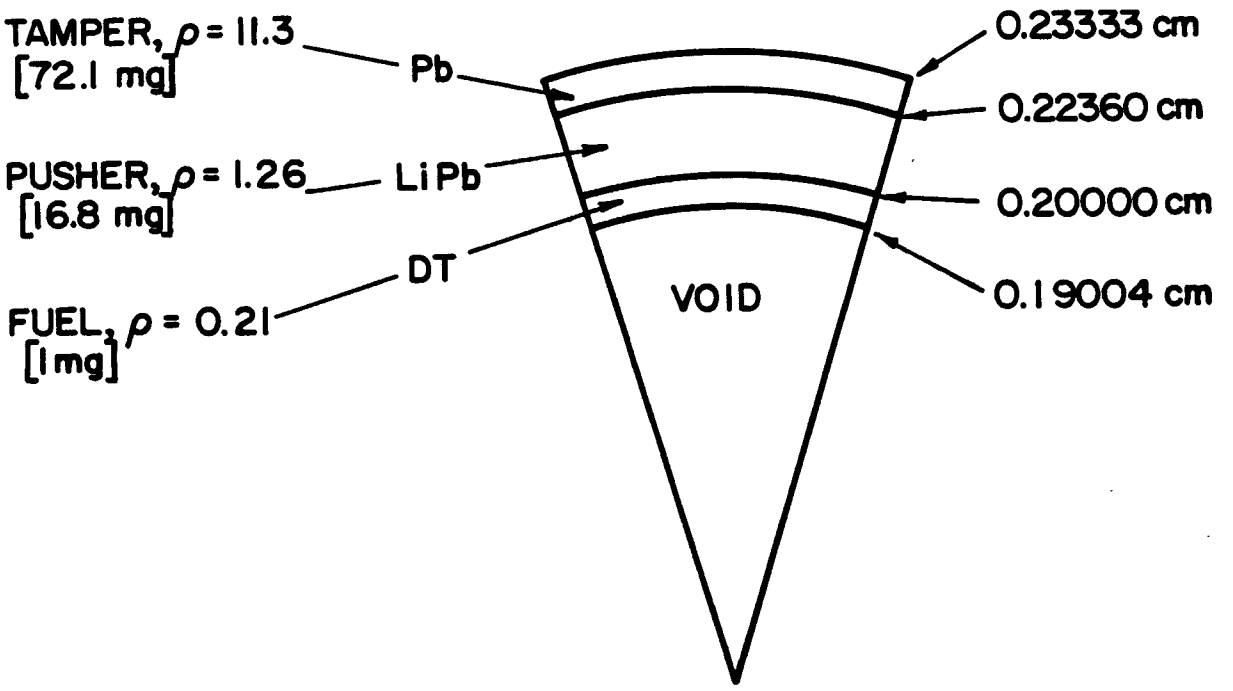

INITIAL TARGET STATE

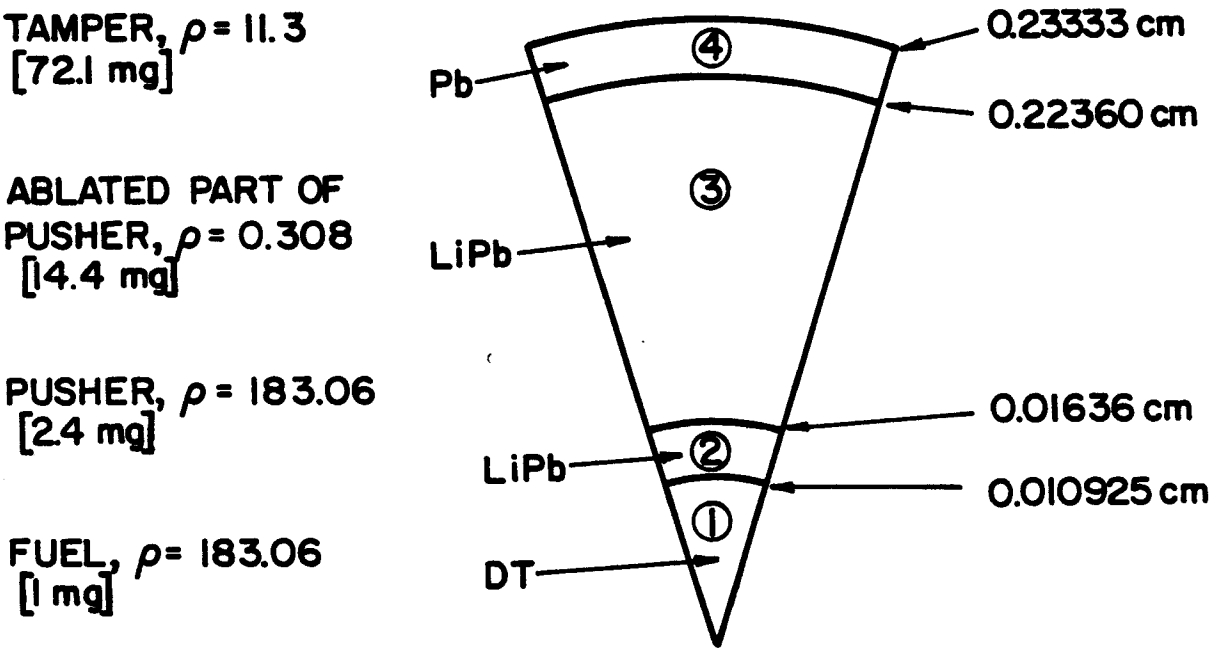

FINAL TARGET STATE

Fig. III.1-5

this target configuration that is used for calculating the neutron, X-ray, and ion spectra.

III.1.1 X-ray and Ion Spectra

The X-ray and ion spectra for the HIBALL target were computed with the PHD-IV hydrodynamics code.[5] The features of this code are given in Table III.1-2. The code was used to simulate the ignition, burn, and disassembly phases of the target dynamics. No attempt was made to simulate the implosion. (See section III.3 for a simulation of the implosion by the MEDUSA code at KfK.) The output X-ray spectrum was computed by collapsing the 33 group Los Alamos astrophysical multifrequency opacity data into 11 coarse groups. No multifrequency opacity data is available for either $Li_{95}Pb_5$ or Pb. In our calculations the $Li_{95}Pb_5$ equation of state and opacity properties were replaced with those of neon and the lead was replaced by iron. The justification for these substitutions is: (1) neon has the same electron number density as $Li_{95}Pb_5$ and (2) iron is the highest-Z material for which we have data. Approximations such as these are quite crude. However, the results of the calculations qualitatively demonstrate some phenomena that would be similar if the correct data were used. Furthermore, the partitioning of the energy between X-rays, ions, and neutrons is very likely to be most dependent on the masses and ρR values of the various materials and not on their specific properties. This is not true for the implosion calculations where such details are extremely important to the compression process. Figures III.1-6 and III.1-7 show the time integrated X-ray spectrum at 0.0312 ns and 3.51 ns following ignition. At 0.0312 ns the thermonuclear burn phase is already completed and the spectrum is characterized by a hard component ($h\nu > 30$ KeV) and a small thermal component. The hard component results from photons from the

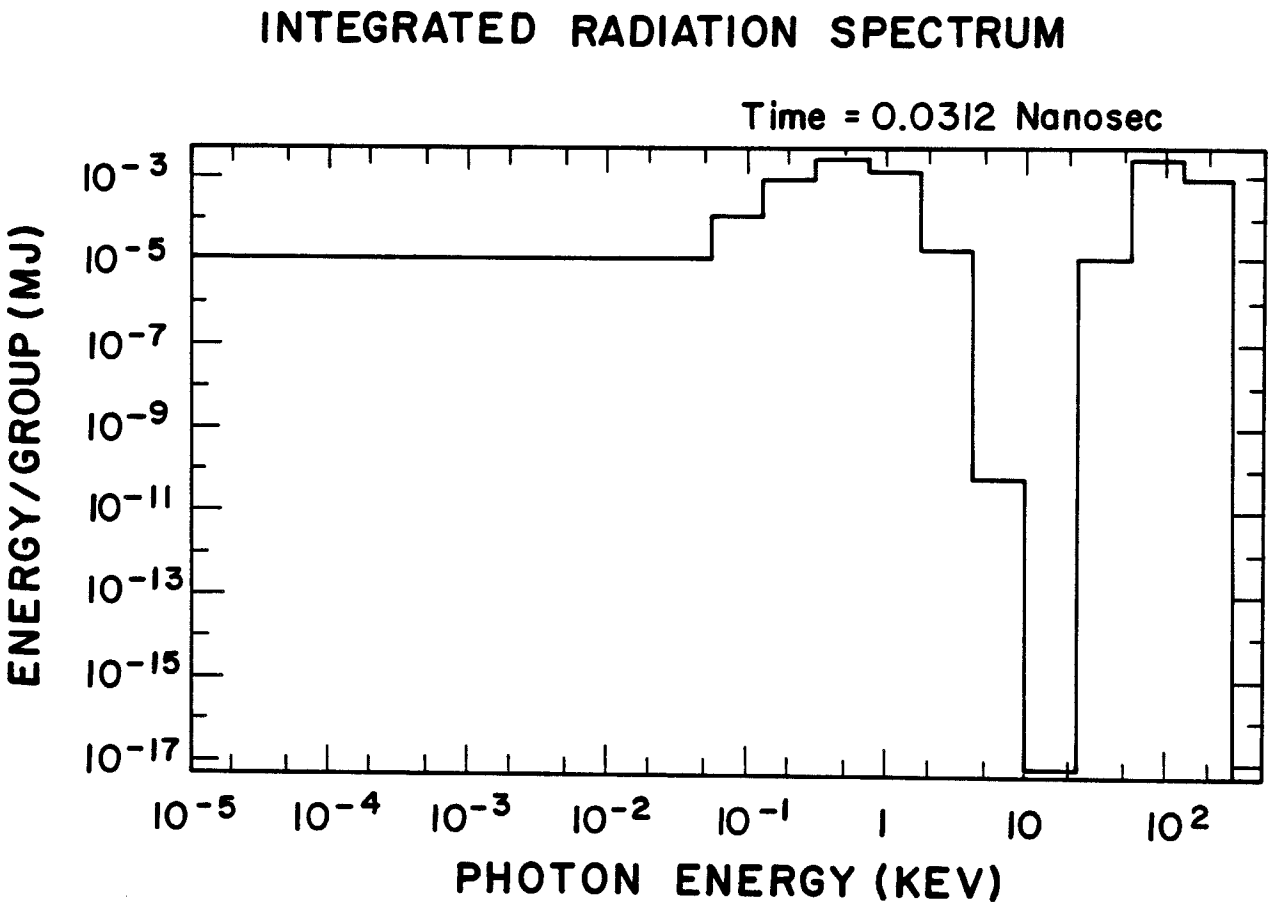
INTEGRATED RADIATION SPECTRUM
Time = 0.0312 Nanosec
ENERGY/GROUP (MJ)
10-3
10-5
10-7
10-9
10-11
10-13
10-15
10-17
10-5
10-4
10-3
10-2
10-1
1
10
102
PHOTON ENERGY (KEV)

Fig. III.1-6

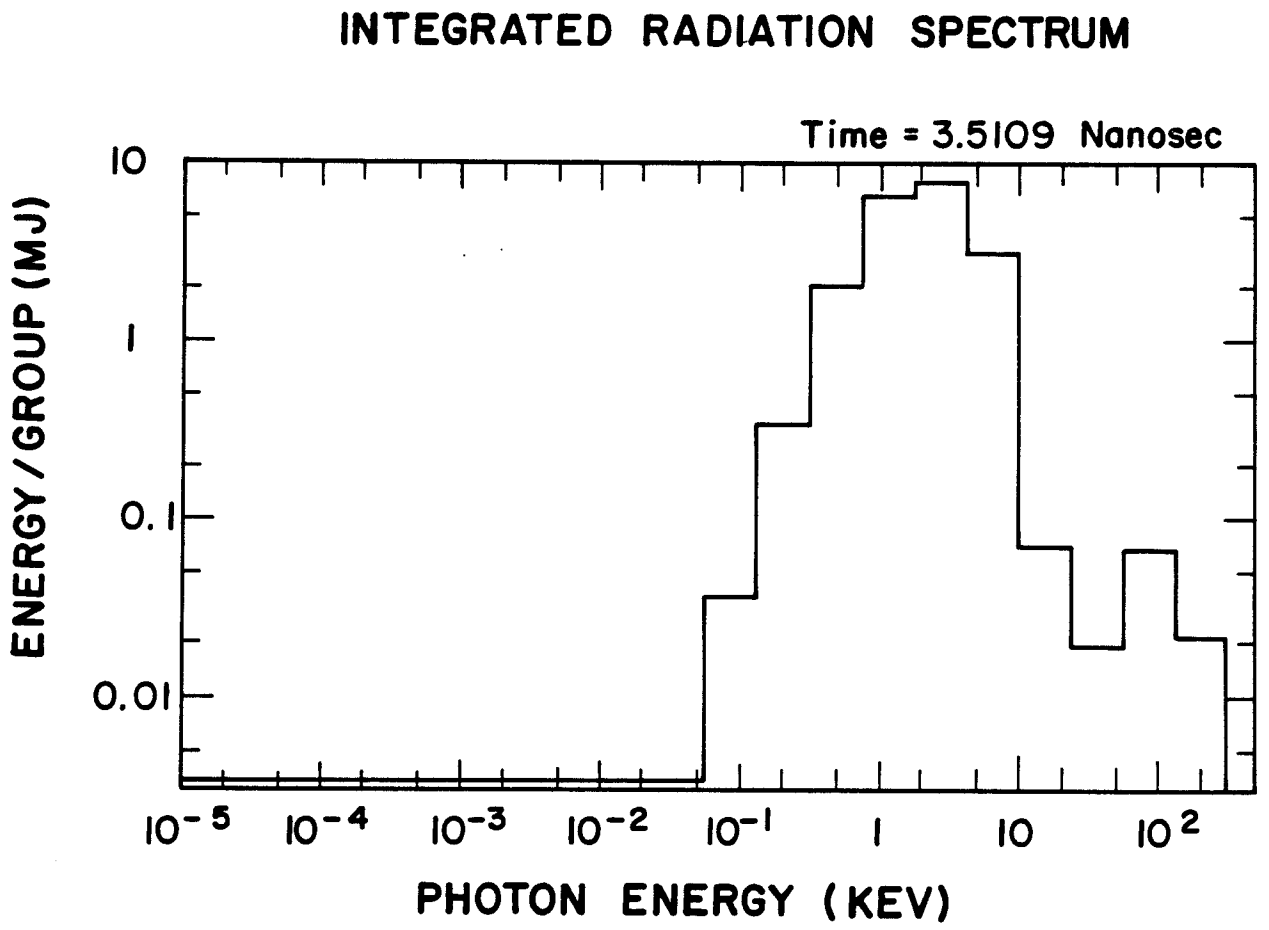
INTEGRATED RADIATION SPECTRUM
Time = 3.5109 Nanosec
ENERGY/GROUP (MJ)
10
1
0.1
0.01
10^{-5}
10^{-4}
10^{-3}
10^{-2}
10^{-1}
1
10
10^{2}
PHOTON ENERGY (KEV)

Fig. III.1-7

Table III.1-2 Major Characteristics of PHD-IV

One-dimensional (planar, cylindrical, spherical) Lagrangian coordinates.

One fluid equation-of-motion with pressure contributions from electrons, ions, radiation, and thermonuclear reaction products.

Two-temperature (electron and ion) energy flow with separate ion and flux limited electron thermal conduction, electron-ion energy exchange, PdV work, radiation emission and absorption coupling terms, and energy sources from ion beam absorption and thermonuclear energy redeposition.

Radiation transport using the multifrequency variable Eddington technique with tabulated opacities for materials of interest.

Thermonuclear reaction rate and species depletion equations for DT, DD, and DHe^3 reactions.

Transport and slowing down of charged-particle thermonuclear reaction products using the time-dependent particle tracking algorithm.

Tabulated SESAME equations-of-state for materials of interest.

Ion beam attenuation by classical slowing down theory.

Execution time of 3 ms/zone-cycle (UNIVAC 1110).

6000 card images (not including EOS data).

78,000 words of storage on UNIVAC 1110.

Written in FORTRAN IV to execute on any large computer.

burning DT fuel with energies above the K-edge of the surrounding high-Z material (8.5 keV for iron and 95 keV for lead). The "hole" in the spectrum is due to the strong absorption of photons with energies above the K-edge of the material. These absorbed X-rays and the alpha particle reaction products heat the target material to temperatures of about 1 keV. The bulk of the target then radiates at this temperature as shown in Fig. III.1-7. At 3.5 ns, the target has reached a quasi-steady state expansion phase. It is cold enough that it has essentially stopped emitting X-rays. At this point, the time

integrated spectrum shows a large thermal component with an effective blackbody shape of about 1 keV. The high frequency tail from the initial burning of the DT fuel is still apparent. The total frequency integrated emission is displayed in Fig. III.1-8 as a function of time. We see that most of the X-ray yield is released by 3.5 ns. The total X-ray yield in this calculation (4 times the computed yield) is 89.5 MJ or 22% of the overall target yield.

The ion spectrum is much more difficult to compute using our lagrangian hydrodynamics model. The ions are treated as a single fluid so no spectral information is available. To obtain the values shown in Table III.1-3 we divide the total kinetic plus thermal energy remaining in the disassembling target at 3.5 ns by the total number of atomic mass units, amu's, in the target. From this value of 0.85 keV/amu we compute the energies of individual ionic species. The ion yield is 21.0 MJ or 5.1% of the overall target yield.

Table III.1-3 Ion Spectra

Normalized Energy	0.85 keV/amu
D	1.70 keV
T	2.55 keV
He-4	3.40 keV
Li-natural	5.90 keV
Pb-natural	176.0 keV

The 14.1 MeV neutron interactions in the target account for the X-ray + ion yield fraction of 27% rather than the 20% coming from the DT fusion reaction. For the purposes of the X-ray and ion yield, as well as spectrum calculations,

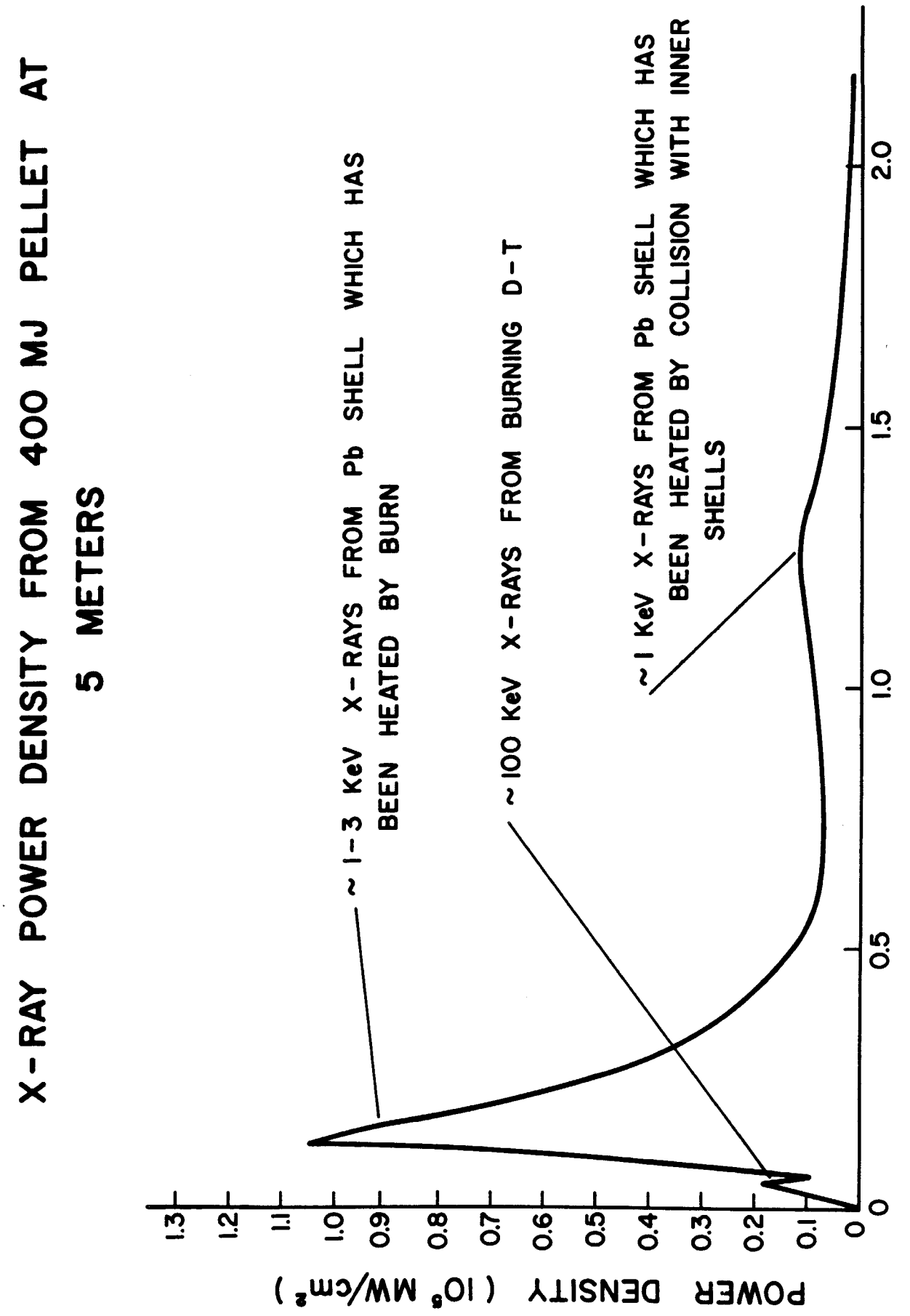
X-RAY POWER DENSITY FROM 400 MJ PELLET AT 5 METERS
~ 1-3 KeV X-RAYS FROM Pb SHELL WHICH HAS BEEN HEATED BY BURN
~ 100 KeV X-RAYS FROM BURNING D-T
~ 1 KeV X-RAYS FROM Pb SHELL WHICH HAS BEEN HEATED BY COLLISION WITH INNER SHELLS
POWER DENSITY (10^5 MW/cm^2)
TIME (nanoseconds)
0
0.1
0.2
0.3
0.4
0.5
0.6
0.7
0.8
0.9
1.0
1.1
1.2
1.3
0.5
1.0
1.5
2.0

Fig. III.1-8

we did not add this deposited neutron energy. Instead, we adjusted the X-ray and ion yields so that the overall energetics is treated consistently.

III.1.2 Target Neutronics and Photonics

Neutronics and photonics calculations are required to determine important fusion reactor parameters such as tritium breeding, nuclear heating, and radiation damage. No neutron-fuel interactions occur in the low density ($\sim 10^{14}/cm^3$) plasma of a magnetic confinement fusion reactor. In an inertial confinement fusion reactor, the DT fuel is heated and compressed to extremely high densities ($\sim 10^{25}/cm^3$) before it ignites. Therefore, neutron fuel interactions cannot be neglected. The spectrum of emerging neutrons is softened as a result of elastic and inelastic collisions with the target constituent materials. Neutron multiplication also occurs as a result of (n,2n) and (n,3n) reactions. This affects the performance of the blanket, first wall, reflector and shield. Neutron-fuel interactions produce gamma photons which contribute to nuclear heating in the blanket. A consistent neutronics and photonics analysis must, therefore, account for neutron target interactions. This is done by performing multigroup neutronics and photonics calculations within the target and coupling them to the blanket calculations.

The target used in the HIBALL fusion reactor design is shown in Fig. III.1-5. Neutronics and photonics calculations are performed within the target at ignition. The multi-group discrete ordinates code ANISN gives time integrated results. An isotropic source of 14.1 MeV neutrons is distributed uniformly in the DT fuel region. A coupled 25 neutron-21 gamma group cross section library is used throughout this work. The library consists of the RSIC DLC-41B/VITAMIN-C data library and the DLC-60/MACKLIB-IV response data library. The same calculations were performed using the ONETRAN finite

element code implemented at KfK. The results of the two calculations are compared later in this section.

Table III.1-4 lists the density data for the final target state used in this work. The target design used in the neutronics and photonics calculations utilizes 1 mg of DT fuel which produces an energy yield of 100 MJ per shot. Since a DT energy yield of 400 MJ is proposed for HIBALL, the results are scaled by a factor of 4. Assuming that the ρR values for the 100 MJ and 400 MJ targets are the same, the neutron and gamma spectra obtained for the 100 MJ yield case can be used for a yield of 400 MJ.

The calculated spectrum of neutrons escaping from the target, which represents the neutron source for the blanket calculations, is given in Fig. III.1-9. The large peak at 14.1 MeV is due to the uncollided flux of neutrons escaping the target. This amounts to 70.75% of neutrons leaking from the target. Local peaking of the flux at 2 and 4 MeV is caused by backward elastic scattering of 14.1 MeV neutrons with D and T, respectively. The lower energy range contains neutrons that have been elastically and inelastically scattered and those produced by (n,2n) and (n,3n) reactions. The average energy of emerging neutrons is 11.98 MeV. The results show that a target neutron multiplication of 1.046 is obtained. This results mainly from (n,2n) reactions in the dense DT fuel and LiPb pusher. The (n,2n) and (n,3n) reactions per fusion obtained using the ANISN and ONETRAN codes are given in Table III.1-5 for the different target regions. Very good agreement between the two codes is obtained.

The spectrum of gamma rays leaking from the target is given in Fig. III.1-10. The spectrum peaks around 0.6 MeV. The average energy of the gamma photons emerging from the target is 1.533 MeV.

Neutron interactions with Li in the target are found to produce 0.0146 tritium atoms per DT fusion reaction. Most of this tritium is produced in ^{7}Li because of the relatively hard spectrum of neutrons in the target. Tritium production in the target is very small compared to that in the blanket.

Table III.1-4 Target Data at Ignition

Region	Composition	Density [g/cm^3]	ρR [g/cm^2]	Atomic Density [atoms/b-cm]
1	D	183.06	2	22.225
	T			22.225
2	^{6}Li	183.06	1	0.4656
	^{7}Li			5.809
	Pb			0.32166
3	^{6}Li	0.308	0.0638	7.834×10^{-4}
	^{7}Li			9.774×10^{-3}
	Pb			5.412×10^{-4}
4	Pb	11.3	0.11	3.2831×10^{-2}

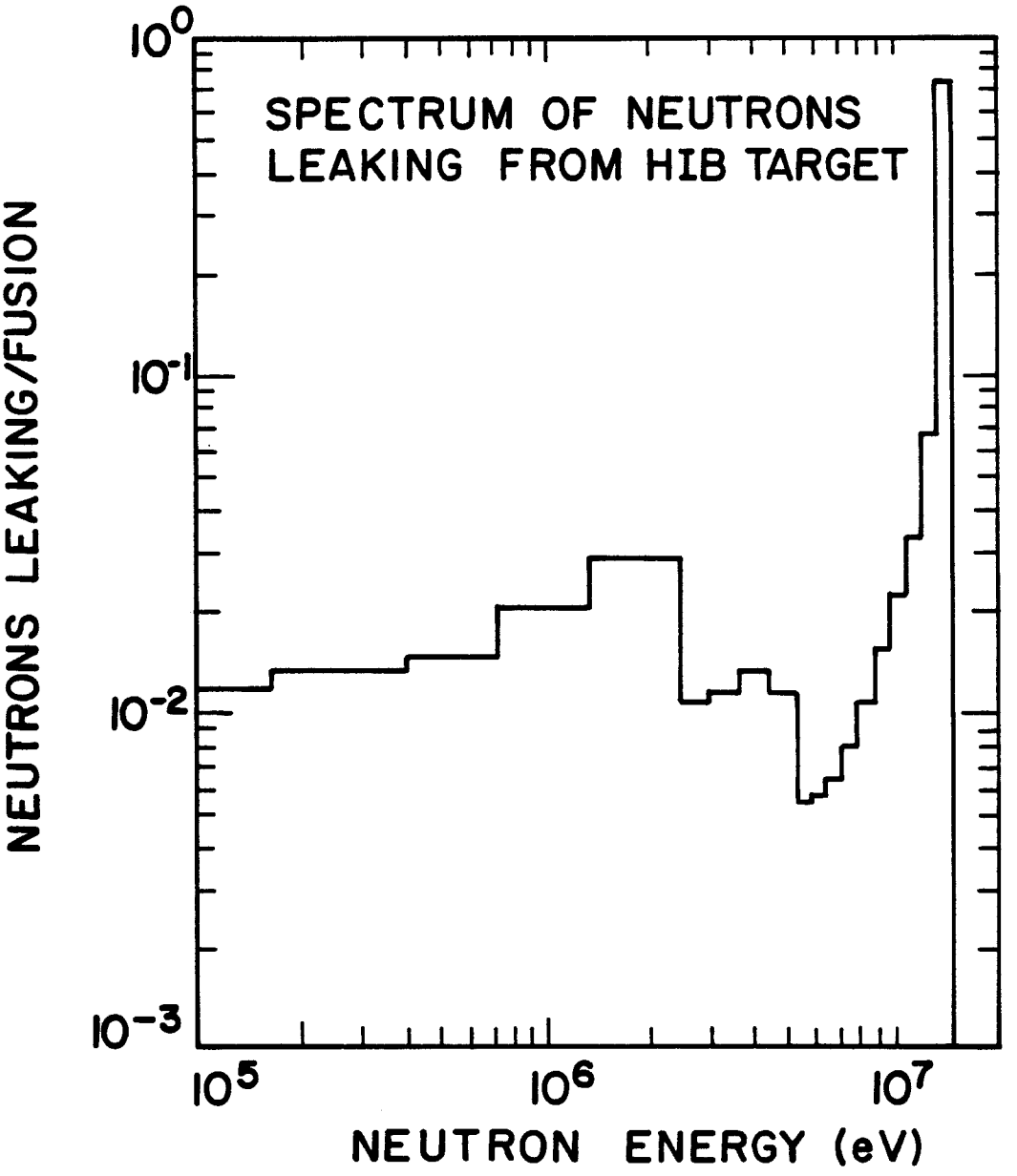
SPECTRUM OF NEUTRONS
LEAKING FROM HIB TARGET
NEUTRONS LEAKING/FUSION
10^0
10^-1
10^-2
10^-3
10^5
10^6
10^7
NEUTRON ENERGY (eV)

Fig. III.1-9

Table III.1-5

	Reactions/Fusion event 1 mg Target (ANISN)		Reactions/Fusion event 1 mg Target (ONETRAN)	
Region	(n,2n)	(n,3n)	(n,2n)	(n,3n)
1	4.0432×10^{-2}	0.0	3.9704×10^{-2}	0.0
2	5.0972×10^{-3}	5.6370×10^{-5}	4.8606×10^{-3}	5.3895×10^{-5}
3	3.6479×10^{-4}	4.0026×10^{-6}	2.5559×10^{-4}	2.8105×10^{-6}
4	6.336×10^{-4}	8.5960×10^{-6}	6.1183×10^{-4}	7.9566×10^{-6}
TOTAL	4.6658×10^{-2}	6.8969×10^{-5}	4.4532×10^{-2}	6.4662×10^{-5}
Neutrons leaking/ per source neutron	1.04589		1.04482	
Gammas leaking/ per source neutron	0.01752		0.01639	

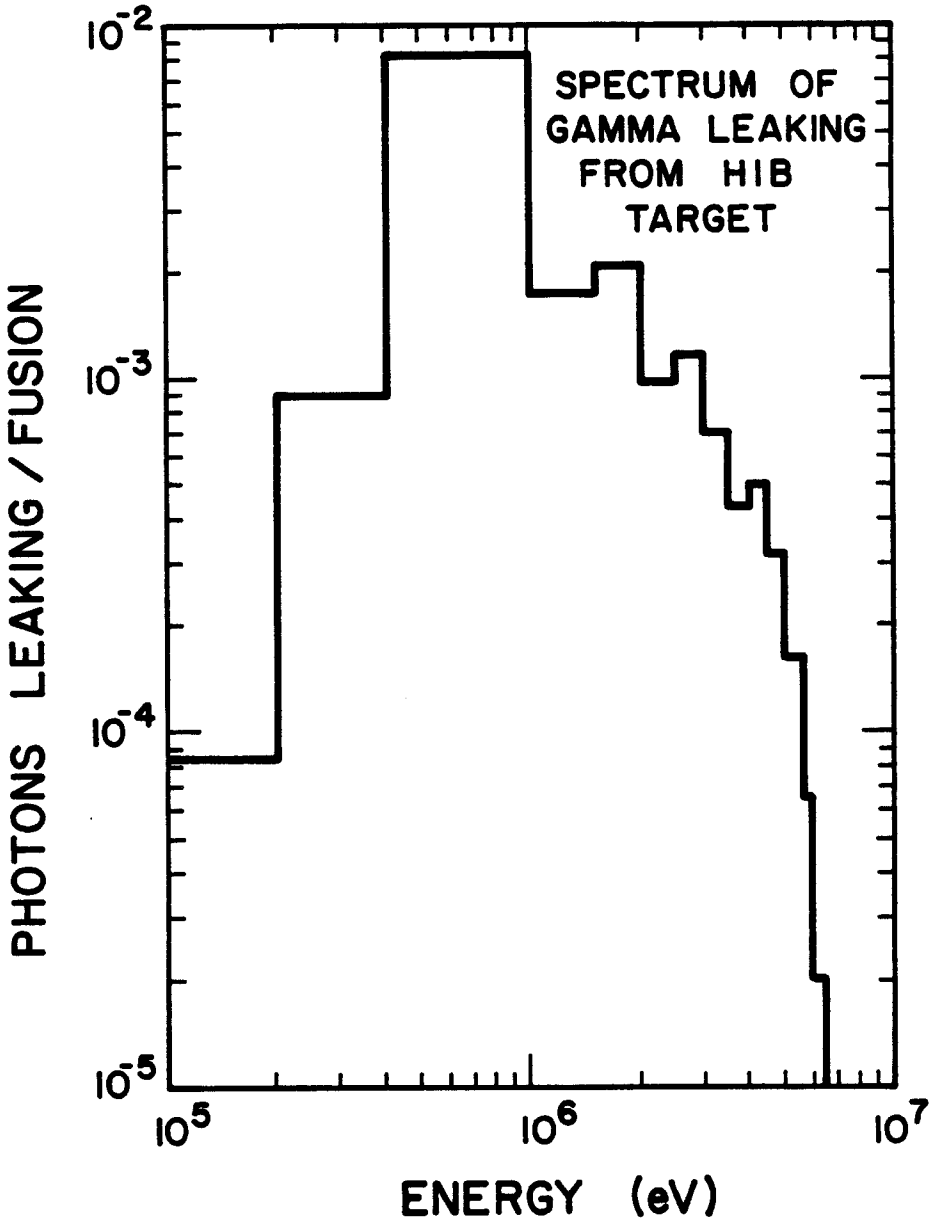
SPECTRUM OF
GAMMA LEAKING
FROM HIB
TARGET
PHOTONS LEAKING / FUSION
10^{-2}
10^{-3}
10^{-4}
10^{-5}
10^{5}
10^{6}
10^{7}
ENERGY (eV)

Fig. III.1-10

Neutron and gamma energy deposition in the target, blanket, first wall, and reflector are calculated using the neutron and gamma spectra and the appropriate kerma factors. Table III.1-6 gives neutron and gamma energy deposition in the different regions of the target. Most of this energy is deposited by neutrons in the DT fuel core. The energy deposited in the target by neutrons and gamma photons is 1.3615 MeV per fusion. When the 3.5 MeV energy carried by the alpha particle emerging from the fusion reaction is added, a total energy of 4.8615 MeV per fusion is found to be carried by X-rays and target debris following the target microexplosion. The energy carried by emerging neutrons is found to be 12.532 MeV per fusion or 71% of the total yield and the energy carried by gamma photons is found to be 0.027 MeV/fusion. The remaining energy of 0.278 MeV/fusion is lost in endoergic neutron reactions with the target materials.

III.1.3 Radioactivity in the Target

Induced radioactivity in the target can be very substantial, depending on the target materials. Radioactivity calculations were performed using the DKR code[7] developed at the University of Wisconsin. Results are displayed in Fig. III.1-11. The DKR code post processes ANISN fluxes to compute the initial activation and then follows the important decay chains to determine how the radioactivity changes with time.

The very high initial activity of 10^5 curies is due to $^{6}Li(n,p)^{6}He$ and $^{7}Li(n,\gamma)^{8}Li$ reactions. These products β-decay with half-lives of 800 ms. The very long term activity is due to ^{205}Pb with a 3×10^7 year half-life. The activity between these two extremes is mostly due to ^{205}Hg and ^{203}Pb with half-lives of 5.5 minutes and 52 hours.

This target radioactivity is a negligible part of the total coolant activity. The target materials are the same as the $Pb_{17}Li_{83}$ coolant that

Table III.1-6 Neutron and Gamma Energy Deposition in the Target

Region	Element	Neutron Heating [eV/fusion]	Gamma Heating [eV/fusion]
1	DT	1.168×10^{6}	0.0
2	^{6}Li	1.70129×10^{4}	2.07881×10
	^{7}Li	1.62950×10^{5}	2.5936×10^{2}
	Pb	6.1056×10^{2}	9.06526×10^{2}
	Region Total	1.805734×10^{5}	1.18667×10^{3}
3	^{6}Li	1.20695×10^{3}	1.26611×10^{0}
	^{7}Li	1.16287×10^{4}	1.57965×10
	Pb	4.35637×10	5.4128×10
	Region Total	1.2879214×10^{4}	71.19061
4	Pb	9.38872×10	1.53527×10^{2}
Total		1.3615×10^{6}	1.14114×10^{3}

protects the first wall, consequently no special separation and handling of the target materials is required in HIBALL.

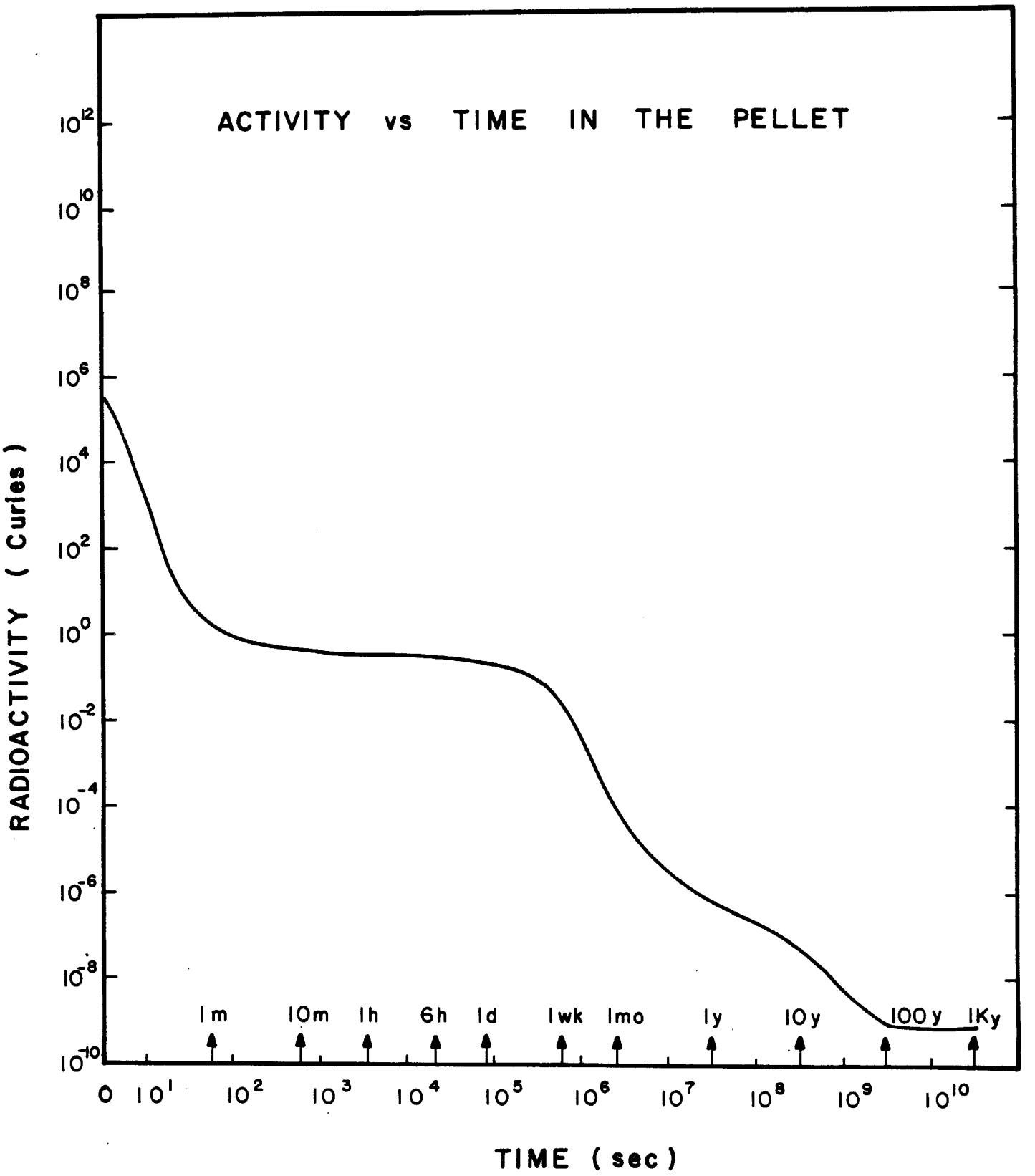
ACTIVITY vs TIME IN THE PELLET
RADIOACTIVITY (Curies)
TIME (sec)
1m
10m
1h
6h
1d
1wk
1mo
1y
10y
100y
1Ky

Fig. III.1-11

References for Section III.1

1. S.E. Bodner, "Critical Elements of High Gain Laser Fusion," NRL Memo Report 4453, Naval Research Laboratory, Washington, D.C., January 1981.

2. R.O. Bangerter, Laser Program Annual Report - 1976, Lawrence Livermore Laboratory Report UCRL-50021-76, June 1977, p. 4-44.

3. R.O. Bangerter and D. Meeker, "Ion Beam Inertial Fusion Target Designs," Lawrence Livermore Laboratory Report UCRL-78474 (1976).

4. G.A. Moses et al., "The SOLASE Conceptual LaserFusion Reactor Study," Proc. of the 3rd Top. Mtg. on the Tech. of Cont. Nuclear Fusion, Vol. 1, Santa Fe, NM, May 1978, p. 448.

5. G.A. Moses and G.R. Magelssen, "PHD-IV, A Plasma Hydrodynamics-Thermonuclear Burn-Radiative Transfer Computer Code," University of Wisconsin Fusion Engineering Program Report UWFDM-194 (unpublished).

6. W. Engles, "A Users Manual for ANISN," RSIC Code Package CCC-254, Radiation Shielding and Information Center, Oak Ridge National Laboratory, Oak Ridge, TN.

7. T.Y. Sung and W.F. Vogelsang, "DKR Radioactivity Calculation Code for Fusion Reactors," University of Wisconsin Fusion Engineering Program Report UWFDM-170 (Sept. 1976).

III. 2 Target Design at MPQ **

The work on target design presented in this chapter has been performed at the Max-Planck-Institut for Quantum Optics (MPQ) in Garching / FRG. It includes a parameter study for pellet gain, an investigation of heavy ion stopping in hot dense plasma and a detailed discussion of a typical heavy ion induced pellet implosion selecting a single-shell design. Strong emphasis has been put on the underlying physics, but all results are directly related to HIBALL and are used to check the "frozen" parameter list for consistency with actual HIF target behaviour. This work represents a first step and leaves important aspects untouched. The effect of irradiation asymmetry on target performance, consideration of double-shell and more complicated designs and optimization between beam and target parameters are some of these aspects. To a certain extent, they will be discussed in chapter III. 4 and in the final HIBALL report.

The parameter study is based on a modified version of the Kidder-Bodner model for pellet gain. The modification consists in a more realistic assumption about the fuel configuration at ignition than used by Kidder and Bodner. The model provides a physical interpretation of the Livermore "conservative" gain curves (see Fig. III.1-1) and reproduces the HIBALL working point (E_{Beam} = 4.8 MJ, Gain 83) with reasonable choices for hydrodynamic efficiency, cold fuel isentrope and fuel pressure at ignition. The theory of heavy ion stopping in hot dense plasma is outlined and used to calculate ranges and deposition profiles for 10 GeV Bi-ions in Pb, Li, and PbLi-alloy relevant for the HIBALL target. Finally, a 1D-implosion of the chosen

**Section III.2 is reproduced exactly as received from the authors, without any retyping or editing.

target configuration yields a detailed picture of the pellet dynamics. Special attention is given to the shock sequence leading to the ignition configuration and how it is related to the pulse shape. Also the growth of Rayleigh-Taylor instability at the absorber-pusher interface is estimated.

III.2.1 Modified Kidder-Bodner model for pellet gain

Pellet gain as a function of beam energy is one of the crucial relations for inertial confinement fusion. Although the dynamics of pellet implosion are very complex, the gain curve can be expressed in terms of a few physical parameters. This has recently been pointed out by S. Bodner.[1] The underlying model had been formulated before by R. Kidder [2]. The fuel configuration at ignition is assumed to consist of a central hot region (spark) surrounded by highly compressed fuel at low entropy as shown schematically in Fig. III.2-1. Ignition will occur in the centre, and burn then propagates into the cold fuel. Propagating burn is essential to achieve high gain. The question of how to achieve such an ignition configuration dynamically is addressed in section III.2.3.

As an important modification of the Kidder-Bodner model, we assume constant pressure p over the total (hot and cold) fuel region. Kidder and Bodner had assumed constant density implying a sharp pressure jump from the hot to the cold fuel region. However, typical implosion runs (see e.g. ref. 3 and section III.2.3) show that the ignition point with maximum fuel ρR and maximum central temperature T_s is generally reached only after the shock, emerging from the centre after shell collapse,

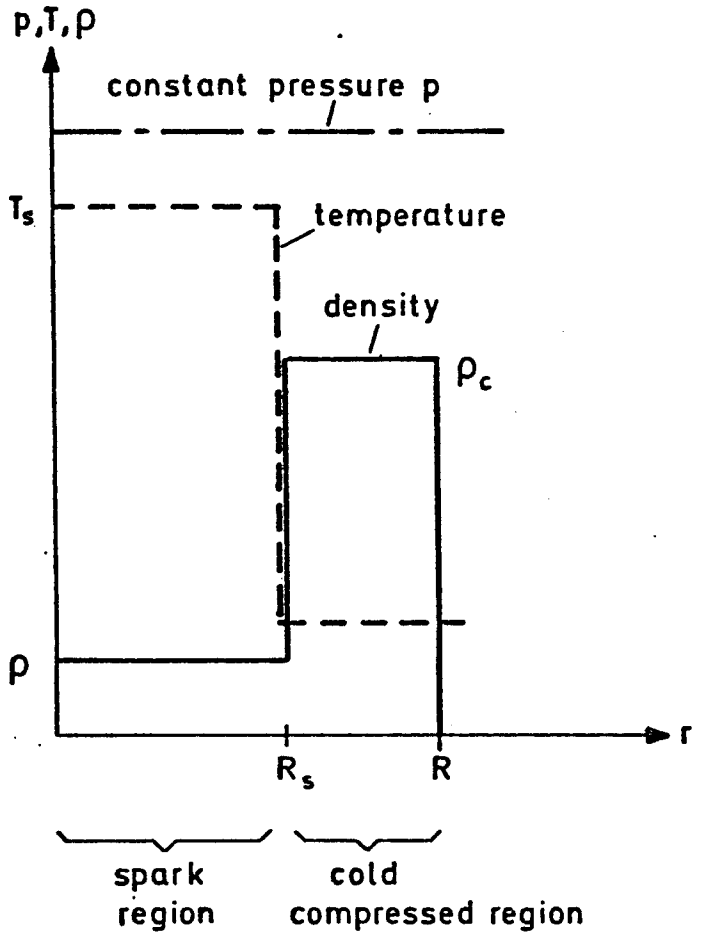

Fig. III.2-1: Profiles of pressure p, temperature T, and density for the schematic ignition configuration

has passed through fuel and pusher. At this time, almost all the inward going kinetic energy has been converted to internal energy, and the pressure is nearly constant over the fuel. This is the realistic ignition situation. Replacing constant density by constant pressure leads to less optimistic gain curves than those discussed by Bodner. This is because now more energy goes into the compressed fuel part.

The model is defined by the following equations. The spark region is described as an ideal gas. Taking as ignition conditions

$$kT_s \geq 5\,keV \tag{1a}$$

$$H_s = \varrho_s R_s \geq 0.4\,g/cm^2 \tag{1b}$$

one obtains for the density ϱ_s, the radius R_s, the mass M_s, and the internal energy E_s of the spark

$$\varrho_s = \frac{\mu_{DT}}{2kT_s} \cdot P \tag{2a}$$

$$R_s = H_s / \varrho_s \tag{2b}$$

$$M_s = \frac{4\pi}{3} R_s^3 \varrho_s \tag{2c}$$

$$E_s = 2 \cdot \frac{3}{2} kT_s \cdot \frac{M_s}{\mu_{DT}} \tag{2d}$$

Here, the atomic weight of DT $\mu_{DT} \cong 4 \times 10^{-24}$ g, and p is the overall pressure.

The highly compressed region is described as a degenerate electron gas with the pressure

$$p = \alpha \cdot \frac{2}{5} n_e \varepsilon_F = 2.34 \cdot 10^{12} \cdot \alpha \varrho_c^{5/3} \quad (\text{cgs units}) \qquad (3a)$$

and the internal energy

$$E_c = \alpha \cdot \frac{3}{5} \varepsilon_F \cdot \frac{M}{\mu_{DT}} = 1.55 \cdot 10^{13} \cdot \alpha M_c \varrho_c^{2/3} \quad (\text{cgs units}) \qquad (3b)$$

The isentrope parameter α denotes the deviation from the completely degenerate expressions and labels different isentropes. Obviously, one has $\alpha \geq 1$. The Fermi energy is given by $\varepsilon_F = \hbar^2 (3\pi^2 n_e)^{2/3} / (2 m_e)$ with the elctron mass m_e and the electron density $n_e = \varrho_c / \mu_{DT}$. In the model, the density ϱ_c of the highly compressed region is obtained from eq. (3a) and its mass M_c from eq. (3b). The total fuel energy $(E_s + E_c)$ is related to the input beam energy

$$E_{Beam} = (E_s + E_c)/\eta \qquad (4)$$

via the hydrodynamic efficiency η. The total fusion energy

$$E_{Fusion} = q_{DT} \cdot M \cdot \phi \qquad (5)$$

is given by the specific DT fusion energy $q_{DT} = 3.34 \times 10^{11}$ J/g, the total fuel mass $M = M_s + M_c$, and the burn rate

$$\phi = H_F/(H_o + H_F) \qquad (6)$$

with the burn parameter $H_o \cong 7$ g/cm^2, the total fuel (ϱR)

$$H_F = \varrho_s R_s + \varrho_c (R - R_s) \qquad (7)$$

and the fuel radius $R^3 = 3M/(4\pi\varrho_c) + (1-\varrho_s/\varrho_c)R_s^3$. The value for H_o corresponds to a freely expanding DT sphere. In actual pellet implosions, pusher material tamps this expansion and increases the burn rate. On the other hand, asymmetry effects will degrade the burn so that the chosen H_o may effectively describe a realistic situation. Finally, the pellet gain is given by

$$G = E_{Fusion} / E_{Beam}$$

Results for $G(E_{Beam})$ are shown in Figs III.2-2 to III.2-4. If the input energy is not sufficient for ignition

$$E_{Beam} < E_s^{ign}/\eta \qquad (8)$$

the model assumptions are $E_c = 0$, $M_c = 0$, $E_s = \eta E_{in}$, $M_s = E_s \mu_{DT}/ 3kT_s$, and $R_s = (3M_s/4\pi\varrho_s)^{1/3} < H_s/\varrho_s$. The break in the gain curves marks the point of ignition and the onset of propagating burn. The hydrodynamic efficiency η, the isentrope parameter α, and the central pressure p are chosen as free model parameters. A standard set obtained for these parameters from explicit code calculations in section 3 is

$$\eta = 0.05, \quad \alpha = 2, \quad p = 0.2\ Tb \qquad (9)$$

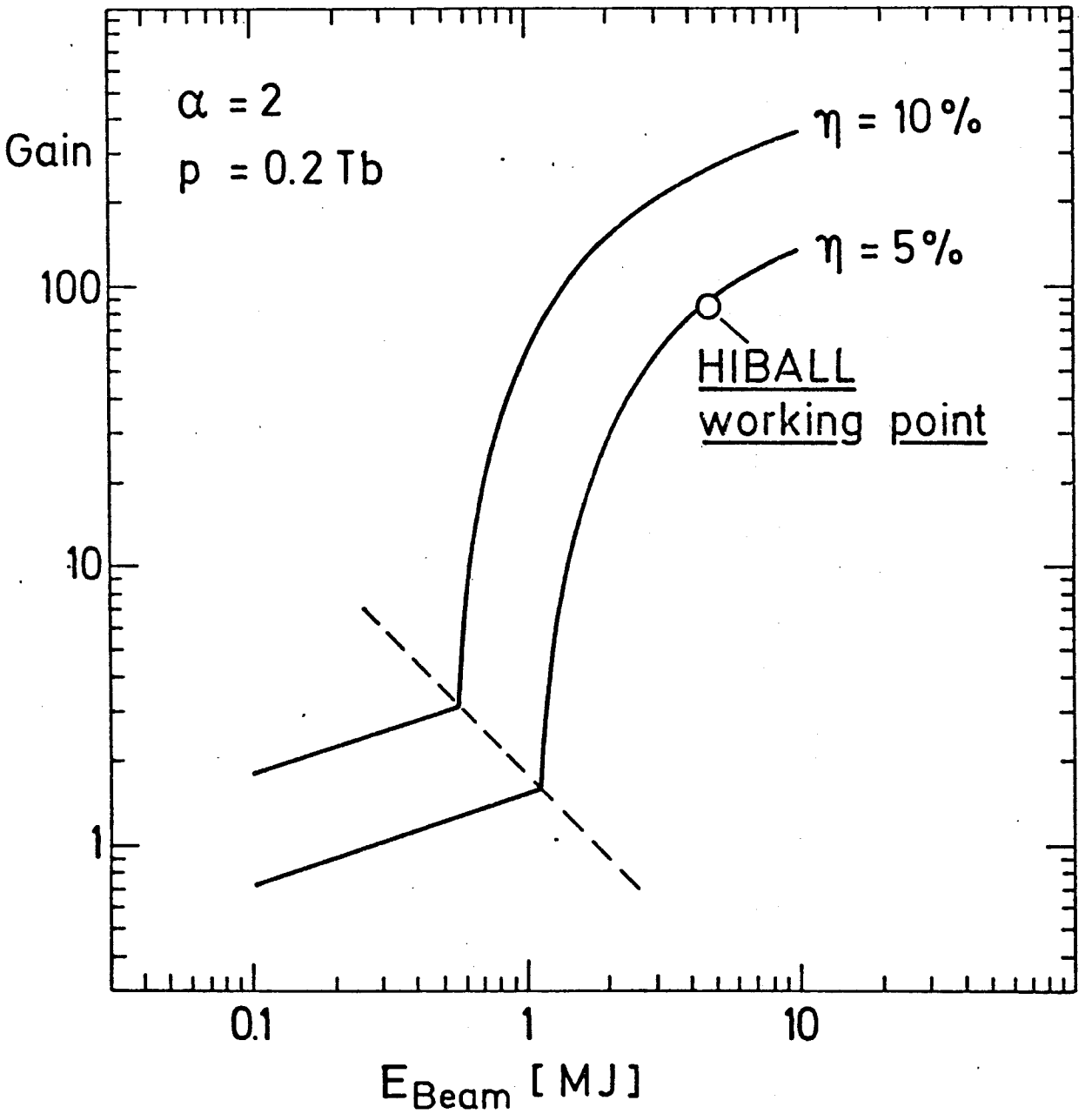

Fig. III.2-2: Gain curves for different hydrodynamic efficiencies, α and p are kept fixed.

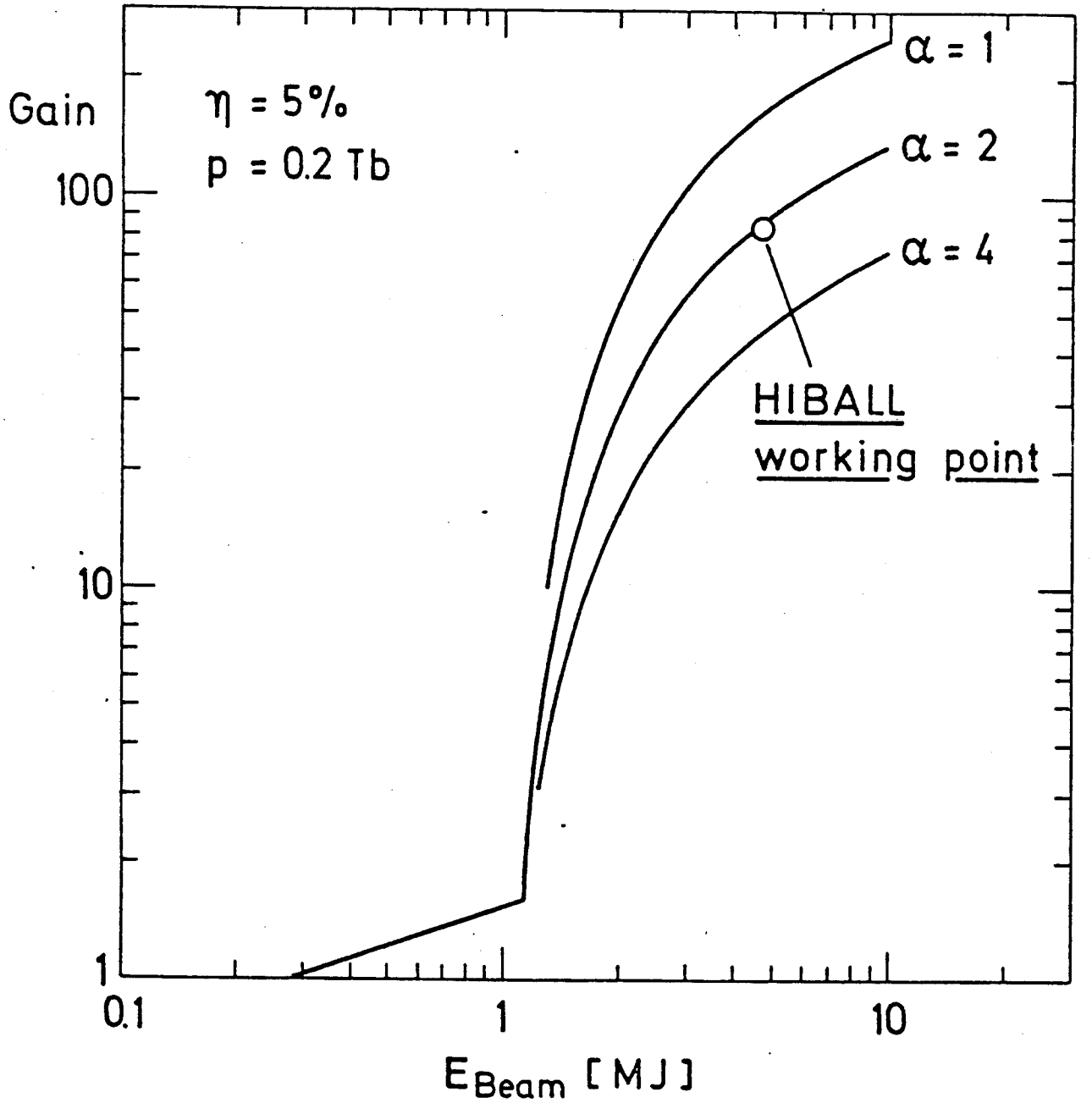

Fig. III.2-3: Gain curves for different cold fuel isentropes, η and p are kept fixed.

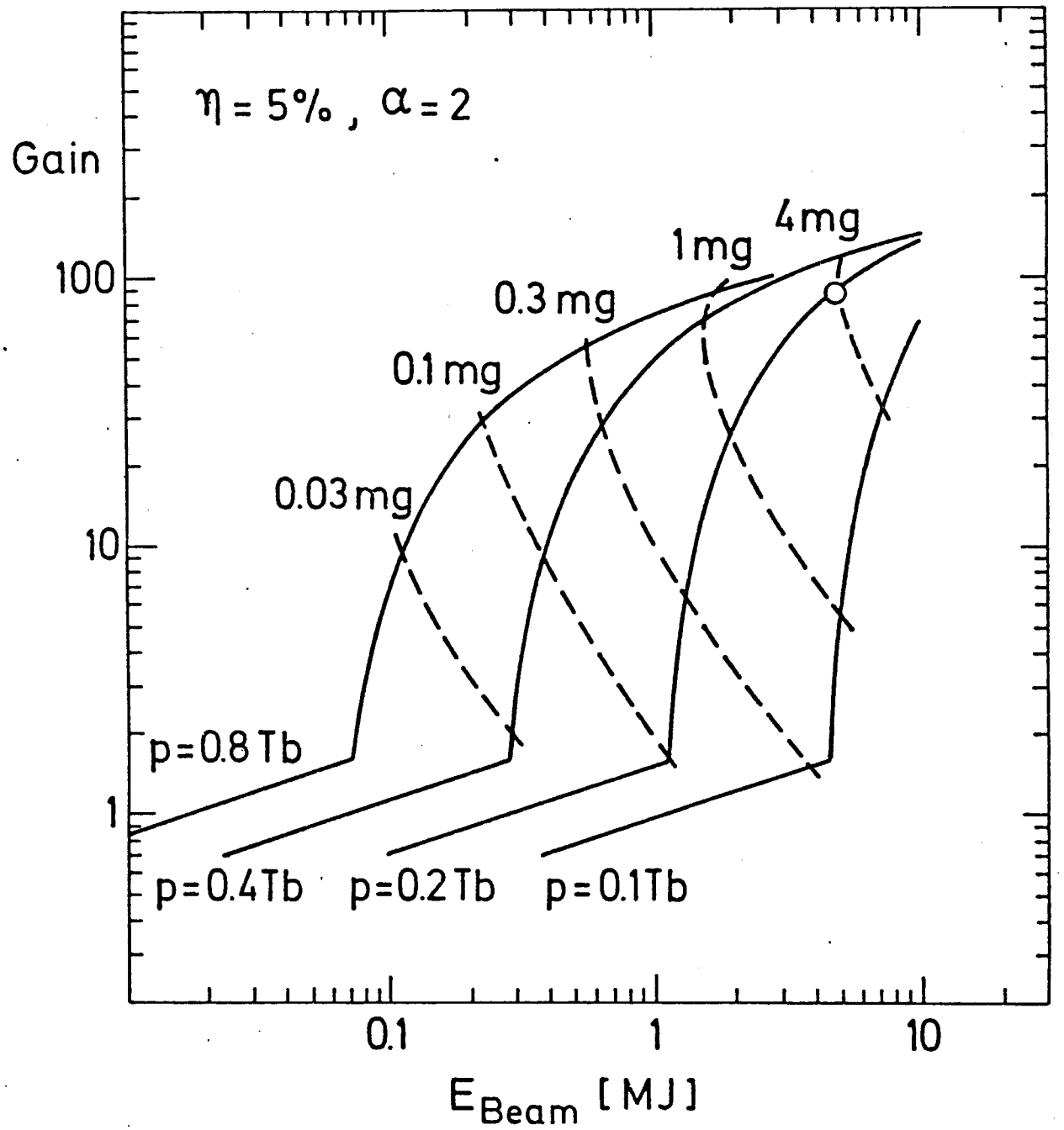

Fig. III.2-4: Gain curves for different central pressures, η and α are kept fixed. The broken lines are curves of equal fuel mass.

The gain curve for these standard parameters as well as neighbouring curves when varying η, α, and p are shown in Figs. III.2-2, -3, and -4, respectively. The standard curve has its ignition point at about 1 MJ. Changing the hydrodynamic efficiency from 5 % to 10 % in Fig. III.2 2, a gain band is obtained which almost reproduces the 'conservative' gain region predicted by the Livermore group.[4] Targets for heavy ion beam fusion have relatively low η and are located at the lower edge of this band. The gain is also lowered by going to higher cold fuel isentropes as seen from Fig. III.2-3; in the region of propagating burn one has $G \sim 1/\alpha$. High central pressures strongly decrease the ignition energy $E_{Beam}^{ign} \sim \rho^{-2}$, but are less important in the high gain regime. This is seen in Fig. III.2-4, where also lines of equal fuel mass are given. At high pressures, the ignition conditions can be achieved with exceedingly small masses. Such small targets may be an option for laser fusion, where sharp focussing and high beam power are possible. For heavy ion beam fusion, however, both these points are difficult to achieve. Therefore one is bound to take relatively large targets.

The working point of the HIBALL reactor design has been chosen as

$$G = 83 \qquad (10)$$

$$E_{Beam} = 4.8 \text{ MJ}$$

which lies on the reference gain curve with the parameters (9). Within the model, one then finds the other pellet parameters as given in Table III.2-1. The spark contains 2.5 % of the fuel mass, but 25 % of the fuel energy. Its density is less than one tenth of the compressed fuel density.

Table III.2.-1 HIBALL Pellet Parameters

total fuel	mass	$M = 4$ mg
	confinement	$(\varrho R) = 3.4$ g/cm^2
	burn rate	$\phi = 30$ %
	radius	$R = 124$ µm
	pressure	$p = 0.2$ Tb
	energy	$E = 240$ kJ
spark	temperature	$T_s = 5$ keV
	mass	$M_s = 0.1$ mg
	confinement	$\varrho_s R_s = 0.4$ g/cm^2
	radius	$R_s = 77$ µm
	density	$\varrho_s = 52$ g/cm^3
	energy	$E_s = 57$ kJ
compressed fuel	density	$\varrho_c = 630$ g/ cm^3
	compressed ratio	$\varrho_c/\varrho_o = 3000$
	isentrope	$\alpha = 2$
	energy	$E_c = 183$ kJ

In the next section, the stopping of heavy ions in hot dense matter is discussed, and stopping powers of Bi-ions are calculated for the absorber materials of the pellet described in section III.2.3. The dynamic design parameters as pulse shape, maximum beam power, absorber pressure, implosion velocity etc. which are needed to achieve the ignition configuration are then discussed.

III.2.2 Heavy ion stopping powers in hot dense matter

III.2.2.1 General considerations

One of the advantages to use heavy ion beams for pellet fusion consists in the high stopping powers. The 10 GeV Bi-ions considered for HIBALL, e.g., are stopped in less than 0.5 mm of a Pb surface layer. So far, however, there exist no precise measurements for ion energies and target regimes of interest for pellet fusion. Stopping data in some cold target materials and for ion energies up to 5 MeV/nucleon have been measured recently at GSI.[5,6] In some cases, these data differ considerably from tables of Northcliffe and Schilling[7]. Tables extrapolated from the new data and covering the range of ion energies 2.5 - 100 MeV/nucleon and various projectile/target combinations have been published by Hubert et al.[8] No experimental information is available for stopping powers in hot dense matter. For pellet applications, one has therefore to rely on theoretical extrapolations.

Fortunately, there are good reasons to believe that classical stopping theory is applicable. As pointed out by Bangerter[9], the typical heavy ion beam for fusion (HIBALL values: 10 GeV Bi-ions, ion velocity $v_B/c \cong 0.3$, particle current at target $\cong$ 25 kA/cm^2) has an ion density of 10^{14} - 10^{15}/cm^3 as compared to a target electron density of $\cong 10^{23}$/cm^3. In this sense, it has to be considered as a dilute beam. The Debye screening length λ_D is 2 - 3 orders of magnitude smaller than the average ion seperation distance. One may therefore hope that anomalous collective effects can be ignored.

The dominant stopping mechanisms are then energy loss due to binary collisions with electrons at distances $r < \lambda_D$ and due to plasmon excitations at distances $r > \lambda_D$. For stopping in partially ionized plasma, it has been claimed that bound electrons at $r > \lambda_D$ do not contribute to the stopping power because of Debye screening[12, 13]. This is incorrect. It would have the consequence that stopping powers first decrease when a target is heated and increase only later at higher temperatures (> 50 eV) when the stopping contribution from the free electrons themselves becomes larger than their assumed screening effect. However, a careful analysis of the energy flow at distances $r > \lambda_D$ (see e.g. Jackson's book[10]) shows that bound electrons in this region contribute to the energy loss just as the free electrons do. Therefore, as long as the ion velocity is large compared to the thermal velocity ($v_{e\ell}^{th}/c \cong 0.003$ for T = 200 eV), the stopping power will monotonically increase with temperature. This is because the number of free electrons increases and energy is more easily transferred to free electrons than to bound ones. As an important result for ion pellet design it follows that ion ranges in cold material represent upper bounds and decrease when the target is heated.

III.2.2.2 The theoretical model for ion stopping

In this subsection, the basic equations for ion stopping in hot dense matter are given. The theoretical frame is kept as simple as possible. Standard stopping theory[10] is generalized and applied to partially ionized dense plasma. The topic has been discussed recently in detail by Mehlhorn[11] and others [12, 13]. The present work basically follows Mehlhorn's description except for a few points explained below.

The electronic stopping power for non-relativistic beams has the general form

$$S = - \frac{4\pi e^4 Z_B^{eff\,2} n_e}{m_e v_B^2} \ln\left(\frac{b_{max}}{b_{min}}\right) \qquad (11)$$

where e and m_e are charge and mass of the electron, Z_B^{eff} is the effective charge of the beam ion and v_B its velocity, $n_e = (\varrho_T Z_T)/(A_T m_p)$ is the electron density with the mass density ϱ_T, the charge number Z_T and the mass number A_T of the target atoms, and m_p is the proton mass. The minimum and maximum impact parameters are given by

$$b_{min} = Max\left\{ \frac{Z_B^{eff} e^2}{m_e v_B^2} \,,\; \frac{\hbar}{m_e v_B} \right\}$$

$$b_{max} = \begin{cases} v_B/\bar{\omega} & \text{for bound electrons} \\ v_B/\omega_p & \text{for free electrons} \end{cases}$$

For the average ionization potential, we have used the expression

$$\hbar\bar{\omega} = 9\,eV \cdot Z_T \cdot (1 + 1.8/Z_T^{1/2}) \cdot \exp\{2.7 \cdot (Z_T^{ion}/Z_T)^2\}$$

which represents a fit to results of ref. 11. The plasma frequency of the free electrons $\omega_p = (4\pi e^2 n_e Z_T^{ion}/m_e Z_T)^{1/2}$. Z_T^{ion} is the average ionization state of target atoms, and $\hbar$ Planck's constant. In the case of 10 GeV Bi-ions, the minimum impact parameter b_{min} is found to be equal to the Coulomb distance ($Z^{eff} e^2/m_e v^2$) over the whole stopping range implying that Bohr's classical stopping formula is valid. For most heavy ion applications, it is incorrect to use the quantum value $b_{min} = \hbar/(m_e v_B)$ which leads to Bethe's stopping formula. This point has been overlooked in a number of papers including Mehlhorn's[11]. Our choice for b_{max} takes into account binary collisions as well as plasmon excitations as discussed in the preceding section.

An important quantity is the effective charge Z_B^{eff} of the beam ion inside the stopping medium, since the stopping powers depend on $Z_B^{eff\,2}$. It is difficult to measure Z_B^{eff} directly, and it has therefore in general been determined indirectly from measured stopping powers on the basis of eq.(11). It is found that Z_B^{eff} is approximately a function of the ion velocity alone and independent of target properties. A good parametrization of existing data has been given by Nikolaev and Dmitriev[14] in the form

$$Z_B^{eff} = Z_B \cdot \left[1 + \left(Z_B^{\alpha} v_o / v\right)^{1/k}\right]^{-k} \qquad (12)$$

with the parameters $\alpha = 0.45$, $k = 0.6$, and $v_o = 3.6 \times 10^8$ cm/sec. We have used this formula taking for the relative velocity between beam ion and electrons $v = (v_B^2 + v_{el}^{th\,2})^{1/2}$ where $v_{el}^{th} = (2kT/m_e)^{1/2}$ is the thermal electron velocity and kT the temperature. The total stopping power is finally obtained by adding the contributions from bound and free electrons

$$\frac{dE}{dR} = \frac{1}{\rho_T}\left(1 - \frac{Z_T^{ion}}{Z_T}\right) \cdot S_{bound} + \frac{Z_T^{ion}}{\rho_T Z_T}\, G(v_B / v_{el}^{th}) \cdot S_{free} \qquad (13)$$

Here, the function $G(x) = (\mathrm{erf}(x) - 2 \times \exp(-x^2)/\sqrt{\pi})$ accounts for the temperature dependence of the Coulomb cross section in the case that the thermal velocity v_{el}^{th} becomes comparable or larger than the ion velocity v_B. It is well known that the description given above breaks down for low ion energies. The Lindhard theory, applicable at low energies, gives for the bound electron contribution

$$S_{bound} = - k \sqrt{E_{ion} / A_B} \qquad (14)$$

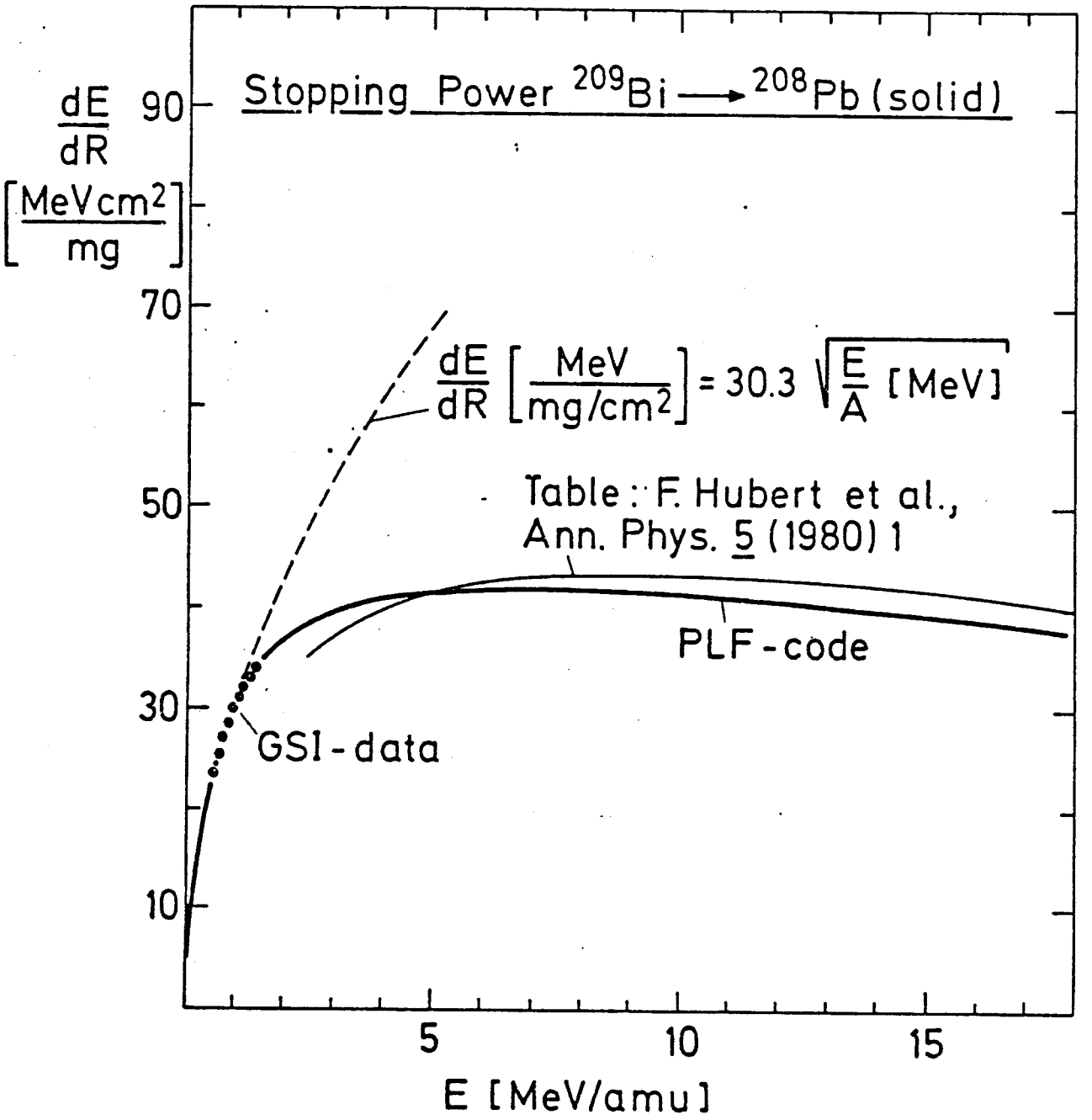

Fig. III.2-5: Stopping powers of Bi on solid PB at low energies.

In order to insure a correct treatment of the energy deposition near the end of the beam range, we have smoothly replaced expression (11) for S_{bound} by the Lindhard expression (14) at small energies, taking the parameter k from recent GSI measurements.[5] The calculated stopping power at small energies for Bi on solid lead is shown in Fig. III.2-5 together with GSI-data and values from the tables in ref. 8.

III.2.2.3 Calculated ranges and stopping powers

As a central result of this study, ranges of Bi-ions on solid Pb, solid Li, and solid PbLi alloy as considered in the HIBALL pellet design are given in Fig. III.2-6 as a function of ion energy in the relevant energy region. The range of 10 GeV Bi on solid Pb is found to be

$$R(10\,GeV\ Bi \rightarrow Pb) \cong 0.30\ g/cm^2$$

in solid Li, it is

$$R(10\,GeV\ Bi \rightarrow Li) \cong 0.13\ g/cm^2$$

For stopping powers at finite temperature, the average ionization Z_T^{ion} of the target plasma has been calculated from the Saha equation using ionization energies derived within Thomas-Fermi approximation. As an example the ionization of Pb-plasma as a function of temperature and density is shown in Fig. III.2-7. Based on these results, deposition profiles of 10 GeV Bi-ions in different materials and at various temperatures relevant for pellet fusion have been calculated as shown in Figs. III.2-8 to III.2-10. With increasing temperature, range shortening is found in all cases. The deposition profile in solid Pb is rather flat, and pronounced Bragg peaks only develop at higher temperatures. In a

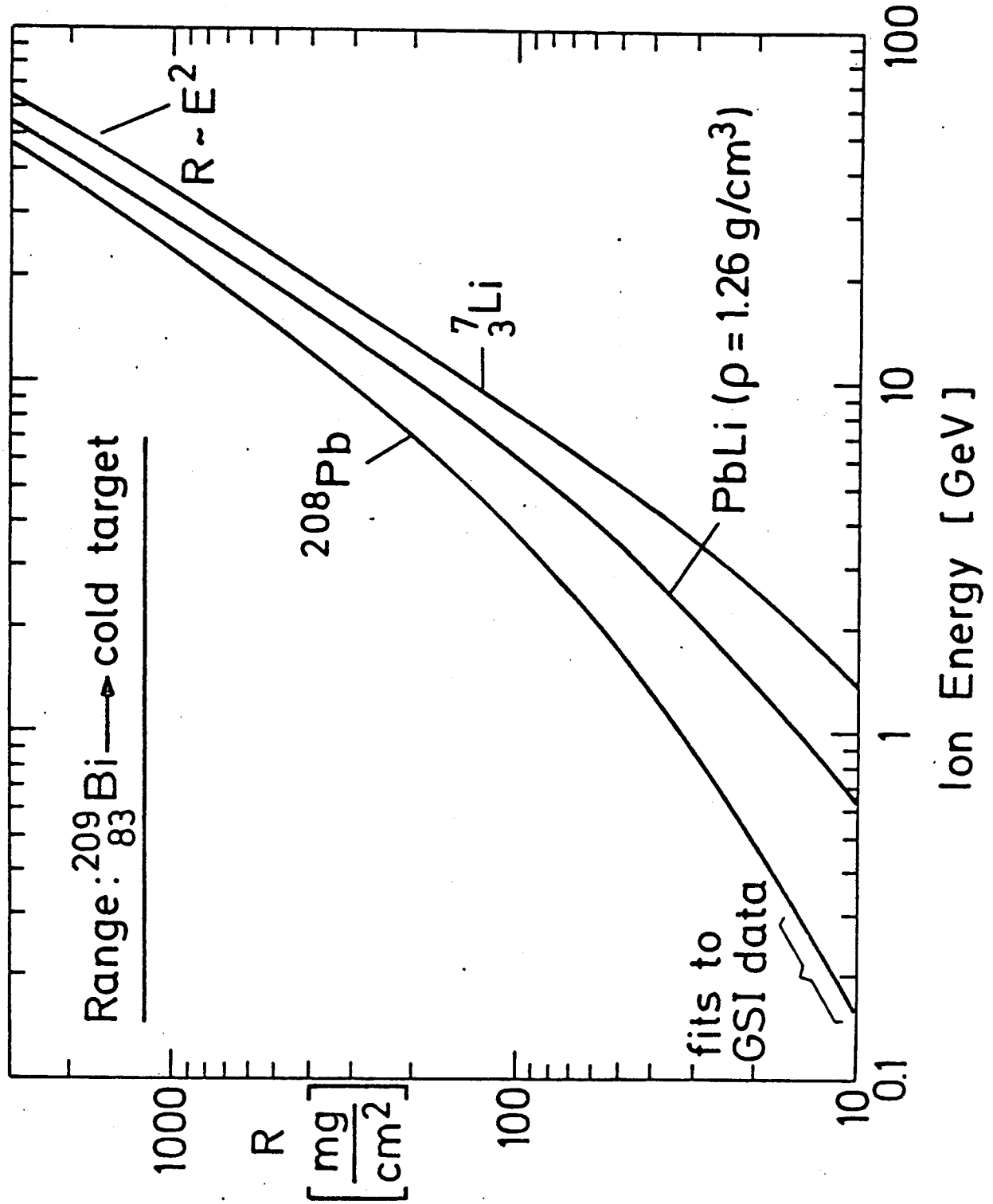

Fig. III.2-6: Ranges of Bi-ions in different solid materials as a function of ion energy.

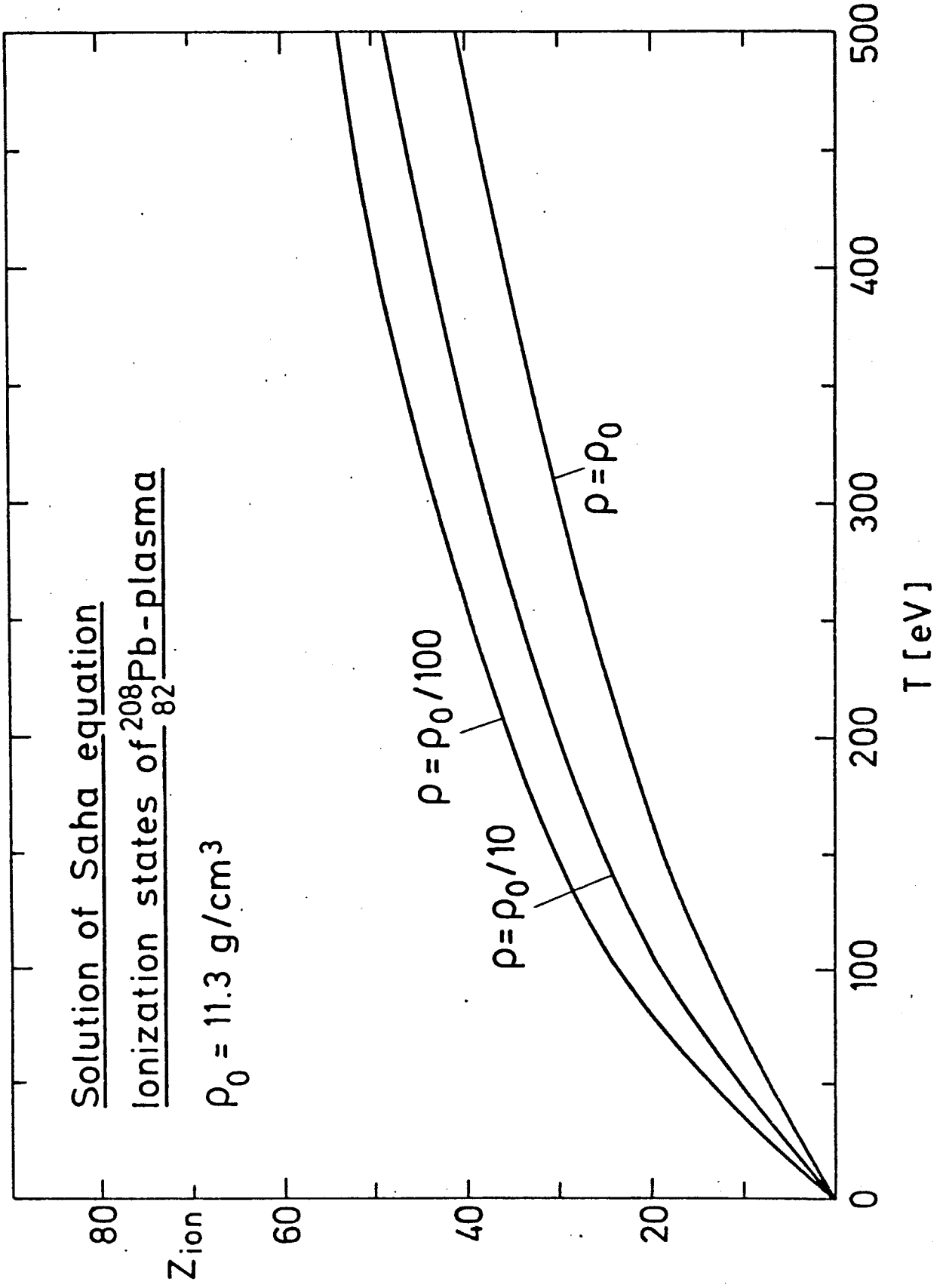

Fig. III.2-7: Average ionization of Pb-plasma as a function of temperature and density.

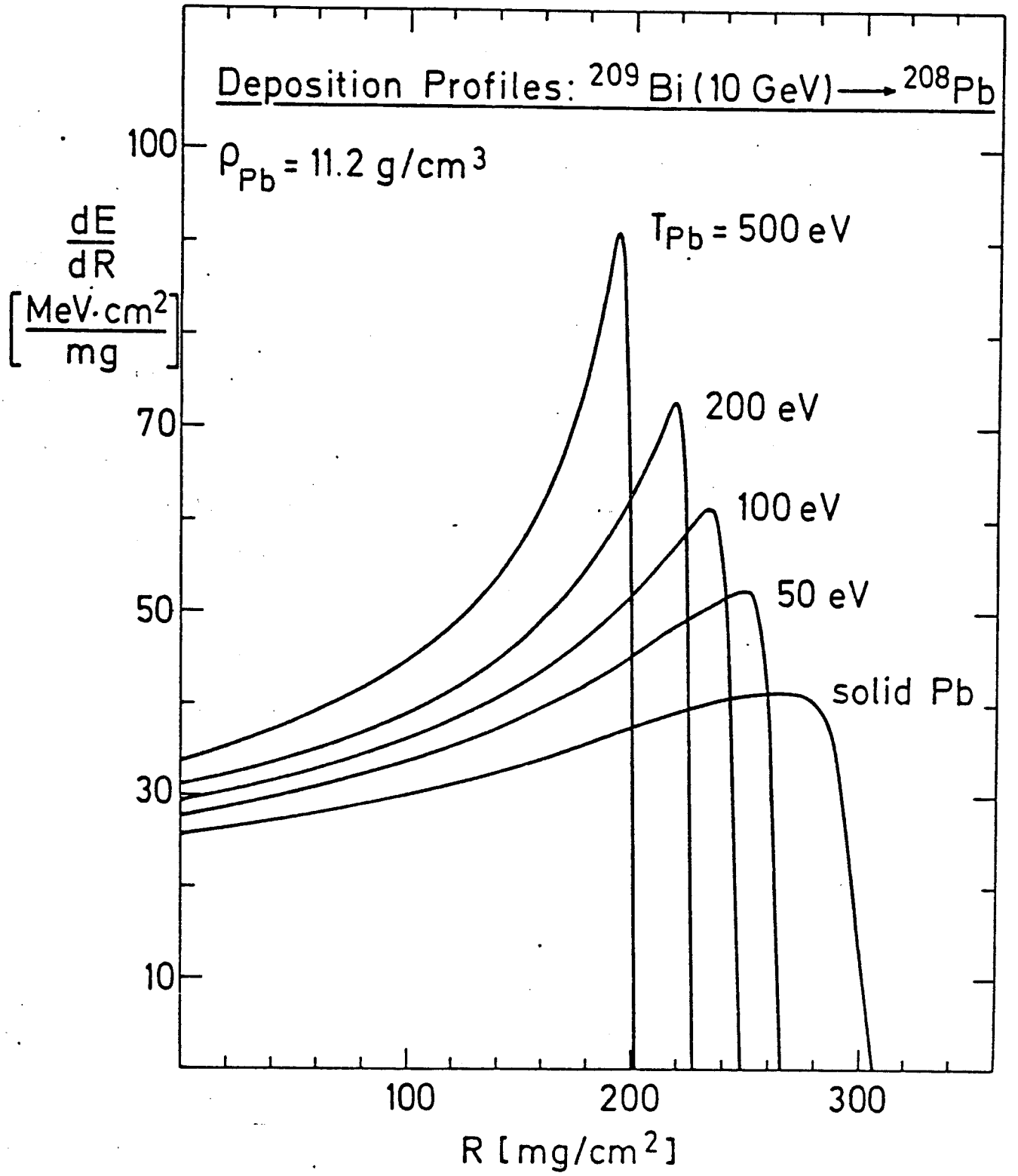

Fig. III.2-8: Stopping power as a function of range for Bi on Pb for different target temperatures.

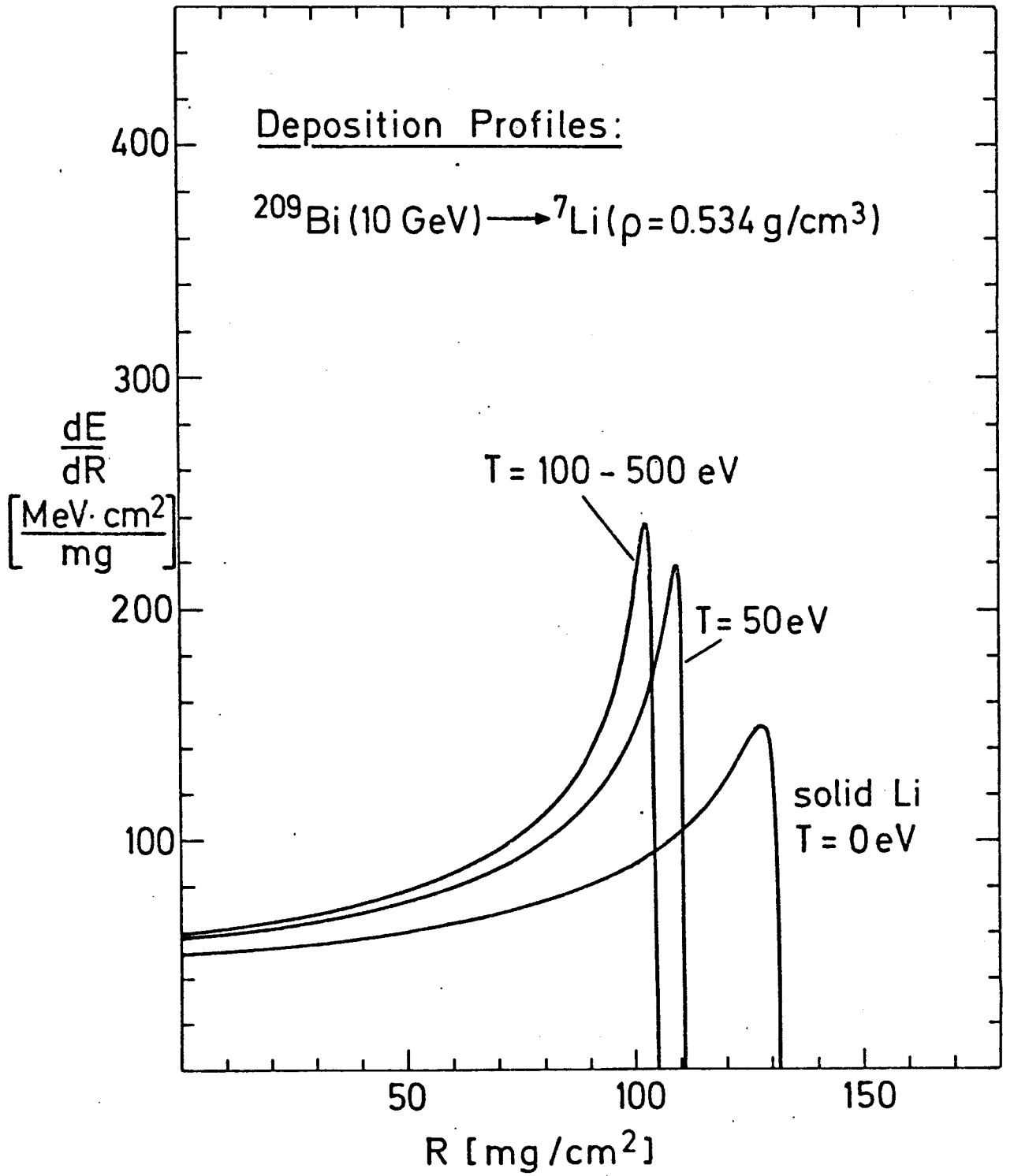

Fig. III.2-9: Same as Fig. III.2-8, but for Bi on Li.

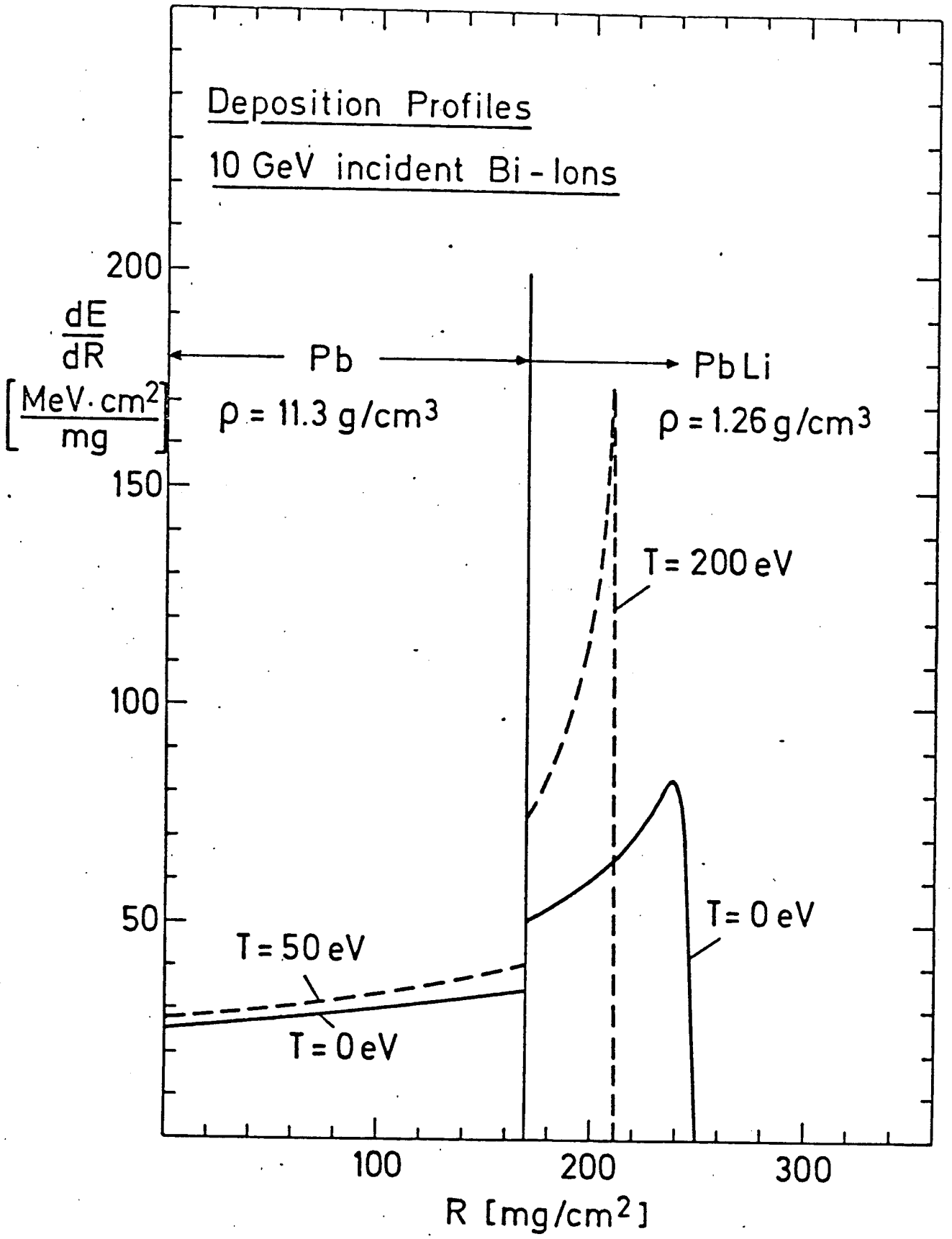

Fig. III.2-10: Energy deposition of 10-GeV Bi-ions in the absorption layers of the HIBALL pellet. Solid line for cold target, broken line for typical temperatures during implosion.

light material like Li, the average stopping is higher than in Pb and the effect of range shortening saturates at a temperature of about 100 eV as seen in Fig. III.2-9. At this temperature, the material is fully ionized.

In Fig. III.2-10, deposition profiles are shown for the HIBALL pellet. The beam first passes through a heavy Pb layer with relatively low stopping power. This layer serves as a tamper. The rest of the beam energy (almost 50 %) is then absorbed in a PbLi layer with low density and high stopping power. It is heated to higher temperatures than the Pb layer. For simplicity, constant temperatures are chosen in Fig. III.2-10 for each layer. They correspond to typical values of the implosion calculation discussed in the next section. It should be noted that deposition profiles of light ion beams show a much more pronounced Bragg peak than the heavy ion beams discussed here. Light ion beams are therefore more suited to create an implosion configuration with a heavy cold tamper outside and a light hot absorber inside which pushes the fuel with high efficiency. The advantage of this design is somewhat reduced when used for heavy ion beam fusion as in the present study.

A further degradation of coupling efficiency between beam and implosion dynamics is due to the fact that, in a realistic situation, the beam arrives at the pellet surface not perfectly focussed (see e.g. ref. 15) The effect of defocussing has been studied in ref. 16. It tends to wash out any Bragg peak in the deposition profile. Since the exact beam properties at target are still uncertain, we have chosen box deposition profiles with constant dE/dR in the following implosion calculation.

III.2.3 A specific pellet design

III.2.3.1 General consideration

In this section, a single shell pellet design is considered, and the results of an implosion calculation are presented in detail. The intention is to provide insight into the dynamics of a heavy ion induced pellet implosion, to check the consistency of the general HIBALL parameters with the requirements of the pellet and to discover critical points. The results indicate that the beam parameters assumed so far are not consistent. Most critical points are ignition and symmetry. The assumed power of 240 TW is too low to insure a stable and igniting implosion, at least for the envisioned single shell design. The presented calculation achieves ignition with 240 TW, but only at the price of a highly optimized pulse shape, a thin pusher (6 mg) and a reduced amount of fuel (2 mg). The required output energy of 400 MJ is obtained due to a high burn rate. However, a rough estimate then shows that the implosion symmetry will be destroyed due to Rayleigh-Taylor (RT) instability. A thicker pusher that survives RT-instability is needed as well as 4 mg fuel to allow for a more realistic burn rate. This will require considerably more beam power for ignition, probably in the order of 500 TW. An alternative approach may be a double shell pellet design which has been found to require less power for ignition due to a central igniter[17].

It should be kept in mind that the present calculations are based on a simple hydrodynamic code (see description below) and are subject to large uncertainties on top of those inherent to pellet design in

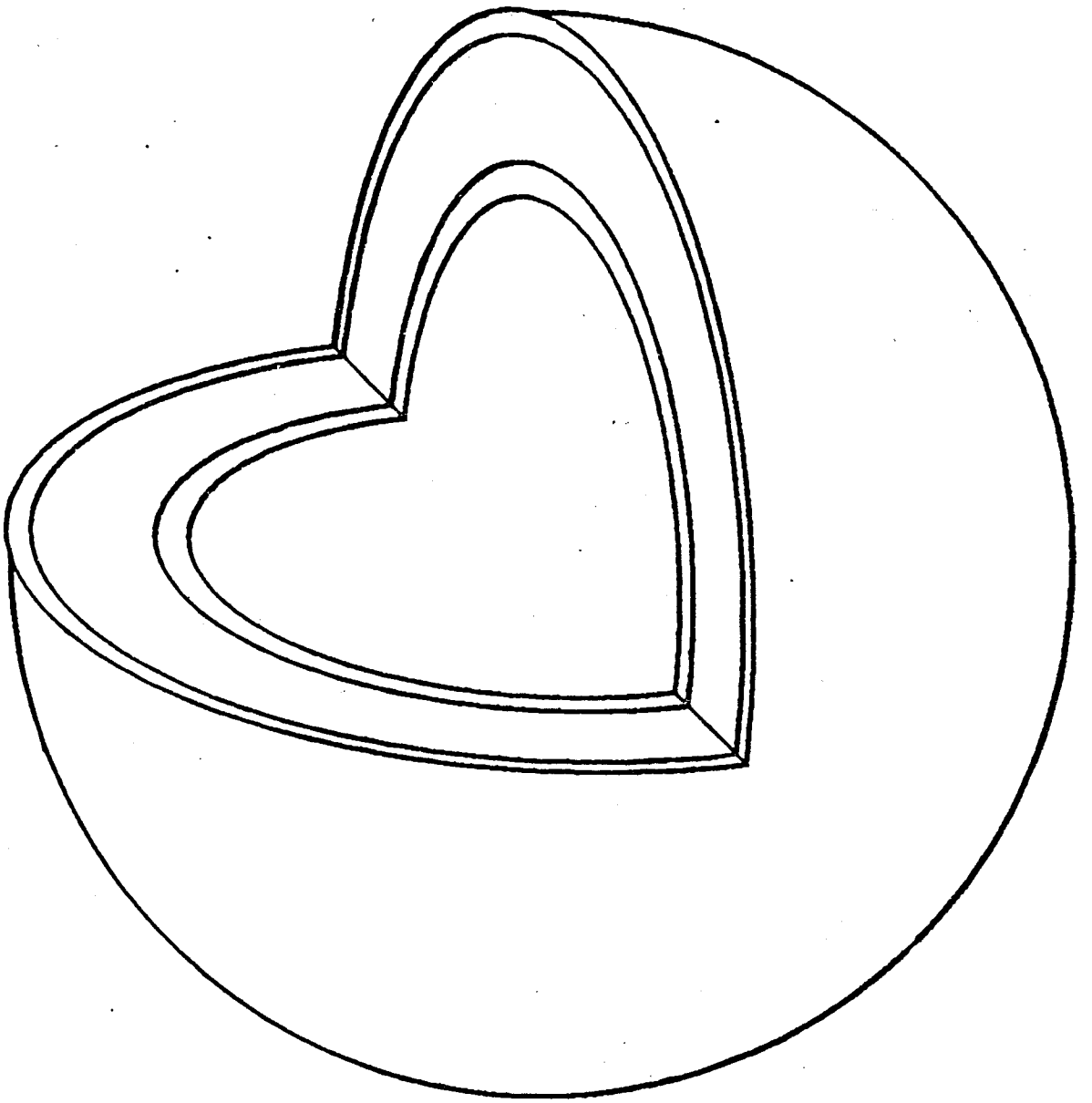

Fig. III.2-11: Perspective view of the HIBALL pellet.

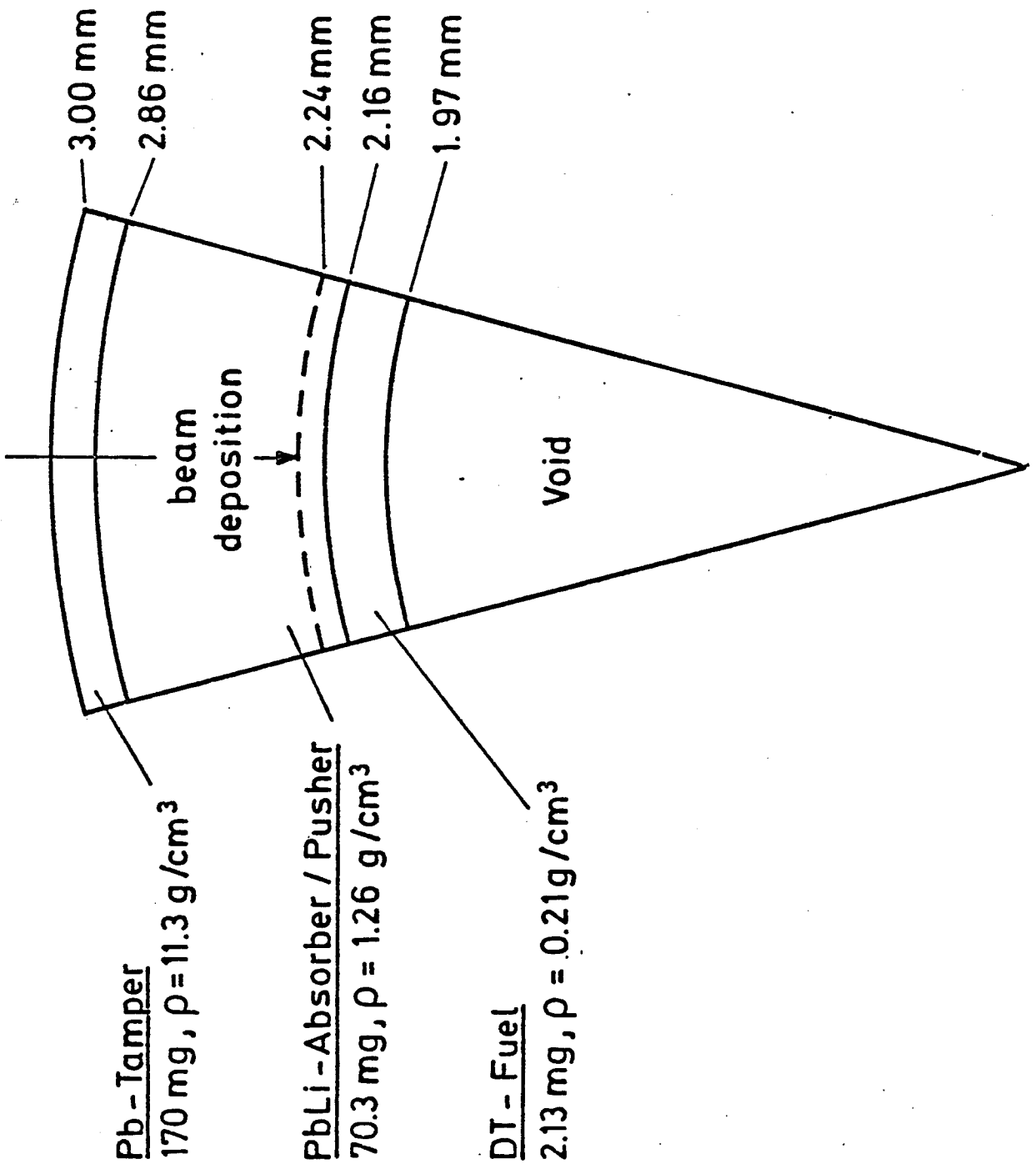

Fig. III.2-12: Sector of the HIBALL pellet

general. A particular problem not further addressed in the following is related to asymmetric irradiation of the pellet in the HIBALL reactor. Due to high density and relatively low temperature in the beam deposition region, lateral heat conduction will be rather ineffective to smooth out these asymmetries, at least in the present design.

III.2.3.2 The pellet configuration

The pellet considered in this work closely follows a design proposed by Bangerter and Meeker[18] for light ion beam fusion. A perspective view is given in Fig. III.2-11. The pellet consists of a spherical hollow shell made of three layers as shown in Fig. III.2-12. The cryogenic fuel is contained in the inner layer, the outer layers are made of low density PbLi alloy and high density Pb. They serve as pusher/absorber and tamper, respectively. The PbLi-alloy replaces the TaCOH material of the Bangerter-Meeker design and has been chosen for reasons of chemical compatibility with the environment in the HIBALL reactor cavity. The main reason for choosing a low density layer in the middle is to have a low density pusher in order to prevent RT-instability at the pusher-fuel interface during the final stage of implosion. The other advantage in having a heavy tamper outside and a light absorber material inside is related to beam target coupling and has already been discussed in the section III.2.2.3.

The masses of the Pb and PbLi layer have been determined such that the interface between these layers is approximately stationary during the implosion and, secondly, by the requirement that beam ions have stopped

in the cold absorber 80 μm before reaching the fuel. This inner region of the PbLi layer is not directly heated by the beam and forms the pusher. The pusher mass (6 mg) as well as the fuel mass (2 mg) have been chosen such that ignition is achieved at a beam power of 240 TW (compare discussion in section III.2.3.1). The outer radius of the pellet has been fixed to 3 mm. This is a minimum value set by the requirements of final beam focussing.

III.2.3.3 The pellet code MINIHY

The 1D-Lagrangian hydrodynamic code MINIHY used for the implosion calculation is characterized by the following physical features:

A. One temperature for electrons and ions

It has been checked that this is sufficient for ion beam driven implosions[19], since energy deposition occurs in dense material and temperatures are typically below 500 eV. This is different from the situation in laser fusion where electron and ion temperatures decouple in the corona.

B. Spitzer thermal conductivity, no flux limit

This is sufficient for the same reasons as mentioned under point A.

C. DT burn with local deposition and free neutron escape

Since this treatment may overestimate ignition, fusion processes are switched on only when the central temperature reaches 5.6 keV. At this temperature, fusion energy production overtakes losses by bremsstrahlung. Fuel depletion is accounted for during burn.

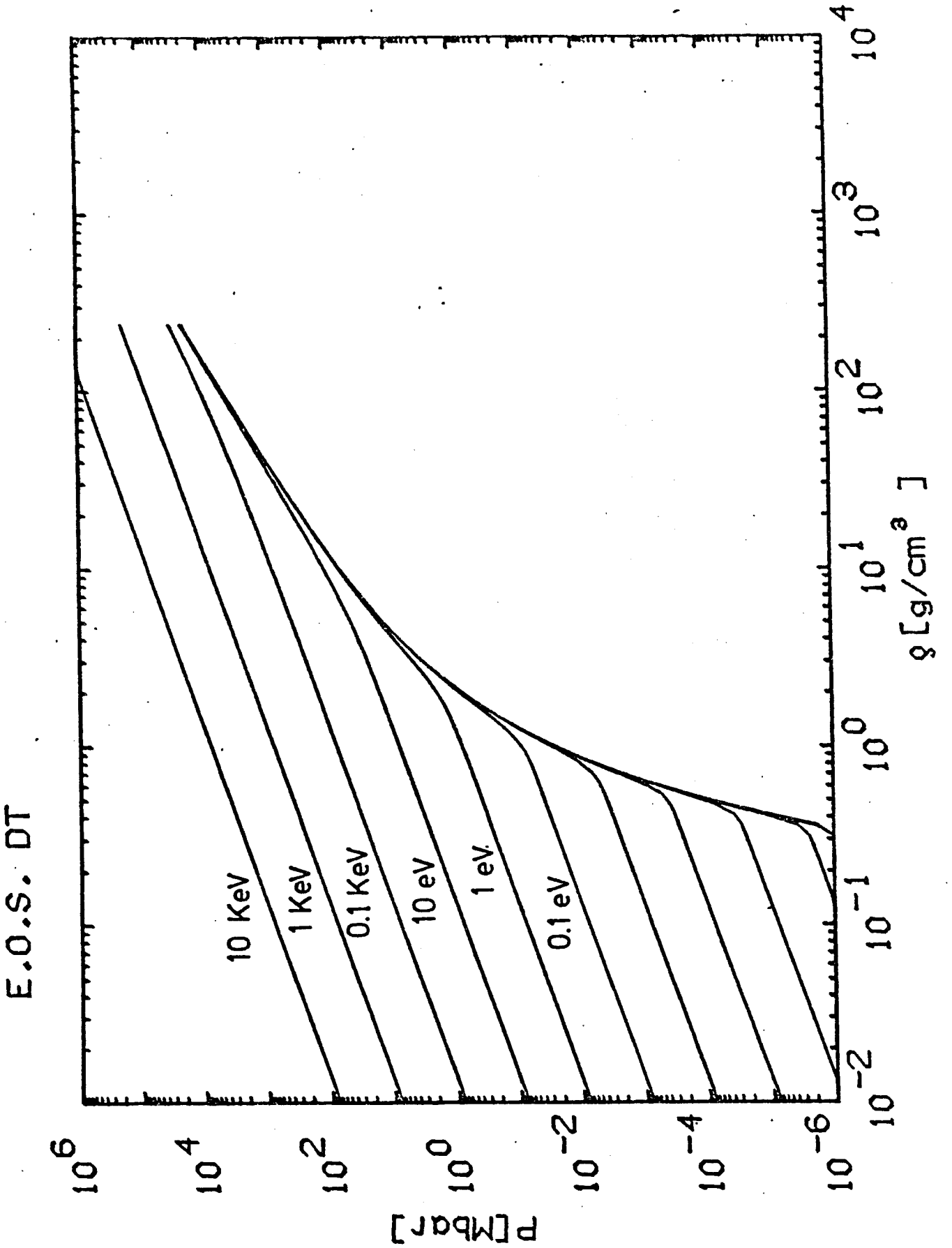

Fig. III.2-13a: Equation of state for DT used in the calculation.

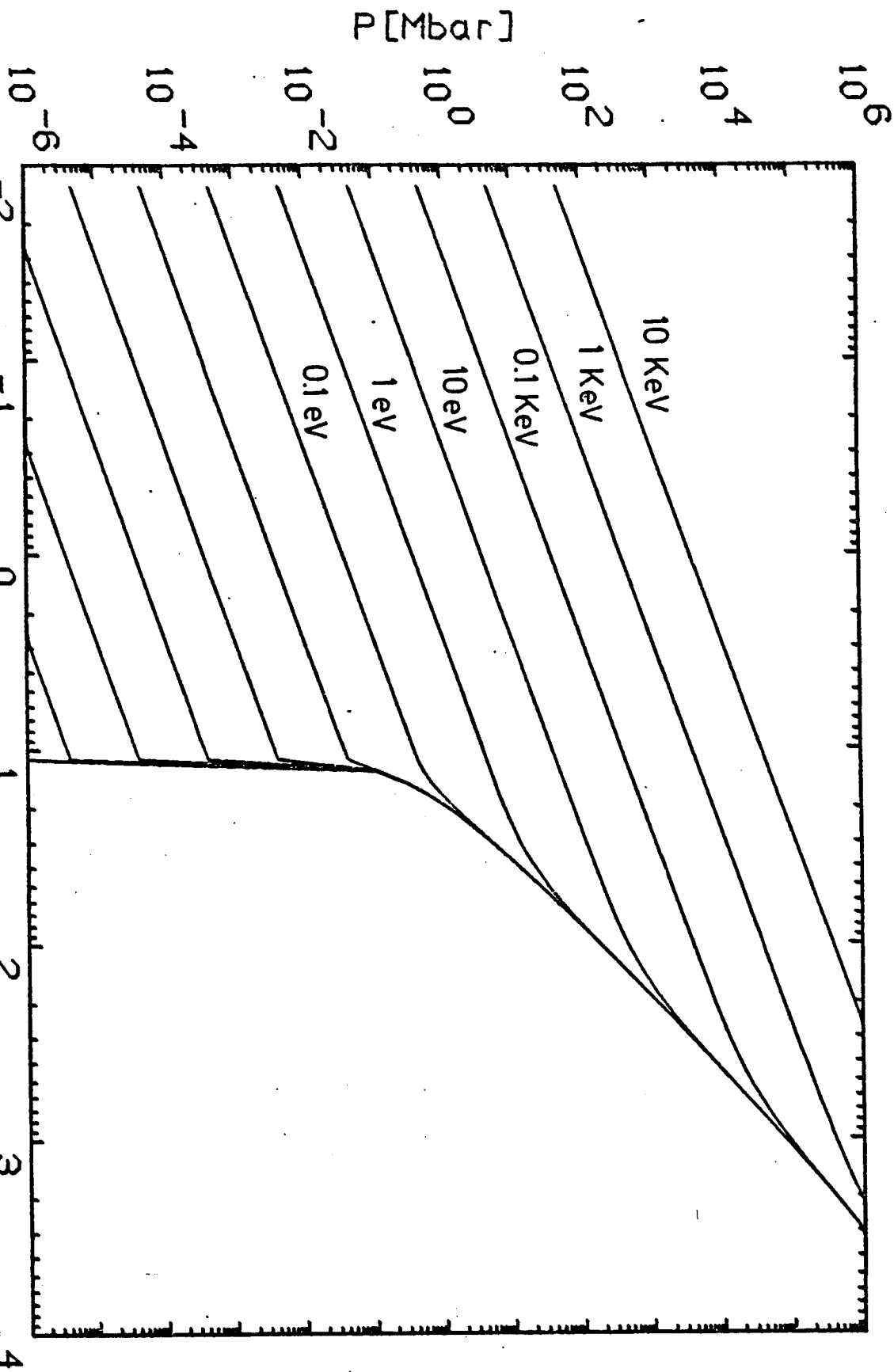

Fig. III.2-13b: Same as Fig. III.2-13a, but for Pb

D. Ideal gas equation of state allowing for electron degeneracy

A crucial point is that the Fermi temperature which controls the transition to the degenerate state is not calculated from the total electron density n_e in the medium (as e.g. in the original version of the Medusa code[20]), but from an effective density of unbound electrons n_e^* which is determined by an ad hoc description of pressure ionization in the form

$$n_e^* = n_e \cdot \exp\{-1/(V_0 n_e)\} \quad .$$

for DT, where $V_0 = 4\pi/3 \quad (\hbar^2/m_e e^2)^3$ is the volume occupied by a bound electron, and for heavier materials in the form

$$n_e^* = \begin{cases} n_e \cdot [1 - \exp(-(\varrho - \varrho_0)/(\beta \varrho_0))] & \text{for } \varrho > \varrho_0 \\ 0 & \text{for } \varrho \leq \varrho_0 \end{cases}$$

where ϱ_0 is the solid density and β an adjustable parameter. In the present calculation, $\beta = 200$ has been chosen for Pb, and $\beta = 50$ for PbLi. To be definite, the isotherms for DT and Pb in the (p, ϱ) plane have been plotted in Figs. III.2-13a and 13b. They show at least qualitatively a reasonable behaviour, in particular near the limiting degeneracy curve which is most important for a correct description of the high compression regions in the implosion.

With a more realistic equation of state, one would have to deposit more energy to create the same driving pressure in the absorber. Also, absorber temperatures would be higher at the same pressures. A critical point will be radiation transport which has not been included in the code, so far. The high-Z Pb layer is optically thick, and radiation

losses through the surface may be estimated by black body radiation. For the proposed pellet design, one finds a loss of 6 kJ for 50 eV surface temperature, 100 kJ for 100 eV, and 1.6 MJ for 200 eV. These are upper limits, but they demonstrate that a careful treatment of radiation as well as a more realistic equation of state are needed in the future development of this work. Nevertheless, no dramatic changes are expected for the overall implosion results. Concerning the beam energy deposition, it has been assumed $dE/\varrho\, dx$ = const (see discussion in section III.2.2.3). The implosion calculation has been performed on a Lagrangian mesh with 100 zones (36 for DT) and with progressively finer zoning towards the inner interface of each layer.

III.2.3.4 The pellet implosion

III.2.3.4.1 The general view

The optimized pulse shape to implode the described pellet configuration and to drive it to ignition is displayed in Fig. III.2-14. It consists of a 20 nsec prepulse at a power level of 2.4 TW and a 10 nsec main pulse at 240 TW with a 2 nsec rise time in between. The pulse is cut of at 32 nsec, since a further continuation would not improve the implosion result. The total pulse energy is 2.7 MJ. The corresponding r-t-diagram of the imploding shell is shown in Fig. III.2-15. The solid lines describe the motion of the outer pellet surface, the interfaces between the Pb, PbLi, and DT layer, and the inner DT surface, respectively. The broken lines display the temperature evolution in the deposition region. Ignition and burn occurs at about 37.7 nsec near R = 0.

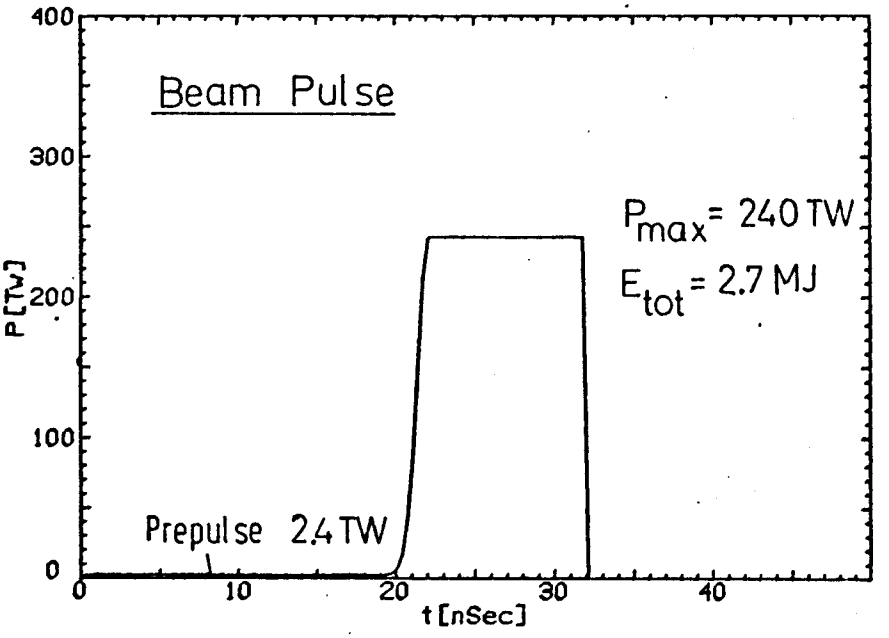

Fig. III.2-14: Pulse shape of the HIBALL design

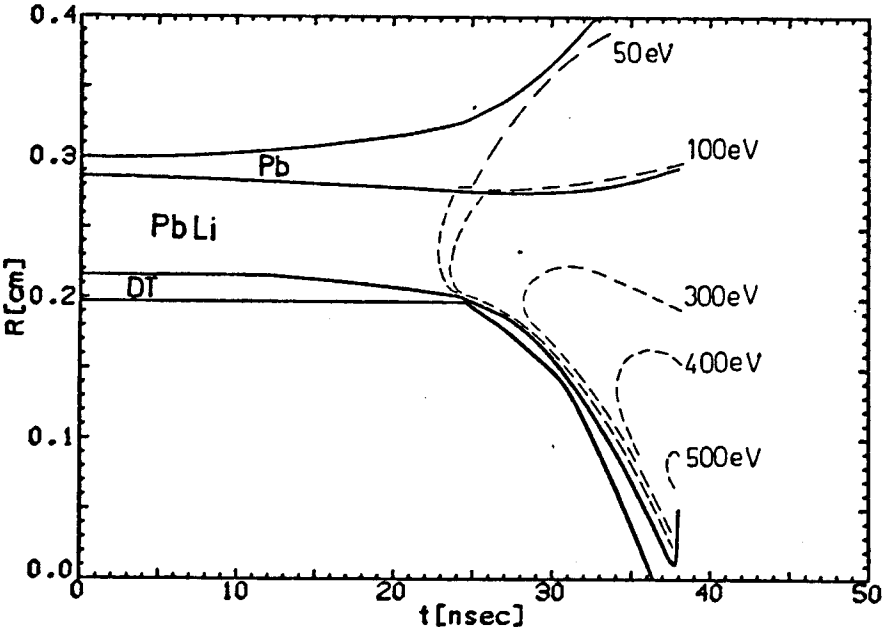

Fig. III.2-15: Implosion of the HIBALL pellet driven by pulse shown in Fig. III.2-14

The ion driven implosion looks rather different from that driven by a laser. It is essentially the explosion of a massive metal shell pushing the fuel at its inner front. The 10 GeV Bi-ions pass through 97.5 % of the shell's mass and deposit their energy deeply inside the volume, whereas laser deposition occurs far outside in a low density corona and the imploding material is driven by an ablating surface. As a consequence, the temperatures in the ion deposition region remain rather low ($\lesssim$ 500 eV) as compared to corona temperatures in laser fusion, and no problem with hot electrons is expected to occur. A disadvantage of the low temperatures is that heat conduction is slow and therefore ineffective to smooth out irregularities due to asymmetric irradiation of the pellet.

III.2.3.4.2 Absorber, pusher, and fuel during implosion

It is instructive to look at the profiles of temperatures Θ, density ϱ, and pressure p given in Figs. III.2-16a-j for different times in conjunction with the r-t-diagram. Fig. III.2-16a shows the unperturbed pellet. The solid points in the broken line for the density mark the interfaces. The profiles at 18 nsec are seen in Fig. III.2-16b. The prepulse has heated the absorber to about 5 eV, the tamper interface stands like a rigid wall, the heated PbLi is flowing inwards, and a sharp density and temperature jump has built up at the border to the unheated PbLi which now forms the pusher. The steep gradients at this interface, formed at early times, stay on through all stages of the implosion. It is subject to severe RT-instability, a point further discussed in section III.2-3.4.5. At 18 nsec, the first shock generated by the prepulse has

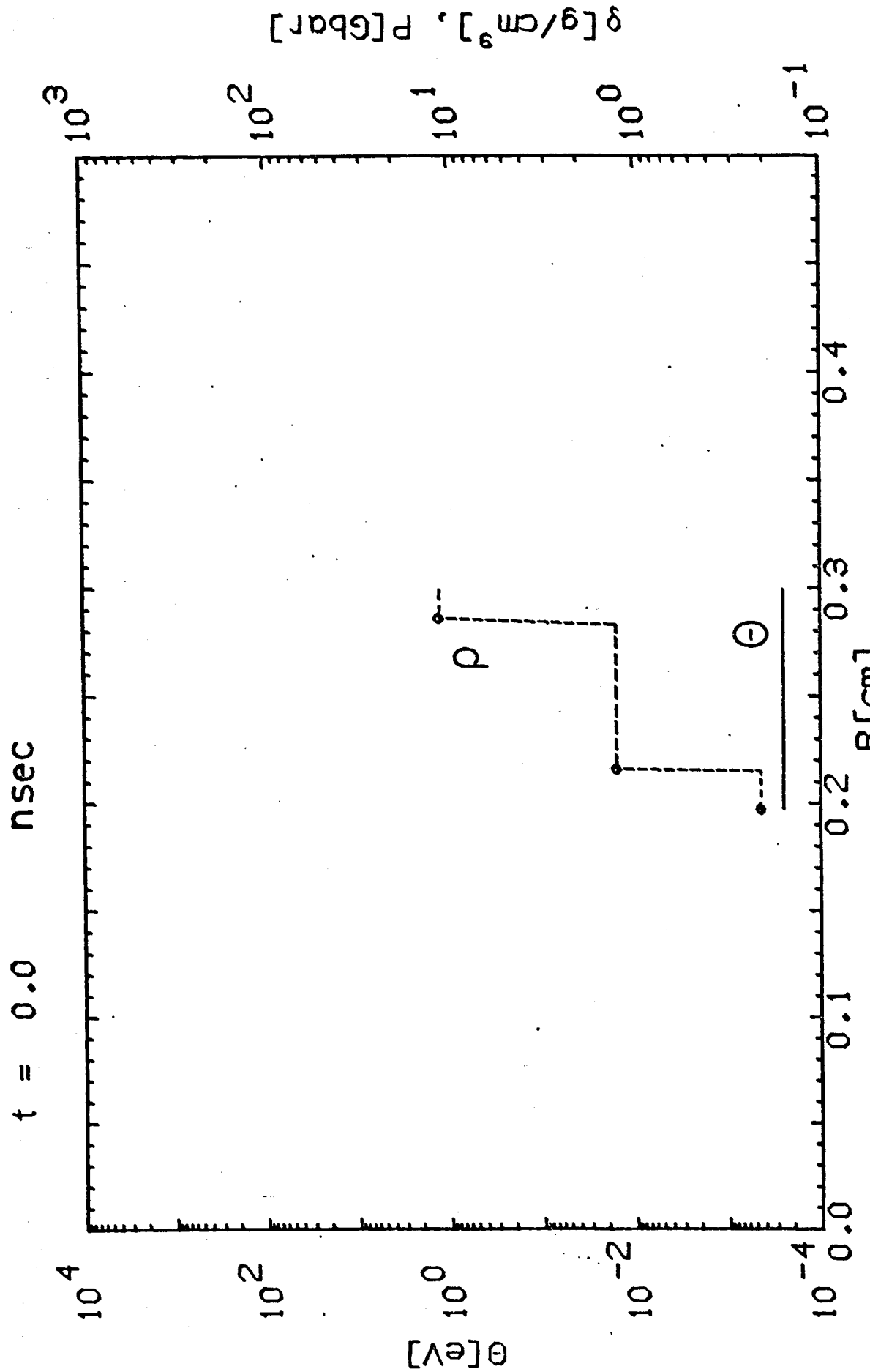

Fig. III.2-16a: Distribution of density ρ, temperature Θ, and pressure p in the pellet at time t = 0. The solid points in the density line mark the interfaces. The pressure is still too low to be seen at this time.

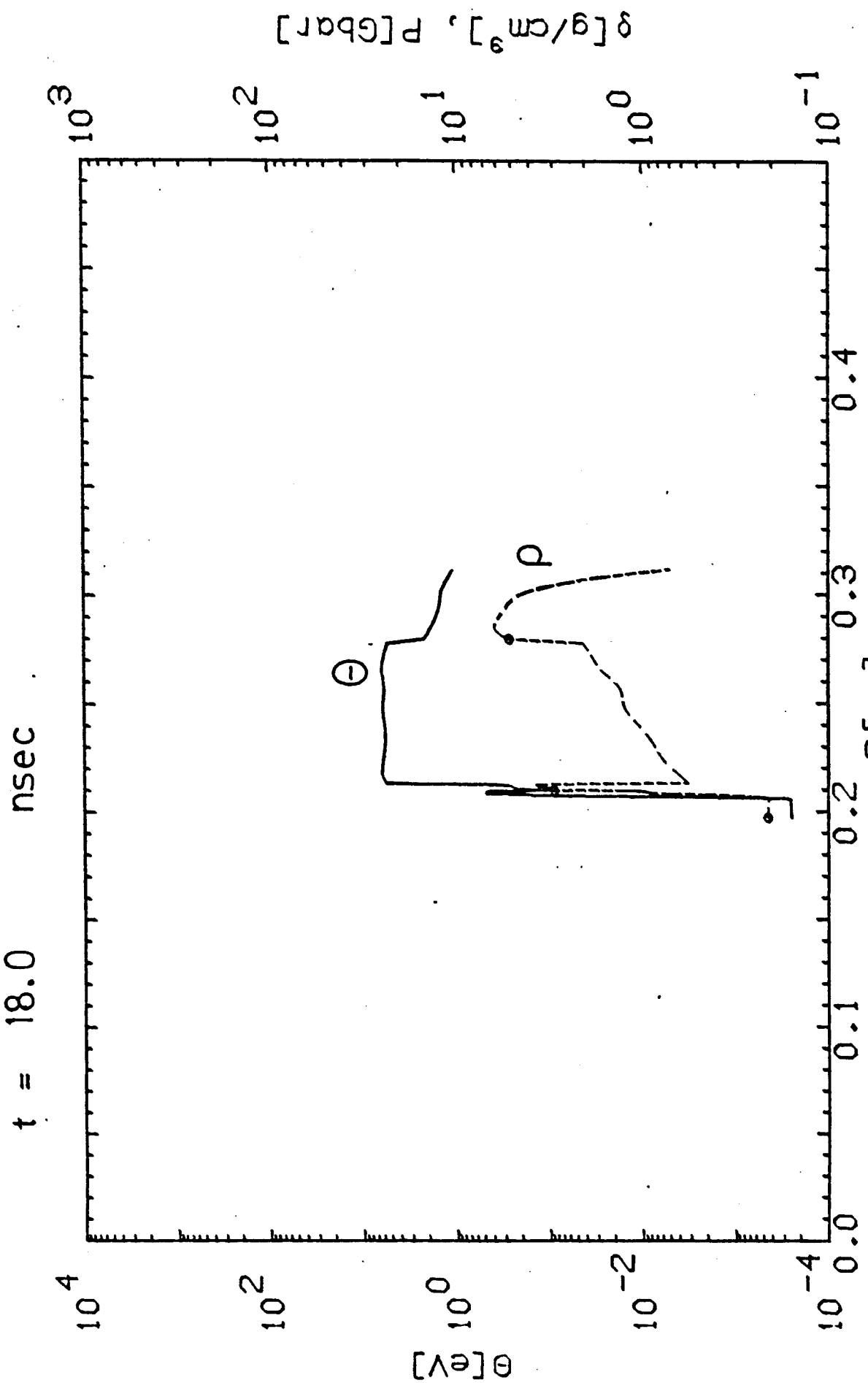
ϱ[g/cm³], P[Gbar]
10³
10²
10¹
10⁰
10⁻¹
Θ[eV]
10⁴
10²
10⁰
10⁻²
10⁻⁴
0.0
0.1
0.2
0.3
0.4
R[cm]
t = 18.0 nsec
Θ
ϱ

Flg. III.2-16b

just entered into the unperturbed fuel. At 24.5 nsec, it has almost reached the inner surface of the fuel closely followed by the second strong shock launched by the main pulse which was switched on at 21 nsec. This is seen from Figs. III.2-16c and 16d. The importance of these two shocks and their relative timing for forming the ignition spark will be discussed in section III.2.3.4.6. Here, one should again pay attention to the r-t-diagram (Fig. III.2-15) and to the way the inner fuel surface is set into sudden fast motion upon arrival of the shocks. It then travels at almost constant speed until the accelerated pusher catches up at about 31 nsec and gives the fuel another kick involving the passage of a third shock through the fuel. This fuel bouncing has been described before by Kidder[3]. It is also important for ignition.

At 36.40 nsec, the inner surface arrives at the centre (void closure). The fuel has now an average velocity of 2.5×10^7 cm/sec. Its kinetic energy amounts to 2.3 % of the input beam energy, whereas its internal energy is only 0.2 %, at this moment. The profiles are plotted in Fig. III.2-16e. A remarkable feature is the temperature distribution in the fuel which steeply rises towards the centre and is forming the ignition region. The pressure has now increased to more than 100 Mbar in the central region and appears on the scale chosen in the diagrams. Typical pressures in the absorber at main pulse time range between 10 and 100 Mbar.

III.2.3.4.3 Ignition and burn

Ignition (defined here as time when the central temperature reaches 5.6 keV) occurs at 37.647 nsec, about 1.2 nsec after void closure. During

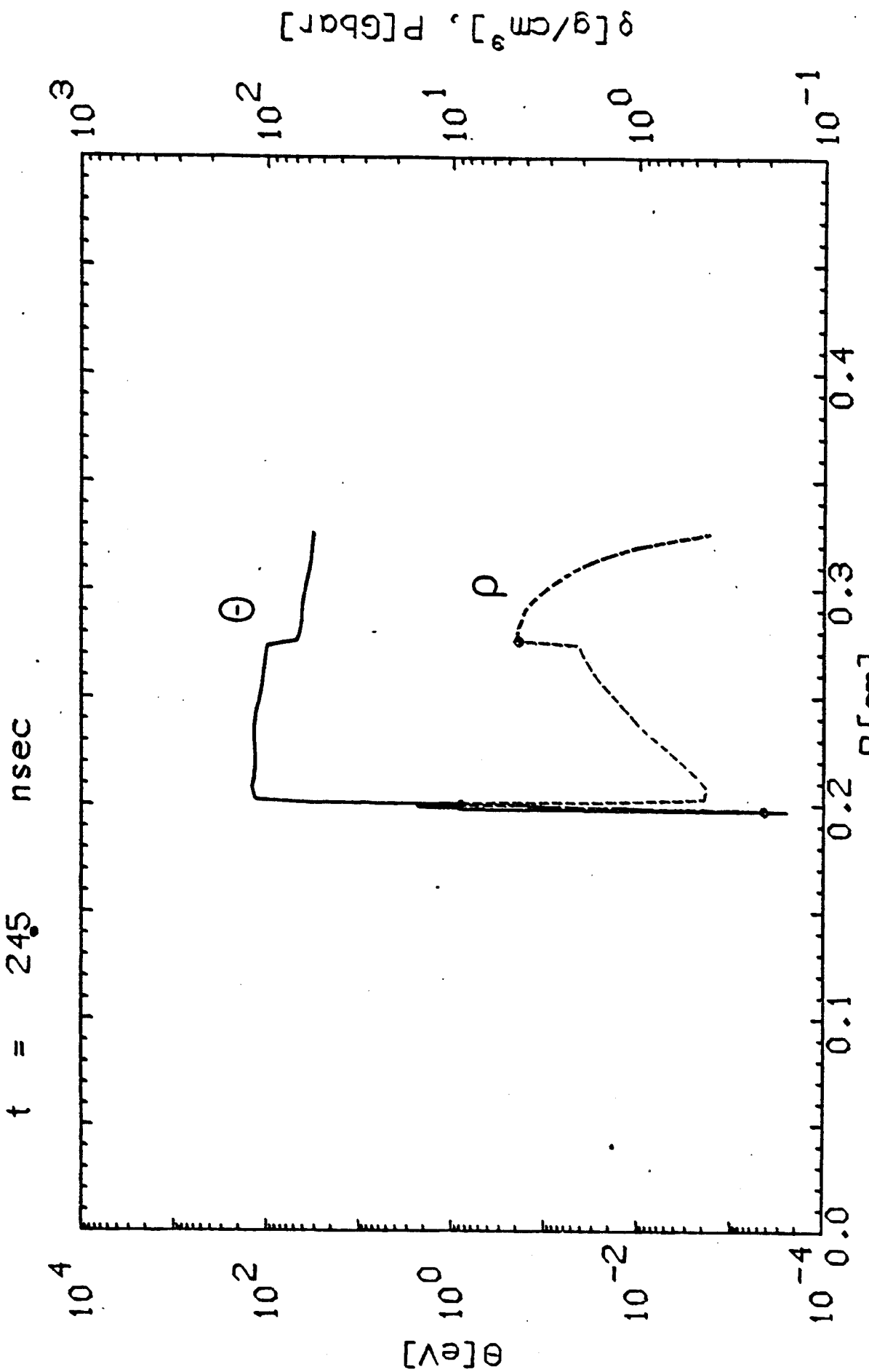
ϱ[g/cm³], P[Gbar]
10³
10²
10¹
10⁰
10⁻¹
θ[eV]
10⁴
10²
10⁰
10⁻²
10⁻⁴
0.0
0.1
0.2
0.3
0.4
R[cm]
t = 245 nsec
Θ
ρ

Fig. III.2-16c

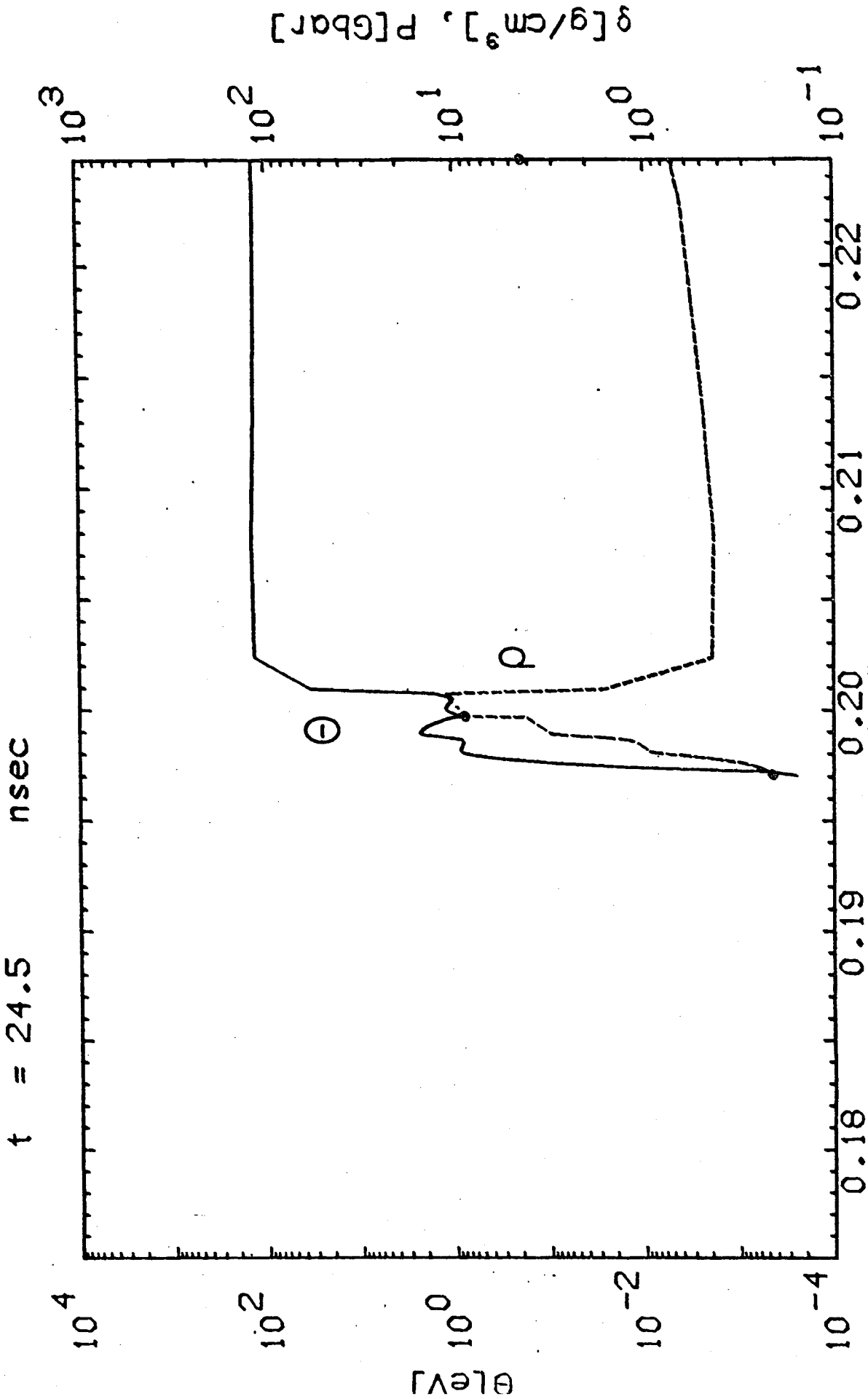

Fig. III.2-16d: Enlarged view of Fig. III.2-16c. First two shocks are seen in fuel.

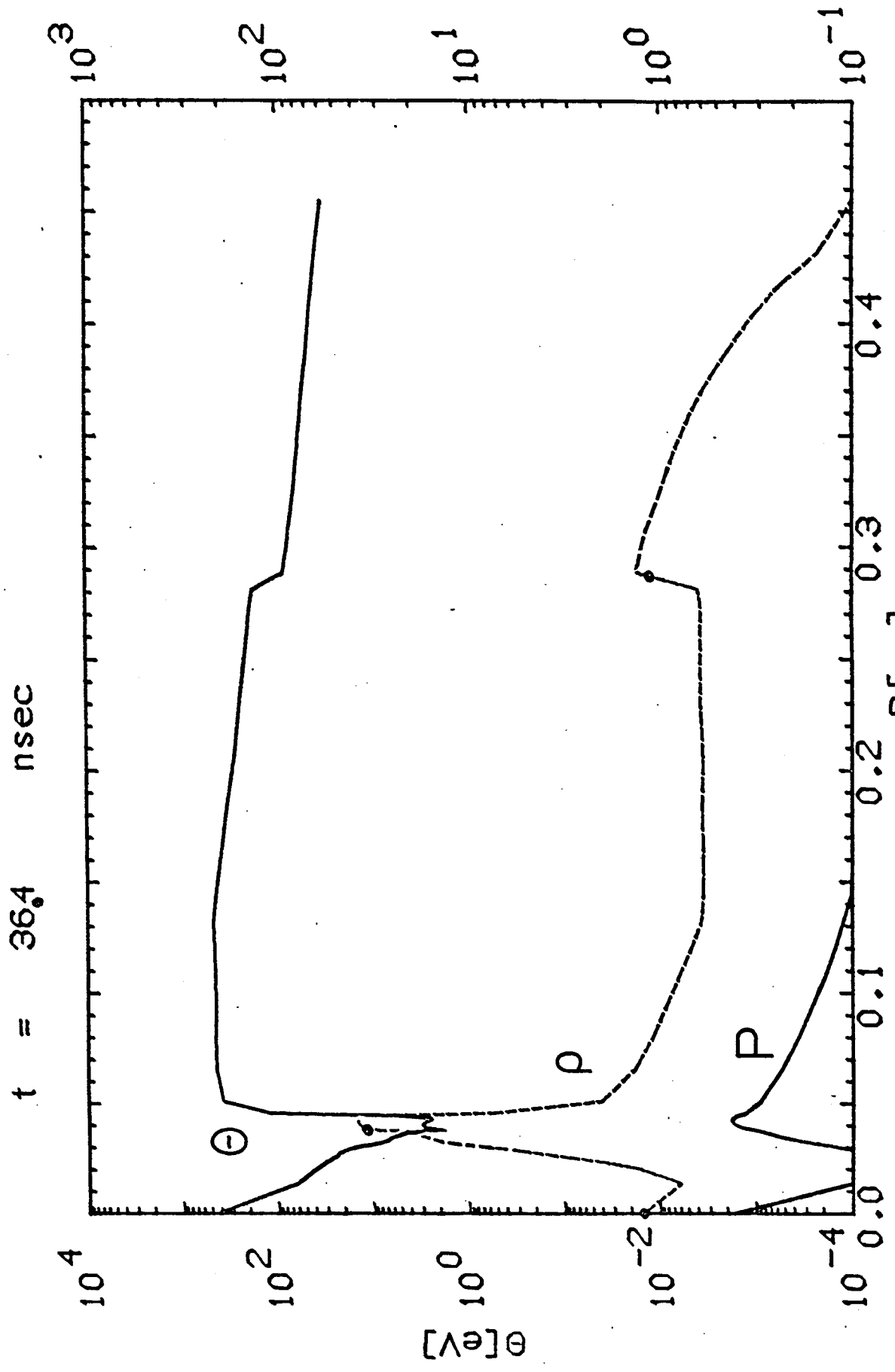

Fig. III.2-16e: Distributions at void closure time. Region of high fuel temperature seen in the centre.

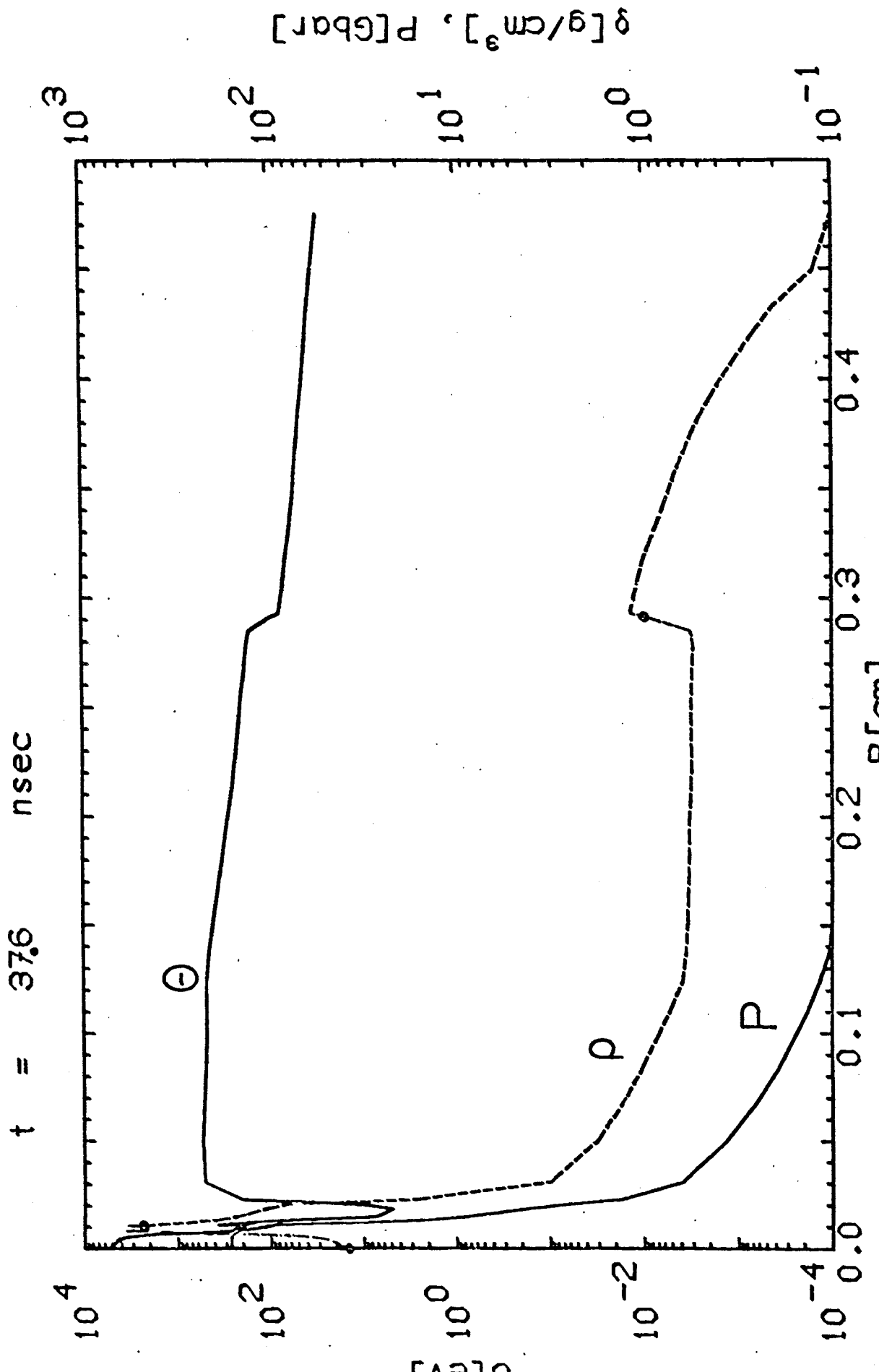

Fig. III.2-16f: Distributions at ignition time.

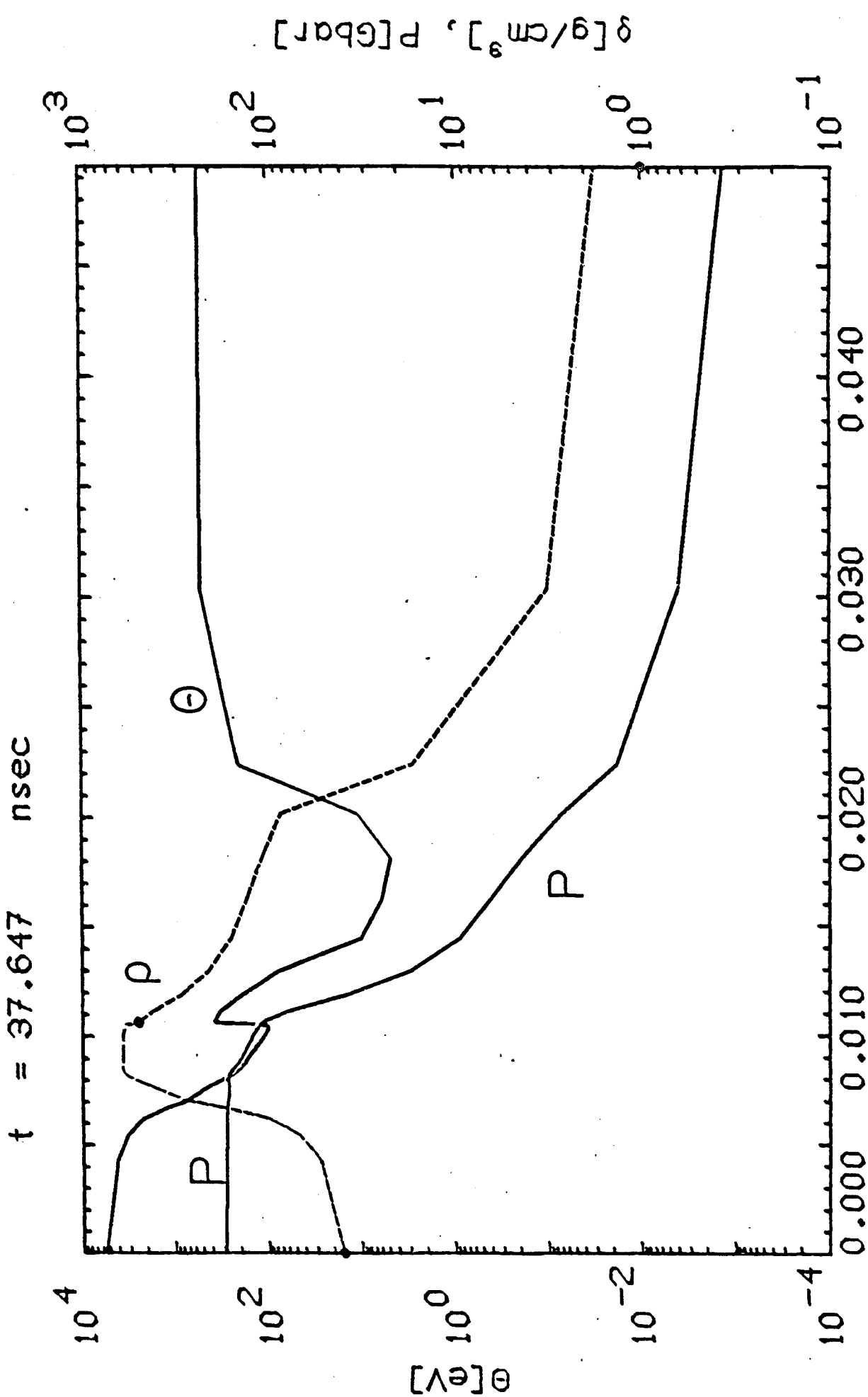

Fig. III.2-16g: Enlarged view of Fig. III.2-16f. The ignition configuration with constant pressure over the fuel is seen for R ≅ 110 μm.

this time, a strong reflected shock has traveled outwards through the fuel and is clearly seen in the pressure profile of Figs. III.2-16f and -16g at a position of 120 μm. (Note that a von Neumann viscosity is used in the hydrodynamic code, and shocks do not appear as sharp discontinuities, but smeared out over several Lagrangian cells). The return shock has finally brought the fuel into the ignition configuration. In Fig. III.2-16g, one should notice

(a) the constant pressure over the fuel of $p \cong 0.17$ Tbar,

(b) the spark region extending to 70 μm with a temperature near 5 keV, a density around 50 g/cm^3 and $(\varrho R)_{spark} \cong$ 0.4 g/cm^2,

(c) the highly compressed fuel region extending from 70 μm to 105 μm with a density plateau at 600 g/cm^3 and a temperature around 150 eV; the total fuel $\varrho R \cong 2.3$ g/cm^2.

These values are very near to those of the HIBALL working point which have been determined within the simple gain model of section III.2.1 and have been listed in Table III.2-1. The present calculation shows that the ignition configuration postulated there can actually be achieved dynamically. In particular, it confirms the key assumption of constant fuel pressure in which our model differs from that of Kidder and Bodner.

At ignition time, the fuel has come almost to rest. The fuel kinetic energy now amounts to 0.07 % of the total input energy, but the internal energy has increased to 4.2 % or 113 kJ. At the same time, there

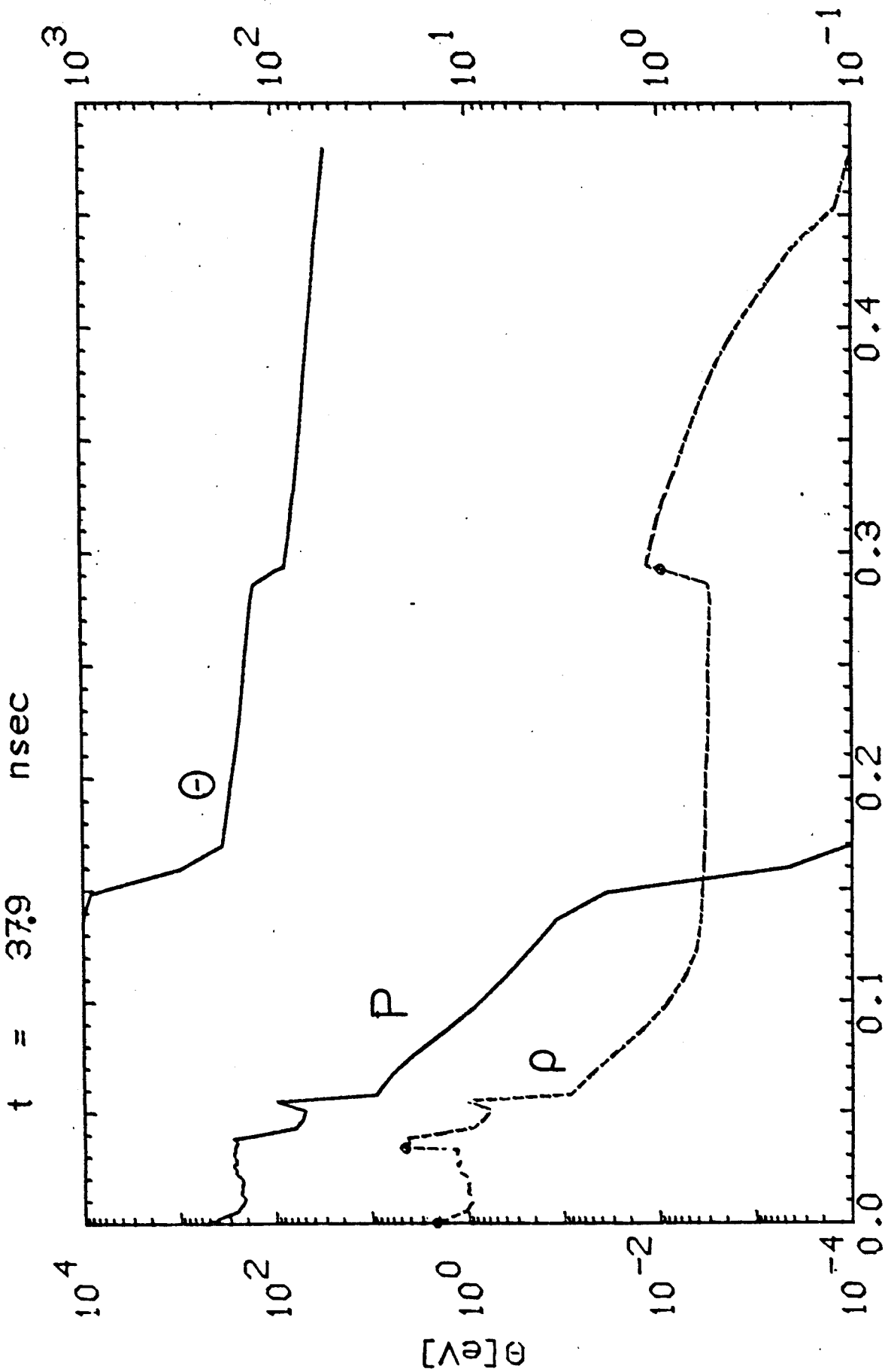

Fig. III.2-16h: Distribution after burn. A heat wave at 0.15 cm is seen travelling to the right far ahead of the burn shock wave at 0.06 cm.

still exists 4.5 % of the energy in form of inward going kinetic energy, mainly located in the massive pusher. The bulk of the energy occurs as internal energy of PbLi ($\approx$ 43 %) and as energy of the tamper (18 % internal, 30 % kinetic). The absorber/tamper interface has hardly moved during the implosion, but about half of the beam energy has been deposited in the tamper and Pb is strongly flowing outwards at this time.

After ignition, it takes roughly 200 psec until burn has spread into the dense fuel region, and fusion energy is released in a short burst of about 20 psec. Fig. III.2-16h displays the situation shortly after burn. The central temperature is now above 10 keV, the burned up fuel is expanding, the outgoing burn shock sits at 0.6 mm, but has been left far behind by a fast moving heat wave with the front located at 1.5 mm. The calculated gain is 212, corresponding to a burn rate of 80 %. Such a high burn rate is probably unrealistic and expected to be degraded by effects (e.g. nonsymmetric implosion) not simulated in our code. In the present calculation, it is explained by the strongly tamping effect of the pusher ($(\varrho R)_{Pusher} \approx 3$ g/cm^2) and its high, inwards directed kinetic energy during burn time.

III.3.4.4 Pulse shape, shocks, ignition

The formation of the ignition spark and how it is related to the pulse shape is now discussed in some more detail. The problem is to drive a certain inner part of the fuel to a much higher isentrope than the rest of the fuel, the entropy of which should be kept as low

as possible. In pure gas dynamics, which are approximately valid for the imploding fuel, the entropy of a fluid element is a constant of motion as long as no shock passes through. The amount of entropy increase due to a shock depends on its strength in a non-linear way. The concept followed in the present design work to achieve an optimal ignition configuration is schematically outlined below and then illustrated by showing the fuel entropy evolution in the code calculation. It involves a sequence of 4 shocks passing through the fuel.

I. Prepulse shock

The prepulse (few TW) launches a 1. shock S1 which homogeneously heats the cryogenic fuel to a temperature of about 0.5 eV.

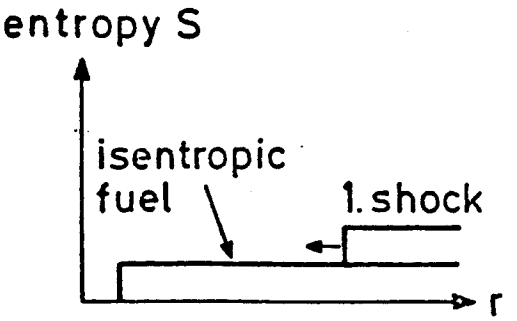

II. Main pulse shock

The main pulse (some 100 TW) launches a second shock S2 into the fuel which is timed to overtake S1 near the inner fuel surface.

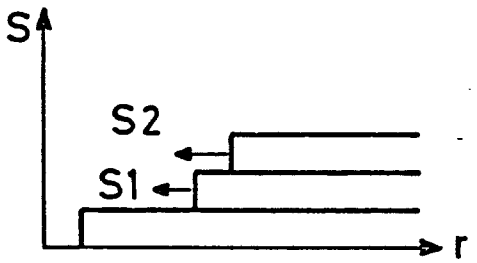

The combined shock S12 is much stronger than the sum of the original shocks and produces a region of higher entropy.

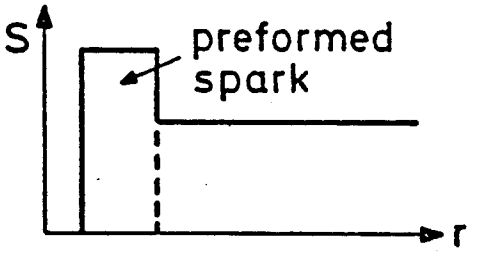

III. The bounce shock

The bounce shock (see section III.2.3.4.2) passes through a sloping density profile near the inner fuel surface and selectively adds entropy to this region.

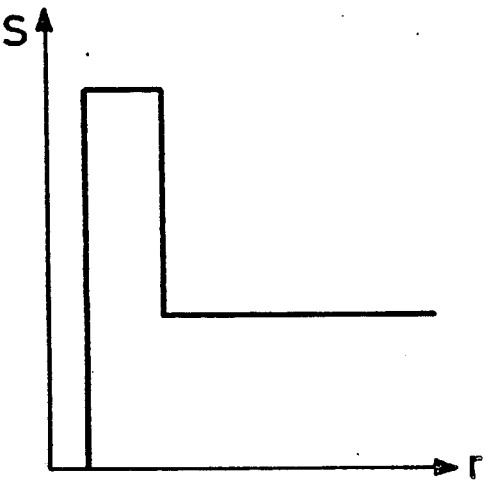

IV. The return shock

The return shock from central collapse finally shapes the spark and brings it to ignition temperature.

In Fig. III.2-17, it is shown to which extent this schematic ignition concept works in the actual code calculation. The ratio ($p/\ ^{5/3}$) normalized to its value for a degenerate electron gas has been chosen as an approximate measure for the entropy and has been plotted over the fluid cells of the Lagrangian mesh for different stages of the implosion Cell. 1 is located at the inner surface of the fuel, cell 36 at the interface with the pusher. For 24 nsec, one observes the first two shocks S1 and S2 as jumps in the entropy distribution (compare the corresponding density jumps in Fig. III.2-16d). At 27 nsec, both shocks have passed the fuel. The timing has been such that S2 has caught up with S1 at Lagrange cell 6, and then the combined shock S12 has propagated further to the left and has generated a region of increased entropy over the last few cells. The preformed spark is clearly seen in the 27 nsec curve. The next increase in entropy is due to the third shock created by fuel bouncing. At 31 nsec,

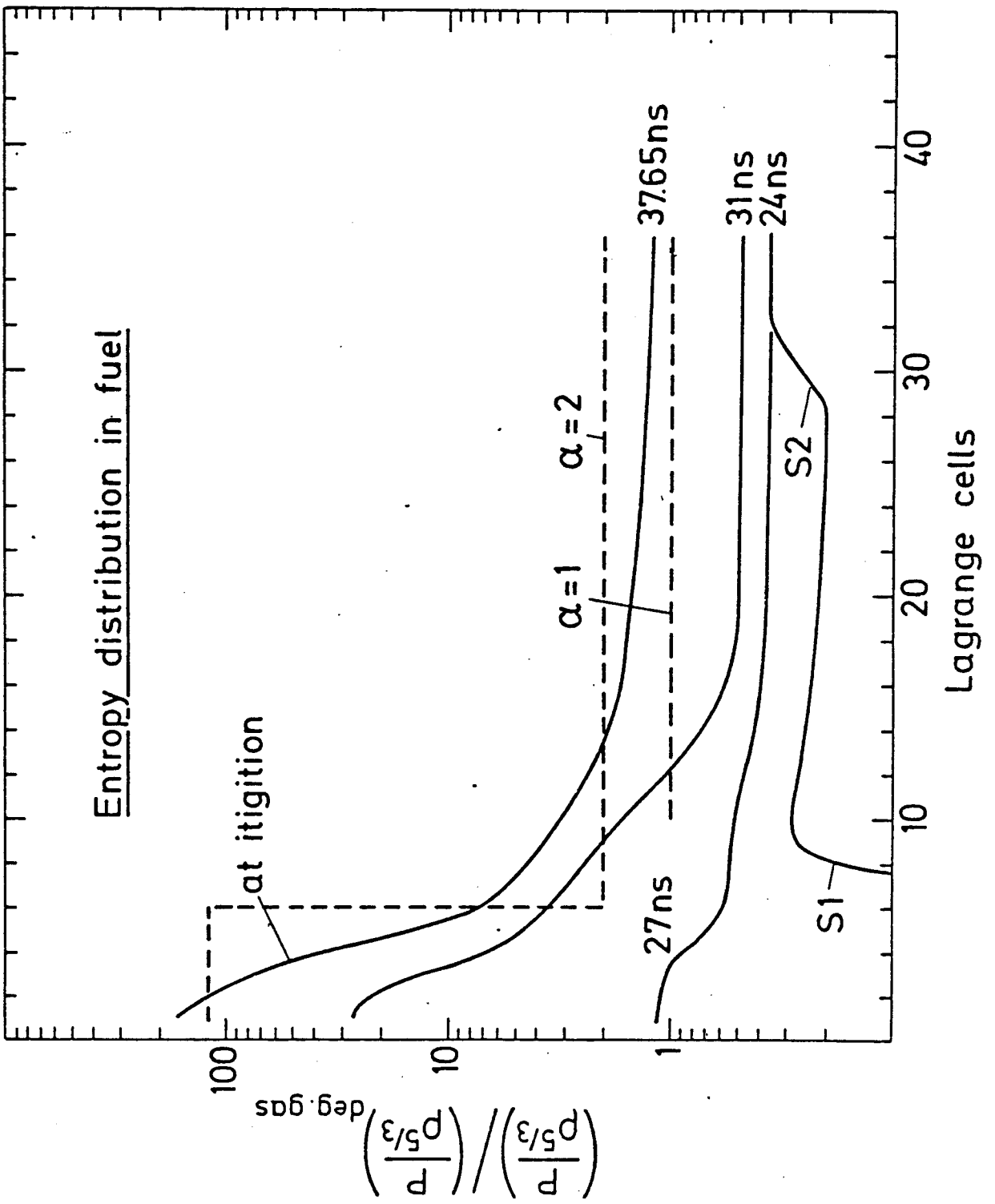

Fig. III.2-17: Time evolution of $(p/\rho^{5/3})$ distribution in fuel.

it has already passed the fuel, but the entropy curve at this time shows what has happened. In propagating through the fuel to the left, the bounce shock has met at Lagrange cell 16 with a rarefaction wave running to the right. This has caused the sharp entropy increase towards the inner surface. Finally, at 37.65 nsec, after passage of the return shock, the $p/\varrho^{5/3}$ curve for the ignition configuration (compare Fig. III.2-16g) is obtained. Its lower part corresponds to the highly compressed, electron degenerate fuel. Notice that this part cannot be directly compared with the other curves of the plot due to the electron degeneracy. Entropy is calculated differently in this case. This becomes clear from the broken curve labelled by $\alpha = 1$ which represents the lowest isentrope possible for the degenerate gas. However, it is interesting that the degenerate branch lies very close to the optimal isentrope $\alpha = 1$. This is indeed an optimal run. Not withstanding the 4 shocks which have gone through the fuel, the overall compression has been almost adiabatic. The $p/\varrho^{5/3}$ distribution assumed in the gain model of section III.2.1 for the HIBALL pellet is given in Fig. III.2.-17 by the broken line $\alpha = 2$, including the spark region at the left with a much higher isentrope. It compares well with the code run.

It is concluded that the idealized ignition configuration assumed by the gain model can approximately be obtained by implosions with optimized pulse shape. With the ignition concept described above, size and form of the spark is mainly determined by the timing of the first 2 shocks which is related to the length of the prepulse and to the power of prepulse and main pulse. The exact values to be chosen also depend on the actual pellet configuration. One problem has been to make the second shock strong enough for reaching final ignition. It has been solved by taking

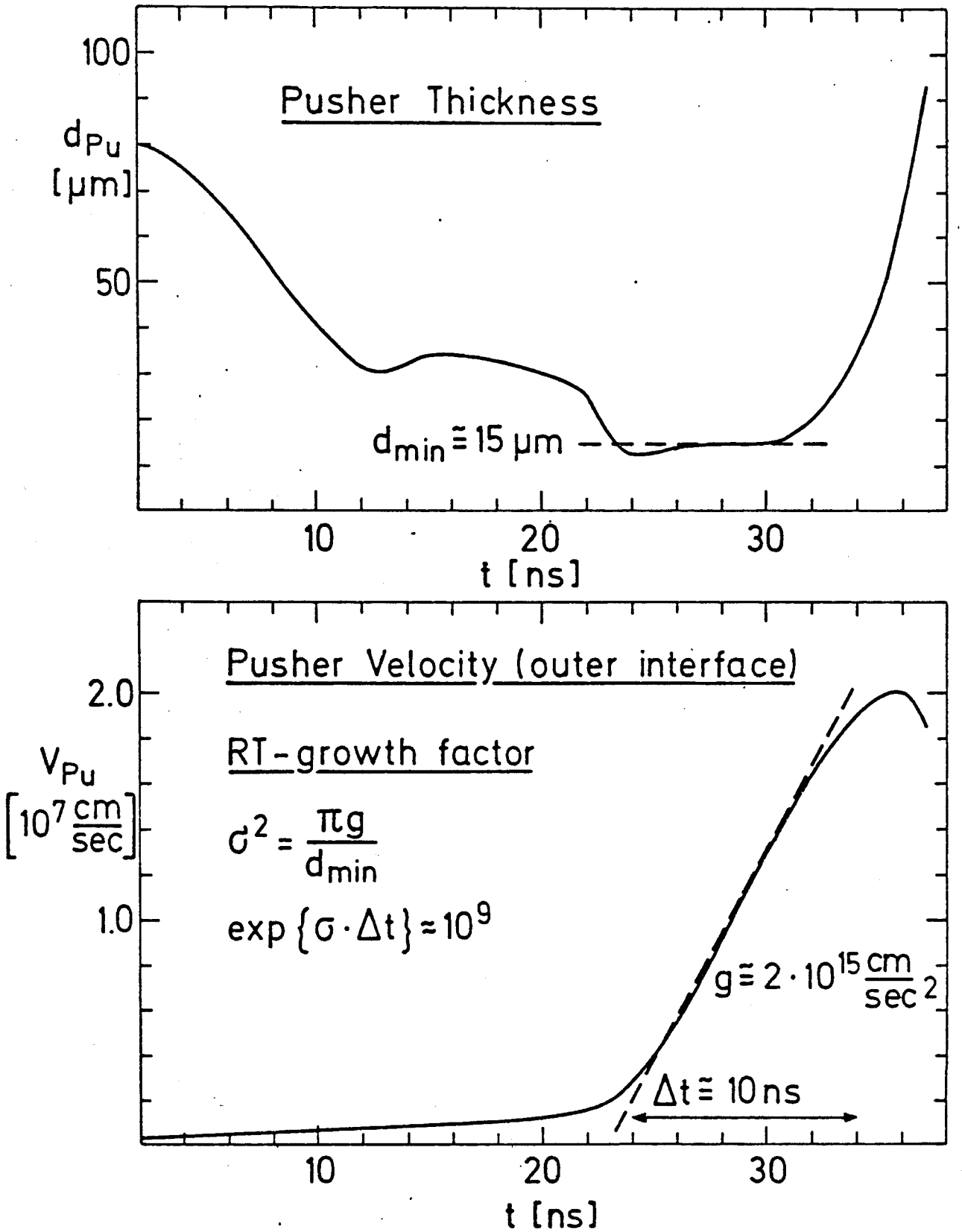

Fig. III.2-18: Pusher thickness and velocity of the pusher/fuel interface as a function of time.

a short rise time of the main pulse. A general experience with these heavy reactor targets is that it is easy, at least in 1D-calculations, to obtain high compression in terms of (ϱR), but it is difficult to achieve high enough temperatures in the centre. The ignition requirement sets the lower bound for the beam power. Certainly more power than 240 TW is needed to make the present design less sensitive to the pulse shape.

III.2.3.4.5 Estimated growth of Rayleigh-Taylor instability

Symmetry is an even more critical point than ignition. A rough estimate shows that the present design fails due to RT-instability. The pusher region is probably not thick enough to survive this fluid instability. Since no 2-dimensional code was available to follow the evolution of the instability in detail, the growth rate has been estimated by applying linear RT-theory for an incompressible fluid. The ingredients for our analysis are given in Fig. III.2-18. The upper plot shows the evolution of pusher thickness with time. It is seen that the pusher is strongly compressed during implosion and has a thickness $d_{min} \cong 15$ µm at the time of maximum acceleration which amounts to $g \cong 2 \times 10^{15}$ cm/sec^2 as seen from the velocity plot in Fig. III.2-18. The pusher is subject to RT-instability, since it has high density and is accelerated by low density absorber material. The density gradient at the interface is very steep (compare Figs. III.2-16b-e), and the Atwood number is $\cong 1$. We have chosen $k_{crit} \cong \pi / d_{min}$ for the wave number of the most critical mode. The exponential growth rate

$$\sigma = (\pi g / d_{min})^{1/2}$$

then leads to an estimated growth factor

$$\exp\{\sigma \cdot \Delta t\} \cong 10^9$$

taking as the relevant implosion time $\Delta t \cong 10$ nsec. Such a growth rate will certainly destroy the symmetry of the pusher during implosion and will prevent burn. According to the simple analysis, a pusher 4 times as thick would lead to a growth factor of $\approx 10^5$ which might be tolerable.[21] It may be that these formulas of linear RT-theory overestimate the growth of the instability and that nonlinear effects (see e.g. ref. 22) not taken into account here improve the situation. But there is little doubt that symmetry is a most critical issue in this design. A more massive pusher may help, although it will be compressed to higher densities and the thickness at maximum acceleration will not increase linearly with mass. Also, a more massive pusher will require more beam power for implosion. The symmetry problem has to be studied in much more detail including the question of initial perturbations and irradiation asymmetry.

III.2.4. Conclusion

A pellet design for heavy ion beam fusion has been presented displaying the different stages of implosion and describing the physical mechanisms such as beam deposition, the relation between pulse shape, shock evolution and ignition, and also pusher dynamics and implosion symmetry. An elementary version of heavy ion stopping theory has been outlined, studying in particular the temperature dependence of stopping powers and ranges. In addition, a gain model has been developed which is based on the results of the explicit design and allows for scaling

of various parameters. It produces gain curves similar to those obtained by the Livermore group and provides a physical interpretation. The model differs from that of Kidder and Bodner in the assumption of constant pressure over the fuel at ignition.

With respect to HIBALL, the gain model yields the HIBALL working point with a gain of 83 at an input energy of 4.8 MJ in a natural way. It corresponds to a hydrodynamic efficiency of 5 % and a compressed fuel isentrope of $\alpha = 2$ in close agreement with the explicit design. Concerning the beam power, however, the code calculation indicates that 240 TW, assumed for HIBALL so far, are insufficient to insure a stable and igniting implosion. The present design achieves ignition at 240 TW only with a highly optimized pulse and will not survive RT-instability. It requires more beam power to improve on both points. Also, consideration of a more realistic equation of state and of radiation losses will increase the requirements on beam power, probably to a level of 500 TW. A final remark should be made with respect to the pulse shape. It has turned out that a carefully timed prepulse is important for effective ignition and should be taken into account in the general HIBALL design.

References

1. S. Bodner, NRL Memorandum Report 4453 (1981).

2. R.E. Kidder, Nucl. Fus. 16 (1976) 405.

3. R.E. Kidder, Nucl. Fus. 19 (1979) 223.

4. J.H. Nuckolls, in LLL Laser Program Annual Report 1979, vol. 2, p. 3-2.

5. H. Geissel, T. Kitahara, Y. Laichter, and P. Armbruster, 'Stopping powers of 0.2-1.4 MeV/u heavy ions in solids', preprint GSI Darmstadt (1980).

6. R. Bimbot, D. Gardes, H. Geissel, T. Kitahara, P. Armbruster, A. Fleury, F. Hubert, Nucl. Instr. Meth. 174 (1980) 231.

7. L.C. Northcliffe and R.F. Schilling, Nuclear Data Tables A7 (1970) 233.

8. F. Hubert, A. Fleury, R. Bimbot, D. Gardes, Ann. Phys. (Fr.) 5 (1980) 1.

9. R.O. Bangerter, Proc. Heavy Ion Fusion Workshop, Report ANL-79-41, p. 415 (1979).

10. D. Jackson, 'Classical Electrodynamics' p. 641ff, Wiley, New York (1975).

11. T.A. Mehlhorn, Report Sand 80-0038 (1980).

12. K.A. Brueckner and N. Metzler, 'Stopping power for energetic ions in solids and plasmas', preprint UCSD (1980).

13. J.E. Rogerson, NRL Memorandum Report 4485 (1981).

14. V.S. Nikolaev and I.S. Dmitriev, Phys. Lett. 28A (1968) 277.

15. K.A. Brueckner, N. Metzler, and R. Janda, Phys. Fluids 24 (1981) 964.

16. K.A. Brueckner and N. Metzler, 'Targets for heavy ion fusion', preprint UCSD (1980).

17. J.D. Lindl and R.O. Bangerter, Report UCRL (1980).

18. R.O. Bangerter and D.J. Meeker, Report UCRL 78474 (1976).

19. S. Jorna, N. Metzler, and P. Hammerling, Phys. Lett. 80A (1980) 308.

20. J.P. Christiansen, D.E.T.F. Ashby, and K.V. Roberts, Comp. Phys. Commun. 7 (1974) 271.

21. R.O. Bangerter, J.D. Lindl, C.E. Max, and W.C. Mead, Report UCRL 77 048 (1975).

22. Ril. McCrory, L. Montierth, R.L. Morse, C.P. Verdon, Phys. Lett. 46 (1981) 336.

III.3 Target Design at KfK

III.3.1 Introduction

At the Institute for Neutron Physics and Reactor Technology, an advanced and extended version of the MEDUSA code is being used to design targets for the ICF reactor study, HIBALL. The design of targets for ICF is a very complicated and involved problem and therefore use of a large computer code such as MEDUSA is essential. In order to be credible such a code must be carefully written and extensively tested on benchmark problems. The original version of the MEDUSA code was written by Christianson, Roberts, and Ashby [3] at the Culham Laboratory, England. The code has been extended by Evans and Bell[4,5] of the Rutherford Laboratory (EOS, fast electron transport, etc.), and Tahir and Laing[6,7] of Glasgow University (radiation transport, ionization, etc.). Further extensions have been made by Tahir and Long[1,2] at KfK, Karlsruhe, in order to transform the code into a fusion design code (multi-shell hollow targets, radiation transport, ionization for heavy elements, etc.) for ion beam fusion, and heavy ion beam fusion in particular. In section III.3.2 the physics and numerical techniques of MEDUSA are presented. In this section the importance of realistic physics for accurate and meaningful simulations is stressed, in particular the fact that a realistic EOS is essential. In section III.3.3 the effect of radiation transport on target simulations is discussed. The energy deposition of ions in hot plasmas is treated in section III.3.4, and in particular the deposition profile in the HIBALL target is presented. Extensive simulation studies of various targets have been carried out during the last year. First of all calculations of a target proposed by Bangerter for light ions are presented. The computer code MEDUSA has been used to reproduce these calculations done at Livermore around 1976, which establishes the credibility of the code as a target design code.

Finally, the HIBALL target has been simulated and first results are presented in section III.3.5. Various conclusions are drawn from these calculations and these are given in section III.3.6.

III.3.2 The Physics and Numerical Methods in MEDUSA

The MEDUSA codes is a well-known and well-tested code, because an intermediate version of the code has been published. The code, however, has been improved and extended in many ways since this version appeared. The physics in the code is as follows,

1. The code is a one-dimensional Lagrangian code which calculates plane, cylindrical and spherical geometry.
2. It is a THREE temperature code, one temperature each for ions, electrons, and thermal radiation. The ions and electrons need separate temperatures in order to give a correct treatment of shock heating. During the burn phase the ion temperature becomes considerably higher than the electron temperature, so this is very important for an accurate study of the physics of the burn phase. It is important also that the radiation field have a separate temperature for reasons explained in section III.3.3.
3. The thermal conduction is due to electrons and radiation and both are flux limited. Flux limited conduction is vital in regions where there are very large temperature gradients, for instance at the outside of the shell and during the burn phase.
4. The code treats any type of multi-shell, multi-material spherical pellet, and can calculate single and double shell targets.
5. Fast electron transport is included as well as a treatment of the ponderomotive force. These facilities are necessary in laser driven targets.

6. Absorption routines for both laser and ion beam fusion are incorporated. At the present time the ion beam deposition is calculated using analytic formulae, in which the range and the deposition profile can be changed.
7. The energy deposition of α-particles produced during the burn is treated locally and the neutrons produced during the burn are allowed to escape freely.
8. The equation of state of the ions is the classical ideal gas EOS. The EOS of the radiation is that of blackbody radiation. The equation of state of the electrons is in general more important than that of the ions because there are more of them. In the original version of MEDUSA the electron equation of state was either that of an ideal gas or of a degenerate or non-denerate (as the case may be) Fermi-Dirac gas. These equations of state have been replaced (although they are still available as options within the code) because they cannot handle problems such as ionization and motion of electrons within the atomic potentials of the ions plus bound electrons. The ionization energy, for instance, represents an important sink of energy which is then not available for compression. Radiation is another such sink, and both these points have been made very strongly by D. Henderson(*) in discussing the dangers of using over-simplified codes. A Thomas-Fermi EOS has therefore been made available and as further sophistication, a corrected Thomas-Fermi model which includes quantum and exchange forces is available. The EOS produces a very good fit to the Los Alamos EOS tables (see Fig. III.3-0), and further allows for the total pressure to be zero at solid densities, so that materials do not expand unphysically when they are cold. Studies that we

*Private communication, "Simple H.I.F. targets are sensitive to physical models".

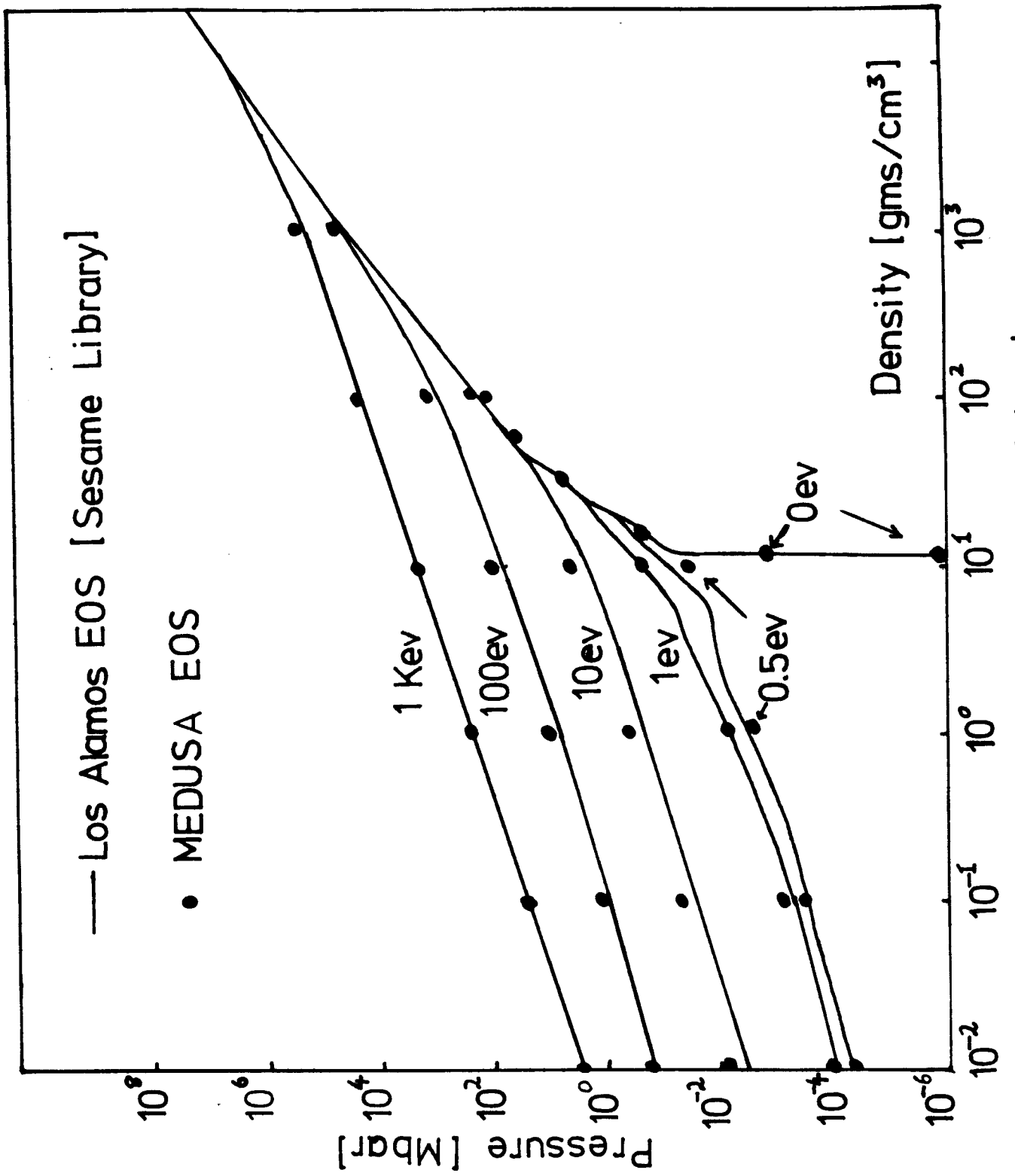

Fig. III.3-0. Equatio of state of Lead

have made show that with the use of an ideal EOS, unrealistically high gains can be produced (even without much tuning), which then disappear when the corrected Thomas-Fermi EOS is used.

9. Ionization states are calculated by use of the SAHA equation, and the average ionization $\langle Z \rangle$ and average squared ionization $\langle Z^2 \rangle$ used in various transport coefficients are also calculated by the SAHA routine. The TRIP time dependent ionization and atomic physics package is also incorporated in the code.

The hydrodynamic and energy equations are solved numerically in MEDUSA. The equation of motion is treated explicitly while the energy equations are solved by the Cranck-Nicolson implicit method and Gauss's elimination scheme. Since the energy equations are non-linear, an iterative scheme is used to check the convergence of the numerical solution. Typically 5 to 10 iterations are required for convergence. Since the equation of motion is solved explicitly, the time step must be restricted by the C.F.L. (Courant, Friedrichs, and Levy) condition. For reasons of accuracy, the time step is also monitored by the time variation of T_e and T_i.

A typical MEDUSA run without radiation transport takes up to 15 minutes of CPU time on an IBM 3032 computer when calculating the 4 mg DT HIBALL target. With radiation transport a typical run takes up to 30 minutes.

III.3.3 The Importance of Radiation Transport in ICF Target Simulations

Radiation effects can be of considerable importance in the ICF target simulations for the following reasons.

The thermal radiation produced by the thermal electrons in the absorption region can preheat the fuel and set the compression on a higher adiabat. This could degrade the final fuel density, which in turn, could reduce the target yield.

The thermal radiation may be helpful in smoothing out irradiation asymmetries.

The radiation losses from the target surface can be significantly large and may be reduced by an appropriate target design.

Radiation may be helpful to propagate thermonuclear burn from the ignition region into the surrounding dense and relatively cold fuel.

From the above considerations it is clear that the radiation can influence the compression and the burn propagation in an ICF target. It is, therefore, very important to include a radiation transport model in the hydrodynamic code, when designing a target for a reactor study. The updated version of the computer code MEDUSA used at KfK includes a steady state, single group radiation diffusion model which can simulate transport of total continuum radiation arising from free-free and free-bound transitions taking place in the plasma. This model has been developed by Tahir et al.[6,8] to simulate radiative preheat effects in laser-compression experiments performed at the Central Laser Facility, Rutherford Laboratory. Some typical results are published in ref. 9 and 10.

It is to be noted that the applicability of the above model requires that the radiation field is in local thermal equilibrium with the electrons. This assumption is valid in the target core but does not hold in the corona region. In the latter region the radiation field may be accurately represented by a multi-group radiation model. In general, multi-group radiation transport models involve a large amount of CPU time. When such a model is included in a hydrodynamic code, the CPU time requirements for the target simulations become prohibitively large. Tahir et al.[12] have proposed a multi-group treatment of radiation transport which will make use of the ICCG[11] numerical methods and will be very efficient compared to the standard

multi-group models. The entire radiation field in this model is divided into a large number of groups (typically 20) which transport radiation energy in real space as well as in energy space. Diffusion in energy space takes place via electron-radiation interaction.

This model is being developed at KfK in collaboration with the Central Laser Facility, Rutherford Laboratory. We will incorporate this model into MEDUSA in order to take account of various radiation effects and to design a target for the HIBALL II reactor study.

III.3.4 Energy Deposition in the HIBALL Target. The Energy Deposition Code GORGON

The distinguishing feature of ion beam fusion is, of course, that the energy is deposited by ions rather than from a laser. The original MEDUSA code was written as a laser fusion code and therefore modifications have to be made in order to transform it into an ion beam target design code. This is being done in two stages. The first stage consisted of using simple analytic formulae for $\frac{1}{\rho}dE/dx$ and these formulae are cold formulae. However, one could expect that energy deposition would change considerable as the material heats up and forms a plasma consisting of free electrons and partially ionized atoms, since scattering from ions and electrons could be expected to be different than from neutral atoms. Hence one needs to develop a code based on a definite physical model that can calculate $\frac{1}{\rho}dE/dx$ as a function of density and temperature within the ranges of interest namely, 0 to 500 eV and ρ_s and $\rho_s/100$. Then as a beam of ions is incident on a target, energy loss in each cell can be calculated as a function of the thermodynamic state of that cell, and this energy loss is then subtracted from the ion energy and the new energy is used to calculate dE/dx in the next cell. This procedure is continued until the ion energy is zero which then defines the range. The ranges of protons

in the 2 to 10 MeV range and heavy ions in the range 5 to 20 GeV are such that they are very well-suited to imploding targets of the size to be encountered in I.C.F. This is not really surprising when one realizes that the lower bound of the mass of DT in the target is fixed by the requirement that the hot burning target should re-absorb the α-particles emitted in the DT reaction.[29] The upper bound is of course fixed by the size of the micro-explosion that can be contained in a reactor chamber. A typical range for Bi^{++} in lead is $\sim 3 \cdot 10^{-2}$ gm/cm^2 or 0.3 mm, for a 10 GeV ion, whereas shell thicknesses for fusion targets are of the order of 0.5 mm.

An energy deposition code, GORGON, based on refs. 14 and 15 has been developed including modifications and extensions described below which are designed to deal with various physical effects. An ion travelling through a charged plasma loses energy mainly to the electrons,[16] by a series of small angle collisions. In each individual collision the amount of energy lost is very small, but because of the long range of the electrostatic forces, there are very many such collisions, so the total energy loss is quite large. The mass of the ion is much larger than the mass of the electron, so that the ion is deflected through small angles and one can consider the ion as travelling in a straight line. The projectile ion is further considered to be a point charge with specified energy, mass and charge (which may change with velocity, see below). The plasma is considered to be either degenerate or non-degenerate as the case may be.

The physical model used in the calculation is based on the distinction between the contribution of bound and free electrons in the target plasma. Free electrons are those having a wave function that extends to infinity (i.e., $\sim e^{i\underline{k}\,\underline{r}}$) and bound electrons are those whose wave function goes as e^{-kr} at large r, therefore not having infinite extent.

The contribution of the bound electrons to the stopping power is calculated according to Bethe's theory[17], taking into account the differences in characteristic excitation energies between a neutral atom and a plasma ion via the Thomas-Fermi model. The contribution of the free electrons is calculated using the dielectric theory for non-degenerate electrons with a more simplified theory being used if the electrons are degenerate.

Calculation of the plasma parameters:

In the model used in this calculation knowledge of the average degree of ionization in the plasma is required, because of the separate treatment of bound and free electrons. This is done using the Thomas-Fermi model of the atom at finite temperature. For this purpose the Thomas-Fermi model is solved using the methods described by Latter[18], which yields values for the electron density distribution in the atomic sphere n(r) for a given density and temperature of the target material, as well as the potential V(r) and the chemical potential α. The number of bound electrons which yields the average degree of ionization is given in the Thomas-Fermi model by,

$$N_b = \frac{32\pi^2}{h^3} \int_{-\infty}^{o} \frac{dE}{[\exp(E-\alpha)kT + 1]} \int_{o}^{r(E)} m[2m(E+eV(r))]^{1/2} r^2 dr \qquad \text{(III.3-1)}$$

where E is the total electron energy, m is the electron mass, T is the temperature, k is Boltzmann's constant, h is Planck's constant and r(E) is the radius which satisfies the condition,

$$eV(r(E)) = - E \qquad \text{(III.3-2)}$$

i.e., where the kinetic energy of the electron just equals its potential energy. From the number of bound electrons the number and density of the free

electrons are determined and used in the calculation of the stopping power due to the plasma free electrons. The calculated structure of the ions is used to determine the bound electrons contribution to the stopping power.

Stopping power due to bound electrons:

The contribution of bound electrons to the stopping power is calculated by Bethe's theory[19], including corrections due to the differences between a plasma ion and a neutral atom. The basic physical parameter is the average excitation energy I, defined by

$$\ell nI = \frac{1}{N} \sum_i \ln(\hbar\omega_i) \qquad \text{(III.3-3)}$$

where N is the number of bound electrons participating in the slowing down process and $\hbar\omega_i$ are the characteristic excitation energies. In these calculations the ω_i's are interpreted as the frequencies of revolution, following Bohr's model[20]. In order to calculate I within the framework of the Thomas-Fermi model one notes that at each radius r, a spectrum of revolution frequencies is determined by the Fermi energy distribution at this radius

$$\omega(r) = [(2/m)\{E + eV(r)\}]^{1/2}/r \qquad \text{(III.3-4)}$$

Here E is the total electron energy. The number of electrons per unit frequency having a revolution frequency ω is,

$$n(\omega) = (32\pi^2\omega^2m^2/h^3)$$

$$x \int_0^{r_{max}(\omega)} r^5 \left(\exp\{[\tfrac{1}{2} m\omega^2r^2 - eV(r) - \alpha]/kT\} + 1\right)^{-1} dr \qquad \text{(III.3-5)}$$

Here $r_{max}(\omega)$ is the radius beyond which the energy which corresponds to ω yields a free electron, i.e.,

$$eV(r_{max}(\omega)) = - E \qquad \text{(III.3-6)}$$

The effective excitation energy is given, within the framework of this model, by

$$\ln I = \frac{1}{N} \int_0^\infty n(\omega) \ell n(\hbar\omega) d\omega \qquad \text{(III.3-7)}$$

A shell correction is included in the calculation by eliminating from the integration in Eqn. (3-7) those electrons for which

$$2mv^2 < \hbar\omega \qquad \text{(III.3-8)}$$

where v is the projectile velocity.

The solution of the Thomas-Fermi model, provides the required values of V(r) (the potential), α (the chemical potential) and n(r) the electron density required in the above integrations.

Stopping power due to free electrons:

The free electron contribution to the stopping power is calculated using the plasma dielectric theory[21,22,23]. The energy loss is given by,

$$\frac{dE}{ds} = - \frac{2e^2 Z^2_{eff}}{\pi\rho} \int_0^\infty k dk \int_0^1 \mu d\mu \ \text{Im} \left(\frac{1}{D(k,\omega=k\mu v)}\right) \qquad \text{(III.3-9)}$$

where ρ is the density, $s = \rho x$ where x is a distance into the material, v is the projectile velocity, k is the wave number, $\mu = \cos\Theta = \underline{k}\cdot\underline{v}/|\underline{k}\cdot\underline{v}|$ D is the dielectric function of the plasma and ω is the frequency. In calculating the

dielectric function a classical, non-degenerate plasma is assumed and collisions in the plasma are taken into account. The collision time is given by,

$$\tau = 3m^{1/2}(kT)^{3/2}\,[4(2\pi)^{1/2}e^4 Z_{eff} n\ell n\Lambda]^{-1} \qquad \text{(III.3-10)}$$

where n is the free electron density, Z_{eff} is the average ion charge, $\ell n\Lambda$ is the Coulomb logarithm. The dielectric function is given by

$$D(k,\omega) = 1 + 2x^2\{1 + xZ(\xi)\}\omega_p^2/\omega^2 \qquad \text{(III.3.11)}$$

where $\xi = x+iy$, $Z(\xi)$ is the plasma dispersion function, $x = \omega/kV_t$, $y = \nu/kV_t$, ν is the collision frequency, V_t is the free electron thermal velocity, $V_t = (\frac{2kT}{m})^{1/2}$. An upper cutoff wave number is used in the integration in eqn. 3-9 following Bethe[19],

$$k_B^{-1} = e^{-\gamma}\hbar/mV_t$$
$$\gamma = 0.5772 \qquad \text{(III.3-12)}$$

Certain additions have been made recently in order to improve the physics in the code and to allow the code to calculate stopping powers for heavy ions. The model now includes an option which allows the calculation of the stopping power of ions in degenerate electrons. This is an important factor for calculating the cold range in metals where up to 5 electrons/atom can be degenerate. Experimental results exist only at room temperature, so the calculations are calibrated on cold material, and it is therefore important to calculate correctly in this limit. The code, as described above, calculates the stopping power of protons very well because the charge on the proton does not change as it passes through the plasma. In principle it could capture an

electron to become a neutral hydrogen atom but since the binding energy is only 13 eV collisions with electrons would prevent this. However for heavy ions say Bi^{++}, entering a plasma, collisional ionization occurs, as does recombination. This is a dynamic process and it takes time for the ion to reach a steady state effective charge when it is travelling at a constant velocity. However, since the velocity is changing continuously it is not clear that the charge state ever reaches a steady state, and it is likely that the effective charge problem should be treated as a dynamic problem. For simplicity in the code at the moment a steady state effective charge formula is used, which is derived by comparing the "cold" experimental results to the Bethe formula. The effective charge is the given by,[24]

$$Z_{eff} = Z_B[1 - 1.034 \exp(-137\beta/(Z_B))^{0.69}] \qquad \text{(III.3-13)}$$

where Z_B is the charge on the ions on the beam, v is the velocity of the ion, and $\beta = v/c$, where c is the velocity of light.

A general formula for dE/dx has the form (from bound electrons),

$$\frac{dE}{dx} = Z_{eff}^2 \omega_p^2 \frac{e^2}{v^2} \quad L \qquad \text{(III.3-14)}$$

where ω_p is the plasma frequency, v is the velocity of the ion, and e is the electron charge. In Bethe's formula L has the form,

$$L_{BETHE} = \ell n \{\frac{2mv^2}{\hbar\omega}\} - \ln(1 - \beta^2) - \beta^2 \qquad \text{(III.3-15)}$$

where $\hbar\omega = I$ is defined above, and m is the electron mass. On the other hand, the classical expression derived by Bohr is given by,

$$L_{BOHR} = \ell n \left(\frac{1.123mv^3}{Z_{eff}e^2\omega}\right) - \ln(1 - \beta^2) - \beta^2/2 \qquad \text{(III.3-16)}$$

A quantum mechanical expression derived by Bloch[13] who attempted to reconcile the two approaches is given by,

$$L_{BLOCH} = \ln \frac{2mv^2}{\hbar\omega} - \frac{1}{2}\ln(1 - \beta^2) - \beta^2/2$$

$$+ \psi(1) - Re\psi\,(1 + iZ_{eff}\alpha/\beta) \qquad \text{(III.3-17)}$$

where ψ is the diagamma function, and α is the fine structure constant.

The Bohr approach is one which uses classical mechanics, and is based on the use of any impact parameter b. For b greater than some impact parameter b_1 collisions are treated as electromagnetic excitations of harmonic oscillators in a constant electric field produced by the passing ion. For $b < b_1$, ions are assumed to scatter from the electrons as if the electrons were free. The Bethe approach uses quantum mechanics and therefore uses momentum transfer to characterize collisions. It considers the ion wave function to be a plane wave of given momentum and treats the ion-atom scattering within the Born approximation. The Bloch approach reconciles these two theories. Block demonstrates that the distant collision part of the Bohr theory is valid quantum mechanically within the dipole approximation. Bloch again assumed that for $b < b_1$ the electrons are free, but relaxed the assumption that the ion should be described by a plane wave. The confinement of the electron within a cylinder of radius b_1 introduces transverse momentum components which interfere with each other under the influence of the scattering potential.

This leads to a scattering cross section which can be very different from the Coulomb cross sections for plane waves.

For very weak scattering b_1 can be large, and plane waves can be used and the Bloch formula tends to the Bethe formula. In the limit of strong scattering wave packets can be constructed which scatter as classical objects and the Bloch formula gives the same results as obtained by Bohr. This happens especially when Z_{eff} is large. In the code the problem is solved by using the larger of two minimum impact parameters, one the quantum impact parameter $\frac{h}{2mv}$ and the other the Bohr impact parameter $(\frac{e^2 Z_{eff}}{mv^2})$, where v is the relative speed between ions and electrons. This effectively changes the Bethe formula over to the Bohr formula.

Another change to the code that has been made, is to include the scattering of the ion off the ions in the plasma. The standard expression originally developed by Chandrasekhar[25] is used. The code can calculate for any type of ion (from hydrogen to uranium) and on any type single element target material, and can be extended to treat mixtures in a simple approximation. Since the code can calculate energy deposition for an ion passing through a degenerate plasma, it can also calculate the energy loss of α particles in degenerate and non-degenerate DT.

The results presented here are confined to those relevant to the HIBALL reactor, and complete results illustrative of the working of the code will be presented elsewhere.[1,26] Figure III.3-1 shows the energy deposition profile of 10 GeV Bismuth ions on lead at 200 eV and in Figure III.3-2 the deposition profile of 10 GeV Bismuth ions in lithium at 200 eV is shown. The deposition profile in the HIBALL target for 10 GeV ions is shown in Figure III.3-3. The range of the ions decreases as the temperature increases from room temperature. Also the deposition profile becomes more peaked at the end of

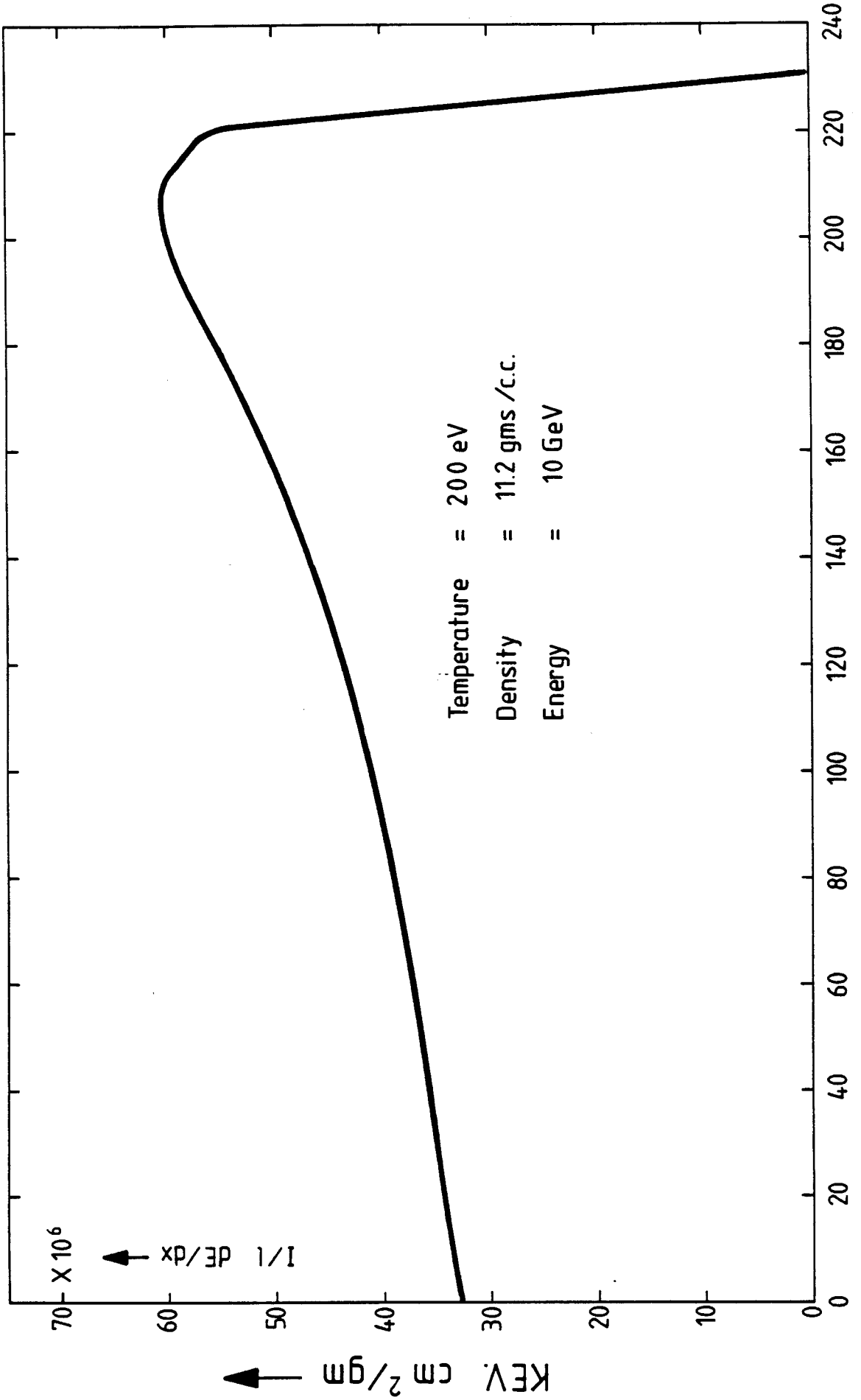

Fig. III·3-1
Stopping power of bismuth ions on lead

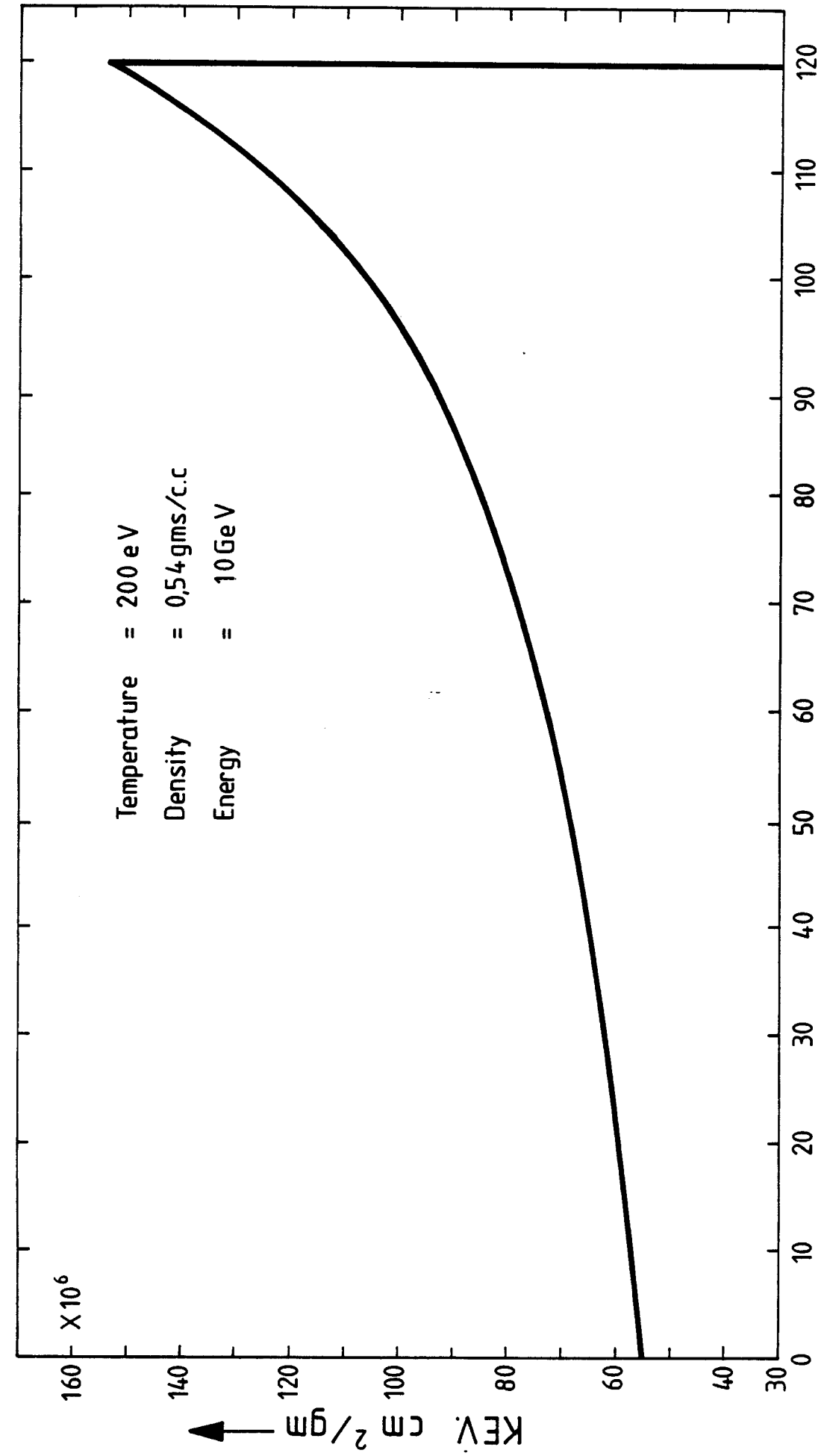

Fig. III·3-2

Stopping power of bismuth ions on lithium

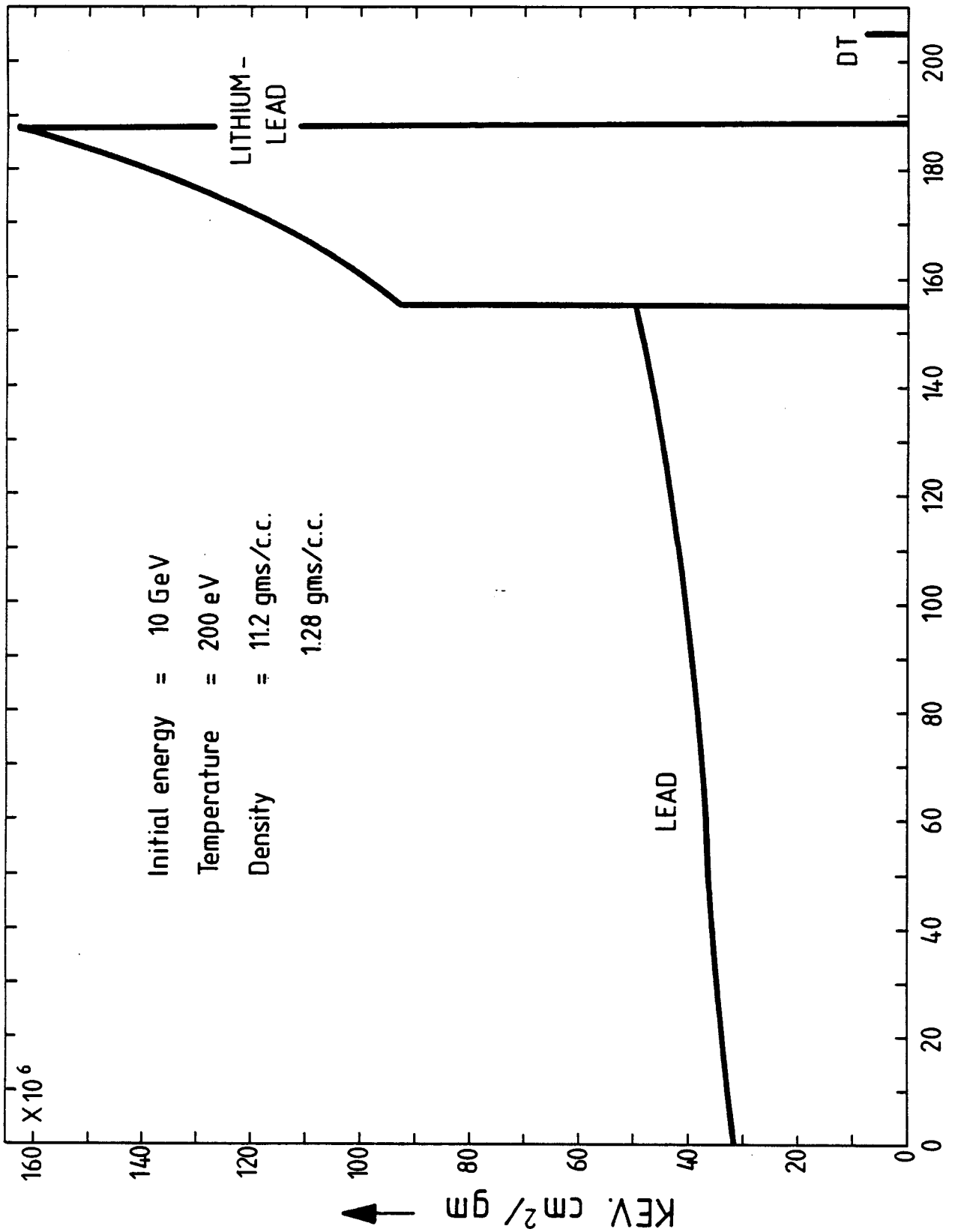

Fig. III·3-3
Bismuth ions on lead and lithium - lead
Hitball pellet

the range as the temperature increases. The reason for this is as follows: At room temperature the energy deposition profile is relatively flat and this comes about because the Bragg peak type profile which would be calculated using Z_B^2 is flattened out by the decrease in Z_{eff}^2 as a function of velocity. As the range is shortened the cutoff occurs at larger values of Z_{eff}^2, so that the flattening effect is much reduced and the Bragg peak starts to reappear. It should be noted here that the peak in the distribution curve always occurs when $V_B \sim V_{el}{}^{Th}$(the electron thermal velocity), and as the temperature increases so does $V_{el}{}^{Th}$, so V_B becomes greater at this point and so does $Z_{eff}(V)$.

In conclusion the assumptions that are inherent in these calculations are briefly considered. The ion is assumed to travel in a straight line and lose energy by small angle scattering to the electrons by excitation and ionization. Hence large angle scattering events are ignored, as these are important only at lower energies. The ions are assumed to slow down independently of each other, that is collective effects (of the beam interaction) are assumed to be absent. This is justified by an argument proposed by Melhorn.[27] For typical beam parameters the interparticle spacing is >100Å, while the relevant shielding distance in both solid and plasma is of the order of 1Å. Hence, in some sense, the particles should not see each other. However this is not the whole story, since one should also consider the time domain. Ions going through a plasma emit plasmons which vibrate with a period $\sim 10^{-17}$ secs. Ions travel typically with a velocity $\sim 3 \times 10^9$ cm/sec, so the time taken to travel 100Å is $\sim 10^{-16}$. Therefore as long as the plasmons are not damped out in ~ 10 oscillations the next ion will see the perturbation produced by the ion in front. Under certain circumstances this could lead to bunching and a coherent motion of the ions, leading to the unstable growth of large amplitude plasma

waves. This could then lead at least to enhanced energy deposition. This effect is currently being investigated to see if such an instability can occur within the parameter space relevant to ICF fusion.

III.3.5 Target Gain Calculations for the HIBALL Reactor Study Using MEDUSA

An ICF target should have a high gain, but there are several other requirements that it should fulfill. The target should be hydrodynamically stable and it should have a reasonable tolerance of irradiation asymmetries. It should also need as low an energy and power as possible to ignite it. Further certain other requirements should be met which do not directly involve target physics considerations. For instance the target should be easy to fabricate and should be made out of relatively cheap materials. It would be desirable that the target produces a minimal amount of radioactivity, that it should be compatible with other materials of the reactor coolant system and finally it should be large enough that the beam can be focussed onto it.

Many of the above requirements impose contradictory constraints. For example, power requirements can be reduced by using shells with large aspect ratio, but such shells are usually unstable.

Bangerter and Meeker[28] proposed a target which fulfills most of the above requirements and is shown in Fig. III.1-2. This is a single shell multi-layered target with a low density, low Z pusher sandwiched between a high density, high Z tamper and the fuel. The heavy tamper serves as a confinement shell to increase the efficiency of implosion. The pusher is seeded with a high Z material to reduce radiative preheat of the fuel. The use of a low density pusher has a number of advantages over a high density pusher. For instance, the pusher can be made relatively thick to reduce hydrodynamic instabilities and yet contain little mass. Also the hydrodynamic instabilities causing pusher-fuel mixing during the final stages of

compression may be eliminated because of the very small density difference between the fuel and the pusher. In addition, this target has a simple structure and is made from inexpensive materials. The simulations of Bangerter and Meeker[28] indicate that in the case of a high Z pusher target comparable to the one shown in Fig. III.1-2, the ρR in the pusher is 10 gm/cm^2. On the other hand, in the present calculations the bulk of the high Z material remains uncompressed and the total ρR of both the pusher and the tamper is less than 1 gm/cm^2. Therefore the latter target would produce less than 10% as much high Z radioactive debris as a target with high Z pushers.

As a first step towards designing the HIBALL target the 1 mg DT Bangerter-Meeker[29] target was simulated at KfK (INR) with the updated version of MEDUSA. To make these calculations computationally simpler the TaCOH pusher was replaced by PbLi, the two have the same mass density and approximately the same electron number density. These results show good agreement with the Bangerter-Meeker results. It is, however, to be noted that a target with 4 mg of DT is required for the HIBALL reactor study. For this purpose the above target has been scaled to a bigger one which contains 4.3 mg of DT in such a way that the two targets have the same aspect ratios. From now on this bigger target will be referred to as the "HIBALL TARGET". Compression, ignition and the burn propagation in this HIBALL target have been simulated. A comparison between the KfK and Bangerter results and results for the 4 mg target are discussed below.

Results

a) 1 mg DT target (Comparison between Bangerter-Meeker and KfK results)

A target very similar to the Bangerter-Meeker[28,29] target, but with PbLi pusher instead of TaCOH, has been simulated using the updated version of MEDUSA. The two materials have the same mass density and approximately same

number of electrons/unit volume. We have used approximately the same deposition profile as in Fig. III.1-4. The pulse shape used in these calculations is shown in Fig. III.3-4 and is relatively simpler compared to the one shown in Fig. III.1-3. A comparison between the KfK results and the Bangerter-Meeker results is given in the following table.

Table III.3-1 Comparison between Livermore and KfK results

	Bangerter-Meeker	KfK
Pulse Energy (MJ)	1.28	2.0
Peak Power (TW)	240	250
Output Energy (MJ)	113	164
Gain	88	84

From the above table it is seen that Meeker and Bangerter have obtained a gain of 88 by using less input energy and practically the same peak power. To get a gain comparable to their value it was necessary to use somewhat higher input energy. The reason for this is that they have used a shaped pulse in their calculations which is designed to minimize shock heating of the fuel. Their target is compressed on a lower adiabat and the input energy requirement is reduced. On the other hand, in the KfK calculations a relatively simpler pulse, shown in Fig. III.3-4 has been used. This pulse shape gives rise to more shock heating of the target and so the compression is placed on a higher adiabat. Consequently, one would require more energy to achieve a high pellet gain. In these calculations 2 MJ input energy is used which compresses the target to give a higher value of ρR as compared to the Bangerter-Meeker calculations. As a consequence one gets larger fractional burnup of DT and more output energy.

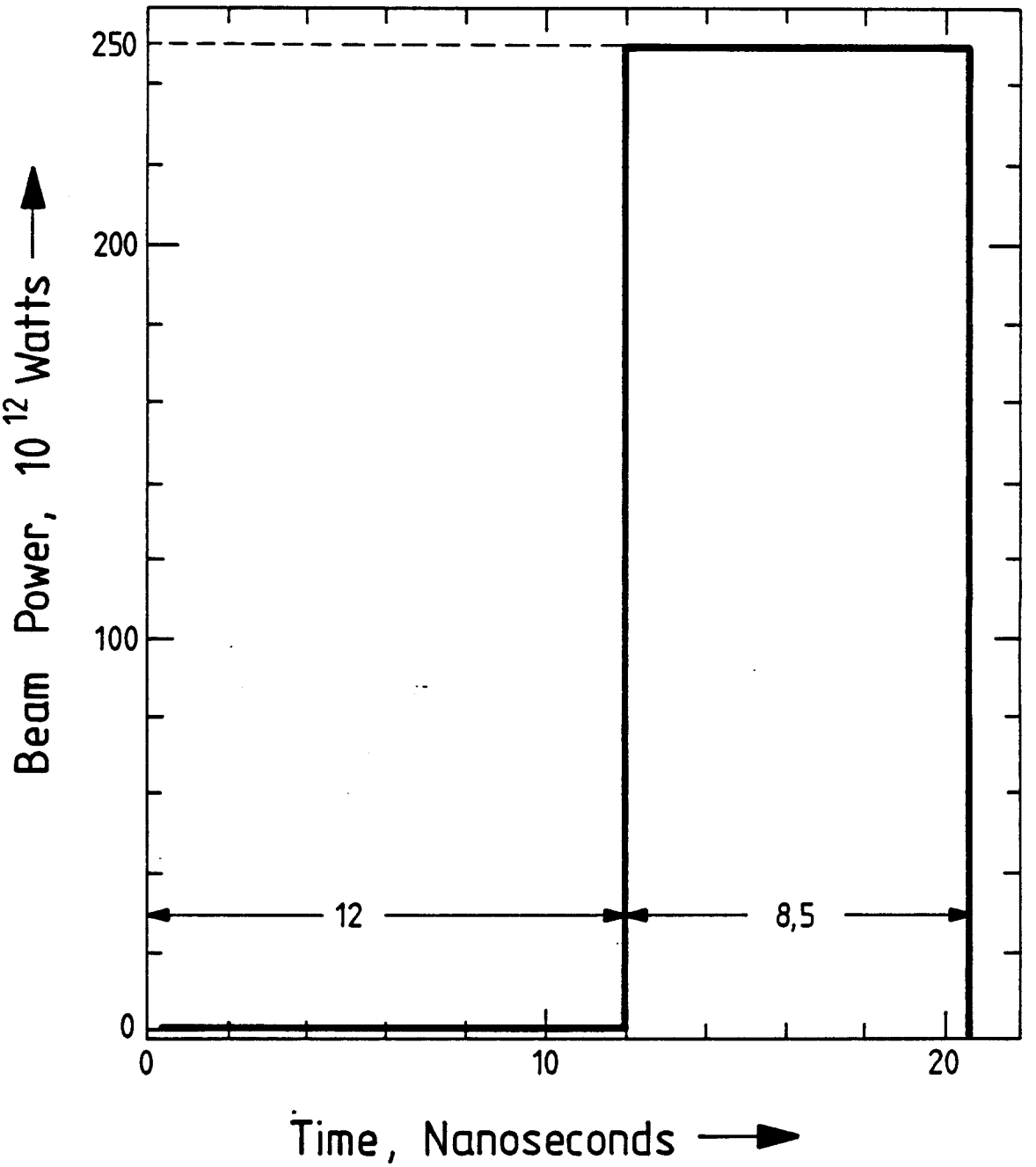

Fig. III·3-4
Beam power as a function of time

It should also be noted that during the final stages of compression the fuel density becomes comparable to the pusher density which is very good for the stability of the pusher-fuel interface. This effect has also been mentioned by Bangerter and Meeker.[28,29]

b) The HIBALL target with 4.3 mg DT

Using the updated version of MEDUSA described in section III.3.2, compression and ignition of the HIBALL target shown in Figure III.3-5 has been simulated. The problem of burn propagation from the central spark region into the surrounding dense and cold fuel has also been studied.

To design an ICF target and tune it for maximum output energy for a possible minimum input energy and power is a very complicated and time consuming problem. The reason for this is that the designer has to work in a multi-dimensional parameter space. The most basic parameter in this space is the type of the target itself which can either be a single shell multi-layered or a composite shell multi-layered target. For the HIBALL target a single shell multi-layered target with the same structural design and aspect ratio as the 1 mg target shown in Fig. III.1-2 has been chosen. The next set of variables which one has to select, are the input energy, the pulse shape and the pulse parameters. Bangerter[29] has mentioned an approximate energy mass scaling relationship according to which one should use 20 to 25 MJ/gm for good target compression. Applying this scaling law the HIBALL target would require 7.5 MJ input energy.

A pulse shape similar to the one shown in Fig. III.3-4 has been used. The choice of correct pulse parameters is another difficult problem. Since each computer run takes about 15 - 20 minutes of the IBM 3032 computer at KfK, it was not possible to vary these parameters blindly (to tune the target). The prepulse and the main pulse lengths were guessed to scale according to

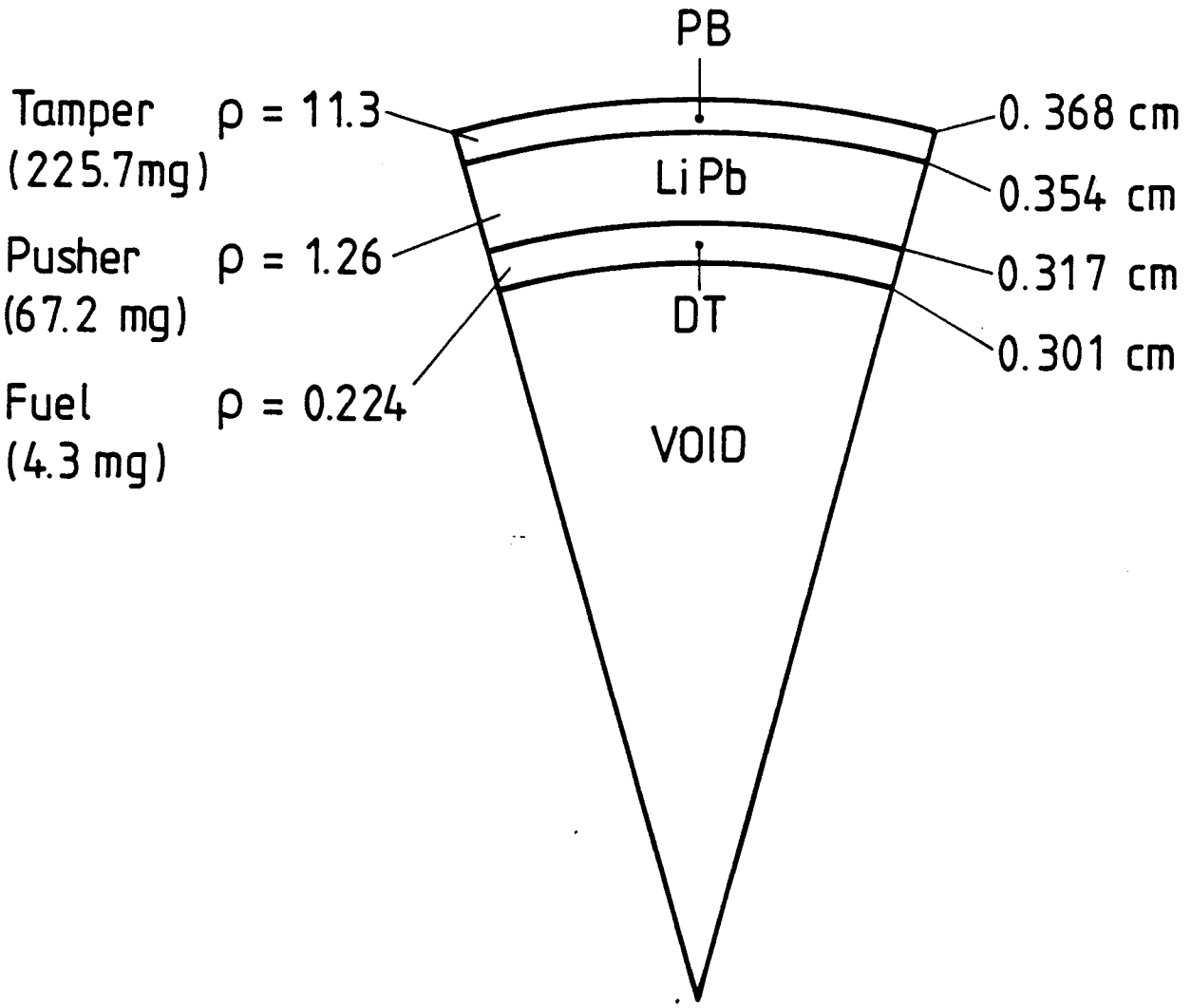
PB
Tamper ρ = 11.3
(225.7mg)
Pusher ρ = 1.26
(67.2 mg)
Fuel ρ = 0.224
(4.3 mg)
LiPb
DT
VOID
0.368 cm
0.354 cm
0.317 cm
0.301 cm

Fig. III·3-5

$m^{1/3}$ times the corresponding values for 1 mg target. The pulse parameters used in these calculations and the target yield are given in Tables III.3-2 and III.3-3 respectively.

Simple analytic formulae have been used to simulate heavy ion deposition in the pellet. The target conditions at the time of ignition are shown in Fig. III.3-6.

Table III.3-2 Pulse Parameters

Prepulse Power	10 TW
Main Pulse Power	600 TW
Prepulse Length	19 ns
Main Pulse Length	12 ns

Table III.3-3 Input Energy and Target Yield

Pulse Energy (MJ)	7.38
Gain	97
Output Energy (MJ)	715

It is to be noted that these calculations are initial and the performance of this target could be improved substantially by further fine tuning. The target yield can be optimized with less input energy and lower peak power by using a shaped pulse.

It should also be noted that one-dimensional codes cannot treat the hydrodynamic instabilities and the effects arising from non-uniform target illuminations. These effects can be studied by two-dimensional codes. Inclusion of the above two effects may degrade the compression substantially

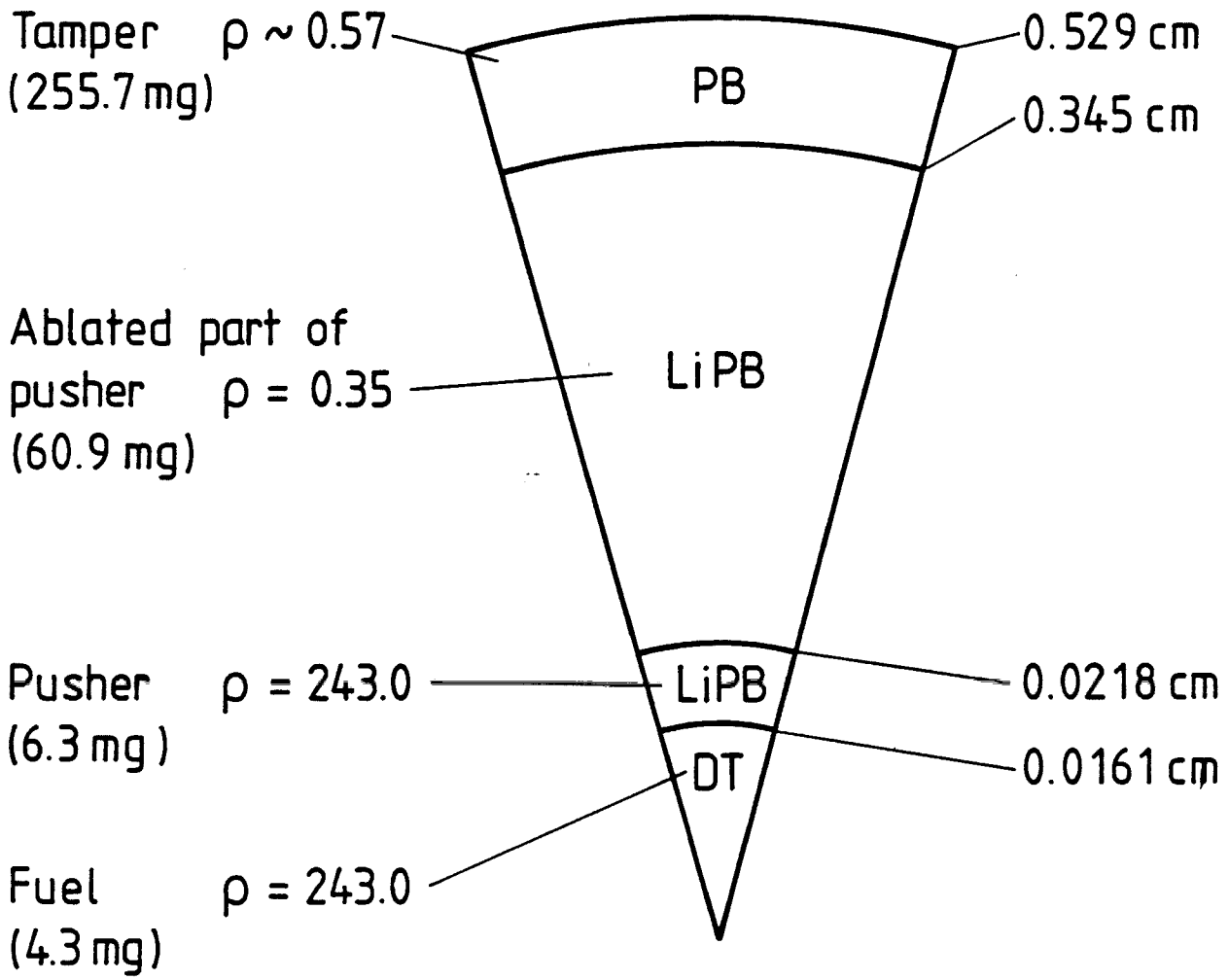
Tamper ρ ~ 0.57
(255.7 mg)
PB
0.529 cm
0.345 cm
Ablated part of
pusher ρ = 0.35
(60.9 mg)
LiPB
Pusher ρ = 243.0
(6.3 mg)
LiPB
0.0218 cm
DT
0.0161 cm
Fuel ρ = 243.0
(4.3 mg)

Fig. III·3-6

which in turn would reduce the target output. According to Meeker* two-dimensional simulations of a typical target show a reduction in gain by up to a factor of 10 compared to the gain obtained by one-dimensional calculations for the same target.

In Fig. III.3-7 the coordinates for the tamper-pusher and pusher-fuel interfaces are plotted as a function of time, respectively. It is seen that the pusher-fuel interface moves inwards as the target gets compressed and ignition starts at about t = 31.0 ns. This is the time when compression achieves its maximum value and corresponds to the switch off time of the pulse. On the other hand, the tamper-pusher interface maintains a steady position during the burn phase and then moves outwards as the target expands. This is because the tamper is very heavy and it does not move in but holds the pusher and the fuel together for a long enough time for nuclear fusion to take place.

The ignition and burn conditions are given in Figs. III.3-8 to III.3-10. We plot log ρ, log P and log T_i as a function of the target radius at three different times. The solid and broken vertical lines represent the pusher-fuel and the pusher-tamper interfaces, respectively. Fig. III.3-8 is plotted at t = 31 ns when the compression has achieved its maximum value. It is seen that the inner 10% of the fuel is heated to ignition temperature but is at a relatively lower density such that the total pressure in the fuel is constant. Figure III.3-9 is plotted after 130 ps and it shows a pressure peak in the ignited fuel region. This is because the charged particles produced in the nuclear reactions deposit their energy and heat up the fuel to temperatures $\sim 10^8$ K. This pressure peak sends a shock wave into the surrounding fuel and the burn spreads radially throughout the fuel. It is seen from Fig. III.3-10

*D. Meeker, private communication.

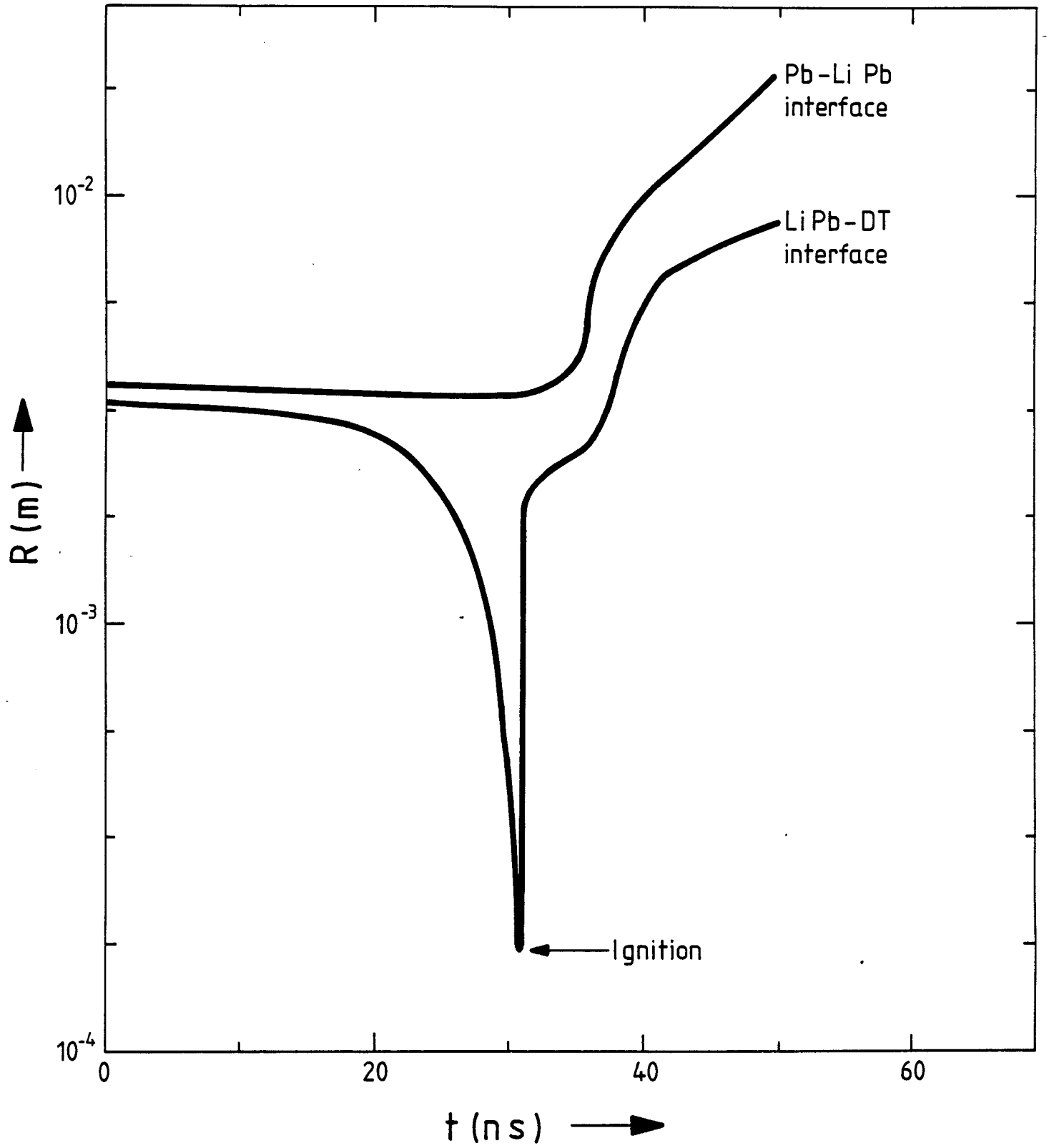
Pb-Li Pb
interface
Li Pb-DT
interface
Ignition
10^{-2}
10^{-3}
10^{-4}
R (m)
0
20
40
60
t (n s)

Fig. III·3-7

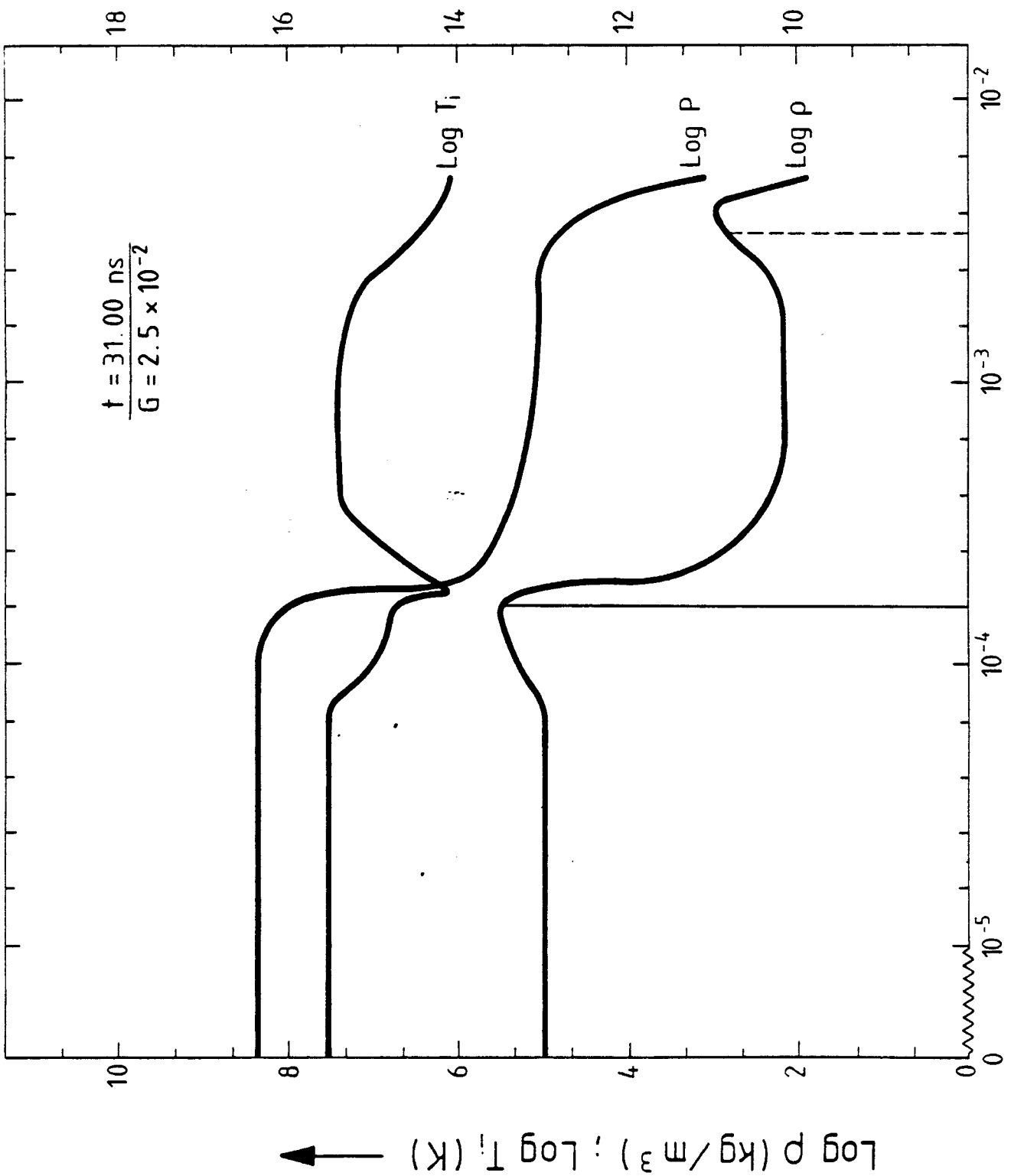
Log P (J/m³)
18
16
14
12
10
Log Tᵢ
Log P
Log ρ
t = 31.00 ns
G = 2.5 × 10⁻²
Log ρ (kg/m³) ; Log Tᵢ (K)
10
8
6
4
2
0
10⁻⁵
10⁻⁴
10⁻³
10⁻²
Radius (m)

Fig. III.3-8

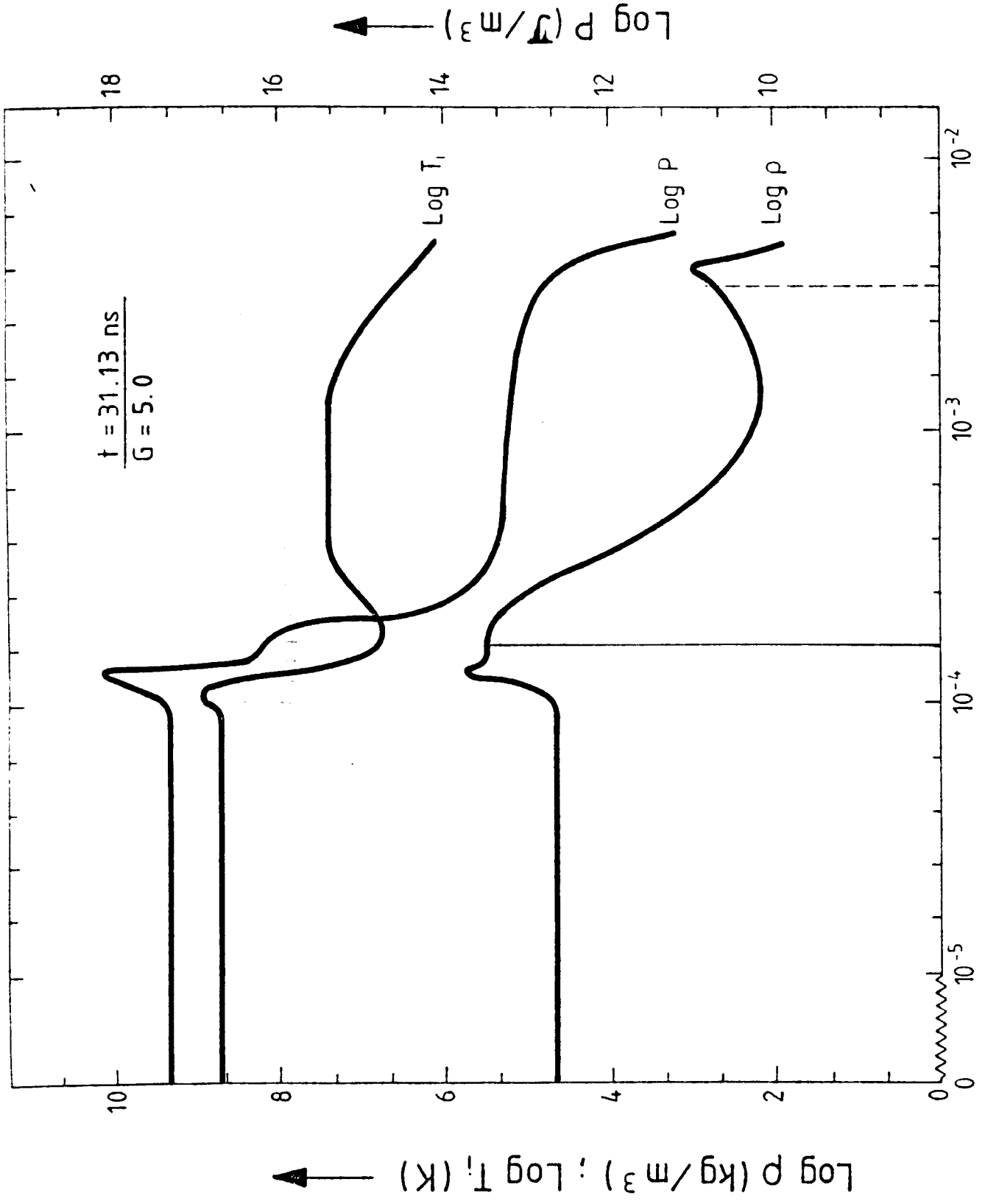
Log P (J/m³)
Log ρ (kg/m³) ; Log Ti (K)
Radius (m)
t = 31.13 ns
G = 5.0
Log Ti
Log P
Log ρ
0
2
4
6
8
10
10
12
14
16
18
10⁻⁵
10⁻⁴
10⁻³
10⁻²

Fig.III.3-9

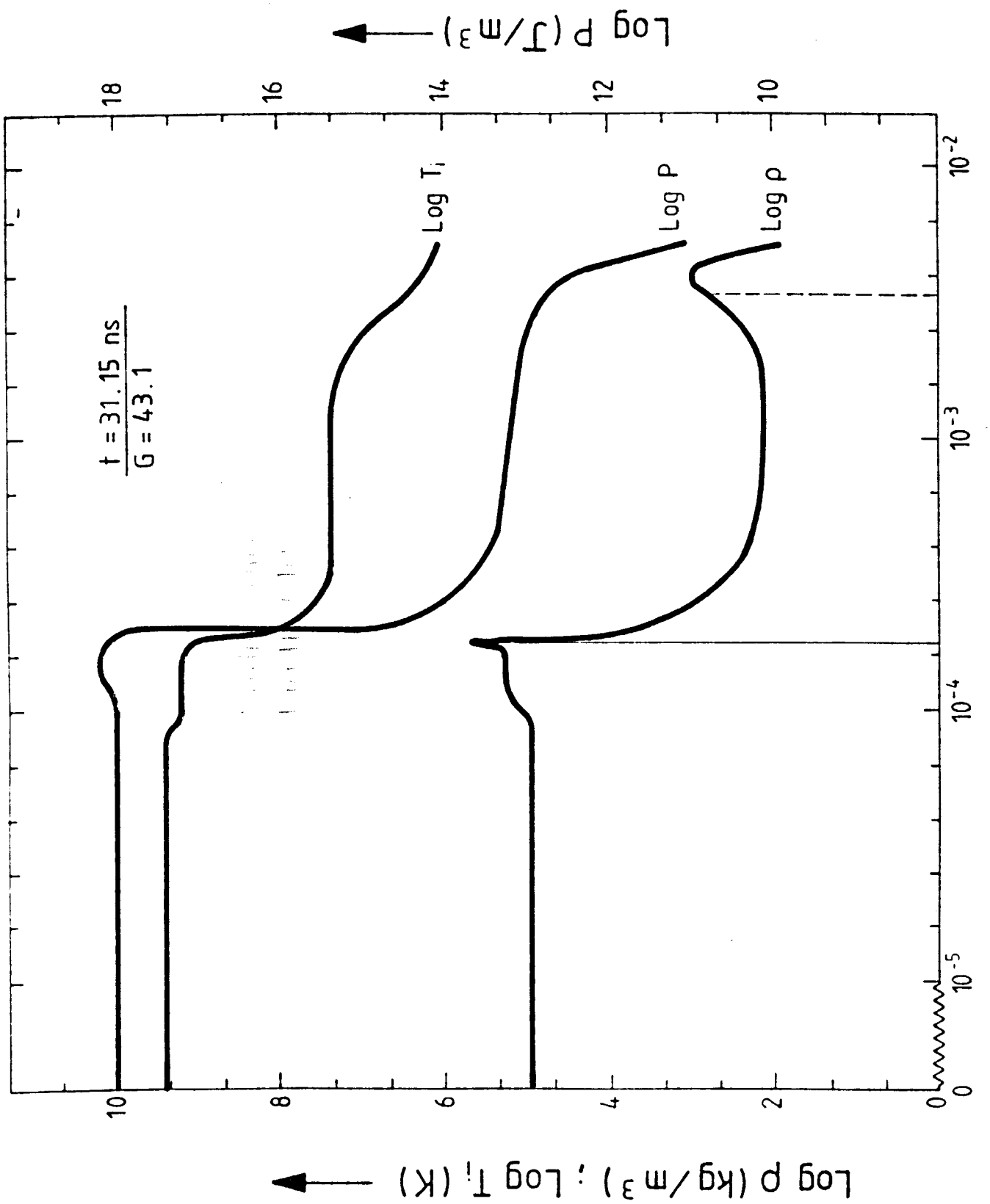
Log P (J/m³)
18
16
14
12
10
Log Tᵢ
Log P
Log ρ
t = 31.15 ns
G = 43.1
10
8
6
4
2
0
Log ρ (kg/m³) ; Log Tᵢ (K)
0
10⁻⁵
10⁻⁴
10⁻³
10⁻²
Radius (m)

Fig.III.3.0

that after 20 ps the whole of the fuel is heated to a temperature ~ 10^9 K. It should be noted that in these calculations radiation transport effects are excluded because of inavailability of opacities for lead. Since the pusher in this pellet is seeded with a high Z element, the radiative preheat effects will be reduced. Also the surface temperature of the target is ~ 100 eV and so the radiation losses will be small. In these calculations we have neglected radiation losses. However, inclusion of radiation transport will help the burn propagation. We expect to include radiation effects in our future calculations of the HIBALL target.

Figure III.3-11 shows the Atwood number at the pusher fuel interface as a function of time. It is seen that towards the end of the implosion the Atwood number decreases rapidly and even becomes negative. This indicates that while the pusher is being decelerated by the high pressure in the fuel, the fuel density becomes comparable to the pusher density. This indicates that our target should be stable to hydrodynamic instabilities which cause pusher-fuel mixing during the final stages of implosion.

III.3-6 Discussion and Conclusion

An advanced and extended version of the well-known MEDUSA code has been transformed into a target design code suitable for heavy ion beam fusion targets. The EOS is vital because it determines to which extent matter can be compressed, and how much energy is needed to do this. Also because the sound velocity is determined from the EOS, the EOS determines the time scale of the whole implosion. The detailed behavior of strong shocks is also determined by the EOS. Hence with a false EOS, targets of the wrong size and structure are likely to be designed. Radiation transport is also important in the design of targets as this can cause preheat of the DT, losses from the surface of the

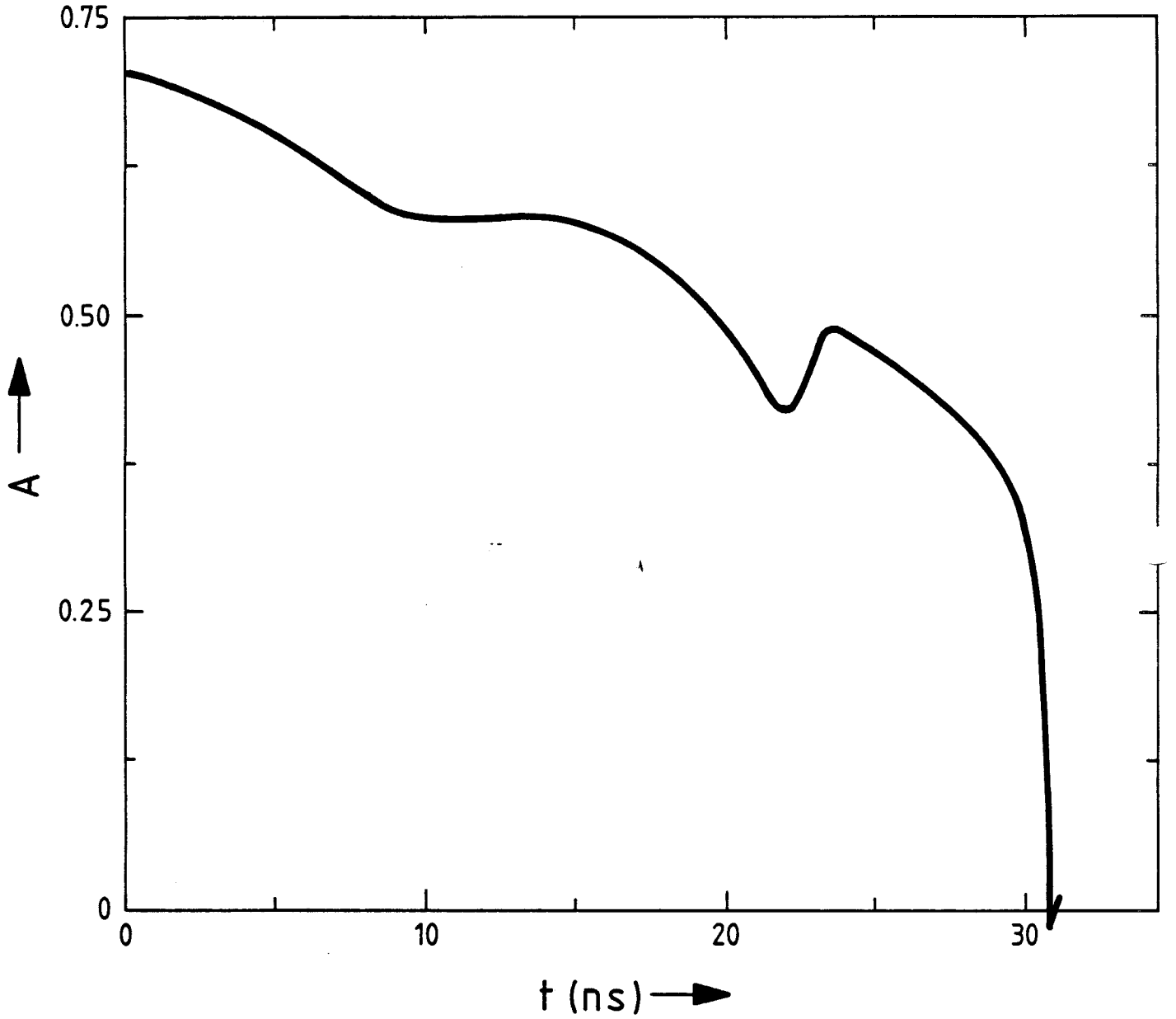

Fig. III·3-11

targets and is important for the propagation of the burn. The HIBALL target has been designed to minimize the deleterious effects of radiation transport.

The energy deposition of ions in ICF target materials has been calculated. A code has been developed which is suitable for the deposition of light and heavy ion beams. Detailed calculations show that range shortening by up to a factor 2 occurs for both heavy and light ions. For heavy ions the deposition profile becomes more peaked as the temperature of the material rises. Typical deposition profiles for the HIBALL target materials and the HIBALL target itself are presented.

The credibility of the MEDUSA code as a target design code has been established by reproducing results obtained by Bangerter for a 1 mg target design. This target has then been successfully scaled up using an $m^{1/3}$ law, to 4 mg of DT. Detailed implosion, ignition and burn phase calculations are presented for this 4 mg HIBALL reactor study target. The gain of this target is 97, with an input energy of 7.4 MJ and an output energy of 715 MJ which is easily sufficient for the designed fusion reactor. Further, detailed tuning and use of a more carefully tailored pulse is expected to increase the gain and decrease the input energy, while still producing over 500 MJ of energy. We found that the gain of the 4 mg target is less sensitive to changes in the ion beam range and the pulse parameters than the 1 mg target. Larger targets are hence less sensitive to parameter changes such as ion beam range, so that range shortening will not have such an effect. Range shortening could be compensated for by ramping the voltage of the incoming ions.

The HIBALL target design has therefore many attractive features. It is a high gain target, and needs reasonable values of input energy and power. It is a relatively simple target, which would make construction reasonably easy, and would also keep the cost down because it contains no expensive material.

The target materials are compatible with the rest of the reactor design, in particular the coolant materials. Since the density of the high Z tamper is low, it produces minimal radioactivity. The target is over 7 mm in diameter and so focussing problems will not be too hard to overcome. The target is stable to pusher-fuel instabilities, and by use of a thick pusher could be made stable to Rayleigh-Taylor instabilities.

References for Section III-3

1. K.A. Long and N. Tahir, "Ion Beam Fusion: Energy Deposition in and Simulations of ICF Pellets," to be published.

2. N.A. Tahir and K.A. Long, "Pellet Simulations for the HIBALL Reactor Study," to be published.

3. J.P. Christiansen, D.E.T.F. Ashby, and K.V. Roberts, "MEDUSA, a One-Dimensional Laser Fusion Code," CPC 7, 271, (1974).

4. R.G. Evans, "Improvements to the MEDUSA Code," Rutherford Laboratory Report, unpublished, June 1980.

5. A.R. Bell, "New Equation of State for MEDUSA," Rutherford Laboratory Report, RL-80-091, (1980).

6. N.A. Tahir, "Simulation Studies of Laser Compression of Matter," PhD Thesis, Glasgow University, 1978.

7. N.A. Tahir and E.W. Laing, Phys, Lett. A, 79A, 321, (1980).

8. N.A. Tahir, E.W. Laing, and D.J. Nicholas, Rutherford Laboratory Report, RL-80-048, (1980).

9. N.A. Tahir and E.W. Laing, Plasma Physics, 22, 1113, (1980).

10. N.A. Tahir and E.W. Laing, Phys. Letts, 77A, 430, (1980).

11. D. Kershaw, J. Comp. Phys. 26, 43, (1978).

12. N.A. Tahir, E.W. Laing, D.J. Nicholas, Rutherford Laboratory Report, RL-80-083, (1980).

13. S.P. Ahlen, Rev. Mod. Phys. 52, 121, (1980).

14. E. Nardi, E. Peleg, and Z. Zinamon, Phys. Fluids 21, 574, (1978).

15. E. Nardi and Z. Zinamon, Phys. Rev. A 18, 1246, (1978).

16. L.D. Landau and E.M. Lifschitz, Quantum Mechanics, Permagon Press, Oxford (1965).

17. H.A. Bethe, in Handbuch der Physik, Springer, Vol. 24, 273, (1933).

18. R. Latter, Phys. Rev. 99, 1854, (1955).

19. H.A. Bethe, Ann. Phys. 5, 325, (1930).

20. N. Bohr, Phil, Mag. 25, 10, (1913).

21. D. Pines and P. Nozières, "The Theory of Quantum Liquids," Benjamin, N.Y., (1966).

22. D. Pines, "Elementary Excitations," Benjamin, (1965).

23. S. Doniach and E. Sondheimer, "Green's Functions for Solid State Physicists," Benjamin, (1972).

24. M.D. Brown and C.D. Moak, Phys. Rev. B6, 90, (1972).

25. S. Chandrasekhar, Principles of Stellar Dynamics, Dover, P. 251, (1960).

26. K.A. Long, "Energy Deposition of Ions and α-particles in ICF Targets," GSI Report 81-3, (1981).

27. T.A. Mehlhorn, SAND80-0038, (1980).

28. R. Bangerter and D. Meeker, LLL Report, UCRL-78474, (1976).

29. R. Bangerter, LLL Report, UCRL-82026, (1978).

III.4 Target Design - University of Wisconsin

There is little question that the key element of inertial confinement fusion is the target. The fortunes of ICF ride on the target performance, thermonuclear yield as a function of driver energy. For commercial applications (i.e., production of electricity) the target gain, or ratio of thermonuclear yield to driver energy, must be large enough to compensate the major inefficiencies of the power plant such as the electrical efficiency of the driver. Furthermore, this minimum gain must be achievable for economically-sized drivers.

A very simple systems analysis of the power cycle within an ICF power plant will predict this value of minimum gain. This cycle is shown in Fig. III.4-1 where the three major components are the target, the energy conversion system, and the driver. The following terms are defined for this system:

$$\eta_D = \text{driver efficiency} = \frac{\text{driver energy on target}}{\text{energy into driver}}$$

$$Q = \text{target gain} = \frac{\text{thermonuclear yield}}{\text{driver energy on target}}$$

$$\eta_t = \text{thermal to electric conversion efficiency}$$

$$f = \text{recirculating power fraction.}$$

Multiplying these factors around the closed loop of Fig. III.4-1 gives

$$\eta_D Q \eta_t f = 1 \quad . \tag{III.4-1}$$

It is clear from the Fig. III.4-1 that the cost of electricity is proportional to

$$\$ \sim (1 - f)^{-1} \quad . \tag{III.4-2}$$

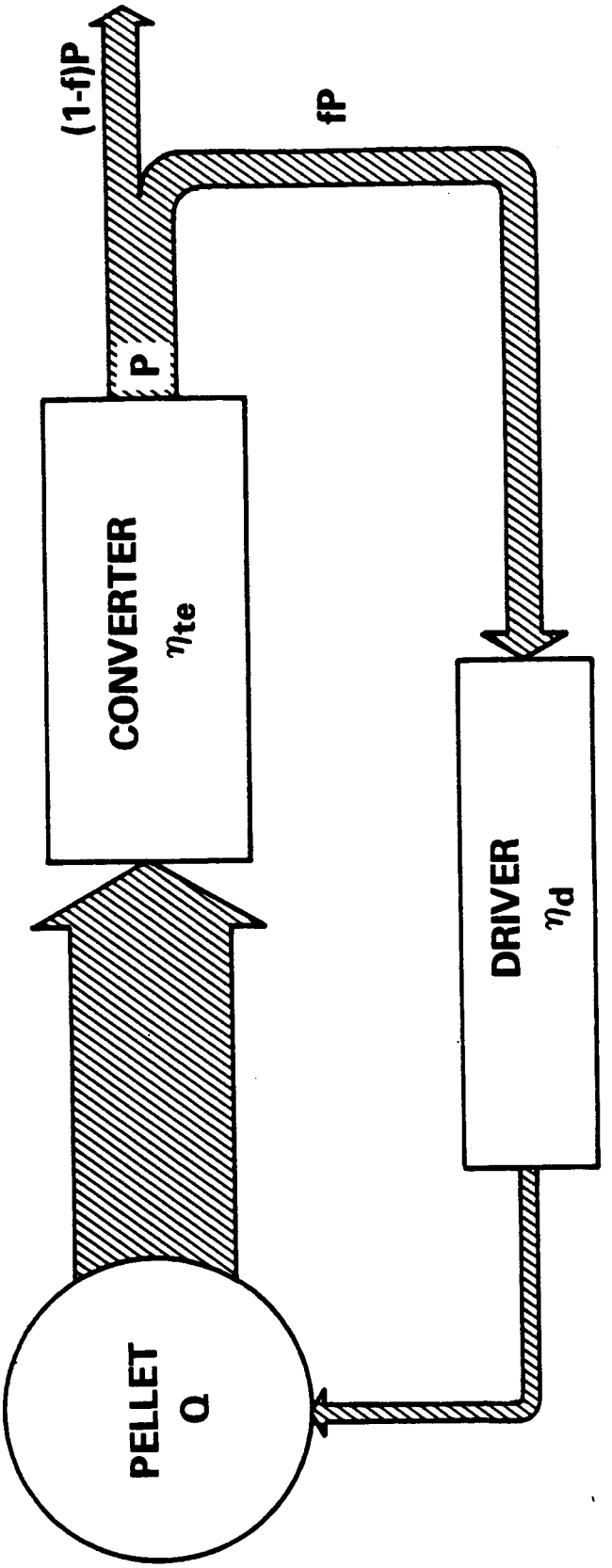

Fig. III.4-1

Power flow in ICF reactor.

This of course is a strong incentive to minimize the recirculating power fraction, f. Historically, a maximum value of f has been taken as 25%, although this value is most certainly quite arbitrary. (We might note that the recirculating power fraction in a nuclear fission reactor is about 5%.) For the sake of specificity we will adopt the 25% convention for our analysis. If we further assume

$$\eta_t = 0.4 \quad , \tag{III.4-3}$$

a reasonable value for a conventional thermal steam cycle, then we are left with a relationship between the target gain and driver efficiency

$$Q\eta_D > 10 \quad . \tag{III.4-4}$$

This product has been labelled the "fusion gain" of the system. The acceptable target gain is therefore dependent on the efficiency of the driver. In our case of ion beam drivers this efficiency may be in a range of 10-40%. Hence the minimum target gain is in a range of 25-100. Any situation where the target gain is much greater than this will naturally lead to smaller recirculating power fractions and more economical electricity production.

We have now established the range of minimum target gain that must be achieved. We next face the question: How much ion beam energy is required to produce this gain? This is a question that is based to a large extent on detailed target design calculations. This is unfortunate because the principle target design tools, large two-dimensional radiation-hydrodynamics computer codes and equation of state and opacity data, are unavailable to all except those working at the three principle nuclear weapons design laboratories, Lawrence Livermore Laboratory, Los Alamos Scientific Laboratory, and Sandia Laboratory. Furthermore, many target designs are classified as secret

restricted data on the grounds that they are somehow related to nuclear weapons design. This problem is partially alleviated by the fact that Lawrence Livermore Laboratory has published general information regarding the performance of ICF targets. An example of their so-called target gain curves is shown in Fig. III.4-2. The solid lines indicate the best possible performance of single and double shelled targets. Single and double shelled target designs are shown schematically in Fig. III.4-3 parts (a) and (d). By "best possible performance" we mean that (1) the target shell configuration is very accurately matched to the intensity profile of the incident pulse of driver energy, and (2) the calculations are performed using a one-dimensional implosion model. Each of these two conditions are in fact unrealistic. First of all, the precise matching of hydrodynamic response to the input pulse of energy is an exercise in "numerical gymnastics." The high gains predicted by the curves in Fig. III.4-2 are often nearly a "delta function" in the target design parameter space. By this we mean that small variations in shell thickness, density, etc., can seriously degrade the result. Critical tolerances are often smaller than the quite sizable uncertainties in the calculational model. Secondly, one-dimensional calculations always over-predict the target gain. Because the actual implosion will not converge to a point, as the one-dimensional model would predict, the ignition condition is generally much more severe than would be indicated by these results.

As a correction to these unrealistic results, the LLL target designers also include a band of performance in Fig. III.4-2 that they label "conservative." This represents a degradation of the idealized results to account for two- dimensional and other unspecified effects that make up the difference between the one-dimensional computer world and the real physical world. The band or range of gain vs. driver energy is meant to represent the uncertainty

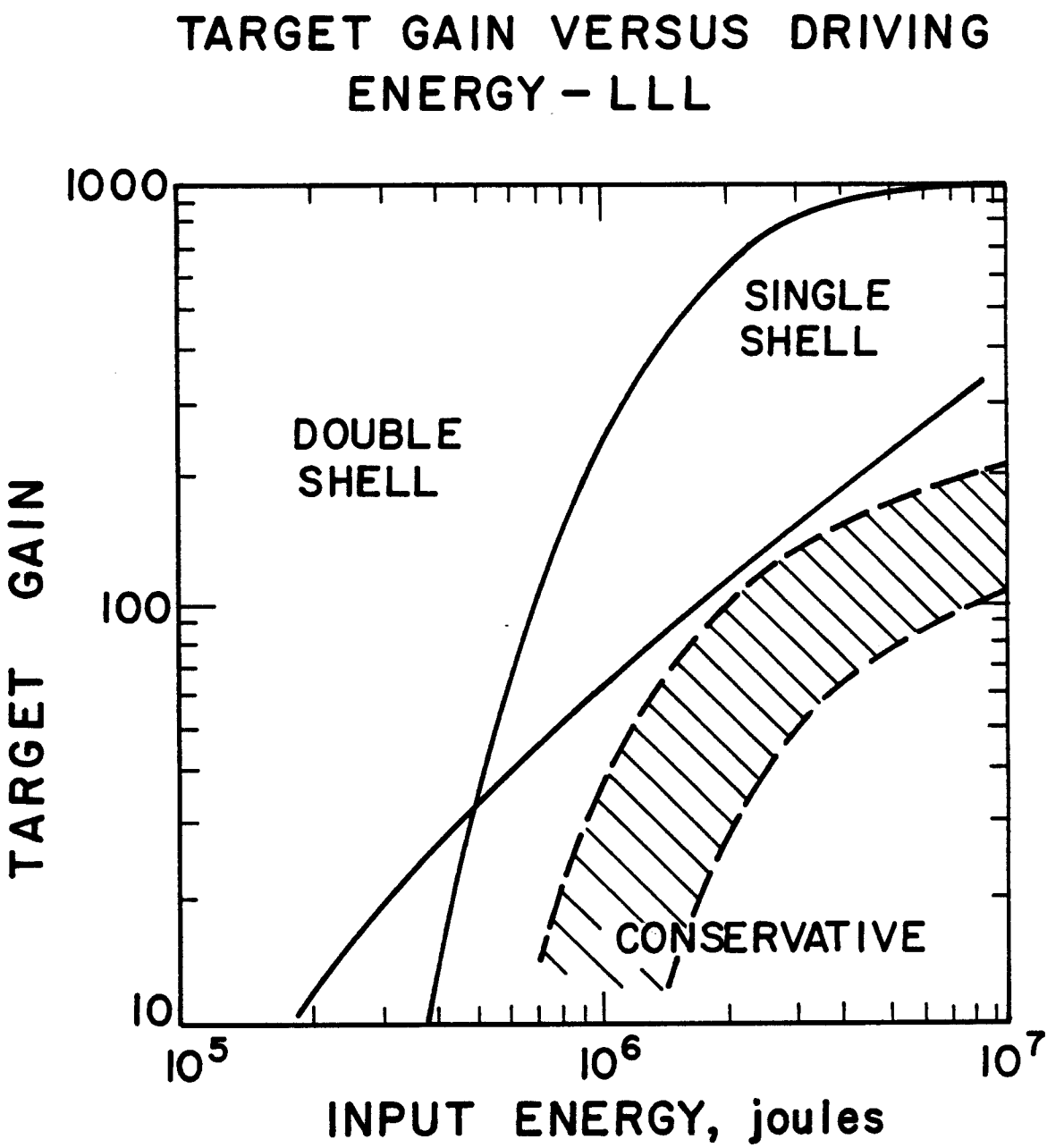
TARGET GAIN VERSUS DRIVING ENERGY - LLL
1000
100
10
TARGET GAIN
SINGLE SHELL
DOUBLE SHELL
CONSERVATIVE
10^5
10^6
10^7
INPUT ENERGY, joules

Fig. III.4-2

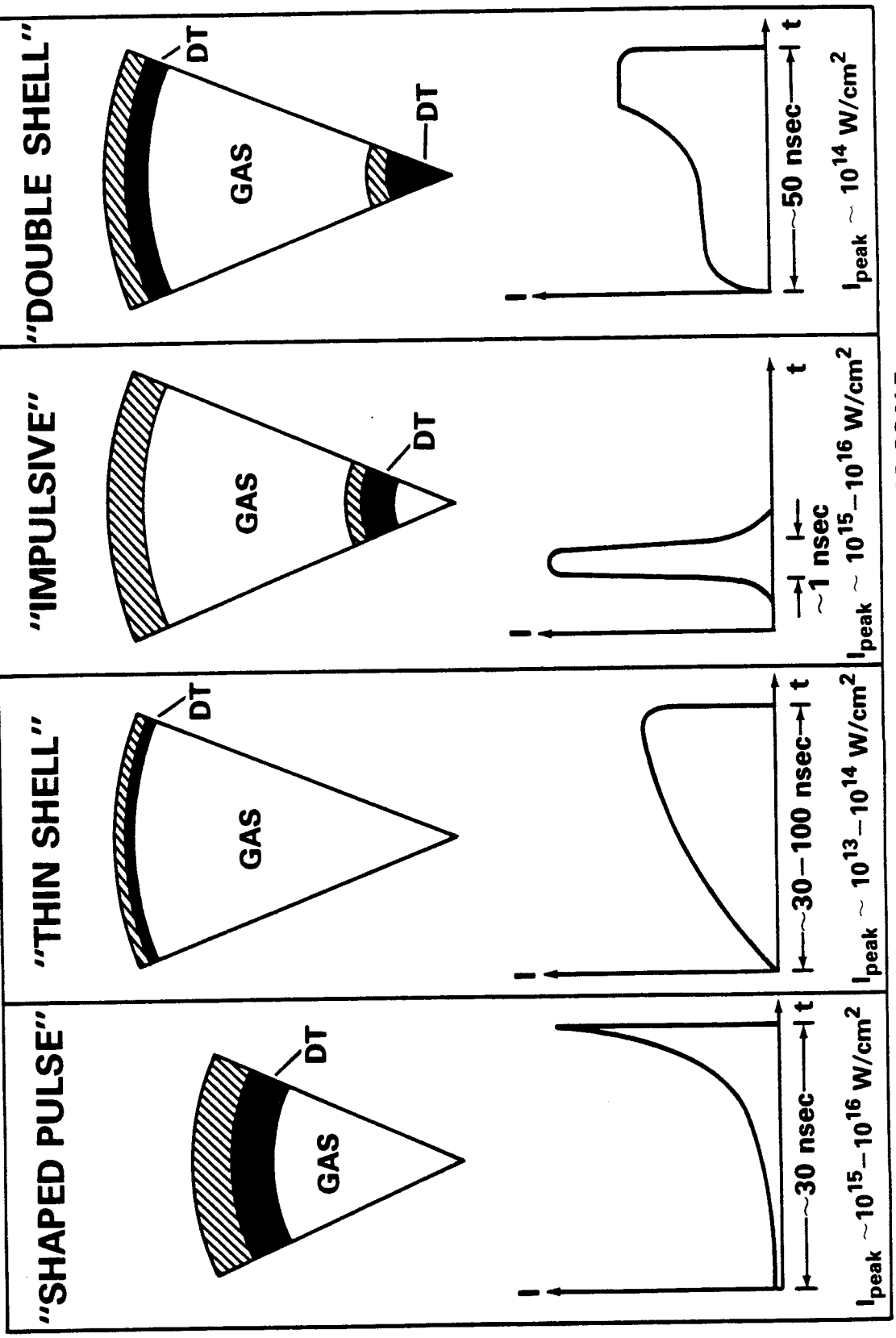

Fig. III.4-3

Different ICF t et designs.

in the calculations. It is important to note that this uncertainty is substantial.

With this valuable information the reactor designer can now determine a range for the driver energy. From our earlier values of Q = 25-100 we get

$$Q = 25 \quad \rightarrow \quad E_D = 0.85 - 2 \text{ MJ}$$

$$Q = 100 \quad \rightarrow \quad E_D = 2 - 8 \text{ MJ} \ .$$

Such large ranges of driver energy are very disquieting. The precise value chosen for a reactor study seems almost arbitrary and in fact it is! To understand this we must ask: How conservative is this band and what does it really mean from the point of view of target design?

This question is answered in section III.2.1 where a simple parameter analysis is used to reproduce the gain curves shown in Fig. III.4-2. To achieve high gain the fuel must be nearly isentropically compressed to high densities (hundreds of times liquid DT density). To achieve this high compression and an efficient hot-spot ignition configuration the fuel must be very symmetrically imploded.

The problem of implosion symmetry cannot be over-emphasized. This symmetry can be destroyed in two ways, (1) nonuniform driving pressures, and/or (2) fluid instabilities. The first is a macroscopic effect. Some parts of the shell are accelerated to greater or lesser velocities and therefore the entire shell does not reach the center of the implosion at the same time. The second problem is much more subtle. In this case, the fluid at the ablation surface during the implosion and the fuel-pusher interface at ignition time are hydrodynamically unstable. Small perturbations in the fluid density tend to grow. This complex subject will not be discussed here in detail. These fluid instabilities can be mitigated by rapid acceleration of

the shells so that the instabilities do not have time to grow and by very high tolerances on the surface finish of the various shells in the target.

Symmetric implosion is a very troublesome problem for directly driven ion beam targets as compared to laser driven targets. This comes from the fact that the ions are depositing their energy very close to the ablation surface whereas laser beams deposit energy at the critical density of the blow-off plasma, Fig. III.4-4. This region between the critical density surface and the ablation surface allows nonuniformities to be smoothed due to lateral conduction. Two-dimensional hydrodynamics calculations by Emery, Gardner and Boris of NRL[1] on thin slab targets demonstrate this smoothing effect. In these calculations they irradiate a slab target with 1.06 μm laser light with a nonuniform spatial profile, Fig. III.4-5. Under extreme circumstances they see very nonuniform density and pressure profiles as shown in Figs. III.4-6 and III.4-7. This study was done parametrically for differing laser intensities (and consequently, different spacing between ablation and critical density surfaces) and these results are summarized in Fig. III.4-8. Here the nonuniformity of ablation pressure is plotted as a function of the ablation-critical density surface spacing for different nonuniformity scale lengths. We clearly see that to hold the pressure variation to a few percent, the scale length of the nonuniform laser profile must be less than or equal to the distance between the critical density surface and the ablation surface. For ion beam targets the ablation surface is directly adjacent to the energy deposition region, because the ions penetrate to such high densities. This implies that ion beam targets such as the one proposed by Bangerter require extremely uniform illumination. Symmetry may possibility be improved by target designs that are beyond the scope of this discussion.

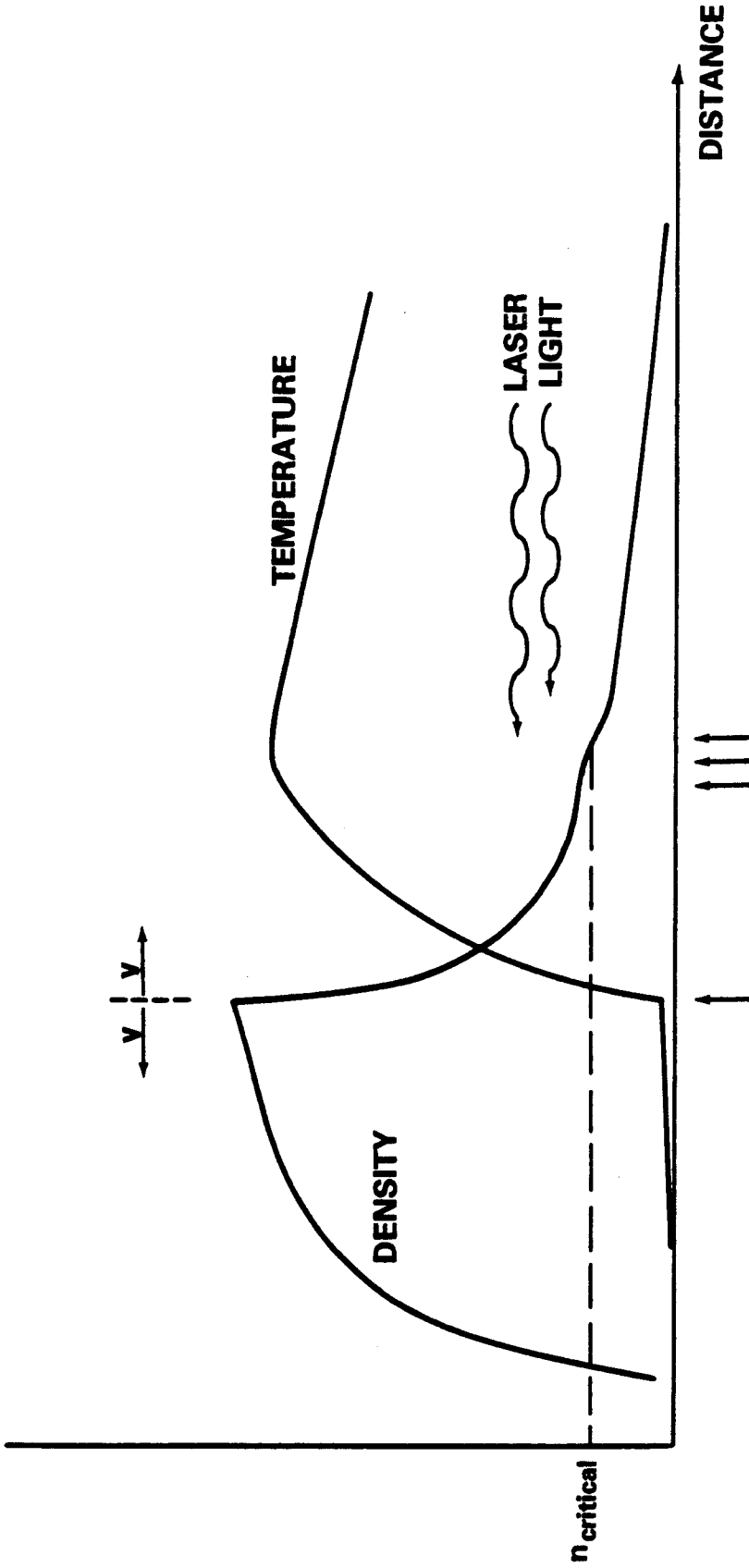

Figure III.4-4

Temperature and density profiles in laser ablated target.

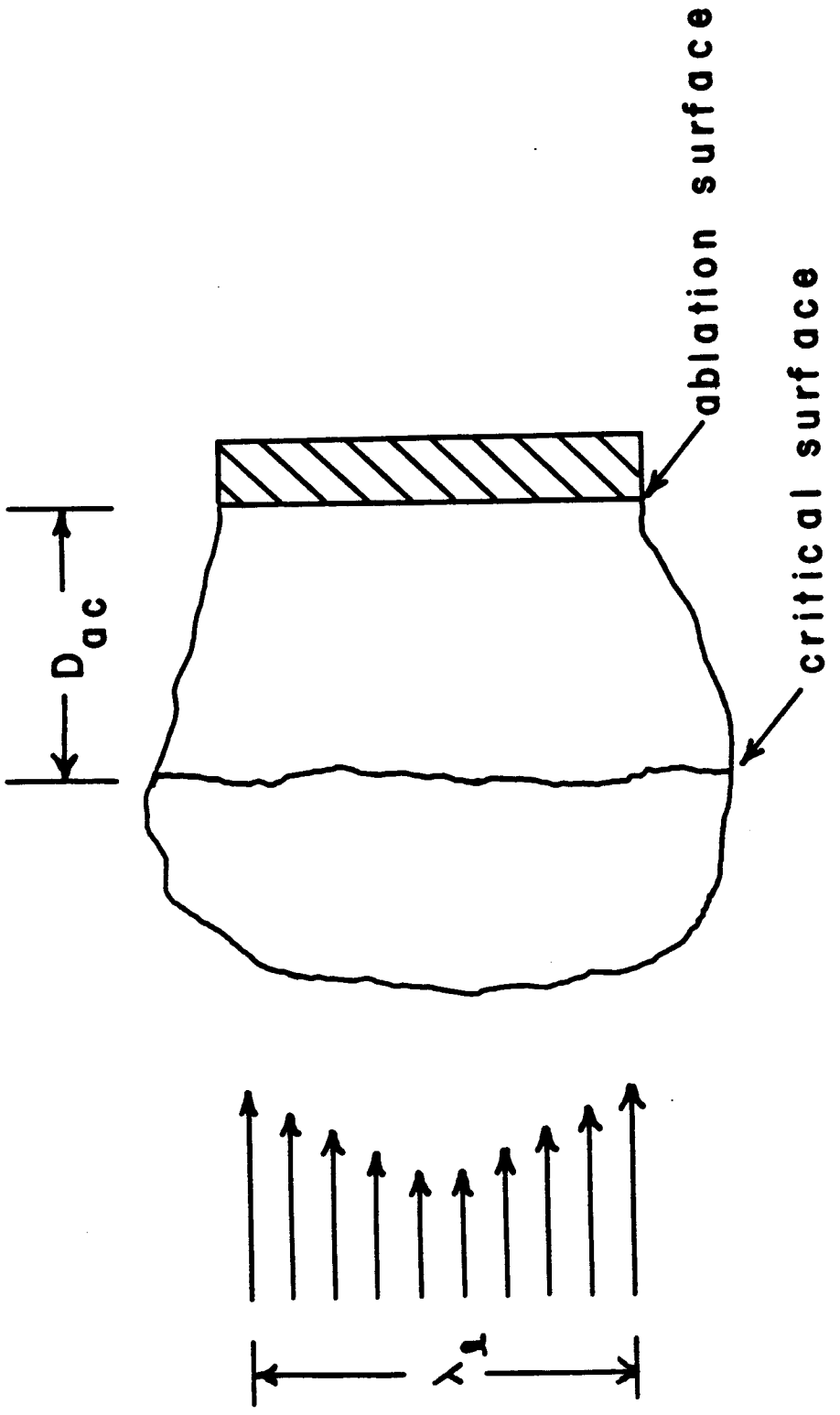

Figure III.4-5
Non-uniform laser spatial profile.

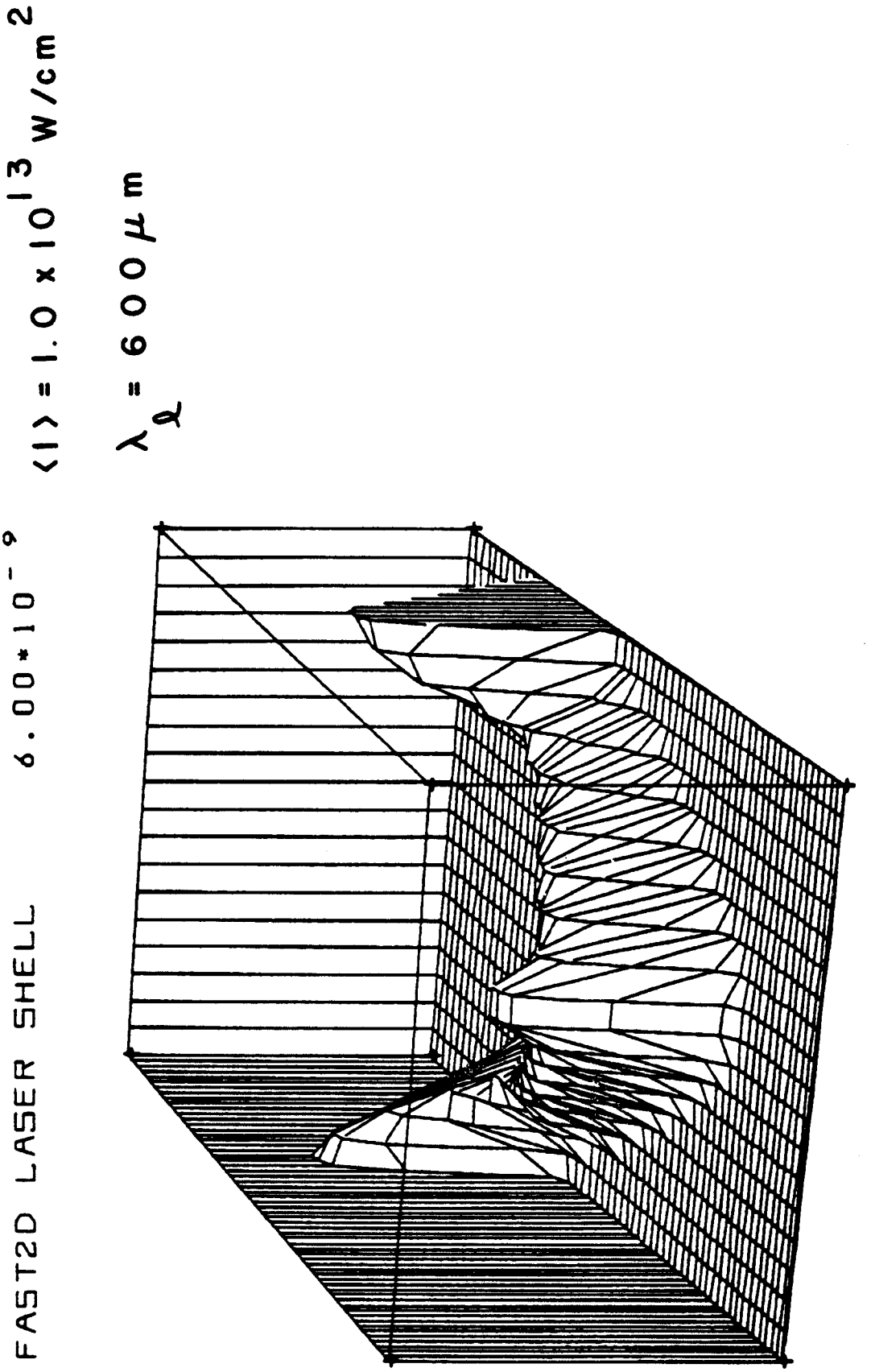

Figure III.4-6
Pressure vs. position for non-uniform laser profile.

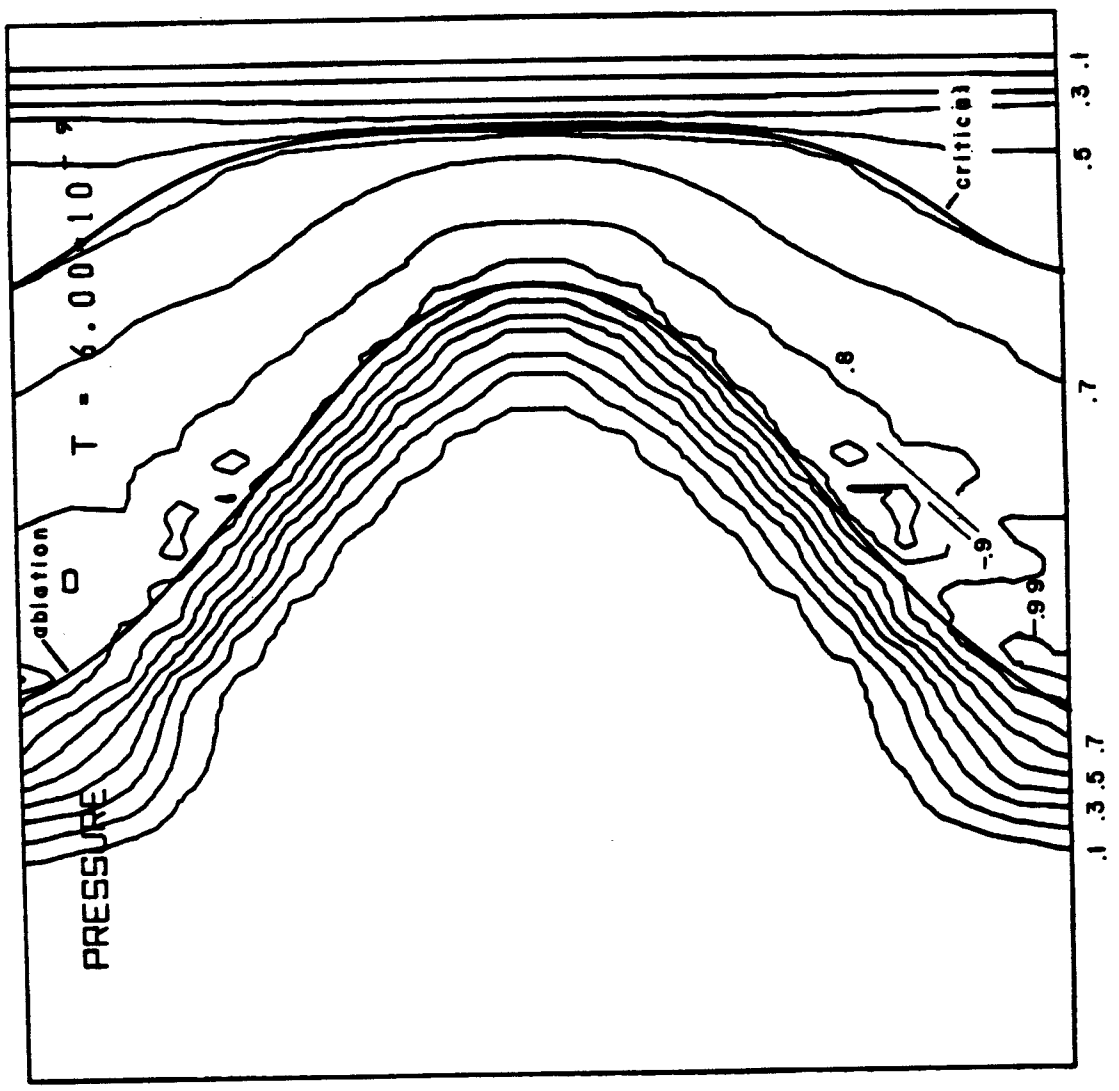

Figure III.4-7
Pressure contours for non-uniform laser profile.

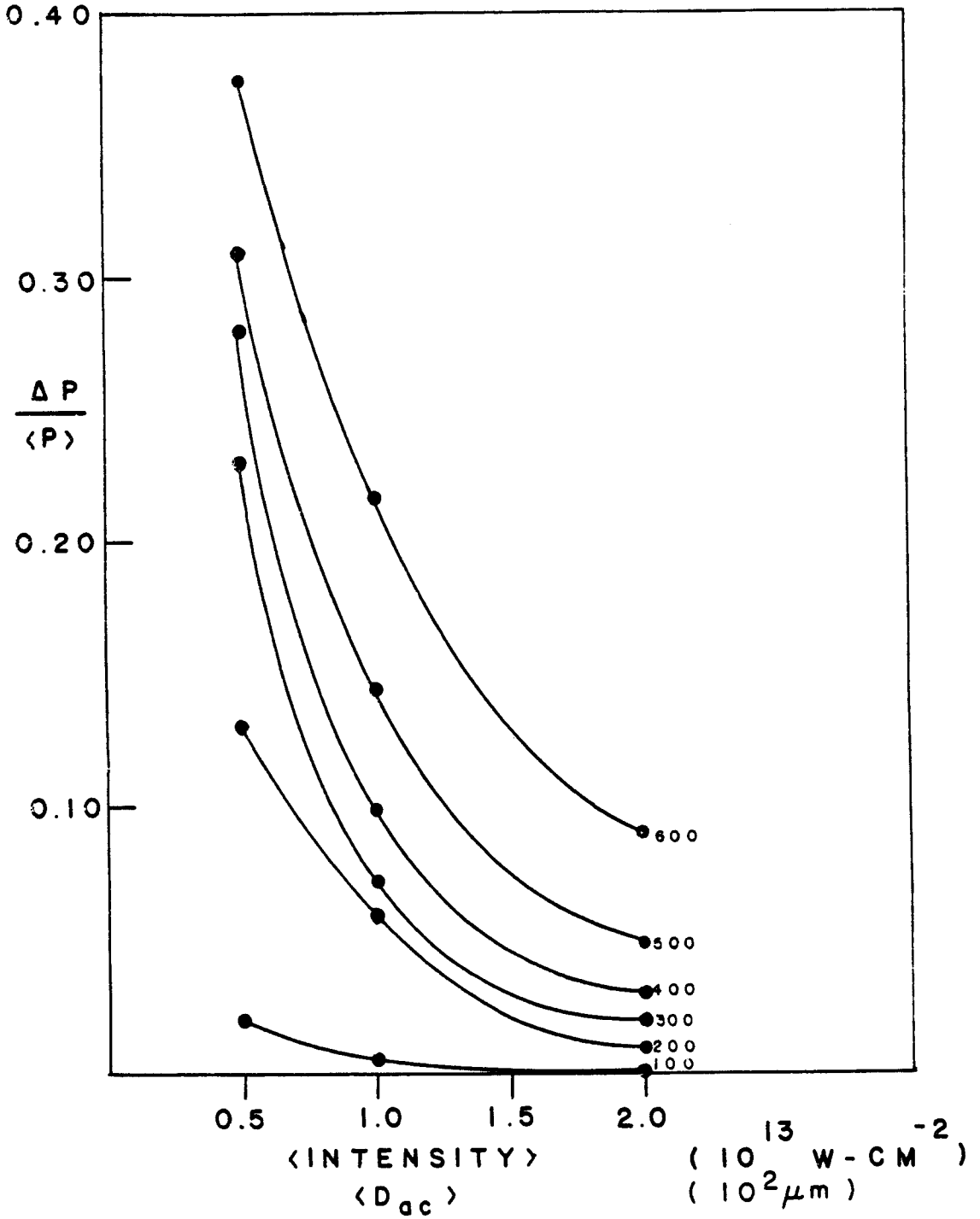

Figure III.4-8

Fractional ablation pressure variation vs. laser intensity.

We have studied the deposition of ions in hot material using the model of Mehlhorn.[2] This analysis is based on the Bethe stopping theory at high ion energy and Lindhard stopping theory at low ion energy. In the transition between these two we interpolate as shown in Fig. III.4-9. Finite temperature effects are then added to these standard models. The theory will not be reproduced here. Instead we show results of calculations for heavy ions stopping in low and high Z material at different temperatures. Figures III.4-10 and III.4-11 show the ranges of 10 GeV bismuth ions in 0.01 solid density gold and aluminum. The range is shortened at higher temperatures. In the case of protons the range begins to re-lengthen at temperatures higher than about 100 eV. Hence the shortest range is associated with about 100 eV material. However, in the heavy ion case, the range is still becoming shorter at 300 eV in both gold and aluminum. The ranges of 10 GeV heavy ions are very much longer than those of 2 MeV protons. In fact, at an aluminum density of 0.027 g/cm^3 the proton energy would be in excess of 10 MeV to have a range that is equivalent to the 10 GeV heavy ions. Heavy ions have a much shorter range in low-Z material than in high-Z material. However, the Bragg peak is not very large and therefore it is more difficult to concentrate energy in a localized region of the target. Figures III.4-12 and III.4-13 show the ranges of 10 GeV uranium ions in gold and aluminum. These are presented for comparison with other researchers since U ions seem to be an unofficial standard for heavy ion beam fusion.

Finally, Fig. III.4-14 and III.4-15 show a comparison between calculations done at the University of Wisconsin using Mehlhorn's model and those done at KfK by Long. His model is discussed in section III.3 of this report. We see remarkably good agreement between these two code calculations.

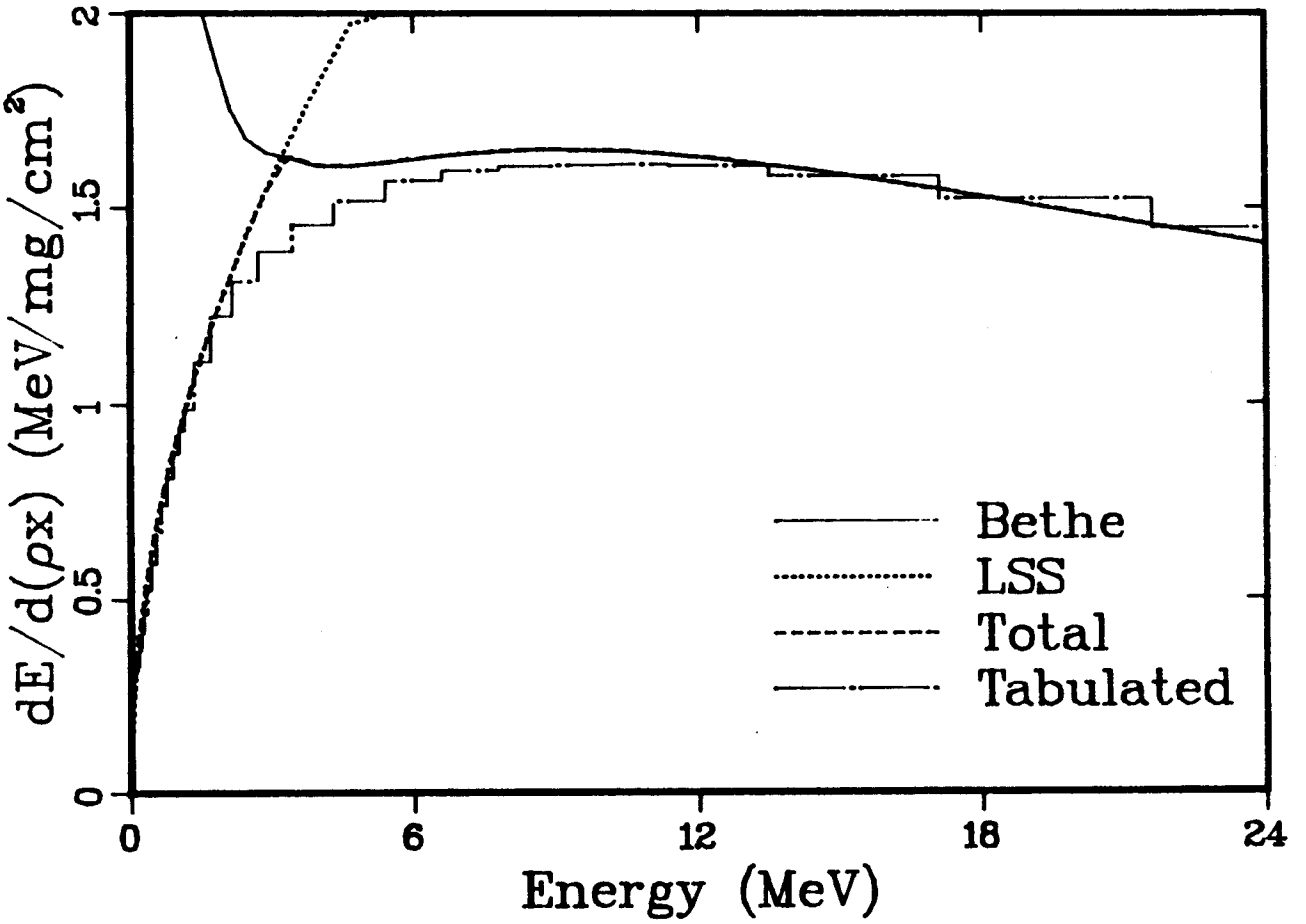

Figure III.4-9

Interpolation of Bethe and LSS theories.

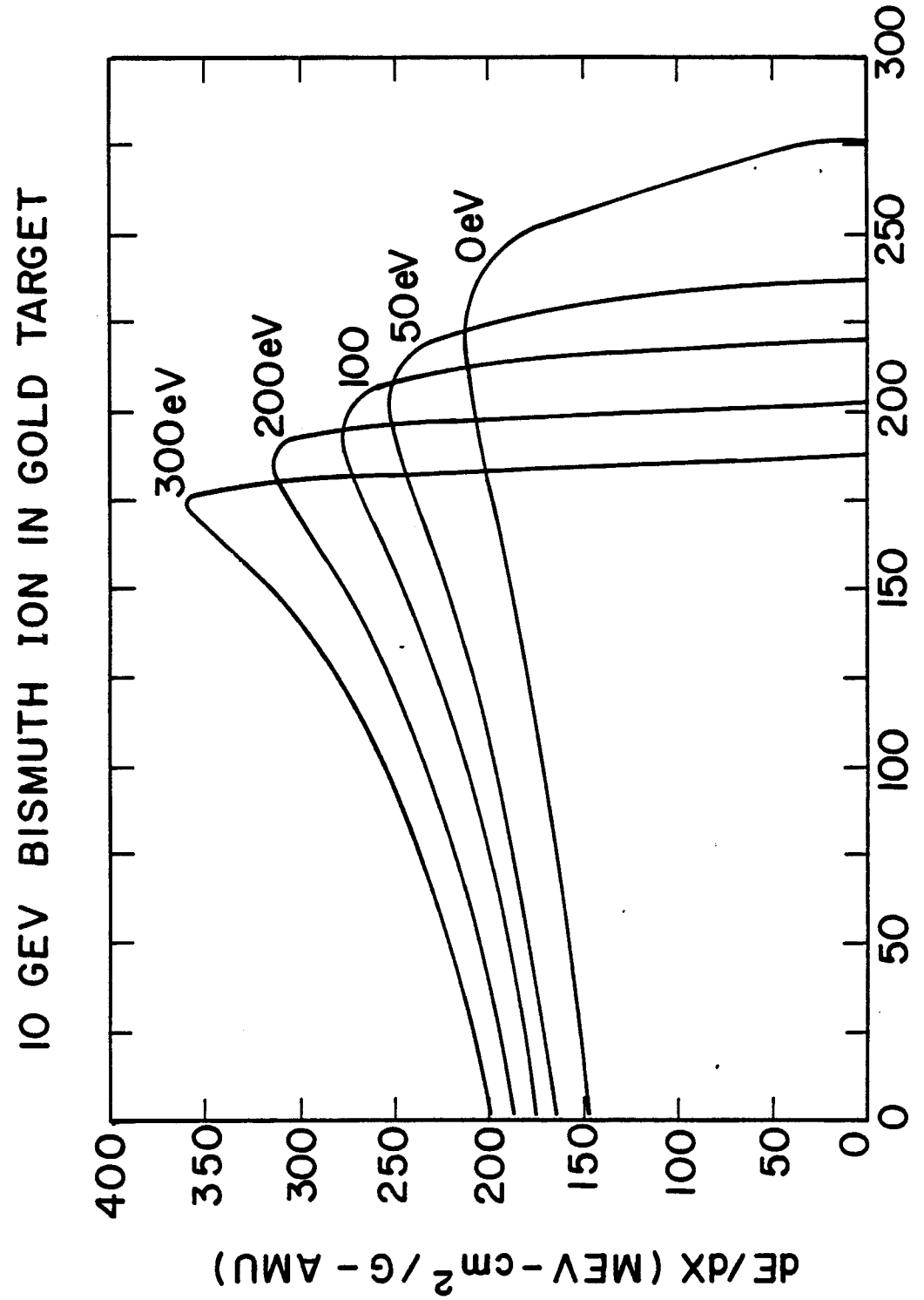

Figure III.4-10

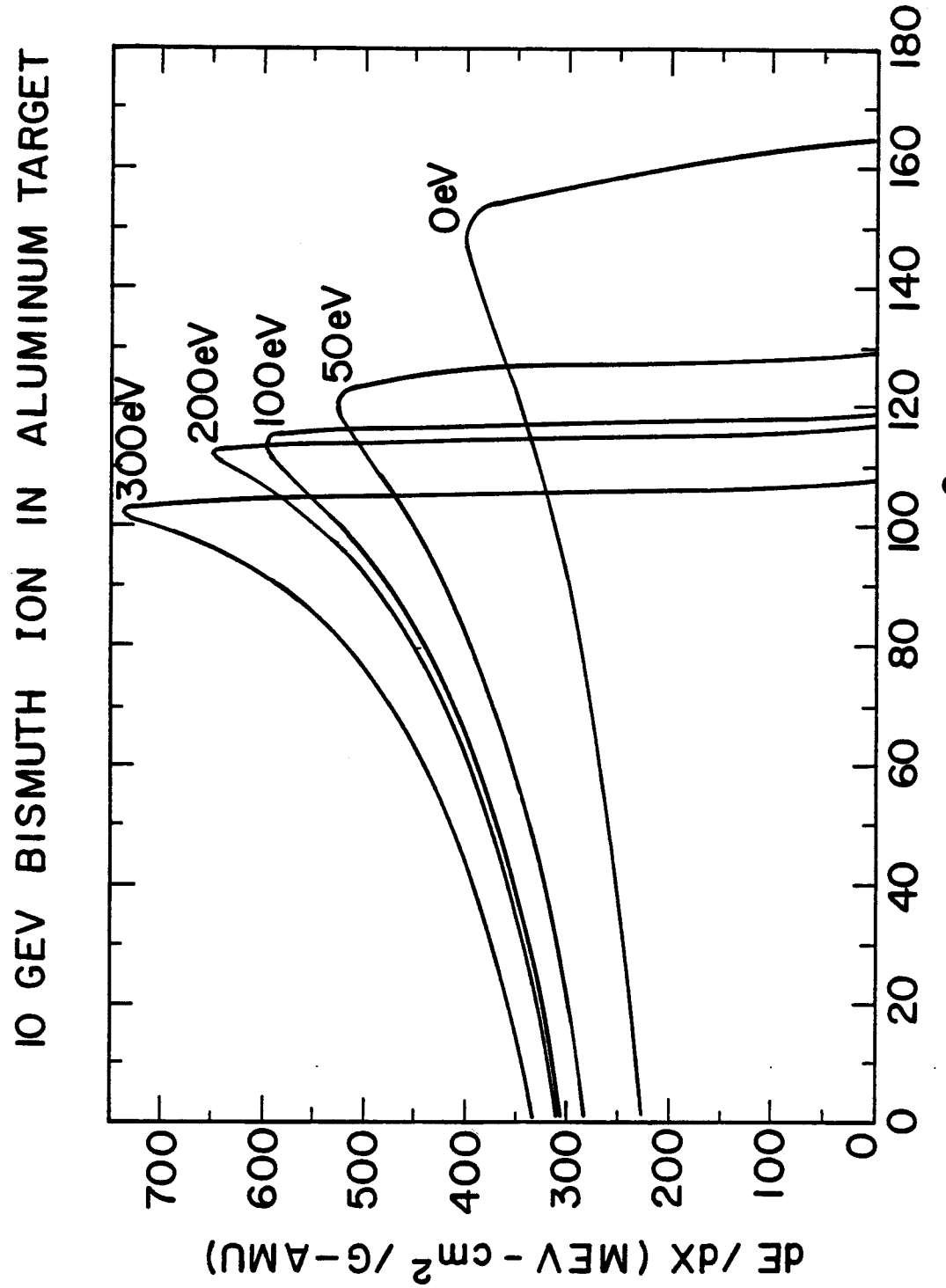

Figure III.4-11

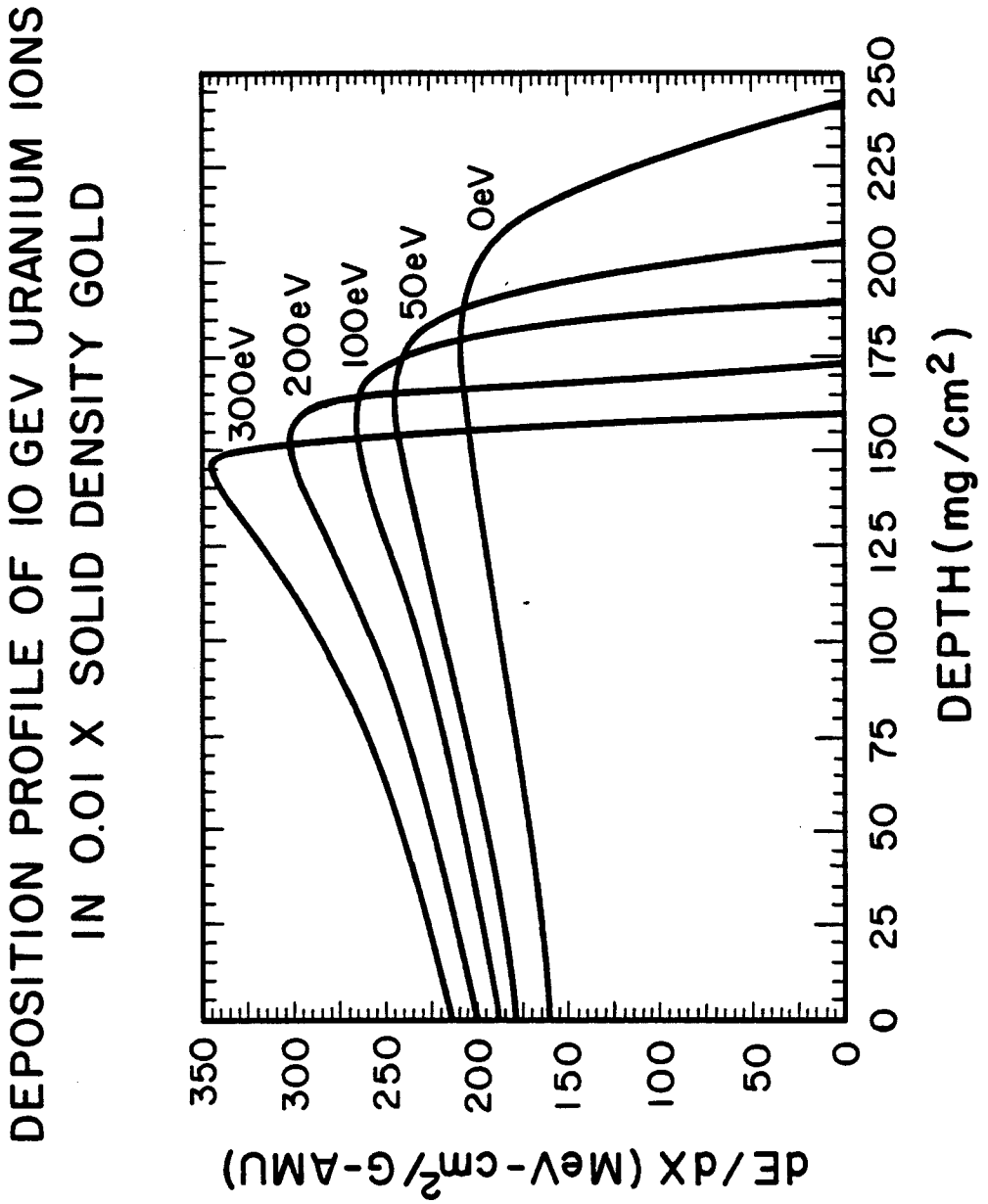

Figure III.4-12

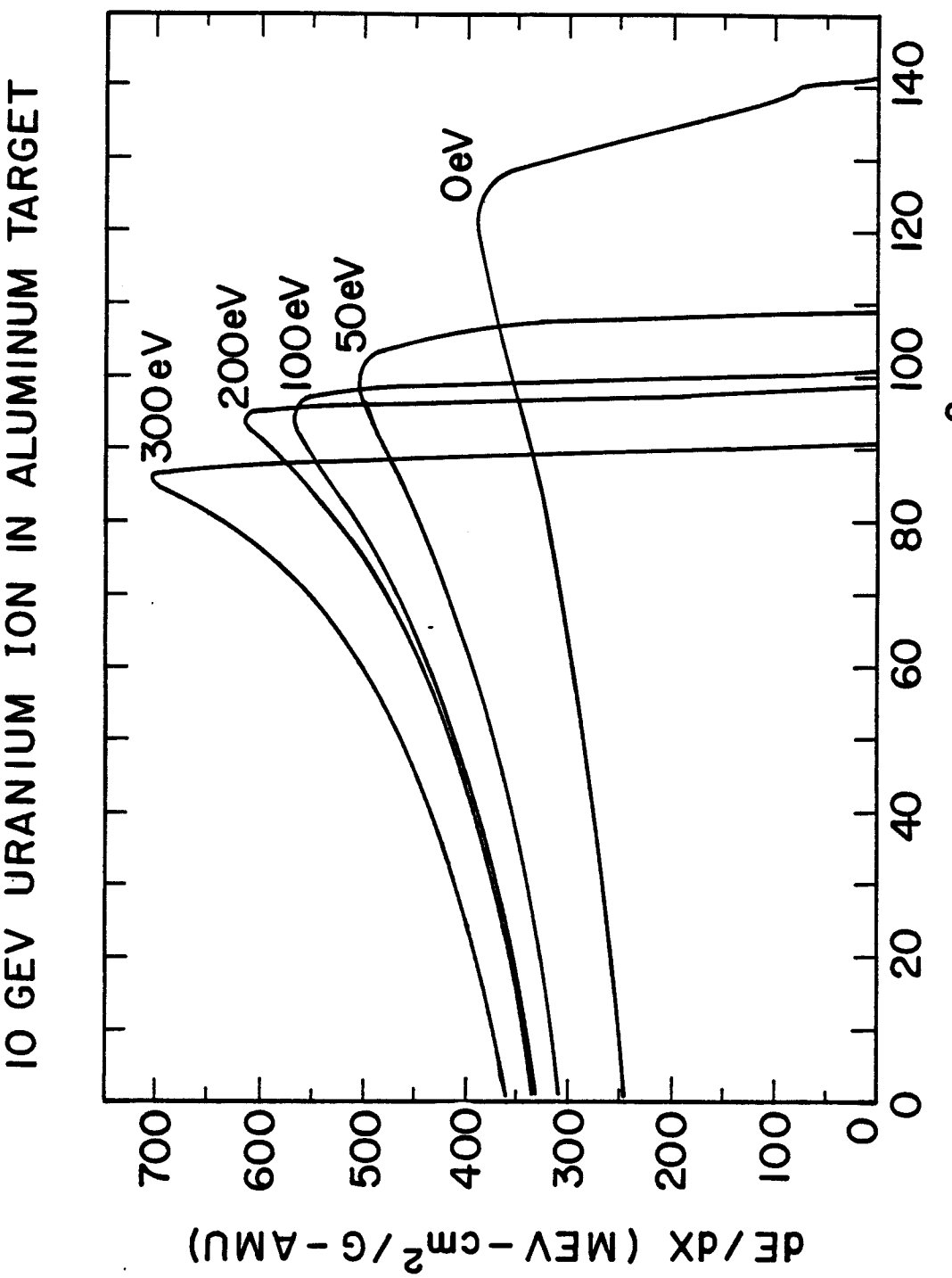

Figure III.4-13

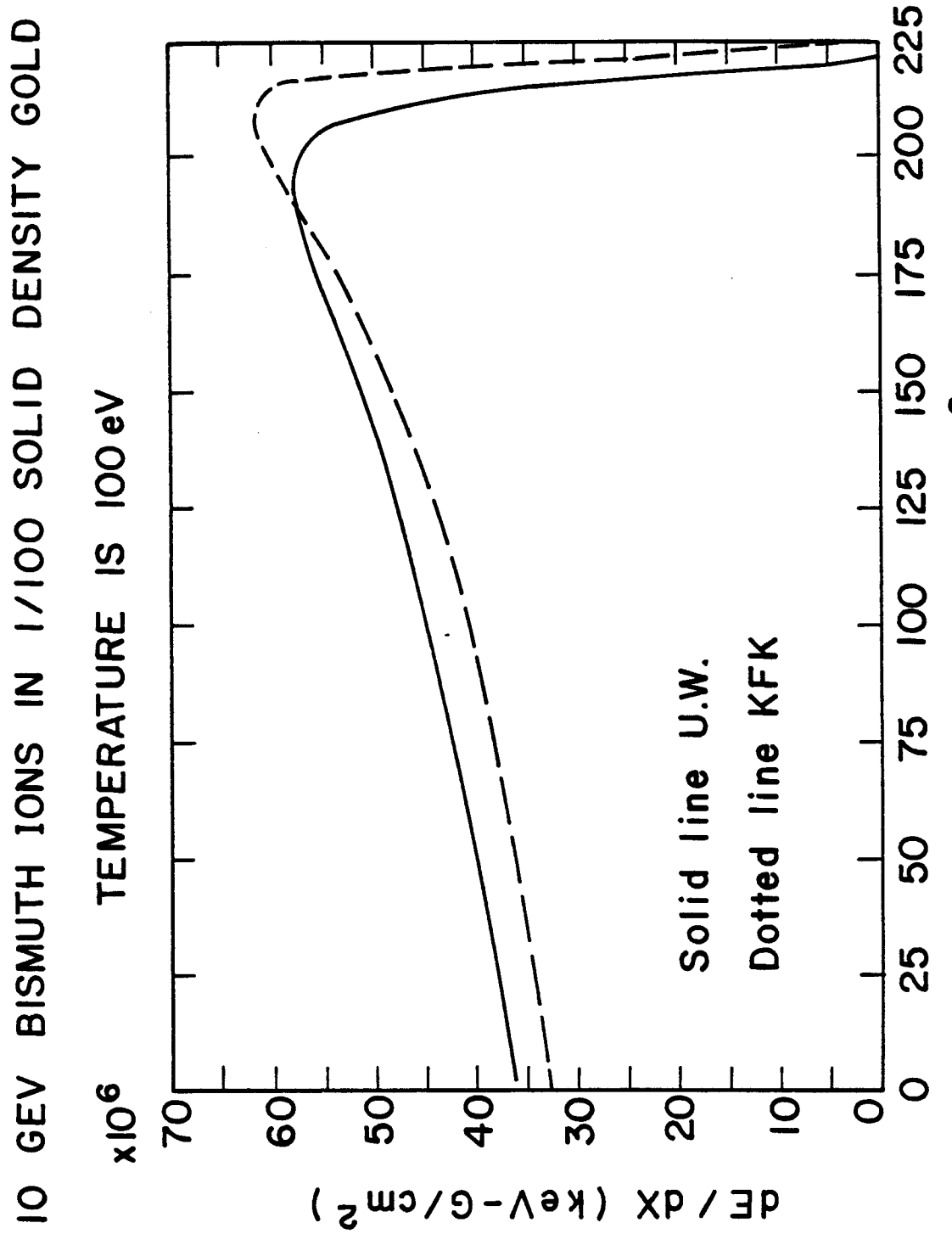

Figure III.4-14

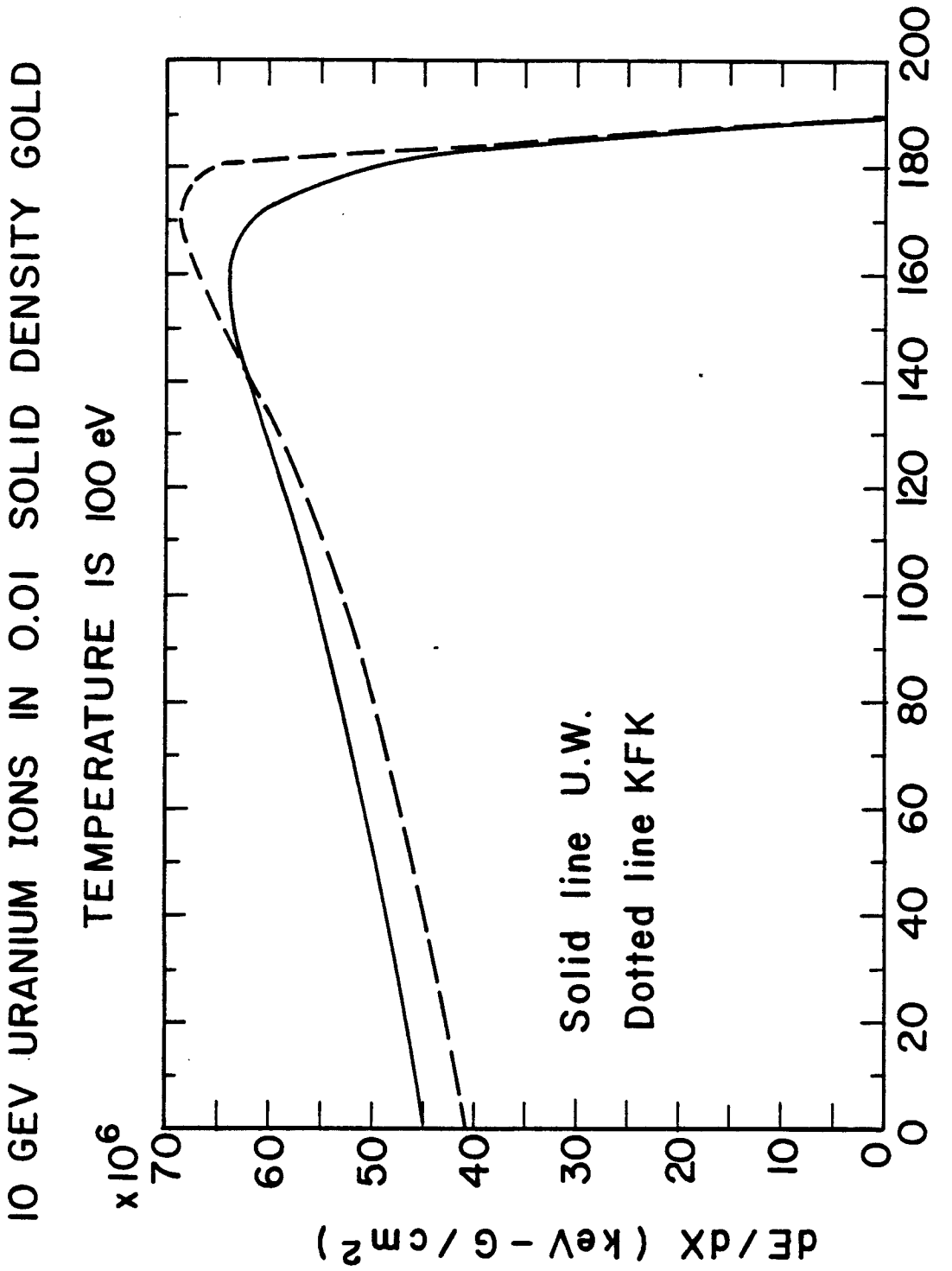

Figure III.4-15

References for III.4

1. M.H. Emery, J.H. Gardner, and J.P. Boris, "Simulation of Laser Beam Nonuniformity Effects," Naval Research Laboratory Report NRL Memo Report 4500, April 1981.

2. T.A. Mehlhorn, "A Finite Material Temperature Model for Ion Energy Deposition in Ion-Driven ICF Targets (U)," Sandia National Laboratory Report SAND80-0038, May 1980.

III.5 Target Delivery

III.5.1 Introduction

The term target delivery comprises two tasks: injecting the cryogenic target into the reactor chamber, and synchronizing the target motion and the ion pulse so that they both reach the focus location at the same time.

General conditions on the injection process are that the target must not be altered to such a large degree that it will not properly implode. This includes limiting the physical damage to the outer shell and, more importantly, the heating during delivery causing the DT fuel to sublimate or melt.

The HIBALL-I design uses ballistic injection, i.e., the target is not guided up to the focus location but travels in free motion for a substantial, final part of its flight time. During this time neither the direction nor the velocity can be corrected. Therefore, lateral deviations (the "scatter circle" of the injector) must be small enough, and the total target travel time must either be very precisely reproducible or the ion pulse has to be timed individually according to the measured target motion rather than by a clock frequency. In this latter case, the intervals between successive explosions will slightly scatter about the nominal value.

The injector described in section III.5.6 meets the scatter circle requirement but not the requirement on total travel time precision. Therefore, the design uses an optical system for longitudinal target tracking. From the results of the tracking the arrival time of the target is predicted and the ion pulse released accordingly.

Alternative "guided" ways of injection are possible and will be mentioned in section III.5.5. Lateral deviations of the target could in principle be compensated for by lateral ion-beam steering (see remark in III.5.9).

III.5.2 Target Positioning Tolerance

The tolerance (admissible inaccuracy) of the target position at ion pulse arrival clearly depends on the target size and on the geometry and intensity distribution of the ion focus. At the focus, each of the twenty beams is assumed to have a circular cross section with a Gaussian radial intensity profile and 80% of the ions within a 3 mm radius (see chapter V). Thus a perfectly positioned 3 mm-radius target will be hit by 80% and missed by 20% of the ions. For a target misplaced by 0.5 mm these figures change to about 78% and 22%, respectively. Since the target is injected along the chamber axis, roughly at right angles with all twenty beams, the same figures will apply approximately to the splitting of the total ion current in case of a longitudinal misplacement (i.e., along the flight path). The current missing the target and thus the power fraction recirculating in the installation would therefore increase by 10% relative if every target were misplaced 0.5 mm upward or downward. For lateral misplacements, the effect is smaller as it obviously multiplies by $|\sin\phi|$ where ϕ is the aximuthal angle between the direction of misplacement and the respective beam. The average of $|\sin\phi|$ over all angles is $2/\pi = 0.64$. Therefore, tolerances of 0.5 mm for the longitudinal and 0.7 mm for the lateral direction are adopted.

Any target misplacement, besides increasing the recirculating power fraction, will also decrease the symmetry of target illumination. We presume the above tolerances to be sufficient also in this respect but the question should be kept in mind for physics considerations.

III.5.3 Target Velocity

The choice of target velocity is clearly related to the longitudinal positioning tolerance. Another important condition is the fact that the ion beams are formed into bunches in the storage rings before being extracted into

the transport lines. Consequently, the ion pulse cannot be released at an arbitrary time but only when the two bunches in each ring are passing the kicker magnets (see chapter IV), i.e., at discrete instants 2.5 μs apart. The easiest way to deal with this difficulty is to choose a velocity low enough so that the distance traveled by the target in 2.5 μs is less than the longitudinal positioning tolerance. The 0.5 mm tolerance then leads to a maximum velocity of 0.5 mm/2.5 μs = 200 m/s.

From the pneumatic injector design point of view a low target velocity is favorable because it relaxes the requirements on the acceleration pressure and length and on the quantity of propellant gas leaving the injector per shot.

A condition leading to a lower bound for the velocity is given by the heating processes before ignition. The target is heated by radiation during the flight time it spends inside the chamber. In addition, with a low velocity the target may have to enter the chamber so soon after the preceding explosion that it finds a sufficiently dense atmosphere for conductive heating and/or condensing on its surface.

The calculations of the following section show that radiative heating at 200 m/s is tolerable (there is a safety margin because a perfectly black target surface was assumed). The flight time spent in the chamber is 33 ms so that the new target enters 167 ms after the explosion of the preceding one. At this time the PbLi vapor density is below 10^{11} atoms/cm^3 (see chapter VI) corresponding to a pressure below 10^{-4} Torr or 13 mPa. The thermal conductivity of the vapor at this pressure should be negligible.

Considering all the above conditions the velocity of v = 200 m/s appears the best choice.

III.5.4 Target Heating During Injection

Since it is importance to keep the fuel in a cryogenic target frozen, the

heating of a target during injection into the chamber should be considered. Using the target shown in Fig. III.5-1, we have studied the transfer of heat from the surface through the DT fuel with a Crank-Nicholson finite difference code. The result of this calculation is the temperature profiles in the target versus time.

The heat flux on the surface of the target is assumed to be due to the blackbody radiation from the cavity surface, which we assumed to be at the maximum first-surface temperature 500°C. This leads to a heat flux of 2.02 W/cm^2. Another possible source of heat is the cavity gas itself, but since this gas reaches a temperature at 167 ms very close to the INPORT tube temperature we have just used the blackbody temperature of the first surface. We have assumed that the target is a perfect absorber and have neglected its re-radiation because its temperature is so far below that of the blackbody radiation, but these are obviously worst-case assumptions. Heat conduction from the gas to the target has also been neglected (see preceding section).

Temperature dependent thermal properties have been used[10,11] with the finite-difference code to obtain the maximum fuel temperatures versus time shown in Fig. III.5-2. In the pusher region we have assumed the PbLi to be entirely Li. Here the maximum fuel temperature of the target was found to be less than 13.7 K after 32.5 ms in the cavity. If the target must travel 6.5 m at 200 m/s, this is the amount of time it remains in the cavity before it is exploded.

The temperature of 13.7 K at the DT-PbLi interface is still below the melting temperature of DT (19.7 K)[1] so that a slight lowering of the injection velocity will not lead to melting of the fuel. Furthermore, the

Fig. III.5-1 HIBALL Cryogenic Target

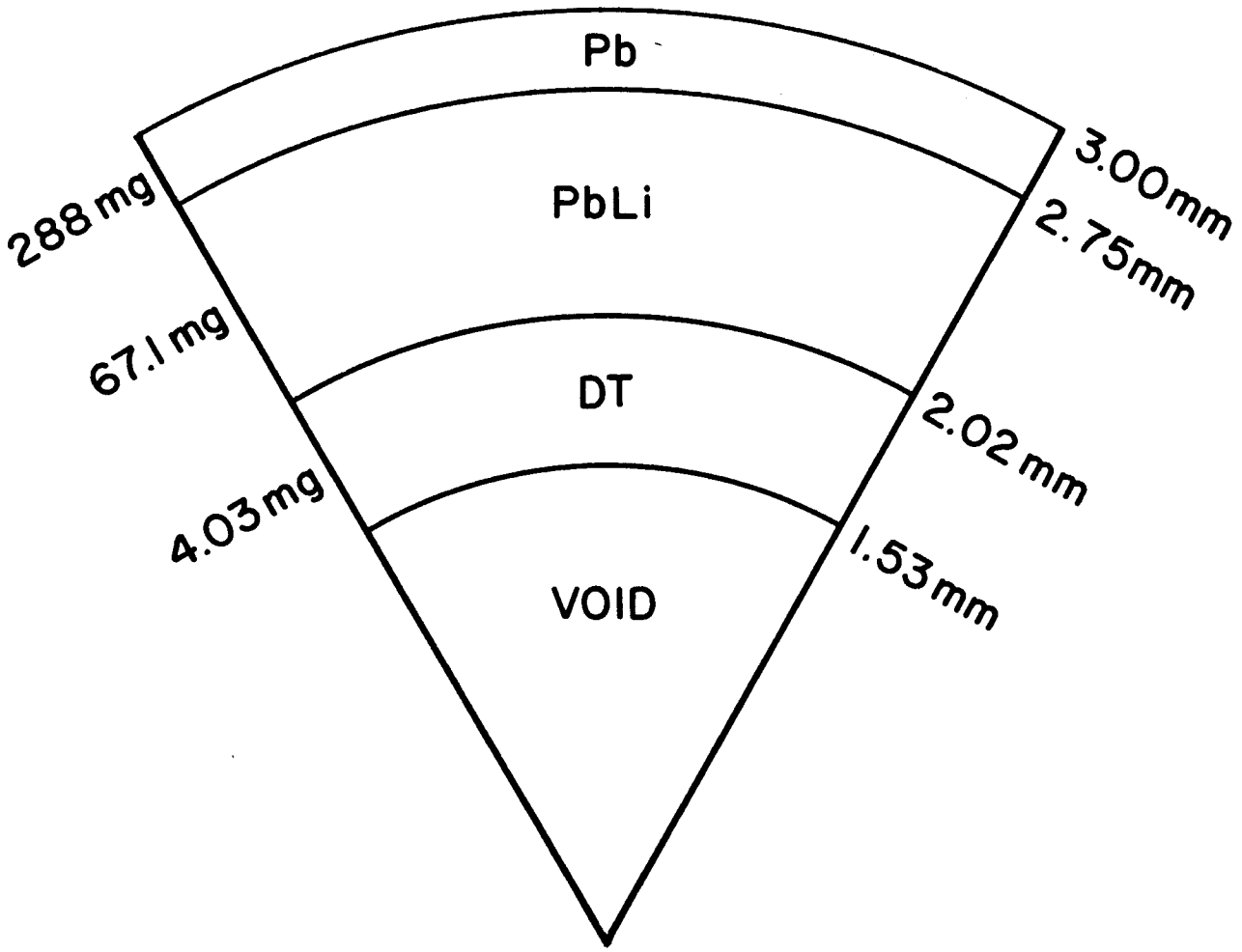

Fig. III.5-2 Maximum Target Fuel Temperature versus Time

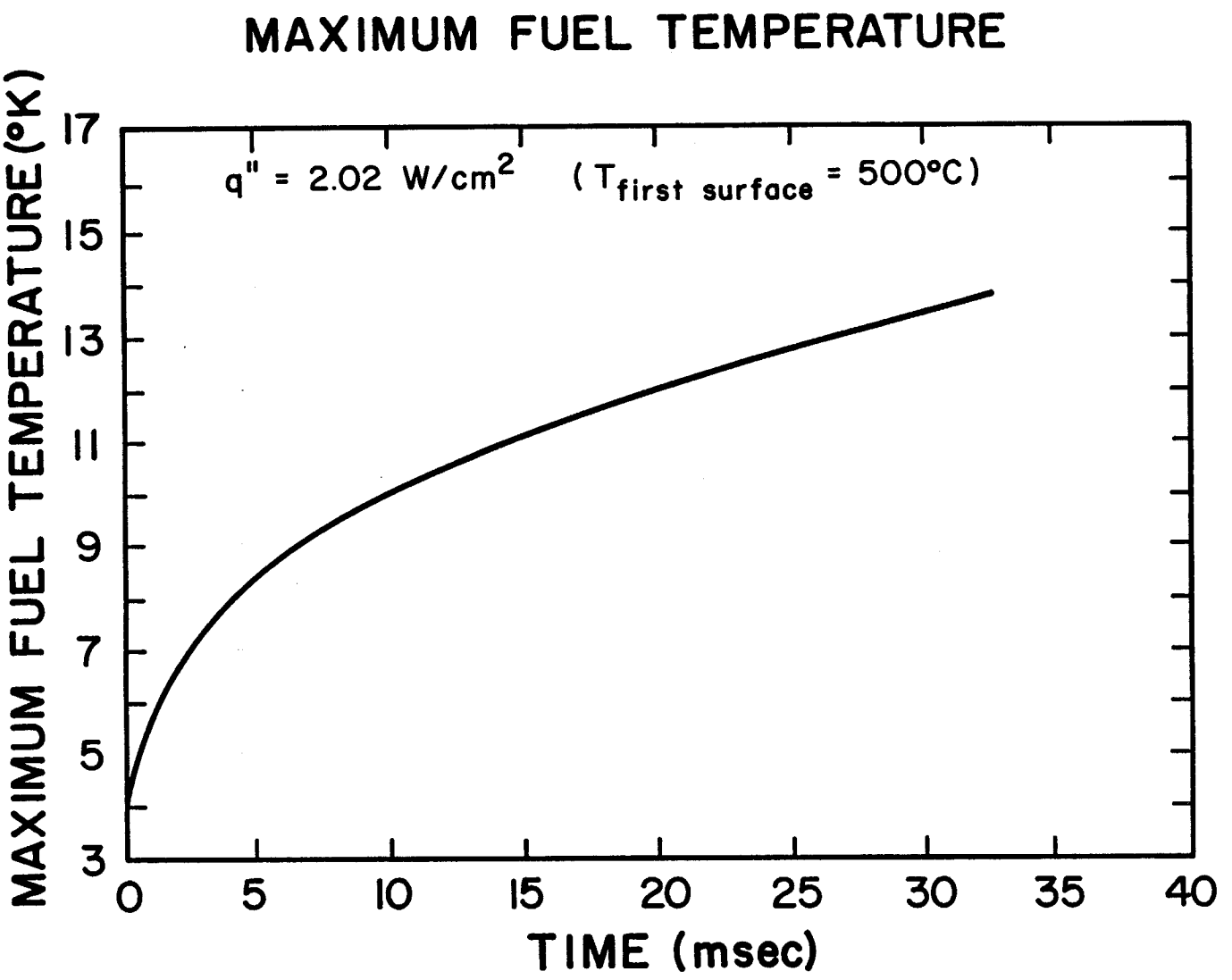

temperature of 11.3 K at the inner boundary of the fuel layer is below the sublimation temperature of DT (14 K)[2].

Temperature profiles in the target are plotted for a few times in Fig. III.5-3. The temperature is found to be almost uniform across the Pb and PbLi shells and to fall off sharply in the DT. This occurs because of the relatively high thermal diffisivity of Pb and Li at low temperatures. Because of the sharp temperature gradient in the fuel, melting will occur at the fuel-PbLi interface long before the whole fuel shell melts. Whether a small amount of melting at this interface is detrimental to the implosion and ignition is an open question, but we avoid controversy by keeping the maximum fuel temperature significantly below the melting point.

There are improvements that can be made to this calculation. Additional sources of heat should be considered as should different initial conditions. The target may have some non-uniform initial temperature distribution due to tritium decay, cooling during storage and heating due to friction during target acceleration. Additional sources of heat on the surface of the target during injection may include laser energy which guides the target to the focus of the ion beams (see III.5). In the future, these considerations must be dealt with as more information about them becomes known.

III.5.5 Injection Methods

There are several techniques that can be proposed for target acceleration to high velocity of 100 to 1000 m/s needed for ICF purposes: gravitational, pneumatic, electrostatic, electromagnetic techniques.

The gravitational acceleration is not suited for velocities of this order because the total vertical flight distance would be too large (some hundreds of meters).

Fig. III.5-3 Temperature profiles in the target

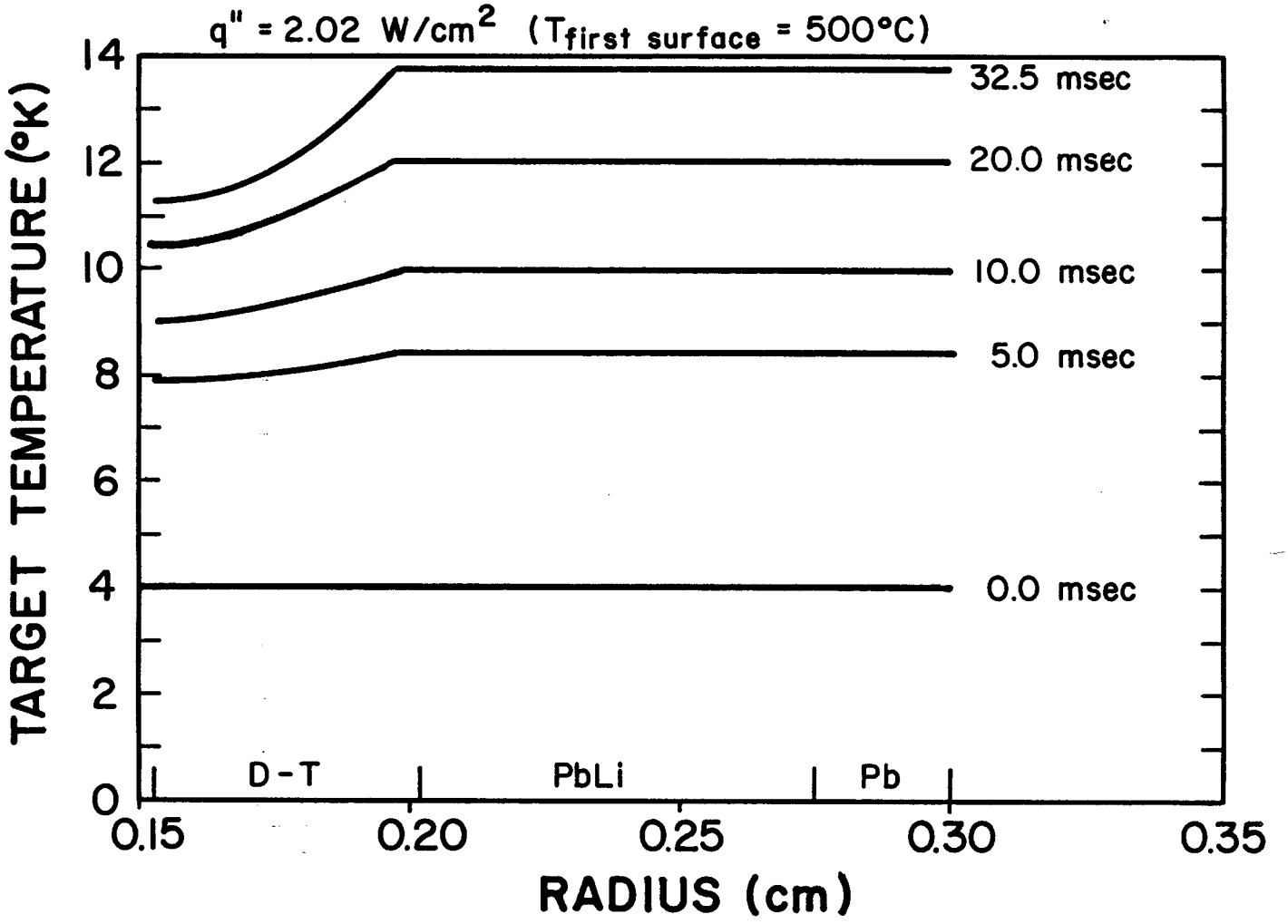

The use of the electrostatic method requires the placement of a high electric charge on the target. To accelerate masses of the order of 1 g and several millimeters diameter to velocities of about 100 m/s a charge-to-mass ratio of roughly 10^{-3} Coulomb/kg and an acceleration field of 10^{6} V/m would be necessary.(3) The experimental basis for such a scheme is too poor at the moment.

To employ the electromagnetic technique the target has to be placed into a conducting carrier driven through an induction tube. Masses of several grams could be accelerated to 100 m/s over a few meters with feasible induction currents.(4) There is, however, the problem of stability of the target carrier motion within the induction tube and the stopping of the carrier after reaching the final velocity. No experiments have been made for such an acceleration scheme. Another problem is the thermal insulation of the target from the carrier material which will be heated by the induced currents.

Pneumatic injection seems to be the most promising method at the moment because there is experience on injection systems used for refueling magnetic-confinement fusion installations.(4,5) Gas gun type injectors are used on the ORMAK and the ISX-B tokamak at Oak Ridge and the WENDELSTEIN VII A stellerator at Garching. Further work in this field is done at Risö and Culham. The purpose of these injection systems is to shoot small cylinders of solid deuterium, also called targets, into a magnetically confined plasma. A high repetition frequency is intended and target velocities up to 10 km/s are envisaged. Up to now deuterium masses of the order of 10^{-4} g have been accelerated to 100 m/s by helium or hydrogen gas at 30 to 40 bars at room temperature. Due to the small target mass an acceleration length of only some decimeters is necessary.

For each of these injection methods the aiming accuracy must be evaluated. It decides whether projectile guiding (and/or ion-beam lateral steering) is needed.

Some methods have been proposed for target (or projectile) guidance. Electrostatic trajectory corrections are suitable if electrostatic acceleration is used because the target is already charged. In any case, devices performing electrostatic trajectory corrections must be arranged outside the reactor chamber to avoid their direct irradiation.

Another class of methods for projectile guidance uses laser beams for trajectory corrections inside the reactor cavity. If a laser beam hits the target and ablates some surface material the target moves in the direction of the resulting recoil momentum. Via the illumination intensity and duration, the amount of ablated matter can be controlled so that the magnitude of the trajectory correction is adjustable.

A method by which the target is laterally guided into the desired position by only one laser beam is proposed by Chang.[6] The target drifts through a conical laser light tube which is adjusted to the aiming point where its inner diameter is just as large as the tolerance of lateral target positioning. The greatest effect of this on target performance should be mainly through additional target heating (see III.5.4).

III.5.6 HIBALL-I Pneumatic Injection System

The injection method which is most suitable from its present technological basis is pneumatic injection. The HIBALL target is vertically injected by a gas gun. Trajectory corrections are not provided. With presently available high-precision air guns a scatter circle radius of less than 0.7 mm at a distance of 12 m can be realized even for horizontal injection.[7] This distance corresponds to just the proposed injection system

(see distance scale of Fig. III.5-4). So the lateral target positioning tolerance of 0.7 mm adopted in section III.5.2 for the given illumination scheme is probably feasible by pneumatic injection without lateral guidance.

High repetition frequencies of several shots per second are also feasible with pneumatic devices.[7] Fast electromagnetic valves with a gas delivery time of the order of 10 ms are available for pressures of the order of MPa (10 Bar).[8]

A 5% reproducibility of the total target travel time, 80 ms, is needed and appears feasible.

The main components of the HIBALL-I injection system are the high pressure propellant gas reservior, the gas gun loader, the gun barrel, the fast gas valve between the reservior and the barrel, the buffer cavity between the barrel and the injection channel which penetrates the top shield of the reactor cavity, and the vacuum pumps providing the low pressure of the buffer cavity. Figure III.5-4 gives a scheme of the system together with the design parameter values.

As a cryogenic target is used in this study it is important that the fuel is not heated to a temperature above 19 K, neither in the cavity nor by friction during acceleration. To avoid heating by the latter source it is appropriate, if not necessary, to put the cryogenic target into a carrier, called a sabot in the following, which is cooled to the cryogenic temperature. Thus, cryogenic sabots, each containing a target, are delivered from a factory to the gas gun. Handling sabots within the injection system requires fewer precautions than the handling of bare targets, especially with regard to the loading of the gun. Furthermore, the sabot protects the target from damage and friction during acceleration. It provides for straight guiding within the gun barrel and isolates the target from the friction heat. The

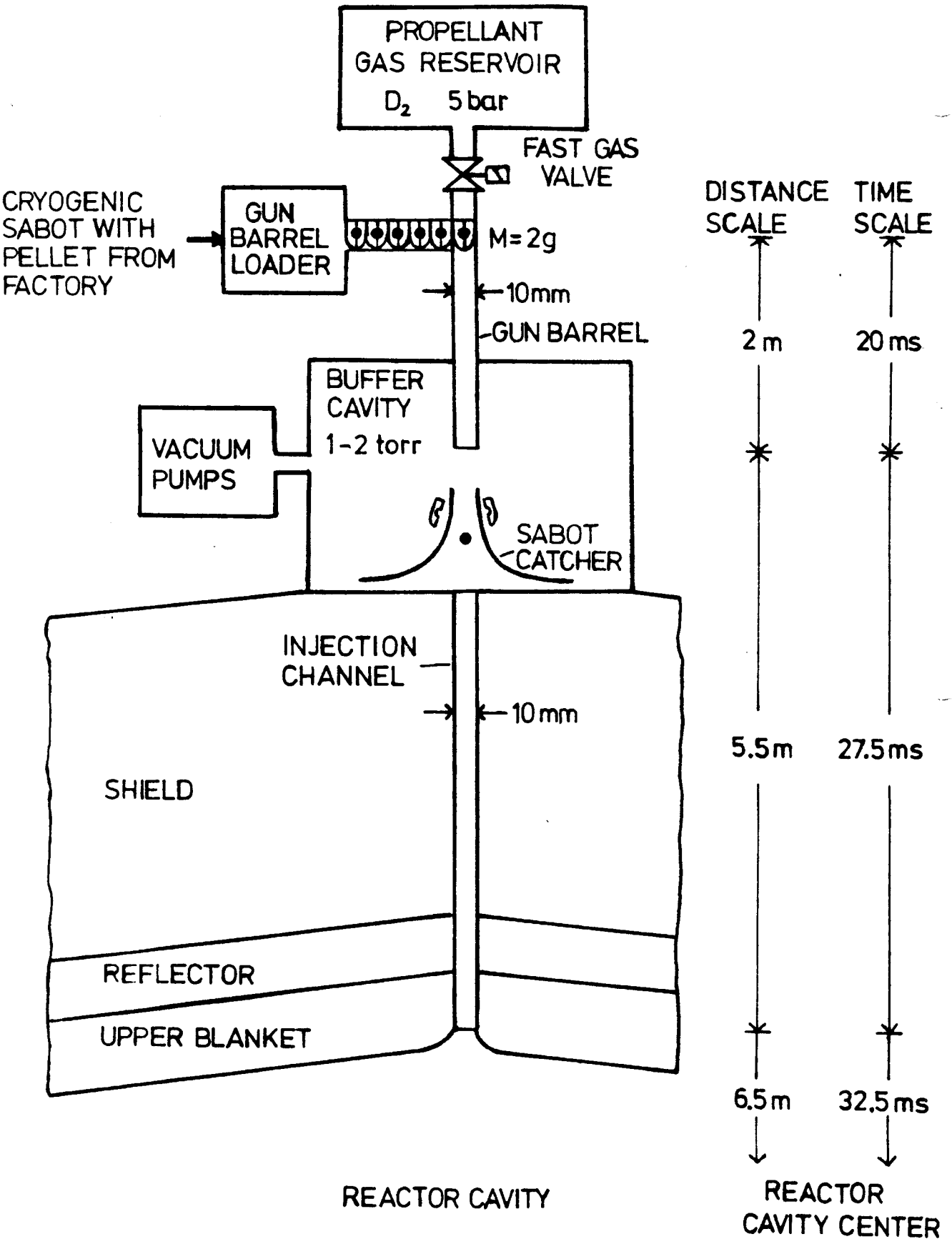

FIGURE III 5-4 SCHEME OF HIBALL-I PNEUMATIC INJECTION SYSTEM AND DESIGN PARAMETER VALUES, PELLET VELOCITY = 200 m/s

latter property requires a low thermal conductivity of the sabot material. The sabot could be made of plastic having a low friction coefficient in contact with the barrel and a high tensile stress allowing for a high acceleration. It consists of two halves separated longitudinally and is removed from the target behind the gun muzzle by a spin given to it during acceleration. To avoid a high mass, the sabot should be hollow with a suitable support structure for the target inside where a contact surface as small as possible should be provided to minimize heat transmission. If the sabot halves do not fit together very tightly the propellant gas, which should be at a low temperature in this case, will enter the sabot so that the halves will be pushed apart when the target enters the low-pressure region behind the gun muzzle. This scheme has to be avoided, however, if a momentum is transferred to the target. Otherwise, target guidance must be provided.

The sabot halves are finally collected by catcher baffles. It would be favorable to choose a sabot material which could be recirculated.

The results of sections III.5.3 and III.5.4 favor a target velocity of 200 m/s, so this value is chosen for this study. Using the sabot concept the dimensions and the mass of the sabot have to be specified. We choose a sabot diameter of 10 mm and a length of about 15 mm. Providing for a hollow, shell-like sabot structure, the sabot mass could be kept at about 1 g (even for a sabot material with mass density of several grams per cubic centimeter). As a reference value for the projectile mass, i.e., the sum of the sabot and target masses, we choose 2 g. To accelerate this projectile to a velocity of 200 m/s a minimum energy of 40 J (0.4 bar-liters) has to be provided by the propellant gas. This corresponds to a minimum gas quantity of 304 Torr-liters per shot. Accounting for the difference between the effective pressure on the projectile and the pressure of the gas reservoir, which generally depends on

the ratio of the specific heats and the temperature of the propellant gas, for the resistance due to the residual deuterium in the gun barrel, and mainly for the energy loss due to friction, we choose an overall efficiency for the kinetic energy transfer to the projectile of 0.5 as a reference value. This means that a propellant gas amount of 608 Torr liters per shot must be provided. Since a certain quantity of the gas will enter the reactor cavity we choose deuterium as a propellant gas for reasons of compatibility. A deuterium amount of 141 mg must be provided for each shot.

The deuterium quantity streaming into the reactor cavity depends on the pressure difference between the buffer cavity and the reactor cavity and on the diameter of the channel connecting both. The buffer cavity will be kept at 1 Torr after the shot assuming adiabatic expansion of the gas. For a mean pressure of 1.5 Torr in the buffer and an injection channel diameter of 10 mm, we obtain a maximum of 1.6 mg dueterium per shot streaming into the reactor cavity, assuming a reactor cavity pressure some orders of magnitude lower than 1.5 Torr.

From the total quantity $(pV)_o$ of 608 Torr liters per shot (or 80 J) a value for the product of the working pressure p_o and the acceleration distance L_a can be derived by dividing $(pV)_o$ by the cross section q of the gun barrel. In our case q = 0.785 cm^2 which gives $p_o L_a$ = 10.2 Bar·m. We choose L_a = 2 m so that the working pressure delivered by the gas reservoir must be about 5 Bar. The actual acceleration corresponds to 2.5 Bar due to the overall acceleration efficiency of 0.5. For L_a = 2 m and v = 200 m/s we obtain a mean target acceleration of 10000 m/s^2. For many materials and the given sabot dimensions this does not imply an intolerable stress on the sabot. The acceleration time is about 20 ms.

The energy loss of the projectile during acceleration due to friction can only be calculated if the sabot is completely designed because the contact area A_s between sabot and the gun barrel, the pressure p_f by which the sabot is pressed against the gun barrel and the materials of sabot and gun barrel must be known. A mean value for the friction power q_f can be estimated using the following expression:

$$q_f = f \quad p_f \quad A_s \quad \bar{v} \qquad \text{(III.5-1)}$$

where f is the friction coefficient and $\bar{v}$ the mean velocity of the projectile during acceleration. Assuming that only 10% of the sabot surface touches the gun barrel which gives in our case a value for A_s of about 50 mm^2, we obtain with p_f = 1 Bar and v = 100 m/s:

$$q_f = f \quad 500 \text{ W} \qquad \text{(III.5-2)}$$

If we use a combination of plastic (for the sabot) and metal with f = 0.05 (Teflon on steel) the friction power is 25 W; taking two metals it may be greater by a factor of ten.

In any case the gun barrel has to be cooled and the target has to be isolated from the friction heat by using a sabot material of low heat conductivity. Furthermore a small contact surface between sabot and target should be provided.

III.5.7 Target Tracking

Longitudinal target tracking means the measurement of two quantities, the target velocity and the time at which the target passes through a fixed plane.

The simple device we propose consists of a laser beam observed by a photosensitive detector and intercepted by the passing target. A beam of 0.2 mm diameter, obtainable by simple lens focussing, is completely intercepted at $v \simeq 200$ m/s within 1 μs. It is therefore certainly possible to derive a timing signal from the light detector with an uncertainty $\Delta t \leq 0.3$ μs. Two of these devices are provided at 5.5 m and 3.0 m above the focus plane (Fig. III.5-5) and furnish the times t_1 and t_2. The distance $s_{12} = 2.5$ m between them is traveled in $T = t_2 - t_1 \simeq 12.5$ ms, and this interval is measured with an uncertainty $\Delta T \leq 0.6$ μs or $\Delta T/T \leq 5 \cdot 10^{-5}$. If $s_{23} = 3$ m is the distance between the second measurement plane and the focus plane the predicted time of target arrival at focus is

$$t_3 = t_2 + (s_{23}/s_{12})T \qquad \text{(III.5-3)}$$

with a maximum uncertainty of

$$\begin{aligned} \Delta t_3 &= \Delta t_2 + (s_{23}/s_{12})\Delta T \\ &= \pm\ (0.3 + (3/2.5) \quad 0.6)\mu s \simeq \pm\ 1\ \mu s\ . \end{aligned}$$

This precision is sufficient as it is less than the interval between two successive possible ion-pulse instants (see III.5.3). The 0.7 mm lateral tolerance of the target trajectory is not a problem since such a deviation in the worst case will cause the interception to start only about 0.1 μs late.

In the last equation the uncertainty of s_{23}/s_{12} has been neglected. In practice this ratio of two fixed distances has to be kept constant within about $5 \cdot 10^{-5}$ which may require temperature control of the respective mechanical supports.

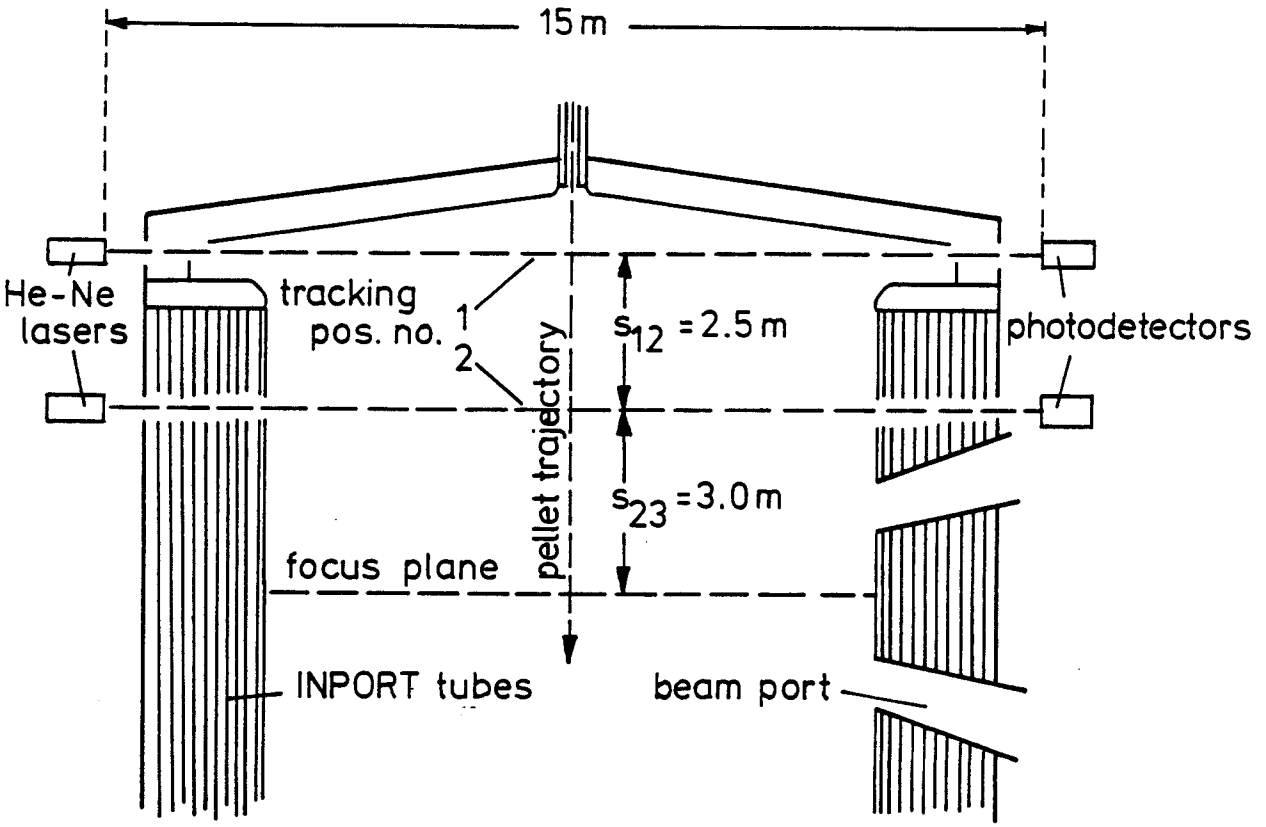

Fig. III.5-5 PELLET TRACKING

The tracking system needs optical windows that have to be protected from condensing vapor as well as from excessive radiation damage. This might be accomplished by a combination of wiping devices and rotating shutters. The lasers and detectors might also be removed out of line of sight with the cavity by using metal mirrors which could be heated to prevent condensation.

III.5.8 Synchronization

Synchronization is achieved basically as follows. Both the target injection and the ion-pulse buildup procedure are started by signals from the master clock of the facility. The ion-pulse buildup procedure is interrupted again by the clock after part of the adiabatic bunching process in the storage rings, and continues upon a signal from the synchronization circuit which evaluates the target tracking information.

Four reactor chambers, denoted A to D, each with a 200 ms average interval between shots, are served by the common driver which therefore works in a 50 ms cycle. The average duration of pulse buildup and delivery is fixed at 45 ms to allow for a maximum deviation of ±5 ms due to target injection scatter.

Figure III.5-6 is an attempt at visualizing the evolvement with time. The target being delivered to chamber B, the driver, the master clock, and the synchronization circuit are each represented by a horizontal line. Every dot means a signal created by the respective component and passed to another component as indicated by a vertical arrow. The start of the driver procedure for a shot to chamber B has been chosen arbitrarily as $t = 0$. The adiabatic bunching is started at 7.5 ms and interrupted at 36 ms. This interval of 28.5 ms suffices to reach about half the final compression of the bunches. In that state the beam is stable enough to be stored for a buffer time period which may be varied arbitrarily from zero to 10 ms in steps of 2.5 μs.

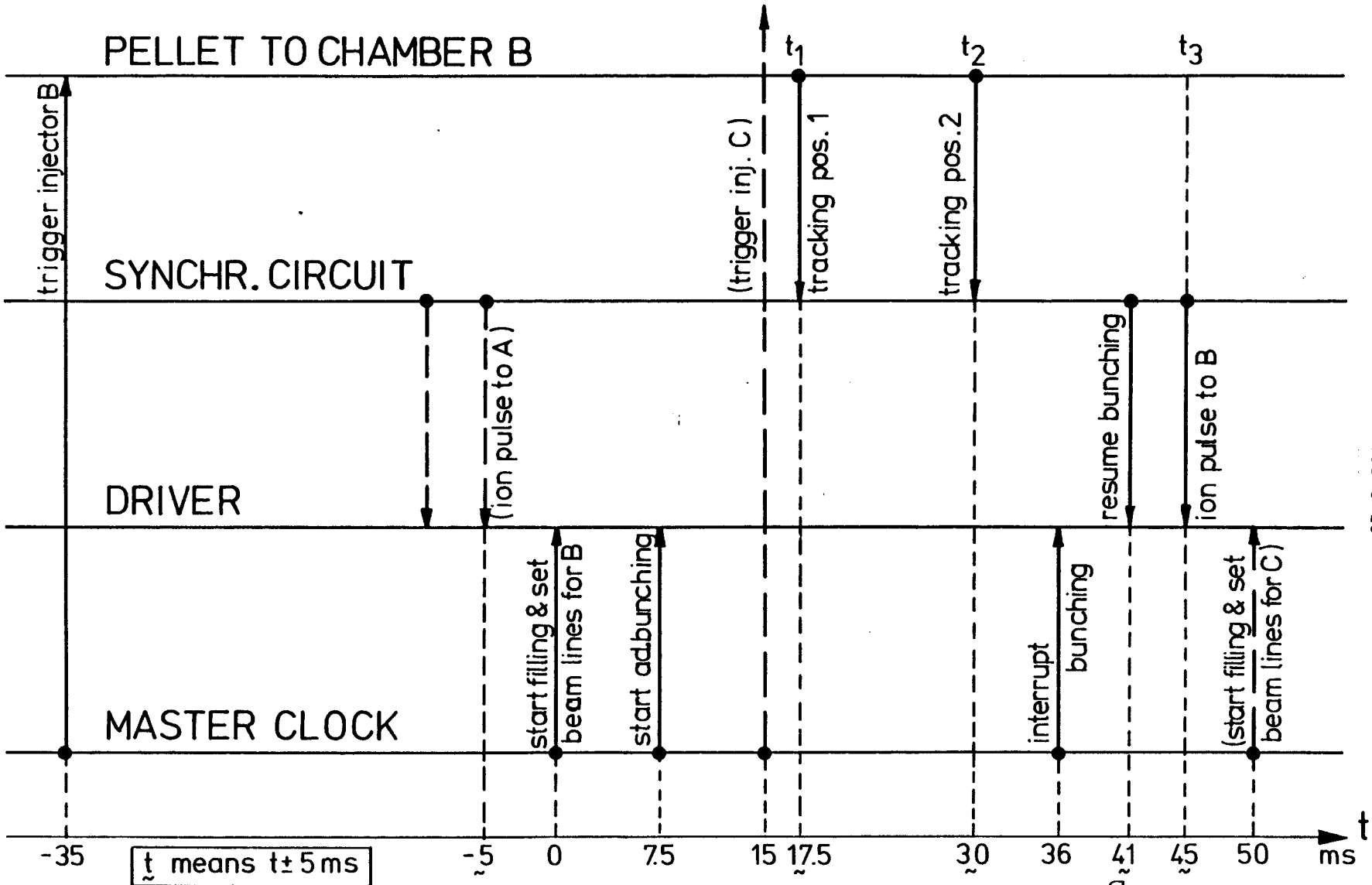

III.5-19

Fig. III.5-6 SYNCHRONIZATION

At about 30 ms (35 at the latest) the target has passed the second tracking position. Allowing 1 ms for signal processing and computation, the t_3 prediction information is thus available before or at the onset of the buffer period. The synchronizing circuit issues the continuation signal which ends the buffer period by resuming the bunching. After another 4 ms the ions are extracted into the beam transport lines. The subsequent passage to the reactor chamber, including the final fast compression, takes only about 10 μs.

III.5.9 Possibilities of Fine Synchronization

It was shown in sections III.5.3 and III.5.4 that by present knowledge, a target velocity as low as 200 m/s can be used and that in this case the ion-pulse arrival time need not be fixed to better than 2.5 μs so that the discretization introduced by the bunching in the storage rings does not present a problem. However, the safety margin with respect to target heating is not large. If a higher velocity such as 500 or 1000 m/s had to be used one or the other of the possibilities described subsequently that offer a fine adjustment within the 2.5 μs interval would be needed in addition to the "coarse" synchronization described above.

The discrete, periodic points in time at which the ion bunches reach the kicker regions are in priniciple determined as soon as the bunching RF voltage is switched on. That instant, situated at about 7.5 ms on the time scale of Fig. III.5-6, might be shifted arbitrarily with a 2.5 μs interval so as to make one of the possible pulse arrival instants coincide exactly with a given time t_3. However, this would require the t_3 prediction to be known already 37.5 ms before t_3. For example, at 500 m/s and a 12 m distance to be traveled from the muzzle, the target would not even have left the barrel at that time. Therefore, this is hardly a useful method.

There is also a way to shift the pattern of pulse instants when the bunches are already existing. It consists in varying, for a limited time, the ion energy. As the ion velocity is in the relativistic domain this will change the revolution period even though the magnetic fields would have to be kept constant for practical reasons. However, the beam trajectory is displaced radially, and the storage ring clearance admits only a very limited variation, corresponding e.g., to a relative change of 10^{-4} in the revolution period. Since the necessary shift is at most ±1.25 μs the t_3 prediction would not be needed 12.5 ms in advance.

The third possibility is ion beam steering in the vertical plane. In this case the necessary shift of the ion arrival time is replaced by a shift of the focus location in space, up or down the target trajectory. At a target velocity of 1000 m/s, a ±1.25 μs change in arrival time can obviously be effectuated by a ±1.25 mm focus shift. The corresponding deflection angle of e.g., 1.25 mm/12.5 m = 0.1 mrad can be produced by air-coil magnets. These magnets and their power supplies are less ambitious components than the storage ring kickers as the deflection angle is smaller and the rise time can be much longer. On the other hand, the magnetic field has to be continuously adjustable by a feedback-loop regulating circuit.

Since a few milliseconds would suffice to adjust the steerer fields the t_3 prediction would not be needed any earlier than it is needed for the coarse synchronization.

It may be noted that similar steerers for the horizontal plane could be used, together with target tracking for lateral deviations, to compensate for excessive direction scatter of an injector.

When considering the cost and energy consumption of a steering system it should be noted that such a system may be necessary anyway for a general,

quasistationary adjustment of the twenty beams so that only the feature of individual shot-to-shot adjustment would have to be added.

References for Section III.5

1. C.K. Briggs, R.G. Hickman, R.T. Tesugawa, P.C. Souers, "Estimated Values of Some Cryogenic Properties of Hydrogen Isotopes," IV-12 to IV-21, Radiation Effects and Tritium Technology for Fusion Reactor, Gatlinburg, Tenn. (Oct. 1979).

2. K.A. Brueckner et al., "Assessment of Drivers and Reactors for Inertial Confinement Fusion," AP-1371, Research Project 1346-1, La Jolla Institute (Feb. 1980).

3. R.G. Tomlinson et al., "Pellet and Laser Beam Space-Time Interaction System Study," R 79-954373-1, United Technologies Research Center, Conn. (Nov. 1978).

4. C.T. Chang, L.W. Jorgensen, P. Nielsen, L.L. Lengyel, "The Feasibility of Pellet Re-Fuelling of a Fusion Reactor," Nucl. Fus., 20, 859 (1980).

5. S.L. Milora, "Review of Pellet Fueling," J. Fus. En., 1, 15 (81).

6. F.R. Chang, "Laser Guided Pellets for Inertial Fusion," Nucl. Fus. 20, 537 (1980).

7. R.W. Conn et al., "SOLASE, A Laser Fusion Reactor Study," University of Wisconsin, UWFDM-220 (Dec. 1977).

8. MPP-Mitteilungen, 103, 2 (1981).

9. M.J. Monsler, "Laser Fusion: An Assessment of Pellet Injection, Tracking and Beam Pointing," Proceedings of the 3rd Topical Meeting on The Technology of Controlled Nuclear Fusion, Santa Fe, New Mexico (May 1978).

10. Y.S. Touloukian, R.W. Powell, C.Y. Ho, M.C. Nicolaou, "Thermophysical Properties of Matter," Vol. 10, Thermal Diffusivity, New York-Washington (1973).

11. H.M. Roder, G.E. Childs, R.D. McCarthy, P.E. Angerhofer, "Survey of the Properties of the Hydrogen Isotopes Below Their Critical Temperatures," NBS Technical Note 641 (Aug. 1973).

III.6 Conclusions and Recommendations

The framework of the target design effort for HIBALL is outlined at the beginning of this chapter. Three separate groups at MPQ, KfK, and UW have participated. The parameters used for this HIBALL study are:

Target Gain	83
Target Yield	400 MJ
Ion Beam Energy	4.8 MJ
Beam Power	240 TW
DT Fuel Mass	4 mg
Target Radius	0.3 cm
Ion Energy	10 GeV
Ion Type	Bi^{2+}

These were fixed at the beginning of the study. Subsequent target design efforts at MPQ and KfK have produced target designs that may differ from these fixed parameters. However, in the process we have learned where changes must be made and future HIBALL designs will reflect the increasing capabilities of the MPQ and KfK target design groups. The future overall reactor designs will be based on their specific target design results.

At this stage we are able to make the following specific statements and conclusions:

1. The ICF target gain model of Bodner has been modified to account for the constant pressure fuel configuration at ignition rather than a constant density configuration. Parametric curves generated by this new model are consistent with the target parameters chosen for HIBALL.

2. The one-dimensional Lagrangian hydrodynamics code MINIHY has been implemented at MPQ as a heavy ion beam target design code. This code includes a heavy ion beam deposition package that includes temperature effects.
3. Implosion studies with MINIHY indicate that the maximum beam power of 240 TW chosen for HIBALL is likely to be too low and a power of approximately 500 TW may be necessary to stably implode a target.
4. Implosion studies with MINIHY also indicate that careful pulse shaping is important to efficient implosions.
5. At KfK, the one-dimensional Lagrangian hydrodnamics code, MEDUSA, has been implemented for use as a heavy ion fusion target design code. The MEDUSA code contains analytic equations-of-stage that match very closely with the SESAME equation-of-state tables from LANL.
6. The MEDUSA code has been tested by successfully reproducing the results of a published light ion target design from LLNL.
7. Calculations with MEDUSA indicate that accurate equations-of-state at high density and low temperature are very important to the accurate simulation of the implosion process.
8. Temperature dependent energy deposition of heavy and light ions can now be computed by a code developed at KfK. Code results were compared to yet another code at UW with remarkably good agreement.
9. From two-dimensional computer simulations of laser irradiated planar targets at NRL we infer that achieving uniform driving pressures with ion beams requires very good illumination uniformity. Much more work is needed in this area.
10. Target injection at 200 m/s is consistent with the switching of the ion beams out of the final storage rings. At this velocity, tolerances on

target position along its flight path can be met by switching the ions out within the 2.5 μs window that is available.

11. An injection velocity of 200 m/s allows the target to reach the center of the cavity without any melting of the cryogenic DT fuel.

In the future, the one-dimensional hydrodynamics codes will continue to be developed. However, they have now reached the stage where useful target design information can be produced so more implosion calculations should also be done. More attention should be paid to multidimensional effects such as target illumination uniformity and Rayleigh-Taylor instabilities during the implosion. Some benchmarking of the various codes used in the HIBALL study could also be attempted.

IV Heavy Ion Beam Driver

IV.1 General Philosophy

IV.1.1 Choice of Ion Species

The mass-to-charge ratio of the ions A/q is chosen so that there are no excessive difficulties impeding the deposition of the energy of these ions into the target ablator, without taking into account the compensating effects of any electrons. The basic criterion is that the target, at its "cold" dimensions will not be charged up to a voltage higher than the accelerating sum voltage (kinetic energy/ion charge), or that the ratio of the pulse charge Q over the sum voltage U_Σ, which quantity may be called "beam capacity", be substantially smaller than the electric capacity of the cold target, $4\pi\varepsilon_o r_{target}$. Formulating two more relations, one for the particle range depending on the kinetic energy and the particle mass, which should be a certain fraction of the target radius r_{target}, and one equation for the required pulse energy QU_Σ, this set of three equations or inequalities has a solution for $A/q > 100$.

If the target would keep its original dimensions during irradiation, at $A/q = 100$ one half of the pulse energy would be invested into electrostatic field energy rather than into ablator heating. The ablating target, however, will send out ions forming a charge sphere which is substantially larger than the cold target, so that indeed the target voltage will be $< U_\Sigma$. Also all the electric fields within the reactor chamber will be so low that the ion motion remains "ballistic" until the ions arrive at the target surface, although these fields are still a matter of concern. Since the occurrence of free electrons is unavoidable, at least within the ablator corona, the electric fields created by the converging and ultimately stopped ion beams have to be a matter of concern and investigation in the future. These free electrons tend to undergo collective acceleration towards the symmetry center (into the target).

Other points of view in the search for a suitable ion species are: low charge-changing cross-sections against collisions with residual gas atoms, or with other ions in the bunches; it should be naturally mono-isotopic, as a matter of costs; easy handling and ionization in the source. For all these reasons we would prefer $^{209}Bi^{2+}$; other choices are $^{133}Cs^{+}$, $^{127}I^{+}$, $^{181}Ta^{+}$ or $^{181}Ta^{2+}$, $^{197}Au^{2+}$. $^{209}Bi^{2+}$ is preferred over Bi^{+} mainly because of the costs for the final focusing lenses which would be nearly prohibitive for an ion stiffness of 200 Tesla-meters, but also because of a slightly lower probability of charge exchange for Bi^{2+} during intra-beam ion-ion collisions.

IV.1.2 Pulse Energy Accumulation

Target implosion requires a driving power of 10^{12} to 10^{13} watts, i.e. a pulse energy of 5 MJ delivered within 10 to 20 nanoseconds. In contrast to the induction linac scheme, this pulse power in HIBALL is not generated in "real time", but a long beam pulse (some milliseconds) is stored, compressed, and then delivered to the target. In the papers of the early HIF workshops[1], this scheme has been called "RF accelerator scenario" (see Fig. IV.1-1).

All the pulse energy is generated in a long RF linac with $U_{\Sigma} = 5 \times 10^{9}$ volts, $I_{beam} = 160$ mA, and $P_{beam} = 800$ MW. Since some short beam pauses are programmed within the pulse, simply by switching the ion current off/on, the pulse has to last 7.5 msec, with a net on-time of 6.3 msec. The particle momentum has to be within a band of a relative width of $\pm 5 \times 10^{-5}$; therefore the beam requires careful debunching. If this band were larger, one would run into difficulties with chromatic aberrations of the final lenses which have to focus the beam onto the target, and a high fraction of the beam would miss the target. The longitudinal emittance of the beam, i.e. the product of beam energy half-width and the pulse time half-width, is critical throughout the scenario, and is more critical than the transverse emittances. While the beam energy is

Fig. IV.1-1

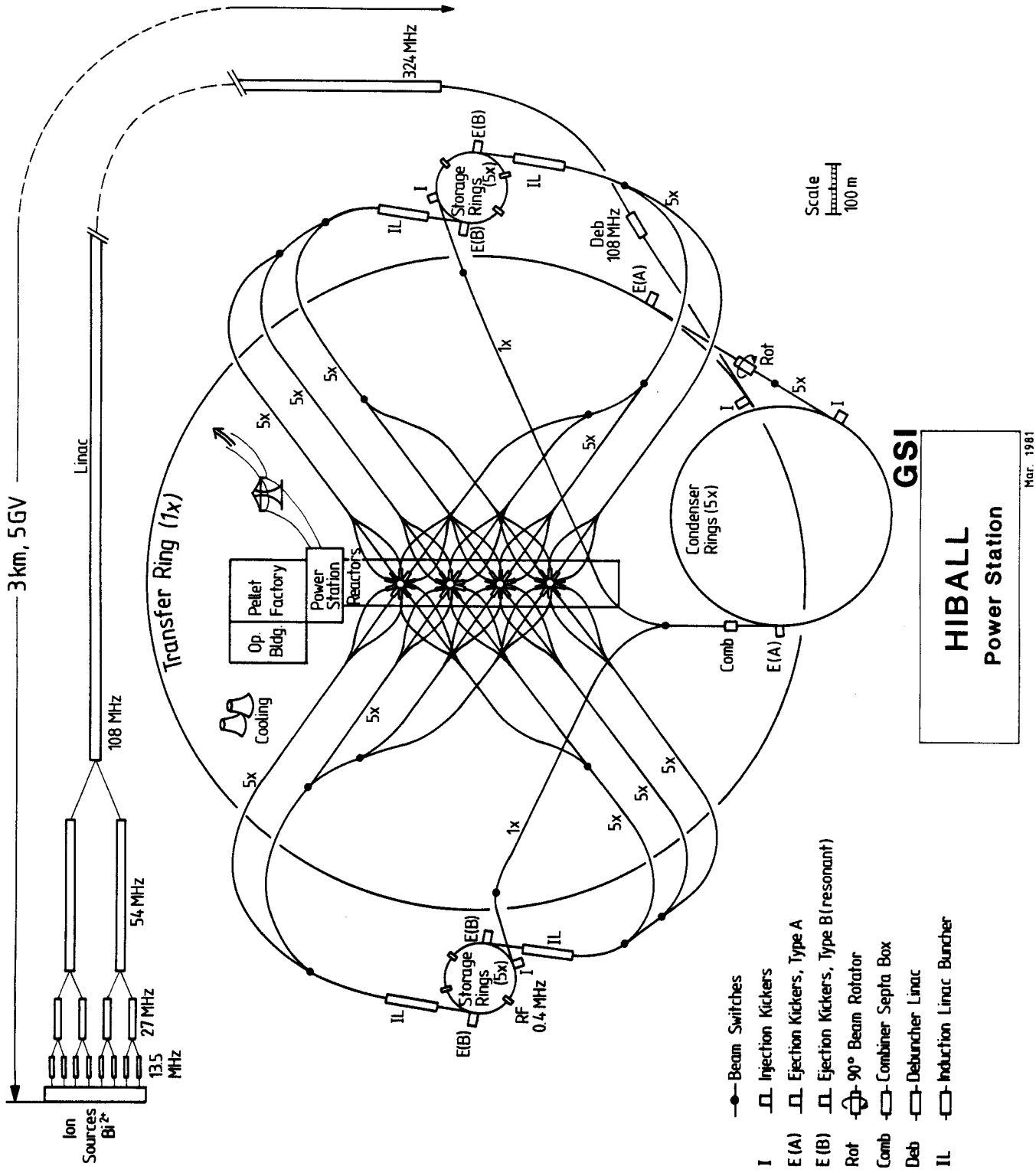
3 km, 5GV
Linac
108 MHz
54 MHz
27 MHz
135 MHz
Ion Sources Bi²⁺
324 MHz
Transfer Ring (1x)
Op. Bldg.
Pellet Factory
Power Station Reactors
Cooling
Storage Rings (5x)
E(B)
I
IL
RF 0.4 MHz
Deb 108 MHz
E(A)
Rot
Comb
Condenser Rings (5x)
5x
1x
Scale 100 m
GSI
HIBALL
Power Station
Mar. 1981
Beam Switches
Injection Kickers
Ejection Kickers, Type A
Ejection Kickers, Type B (resonant)
90° Beam Rotator
Combiner Septa Box
Debuncher Linac
Induction Linac Buncher

being generated in the linac, it is piecewise stored in a set of storage rings. It is convenient to think of the storage rings in terms of electric capacitors. The "coherent" space charge limit, which indicates at which stored electric charge Q an allowable tune shift $\Delta\nu$ (difference of betatron oscillation numbers per revolution) occurs, is proportional, among other factors, to the accelerator voltage U_Σ. For long-term storage, $|\Delta\nu|$ is restricted to values < 0.25, or even lower. For a few turns, $|\Delta\nu|$ of even a few units may be tolerated. Other important factors are the transverse emittances ε_H or ε_V of the stored beam, and the bunching factor $B_F = \bar{I}/\hat{I}$, where $\hat{I}$ is the spatial maximum and $\bar{I}$ the average circulating beam current. Non-relativistically, the coherent space charge limit can be expressed as

$$Q = 8\pi^2 \varepsilon_o \, \Delta\nu_H \, \varepsilon_H \left(1 + \sqrt{\frac{\varepsilon_V}{\varepsilon_H}}\right) B_F \, U_\Sigma$$

$$= 1400 \text{ pF/m } \Delta\nu \, \varepsilon_T \, B_F \, U_\Sigma \qquad \text{for } \varepsilon_H = \varepsilon_V = \varepsilon_T \ .$$

(Shape factors quoted in the original literature (CERN) are in the order of unity in the cases considered here.)

Again, aberrations of the final lenses determine the allowable transverse emittances ε_T. For a target of 3 mm radius, the emittance should not be greater than 60 mm mrad = 6×10^{-5} m per channel or per storage ring, or at least a product of $\varepsilon_H \varepsilon_V = 3600$ (mm mrad)^2 should not be surpassed. Therefore, the electric charge of 10^{-3} Coulomb per pulse has to be distributed into 10 storage rings, of a capacity of 0.02 pF each, to ensure that in none of them $\Delta\nu = 0.25$ is surpassed at $B_F = 1$, or $\Delta\nu = 0.5$ at B_F at 0.5, and so on. For more precise numbers, refer to Fig. IV.1-2. The limits for $\Delta\nu$ which are really safe are not well established; they may be even higher.

Fig. IV.1-2

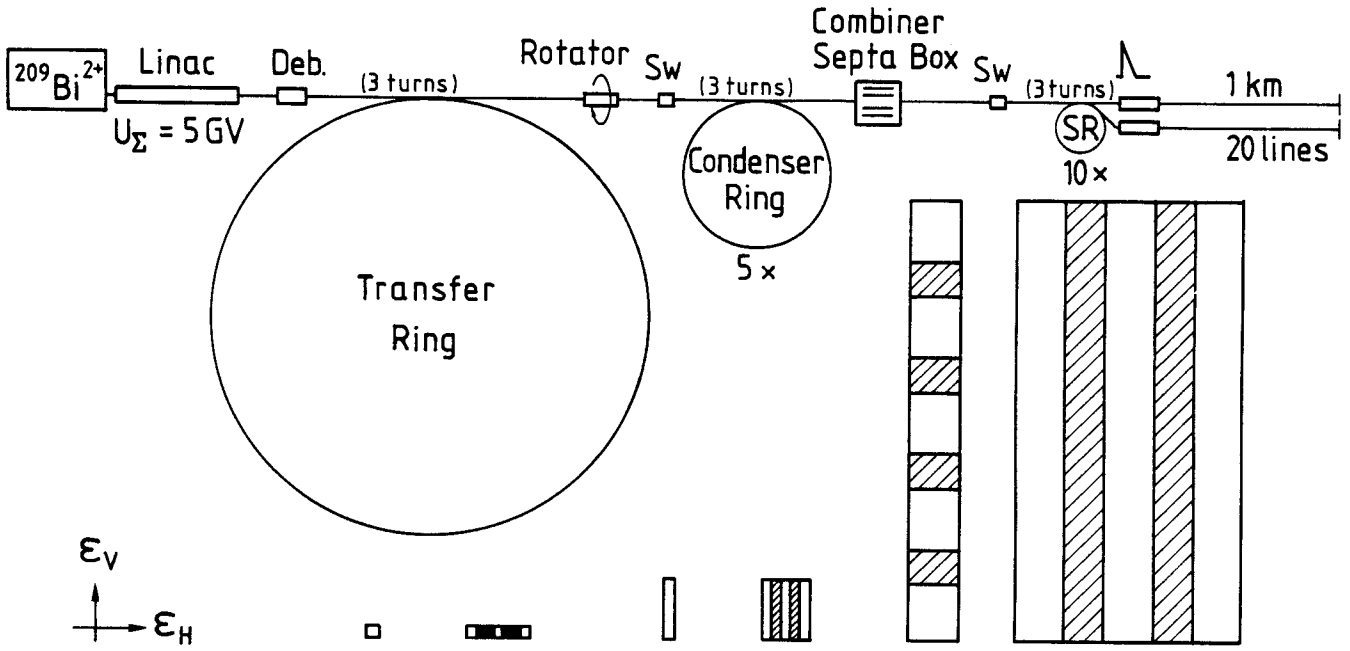

		TR		CR		SR	
Stack. Factor	3		3		5	3	
Dilution Factor	2		1.67		1.5	1.5	
$\varepsilon_H/10^{-6}$ m	2	12	2	10	10	45	
$\varepsilon_V/10^{-6}$ m	2	2	12	12	90	90	
B_F (bunch factor)		0.95		0.95		0.95	0.5 / 0.08
$-\Delta\nu_H$ (hor. tune shift)		0.356		0.287		0.277	0.526 / ≈3.3
$-\Delta\nu_V$ (vert. tune shift)		0.872		0.262		0.196	0.372 / ≈2.3
$C = \overbrace{8\pi^2\varepsilon_0}^{700\ pF/m} \lvert\Delta\nu_i\rvert B_F\varepsilon_i(1+\sqrt{\varepsilon_j/\varepsilon_i})/10^{-15}F$		4		4		20	
$W = U_\Sigma^2 \cdot C$ / MJ per ring		0.1		0.1		0.5	
$\hat{I}$/Amp	0.16	0.47		1.4		21 / 40 / 250	Target: 2500 p. channel
$\Delta p/p$	$\pm 5\cdot10^{-4}$	$\pm 5\cdot10^{-5}$				$\pm 8\cdot10^{-5}$ / $\pm 5\cdot10^{-4}$ / $\pm 5\cdot10^{-3}$	
τ_{rev}/μsec		45		15		5	
Max. residence time/msec		0.25		1.5		20...40	

EMITTANCES AND CURRENTS HISTORY, HIBALL POWER STATION SCENARIO, JUNE 1981
5 MJ WITHIN 20 NSEC FROM 20 BEAMS: $^{209}Bi^{2+}$ OF 10 GEV

It is worth noting that the coherent space charge limit is not explicitly dependent on the ring circumference. To obtain pulses as short as possible after (fast) extraction, the rings should be as compact as possible. We anticipate that future developments of superconducting magnet technology will make possible lattices of $\overline{B} \simeq 1.4$ Tesla (with local magnetic fields of 4.5 Tesla), in which Bi^{2+} ions circulate with a revolution time of 5 μsec. With respect to the chromatic aberrations of the final lenses, it turns out that only half of the 5 μsec, namely 2.5 μsec can be processed in one beam channel, and that each ring needs two exits, resulting in 20 beam lines into the target chamber. This number of beam lines is needed for another reason, namely the space-charge transport capacity of individual channels (see Chapter V). On one hand, therefore, it is not necessary to look for denser ring lattices; on the other hand, less dense lattices would require a larger number of exits per ring, or a larger total number of beam lines, or alternatively a narrower $\Delta p/p$ distribution in the rings. It seems as if there is no other reasonable choice for $\overline{B}$, at least for the given set of target parameters.

The assumption of what energy or momentum spread is reasonable in the ring for the forementioned consideration is a result of evaluations of linac particle dynamics, as a trade-off with current-transport considerations. The figure of $\Delta p/p = \pm 5 \times 10^{-5}$ then is the lower limit of what can be achieved with a careful design of the first part of the linac, the RFQ section, and under the assumption of conservation of the longinal emittance.

Two risks are worth mentioning. One is the question of whether debunching a beam in order to arrive at a very good energy definition is possible under the influence of (nonlinear) longitudinal space charge forces. The other is the risk of self-bunching of the beam into erratic bunch modes while coasting in the storage rings. It is known that this self-bunching occurs at

a given level of $\hat{I}/(\Delta p/p)$, and that it is dependent on the number of coasting revolutions. Both questions are the subject of experimental investigations planned on the SNS proton ring at Rutherford Laboratory which will be constructed in the next few years. It is planned to check measures (active feedback) to push $\hat{I}/(\Delta p/p)$ to as high a level as possible.

Next a description of how the beam is put into the storage rings will be given. The part of the linac beam which is to be wrapped into one storage ring has a (virtual) length of 0.675 msec βc = 62.5 km, which is 135 times the circumference of a storage ring. It is, physically and technically, impossible to do a 135-turn radial multiterm injection. Since a combined radial-vertical stacking procedure also seems to be too difficult, (handling a beam power of 800 MW (!)), the next idea is to wrap the beam in a large "transfer" ring radially, say 10 turns, extract it, rotate it by 90°, and wrap it radially again by, say, 15 or 20 turns. Besides the fact that a turn number as high as 10 is still too risky, the additional difficulty is that the coherent tune shift of the beam in the transfer ring is so high that the transverse stacking procedure is disturbed (the same 10^{-4} Coulomb as in the storage ring, with a far smaller transverse beam emittance). So this scheme proves to be impossible.

One solution, a multiplicity of transfer rings all being discharged at one time into one of the storage rings, has been proposed by N.M. King.[2] A still lower risk solution is given here; see Fig. IV.1-1. A transfer ring with a circumference nine times that of a storage ring is filled with three turns. After extraction the beam is rotated by 90° and injected into one of five "condenser" rings, again with three turns. This is repeated five times until all the five condenser rings have been filled. All five rings are discharged simultaneously, their beams are combined in an inverse static beam splitter (as it is in use at UNILAC for 3 beams) and injected into the storage

rings, again with three turns. Now stacking has been done in four steps, with the associated stacking factors of 3,3,5,3, whose product is 135. Though the associated dilution factors also multiply up to the fourth power, the product is small since each of the factors can be kept small when only three turns are stacked.

As proof of physical consistency, the beam emittances, tune shift, currents, etc., are listed in Fig. IV.1-2. The time schedule for the linac pulsing, and the destinations of the individual parts of the linac pulse, are indicated in Fig. IV.1-3.

Up to now, ten energy stores have been filled with all the driving energy needed. If discharged through the 20 extraction channels, the 2.5 μsec long pulses would still be too long. The momentum width in the stored beam of $\Delta p/p = \pm 5 \times 10^{-5}$ allows us to shape the contents into pulses of 20 nsec length and $\pm 5 \times 10^{-3}$ relative momentum half-width, of elliptical phase-space configuration.

Though this is simply possible from Liouville's theorem, the expense for doing this is not trivial. First of all, it requires careful adiabatic bunching in the storage rings, by means of multiplying an RF voltage of exponentially increasing amplitude. Since in the beginning the synchrotron frequency is very low, it requires many milliseconds until a bunching factor of $B_F = 0.5$ is reached. From there on, bunching is faster, but the required RF amplitudes become higher and higher. Therefore, from a suitably chosen point on, bunching should no longer be adiabatic but "fast".

One part of fast bunching is done in the storage rings themselves, by means of the RF cavities (0.4 MHz) whose voltage is raised to a high value suddenly. The second part is done outside the rings in an induction linac

Fig. IV.1-3

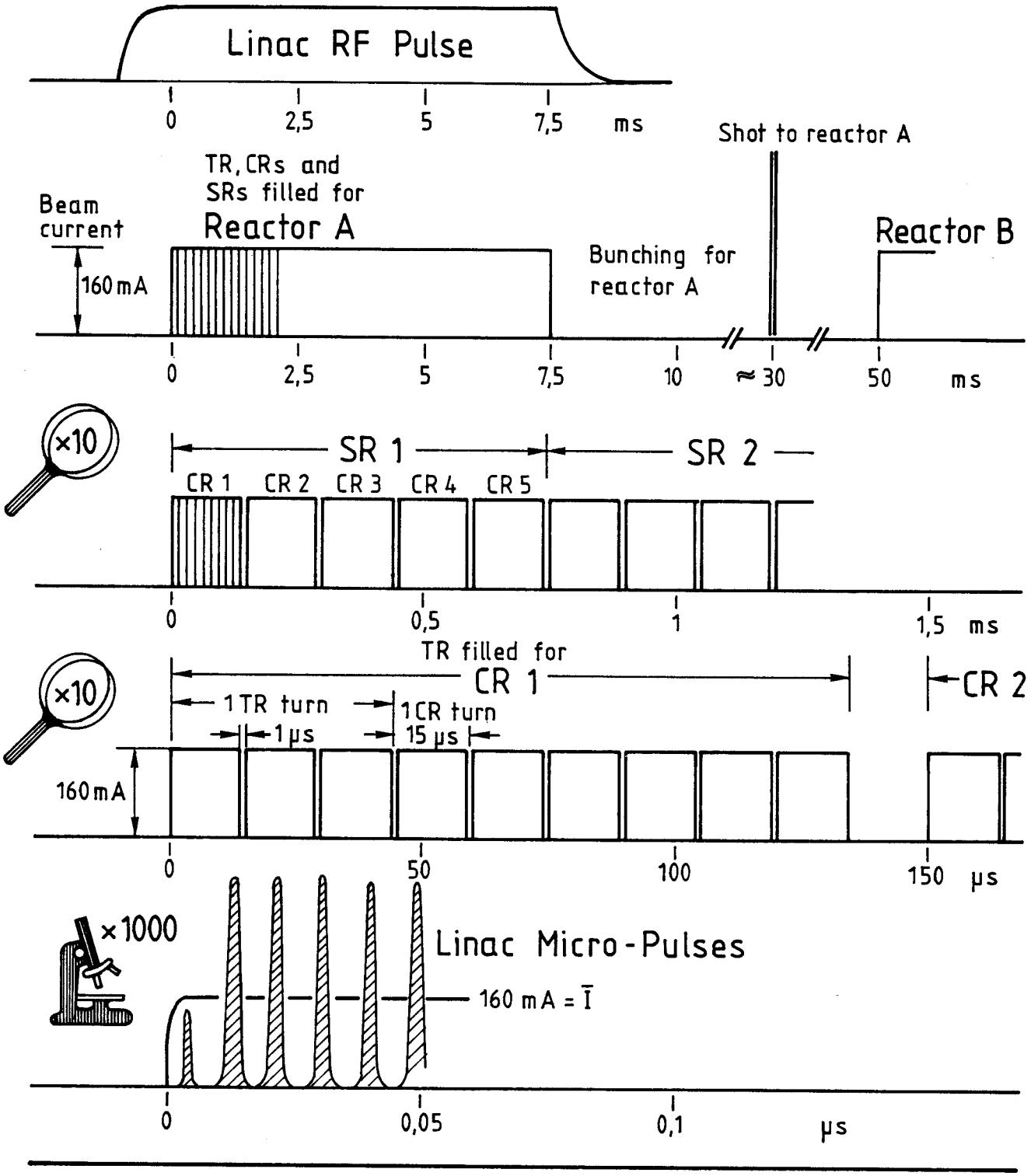

LINAC PULSE TIMING

- HIBALL -

Mar. 81

with sawtooth voltage, and the bunch comes to a time focus after a roughly 1 km long drift. Because of the importance to the investment costs, the details of this procedure are described in a separate section (IV.9).

References for Section IV.1

1. Proceedings of Heavy Ion Fusion Workshops: New York, Oct. 17-21, 1977, BNL-50769; Argonne, Sept. 19-26, 1978, ANL-79-41; Berkeley, Oct. 29-Nov. 9, 1979, LBL-10301/SLAC-PUB-2575.

2. N.M. King, J.R.M. Maidment, "A Storage Ring System for HIF," RL-81-007 (1981).

IV.2 Ion Source

The design goals for the ion source are 50 mA of heavy ions with $A/q \simeq 110$ and a normalized emittance ε_n ($\varepsilon_n = \beta\gamma\varepsilon$, $\varepsilon = F/\pi$, F = area of emittance figure) of $\varepsilon_n < 2 \times 10^{-7}$ m. The desired brightness $B_n = I/\varepsilon_n^{vert}\ \varepsilon_n^{hor}$: $B_n > 1.25 \times 10^{12}$ A/m^2 implies that the space charge of the extracted ion beam is almost completely compensated. Therefore, the source must provide a homogeneous, stable emitting surface, and the extraction system includes an electron suppressing electrode.

The emitting surface may be either solid (contact ionization sources, limited to very few materials like cesium) or a plasma sheath. As the future knowledge of charge exchange cross sections within the beam may ultimately determine the choice of the ion species a plasma source with its wide range of feeding materials offers great advantages over the former one and was preferred here.

The plasma of our source is generated by a low voltage, heated cathode discharge within a cylindrical anode, and confined radially by a magnetic multipole and axially by two reflector electrodes. This geometry has proved its value with Q (quiet plasma) machines[1] and neutral injection sources.[2]

As a first model, we developed a source for operation with gases, ELSIRE (Einzel-Ladungs-Schwer-Ionen-Reflex-Entladung)[3] which yielded, for example, 26 mA Xe ions with a brightness of $B_n = 1.5 \times 10^{12}$ A/m^2, using a 7-hole extraction system with 0.5 cm^2 total aperture area. An extension of the extraction area up to 1.5 cm^2 is possible and should result in about a 75 mA ion current. Single hole extraction (0.2 cm^2 area) was also tried and gave 4.3 mA with $B_n = 1.37 \times 10^{13}$ A/m^2, but at the extraction voltages involved (20-50 kV) one cannot enlarge this one aperture without severely losing brightness. This limitation may be lost when one extracts directly with a several hundred kV

extraction voltage, using a 4-electrode system. A first step in this direction, designing a 75 kV 4-electrode system, has actually been started.

ELSIRE was extensively tested with helium for high current accelerator experiments,[4] and exhibited good reliability and stable operation without interruption for 50 hours (50 Hz pulses, each one 2 ms long).

For the generation of metal plasmas, the source HORDIS (Hot Reflex Discharge Ion Source)[5] was constructed. It has an electrode configuration identical to that of ELSIRE, but all electrodes are suspended on poorly heat-conducting structures and run hot during source operation. The metal vapor is produced in an oven and conducted through the cathode into the discharge volume. First tests showed that the discharge can be run in a pure metal plasma after the source had been heated up using an auxiliary gas.

The ion species of interest for HIBALL is $^{209}Bi^{2+}$. For a copious production of the second charge state the discharge must be run at quite high power as then both voltage and density of the ionizing electrons are enhanced. High plasma density, on the other hand, means that the extraction apertures must be small, in order not to have the terminating plasma sheath protruding outwards which would cause a badly mismatched beam.

At an oven temperature of 990°C, an 8 mA bismuth beam was extracted from 0.34 cm^2 (7 holes) area at 31 kV. This beam contained 3.2 mA (28% particles) of Bi^{2+}, the brightness for Bi^{2+} then was $B_n > 5 \times 10^{11}$ A/m^2 (calculated from the beam line acceptance; the emittance was not measured). While it seems impossible to further raise the relative abundance of the Bi^{2+} charge state, there is a good chance to increase the total ion beam current by using 13 or even 19 extraction holes.

For still larger extraction areas the source discharge chamber has to be modified. So, presently a wider source, HORDIS II, is in the design state.

One should underline, however, that the calculated lower limit for the brightness is a factor of 3 beneath the design value, and increasing the extraction area can never lead to higher brightness, even with proportionally growing absolute ion current.

Therefore, from the viewpoint on the ion source, ions like In^+ or $^{127}I^+$ are much preferrable as the first charge state can always be extracted with more than 95% abundance. Reduced discharge power, then, would be also beneficial for source life-time and reliability. Once Bi^{2+} is given up, one should also think again of Xe^+ (possibly one enriched isotope) or $^{133}Cs^+$ as candidates.

When employing singly charged, mono-isotopic ions, one can also leave out mass separation before the pre-accelerator and thus eliminate another difficulty, that is, the emittance growth due to loss of space charge compensation and aberrations. This effect had been encountered during the helium experiments.[4] The emittance grew by a factor of 5 when the beam was passed through a magnetic quadrupole triplet. On the test stand this growth could only partially be reduced by once more compensating the space charge, raising the background pressure in the beam line behind the lens. It is doubtful, however, if this technique can be applied to a pre-accelerator beam line. A low voltage beam line as short as possible is therefore strongly indicated by the experiences gained.

References for Section IV.2

1. R. Limpaecher, K.R. McKenzie, Rev. Sci. Instr. 44, 726 (1973).

2. A. Goede, R.S. Green, B. Singh, 8th Europ. Conf. on Controlled Fusion and Plasma Physics, Prague (1977).

3. R. Keller, 3rd Int. Conf. Ion Implantation: Equipment and Technology, Kingston (1980).

4. J. Klabunde, N. Angert, R. Keller, P. Spädtke, J. Struckmeier, H. Trautmann, Particle Accelerator Conf., Washington (1981).

5. R. Keller, F. Nöhmayer, P. Spädtke, to be published.

IV.3 Low-Velocity Accelerator Tree

Several reasons dictate the start of linac acceleration with a low RF frequency, in the specific case, of 13.5 MHz. To have a safe and reliable pre-acceleration technology with quick access to the sources, and to facilitate adiabatic bunching in an RFQ structure, the platform voltage should not be above 0.5 MV. This is our specific choice, based on UNILAC experiences. There are approaches of another group (ANL) with considerably higher static pre-acceleration voltage, losing some of the abovementioned features without arriving at a considerably higher basic frequency.

Always, the velocity βc of the very heavy ions is low, and to arrive at a reasonably long drift tube length, $\beta\lambda/2$, to house the focusing quadrupoles, the only way is to choose the wave length λ high enough or the frequency $f = c/\lambda$ low enough.

A second reason is the space charge transport limit of linear accelerators. For a given transverse acceptance, this limit is proportional to the spatial betatron frequency, σ_0/S, where σ_0 is the phase advance of the betatron oscillation per unit cell length S. In the case of a magnetically, or better, electrostatically focused linac, where the number of quadrupoles of one polarity within one FODO group has no principal limit, the main point of view for the frequency choice is a technical one. For an RFQ accelerator the period length is $\beta\lambda$. Generally, the frequency choice in both cases is not substantially different, but the RFQ accelerator, because of a higher σ_0/S, has the higher beam transport capability. The frequency then should be chosen so that $\sigma_0 \simeq 1$ radian, with the electric field strength limited by sparking.

This low frequency, on the other hand, allows one to multiply the beam current in subsequent accelerator sections by injecting into them several (here, two) beams out of a corresponding number of linear accelerators. This

must always be accompanied by a jump of the RF frequency by at least this factor. By this jump of frequency an appropriate number of new RF buckets is created into which the bunches of the injecting linacs are installed, simply by a transversely deflecting RF field of the frequency of the foregoing section. Doing this repeatedly, the low-velocity end of the linac then has the shape of a tree with, e.g., 8 branches of 13.5 MHz confluent into one beam at 108 MHz. This so-called "funneling" scheme is an old idea and is based on several favorable effects:

a) At constant acceleration gradients, and constant equilibrium phase, the bunch width of a beam shrinks like $\beta^{-3/4}$, the well-known phase damping. If the frequency is suddenly doubled, the bucket shape ratio changes with $f^{1/2}$ in such a manner that a matched beam would then have a smaller phase width as $f^{-1/4}$. Generally, at a frequency jump rebunching is necessary to match the beam into the new bucket shape, and it is necessary anyway in order to transport the beam across the funneling deflector (it is also the same reason for which transverse lenses are needed). In total, one can double the frequency after every piece of linac which doubles the particle velocity, provided the acceleration gradient E_{eff} and the equilibrium phase ϕ_s remain unchanged.

In our specific case the adiabatic bunching process is finished at $\beta = 1\%$, or W = 10 MeV, a sum voltage of $U_\Sigma = 5$ MV, at a frequency of 13.5 MHz, and at an acceleration gradient of $E_{eff} = 0.6$ MeV/m. At $\beta = 8\%$, W = 600 MeV, $U_\Sigma = 300$ MV, or after roughly 200 m length of structure, all eight beams have been combined into one at 108 MHz. Since there $E_{eff} = 2$ MV/m, the phase width is only $60° \cdot (0.6/2)^{1/4} = 44.4°$. For this reason, one might combine the beams even earlier.

b) The transverse space charge "bottleneck" of any linear accelerator is found at its beginning, at low velocities. This is true also at the frequency jumps, as it is seen from analysis of any available formula, or from a simple consideration. Though in a specific structure the geometric length of individual bunches increases slightly as $(\beta\lambda)^{1/4}$, it is compressed again to its original length at a frequency jump with proper longitudinal matching. Also with a constant transverse tune σ_T, the transverse dimensions do not change. Overall, the volume of an individual bunch, and hence the local forces (transverse and longitudinal) seen in the moving frame of the bunch, remain in the same order of magnitude; otherwise the dimensions of the bunch could not remain constant. This consideration is only non-relativistic; with the approach to the velocity of light the space-charge limits are at higher currents.

In the bunch frame, neighboring bunches are shifted away from the observer's bunch; this fact may slightly modify longitudinal space charge forces. But, at a frequency jump, new bunches are inserted, and the observer has the impression of seeing neighboring bunches as close as at the beginning of the foregoing cycle. So, if the space charge limits have been checked for a piece of linac which doubles the particle velocity, one can rely upon the ratio of space-charge forces to external forces being the same again after doubling the frequency and doubling the beam current by inserting new bunches into the new buckets.

After explaining the physical conditions, a technical description of the low-velocity linac tree is to be given. At the beginning, there are eight (alternatively 16) sources, followed by a charge selection and a fast chopping device. For reasons of maintenance, the source should be arranged on separate high voltage platforms, rather than on a common platform. Each platform is on

a positive voltage of 252 kV, powered by a power supply for at least 10 mA, buffered by a capacity of least 75 nF (voltage drop less than 5 kV when 375 μC = 50 mA x 7.5 ms are taken), and housed in an RF-tight cabinet. Static acceleration columns for high current (20 mA ions) are under development; it is sure that they can be made with good optical properties.

Arriving at ground potential, the beam is focused into the transverse acceptance of an RFQ accelerator which will be described in the next section. Here the beam is still a d.c. beam. One or two wide-aperture triplets, and a space-charge correction lens will be needed.

The linac tree begins with 8 parallel RFQ linacs at 13.5 MHz, followed by 4 parallel Widerøe linacs of 27 MHz, 2 parallel Widerøe or Alvarez linacs of 54 MHz, and one Alvarez linac whose first section operates at 108 MHz. In-between, funneling and rebuncher sections combine the beams.

IV.4 RFQ Section

At low particle velocities, focusing by electric quadrupole fields is more effective than by magnetic fields. Feeding the quadrupoles with RF, a higher field strength can be maintained compared with dc voltages, especially since support insulators can be avoided. Though RF power is more expensive to produce than the same amount of dc power, with a careful design one can build the accelerator at a far lower expense per megavolt than a drift tube linac with static focusing devices.

This explains why adiabatic bunching of a dc beam into RF buckets is mostly mentioned in connection with RFQ structures. Adiabatic bunching which in principle is possible with any linac type, demands a certain additional length of linac which normally is regarded to be too expensive for this purpose. An additional reason is that transverse focusing should be very vigorous to avoid excessive long-trans coupling (especially the parametric coupling resonance), and this again would make other structures than the RFQ less effective. Especially, the combination of currents of $^{209}Bi^{2+}$ ions of 20 mA, adiabatic and loss-free bunching out of a particle energy of 0.5 MeV and a frequency of 13.5 MHz is only possible with RFQ techniques.

In an ingenious concept Kapchinskij and Teplyakov[1] have demonstrated how to use RFQ techniques in the most efficient way. Since then, several groups have begun to design or to build RFQ structures, the most successful of which was at Los Alamos. Nearly all of these were for protons or light ions ($A/q < 3$); also the original concept of Kapchinskij and Teplyakov was designed for light ions at fairly high frequencies (> 100 MHz).

Beside an incomplete design of D. Swenson[2] for very heavy ions ($A/q = 100$) the only effort to design an RFQ accelerator for these ions (or even heavier ones) at low frequencies around 10 MHz up to now has been made jointly

by GSI of Darmstadt and the University of Frankfurt. The RF system of this accelerator is quite different from the light ion types.[3] Its features are good power economy in spite of a high capacitive load of the RF cavity (or a good "shunt impedance"), and very good stability of the voltage distribution along the accelerator against disturbing influences (capacitances, geometric errors). A proton model of this design, scaled down 1:4 has been put into operation. Now (1981) a prototype of a full-scale accelerator cavity is built, with a slightly smaller transverse acceptance. As a novelty, so-called radial matching sections are installed at the beginning as well as at the end. By this measure it is tried to keep the transverse emittance blow-up as small as possible. We hope for an emittance blow-up factor as small as 1.5 to 2.0, and this hope is nourished by calculations of the Los Alamos group. A maximum blow-up factor of 3.0 would be tolerable.

A specific problem with adiabatic bunching is the longitudinal emittance of the beam. Without a so-called shaper section, the longitudinal emittance is determined by the fairly large longitudinal acceptance of the so-called "gentle-buncher" into which the beam is filamentated. To decrease the emittance, i.e. to avoid some of the filamentation, a so-called "shaper section" is used before, with no acceleration at all, but with a rising longitudinal field amplitude. Its problem is that it should be very long to be very effective. With a 1 m long shaper, 18 $\beta\lambda$ periods, the longitudinal emittance is 50 degrees x keV/amu, compared with 140 deg x keV/amu without any shaper. The longitudinal emittance should be smaller than 25 deg x keV/amu for the HIBALL accelerator. At the time of writing we try to determine how long the shaper should be. A longer shaper does not improve the capture efficiency substantially, which is now 80 to 90%. Figure IV.4-1 shows a longitudinal section through the RFQ cavity prototype.

Fig. IV.4-1

This figure was unavailable at time of printing.

References for Section IV.4

1. I.M. Kapchinskij, V.A. Teplyakov, Pribory i Tekh. Eksp. (1970), 19-22; I.M. Kapchinskij, IHP-INZH 72-29, Serpukhov 1972; translation: GSI-tr-14/76.

2. D.A. Swenson, Proc. HIF Accel. Study, Berkeley, CA (Oct./Nov. 1979).

3. R.W Muller, GSI 79-7 (1979).

IV.5 Widerøe and Alvarez Sections

This is the most conservative and best developed part of the facility. Though it has to be designed for a lower specific ion charge q/A, its technical features may be widely identical with the GSI design of UNILAC cavities, except for the total lengths. Descriptions have to be omitted here, they may be taken from the literature.[1-3] Figure IV.5-1 gives a parameter table of the linac.

While UNILAC is composed of 27.1 and 108.4 MHz structures only, there will be an intermediate 54.2 MHz structure also, probably of the Widerøe design. This structure has not yet been detailed.

Calculations and experiments done recently[4] show that the beam transport capability of the Widerøe structure is sufficient for HIBALL, except the first part of UNILAC cavity W1, the very first one, which in HIBALL will be replaced by an RFQ cavity, see section IV.4.

The last part of the linac, but the largest one as measured in terms of length of structure and installed power, is a 325.2 MHz Alvarez structure. This frequency is preferred over 216.8 MHz because there is no mature power-amplifier technology available between 108 MHz (upper end of FM radio) and the onset of klystron technology for which only recently high-power klystrons of 324 MHz have been developed. This consideration was one of the important reasons of the frequency choice (108 and 324 MHz) for the SNQ Project,[5] a 1.1 GeV proton linac for an intense neutron source. In this project also the type of structure changed in favor of the "disc-and-washer" structure at this frequency jump. We are, however, not able to choose another type of cavity than the Alvarez structure for two reasons: (1) For reasons of space charge transport we have to provide one quadrupole magnet per $\beta\lambda$, i.e. the length of one FODO period should not be more than 1 $\beta\lambda$; so we may not choose a structure

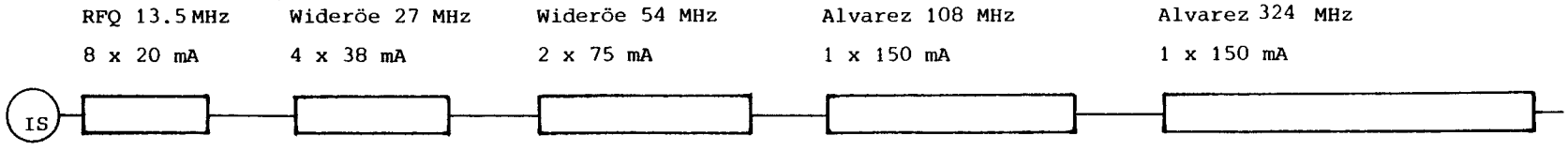

β in %	1,5	3	6	12	32	
W in MeV/u	0,1	0,4	1,7	6,5	50	
ΔU in MV	10	30	130	480	4350	Σ = 5000 MV
Acc. Rate in MV/m	0.5	1	1.25	1.5	1.75	
Length in m	20	30	104	320	2500	Σ = 3000 m
RF Peak Power in MW/m	0.03	0.034	0.05	0.072	0.1	
RF Peak Power per Section	4.8	4.4	10.4	23	250	Σ = 293 MW
RF Duty Factor	0.154	0.154	0.154	0.164	0.155	
Average RF Power	1.22	0.68	1.6	3.8	38.5	Σ = 45.8 MW

Comments: Acc.Rate = $E_o \cdot T \cdot \cos\phi_s$
E_o = Average Axial Field
T = Transittime Factor ∿ 0.86
ϕ_s = Synchron.Phase Angle = - 30°
RF Peak Pwr in MW/m = E_o^2/Z_o
Z_o = Shunt impedance = 50 MΩ/m

Fig. IV.5-1: Preliminary HIBALL Linac Parameters

of "separate functions". (2) The main parameter that determines whether the shunt impedance (which is a figure of merit for optimal power economy) is near its maximum, is the particle velocity. $\beta = 0.32$ is well within the domain of Alvarez, and clearly outside the domain of disc and washer. A little problem seems to arise from the diameter of drift tubes which cannot be scaled down to proportional to λ since the bore diameter does not scale this way. Nevertheless, even if the optimum of drift tube diameter (about 5 to 10% of λ) cannot be matched, the shunt impedance still is higher at 325.2 MHz than at 216.8 MHz. Moreover it is hoped to draw advantage from the newly-developed permanent-quadrupole magnet technology[5] by designing smaller (and energy-conserving) drift tubes.

Probably it will not be necessary to equip the linac with remote handling maintenance devices, in contrast to high-intensity proton and deuteron machines. If ions hit solid materials, elastic and inelastic scattering dominate largely over nuclear reactions. At UNILAC, residual radioactivity in linac components is negligible except in the beam splitter septa which routinely are hit by a large fraction of the beam. However, this device too does not require remote handling. In HIBALL, beam intensities are three or four orders of magnitude higher. Then drift tubes etc. will become slightly radioactive, but only septa in the storage rings will require remote handling.

The RF amplifier systems probably will look a little different from UNILAC techniques. 50% to 75% of the RF power, about 800 MW, will be taken by the beam. Then the 50 Ohm power transmission lines between the amplifiers and the accelerator structures which, though expensive, represent an advantage for status diagnostics under a small beam load, are no longer very reasonable. Instead, we may think of tetrode amplifiers which are coupled directly, on a high impedance level, to the accelerator structures. This may result in

smaller units also, the modularity of these units may improve the reliability. These trends at present do not apply to klystron amplifiers which normally have to operate into a matched waveguide line.

References for Section IV.5

1. K. Kaspar, "The Prestripper Accelerator of the UNILAC," Proton Lin. Acc. Conf., Chalk River (1976).

2. D. Böhne, "The UNILAC, Development and Present Status," Proton Lin. Acc. Conf., Chalk River (1976).

3. T. Niewodniczanski, E. Malwitz, "Mechanical Design Features of the UNILAC," Proton Linear Acc. Conf., Los Alamos (1972).

4. J. Klabunde et al., "High Current Expeiments in a Widerõe Structure," IEEE Trans. NS-28 (1981), 345-2, Accel. Conf., Washington, D.C. (1981).

5. J.E. Vetter (Ed.), "The Basic Concept of the SNQ Lin. Accelerator," KfK 3180 B (June 1981).

IV.6 Funneling

The purpose of the funneling sections has been described in section IV.1, and is shortly repeated here.

In linacs, the frequency can be doubled each time the velocity of particles has been doubled. At this point, one can combine the beams of two foregoing linacs into the one of higher frequency without any disadvantages concerning space charge containment, since the linac of higher frequency contains double the number of RF buckets. One needs, however, a switch which brings the beams of both foregoing linacs into a common beam axis.

Though in principle one would need a deflector with a step-function behavior (meander or trapez function), in practice a sine function deflecting field will do. The frequency of the deflecting field is that of the foregoing linac, i.e. to combine the beams of two 54.2 MHz linacs into one 108.4 MHz linac, one would use a 54.2 MHz transverse deflector.

Another question is whether the electric field necessarily travels along with the beam pulses, or whether a standing-wave cavity may be used. In the case of sinusoidal field, the field strength which can be generated is high enough to apply a standing wave. The practical problem of a funneling section is that rebunching cavities (for properly matching into the next structure), quadrupole lenses, bending magnets and a septum magnet also have to be arranged in the beam path.

Because of the limited "aperture" of the "time lenses", as rebunchers can be looked at, given by the useful phase width of the sinus curve which has to be sufficiently linear, the space between two rebuncher cavities, or the distance to the objects which have to be matched to, is limited to a few meters. Generally, funneling sections tend to be short and crowded. This problem is looked at by K. Bongardt at KfK. A preliminary design is shown in Fig. IV.6-1,

Fig. IV.6-1

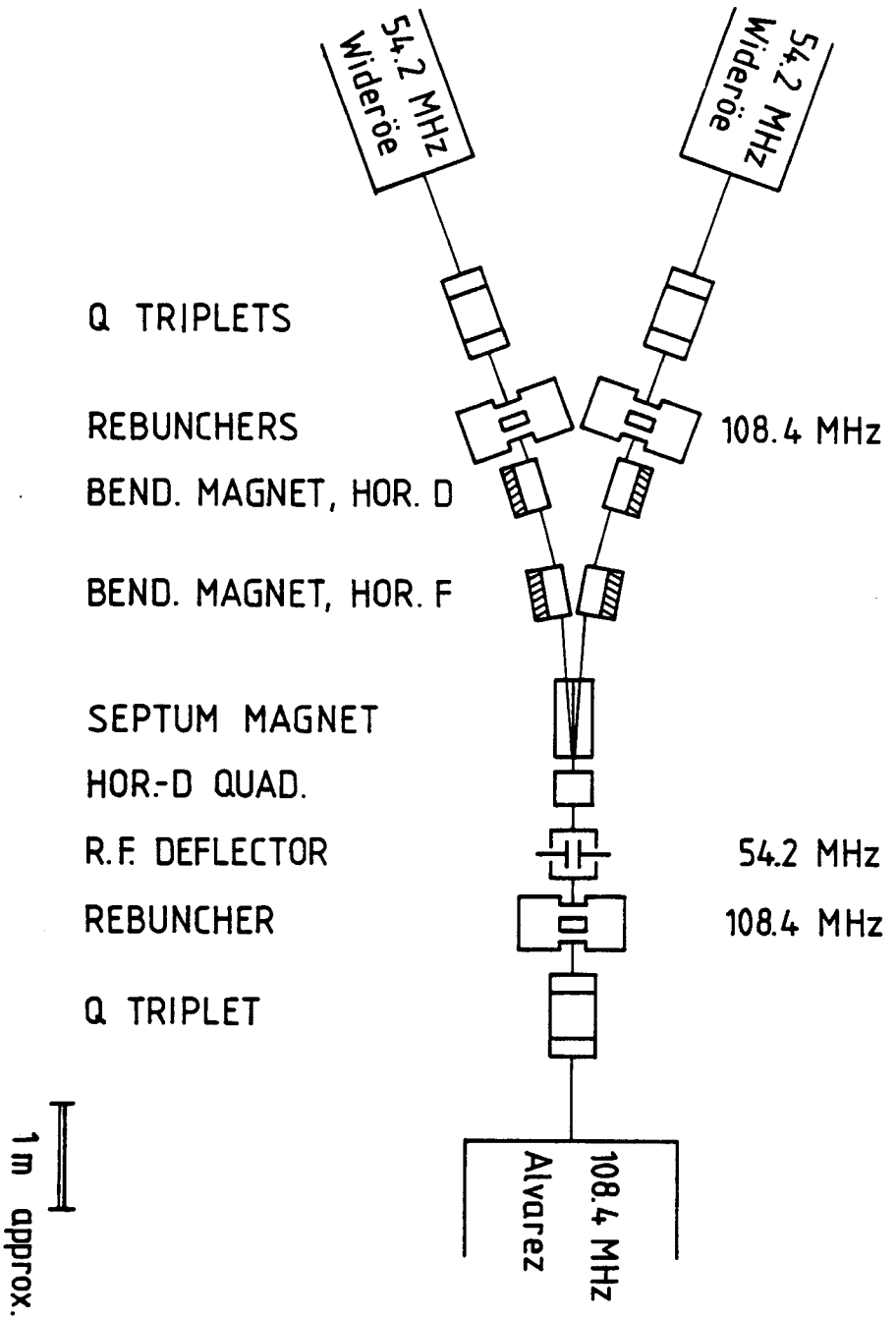

EXAMPLE FOR A FUNNELING SECTION

based on a two-rebuncher-cavity design (which gives enough flexibility for matching).

IV.7 Rings, Lattice, and Magnet Technology

The purpose of the storage ring system, its basic properties and how it fits into the driver concept of HIBALL have been described in Chapter IV.1. Here, additional technical details will be discussed. No significant problems are expected to occur in the transfer ring or in the condenser rings due to their large circumference, the relatively low coasting beam current, and the lower electric charge. Therefore, attention is focused on the small storage rings where part of the necessary bunching procedure takes place. These rings have to be built as compact as possible to minimize the revolution time. On the other hand, that may induce practical problems if the available space in the magnet lattice is too limited for installing beam sensors, RF cavities, correction magnets, and beam manipulating elements.

IV.7.1 Magnet Lattice

The most efficient high-quality lattice for providing alternating gradient transverse focusing is that composed of FODOFODO-cells with bending dipoles placed in space O between quadrupoles F and D. For simultaneous extraction of two bunched beam segments it is convenient that the lattice be made up of 4 identical sectors, the superperiods, each of them consisting of 10 normal periods of 11.58 m length. That puts the betatron tune ν near 10. Besides the two straight sections for extraction purposes, there are two other straights to be used for beam injection and for installing bunching cavities. In each half normal period about 1.6 m are provided to install additional equipment. The preliminary lattice data are summarized in Table IV.7-1.

Table IV.7-1. Magnetic Lattice Data

Lattice Parameters	
Magnetic rigidity of the beam	107.7 Tm
Number of superperiods	4
Number of normal periods	40
Betatron tune	near 10
Circumference of the ring	463.1 m
Length of a superperiod	115.8 m
Length of a normal period	11.6 m
Free space per half normal period	1.6 m
Dipoles	
Total number	144
Number per half normal period	2
Deflection angle	2.5°
Length	1.09 m
Additional free space	0.25 m
Bending radius	25.05 m
Assumed magnetic field strength	4.30 T
Average dipose field	1.43 T
Sagitta	0.06 m
Quadrupoles	
Total number	80
Length	0.63 m
Additional free space	0.20 m
Field gradient	41.9 T/m
(approximate value under assumption of 90° phase advance)	

Schematic layout of half a normal period:

Element:	Quadrupole	Drift Space	2 Dipoles	Drift Space	Quadrupole
Length/m:	0.63	0.45	2.68	2.02	0.63

A more detailed parameter list, including ion optical data, is in preparation.

For additional data see also the complete HIBALL parameter list.

IV.7.2 Magnet Technology

Whereas the transfer ring as well as the condenser rings will be built by using the well established technology of normal conducting magnets, advanced technology superconducting excitation coils should be applied in the case of storage rings. In the light of the current state-of-the-art in the field in superconducting magnets, it will be feasible in the near future to construct the storage rings on the basis of this technology. The problems are less severe than in accelerating synchrotrons because of the fact that no fast pulsing of the magnets is necessary. The biggest advantage is the much lower power consumption of superconducting magnets.

The magnetic inductions of present dipole magnets for accelerators vary between 4 T and about 5 T. This field region can be realized using superconductors of Nb/Ti in a copper matrix, and one can rely on a well proven technology. The present design value for the central induction of 4.3 T is well below the limit of 5 T where difficulties seem to increase rapidly.

A bore size of at least 60 mm is needed. Both solutions -- warm or cold iron -- are realized at present. A decision in that respect could be based on the following points:[1]

- The danger of permanent heat input into the helium by means of RF losses and beam induced currents in the chamber wall is avoided using a warm bore. Especially the high peak currents in HIBALL may create severe problems.
- In the case of beam losses there is no danger of evaporation of frozen impurities from the walls.
- The machine vacuum tube completely at room temperature enables the installation of insertions without interference with the cryogenic system.
- One of the most serious disadvantages of cold iron is the high mass to be cooled down to helium temperature. This means extremely long cooling and

heating times which are very uncomfortable in many cases (tests, replacement in the ring).

- Furthermore it is not easy to avoid difficulties due to the difference in thermal contraction of magnetic steel and the coils.
- In cases where the iron is too close to the coils, saturation effects may cause field distortions which have to be corrected.
- On the other hand, one has the following advantages: coils are easier to align centrally within the iron bore. Magnetic forces can be safely taken at the low temperature of the coil without heat losses. The iron is closer to the coils, which requires less ampere turns for the same field and useful diameter.

The advantages and disadvantages of warm iron are naturally the inverse of those of cold iron.

The final selection should be postponed until extensive experience and information is available from other superconducting systems either already in fabrication or being proposed. Many components and details might still be improved, and completely alternative designs cannot be excluded at the present time. Certainly, the reliability and reproducibility of current superconducting magnets has to be raised considerably.

Assuming about 200 m of magnets per storage ring and a necessary cooling power of about 3 W/m to be delivered at the cold part of the magnet, leads to 600 W of total cooling power per ring. Facilities of up to 3000 W can be built already at present time. Consequently, it would be reasonable to use one cooling facility for a group of 5 storage rings.

References for Section IV.7

1. HERA-Report; ECFA 80/42; 17 March 1980; DESY HERA 80/01.

IV.8 Beam Handling in the Rings (Kickers)

IV.8.1 Injection and Extraction

In the present concept, multiturn injection is used to fill the transfer ring as well as the condenser and storage rings. In any case the principal element is a septum magnet which transports a new turn of beam into the ring and lets pass the previously injected turns of beam on the other (field-free) side of the septum. The septum has to be thin so that the new and the old turns can be stacked next to each other with a minimum of separation between them. The thickness of the septum will be optimized with respect to its cooling properties and the tolerable beam losses. As successive turns are stacked, since it is impossible to move the septum that rapidly, the orbit of the already injected beam is moved by 2 pairs of fast orbit-bump magnets located approximately +90° and -90° betatron phases from the exit of the septum. It will be necessary to shift the bumped orbits in times of the order of 1 μsec. In order not to restrict the acceptance, the bumped orbits are only allowed to appear in the injection straight section. Because of the fact that only 3 turns are injected in the horizontal plane of each ring it should not be a problem to keep the emittance dilution factor well below a value of 2 as required by the present scheme. The filling of the second transverse plane is accomplished by rotating the beam by $\pi/2$ between the transferring and the condenser rings, followed by another stacking procedure in the horizontal plane. Solutions to all these problems are on hand in the frame of the current state-of-the-art of accelerator technology.

Alternatively, a corner septum could be used to stack the beam simultaneously in both transverse planes. That could possibly lead to a simpler configuration with respect to the transfer and condenser rings. But, however, that method has not yet been considered in more detail.

After bunching, two bunches exist in each storage ring and have to be extracted simultaneously by fast kicker magnets. The extraction equipment will be installed in two straight sections on opposite sides of the storage rings.

IV.8.2 Kicker Magnets

The characteristic properties and the technological problems of kickers vary with rise time, flat top time and strength of the kicker field.

The required field strength is determined by the necessary deflection angle ζ, the magnetic rigidity of the beam BR and the allowed length of the kicker magnet itself:

$$\text{kick [Tm]} = \zeta \text{ [rad]} \; BR \text{ [Tm]} \quad .$$

The corresponding kicker parameters needed for the three types of rings used in the HIBALL concept are given in Table IV.8-1

A rough estimation of the necessary voltage V, current I and consequently of the required power is possible by using the relations

$$V \text{ [V]} = \frac{w \cdot k}{\tau_R} \quad , \quad I \text{ [A]} = \frac{h \cdot k}{\mu_o \cdot \ell}$$

where ℓ, h, w [m] are the mean length, height, and width of the aperture, τ_R [sec] is the rise time, and k [Tm] the kick needed. The required voltages are in the range from 10 to 100 kV and the corresponding currents vary between 5 and 20 kA.

In principle no problems are expected to occur in the final phase of construction of such kicker magnets from a technological point of view. However, solvable difficulties may arise in connection with the long flat top of type A magnets, and with the limited length of about 3 m allowed in the storage

Table IV.8-1. Kicker Magnet Parameters

	Deflection Angle [mrad]	Rise Time [μsec]	Flat Top [μsec]	Type
Transfer Ring	2.5	< 1	45	A
Condenser Rings	2.5	< 1	15	A
Storage Rings	6.0	1.5	0.5	B

rings. The characteristic parameters have to be carefully optimized against each other. In any case, prototypes of final size have to be built and tested in advance.

Probably, type B kickers have to be split into several modules driven by discharges of high-voltage L/C-pulse forming networks, which is a proven method for generating kicker pulses of constant current (low ripple and overshoot, etc.). The kicker modules themselves may be designed as asymmetric C-shaped ferrite magnets. Cooling water channels have to be provided in the condenser plates in order to keep the inserted ferrite pieces below their Curie temperature. Alternatively, a design without ferrite may be worthwhile considering. According to the literature,[1] in this case about twice the amount of current and comblike conductors are required for a sufficiently good dipole field.

Methods have also been suggested[2] to recycle at least 50% of the energy stored in such kickers.

References for Section IV.8

1. G. Schaffer; IKOR-Report; Jül-Spez-114; June 1981.
2. G. Schafer; KfK; April 1981 (unpublished).

IV.9 Bunching

IV.9.1 Bunching in the Storage Rings

Starting from a coasting beam (21 A; 5 μsec revolution time) two bunches (250 A; 200 nsec length) have to be created, with as little loss of particles as possible. The most tedious part is the first one which has to occur carefully and slowly so that substantial dilution of the longitudinal emittance is avoided. A sinusoidal RF voltage of 0.4 MHz is applied, starting with an amplitude of less than 1 kV (per turn) modifying $\Delta p/p$ by 5×10^{-5} over 500 revolutions), and the RF amplitude is increased exponentially with time. It is estimated that it takes at least 10 msec (200 revolutions) until a bunching factor $B_F = 0.5$, bunch length of 1.59 μsec, has been reached at an RF amplitude (integrated over the circumference) of 2 KV per revolution.

Proceeding with adiabatic bunching, the bunch length Δt shrinks as the inverse 1/4th power of the RF voltage:

$$\Delta t \sim B_F \sim U_{RF}^{-1/4} \quad .$$

To arrive at a bunch factor of 1/12 (bunch length of 250 nsec), U_{RF} has to be raised to as much as 2.6 MV. This is probably too high a voltage, in view of the ceramic windows of the cavities.

Instead of this totally adiabatic procedure, one would prefer a mixed procedure: bunching is adiabatic until $B_F = 0.3$ to 0.25 has been reached, at a voltage of about 20 kV. Then voltage is raised suddenly, within a few microseconds, to 200 kV. Thereafter the phase space ellipse begins to rotate; when it is in a vertical position, the bunches are extracted. In this non-adiabatic procedure, the shortest bunchwidth is proportional to $U_{RF}^{-1/2}$:

$$\frac{B_{F1}}{B_{Fo}} = \left(\frac{U_{RFraised}}{U_{RFo}}\right)^{-1/2}$$

that means that $B_F = 1/12$ is achieved with 200 kV.

Since the high RF voltage is applied to a bunch of ±60° phase extent, and the bunch is further compressed by a factor of 3 only, it is allowed to be a sine and not sawtooth. We estimate it to be dangerous to have ferrite cavities in the rings, except for the purpose of active feedback for suppression of spurious bunch modes, and with the feedback amplifier being switched on. This is a technique which will be investigated experimentally in the SNS at Rutherford Laboratory. If the feedback amplifier were very powerful one could also apply the bunching voltage directly into this cavity. Some kilovolts would suffice to perform the whole bunching process, with no adiabatic bunching process before. The question whether this technique will be successful is very open, and our description is not based on this (however very advantageous) method.

The storage ring vacuum must be closed from the volume of the RF cavities (with or without ferrites) by a cylindric ceramic window, because the ring vacuum has to be at a pressure of 10^{-12} torr. This limits the RF voltage to about 100 kV (amplitude) per RF cavity, and two or three RF cavities have to be installed per ring.

The RF cavities may be shared by all rings of a ring package (of 5 rings). This sharing does not mean the loss of freedom to bunch the contents of the 20 final beam lines individually in different ways, in order to shape the pulse. Individually bunching is performed by the induction linacs outside the rings (see next subsection), of which there has to be really one per beamline.

IV.9.2 Induction Linac Compressor

IV.9.2.1 Introduction

After the 20 beam pulses are simultaneously extracted from the 10 storage rings, final compression of each beam is initiated with an induction linac compressor. Each compressor, 20 required, applies a 150 MV (300 MeV) voltage ramp to the beam in 250 kV steps forcing the 200 nsec beam pulse to be ballistically focused to 20 nsec at the target chamber.

A compressor can be viewed as consisting of a beam transport system and induction linac sections which are described below.

IV.9.2.2 Beam Transport System

Each beam will be transported through a compressor with a periodic FODO system which is matched to storage ring extraction. Compressor beam transport parameters are tabulated in Table IV.9-1.

Table IV.9-1. Compressor Beam Transport Parameters

Period	8 m
Occupancy Factor	1/8
Tune Shift	60°-36° (vertical)
	60°-18° (horizontal)
Nominal Current	250 amp
Beam Radius	0.052 m
Focusing Strength	53.2 T/m

Allowing 25% beam radius clearance, the following focusing magnet parameters are obtained:

Table IV.9-2. Focusing Magnet Parameters

Bore Tube Radius	0.065 m
Bore Tube Radius Field	3.46 Tesla
Effective magnetic length	0.50 m

Superconducting cosine coil quadrupoles are envisioned for the beam transport system.

IV.9.2.3 Induction Linac Systems

The induction linac sections of the compressor consist each of 12 modules. Each module is fed with a suitably tailored high voltage pulse so that a ramped voltage of 250 kV maximum is applied to the beam pulse. Thus each section applies a 3 MV voltage tilt to a beam pulse and 50 sections (600 modules) provide the required 150 MV.

A conceptual induction linac section is shown in Fig. IV.9-1. A module consists of a ferrite core (nickel-zinc-ferrite), a high voltage supply loop which also functions as the ferrite core support, an insulator and the housing with the feed connection. The housing is filled with oil for high voltage insulation.

The design shown is of simple construction and basically consists of just 2 assemblies. Each ferrite core (fabricated with such shapes as rings, segments or blocks) is captured by a core support and welded to the outer housing; this makes up the core housing assembly. All the insulators are welded together with intermediate short tubes, each containing a captured helical spring contact, which with a pump-out makes up the section insulator assembly. To assemble a section, the insulator assembly is inserted into the core-housing assembly. An oil seal is provided at either end of the core-housing

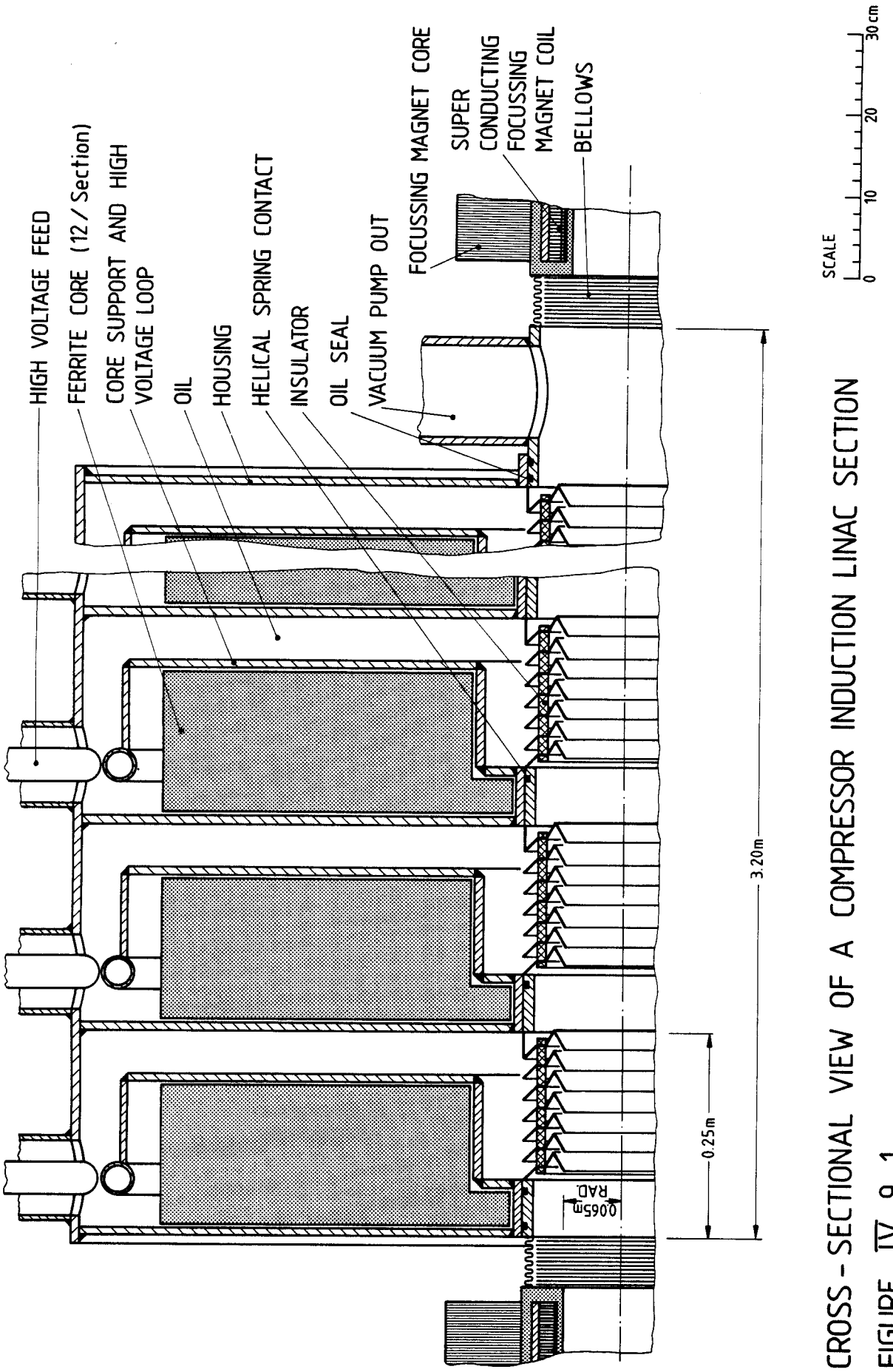

CROSS-SECTIONAL VIEW OF A COMPRESSOR INDUCTION LINAC SECTION

FIGURE IV. 9-1

for oil containment. An advantage of this design is that the potentially troublesome components, the insulators and helical springs, can be readily accessed by removing the section insulator from the core-housing.

Compressor length including the beam transport is 200 m with a 0.75 MV/m peak voltage gradient. Relevant module dimension and parameters are tabulated in Table IV.9-3.

Table IV.9-3. Induction Module Dimensions and Parameters

Module Length	0.25 m
Core Length	0.17 m
High Voltage Oil Spacing	0.05 m
Bore Radius	0.065 m
Core Inner Radius	0.135, 0.185 m
Core Outer Radius	0.56 m
Module Outer Radius	0.66 m
Insulator Gradient	17 kV/cm
Ferrite Core Weight	725 kg
Core Loss Energy	24 Joules
Module Stored Energy	64 Joules
Module Peak Current	2050 amp
Module Power at 20 Hz	1280 kW

The design represents a conservative approach but actual performance must be verified with prototype testing. With module development effort and newer ferrites, it may be possible to operate the compressor at a higher gradient.

Also, the tradeoff between a higher compressor voltage gradient (requiring more ferrite) and a shorter transport line needs to be examined.

The requirements for the 20 compressors are tabulated in Table IV.9-4. The estimated costs (1981), with power supplies, are $33,000 (73,000 DM) per module. The quadrupole magnets are not included; they are cost items of the beam lines.

Table IV.9-4. Requirements for 20 Compressors

No. of Modules	12,000
Total Weight of Ferrite	8,100 tons
Total Stored Energy	0.77 MJ
Total Power	15.3 MW

IV.10 Driver Efficiency

IV.10.1 Introduction

Efficiency is meant to be the particle beam power delivered from the driver divided by the overall power consumption of the driver facility. The fact that a fraction of the beam might miss the target is not included here. The figure below illustrates the simplified power flow diagram of an inertial confinement fusion power plant.

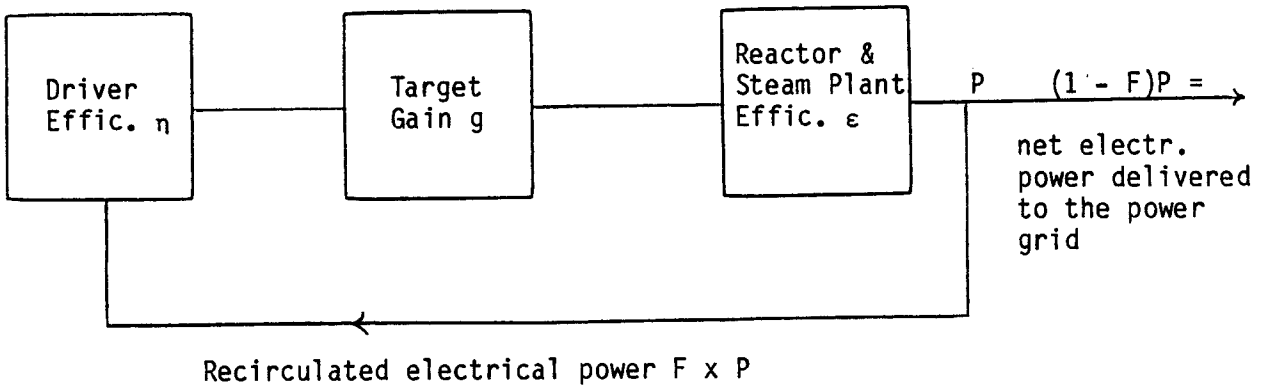

If the fraction of the recirculated power F is chosen to be 1/4 and the thermal efficiency ε of reactor and turbine system is 1/3, then $\eta \cdot g \geq 12$. This immediately demonstrates the implication for the target design: a particle beam driver with an efficiency η of about 1/4 requires a target gain of only ≥ 48, which is regarded to offer many encouraging options in target design. In the case of a laser beam driver the efficiency is presently considered to be less by an order of magnitude and hence the success of an appropriate target design is less certain. While a laser beam efficiency of 2.5% still is a design aim, the corresponding figure of nearly 25% for a particle beam driver will be shown to be realistic. It is neither the purpose of this contribution to calculate this number with the highest possible perfection nor

to make suggestions for further improvements. It is rather the aim to identify accelerator components and subsystems which are most determinative for the overall efficiency and separate them from the others, for which power consumption is not a stringent design parameter.

IV.10.2 The Accelerator

For a beam current equal to 0, the efficiency is also 0. For an extremely high current, the efficiency approaches the conversion efficiency of main power into RF power, typically 0.54. For current values in between both extremes, the efficiency strongly depends on accelerator parameters and hence the machine design must be known, partly in detail. The lay-out of the linac was described in section IV.5 and the numbers given in Fig. IV.5.1.

Most data have been chosen to be similar to the UNILAC. A fourth frequency jump to 324 MHz, which is not correlated to a funneling step, was tentatively included. It was the potential of (a) cutting down the linac cost; (b) increasing the RF efficiency, because it is the lowest frequency, at which a klystron ($\eta \sim 70\%$) seems realistic; (c) the filling time of the cavities being lower by a factor of 3 and hence the RF duty factor being more favorable compared to the beam duty factor; and (d) the possibility of a fourth funneling step, if source currents ultimately fall short or more redundancy is deemed necessary.

An RF power source for 324 MHz will become available soon. However, the RF efficiency figure assumed here is based on the 108 MHz tetrode amplifiers of the UNILAC, hence, the result is overly conservative. The shunt impedance of the linac structure, which is nearly as determinative for the overall efficiency as the RF conversion efficiency, was derived from the UNILAC Alvarez section, 50 MΩ/m. This figure includes losses for end-walls, tuners, etc. This figure might be more favorable for a 324 MHz structure, provided the

drift tube diameter could be decreased from the 20 cm value, used in the UNILAC, to 12-14 cm by using permanent magnet quadrupoles.

The same shunt impedance figure of 50 MΩ/m is assumed for the Widerøe sections too, though this type of structure has a typically higher value. But it is strongly dependent on the particle velocity and frequency and cannot be derived more accurately without a more detailed cavity design. The same is true for the transit time factor: only a final design can yield a more accurate number. Here an average value of the UNILAC Alvarez section is used, T = 0.86. Another number, which determines the linac efficiency, is derived from the UNILAC: the net acceleration rate of 1.75 MV/m. This value is usually selected by a cost optimization of linac length versus RF power installation and usually does not include efficiency considerations. The adapted UNILAC number results in a linac length of 3 km, which actually is the length of the longest linac presently in existence. If the linac length would be doubled the linac efficiency would be 38.5%, rather than 33.3%, as in the proposed design. For the drift tube quadrupoles, permanent magnets are assumed and a DC doublet will be used every 10 m between the cavities for matching purposes. It is not clear from the particle dynamics standpoint whether this limited amount of focusing adjustment is adequate for a beam stability between zero and full beam current. If this idea has to be abandoned the linac efficiency drops from 33.3% to approximately 31%.

Compared to the linac, the transfer ring, the condenser rings, the storage rings, the beam manipulation components and the long beam transport paths are by far less determined at the present stage of the HIBALL scenario. Fortunately, the power consumption of those items, 75 MW, does not dominate the power balance, as the linac with its 300 MW does. Therefore the concern about this final part of the facility is more of a question of feasibility and

cost rather than efficiency. The use of superconducting magnets is almost obligatory. Permanent magnets could be used for beam transport lenses, but hardly for the high fraction of bending dipoles. If room temperature magnets ultimately have to be used, the power requirement of 62 km of beam transport length, including the rings, would go up by a factor of 10 approximately and the overall efficiency would drop from 26% to 17%. In addition, the lay-out of storage rings, beam rotators and final lenses would have to be revised drastically. Among the beam manipulation components, the bunching cavities in the rings and the induction linac, which is included as the final bunch compressor in each of the 20 beam lines, are not yet determined in their electrical parameters and may influence the power balance more significantly.

IV.10.3 The Power Balance

The listing of individual power requirements is based on average values. That means that except for the obvious continuous power consumers, the peak power must be determined and then be multiplied by the individual duty factors, which also must include build-up times and pauses. Therefore the timing scheme of the beam pulse and the excitation pattern of the linac and the beam manipulation elements was determined.

A) Peak Beam Power	150 mA x 5 GV =	750 MW
Average Beam Power	750 x δ_{beam} =	100 MW
B) RF Power Requirement = Beam Pwr + Linac aver. RF Pwr =		145.8 MW
estim. RF Pwr for Rebunchers and Funneling Cavities		2.2 MW
		148 MW

Conversion Eff. Main Pwr/RF Pwr =	0.54	
Main Power of RF Installation = 148/0.54 =	275	MW
Conventional Lenses and Steering Magnets 10 kW per 10 m =	3	MW
Vacuum, Controls, Miscel. 1 kW per m	4	MW
Cooling Plant to Remove 150 MW Power Losses: 150 x 0.12 =	18	MW
Total Linac Main Power Consumption	300	MW

$$\text{Linac Efficiency} = \frac{\text{Beam Pwr}}{\text{Total Main Pwr}} = \frac{100}{300} = 33.3\%$$

C) Rings, Beam Transport, Beam Handling, Final Focusing

Length of Beam Path:

First Transfer Ring	3.20 km
5 Condenser Rings	6.94 km
10 Storage Rings	4.63 km
20 Long + 80 Short Transp. L.	48.00 km
	62.77 km

Magnet Filling Factor	~ 0.5
Total Length of Supercond. Magnets	31.40 km
Power Loss at 4°K	2 W/m
Total Refrigerator Capacity at 4°K	62 kW
Conv. Eff. of Refr. Plant Including Utilities	450:1
Cooling Plant Main Power Requirement	28 MW
80 Correction Dipoles at Beam Line Ends	16 MW
Bunching Cavities and Ind. Linac (estim.)	12 MW
20 Slow Switching Magnets (estim.)	4 MW
22 Kicker Magnets	2 MW

22 Septum Magnets	3 MW
Vacuum, Controls, Miscel. 0.2/kW/m	10 MW
	75 MW

$$\text{Total Facility Efficiency} = \frac{\text{Beam Power}}{\text{Linac + Ring + Transp. Pwr Consumpt.}}$$

$$= \frac{100}{300 + 75} = 26.7\% \quad .$$

IV.10.4 Conclusions

1. An overall efficiency of about 25% is realistic for a heavy ion fusion driver, when all beam transport magnets are based on superconducting technology.
2. Reliability and redundancy considerations, potential reserves in beam power and derating of crucial component characteristics have all the tendency to decrease the overall efficiency.
3. The most decisive figure is the conversion efficiency of main power into RF power. If this figure would be 70% (which is expected in the near future), rather than the assumed 54%, the overall efficiency would go up from 26.7% to 32%.
4. The funneling section of the chosen linac contributes only about 1.5% to the total power losses and can therefore be designed freely without degrading the efficiency.

V. Beam Transmission and Final Focusing

V.1 General Theory

V.1.1 Introduction

Transport of beams from the accelerator to the target chamber and focusing on a small target are key issues in heavy ion fusion. Their solution determines most of the parameters of the accelerator scenario. The option of transporting beams ballistically as though in vacuum -- without neutralization -- has been recognized as a major advantage of using heavy ions and will be considered here. The alternative use of a plasma channel for final transport of heavy ions -- similar to light ion fusion schemes -- requires considerable additional theoretical and also experimental work before it can be assessed in a reactor design.

The compatibility of nearly vacuum propagation with the cavity design (wall protection, pumping, etc.) will be considered in section V.6 and a proper definition of the vacuum by stripping considerations will be given later in section V.5. A crucial cavity design parameter that determines final transport is the stand-off distance of final focusing magnets from the target (8.5 m). Because of limited space, the number of beam lines (including shielding) is confined to approximately ten on a circumference, hence the use of two rows of beam ports demands a particle current per beam line of the order of 1 kA. It was also felt that elliptic entry ports (with noticeably vertical elongation) rather than circular entry ports of the same area could be advantageous to the design of coolant tubes and possibly be helpful for correcting geometric aberrations of the final magnets.

In addition to these cavity related constraints there are beam dynamics limitations which have to be incorporated into the final transport design. Space charge plays an important role here and is a novel feature compared with

designs of existing high energy beam lines that usually have negligible space charge effects. The current transport limit in the long periodic beam line connecting with the accelerator is not serious as long as low charge states are chosen (q = 1,2). In fact, recent computer simulations have shown (see V.1.2 and Ref. 3) that under certain conditions there is no limit to the transportable current from the physics point of view. Electrostatic repulsion in the final drift can be controlled by increasing the beam divergence, hence the entry port radius. The lens aperture is limited, however, by spherical aberrations and it was felt that a 10-20% increase over the emittance controlled divergence would be reasonable. From the standpoint of aberrations the emittance and momentum spread should be as small as possible. For constant target requirements this is possible only at the expense of the accelerator size. A reasonable compromise has been found in the parameter space around 60 π mm-mrad average horizontal-vertical emittance and 1/2-1% momentum spread.

As to the level of confidence one may have in the transverse transport considerations, we note that computer simulation studies performed at the Naval Research Laboratory and at the Max-Planck-Institut für Plasmaphysik with different codes have led to excellent agreement and also confirm predictions from analytic theory. The situation is different with regard to longitudinal dynamics and longitudinal-transverse coupling under strong space charge conditions during longitudinal compression, which require future work. For the present study a first-order approach has been made by using the longitudinal envelope equation.

During the performance of this study progress has been made also with regard to the development of design programs to treat the final focusing problem. At the University of Giessen, a very flexible computer program GIOS has been

Fig. V.1-1

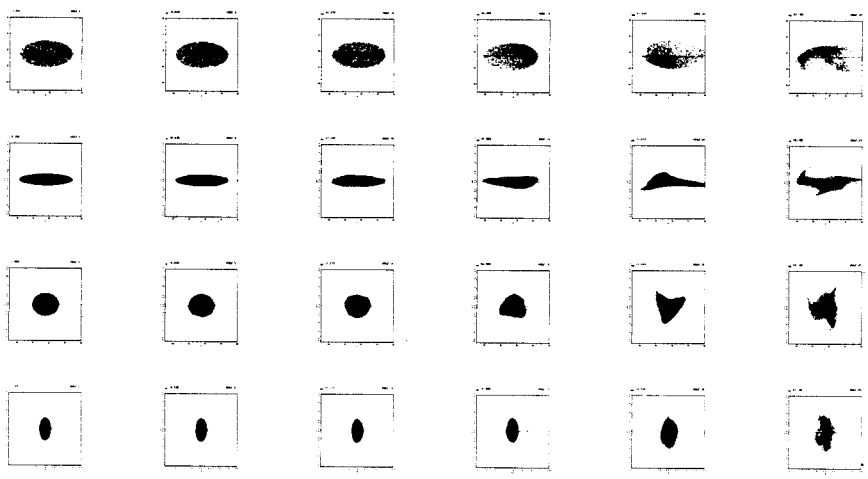

developed for the design of complex beam guidance systems up to third order. An extension of GIOS to treat beams carrying space charge is under progress. At the Max-Planck-Institut für Plasmaphysik the program SCOP1 has been developed with main emphasis on the treatment of space charge and some design capabilities, including third order effects.

V.1.2 Transverse Stability of Periodic Transport

Beam transfer from the storage rings to the target chamber requires a length of the order of a kilometer to perform longitudinal bunch implosion. It is necessary to ensure transport over a large number of periods of a quadrupole alternating gradient focusing lattice without emittance dilution.

For zero intensity, the requirement for stable trajectories is $\sigma_0 < 180°$, with σ_0 the phase advance per focusing period, to avoid a half-integer resonance with the focusing period. For finite intensity, the defocusing space charge force depresses the tune to a value $0 < \sigma < \sigma_0$ and as a new phenomenon collective modes of oscillation can be in resonance with the focusing period, which may lead to emittance growth unless σ_0 and σ are constrained to stable bands.

Analytic theory[1] and computer simulation[2,3] have suggested that instability of the envelope mode is suppressed if $\sigma_0 < 90°$, and instability of the "third order" mode if $\sigma_0 < 60°$. This "third order" mode is evolving with three arms in x-p_x or y-p_y phase space and is quite insensitive to the type of distribution function (Fig. V.1-1). The remaining higher order mode instabilities do not spoil the r.m.s. emittance if σ is depressed to small values.[3]

Different emittances in the horizontal and vertical planes may give rise to emittance transfer. The underlying mechanism is a space charge induced coupling instability and requires considerable energy anisotropy and strong tune depression.[3] In most cases the onset of instability is suppressed if

strong tune depression is avoided, for instance $\sigma/\sigma_0 \gtrsim 0.3$ in both planes for $\varepsilon_x/\varepsilon_y = 4$ (see Fig. V.1-2 with linear current ramp to simulate bunch implosion). This limits the current performance compared with equal or almost equal emittances, where no limit has been found so far.

It is convenient to express the current in the channel in terms of the scaled space charge parameter Q' and maximum amplitude u_m (see Ref. 4)

$$I/q = 3.66 \times 10^6 \ (A^{1/3}/q^{4/3}) B_Q^{2/3} (\beta\gamma)^{7/3} \varepsilon^{2/3} Q'/\mu_m^{2/3} \ [A] \qquad (V.1\text{-}1)$$

where $Q'/\mu_m^{2/3}$ (Laslett's "figure of merit") is a function of the tune depression σ/σ_0 (see Fig. V.1-3) and the remaining quantities are:

- A atomic weight
- q charge state
- B_Q pole tip field (Tesla)
- β v/c
- ε unnormalized emittance [m-rad] (for unequal emittances the larger one)

V.1.3 Longitudinal Bunch Compression

Longitudinal drift bunching is described by an envelope equation[4]

$$z_m'' = \frac{\varepsilon^2}{\gamma^4 z_m^3} + \frac{3}{2}\frac{q^2}{A}\frac{g}{\beta^2\gamma^5}\frac{Nr_p}{z_m^2} \qquad (V.1\text{-}2)$$

with: z_m = envelope in z

ε = $1/\pi$ x emittance in $(z, \Delta p/p)$

N = total number of ions

r_p = classical proton radius (= 1.52×10^{-18} m)

Equation (V.1-2) assumes a linear space charge force, i.e. parabolic line charge density. This assumption is consistent with a particular distribution

Fig. V.1-2

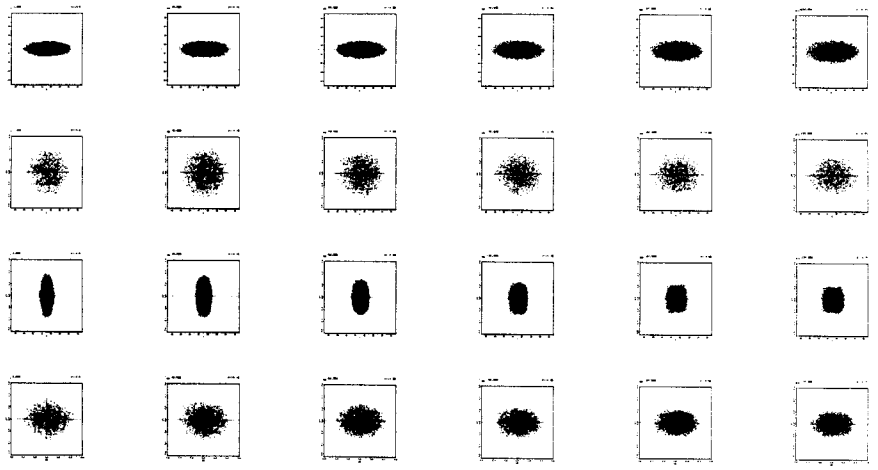

Fig. V.1-3

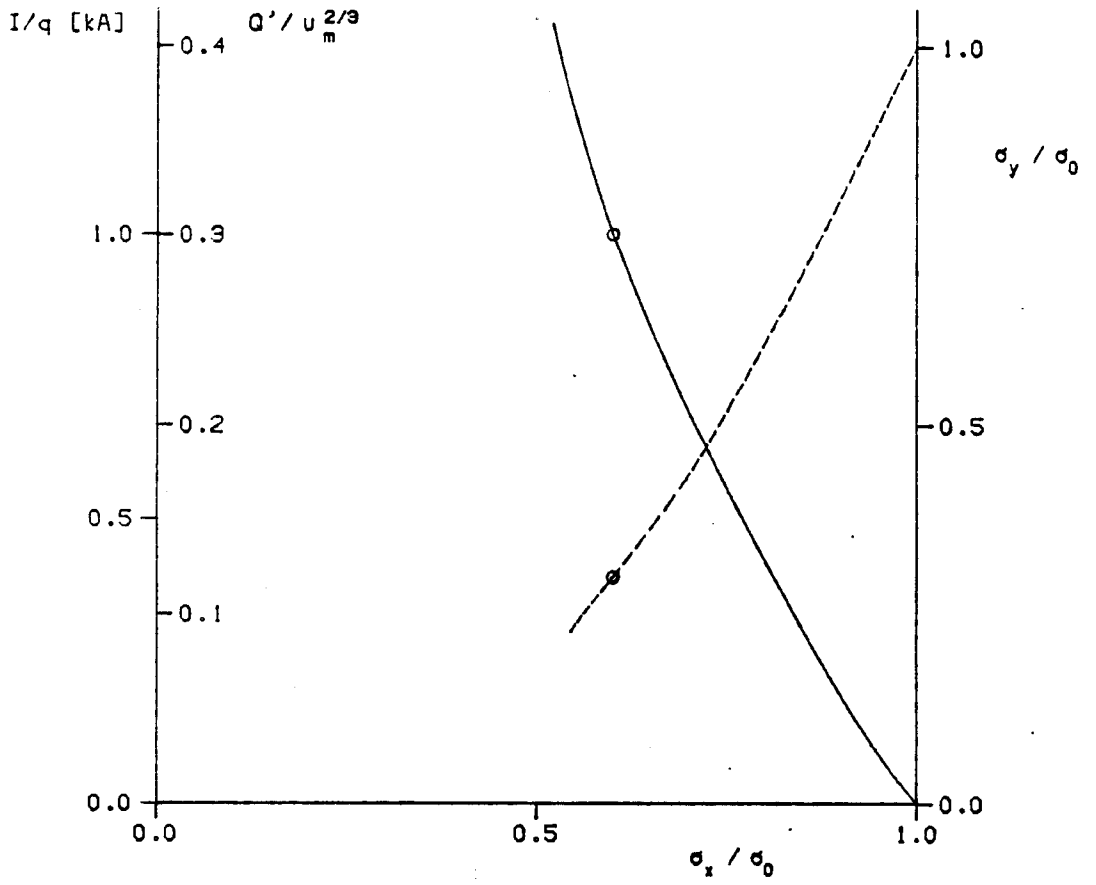

Fig.V.1-3. Intensity coefficient vs.tune depression in x for a $\sigma_o = 60^o$ symmetric FODO lattice and $\varepsilon_x/\varepsilon_y = 4$. I/q as example for HIBALL parameters. The dashed line gives the corresponding tune depression in y and the circles indicate stability limits beyond which emittance transfer is possible.

function (see Ref. 5), whereas in practice deviations from the linear force compression must be expected due to the presumably Gaussian shaped distribution function. In addition, the geometry factor g depends on the transverse position. For a uniform density beam of radius, a, in a pipe with radius, b,

$$g = 1 + 2 \ln (b/a) - (r/a)^2 \qquad \text{(V.1-3)}$$

Hence it varies between $1 + 2 \ln (b/a)$ and $2 \ln (b/a)$ from the center to the edge of the beam. A quantitative evaluation of this non-ideal compression scheme and the associated longitudinal emittance dilution requires a simulation program employing r-z or x-y-z geometry. A simulation code solving Poisson's equation in r-z geometry in a long circular cross section pipe is presently being tested at the Max-Planck-Institut für Plasmaphysik.

In spite of these limitations Eq. (V.1-2) is a useful starting point to describe the longitudinal bunching process. The initial tilt of the phase space ellipse is provided by the ramped voltage of an induction linac section of several hundred meters length. The phase space rotation is completed in a long drift space (see Fig. V.1-4).

Assuming constant longitudinal emittance during bunching, the coherent initial momentum spread $(\Delta p/p)_i$ necessary to achieve the desired final pulse length can be easily derived from Eq. (V.1-2) by carrying out an integration (see Ref. 4). For large compression ratio we have,

$$(\Delta p/p)_i^2 = (\Delta p/p)_t^2 + 3 \frac{q^2}{A} \frac{g}{\beta^2 \gamma} \frac{N r_p}{z_t} \quad . \qquad \text{(V.1-4)}$$

Note that the incoherent momentum spread at target $(\Delta p/p)_t$ is reduced below $(\Delta p/p)_i$ because of the space charge repulsion which becomes effective close to

Fig. V.1-4

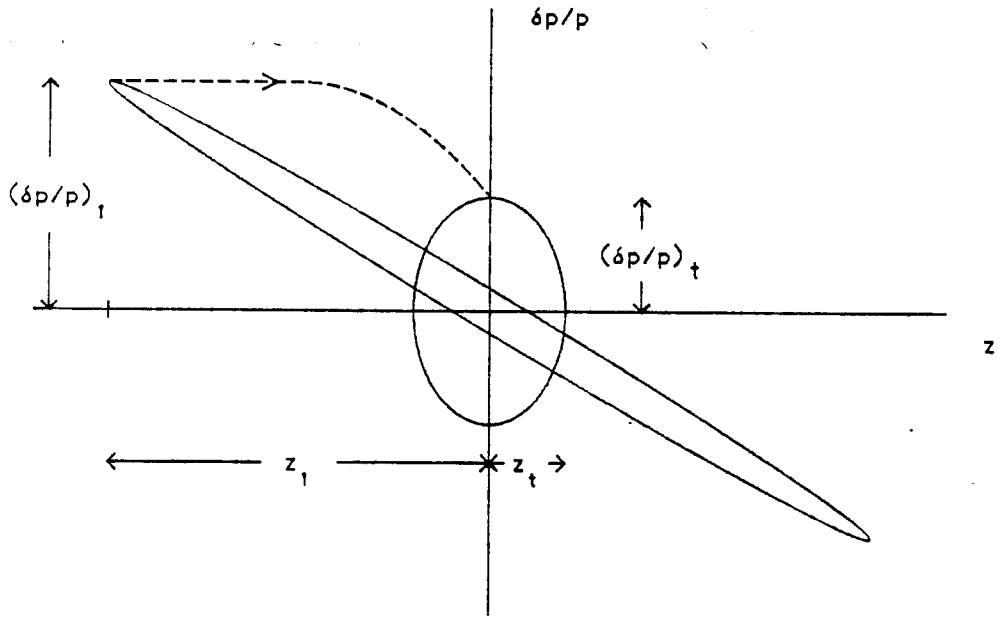

Fig.V.1-4. Ellipse rotation in longitudinal phase space for longitudinal bunch implosion under space charge conditions

the end of the bunching process, when the line charge density has almost come to its final high value.

The necessary drift length is approximately given by

$$L \sim \gamma^2 z_i/(\Delta p/p)_i \quad .$$

$(\Delta p/p)_t$ is limited by chromatic aberrations of the final focusing system. The final momentum transmission of a long beam line with bending sections will set a limit to $(\Delta p/p)_i$, but it is assumed here that the final focusing constraint on $\Delta p/p$ is more stringent and thus determines the momentum width in the storage rings.

V.1.4 Final Focusing Constraints

A final quadrupole doublet or triplet is adequate to perform focusing onto the small target. The large beam size required in the final lens is matched to the periodic transport line with several quadrupoles. There is not a unique way of defining an appropriate final focusing system and some thought is necessary to keep both chromatic and geometric aberrations at as low a level as desirable with regard to the constraints imposed by storage ring considerations. Second order chromatic aberrations (dependence of focal length on momentum) are given by (Ref. 6):

$$\Delta x \sim \frac{\Delta p}{p} \frac{1}{x_t'} \int_0^{s_t} (x')^2 \, ds \qquad \text{(V.1-5)}$$

with $x_t' \equiv dx/ds$ at target, and similar for y. A simple estimate results in

$$\Delta x \sim \alpha \frac{\varepsilon L}{r_o} \frac{\Delta p}{p} \qquad \text{(V.1-6)}$$

with: r_o = target radius

L = distance F.F.M.-target

ε = transverse emittance.

The coefficient α exceeds unity for a focusing system with quadrupoles only. Its actual value depends on the first order design and can be minimized according to Eq. (V.1-5) by an appropriate setting of sufficiently many matching quadrupoles so as to avoid unnecessary fluttering of envelope.

Sextupole correction of chromatic aberrations has not been attempted here, but we have tried to keep $\Delta p/p$ at the level of ± 0.005 where correction is unnecessary. Due to the variation of space charge defocusing within the bunch and with distance from the target there is concern that sextupoles might do more harm than good if they are used according to concepts developed for high energy beam lines without space charge (Ref. 7). Further study is required to clarify sextupole correction in the presence of varying space charge.

According to Ref. 8 third order geometric aberrations are tolerable if

$$\varepsilon \lesssim 0.15\, r_o^{5/4}\, \rho^{-1/4} \quad . \tag{V.1-7}$$

Here ρ is the radius of curvature related to the pole-tip field, and the coefficient 0.15 is about the minimum value that can be achieved by a large class of focusing systems. A brief examination shows that for HIBALL parameters with $\rho \gtrsim 25$ m ($B\rho$ = 106 T-m) the spot size will be spoiled by aberration if ε exceeds in both planes the value 30 mm-mrad. We note that the aberration properties of the Reference Design are very well described by Eq. (V.1-7) as detailed calculation will show.

References for Section V.1

1. L. Smith et al., LBL-Rep. HIFAN 13-15, Berkeley (1977).

2. I. Haber, IEEE Trans. Nucl. Sci. NS-26, 3090 (1979).

3. I. Hofmann, IEEE Trans. Nucl. Sci. NS-28, 2399 (1981).

4. G. Lambertson et al., IEEE Trans. Nucl. Sci. NS-24, 993 (1977).

5. D. Neuffer, IEEE Trans. Nucl. Sci. NS-26, 3031 (1979).

6. K.G. Steffen, High Energy Beam Optics, Interscience Publishers, New York, 1965.

7. K.L. Brown and J.M. Peterson, Proc. of the Heavy Ion Fusion Workshop, Berkeley, Oct. 29 - Nov. 9, 1979, SLAC-PUB-2575 (1980).

8. D. Neuffer, Proc. of the Heavy Ion Fusion Workshop, Argonne, Sept. 19-26, 1978, ANL-79-41 (1979).

V.2 Final Transport and Focusing for HIBALL

V.2.1 Periodic Transport Lattice for Imploding Bunch

The goal is to transport and simultaneously bunch individual beamlets (20 per cavity) from the accelerator to the target with the following specifications at target:

particle current/beam (averaged over pulse)		1.2 kA
unnormalized emittance:	vertical	120 π mm-mrad
	horizontal	30 π mm-mrad
momentum spread $\Delta p/p$		± 0.005
pulse length		20 nsec

The requirements to achieve this by ten-fold drift bunching are (see Fig. V.2-1)

initial momentum spread $\Delta p/p$ (coherent + incoherent)	± 0.017
induction linac voltage	$\sim$ 300 MeV
length of induction linac	$>$ 150 m
drift distance (induction linac-target)	655 m

There are several options to determine the periodic lattice of these beam lines. The maximum particle current at the end of the periodic lattice is 1.0 kA, assuming a flat pulse shape (note that the final current of 1.2 kA is achieved after drifting through 60 m of large diameter final focusing lenses where space charge is less important). While it is clear from Eq. (V.1-1) that quadrupoles at the 1 kA particle current level have to be superconducting (4 T), it appears attractive to divide the lattice at lower currents into

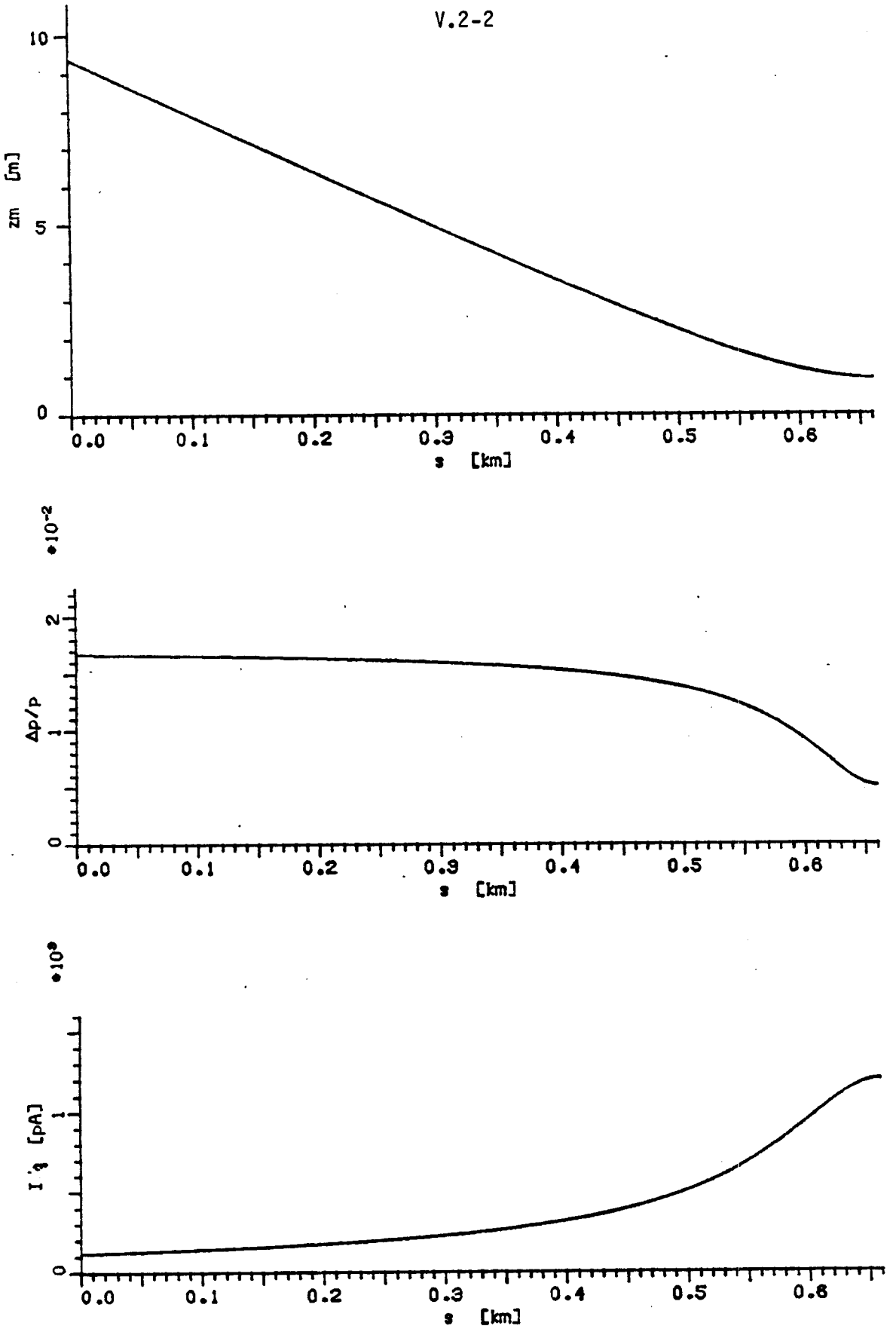

Fig.V.2-1. Longitudinal bunch compression by ten-fold drift bunching between induction linac and target. Longitudinal envelope z_m[m], momentum spread $\Delta p/p$ and particle current I/q [kA] according to envelope equation (with g = 2) as function of distance s from induction linac.

sections with normal conducting (< 2 T) and permanent (< 1 T) magnets. The split is performed according to

$$\frac{I}{q} \lesssim 410 \times B_Q^{2/3} \text{ [A]} \qquad \text{(V.2-1)}$$

with an upper limit of 0.3 for $Q'/u_m^{2/3}$ equivalent to a tune of $\sigma_{vert} = 36°$, $\sigma_{hor} = 18°$ at the end of each lattice section (see stability discussion in section V.1.1). Within a section the lattice is exactly periodic except for the first few magnets that are assumed to perform matching into the changed lattice structure. Details of this lattice are given in Table V.2-1.

lattice	FODO (symmetric)
occupancy factor	$\eta = 1/2$
zero intensity tune	$\sigma_o = 60°$
tune at max. current in each section	$\sigma_{vert} = 36°$
	$\sigma_{hor} = 18°$
length	595 m
bending radius	150/220 m
average dipole field	0.707/0.482 T

Table V.2-1. Periodic Transport Lattice for Rising Beam Current (The Beam Tube Diameter is Assumed 25% larger than the Actual Beam Diameter)

Cell	Part. Current [A]	Pole-Tip B_Q [T]	Max. Beam Diam. [m]	Gradient B_Q/a[T/m]	Length of Cell [m]
1-51 (0-415 m)	120-350	1	0.102	15.7	8.142
52-69 (415-508 m)	350-560	2	0.082	39.0	5.162
70-100 (508-595 m)	560-1000	4	0.060	133.3	2.790

V.2.2 Final Focusing - Reference Design

A reference design for the final focusing has been determined along the following lines:

1. In order to keep the beam size and thus second order chromatic and also third order geometric aberrations as small as possible (without correction) the maximum obtainable focusing power is put into the first two quadrupoles, which calls for superconducting magnets. It is assumed that the field at the conductors is limited to 10 Tesla, with a 50 cm thick shield included in the aperture.
2. Matching of the large beam size in the final magnets to the small beam size in the periodic transport is performed as smoothly as possible, searching for a minimum of the integral in Eq. (V.1-5), which determines the size of chromatic aberrations.

The design has been performed using the computer program SCOP1 (space charge optics program 1) developed at the Max-Planck-Institut für Plasmaphysik. The program has two options:

A. Integration of the Kapchinskij-Vladimirskij envelope equations for first-order design.
B. Raytracing of a random set of trajectories with initial K-V distribution in transverse phase space and square distribution in momentum space. It assumes a linear space charge force derived from the r.m.s. beam envelopes calculated at each time-step. Second order chromatic and third order geometric aberrations can be turned on as well as multipole fields for correction.

Both options use fitting routines for matching (A) and correction (B). Results can be checked with the particle-in-cell code SCOP2 for arbitrary initial distribution with self-consistent space charge force calculation.

First Order Design

The results of a design with hard-edge quadrupoles are shown in Table V.2-2 and Fig. V.2-2. Note that the first order spot diameter is taken 5 mm to account somewhat for a nonideal beam profile. The plotted beam size has been assumed everywhere 25% larger than the r.m.s. size (K-V envelope) for the same reason.

Higher Order Effects and Beam Characteristics on Target

A distribution of momenta and deviations from paraxial focusing result in an increased spot size. A momentum width of ± 0.005 can be accomodated in the 3 mm radius spot. The situation is different with regard to third order geometric aberrations. Without correction only 40% of the intensity hit the target and it takes a 10 mm radius target to contain 80% of particles, the actual spot being elliptic rather than circular.

Applying fields with octupole symmetry in Q_3, Q_7 and Q_8 has brought some improvement to the degree that a fairly circular spot is obtained with 80% of the particles contained in a radius of 5 mm. This modest improvement might be due to the first order design which does not allow effective (i.e. sufficiently independent) coupling of octupoles to the various aberration terms. In a previous design it has been possible to almost entirely correct aberrations with three octupoles,[1] but this design had a larger momentum sensivitity. No attempt has been made to optimize the design for reduced geometric and chromatic aberrations, which will be desirable for future work.

Nonparaxial effects due to a nonuniform space charge have been found in previous work[2] to be comparatively small under similar conditions (similar electric current and beam size, which led to a 20% intensity reduction within the first order spot size).

Table V.2-2. Reference Design Specifications With Hard-Edge Quadrupoles

Unnormalized emittance (r.m.s.) (no dilution in periodic transport)	
vertical	120 π mm-mrad
horizontal	30 π mm-mrad
Particle current/beam	1.2 kA
First order spot diameter	5 mm
Distance F.F.M.-target	8.5 m
Total length of final focusing	60.374 m
Length of quadrupoles	2.683 m
Drift sections between magnets	1.789 m
Drift section after period. transp.	17.890 m
beam size (1.25 x r.m.s. diameter)	
at exit of periodic transp.	7 x 3 cm
inside front magnet (Q_8)	120 x 60 cm

Gradients [Telsa/m]

Q_1	Q_2	Q_3	Q_4	Q_5	Q_6	Q_7	Q_8
0.711	4.762	6.561	4.722	1.611	2.868	8.221	7.922
F	D	F	D	F	F	D	F in vertical direction

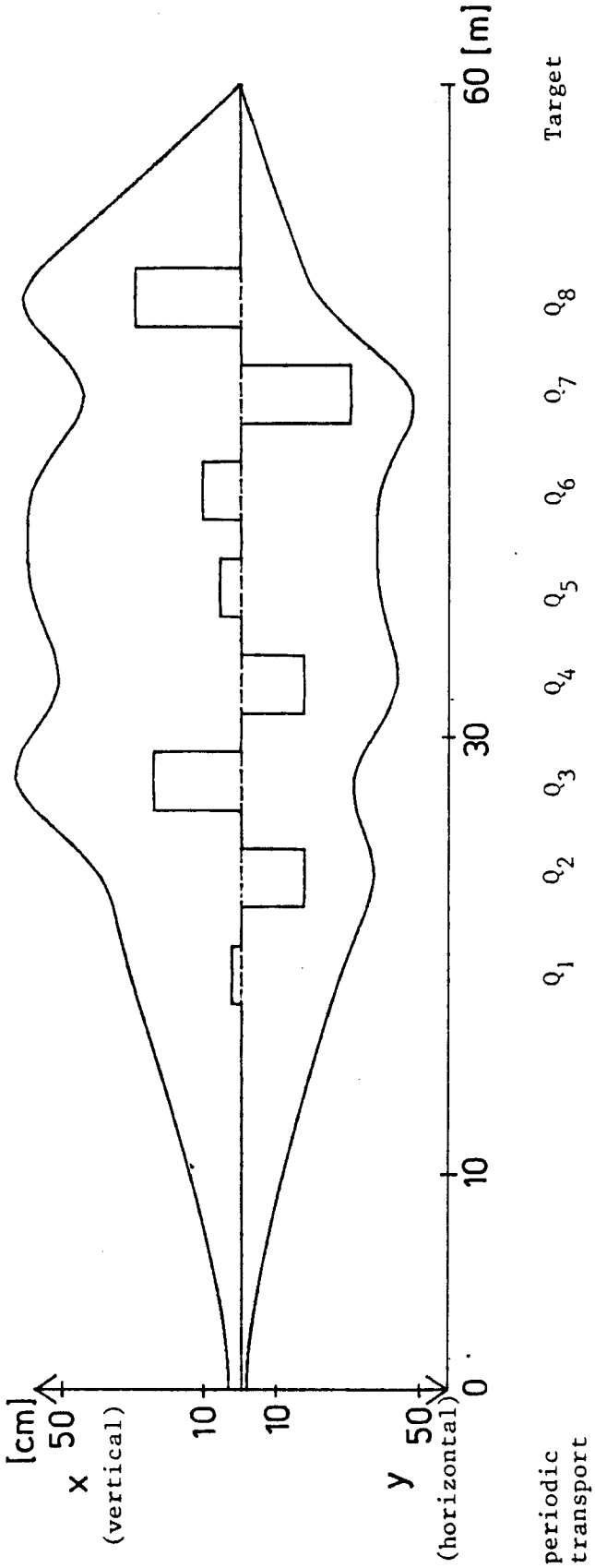

Fig.V. 2-2 . Reference design for final focusing employing 8 quadrupole magnets for beam transfer from the periodic lattice to the target. The square line represents the focusing strength (gradient) in vertical direction.

Summarizing, the present reference design delivers about 50% (or 40% without octupoles) of the beam intensity on a target with 3 mm radius. The remaining intensity is spread out because of aberrations. Third order geometric aberrations are the dominant constituent; octupoles have been shown to give an improvement at least in principle. The size of the uncorrected aberrations is not discouraging, and it is conceivable that the desired spot can be achieved with improved design.

V.2.3 Study of the Overall Beam Line Arrangement

When designing the final focusing system one must pay attention not only to the geometry and field distribution of the last quadrupole lens multiplet but also to the preceding last section of the beam guidance system. Though many different arrangements are feasible it seems inevitable that the final focusing quadrupole lenses will be arranged along lines inclined relative to a horizontal plane of symmetry. The beam guidance system which must feed these inclined beam lines must deviate even more from this horizontal plane of symmetry. An example of a possible overall arrangement is shown in Fig. V.2-3. Though here quadrupoles of maximal flux densities of 5 T are assumed, the bending magnets are postulated to have only 3.2 T. Attention should here be paid to the fact that the apexes of the vertically curved beam guidance systems are more than 20 m above and below the horizontal plane of symmetry. Since altogether 20 beam lines are planned, 10 arrangements as in Fig. V.2-3 must be foreseen, the planes of which are inclined by 36° relative to each other with the axis of rotational symmetry of the reactor vessel being common to all. Thus there is a true three-dimensional structure to be built having a radius of about 200 m and a height of about ±20 m. Most probably, such a structure is best built underground. In any case the costs for the complex civil engineering should be considered.

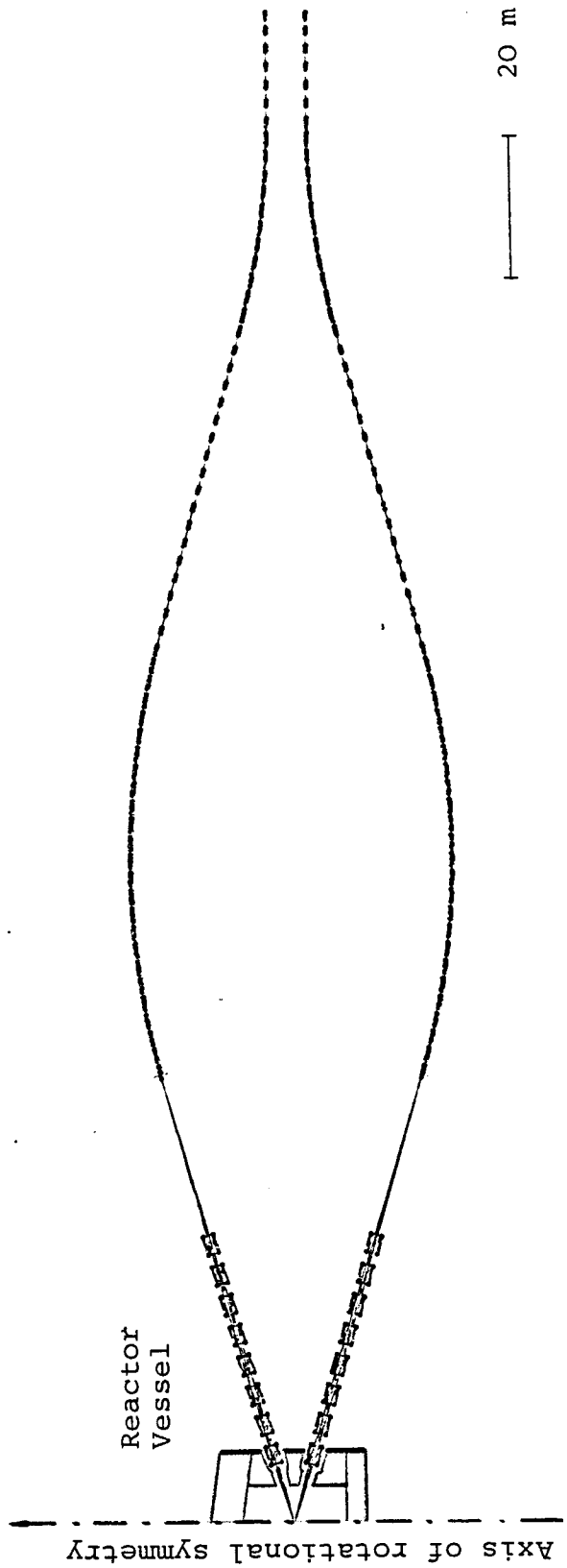

Fig. V.2-3 The possible overall arrangement of a radial section of the final focusing quadrupole and the final portions of two beam lines. For each of these beam lines three unit cells are shown which altogether feed final focusing lenses which are inclined by $\pm 16^{\circ}$ to a horizontal plane of symmetry. Note that 10 such beam line arrangements are necessary for the final system and that the planes of these arrangements are inclined relative to each other by 36° with the axis of rotation of the reaction chamber being common to all.

References for Section V.2

1. I. Hofmann, HIBALL Workshop KfK Karlsruhe, Germany, Jan. 22-23, 1981.

2. I. Bozsik and I. Hofmann, Proc. of the Conference on Charged Particle Optics, Giessen, FRG, 1980, to be published in Nucl. Instr. and Meth.

V.3 Final Focusing Quadrupole Design

Within the set of final focusing quadrupoles in each beam line, the most severe constraints for design and operation must be met by Q_7 and Q_8. They are subjected to fusion neutrons more strongly than the other quadrupoles, and they have to provide a magnetic gradient of g = 8 T/m to a beam of diameter 2a = 1.2 m. The product g·a of gradient and minimum aperture radius is almost 5 T, excluding the efficient utilization of ferromagnetic poles.

The quadrupole field must therefore be generated by an appropriate current distribution (Fig. V.3-1) which is standard practice in the layout of superconducting quadrupole magnets.(1)

For the HIBALL quadrupoles, the current carrying conductors may be normal conducting or superconducting. Normal conducting coils, e.g., of copper and inorganic insulation, may be subjected to 10^{12} rad before their performance degrades. For a reasonable lifetime of the coils, the radiation shielding must be at least 0.2 m thick, yielding a minimum inner coil radius of 0.2 m + a = 0.8 m. Each quadrupole of this type would consume 20 to 50 MW of electric power depending on the trade-off between current density and radial thickness (weight, materials cost). With a lifetime of about 1 year, these coils would require frequent maintenance. Power balance and frequent remote repair excludes the use of normal conducting coils in HIBALL final focusing systems.

For superconducting coils, the shielding requirements are dictated by the operating temeprature of 4.2 K or below much more strongly than by radiation damage considerations. The heat load into the coils may be sufficiently reduced by a neutron- and γ-shield of 0.6 m which, together with cryostat and supports, gives an inner coil radius of 1.3 m. It can be assumed that with these parameters, a superconducting coil will operate for about 30 years of

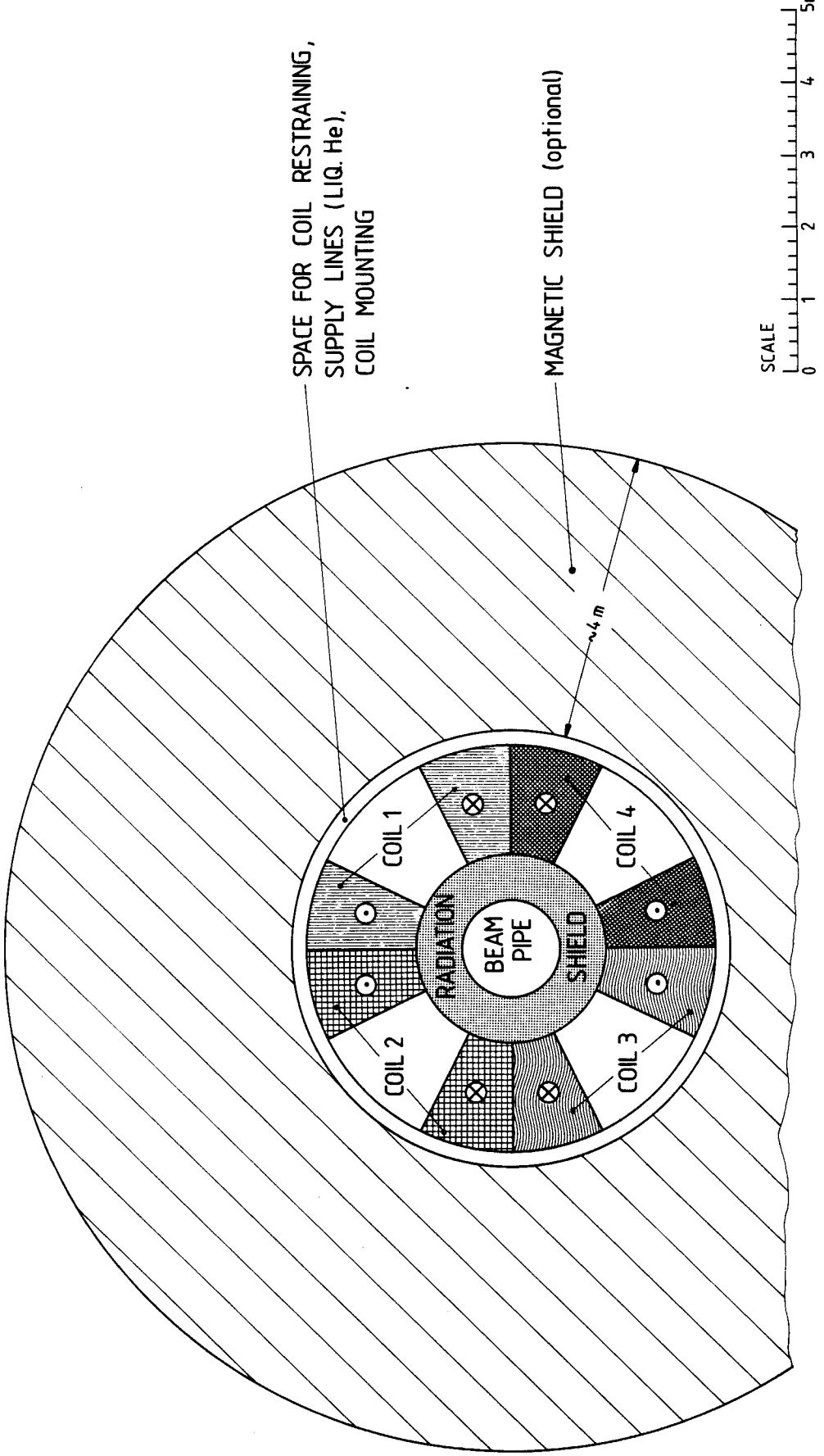

SCHEMATIC CROSS SECTION OF SUPER CONDUCTING END FOCUSSING QUADRUPOLE

FIGURE V. 3-1

lifetime before radiation damage of the insulation becomes an issue. The Nb-Ti superconductor itself is relatively insensitive to radiation.

The main parameters of a conceptual quadrupole are given in Table V.3-1, its cross section is shown in Fig. V.3-1.

Table V.3-1. Parameters of Final Focusing Quadrupole

Inner coil radius	1.3 m
Outer coil radius	2.3 m
Radiation shield thickness	0.6 m
Field gradient in coil midplane	8 T/m
Average current density in coil	2 kA/cm^2
Peak induction in coil	12 T
Superconductor	- Nb_3Sn
	- NbTi in low field regions
Length of coil straight section to achieve a focusing strength of 20 T/m•m	~ 2.5 m
Overall coil length	4-6 m
Iron shield thickness (optional)	$\gtrsim$ 4 m

These parameters represent the limits of presently conceivable superconductor technology. In particular, the average current density cannot be increased:

- Large magnets ($\gtrsim 10^8$ J) require a fully stabilized superconductor, i.e. a sufficient amount of good normal conducting material must be provided in parallel with the conductor.

The Lorentz forces which have a particularly complicated pattern in multipole magnets must be accommodated without conductor degradation. A large fraction of the coil cross section must therefore be taken by steel or similar materials.

The current density and peak field attained correspond to parameters which are presently discussed for large superconducting magnets in tokamaks and mirrors.

Two aspects of the magnet design require special attention as they relate to the overall layout of HIBALL:

a) If the stray field must be shielded, iron of about 4 m radial thickness is needed (about 1500 tons per quadrupole). If this shielding is not considered, the mutual distortion of fields in neighboring beam lines and the stray field in the reactor chamber must be taken into account.

b) The overall axial length of the quadrupoles is determined by the coil and type, i.e. the spatial pattern in which the direction of current carrying conductors is reversed. At least 6 m of total length result if the coil end is provided in the same radial region in which the coil itself is situated (see Fig. (V.3-1). If the coil end is bent radially outward, the total length comes down to about 3.5 m but the radial dimensions and thus the magnetic shielding requirements are aggravated.

Reference for Section V.3

1. H. Brechna, Superconducting Magnet Systems, Berlin, Heidelberg, New York; Spring 1973, Techn. Physik in Einzeldarstellungen Bd. 18.

V.4 Shielding of Final Focussing Magnets

V.4.1 Introduction

Fusion reactors are required to accommodate a variety of penetrations. The purpose and size of these penetrations vary depending on the reactor type.[1-3] However, in all cases proper shielding is required to protect the vital components in the penetration from excessive radiation damage caused by radiation streaming. The major penetration in a heavy ion beam fusion reactor is the ion beam line. Such a penetration is characterized by a large area ($\sim$ 1 m^2). Furthermore, a large number of these penetrations ($\sim$ 20) is required to provide uniform illumination of the target.

The HIBALL reactor utilizes twenty 10 GeV Bi^{++} ion beams to bring the target to ignition. Each beam port is rectangular in shape with a height of 102.8 cm and a width of 34.3 cm at the reactor cavity wall of radius 7 m. There will be 8.14×10^{16} neutrons streaming through each beam line penetration per shot for a DT yield of 400 MJ. A number of superconducting magnets are arranged along the beam line to focus the ion beam to a spot 6 mm in diameter at the target. Adequate penetration shielding is required to protect these beam focussing magnets from excessive radiation damage.

Various beam line penetration shield shapes have been considered to assess their effectiveness in reducing the radiation effects in the HIBALL beam focussing magnets. A three-dimensional neutronics and photonics analysis must be performed to account for the geometrical complexity of the penetration. The design criteria used to determine the shielding requirements for the magnets are:

1) A 50% radiation induced resistivity increase in the copper stabilizer which corresponds to 1.4×10^{-4} dpa (displacements per atom).

2) A radiation dose of 5×10^{9} Rad in the epoxy electrical insulation.

3) A peak nuclear heating of 10^{-4} W/cm^3 in the magnet.

V.4.2 Calculational Model

The blanket region in HIBALL is 2 m thick and consists of SiC tubes through which $Li_{17}Pb_{83}$ liquid metal eutectic flows. The tubes occupy 33% of the blanket region. A cylindrical vacuum wall having a radius of 7 m is used. The first wall is made of ferritic steel (HT-9) and is 1 cm thick. A 0.4 m thick reflector composed of 90 v/o ferritic steel structure and 10 v/o $Li_{17}Pb_{83}$ coolant is used. The reactor utilizes a 3.5 m thick concrete biological shield. A more detailed discussion is given later in section VI.3. Because of its small thickness and negligible effect on radiation damage in the penetration, the first wall is neglected in the present analysis. The results presented here are based on a DT yield of 400 MJ and a repetition rate of 5 Hz yielding 7.1 x 10^{20} fusion neutrons per second. Neutron multiplication, spectrum softening and gamma production in the target have been taken into account by performing one-dimensional neutronics and photonics calculations[4] in the spherical target using the discrete ordinates code ANISN[5] as described in section III.1.

The final focussing system in HIBALL which focuses the beam from the periodic beam line onto the target, consists of eight quadrupole magnets. The total length of the system is 60.4 m. Each quadrupole has a length of 2.7 m with the drift sections between the quadrupoles being 1.8 m long. Figure V.4-1 shows the vertical and horizontal envelopes for the beam as it is transported from the periodic line to the target. The positions of the eight quadrupoles used for focussing the beam are also shown. The inner dimensions of the magnet shield have been chosen to be at least 2 cm larger than the beam size, as determined from the envelopes in Fig. V.4-1, at all places along the penetration.

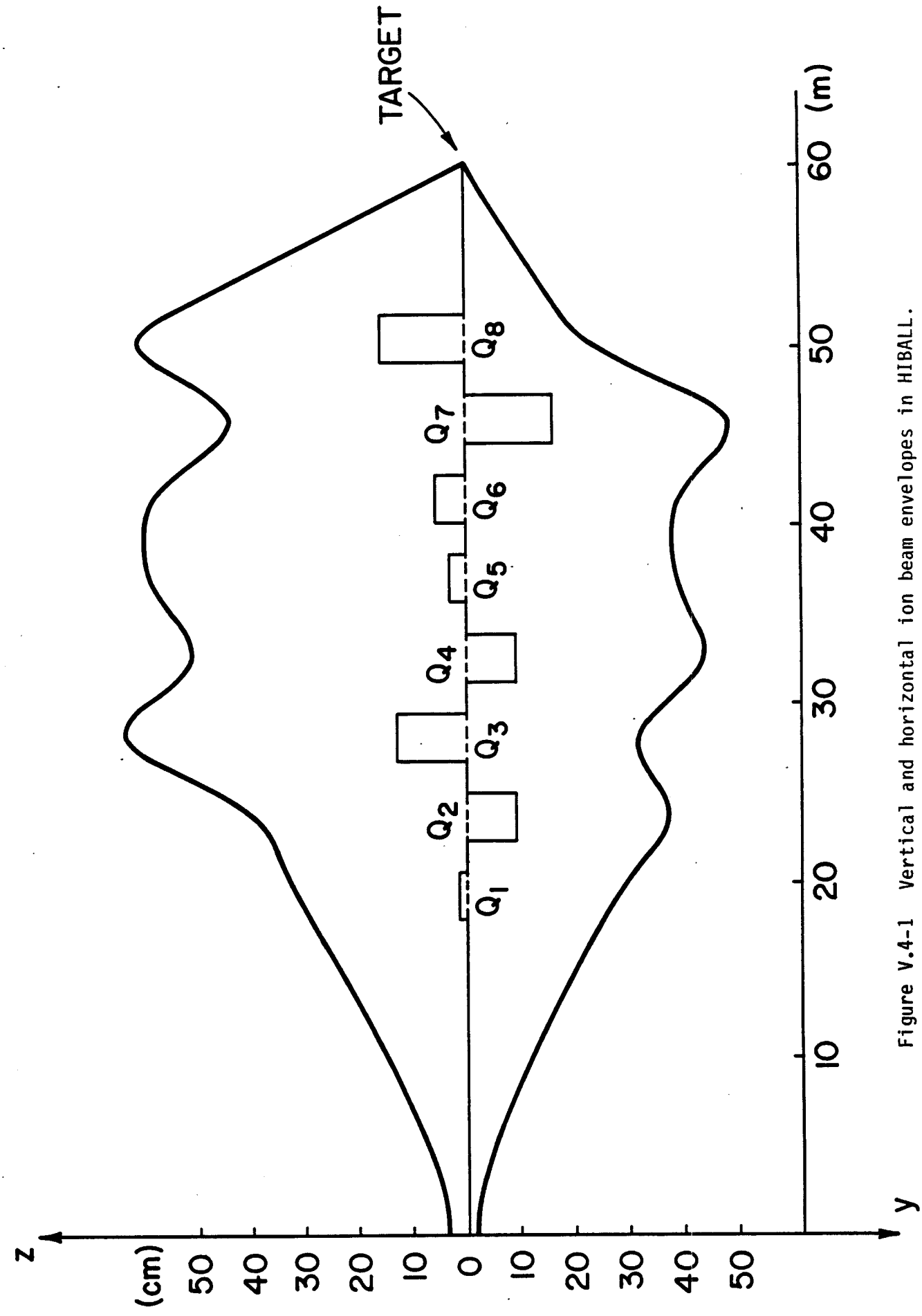

Figure V.4-1 Vertical and horizontal ion beam envelopes in HIBALL.

The 20 beam ports are arranged in two rows which are symmetric about the reactor midplane (z=0). The beam ports are 4 m apart vertically at the reactor vacuum wall. Because of symmetry only half a penetration is modelled in the present analysis with reflecting albedo boundaries used at the planes of symmetry. Consequently, only 1/40 of the reactor is modelled. This corresponds to a "pie slice" of the upper half of the reactor with an azimuthal angle of 18°. The angle between the centerline of the beam line penetration and the reactor midplane is 16°. The axes are rotated by 16° around the y axis for the penetration centerline to coincide with the x axis of the calculational model. This simplifies the description of the penetration geometry. Figure V.4-2 gives the vertical cross section for the focussing magnets and shield. Figure V.4-3 gives the cross section at the plane z'=0. Each quadrupole has a length of 2.7 m and a thickness of 1 m. Each magnet coil is modelled to have 7.52 v/o NbTi superconductor coils, 67.48 v/o copper stabilizer, 15 v/o liquid helium coolant, and 10 v/o insulation. The magnet shield is taken to be made of 60 v/o 316 SS, 15 v/o Pb, 15 v/o B_4C and 5 v/o H_2O coolant. The shield has a minimum thickness of 0.5 m in the quadrupole sections. The inner surface of the shield in the quadrupole section is tapered such that it does not see direct line of sight 14.1 MeV source neutrons. This will be shown to be more advantageous than using a shield with flat inner surface.

The neutronics and photonics calculations were performed using the three-dimensional Monte Carlo code MORSE.[6] A coupled 25 neutron - 21 gamma group cross section library was used. The library consists of the RSIC DLC-41B/VITAMIN-C data library[7] and the DLC-60/MACKLIB-IV response data library.[8] Since only 1/40 of the reactor is considered, we start with 1.775×10^{19} 14.1 MeV fusion neutrons per second and perform target calculations to determine

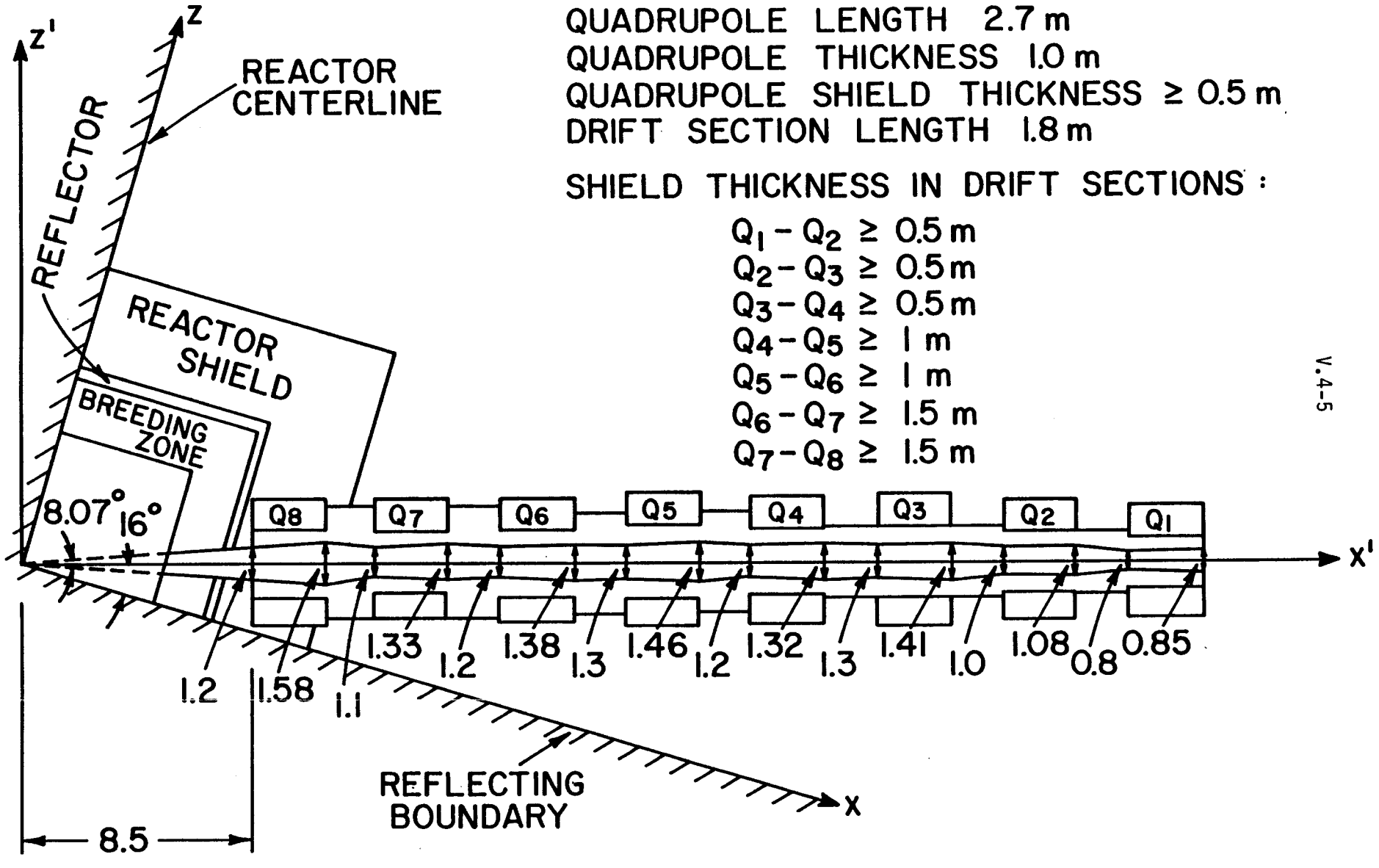

Figure V.4-2 Vertical cross section for focussing magnets and shield.

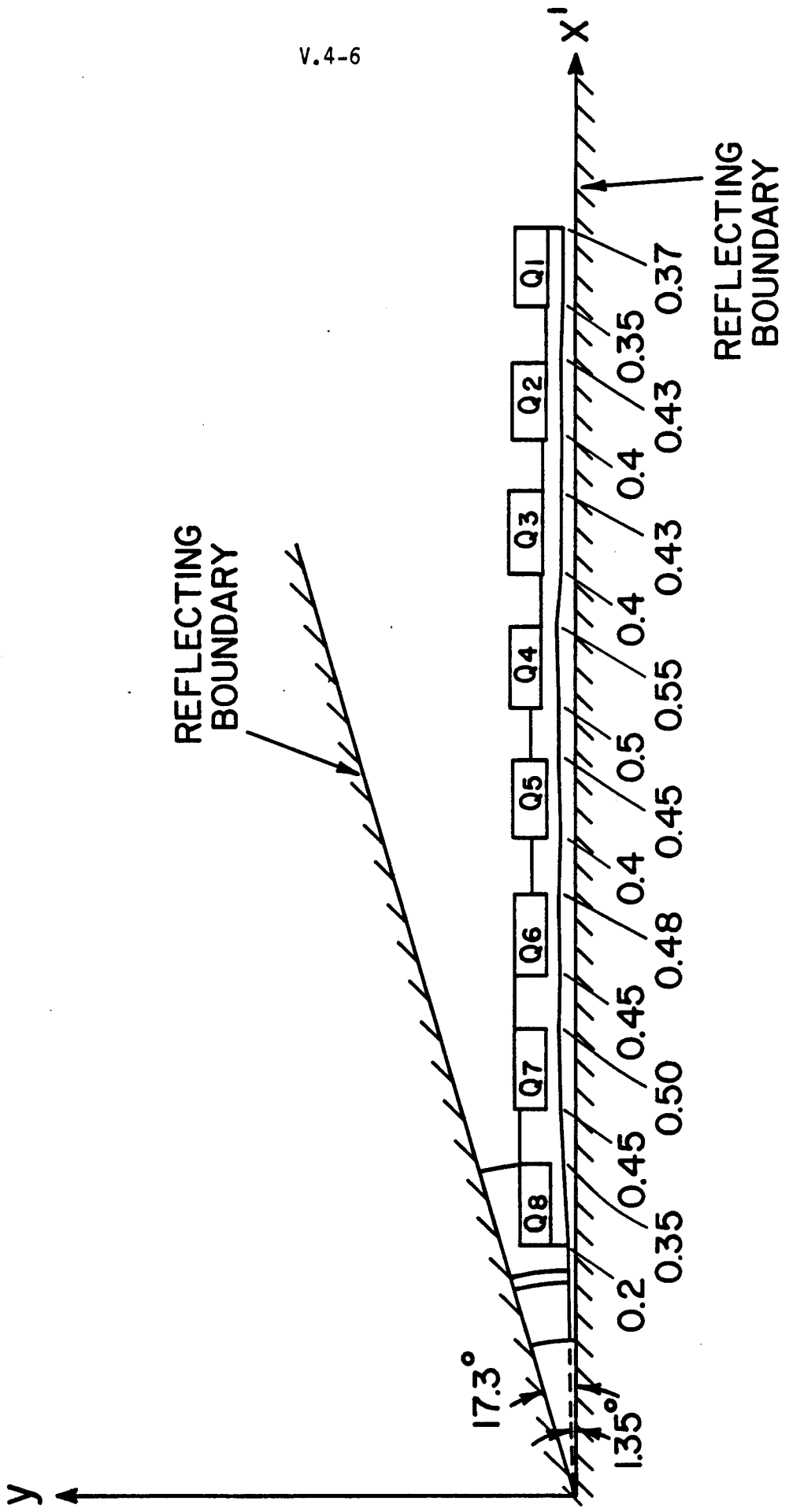

Figure V.4-3 Cross section at plane z'=0 for focussing magnets and shield.

the source intensity and spectrum for neutrons and gammas emitted from the target. These source neutrons and gammas are considered to be emitted isotropically at the origin.

In order to get statistically adequate estimates for the flux in the focussing magnets with a reasonable number of histories, an angular source biasing is used. The biasing technique is similar to that used previously for the analysis of the end plug of a tandem mirror fusion reactor.[3] However, in this case, the distribution is biased in both polar and azimuthal angles.

The distribution function from which the polar and azimuthal angles are picked is

$$P(\underline{\Omega})\ d\underline{\Omega} = P(\mu)\ P(\phi)\ d\mu\ d\phi\ . \qquad \text{(V.4-1)}$$

For the unbiased isotropic distribution we have

$$P(\mu) = 1\ ,\ (0 < \mu < 1)$$

and

$$P(\phi) = 10/\pi\ ,\ (0 < \phi < \frac{\pi}{10})$$

where $\mu=\cos\theta$, and θ and ϕ are the polar and azimuthal angles with respect to the frame xyz. If the biased distribution function is given by

$$P'(\underline{\Omega})d\underline{\Omega} = P'(\mu)\ P'(\phi)\ d\mu\ d\phi\ , \qquad \text{(V.4-2)}$$

the statistical weight of the source should be modified by the ratio of the

unbiased to the biased distribution functions at any particular solid angle (θ,ϕ) for the final estimates to be unbiased. Therefore, the weight for the biased case, w', is related to the weight for the unbiased case, w, by

$$w' = w \frac{P(\mu)P(\phi)}{P'(\mu)P'(\phi)} . \qquad (V.4\text{-}3)$$

In this work, μ is picked from a biased distribution which forces 90% of the source neutrons to have $\theta_p - \frac{\Delta\theta_p}{2} < \theta < \theta_p + \frac{\Delta\theta_p}{2}$, where $\theta_p = 74^0$ is the angle between the axes x' and z, and $\Delta\theta_p = 8.07^0$ as shown in Fig. V.4-2. A schematic of the biased and unbiased distributions for μ is given in Fig. V.4-4(a). The azimuthal angle, ϕ, is picked from a biased distribution that forces 90% of the source neutrons to have $0 < \phi < \Delta\phi_p$, where $\Delta\phi_p = 1.4^0$ is the azimuthal angle in the plane z=0 subtended by the penetration. A schematic of the biased and unbiased distributions for ϕ is given in Fig. V.4-4(b). After picking μ and ϕ, the direction cosines of the source particle with respect to the frame xyz are calculated. An orthogonal transformation is performed to determine the corresponding direction cosines with respect to the frame x'yz' used in the calculations.

Because of the $1/R^2$ geometrical attenuation, the largest radiation effects occur in the magnets closer to the source. For this reason and to reduce the computing time, only the last two quadrupoles Q_7 and Q_8 are modelled. The geometry for the computational model used is given in Fig. V.4-5. Each quadrupole is divided into three zones and each quadrupole shield is divided into two zones. Zone 12 represents the biological shield. Zones 13 and 14 represent the reflector and blanket, respectively. The inner vacuum region (zone 15) is extended to the region outside the biological shield and the focussing magnets. This allows the neutrons leaking out of the biological

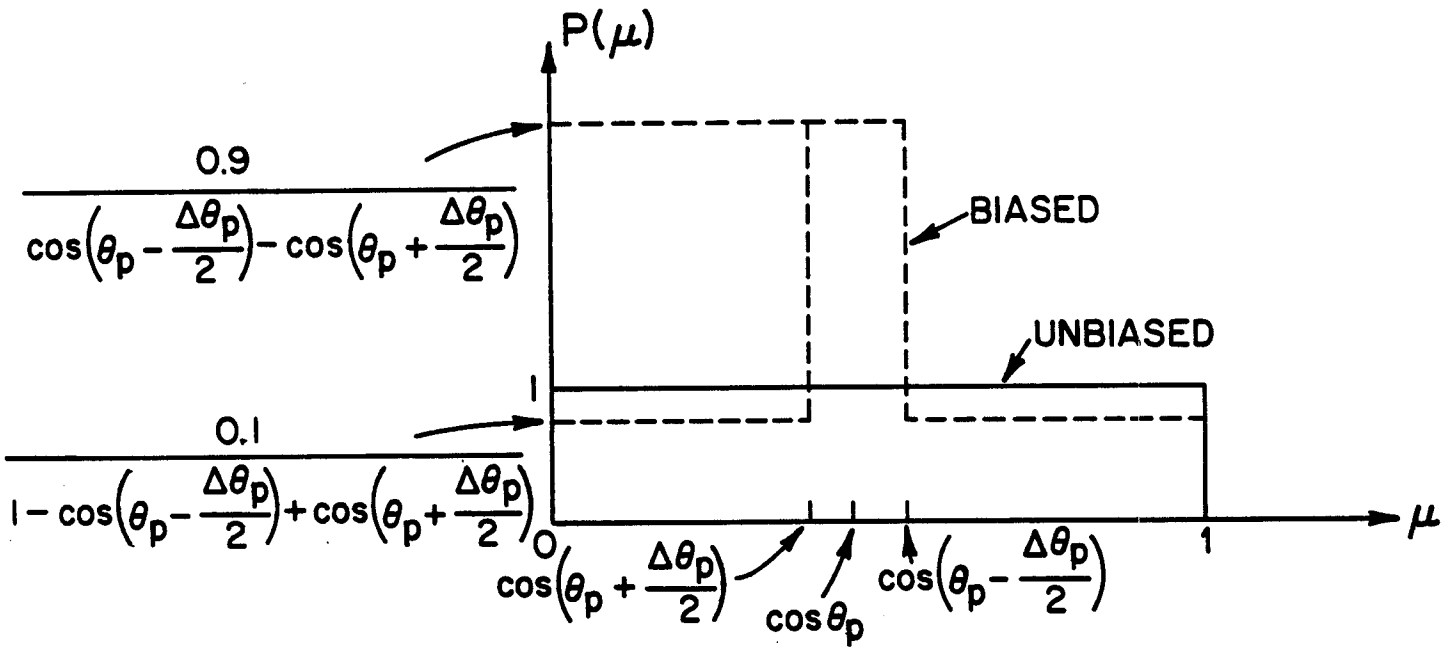

(a) ANGULAR BIASING FOR POLAR ANGLE

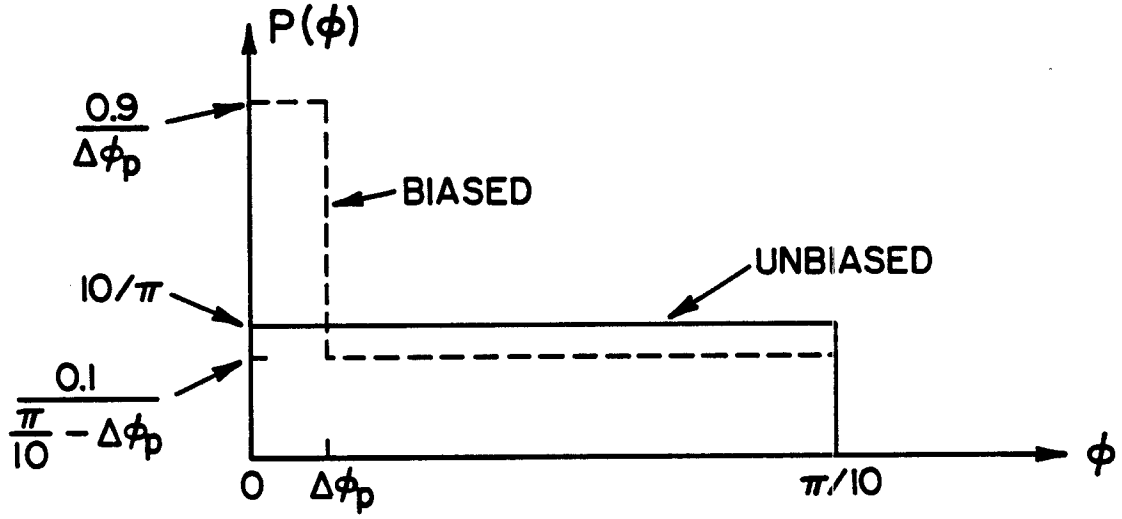

(b) ANGULAR BIASING FOR AZIMUTHAL ANGLE

Figure V.4-4 Angular source biasing scheme.

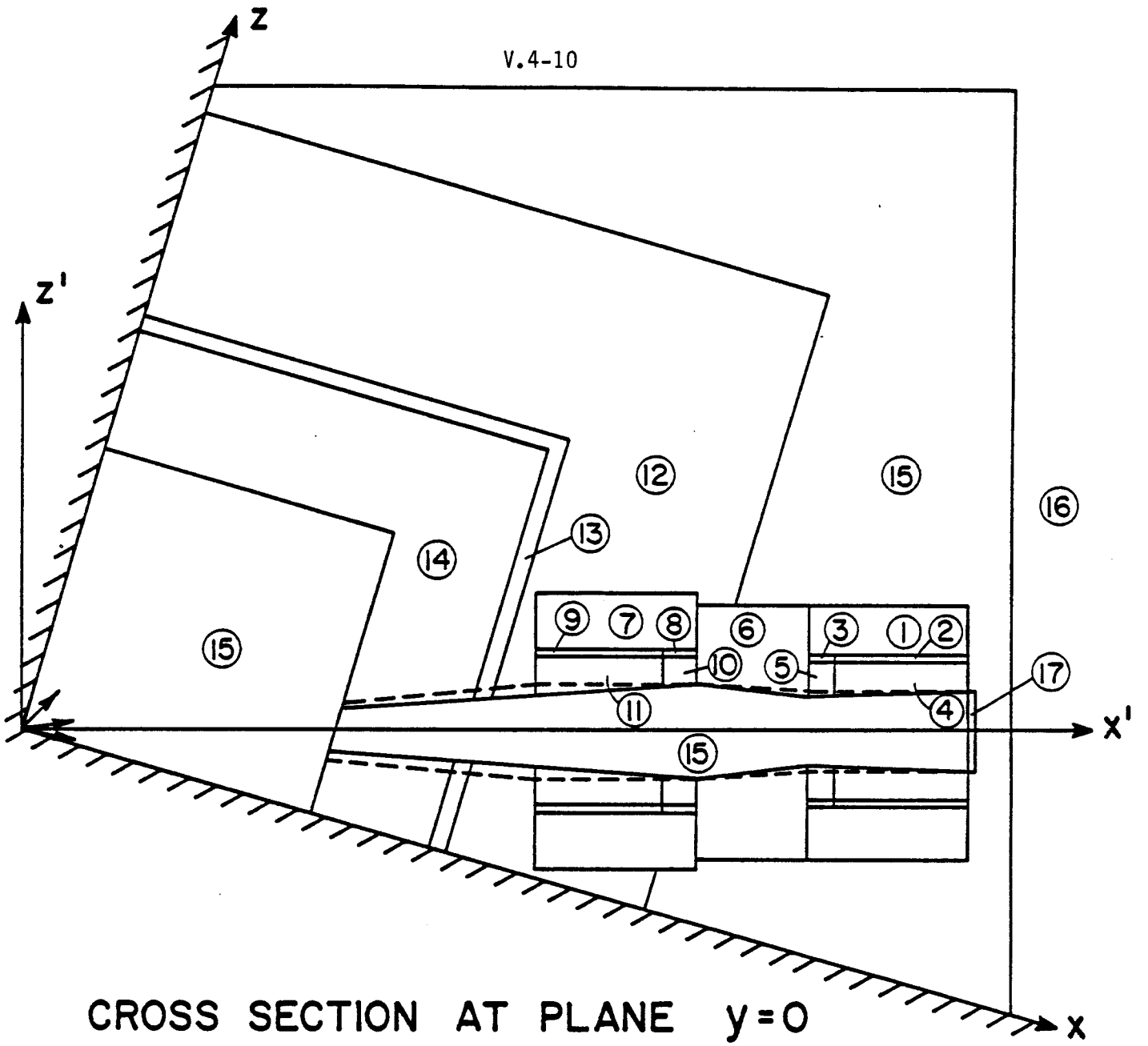

CROSS SECTION AT PLANE y=0

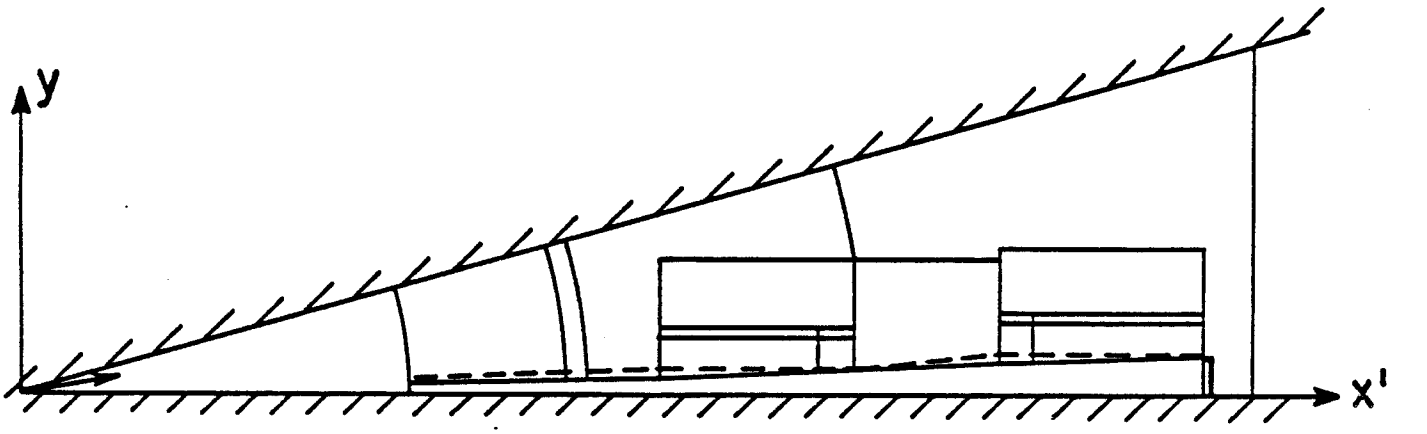

CROSS SECTION AT PLANE z'=0

Figure V.4-5 Geometry of computational model for final two focussing magnets.

shield to have additional collisions in the focussing magnets instead of being discarded as they would be if an outer vacuum region is used. To quantify leakage from the penetration a 1 cm thick penetration plug is designated as zone 17. The dotted lines in Fig. V.4-5 represent the geometry for a flat shield in the quadrupole sections. The solid lines represent the case with the shield being tapered in the quadrupole sections. Table V.4-1 gives the dimensions and material composition used in the different zones. The results presented here are obtained using 20,000 histories in the Monte Carlo problem.

V.4.3 Results and Discussion

The effect of tapering the shield in the quadrupole sections on the flux in the magnets was investigated. The geometrical models used for the flat and tapered shield cases are shown in Fig. V.4-5. In the tapered shield case, the shield is tapered along the direct line of sight of source neutrons. In this case, no direct 14.1 MeV source neutrons impinge on the part of the shield in the quadrupole sections. All source neutrons impinge on the inner surface of the shield in the drift section. Table V.4-2 shows the effect of tapering the shield on the neutron scalar flux in the different penetration zones.

It is clear from the results in Table V.4-2 that tapering the shield in the quadrupole sections reduces the neutron flux in the magnets. The peak neutron flux in quadrupole 7 occurring in zone 3 is reduced by a factor of 1.8 when the shield is tapered. On the other hand, the peak neutron flux in quadrupole 8 occurring in zone 8 is reduced by an order of magnitude. The effect of shield tapering on the flux in quadrupole 8 is more pronounced than that in quadrupole 7 because scattering of 14.1 MeV neutrons is highly forward peaked. It is clear also that the flux in the shield for quadrupole 8 is reduced significantly by tapering. The reason is that in the tapered case no direct line of sight source neutrons reach zones 10 and 11 and neutrons reach

Table V.4-1 Zones Used to Model the Final Two Focussing Quadrupoles and Their Shields

Region	Zone Number	Length (m)	Thickness (m) Tapered Shield	Flat Shield	Material Composition
Quadrupole 7	1	2.7	.9	.9	7.52 v/o NbTi + 67.48 v/o Cu
	2	2.2	.1	.1	+ 15 v/o Liq. He + 10 v/o
	3	.5	.1	.1	Insulation
Shield for Q_7	4	2.2	.5-.55	.5	60 v/o 316 SS + 15 v/o Pb
	5	.5	.54-.56	.5	+ 15 v/o B_4C + 5 v/o H_2O
Drift Section Shield	6	1.8	1.37-1.56	1.35-1.50	
Quadrupole 8	7	2.7	.9	.9	7.52 v/o NbTi + 67.48 v/o Cu
	8	.5	.1	.1	+ 15 v/o Liq. He + 10 v/o
	9	2.2	.1	.1	Insulation
Shield for Q_8	10	.5	.5-.54	.5	60 v/o 316 SS + 15 v/o Pb
	11	2.2	.53-.69	.5	+ 15 v/o B_4C + 5 v/o H_2O
Biological Shield	12	-	3.5	3.5	95 v/o Concrete + 5 v/o H_2O
Reflector	13	-	.4	.4	90 v/o ferritic steel + 10 v/o $Li_{17}Pb_{83}$
Blanket	14	-	2.0	2.0	98 v/o $Li_{17}Pb_{83}$ + 2 v/o SiC (.33 d.f.)
Inner Vacuum	15	-	-	-	Void
Outer Vacuum	16	-	-	-	Void
Penetration Plug	17	-	.01	.01	316 SS

Table V.4-2 Effect of Tapering the Shield on the Flux Estimates in Penetration Zones

Region	Zone Number	Neutron Scalar Flux (n/cm^2 s) Flat Shield	Tapered Shield
Quadrupole 7	1	2.767×10^8 (0.60)*	1.631×10^8 (0.77)
	2	4.504×10^9 (0.40)	3.441×10^9 (0.52)
	3	2.156×10^{10} (0.38)	1.217×10^{10} (0.48)
Shield for Q_7	4	1.552×10^{12} (0.13)	7.728×10^{11} (0.14)
	5	3.606×10^{12} (0.17)	2.224×10^{12} (0.15)
Drift Section Shield	6	1.299×10^{12} (0.09)	9.765×10^{11} (0.08)
Quadrupole 8	7	7.388×10^9 (0.75)	9.720×10^6 (0.77)
	8	9.854×10^{10} (0.76)	9.758×10^9 (0.69)
	9	1.780×10^{11} (0.50)	NS**
Shield for Q_8	10	6.624×10^{12} (0.14)	8.108×10^{11} (0.18)
	11	8.181×10^{12} (0.11)	1.980×10^{11} (0.30)
Penetration Plug	17	5.936×10^{13} (0.13)	5.368×10^{13} (0.10)

* Numbers in parentheses are fractional standard deviations.

** No score in this zone for the 20,000 histories used.

these zones only after having collisions in the drift section shield (zone 6). On the other hand, the neutron flux in the shield for quadrupole 7 decreases only slightly because the 14.1 MeV source neutrons have a larger chance to go in the forward direction into zones 4 and 5 than to go in the backward direction into zones 10 and 11 after colliding in the drift section (zone 6). The neutron flux at the first surface of the HIBALL blanket at the reactor midplane is 2.364×10^{14} n/cm^2 s. This implies that the peak flux in the

focussing magnets is more than four orders of magnitude lower than the flux at the first surface of the blanket.

The neutron leakage flux at the penetration plug is 5.368 x 10^{13} n/cm^2 s for the tapered shield case. The direct line of sight 14.1 MeV neutron flux leaking from the penetration is 2.398 x 10^{13} n/cm^2 s which amounts to 45% of the neutron leakage flux. It is clear from the results in Table V.4-2 that the neutron flux in the penetration plug decreases by tapering the shield. The reason is that the amount of neutrons leaking after colliding along the penetration decreases when no direct line of sight source neutrons are incident on the shield for quadrupole 7. Even though an appreciable amount of neutrons are leaking through the penetration modelled here, this does not pose a serious problem because only the last two quadrupoles are modelled here. The other six quadrupoles are shielded in the same manner as shown in Figs. V.4-2 and V.4-3. Considering $1/R^2$ attenuation, the neutron leakage flux at quadrupole 1 is estimated to be 7.257 x 10^{12} n/cm^2 s.

Further modification in the shape of the shield in the drift section is considered to improve the effectiveness of the penetration shield. The inner surface of the shield in the drift section is tapered at both ends such that it coincides with the direct line of sight from the source as shown in Fig. V.4-6. In this case, all source neutrons impinge on a vertical neutron dump in the shield. This increases the minimum distance between the magnet and the point on the surface of the shield where the source neutron has its first collision and is expected to reduce the radiation damage in the magnets. Two positions are considered for the neutron dump as shown in Fig. V.4-6.

Table V.4-3 gives the atomic displacements per full power year (FPY) in the Cu stabilizer in the different magnet zones for the cases of flat shield and tapered shield with the different options for the drift section shield

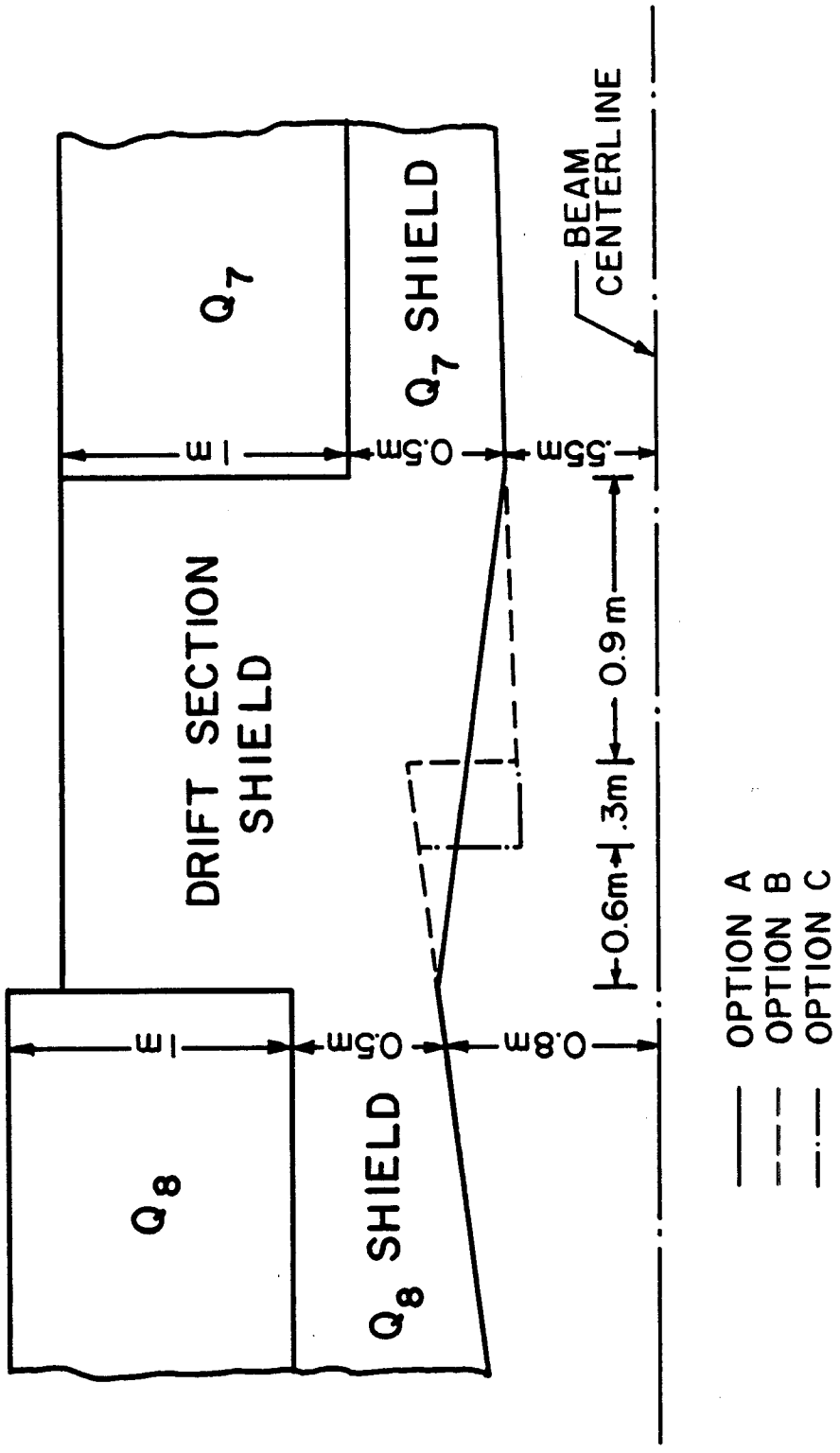

Figure V.4-6 Options for tapering drift section shield.

Table V.4-3 Effect of Penetration Shield Shape on DPA Rate in the Copper Stabilizer

Region	Zone Number	DPA Rate (dpa/FPY) Flat Shield	Tapered Shield in Quadrupole Section Option A	Option B	Option C
Quadrupole 7	1	2.167×10^{-6}	1.142×10^{-6}	1.023×10^{-7}	NS
	2	3.129×10^{-5}	3.686×10^{-5}	1.256×10^{-5}	NS
	3	9.115×10^{-5}	9.702×10^{-5}	1.600×10^{-5}	2.710×10^{-6}
Quadrupole 8	7	1.690×10^{-5}	1.742×10^{-7}	NS	1.749×10^{-8}
	8	6.182×10^{-4}	1.151×10^{-4}	NS	4.483×10^{-6}
	9	1.056×10^{-3}	NS	NS	7.580×10^{-7}

shown in Fig. V.4-6. Notice that even though the scalar flux in zones 2 and 3 of quadrupole 7 decrease when the shield is tapered with option A (Table V.4-2), the dpa rate slightly increases. The reason is that when the shield is tapered, all 14.1 MeV source neutrons fall on the drift section shield (zone 6) instead of falling on zones 4 and 5 as well. Since elastic scattering of high energy neutrons is highly forward peaked, this results in a slight increase in the high energy flux in zones 2 and 3 of quadrupole 7 yielding higher dpa values. As the neutrons slow down in the shield the scattering becomes more isotropic with the low energy flux decreasing in zones 2 and 3. The net effect is to decrease the total neutron scalar flux as shown in Table V.4-2. On the other hand, tapering the shield with option A results in significant reduction in the dpa rate in quadrupole 8.

If shielding option B is used, it is found that the peak dpa rate in quadrupole 7 is decreased by a factor of ~ 6 as compared to option A in

addition to decreasing the peak dpa rate in quadrupole 8 significantly. In the run of 20,000 histories, no contribution was obtained in quadrupole 8. Because scattering is forward peaked at high neutron energies, locating the source neutron dump halfway between Q_7 and Q_8 results in considerable reduction in damage in Q_8 and a smaller reduction in Q_7. Using option A the peak damage occurs in Q_8 while it occurs in Q_7 when option B is used. In option C, the source neutron dump is moved closer to Q_8. This is found to decrease the peak dpa rate in Q_7 considerably and increase the peak damage rate in Q_8 only slightly. The peak in Q_8 when option C is used is a factor of ~ 25 lower than that when option A is used.

Table V.4-4 gives the radiation dose rate in the epoxy electrical insulation in the different magnet zones for the different geometrical options considered. Again, it is clear that significant reduction in the radiation dose is obtained when the suggested shield geometrical modifications are adopted. The results given in Table V.4-4 include the contribution from both neutron and gamma energy deposition. Table V.4-5 gives the peak dpa rate, the peak radiation dose, and the peak power density in the focussing magnets for the different geometrical options considered. It is clear that the tapered shield with option C is the most effective shield design. Using option C for the drift section shield is found to result in a peak dpa rate in the Cu stabilizer of only 4.483×10^{-6} dpa/FPY. The neutron leakage flux at the penetration plug is found also to decrease to a value of 4.615×10^{13} n/cm^2 s with option B and 3.361×10^{13} n/cm^2 s for option C. This results from increasing the attenuation distance in the shield for neutrons impinging on the source neutron dump.

Radiation damage to the stabilizing material in the superconducting magnets results in increasing the electrical resistivity. The radiation induced

Table V.4-4 Effect of Penetration Shield Shape on Radiation Dose Rate in the Epoxy Insulation

Region	Zone Number	Radiation Dose Rate (Rad/FPY) Flat Shield	Tapered Shield in Quadrupole Section Option A	Option B	Option C
Quadrupole 7	1	5.220×10^{6}	2.149×10^{6}	7.966×10^{5}	1.625×10^{2}
	2	5.914×10^{7}	7.637×10^{7}	1.978×10^{7}	7.390×10^{3}
	3	1.831×10^{8}	2.195×10^{8}	2.526×10^{7}	4.174×10^{6}
Quadrupole 8	7	4.961×10^{7}	3.350×10^{5}	NS	1.031×10^{5}
	8	1.616×10^{9}	2.552×10^{8}	NS	7.188×10^{6}
	9	3.467×10^{9}	NS	NS	1.250×10^{6}

Table V.4-5 Effect of Penetration Shield Shape on Peak Values of DPA, Radiation Dose, and Nuclear Heating in the Focussing Magnets

	Flat Shield	Tapered Shield in Quadrupole Section Option A	Option B	Option C
Peak dpa/FPY in Cu Stabilizer	1.056×10^{-3}	1.151×10^{-4}	1.600×10^{-5}	4.480×10^{-6}
Peak Radiation Dose in Insulation	3.467×10^{9}	2.552×10^{8}	2.526×10^{7}	7.20×10^{6}
Peak Power Density (W/cm^3)	4.380×10^{-3}	2.44×10^{-4}	3.554×10^{-6}	5.350×10^{-7}

resistivity is related to the number of displacements per atom in the stabilizer. A 50% radiation induced resistivity increase in the copper stabilizer is considered as a design criterion. A resistivity of this amount is produced by a damage level of 1.4×10^{-4} dpa. This value is obtained using the relation between the induced resistivity in Cu, ρ_i and the total displacements per atom, d, given by the following equation:[9]

$$\rho_i = 3 \times 10^{-7} \left(1 - e^{-563d}\right) \Omega \cdot \text{cm} . \qquad \text{(V.4-4)}$$

However, recovery is possible by annealing. Increasing the time span between required anneals is desirable for reducing the maintenance cost. Decreasing the number of anneals required during the reactor lifetime also minimizes any possible undesirable consequences of cyclic irradiation. Using the shield design with option C, the maximum period of operation without annealing is ~ 31 full power years. This is compared to 8.5 FPY when option B is used and ~ 1 FPY when option A is used. If a flat shield design is used, one needs to anneal every ~ 45 days. This implies that when the shield design with option C is used, no annealing is needed for an estimated reactor lifetime of 20 full power years.

The radiation effects on the insulator are not reversible and it is essential that it lasts the whole reactor lifetime. The design limit used for the radiation dose in the epoxy electrical insulator is 5×10^9 rad. The results show that for an estimated reactor lifetime of 20 full power years, the designs with options B and C result in an accumulated radiation dose well below the design limit, while the designs with a flat shield and with option A do not satisfy the design criterion. The design limit on the peak power density is set to be 10^{-4} W/cm^3. It is clear from the results of Table V.4-5

that the tapered shield design with options B and C satisfy this design criterion while the designs with a flat shield and option A do not fulfill this requirement. It is concluded from the results presented here that a magnet shield which is tapered in the quadrupole sections with option C for the drift section shield shape satisfies the design criteria on the radiation dose in the insulator and the nuclear heating in the magnet with the possibility of eliminating the need for magnet annealing during the whole reactor lifetime.

Our calculations show that the edges of quadrupole 8 close to the reflector are exposed to relatively high levels of radiation because of the poor shielding effectiveness of concrete. To meet the design criteria, the dpa rate, radiation dose and power density at the corner of Q_8 close to the reflector need to be reduced by factors of 5, 10, and 40, respectively. This can be achieved by surrounding the magnet at these spots by more effective shielding. Tungsten can be used to attenuate neutrons and hence reduce the dpa and neutron heating. Lead can also be used to attenuate the high gamma flux which is the main source for nuclear heating in these parts of the magnet.

V.4.4 Summary

Tapering the shield in the quadrupole sections in such a way that all direct line of sight 14.1 MeV source neutrons fall on the inner surface of the drift section shield was found to reduce the radiation damage in the magnets. Several options for the shape of the shield in the drift sections were analyzed. The smallest radiation effects in the magnet were obtained when the inner surface of the shield in the drift sections was also tapered resulting in a vertical neutron dump between the magnets. Better shielding was obtained when the neutron dump between the last two quadrupoles was placed closer to the last quadrupole. With this design, the period between required magnet

anneals was increased to ~ 31 full power years compared to 45 days for the flat shield design. This implies that using the recommended shield design, the need for annealing during the reactor lifetime can be eliminated completely. The recommended shield design reduces the peak radiation dose in the insulator allowing it to last for the whole reactor lifetime. The peak power density in the magnet is also reduced significantly. We conclude that with proper shield design the final focusing magnets for HIBALL can be protected sufficiently so that radiation damage will not limit their lifetime and that the nuclear heating loads are not serious.

References for Section V.4

1. J. Jung and M.A. Abdou, Nuclear Technology, 41, 71 (1978).

2. M. Ragheb, A. Klein, and C.W. Maynard, Nuclear Technology/Fusion, 1, 99 (1981).

3. M. Ragheb and C.W. Maynard, UWFDM-398, University of Wisconsin (1981).

4. M. Sawan, W. Vogelsang, and G. Moses, UWFDM-395, University of Wisconsin (1980).

5. RSIC Code Package CCC-254, "ANISN-ORNL", Radiation Shielding Information Center, ORNL.

6. RSIC Code Package CCC-203, "MORSE-CG", Radiation Shielding Information Center, ORNL.

7. RSIC Data Library Collection, "VITAMIN-C, 171 Neutron, 36 Gamma-Ray Group Cross Sections Library in AMPX Interface Format for Fusion Neutronics Studies", DLC-41, ORNL.

8. RSIC Data Library Collection, "MACKLIB-IV, 171 Neutron, 36 Gamma-Ray Group Kerma Factor Library", DLC-60, ORNL.

9. M. Abdou and R. Roussin, ORNL/TM-3706, Oak Ridge National Laboratory (1976).

Figure Captions for Section V.4

Figure V.4-1 Vertical and horizontal ion beam envelopes in HIBALL

Figure V.4-2 Vertical cross section for focussing magnets and shield

Figure V.4-3 Cross section at plane z'=0 for focussing magnets and shield

Figure V.4-4 Angular source biasing scheme

Figure V.4-5 Geometry of computational model for final two focussing magnets

Figure V.4-6 Options for tapering drift section shield

V.5 Considerations for Future Design

To focus several intense ion beams on a spot of 3 mm radius it is advantageous to choose ion beams with differently large phase space areas in the horizontal and the vertical planes. One main reason for this is that the INPORT tube protection of the reactor vessel is easier to fabricate by requiring vertically long and horizontally narrow beam apertures instead of round openings of equal area. Another main reason is that the choice of unequal phase space areas simplifies the correction of image aberrations of the final focusing lens system. Some problems in this case arise in the design of the beam guidance systems which mainly result in larger beam apertures and thus larger magnet elements. To accommodate the required phase space area of about 30 x 120 $\pi^2 mm^2$ $mrad^2$ for 20 beam lines a horizontal phase space area of 30 π mm-mrad and a vertical phase space area of 120 π mm-mrad, each was chosen as basis of all geometric designs in this section, resulting in beam apertures of ±110 and ±340 mm in the middle of the 3 m thick wall of the reactor vessel.

In order to achieve a homogeneous bombardment of the target and at the same time allow a Pb-Li flow which is as little disturbed as possible the 20 beam lines were arranged in 10 pairs inclined by ±16°. An even more homogeneous bombardment of the target would be feasible by choosing not only two but three or possibly four rows of beam lines each of which transmits a smaller phase space. This may be understood as a smaller lateral phase space for a beam pulse of equal length or, which may be of high importance, a shorter ion pulse for beams of constant lateral phase space.

Since all focusing lenses must be placed outside of the reactor vessel their diameters must be larger than the openings in the reactor wall resulting in quite bulky magnets of high flux densities. To keep these lens diameters

within limits it seems reasonable to use as short lenses as possible. Thus superconducting quadrupole lenses with high magnetic flux densities are attractive. Unfortunately cooled superconductors are rather sensitive to ionizing radiation so that rather well-designed shielding against neutrons is necessary. However, such radiation shields increase the lens apertures considerably. For lens coils which have a direct view to the target this increase in diameter is about ±500 mm so that the cross section within any lens is mainly filled by shielding material and only to a minor percentage by the ion beam. For lens coils which have no direct view to the target this increase in diameter is around ±300 mm.

In the design of such final focusing lenses attention must be paid to the existing space charge of the ion beams. Since ion beams of comparable intensities are not yet available experimentally it is difficult to predict to what extent the positive charge of ions is compensated by slow electrons or slow negative ions within the beam. The predictions of achievable space charge compensations vary from 0% to 100% since it seems possible to modify the experimental conditions to favor either one of these limits.

As long as no experimental information on such ion beams is available it seems most useful to either look for solutions which are relatively insensitive to varying space charge by avoiding narrow beam cross overs and long drift distances[1] (most probably, however, the required focusing precision cannot be preserved over a wide range of space charge values). We could also look for solutions in which the effects of varying space charge can be compensated by varying the magnet flux densities in some or all lenses of the final focusing section. Since both types of solutions can be expected to work only for narrow regions of space charge compensation, any design for an arbitrarily chosen fixed percentage can only be an example.

To provide a summary about possible solutions for the final focusing lens systems and at the same time pay some attention to the mentioned problems we shall below discuss three principle solutions:

1. The first type of lens system consists of 6 or 8 quadrupoles to which the rather narrow ion bundle from a beam transport line is matched by normally 3 additional quadrupoles.[2] Though such solutions seem quite reasonable at first and second sight, they all have the draw-back that the lens coils have a direct view to the fusion target and thus require heavy shielding. While the final focusing lenses of the reference design (see section V.2) require maximal magnetic flux densities in excess of 4 T at the beam envelope, resulting in more than 8 T at the quadrupole coils outside of the heavy shielding, it is also possible to find solutions for which the maximal flux densities stay below 2 T at the beam envelope. Thus good magnet iron could be used to concentrate the magnetic flux without saturation effects in the pole tips. This would result in considerably less costly systems for which the shielding problem is much simpler. Such solutions, however, must be expected to have increased image aberrations so that possibly the acceptable phase space for each ion beam must be reduced slightly in order that the major portion of the ions in a beam can be delivered to the target.
2. The second type of lens system consists not only of quadrupole lenses but also includes magnetic sector fields in the lens arrangement outside of the reactor vessel so that only the first sector field (see Fig. V.5-1a) has a direct view to the fusion target. Consequently, the radiation shielding for all following quadrupole lenses must only increase the corresponding lens diameters by about 0.3 m. However, it should not be overlooked that the first one of these lenses is no longer 10 m away from

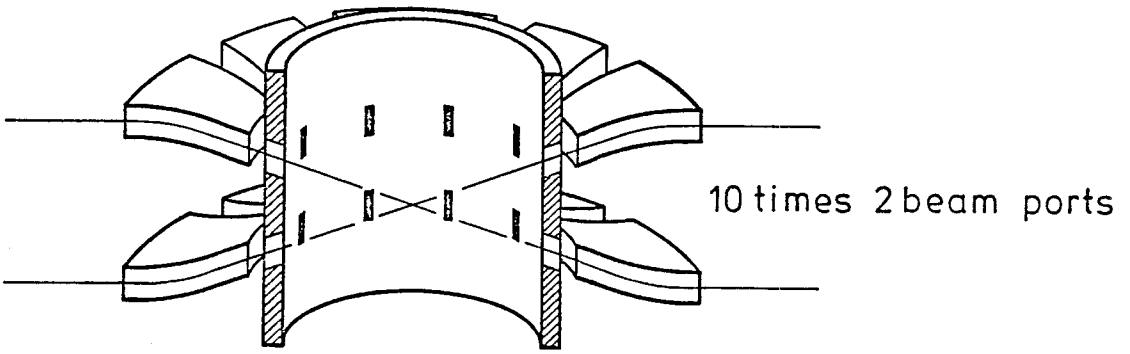

(a)

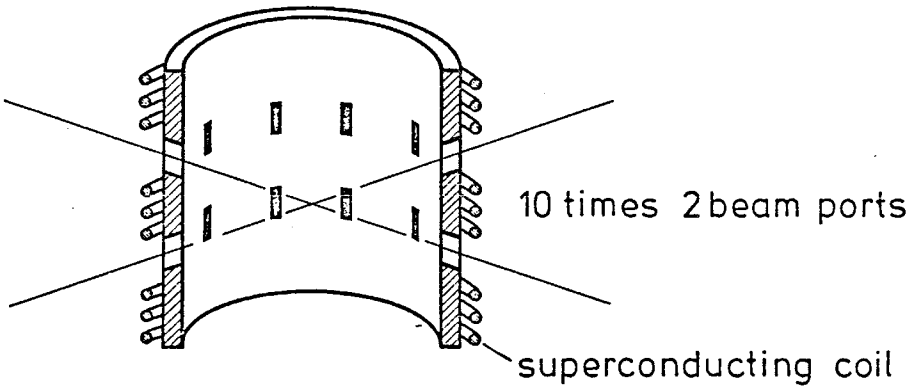

(b)

Fig. V.5-1 Two possible arrangements of a last sector field in the final focusing system are shown which both reduce the radiation level for the final focusing quadrupoles. One first solution (a) postulates vertically deflecting dipole fields immediately outside of the reactor vessel. Note here the race track design of the sector fields which allows tolerable fringing fields and limited amounts of iron. A second solution (b) assumes a large magnetic coil to form a magnet flux parallel to the vessel axis. In this case the optical elements outside of the reactor vessel must focus the ion beam not onto the fusion pellet but to a point about 1 m away from it so that the magnetic field in the reactor vessel can bring it onto the pellet.

the fusion target, that is, the radius of the reactor chamber, but almost 20 m. Thus the lens diameters must be rather large at least in the vertical direction because of the aperture angles of ±40 mrad which are only slightly modified by the first sector field (see Fig. V.5-2). Because of the high rigidity of the ion beams under consideration, the angle of deflection of this first sector field cannot be very large. One should postulate, however, that it must completely separate the ions from the neutron beam at the boundary of the reactor vessel. Choosing a sector magnet of 2 T (or 4 T) one thus finds from simple geometry a deflection angle $\phi_0 \simeq 15°$ (or $\simeq 19°$) and a magnet length of $\rho_0\phi_0 \simeq 8.2$ (or $\simeq 5.8$) meters. In spite of these rather small differences, it seems advantageous to use a sector magnet of 2 T so that good magnet iron can be used to concentrate the magnetic flux and to avoid any problems arising from a high radiation dose. The corresponding magnet is preferably constructed in the race track design as indicated in Fig. V.5-1a.

3. A third type of lens system requires a large preferably superconducting coil to be wound around the reactor vessel (see Fig. V.5-1b) so that a magnetic flux parallel to the axis of this vessel is created. For an optical system outside of the reactor vessel then the ions seem to be focused to a point almost one meter away from the target. Forming a channel of shielding material which is directed towards the virtual target position the neutron and γ-radiation from the target can be shielded effectively. The shielding material can be partially the Pb-Li cooling liquid and partially explicit shielding material placed in and a little outside of the reactor wall. Depending on the design of the Pb-Li sheet probably only a minor amount of shielding material must be added to the reactor wall so that one can employ quadrupole lenses similarly as in case 1.

The conclusions of the previous analysis can be stated as follows:

1. The magnitude of the space charge to be taken into account is unknown for all three focusing schemes. Corresponding experimental investigations of the magnitude of space charge compensation seem indispensable. This includes investigations in the presence of strong magnetic fields.
2. A system as shown in Fig. V.5-2 deflects the ion beam vertically by two magnets. In this design the highest and the lowest points of the two ion beams stacked on top of each other vertically are only about 5 m above and 5 m below the plane of symmetry of Fig. V.5-1a. Systems as shown in Figs. V.5-2 and V.5-3 include much longer straight sections so that vertical deflections can occur only in the beam guidance lines. The highest and lowest points of the two ion beams in these two cases thus are more than 20 m above and below the plane of symmetry as outlined in section V.2.3.
3. Detailed calculations of image aberrations of the final focusing lenses should be performed as soon as the questions of point 1 are better known or reasonable assumptions can be made and as soon as one has fixed a first order design. In such calculations, the effects of the complex beam guidance systems must be included since their influence is not negligible.

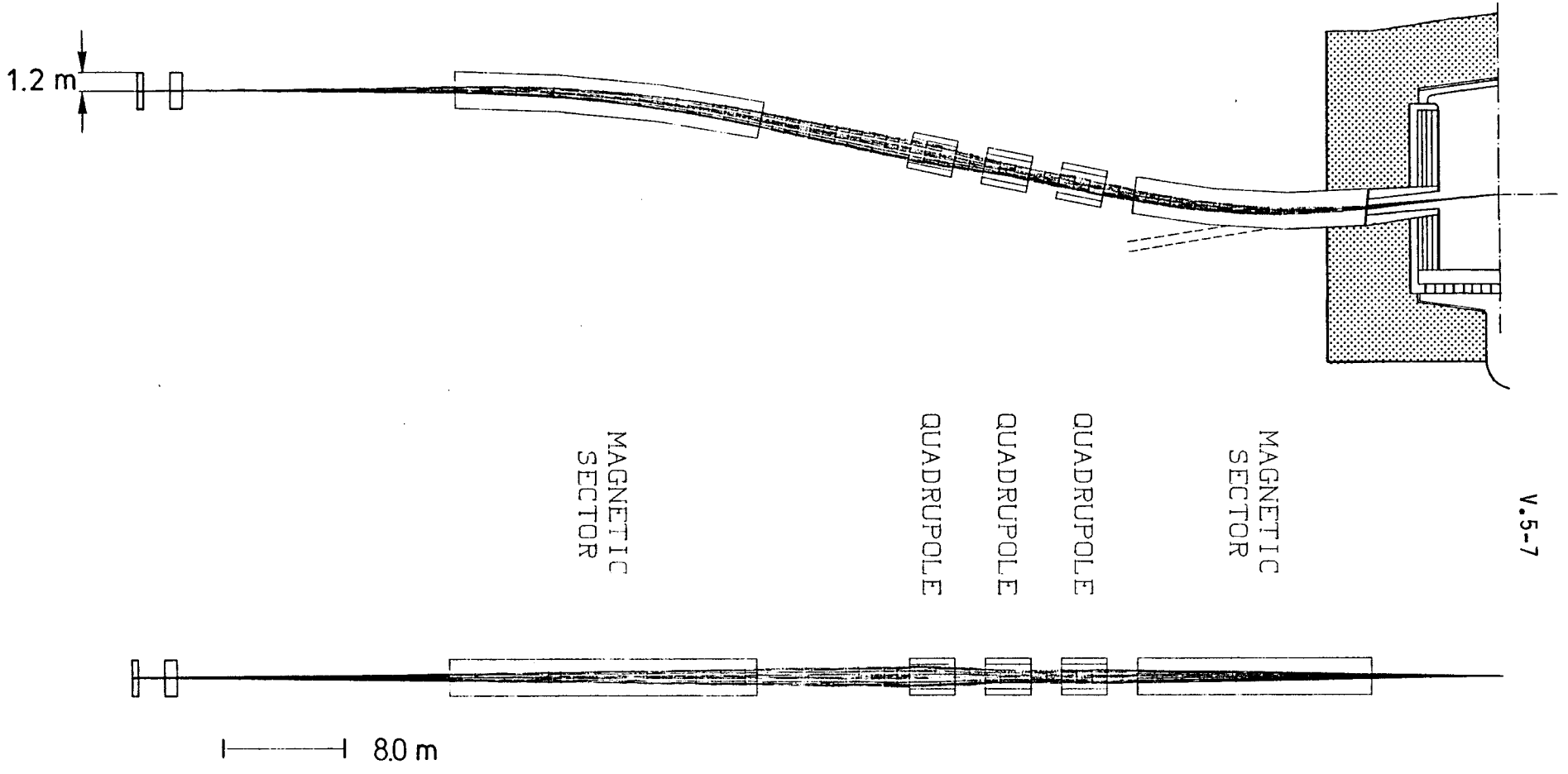

Fig. V. 5-2: Final focusing lens system which uses a magnetic sector field as its last element is shown in a vertical (upper part) and horizontal (lower part) projection. This sector magnet deflects the ion beam so that all quadrupole lenses upstream are out of sight of the fusion pellet and thus subject to a considerably reduced neutron flux only. The neutron and γ-radiation beam is indicated by dashed lines. The draw-back of this design is that the length of the first 2T sector field is 8.2.m so that the first quadrupole lens is about 17m away from the fusion pellet. Because of the large phase space area of 30.120 mm^2 $mrad^2$ the beam radii of these quadrupole lenses then are almost 2 m with flux densities of about 6 T.

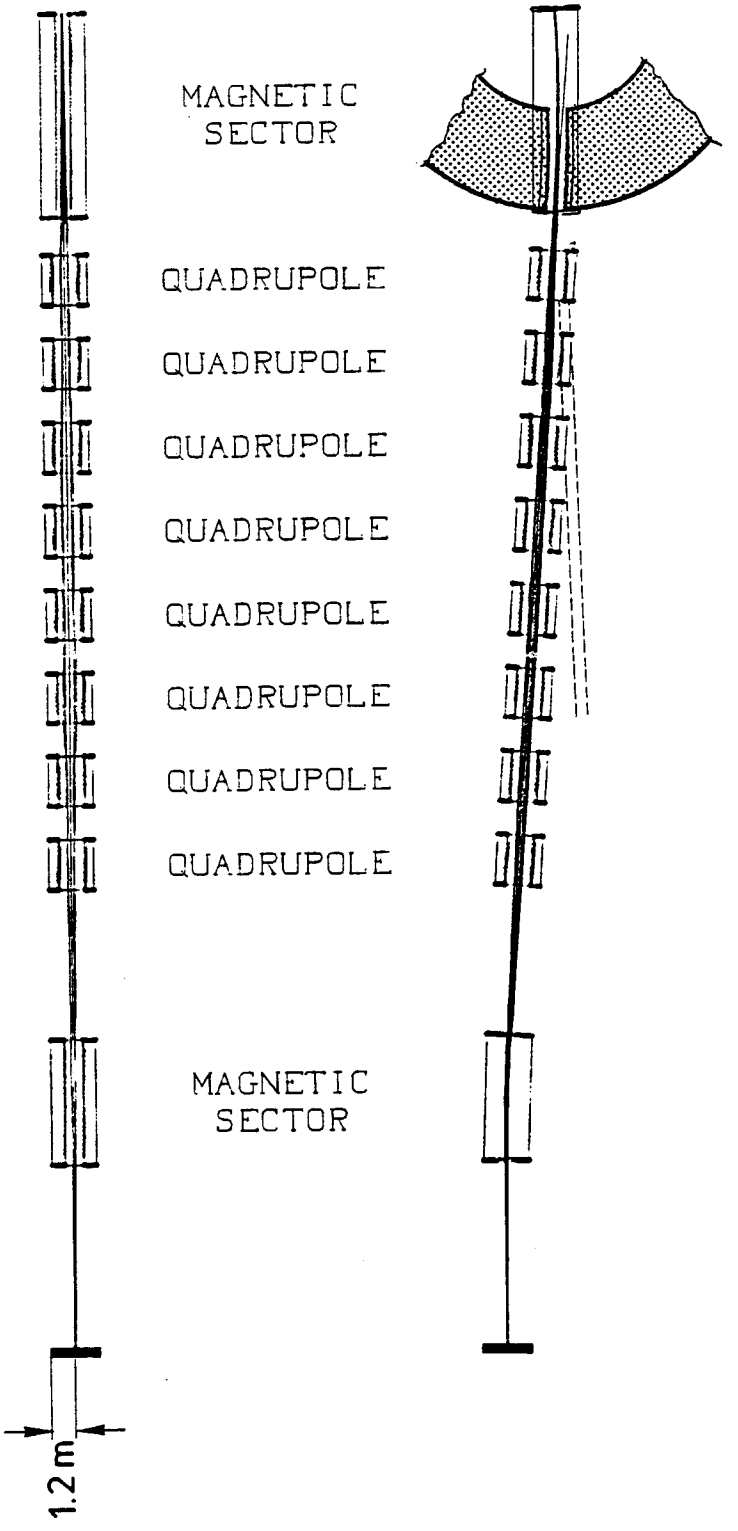

Fig. V. 5-3: A quadrupole lens octett preceded by a sector field and followed by a dipole field of 1T formed by the large coil of fig. V. 5-1b is shown in a vertical (upper part) and horizontal (lower part) projection. Because of the magnetic beam deflection in the reactor vessel the neutron and γ-radiation is already considerably reduced at the reactor wall so that only limited shielding is necessary in the quadrupole lenses and the beam line. Note the neutron and γ radiation indicated by dashed lines.

References for Section V.5

1. G. Krafft, Univ. of California, private communication, October 1980.

2. I. Hofmann, MPP-München, private communication, January 1981.

V.6 Beam Stripping Theory

V.6.1 Stripping Cross Section

The total inelastic scattering cross section for Bi^{+2} on Pb has been calculated in Born approximation by Y. K. Kim.[1] Following the method described in Ref. 2, he has calculated the parameters given in Table V.6-1, which are to be inserted in formulas (1)-(4) of Ref. 2. Table V.6-2 gives the atomic properties needed in the calculation. Kim finds

$$\sigma_{in} = 2.2 \times 10^{-16} \text{ cm}^2/\beta^2 \quad .$$

The first order correction to this formula is estimated to be given by the factor[1]

$$1 - 0.002/\beta^2 \quad ,$$

so that the Born approximation should be very good at $\beta^2 = 0.1$. If we assume that the stripping cross section is 1/3 of this, then

$$\sigma_{st} \doteq 0.7 \times 10^{-16} \text{ cm}^2/\beta^2 \quad .$$

For $\beta^2 = 0.1$, this is

$$\sigma_{st} \doteq 7 \times 10^{-16} \text{ cm}^2 \quad .$$

The best estimate of Pb density in the target cavity when the beam enters is 4×10^{10} atoms/cm^3. This is below the equilibrium density at 470°C which is 8×10^{10} atoms/cm^3. If we take the latter figure as more conservative, we

Table V.6-1 Bethe Cross Sections for the Excitation of Bi^{2+} by Pb (see Ref. 2)

Quantity	Value
$I_{in,el}$	5634.1
$I_{in,in}$	161.83
$\gamma_{in,el}$	-68080.5
$\gamma_{in,in}$	$\sim$ -172150*

*In Eq. (17) of Reference 2, $-2E_{total}$(a.u.) was used instead of S(1). This leads to a value of $|\gamma|$ larger than the correct one.

Table V.6-2 Atomic Properties of Bi^{2+} and Pb

Property*	Bi^{2+}	Pb
Z_N	83	82
Z_e	81	82
$-E_{total}$(a.u.)	21539.4	20889.3
$\langle r^2 \rangle_{6p}(a_0^2)$	6.914	11.423
I.P.$_{6p}$ (eV)	25.08	6.91
S(-1) (Ryd^{-1})	9.433	14.482

*Based on Dirac-Fock wave functions.

get for the mean free path

$$\ell_{st} \sim 150 \text{ m} \quad .$$

The fraction of beam stripped is

$$1 - \exp(-7\text{m}/150\text{m}) \sim 5\% \quad .$$

V.6.2 Beam Loss on Target Due to Stripping

Stripping of a beam ion from q = 2 → 3 results in a larger deflecting force due to the beam space charge. The displacement at target depends on the distance of the projectile from the target as well as from the beam axis at the moment of stripping.

In order to determine what fraction of stripped ions actually miss the target we introduce a loss factor λ in the rate equation

$$dn(s) = -\sigma_{st}\rho n(s)\lambda(s)\, ds \qquad \text{(V.6-1)}$$

with ρ the background gas density, n the beam density (atoms/cm^3) and s the distance from target. We have calculated λ for different values of s by tracing trajectories of a randomly distributed set of 100 ions (initial K-V distribution) stripped at distance s and moving under the influence of the space charge force of the focused beam, which results from the zero order envelope motion (see Fig. V.6-1). This is valid if only a small fraction of the beam is stripped. By integrating $\lambda(s)$ from 7 m up to the target one finds that the actual loss is only 1/2 the fraction of beam stripped.

Fig. V.6-1

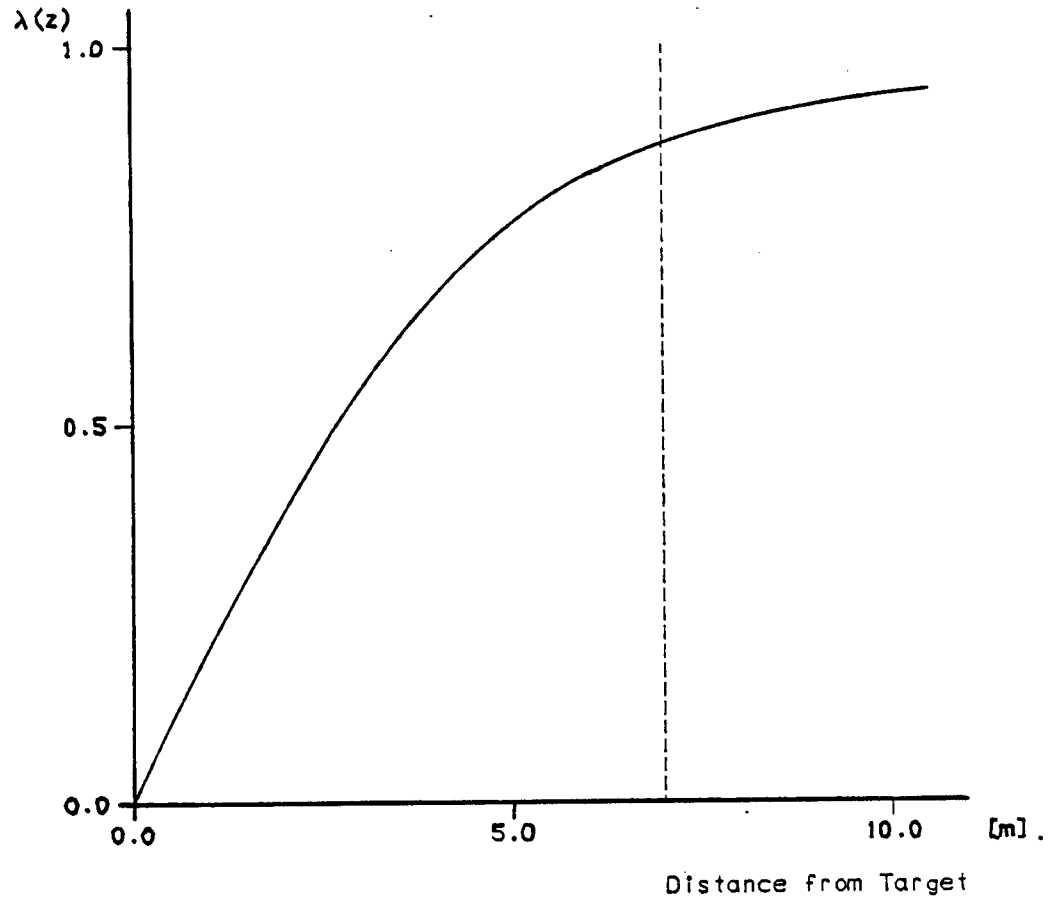

Fig.V.6-1. Loss factor λ(s) (lost ions/stripped ions) as function of distance from target for HIBALL beam and an assumed K-V transverse distribution.

V.6.3 Discussion

For the equilibrium density of Pb at 470°C, i.e. 8×10^{10} atoms/cm^3 the predicted stripping is 5% and the loss on target 2.5%. These rates might be up to a factor of two larger if the ratio $\sigma_{st}/\sigma_{in} = 1/3$ is too optimistic. A more accurate calculation of σ_{st} could be carried out by subtracting from σ_{in} the dominant discrete excitations of Bi^{++} by Pb; this would involve several months of computational effort. On the other hand very crude estimates of non-Born corrections suggest a reduction of the cross sections of 20-30% at the energy considered.(3)

All this amounts to the conclusion that the assumed stripping cross section, 7×10^{-16} cm^2, is probably conservative and leads to less than 5% loss for the assumed background gas density.

We note that beam neutralization due to background gas ionization is negligible here, contrary to a lithium cavity fill gas, where the relevant ionization cross section is an order of magnitude larger than the beam stripping cross section.(4)

References for Section V.6

1. A.K. Kim, Argonne National Laboratory, Argonne, IL, private communication. We are grateful to Dr. Kim for supplying us with the results of these calculations.

2. G.H. Gillespie, Y.K. Kim, and K.T. Cheng, Phys. Rev. A 17, 1284 (April 1978).

3. G.H. Gillespie, private communication (1981).

4. G.H. Gillespie, Heavy Ion Fusion Beam Transport Workshop, LASL, Los Alamos, NM, Aug. 26-27, 1980.

VI Cavity Design

VI.1 General Requirements, Description, and Reference Parameters

VI.1.1 Requirements

The requirements imposed on the design of the cavity for HIBALL are determined by a number of sometimes conflicting considerations. A strict definition of the cavity is that part of the chamber inside the first material wall. For the purposes of this section the definition is expanded to include the entire chamber including reflectors, shields, and the top and bottom portions. The basic requirements are: (1) the cavity be able to dissipate the energy from the target in a coolant operating at temperatures consistent with material requirements and the necessity to produce steam suitable for operation of a steam turbine driven generator, (2) the atmosphere in the cavity be such that the heavy ion beam can be focussed on the target, (3) the system be maintainable in a reasonable fashion, (4) the system be able to breed tritium at a breeding ratio greater than or equal to unity, (5) the tritium be recoverable without undue accumulation of tritium in the breeding material, and (6) the dose rate outside the shielding be at an acceptable level.

The two requirements which have the greatest impact are the need to dissipate the target energy and propagate the beam through the chamber to the target. The fusion yield of the HIBALL target is 400 MJ and the repetition rate is 5 Hz, yielding a fusion power of 2000 MW per chamber. The time dependent neutronics studies reported in section VI.3.4 indicate that because of endothermic reactions in the target the actual energy available is slightly less, i.e. 394 MJ/shot. Of these 396 MJ, 285 MJ is carried by neutrons of average energy of 12 MeV, 88 MJ is contained in X-rays emitted from the target, and 21 MJ by the target debris, i.e. He, unburned D and T, Pb, and Li. A very small amount appears as high energy gamma radiation. This means that al-

though the greatest part of the energy is carried by the neutrons and therefore is volumetrically deposited in the blanket materials, a significant amount, viz. 109 MJ, is in a form that would be deposited on or very near the surface of any material surrounding the target.

VI.1.2 INPORT Concept

A persistant technical problem in the Inertial Confinement Fusion (ICF) field has been the protection of the first load bearing walls from target debris, x-rays, and neutrons. Various schemes have been proposed in the past: swirling liquid metal pools[1], wetted walls[2,3,4,5], magnetic protection[6], gaseous protection[7], dry wall ablative shields[8-11], and free falling sheets of liquid metals[12-15]. None of these schemes have been completely satisfactory, but the liquid metal protection scheme, HYLIFE[15], seems to be the best developed thus far.

One disadvantage with the HYLIFE scheme is the disassembly of the liquid metal columns after each shot and the need to reestablish the stream before the next target can be injected. This results in small ΔT, high recirculation rates, and large pumping powers, especially for the Pb-Li alloys. Ideally, one would like to develop a scheme which would slow down the flow of liquid metal so that it can absorb the energy of several shots before exiting the reactor.

Such a scheme was developed in late 1979 for the HIBALL project. The basis of this new design is the use of woven SiC tubes which are flexible, sufficiently strong, compatible with Pb-Li alloys used in HIBALL, and porous enough to allow liquid to cover the surface while the bulk of the fluid flows down the center of the tube (Fig. VI.1-1). This idea is called the INPORT concept, standing for the Inhibited Flow - Porous Tube Concept. The film thickness of roughly 1 mm is sufficient to absorb the energy from x-rays and

Figure VI.1-1

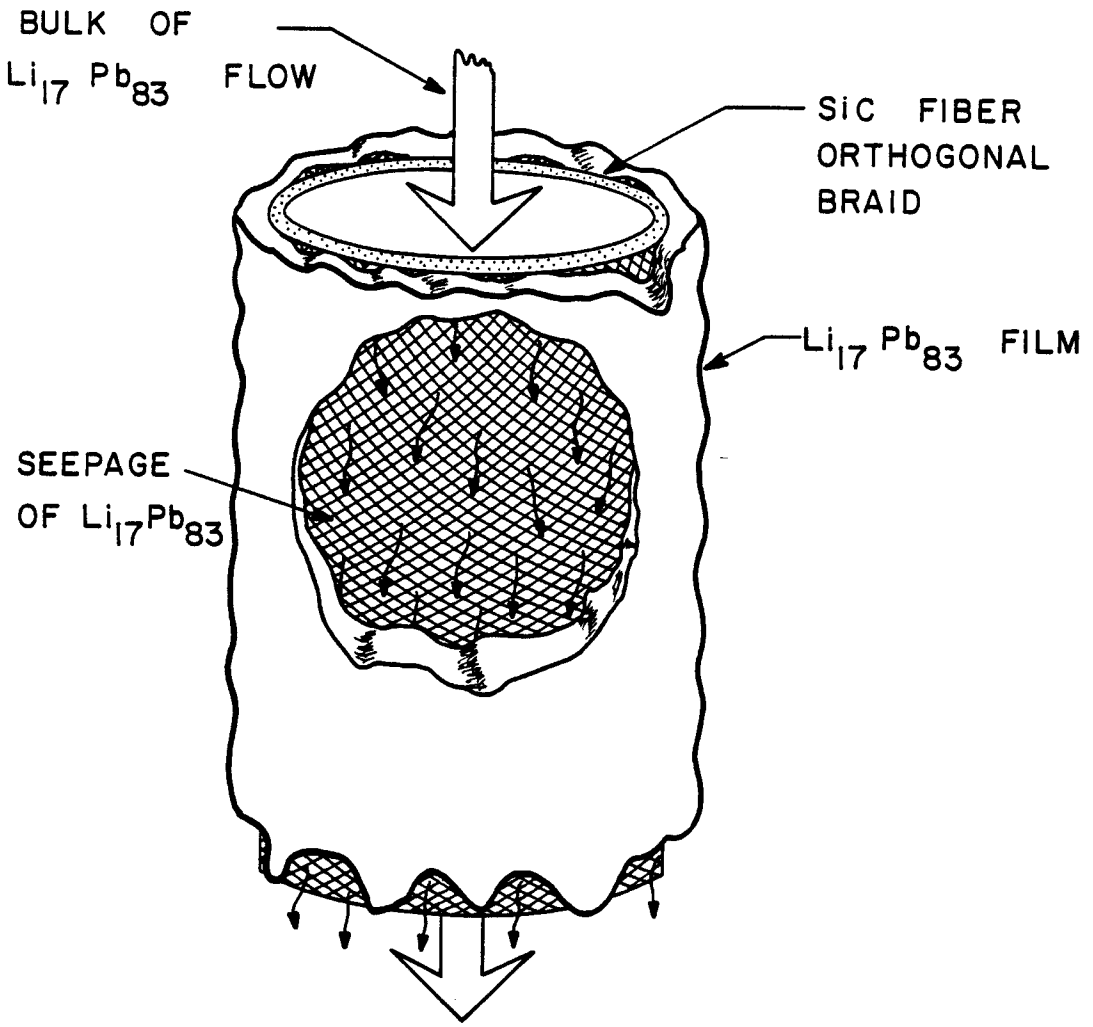
BULK OF
Li_{17} Pb_{83} FLOW
SiC FIBER
ORTHOGONAL
BRAID
Li_{17} Pb_{83} FILM
SEEPAGE
OF $Li_{17}Pb_{83}$

target debris while several banks of tubes provide enough Pb-Li alloy to considerably moderate the neutron flux and reduce the total damage and damage rate in the first wall (Fig. VI.1-2).

A schematic of how the porous tube structure fits into the HIBALL chamber design is given in Fig. VI.1-3 and the overall chamber design is shown in Fig. VI.1-4. A few of the major operating parameters are given below:

Tube radius, cm (Number) - inner rows	1.5/(1230)
- outer rows	5/(3070)
Inlet/outlet temp. of $Pb_{83}Li_{17}$	330/500°C
Max. flow velocity (front tube)	5 m/s
Target yield x frequency of shots	400 MJ x 5 Hz
Energy flux to first Pb-Li surface	35 J/cm^2
Condensation time to 10^{-5} torr (at RT)	0.15 sec
dpa in HT-9 FW per FPY w/o INPORT units	21
dpa in HT-9 FW per FPY with INPORT units	2.7

It is clear that the INPORT concept enhances the promise of ICF reactors and it should remedy one of the more serious drawbacks of the HYLIFE concept, the disassembly after each shot. The rest of this section will discuss, in more detail, how the INPORT concept fits into the HIBALL design.

VI.1.3 Mechanical Description of Cavity

The cavity is an upright cylinder with internal dimensions of 11.5 m height on axis and 10 m in diameter, Fig. VI.1-4. From the center and outward in all directions, the cavity is characterized by three distinct zones, the blanket, reflector and shield. In the vertical sides of the cavity, the blanket consists of a 2 m thick zone of SiC tubes through which $Li_{17}Pb_{83}$ is

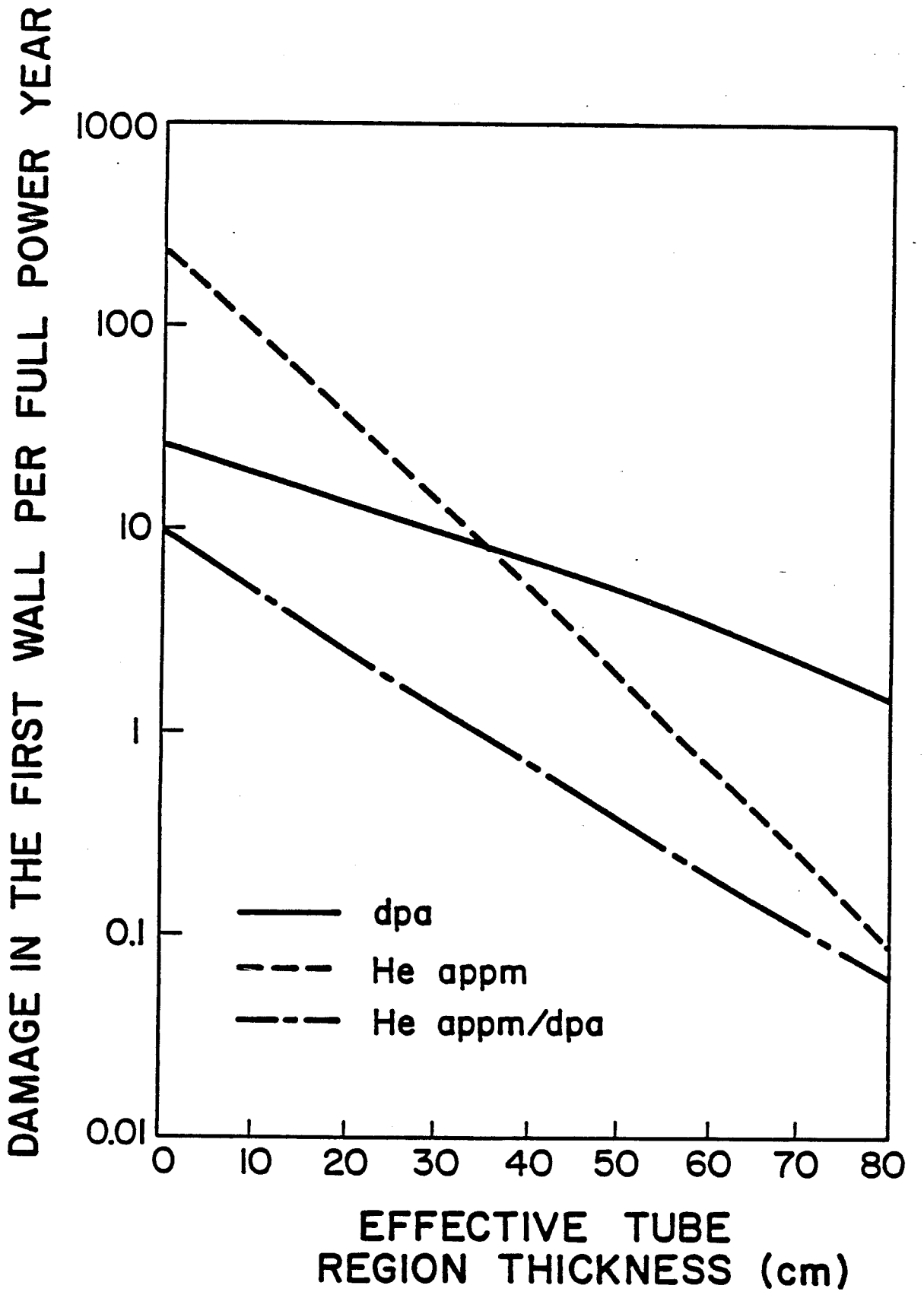

Fig. VI·1-2 Effect of INPORT tubes on Damage in HT-9 first wall.

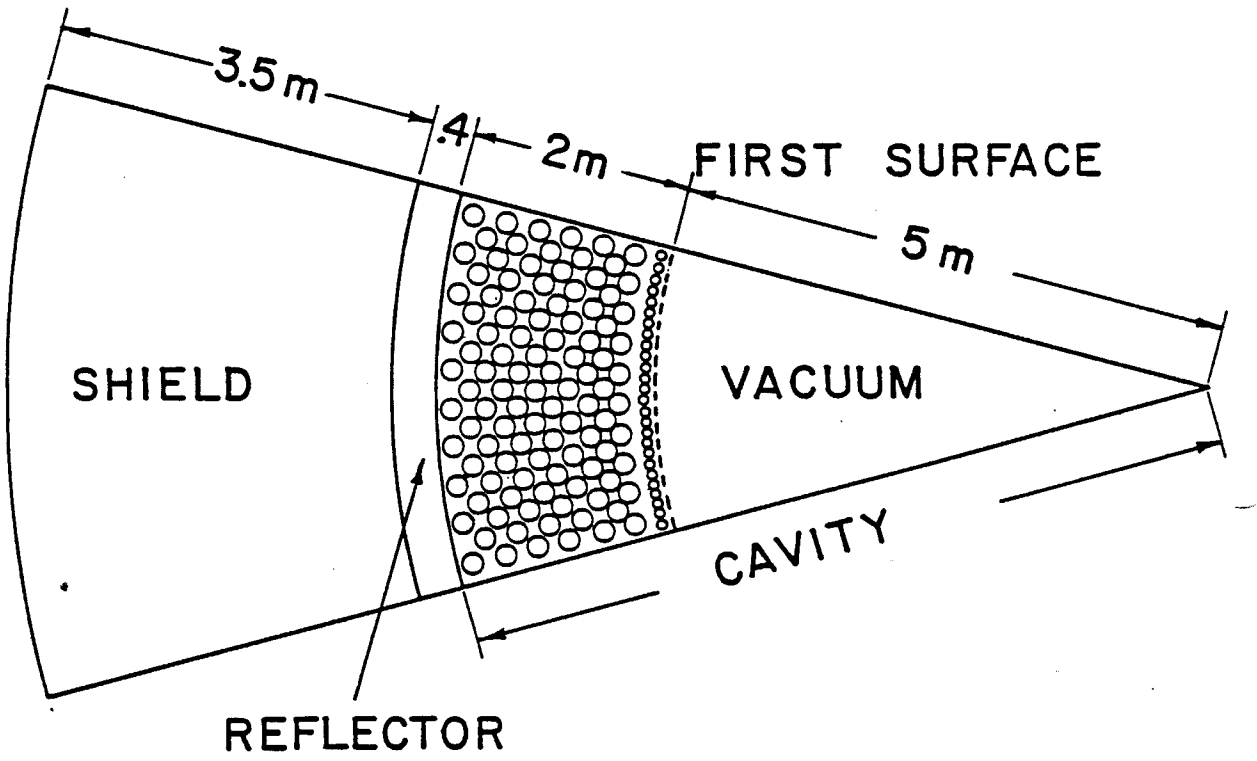

Fig. VI.1-3

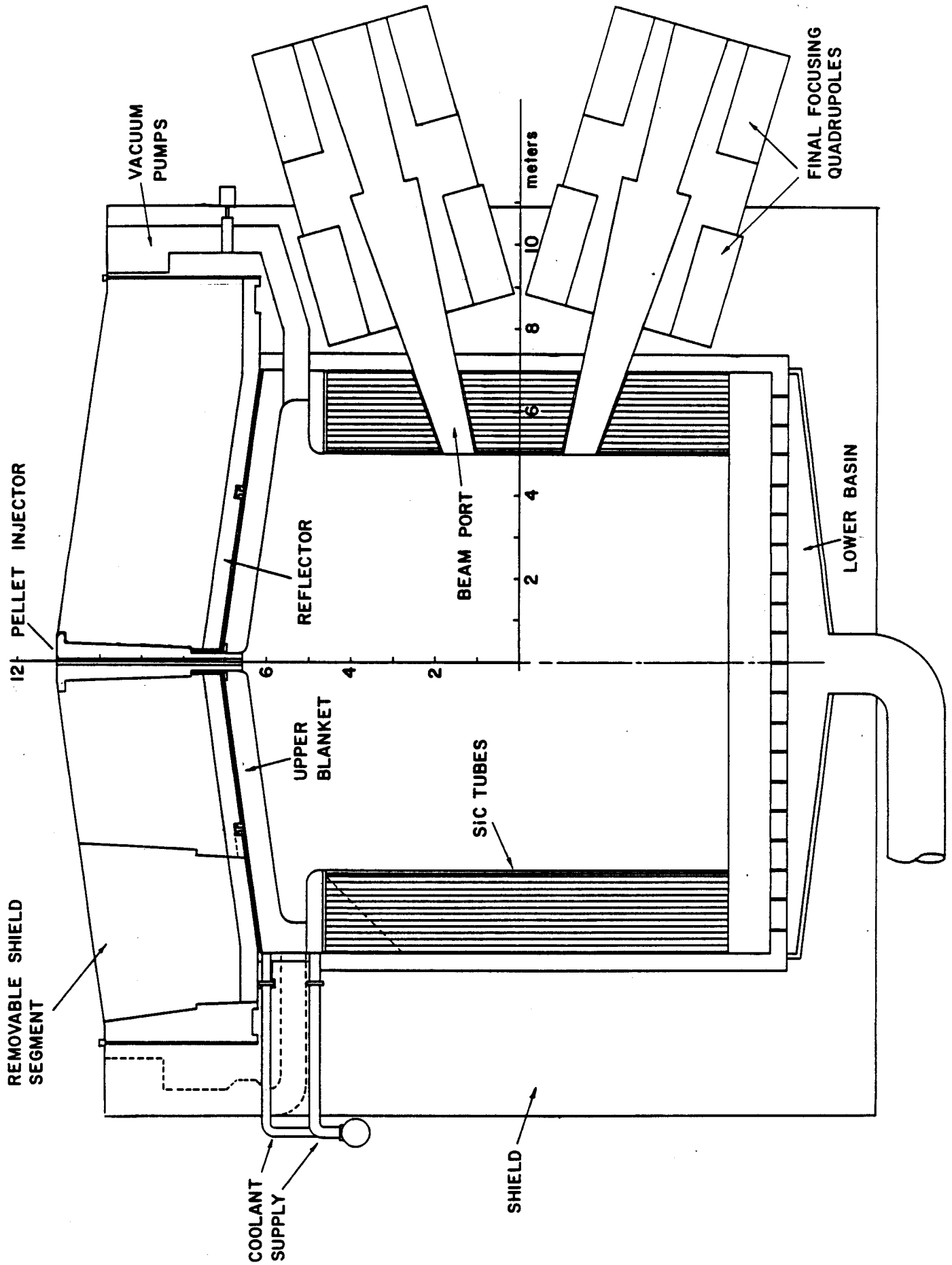
VACUUM PUMPS
FINAL FOCUSING QUADRUPOLES
meters
10
8
6
4
2
PELLET INJECTOR
REFLECTOR
BEAM PORT
LOWER BASIN
12
6
4
2
UPPER BLANKET
SiC TUBES
REMOVABLE SHIELD SEGMENT
COOLANT SUPPLY
SHIELD

Fig. VI.1-4

circulated, Fig. VI.1-3. It is followed by a reflector zone made of HT-9 which is 40 cm thick and finally by the shield, which is primarily concrete and is 3.5 m thick. The top of the cavity has wedge shaped blanket modules, 50 cm thick which are also filled with $Li_{17}Pb_{83}$. They too are followed by 40 cm of HT-9 reflector and a 3.5 m concrete shield. The bottom of the cavity has a pool of $Li_{17}Pb_{83}$ one meter thick, followed by a 40 cm thick reflector which has holes in it to allow the coolant to drain out. A catch basin then directs the flow to an outlet tube through which it is pumped to the steam generator. The rest of the material that follows is a concrete shield.

The top of the cavity has a unique design. Although the blanket modules are designed to stay stationary, the reflector and shield is capable of being rotated about the central axis. This is needed to provide access to the blanket modules for replacement and will be discussed further in Chapter IX. The upper blanket modules are locked to the reflector by means of studs which fit in milled slots. During reactor operation when the modules are filled with $Li_{17}Pb_{83}$, the stud latches are actuated and the modules are locked to the reflector. However, during servicing when the modules are drained of all the breeding material, the stud latches are de-activated. At this time the blanket modules are only supported on the outer periphery and in the center of the cavity, where they are attached to a central hub. This makes it possible to rotate the reflector and shield while the blanket modules remain stationary.

The cavity is sealed to the outside by a liner which is welded to the reflector at the upper end of the cavity. A circumferential weld (or seal) between the liner on the stationary part of the top shield and the rotatable part maintains the cavity atmosphere during operation.

At the junction between the top blanket modules and the SiC tubes, there are 30 apertures, 65 cm high and 1.2 m wide. These are the vacuum system ports. The vacuum ducts which are concealed from direct line of sight of neutrons lead to pumping stations located in the upper corner of the reactor cavity. These pumps are used to evacuate the cavity prior to operation and to pump the non-condensable gases, such as the hydrogen species and the helium. The pumping system is discussed further in section VI.5.

There are 20 beam ports in each cavity. Each two beams come in at ± 16° to the horizontal, spaced at 36° circumferentially. The blanket is divided in such a way that every third module has two beam ports built in. At the first surface (5 m radius) the beam ports are 23 cm wide and 74 cm high. Distribution manifolds surround the beam tubes such that the SiC tubes are attached to them on the top and bottom. Each beam transport line is attached to the cavity at the point of entry and constitutes the vacuum interface between the cavity and the beam handling system.

VI.1.4 Chamber Parameters

Table VI.1-1 presents reference parameters which have been used as a basis for the calculations in the following sections of this chapter. These values were chosen on the basis of: (1) defining the nature and role of the system, (2) consistency with known materials characteristics of various parts of the system, or (3) as a result of previous calculations. A more detailed parameter set is given in Appendix A.

Table VI.1-1

Cavity and INPORT Region	
Neutron energy/shot (MJ)	285
X-ray energy/shot (MJ)	90
Debris energy/shot (MJ)	21
Gamma energy/shot (MJ)	< 1
Cavity shape	cylindrical
Cavity diameter to vacuum wall (m)	14
Cavity height at center (m)	11.5
Coolant and breeding material	$Pb_{83}Li_{17}$ (natural)
INPORT tube structural material	SiC
INPORT region support structure	HT-9
First surface radius (m)	5
INPORT tube region packing fraction	0.33
INPORT tube length (m)	10
INPORT tube diameter (cm)	
First two rows	3
Remainder	10
Number of first row tubes	1230
Number of remaining tubes	3060
Number of Beam penetrations	20
Total area of beam penetrations at the first surface (m^2)	3.6
Pb atom density (x 10^{-10} atom/cm^3) just before shot	4
Noncondensible atom density at 500°C (x 10^{-10} atoms/cm^3)	0.13
Chamber top thickness (m)	0.5
Coolant volume fraction	0.97
Bottom region thickness (m)	1
Coolant volume fraction	1
Vacuum Wall (first material wall)	
Structural material	HT-9
Inside diameter (m)	14
Thickness (m)	0.01

Table VI.1-1 (continued)

Reflector	
Structural material	HT-9
Coolant	$Pb_{83}Li_{17}$
Coolant volume fraction	0.9
Inside diameter (m)	14.02
Thickness (m)	0.4
Shield	
Structural Material	Concrete (unreinforced)
Coolant	H_2O
Coolant volume fraction	0.05
Inside diameter (m)	14.82
Thickness (m)	3.5
$Pb_{83}Li_{17}$ Coolant	
Inlet temperature (°C)	330
Outlet temperature (°C)	500
Pressure (MPa)	0.2

References for Section VI.1

1. A.P. Fraas, "The BLASCON - An Exploding Pellet Fusion Reactor," Oak Ridge National Laboratory, Oak Ridge, TN, TM-3231 (July 1971).

2. L.A. Booth, "Central Station Power Generation by Laser Driven Fusion," Nucl. Eng. and Design 24, 263, North-Holland Publishing Co. (1973).

3. J. Hovingh, J.A. Maniscalco, M. Peterson, R.W. Werner, "The Preliminary Design of a Suppressed Ablation Laser Induced Fusion Reactor," Proc. 1st Top. Mtg. on the Tech. of Controlled Nucl. Fusion, I, 96, San Diego, CA (1974).

4. J.K. Baird and V.E. Anderson, "Combination First Wall and Parabolic Lithium Mirror for a Laser-Driven Pellet Fusion Reactor," Proc. 6th Symp. on Eng. Prob. of Fusion Research, 1015, San Diego, CA (1976).

5. R.R. Holman and W.P. Kovacki, "Conceptual Approach to Laser Fusion Hybrid Reactor," Trans. ANS 1977 Summer Mtg., 56, New York, NY (1977).

6. T. Frank, D. Freiwald, T. Merson, J. Devaney, "A Laser Fusion Reactor Concept Utilizing Magnetic Fields for Cavity Protection," Proc. 1st Top. Mtg. Tech. of Controlled Nucl. Fusion, I, 83, San Diego, CA (1974).

7. B. Badger et al., "SOLASE, A Laser-Fusion Reactor Study," University of Wisconsin Fusion Design Memo UWFDM-220, (Dec. 1977).

8. F.H. Bohn, H. Conrads, J. Darvas, and S. Forster, "Some Design Aspects of Inertially Confined Fusion Reactors," Proc. 5th Symp. of Eng. Prob. of Fusion Research, 107, Princeton, NJ (1973).

9. J.M. Williams, F.T. Finch, T.G. Frank, and J.S. Gilbert, "Engineering Design Considerations for Laser Controlled Thermonuclear Reactors," Proc. 5th Symp. of Eng. Prob. of Fusion Research, 102, Princeton, NJ (1973).

10. S.G. Varnado and G.A. Carlson, "Considerations in the Design of Electron-Beam-Induced Fusion Reactor Systems," Nucl. Tech. 29, 415 (June 1976).

11. J. Hovingh, "First Wall Studies of a Laser Fusion Hybrid Reactor Design," Proc. 2nd Top. Mtg. on the Tech. of Controlled Nucl. Fusion, II, 765, Richland, WA (1976).

12. R.J. Burke, "Outline for a Large-Pulse Electron-Beam-Ignited Fusion Reactor," Argonne National Laboratory, Argonne, IL, CTR/TM-31 (1974).

13. W. Seifritz and H. Naegel, "Uranium and Thorium Shells Serving as Tampers of DT-Fuel Pellets for the Electron-Beam-Induced Fusion Approach," Trans. ANS 21, 18 (1975).

14. J.R. Powell, O. Lazareth and J. Fillo, "A Liquid Wall Boiler and Moderator (BAM) for Heavy Ion-Pellet Fusion Reactors," Brookhaven National Laboratory, Long Island, NY, BNL-50744 (Nov. 1977).

15. W.R. Meier and J.A. Maniscalco, "Reactor Concepts for Laser Fusion," Lawrence Livermore National Laboratory, Livermore, CA, UCRL-79694 (1977).

VI.2 Impulse Response of INPORT Tubes

VI.2.1 Impulse Characterization

When the PbLi is vaporized by the target generated X-rays, a reactive impulse imparts radial acceleration to the first two rows of the tube bank. One can conservatively estimate the bulk kinetic energy of the vaporized fluid to be equal to the thermal energy of the gas.

$$(3/2)\ (M_{gas}/m_{ion})\ k_B T_{gas} \doteq (1/2)\ M_{gas}\ V^2 \qquad \text{(VI.2-1)}$$

Here the left-hand-side represents the thermal energy of the gas which is equal to the deposited X-ray energy less the energies of ionization and vaporization. The bulk velocity of the gas is denoted by V while m_{ion} represents the average mass of ions in the gas. For the case of 87.6 MJ of X-ray energy and 13.3 kg of vaporized PbLi, T_{gas} = 1.26 eV. The reactive impulse equals $M_{gas}V$.

$$\Delta I = M_{gas}\ (3k_B T_{gas}/m_{ion})^{1/2} \qquad \text{(VI.2-2)}$$

$$= 1.89 \times 10^9 \text{ dyne-sec.}$$

This can also be expressed as an impulsive pressure per unit surface area.

$$\Delta P = 600 \text{ dyne-sec/cm}^2 \qquad \text{(VI.2-3)}$$

The preceding estimate is conservative since it is assumed that all vaporized atoms are initially moving towards the center of the cavity with their thermal velocity. This will clearly overestimate the reactive impulse.

VI.2.2 Stiffened INPORT Tubes

VI.2.2.1 General Characterization

Both stiffened and unstiffened silicon carbide tubes were considered for the INPORT units. In the former case the woven tubes are rigidized with a SiC binder or matrix but with a porous wall. Such members resist transverse loading by flexural action, not unlike structural beams. A general formulation is developed for stresses, deflections and frequencies. For uniform impulsive pressure, design data is presented which identifies the basic mechanical characteristics of these elements.

VI.2.2.2 Dynamic Analysis

The principle equation of motion governing the transverse vibration of the tube is given by

$$EI\ \partial^4 y(x,t)/\partial x^4 + \bar{m}\ \partial^2 y(x,t)/\partial t^2 = p(x,t) \qquad \text{(VI.2-4)}$$

where E = elastic modulus

I = cross section moment of inertia

$\bar{m}$ = mass per unit length

$p(x,t)$ = dynamic pressure (force per unit length)

t = time

$y(x,t)$ = transverse displacement.

The coordinate system and loading are shown on a typical span of tubing in Fig. VI.2-1.

To determine the natural frequencies of the tube, the external load is set equal to zero, resulting in the differential equation for free vibration. A solution of the form

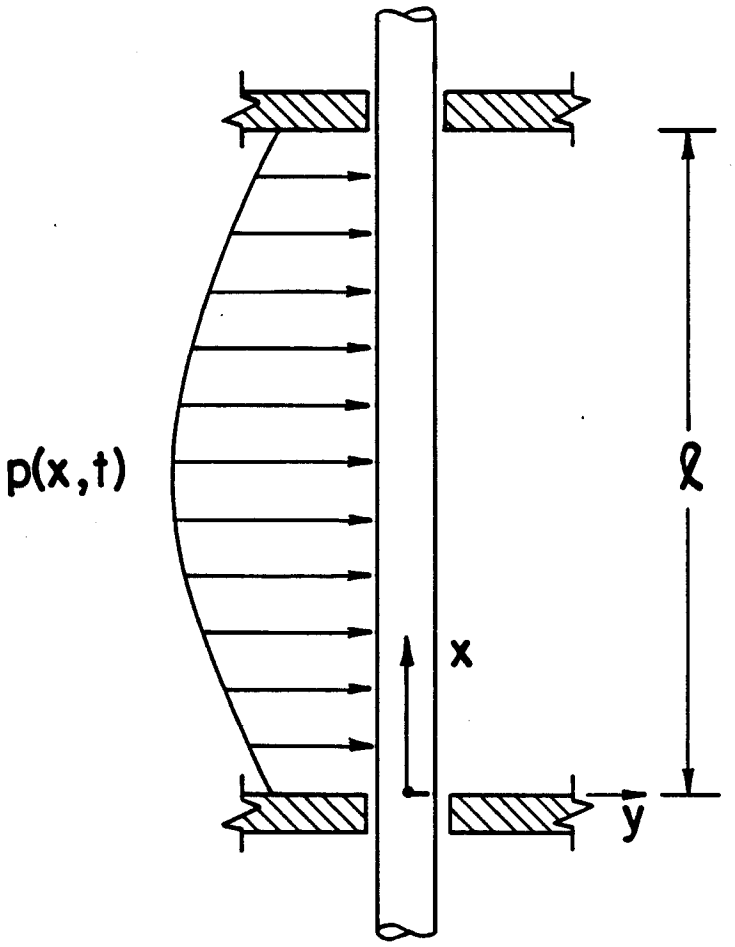

Fig. VI.2-1

$$y(x,t) = \Phi(x)\ Y(t) \qquad \text{(VI.2-5)}$$

is substituted into Eq. VI.2-4, leading to

$$\frac{EI}{\bar{m}\ \Phi(x)} \frac{d^4\Phi(x)}{dx^4} = \frac{1}{Y(t)} \frac{d^2Y(t)}{dt^2} \ . \qquad \text{(VI.2-6)}$$

With x and t being independent variables, the preceding equation can be satisfied only if both sides are set equal to a constant, producing two ordinary differential equations. Choosing ω^2 for this constant, these equations will have solutions of the form

$$Y(t) = C_1 \sin \omega t + C_2 \cos \omega t \qquad \text{(VI.2-7)}$$

$$\Phi(x) = A \sin ax + B \cos ax + C \sinh ax + D \cosh ax \qquad \text{(VI.2-8)}$$

where

$$a^4 = \bar{m}\ \omega^2/EI \ .$$

The tubes would be continuous through any intermediate support, if provided, with the deformed shape for any span characterized by zero slope change and zero deflection at each end. Thus, the boundary conditions are

$$y(o,t) = y\ (\ell,t) = 0$$

$$\partial y(o,t)/\partial x = \partial y(\ell,t)/\partial x = 0 \ . \qquad \text{(VI.2-9)}$$

With these and Eq. VI.2-8 the following transcendental equation is obtained.

$$\cos a\ell \cosh a\ell = 1 \qquad \text{(VI.2-10)}$$

This equation generates an infinite number of discrete eigenvalues, $a_n(n=1,2,3,\ldots)$, which are obtained numerically and are related to the natural frequencies ω_n by

$$\omega_n = a_n^2(EI/\bar{m})^{1/2} \qquad n = 1,2,3, \ldots \qquad \text{(VI.2-11)}$$

Corresponding to each natural frequency is a characteristic shape or eigenfunction

$$\Phi_n(x) = C_n[(A_n/B_n)(\sinh a_n x - \sin a_n x) + \cosh a_n x - \cos a_n x] \qquad \text{(VI.2-12)}$$

where

$$A_n/B_n = (\cos a_n\ell - \cosh a_n\ell)/(\sinh a_n\ell - \sin a_n\ell)$$

and C_n is an arbitrary constant.

After the mode shapes and frequencies have been determined, a modal-superposition method of analysis can be used to solve for the dynamic response of the forced vibration. Thus, any displacement can be expressed by superimposing appropriate amplitudes of the vibration mode shapes for the structure. This can be written as

$$y(x,t) = \sum_n \Phi_n(x)\, Y_n(t) \qquad \text{(VI.2-13)}$$

Using an energy solution, Lagrange's equation is applied to the system

$$d[\partial K/\partial \dot{Y}_n(t)]/dt + \partial U/\partial Y_n(t) = \partial \Omega_e/\partial Y_n(t) \qquad \text{(VI.2-14)}$$

where K = total kinetic energy

U = total flexural strain energy

Ω_e = external work

and $(\cdot)$ denotes differentiation with respect to time, t. The kinetic energy for the entire system is given by

$$\begin{aligned} K &= (1/2)\ \bar{m} \int_0^{\ell} \dot{y}(x,y)^2\ dx \\ &= (1/2)\ \bar{m} \int_0^{\ell} [\sum_n \Phi_n(x)\ \dot{Y}_n(t)]^2\ dx \\ &= (1/2)\ \bar{m} \sum_n \dot{Y}_n^2(t) \int_0^{\ell} \Phi_n^2(x)\ dx \end{aligned} \qquad \text{(VI.2-15)}$$

where $\bar{m}$ is considered to be constant over the span and orthogonality of the mode shapes has been utilized.

The work done by external forces is

$$\begin{aligned} \Omega_e &= \int_0^{\ell} p(x,t)\ y(x,t)\ dx \\ &= \int_0^{\ell} p(x,t)\ [\sum_n \Phi_n(x)\ Y(t)]\ dx\ . \end{aligned} \qquad \text{(VI.2-16)}$$

Considering $p(x,t) = P(x)\ f(t)$, where $P(x)$ is the spatial load distribution and $f(t)$ is the time function, the external work becomes

$$\Omega_e = f(t) \sum_n Y_n(t) \int_0^{\ell} P(x)\ \Phi_n(x)\ dx\ .$$

Substituting into Eq. VI.2-14 yields

$$\bar{m}\,\ddot{Y}_n(t)\int_0^{\ell}\Phi_n^2(x)\,dx = \partial U/\partial Y_n(t) = f(t)\int_0^{\ell}P(x)\,\Phi_n(x)\,dx$$

or (VI.2-17)

$$\ddot{Y}_n(t) = \omega_n^2\,Y_n(t) = f(t)\int_0^{\ell}P(x)\,\Phi_n(x)\,dx/\bar{m}\int_0^{\ell}\Phi_n^2(x)\,dx\ .$$

Eliminating the time dependency, the modal static deflection can be defined as follows.

$$Y_{n\ st} = \int_0^{\ell}P(x)\,\Phi_n(x)\,dx/\bar{m}\,\omega_n^2\int_0^{\ell}\Phi_n^2(x)\,dx\ . \qquad \text{(VI.2-18)}$$

To determine the dynamic response, the static response is multiplied by the dynamic load factor (DLF). More descriptively this could be identified as a dynamic load function, representing the time function of the loading for an equivalent single degree of freedom system. Additional details on this can be found in Reference (1). The total deflection at any point is given by

$$y(x,t) = \sum_n \Phi_n(x)\,Y_{n\ st}\,(DLF)_n\ . \qquad \text{(VI.2-19)}$$

The dynamic bending moment can be determined from

$$M(x,t) = EI\,\partial^2 y(x,t)/\partial x^2 = EI\sum_n Y_{n\ st}\,d^2\Phi_n(x)/dx^2\ DLF_n\ . \qquad \text{(VI.2-20)}$$

The flexural stess in the tube is

$$\sigma(x,t) = M(x,t)\,R_o/I = ER_o\sum_n Y_{n\ st}\,d^2\,\Phi_n(x)/dx^2\,(DLF)_n\ . \qquad \text{(VI.2-21)}$$

Here R_o represents the outer radius and the stress is associated with points at the outer surface.

VI.2.2.3 Quantitative Results

The preceding work identifies principle equations for stiffened tube response. Complete details were incorporated into a computer program for the determination of numerical values.

The fundamental frequency curves are shown as functions of tube length for various radii and thicknesses in Figs. VI.2-2, 2-3 and 2-4. These include the mass of the PbLi. It can be seen that for lengths greater than 800 cm, frequencies are very low and relatively constant. For lengths less than 200 cm, the fundamental frequencies rise very quickly. To avoid resonance, these results indicate that the effective length (between supports) should be considerably less than the full length of 10 m. Figure VI.2-5 shows deflection results based upon a dynamic load factor of unity for a single impulse, i.e., resonance is not considered. As the tube thickness and inner radius decrease, e.g., 1 mm x 1.5 cm, the transverse displacements rise very rapidly. Similar effects can be expected for flexural stresses. In Fig. VI.2-6, the value predicted for an INPORT unit with a radius, thickness and length of 1.5 cm, 1 mm, and 10 m is unacceptably high.

Natural frequencies can be raised substantially above the repetition rate while deflections and stresses are reduced if an intermediate support mechanism is employed. Figure VI.2-7 is a conceptual representation for a ring support which sustains the radial impulsive forces by self-equilibrated circumferential tensile stresses. Such a design precludes the necessity to transmit thrust to the outer wall. Small radial dimensions, as implied by the sketch, would generally be important to reduce thermal stresses caused by

Fig. VI.2-2

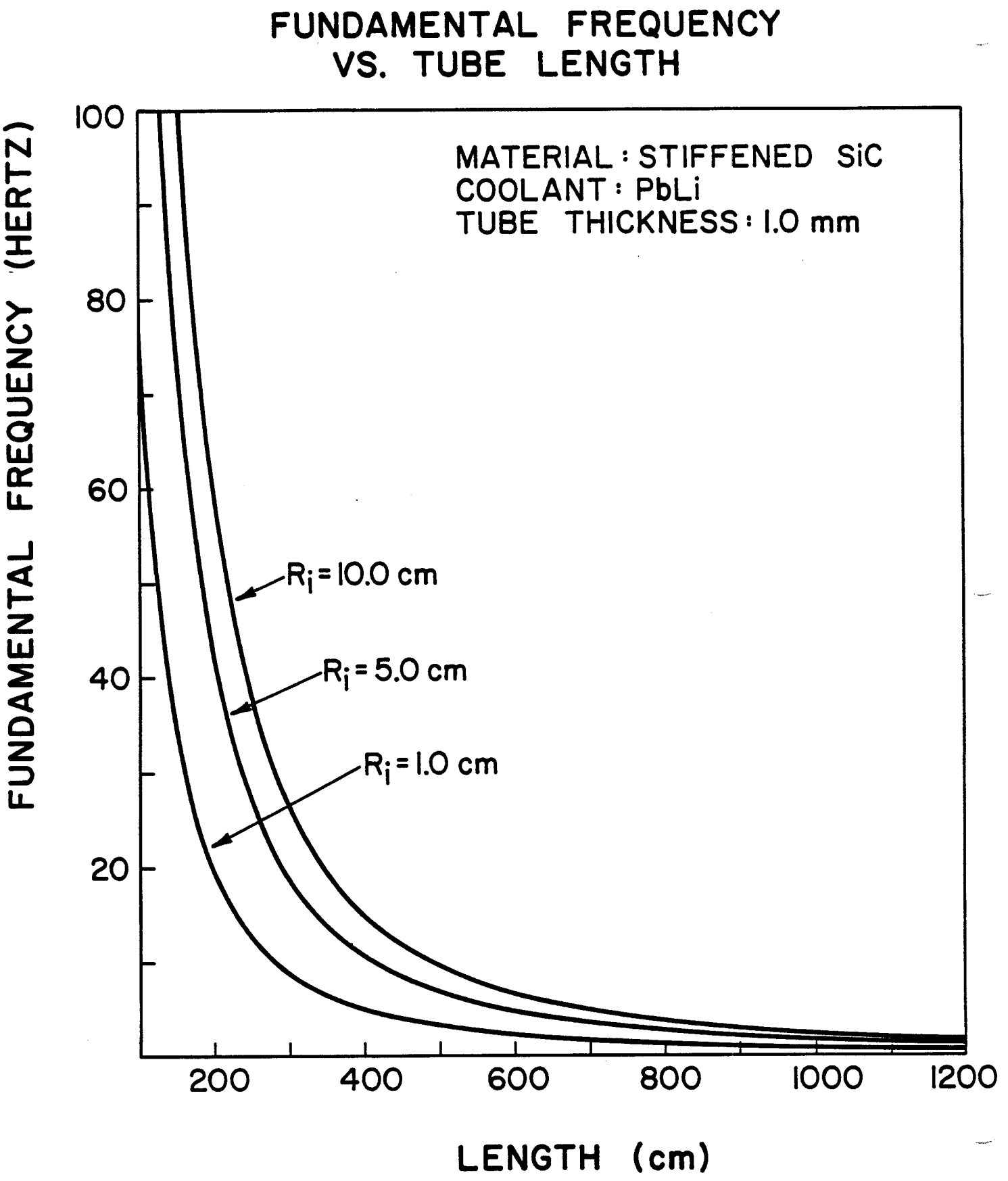
FUNDAMENTAL FREQUENCY
VS. TUBE LENGTH
MATERIAL : STIFFENED SiC
COOLANT : PbLi
TUBE THICKNESS : 1.0 mm
R_i = 10.0 cm
R_i = 5.0 cm
R_i = 1.0 cm
FUNDAMENTAL FREQUENCY (HERTZ)
100
80
60
40
20
200
400
600
800
1000
1200
LENGTH (cm)

Fig. VI.2-3

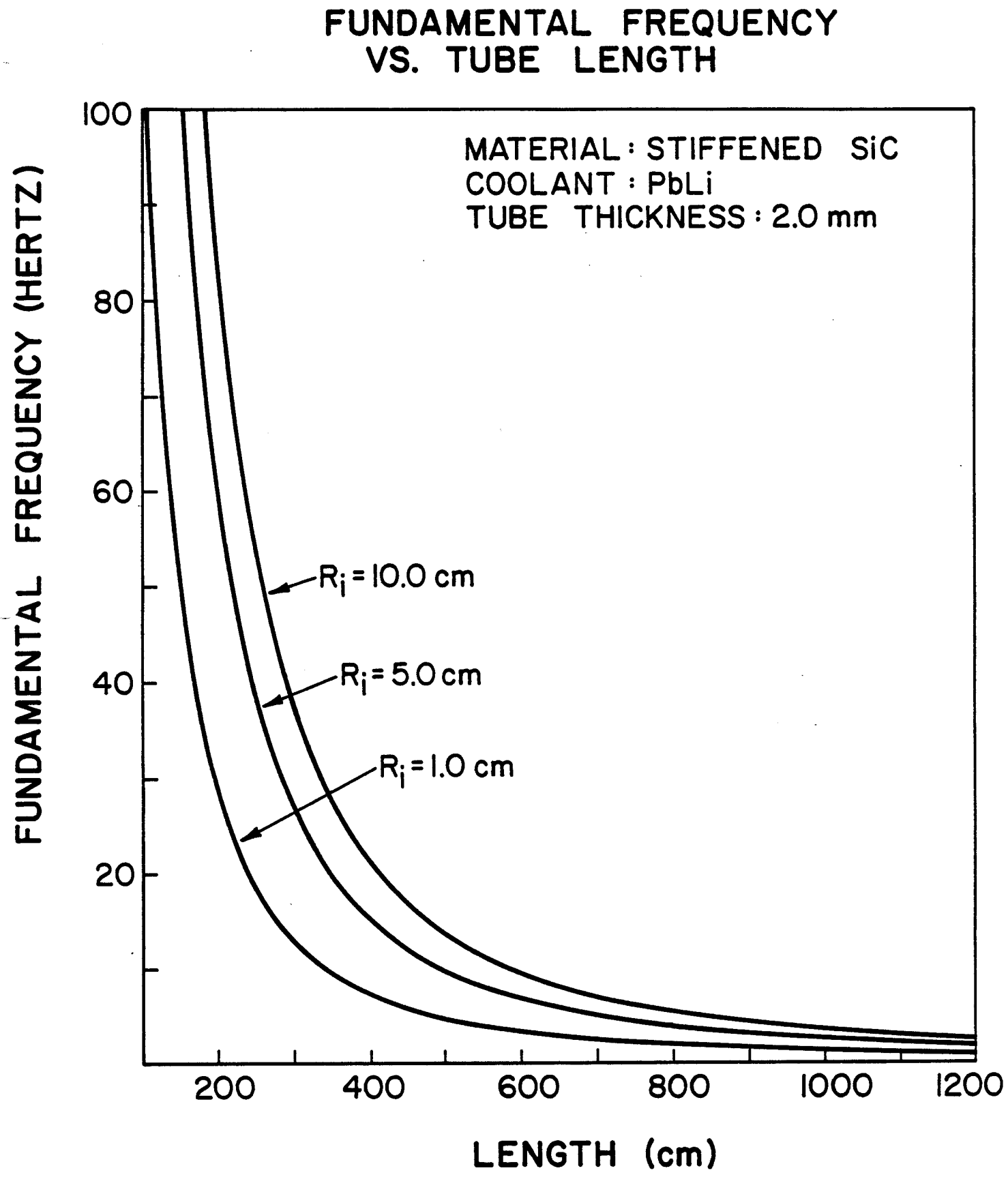
FUNDAMENTAL FREQUENCY
VS. TUBE LENGTH
MATERIAL : STIFFENED SiC
COOLANT : PbLi
TUBE THICKNESS : 2.0 mm
R_i = 10.0 cm
R_i = 5.0 cm
R_i = 1.0 cm
FUNDAMENTAL FREQUENCY (HERTZ)
100
80
60
40
20
200
400
600
800
1000
1200
LENGTH (cm)

Fig. VI.2-4

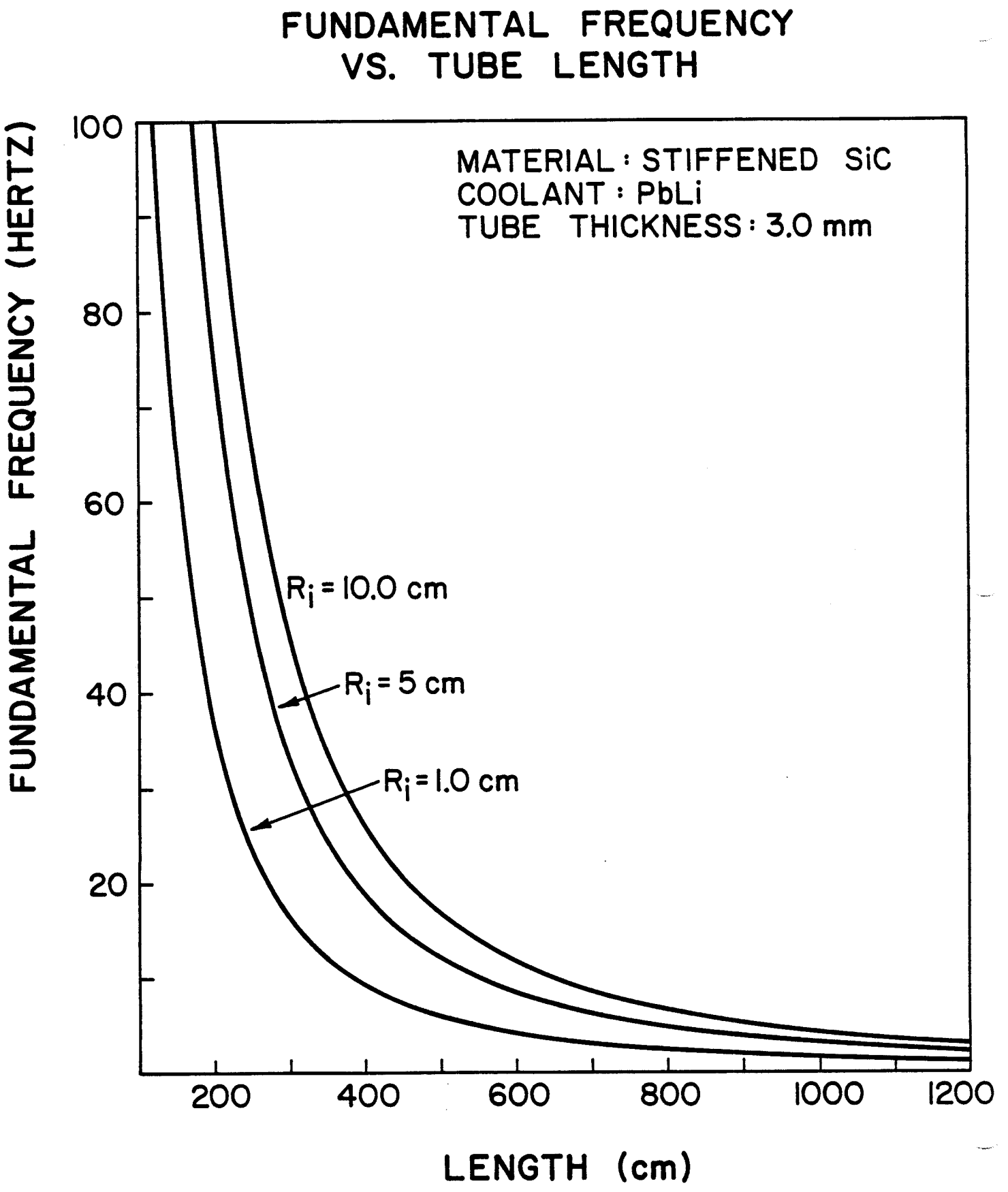
FUNDAMENTAL FREQUENCY
VS. TUBE LENGTH
MATERIAL : STIFFENED SiC
COOLANT : PbLi
TUBE THICKNESS : 3.0 mm
R_i = 10.0 cm
R_i = 5 cm
R_i = 1.0 cm
FUNDAMENTAL FREQUENCY (HERTZ)
100
80
60
40
20
200
400
600
800
1000
1200
LENGTH (cm)

Fig. VI.2-5

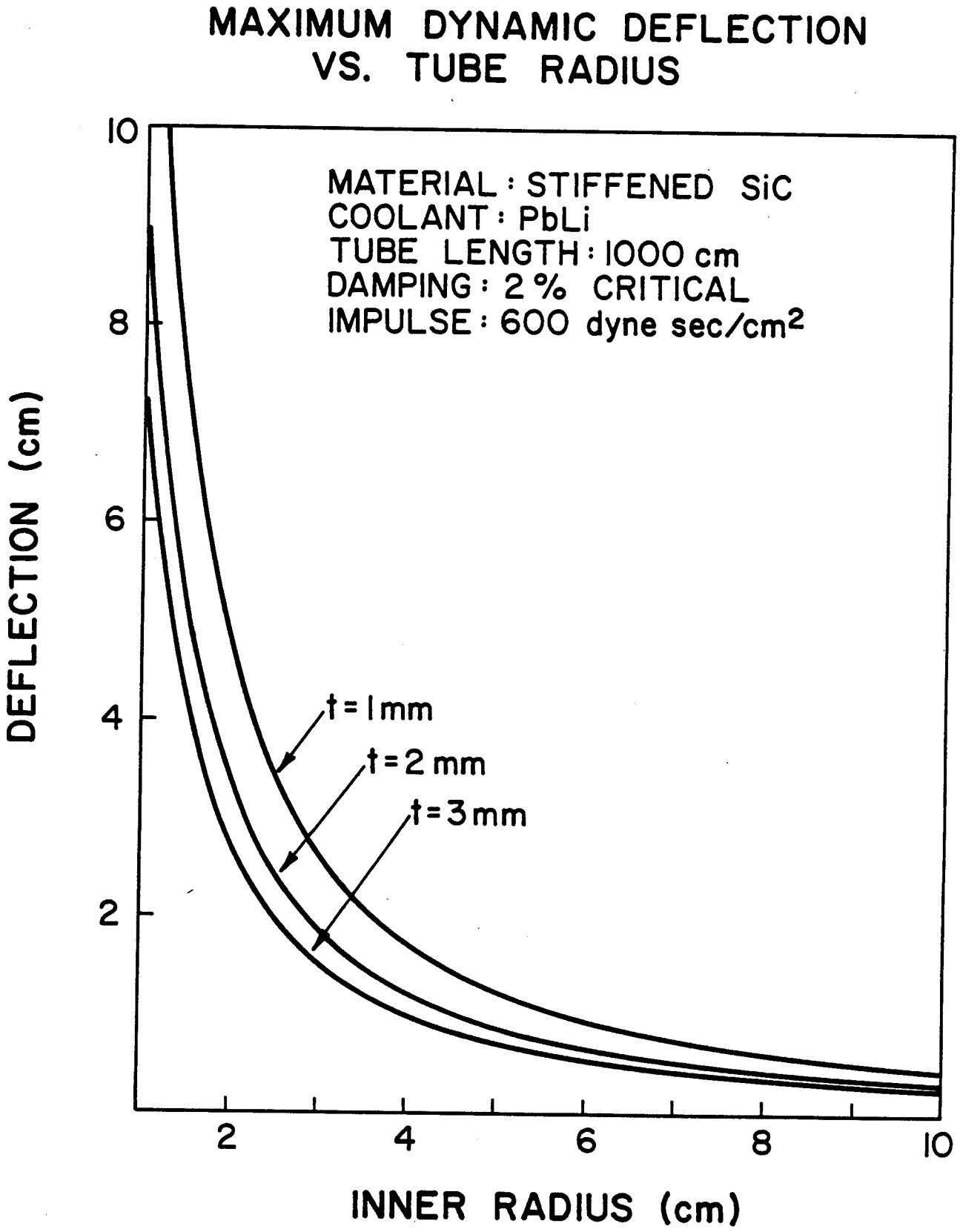
MAXIMUM DYNAMIC DEFLECTION
VS. TUBE RADIUS
MATERIAL : STIFFENED SiC
COOLANT : PbLi
TUBE LENGTH : 1000 cm
DAMPING : 2 % CRITICAL
IMPULSE : 600 dyne sec/cm2
t = 1 mm
t = 2 mm
t = 3 mm
DEFLECTION (cm)
INNER RADIUS (cm)
2
4
6
8
10

Fig. VI.2-6

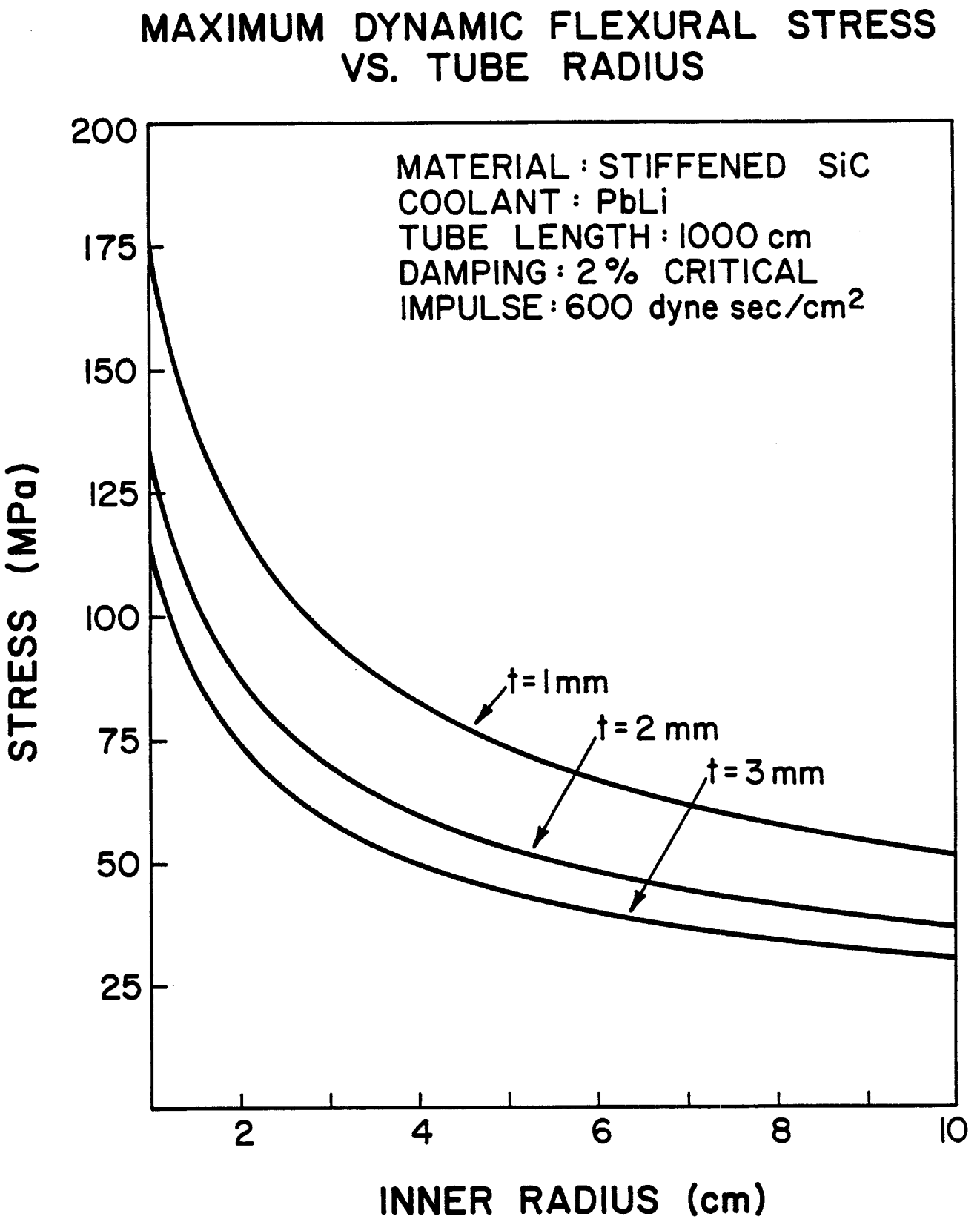
MAXIMUM DYNAMIC FLEXURAL STRESS VS. TUBE RADIUS
MATERIAL : STIFFENED SiC
COOLANT : PbLi
TUBE LENGTH : 1000 cm
DAMPING : 2 % CRITICAL
IMPULSE : 600 dyne sec/cm²
t = 1 mm
t = 2 mm
t = 3 mm
STRESS (MPa)
200
175
150
125
100
75
50
25
2
4
6
8
10
INNER RADIUS (cm)

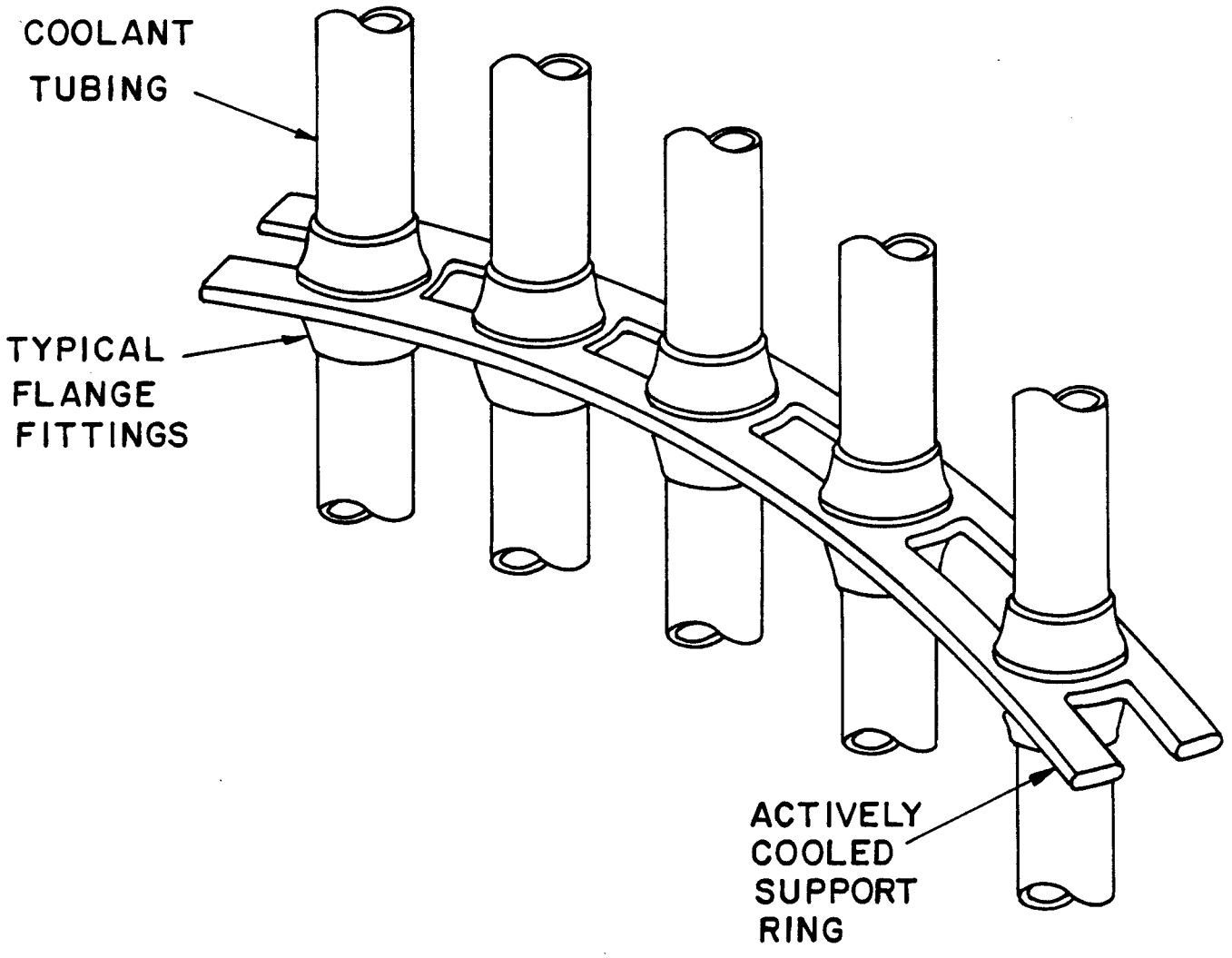
COOLANT
TUBING
TYPICAL
FLANGE
FITTINGS
ACTIVELY
COOLED
SUPPORT
RING

Fig. VI.2-7

radial temperature gradients. Active protective cooling would still be essential.

A combination of reasons led the decision to use unstiffened rather than stiffened SiC tubes for the INPORT units. In the latter case, the geometry is that of a somewhat delicate structure requiring extra care in fabrication and handling. The analysis has shown that resonance, large deflections and stresses are potential problems without supplementary structural support which of course is another addition to complexity. The stiffened tubes also involve untested manufacturing techniques and unknown additional expenses as well. By comparison, unstiffened tubes do not appear to have such disadvantages while possessing inherent desirable features. Their mechanical response characteristics are discussed in the work which follows.

VI.2.3 Mechanical Response of Unstiffened INPORT Tubes

VI.2.3.1 General Characteristics

The term "unstiffened" used here denotes a tube woven from silicon carbide fibers alone. The wall is pliable and porous, essentially cloth-like. A small percentage of fibers will run axially in the wall to enhance the tensile load carrying capacity.

As structural members, such units resist lateral loading by tensile force action alone, i.e., having negligible shear and bending resistance. For the dynamic response, dissipation is accounted for by including viscous damping in the system. In the work which follows, two support modes are considered separately. The first involves suspension from the upper end with the lower free to move while the second has the bottom end constrained in addition.

VI.2.3.2 Equilibrium Equations and Vibration Modes-One Point Suspension

The notation and coordinate system for the equilibrium equations is shown in Fig. VI.2-8. On the element, T represents the tension while ρ and g denote

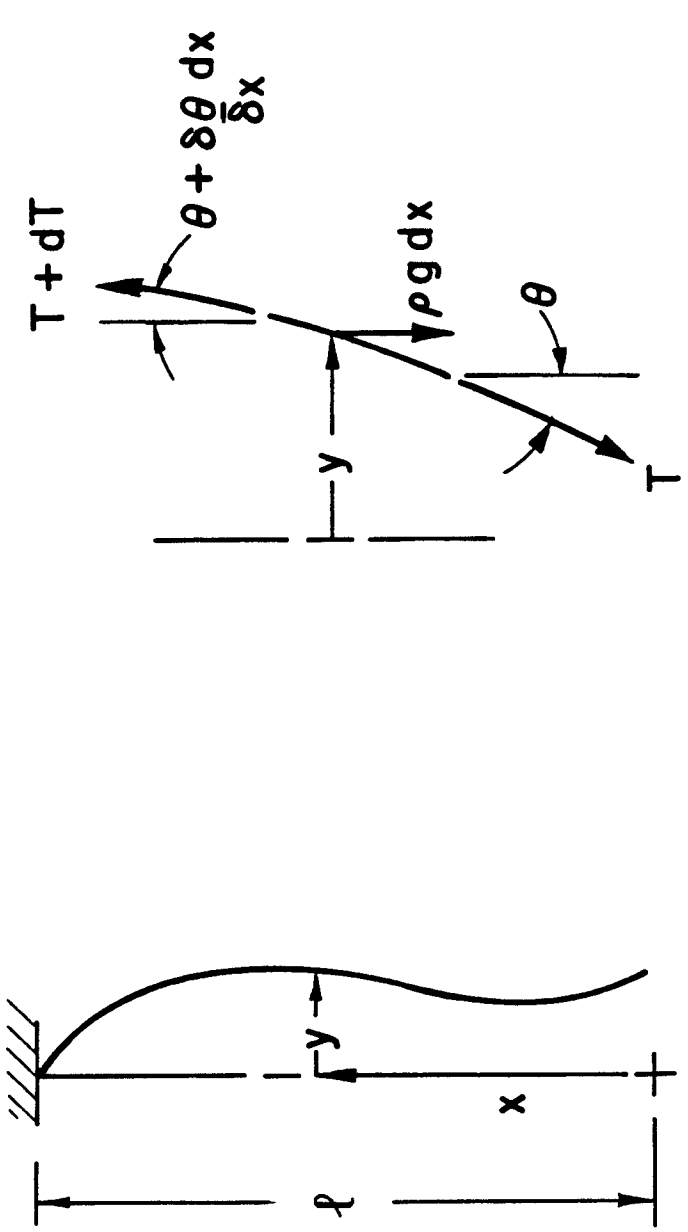

Fig. VI.2-8

the mass density per unit length and the gravitational constant, respectively. At a generic location x, the lateral displacement component is taken to be y. For response characterized by small slope changes, equilibrium in the axial direction requires the tension gradient to be equal to the weight per unit length,

$$dT/dx = \rho g$$

or

$$T = \rho g x \qquad \text{(VI.2-22)}$$

from the condition that the tension is zero at the lower end. In the transverse direction, the equilibrium statement can be reduced to

$$T\ \partial\theta/\partial x + \rho g \theta = \rho\ \partial^2 y/\partial t^2 \qquad \text{(VI.2-23)}$$

in which t denotes time. The two preceding equations can be combined into

$$x\ \partial^2 y/\partial x^2 + \partial y/\partial x = \partial^2 y/g\partial t^2\ . \qquad \text{(VI.2-24)}$$

Characteristic solutions may be developed by taking the displacement as a product of functions in the variables: X(x) T(t). Thus

$$\ddot{T}/gT = xX''/X + X'/X = -\lambda^2\ . \qquad \text{(VI.2-25)}$$

It follows that the solution for the time-dependent component is

$$T = A \cos \lambda\sqrt{g}t + B \sin \lambda\sqrt{g}t \qquad \text{(VI.2-26)}$$

where λ, A and B are constants. The equation for the spatial component is of the form

$$(x^r y')' + (ax^s + bx^{r-2})\, y = 0$$

the solution of which can be expressed in terms of Bessel Functions of the first and second kind, J_ν and Y_ν. In general the parameters and solution are

$$\alpha = (1-r)/2 \qquad \gamma = (2-r+s)/2$$

$$k = 2|a|^{1/2}/(2-r+s)$$

$$\nu = [(1-r)^2 - 4b]^{1/2}/(2-r+s)$$

$$y = x^\alpha [CJ_\nu(kx^\gamma) + DY_\nu(kx^\gamma)]$$

where C and D are arbitrary constants. For this specific case

$r = 1$	$b = 0$	$a = \lambda^2$	$s = 0$
$\alpha = 0$	$\gamma = 1/2$	$k = 2\lambda$	$\nu = 0$.

Thus

$$X = CJ_0(2\lambda x^{1/2}) + DY_0(2\lambda x^{1/2}) \qquad \text{(VI.2-27)}$$

Since Y_0 becomes arbitrarily large as x tends to zero, it is necessary to delete this component, or simply set D equal to zero. Satisfaction of the

boundary condition at the upper support is also necessary.

$$y(\ell,t) = 0 \qquad \therefore J_o\,(2\lambda\ell^{1/2}) = 0\ .$$

The roots are

$$2\lambda\ell^{1/2} = 2.4048,\ 5.5201,\ 8.6537,\ \text{etc.}$$

However, the natural frequencies can be defined as

$$\omega_n = \lambda g^{1/2}$$

and thus, for example, the fundamental is

$$\omega_1 = 1.2024\ (g/\ell)^{1/2}\ \text{(rad/sec)}$$

From this it can be seen that system frequencies are determined essentially by the unsupported length. For a length of 10m, the fundamental frequency is

$$\omega_1 = 0.1877\ \text{Hz}$$

The first ten natural frequencies are listed with Fig. VI.2-9. The mode shapes corresponding to the first three natural frequencies are also shown.

VI.2.3.3 Forced Response - One Point Suspension

The general form for the transverse displacement can be obtained using superposition of characteristic solutions.

Fig. VI.2-9

NATURAL VIBRATION MODES OF 3 cm × 10 m INPORT TUBES

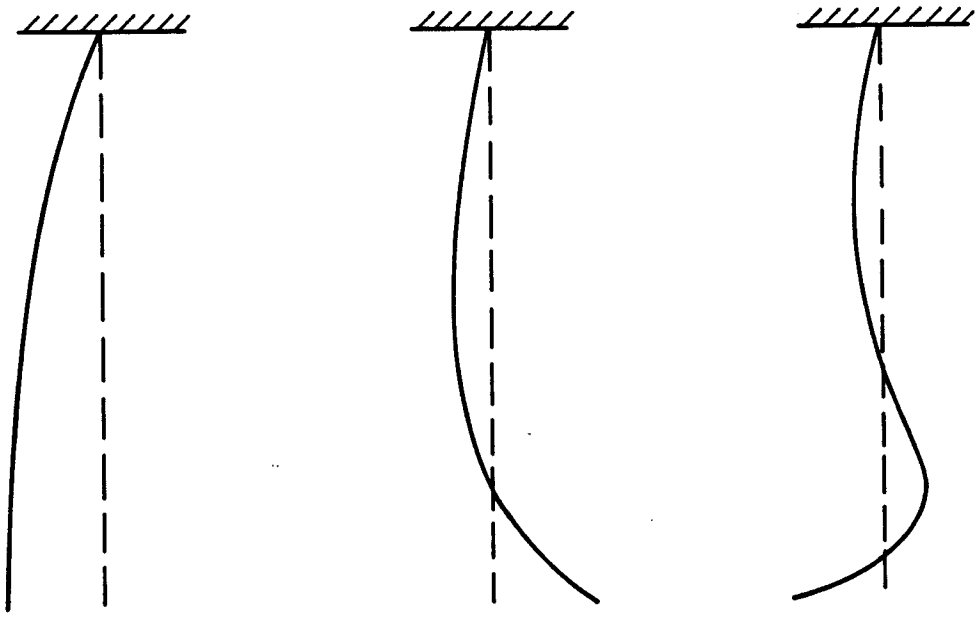

0.1877 Hz 0.4309 Hz 0.6756 Hz

MODE NO.	NATURAL FREQUENCY (Hz)
1	0.1877
2	0.4309
3	0.6756
4	0.9205
5	1.1656
6	1.4519
7	1.7042
8	1.9566
9	2.2089
10	2.4613

$$y(x,t) = \sum_{m=1}^{\infty} J_o(2\lambda_m x^{1/2})[A_m \cos(\lambda_m g^{1/2} t) + B_m \sin(\lambda_m g^{1/2} t)] \quad \text{(VI.2-28)}$$

For a single impulse the initial conditions are

$$y(x,o) = 0 \qquad \partial y(x,o)/\partial t = f(x) \quad \text{(VI.2-29)}$$

With these and orthogonality of the solutions,

$$A_m = 0 \quad B_m = \int_o^{\ell} f(x)\, J_o(2\lambda_m x^{1/2})dx / g^{1/2}\lambda_m \int_o^{\ell} J_o^2(2\lambda_m x^{1/2})dx \quad \text{(VI.2-30)}$$

In this work, f(x) is taken as a uniform initial velocity $\dot{y}_o$. Then after evaluating the integrals in Eq. VI.2-30, the result is

$$B_m = \dot{y}_o/\lambda_m^2 (g\ell)^{1/2} J_1(2\lambda_m \ell^{1/2}) \quad \text{(VI-2-31)}$$

Thus the formal solution is complete for the initial impulse problem. Numerical results are obtained from a computer program based upon the preceding analysis. Calculations include the weight of the PbLi, the SiC and the outer surface film.

The displacement profile following an impulse at rest is initially very uniform. A typical result is shown in Fig. VI.2-10 at a time of 0.20 sec. This is the instant at which a second impulse would occur in operation. However if the excitation is limited to a single shot, and motion allowed to develop for larger values of time, the shapes become somewhat complex as shown qualitatively in Fig. VI.2-11. The quantitative time histories of Figs. VI.2-12 and VI.2-13 correspond to this case also. The maximum midpoint and tip deflections are approximately 16 and 55 cm, respectively. It was felt

Fig. VI.2-10

DEFLECTION PROFILE OF 3 cm TUBE AT t = 0.20 sec

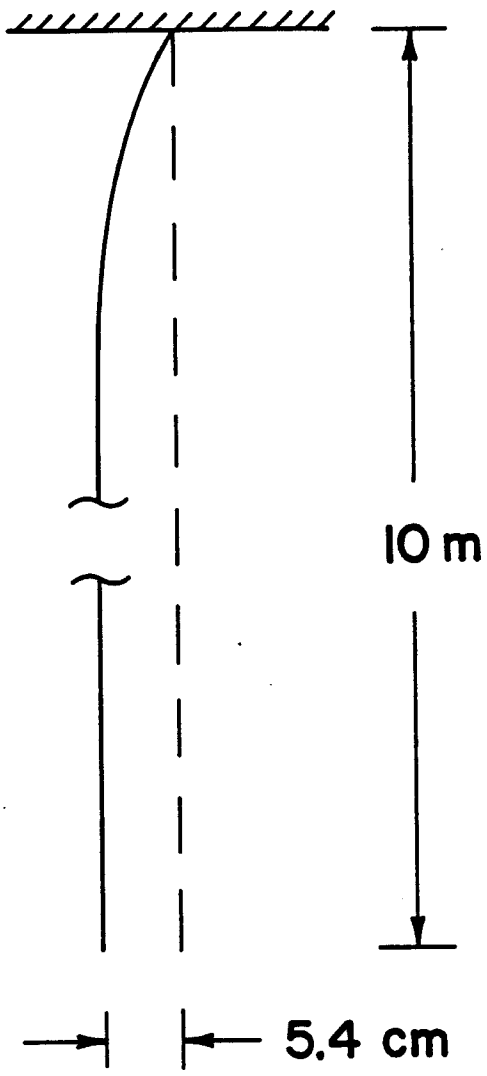

DEFLECTED SHAPES OF 3 cm TUBES AT VARIOUS TIMES AFTER UNIFORM IMPULSE

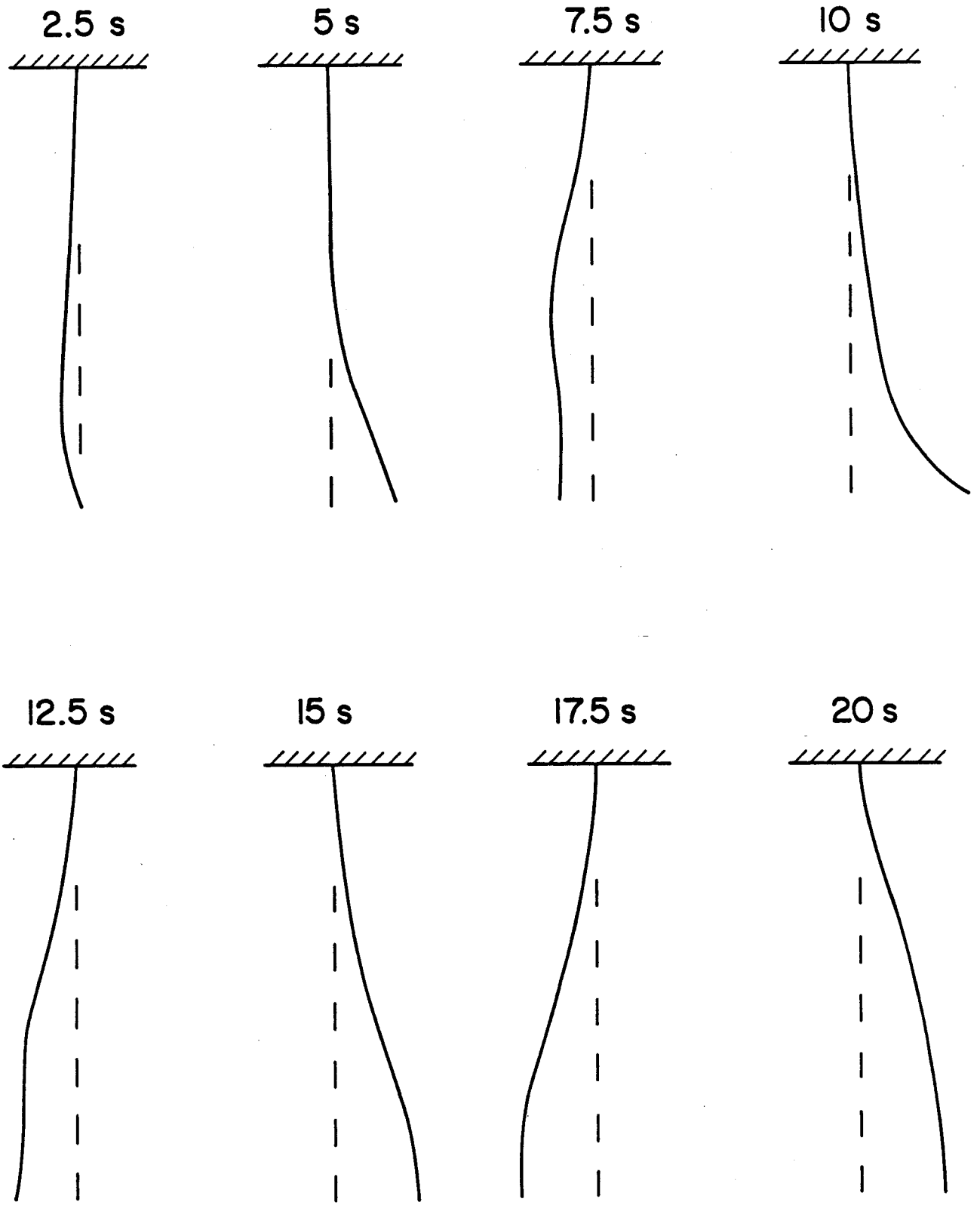

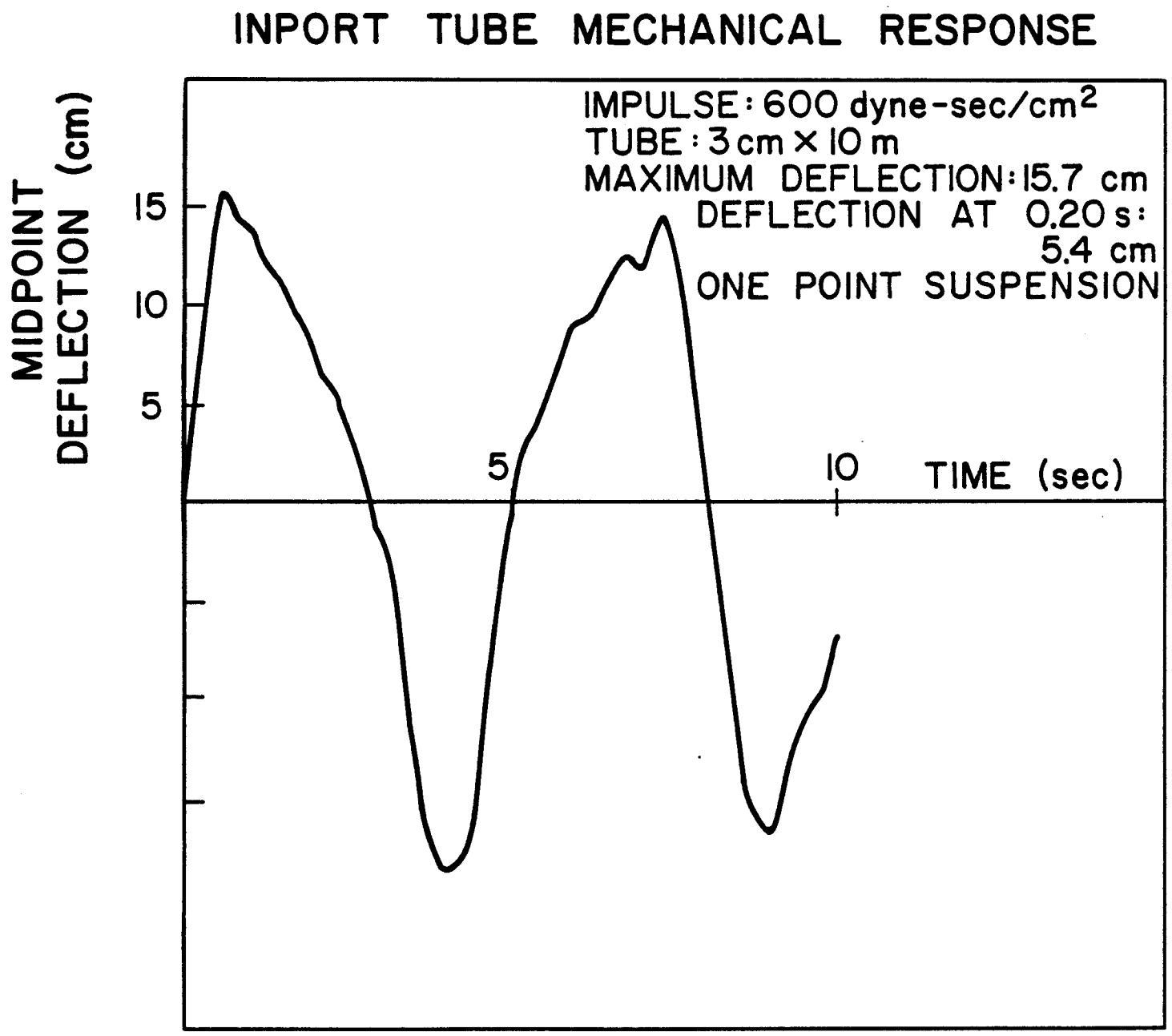
INPORT TUBE MECHANICAL RESPONSE
IMPULSE: 600 dyne-sec/cm²
TUBE: 3 cm × 10 m
MAXIMUM DEFLECTION: 15.7 cm
DEFLECTION AT 0.20 s: 5.4 cm
ONE POINT SUSPENSION
MIDPOINT DEFLECTION (cm)
15
10
5
5
10
TIME (sec)

Fig. VI.2-12

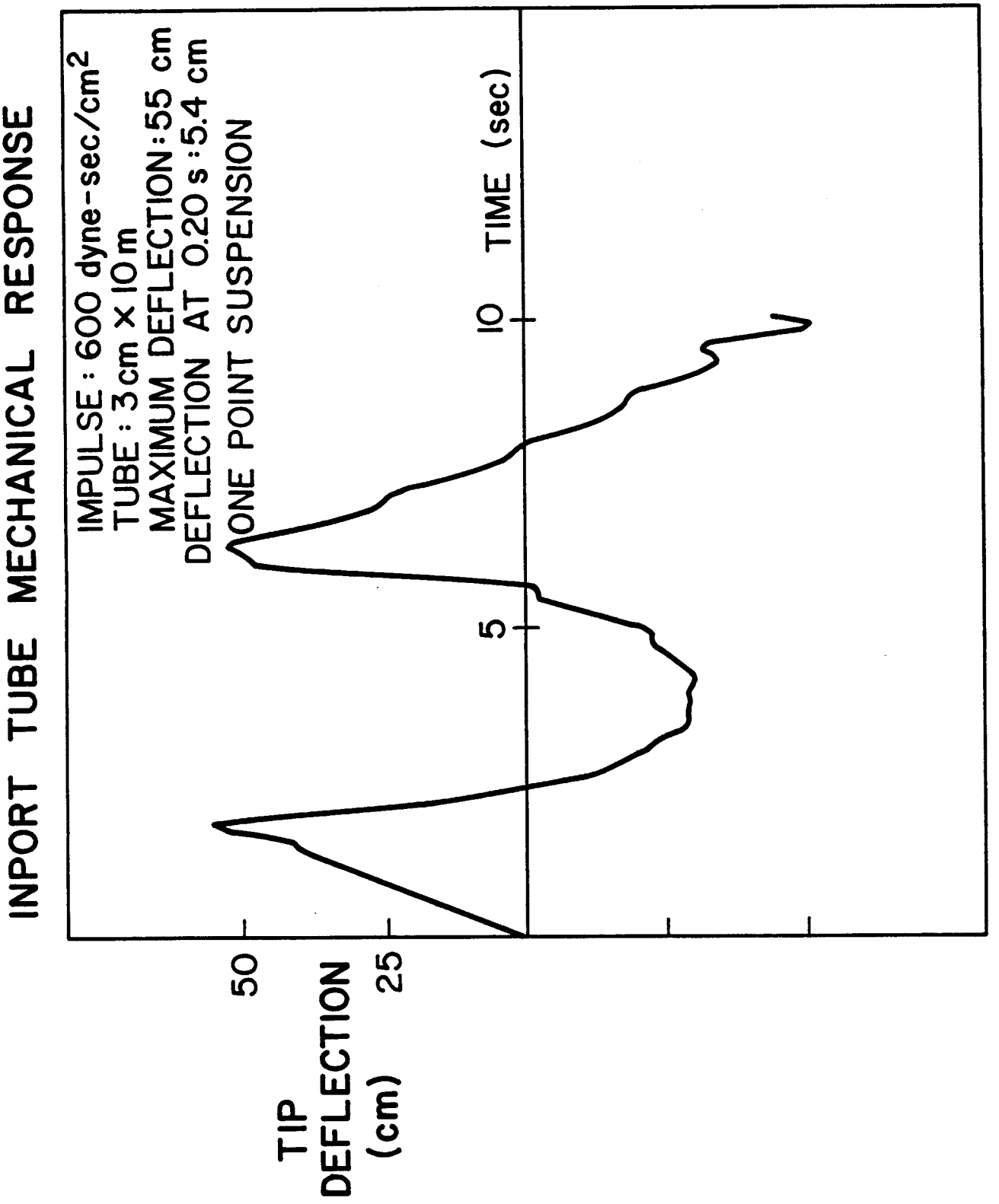
INPORT TUBE MECHANICAL RESPONSE
IMPULSE : 600 dyne-sec/cm²
TUBE : 3cm × 10m
MAXIMUM DEFLECTION : 55 cm
DEFLECTION AT 0.20 s : 5.4 cm
ONE POINT SUSPENSION
TIP DEFLECTION (cm)
50
25
5
10
TIME (sec)

Fig. VI.2-13

that as typical values, these displacements were excessive, particularly on a single shot basis.

VI.2.3.4 Analytical Outline - Two Point Suspension

In order to control deflections, it has been proposed to constrain the bottom as well as the top of the INPORT tubes. The background analysis for this case is briefly outlined in the work which follows.

The principle equation of motion is

$$\partial^2 y/\partial t^2 - (T/\rho)\, \partial^2 y/\partial x^2 + 2b\partial y/\partial t = 0 \qquad \text{(VI.2-32)}$$

in which b is a viscous damping coefficient. The initial conditions and boundary conditions are

$$y(x,o) = f(x) \qquad \partial y(x,o)/\partial t = g(x)$$

$$y(o,t) = o \qquad y(\ell,t) = o \qquad \text{(VI.2-33)}$$

The solution form is taken as

$$y(x,t) = \sum b_n(t) \sin n\pi x/\ell$$

with

$$f(x) = \sum f_n \sin n\pi x/\ell = \sum b_n(o) \sin nx/\ell$$

$$g(x) = \sum g_n \sin n\pi x/\ell = \sum \dot{b}_n(o) \sin n\pi x/\ell \qquad \text{(VI.2-34)}$$

i.e., $b_n(o)$ and $\dot{b}_n(o)$ are the Fourier coefficients of $f(x)$, $g(x)$. With the preceding, the solution to Eq. VI.2-32 can be expressed as

$$y(x,t) = e^{-bt} \sum [f_n \cos \bar{\omega}_n t + (g_n + bf_n)/(\sin \bar{\omega}_n t)/\bar{\omega}_n] \sin n\pi x/\ell \ . \quad \text{(VI.2-35)}$$

For a single impulse, with no initial displacement

$$f_n = o$$

$$\partial y(x,o)/\partial t = g(x) = I(x)/\rho$$

where $I(x)$ is the impulse per unit length. Thus Eq. VI-2-35 becomes

$$y(x,t) = (2e^{-bt}/\rho\ell) \sum [\int_o^\ell I(u) \sin(n\pi u/\ell)du] \frac{\sin \bar{\omega}_n t}{\bar{\omega}_n} \sin \frac{n\pi x}{\ell} \ . \quad \text{(VI-2-36)}$$

If a more general force is imposed, $F(x,t)$ per unit length,

$$y(x,t) = \frac{2e^{-bt}}{\rho\ell} \sum \int_o^\ell \int_o^t F(u,\tau) \sin \frac{n\pi u}{\ell} \sin \frac{n\pi x}{\ell} \sin \frac{\bar{\omega}_n(t-\tau)}{\bar{\omega}_n} d\tau du \ .$$

VI.2.3.5 Numerical Results - Two Point Suspension

The response of the INPORT tubes was first determined for a single impulse, uniformly distributed along the length. Figures VI.2-14 - VI.2-17 show the time histories of the midspan displacement for various levels of damping. The amount of damping is expressed as a fraction of the so-called critical value, i.e., the damping coefficient which would produce non-oscillatory response. The peak values shown for a single pulse appear acceptable.

The program was extended to determine INPORT tubes response under repetitive impulses at 5 Hz. Figure VI.2-18 corresponds to "start up", with the initial velocity and displacement zero. At the end of 0.20 sec the velocity

Fig. VI.2-14

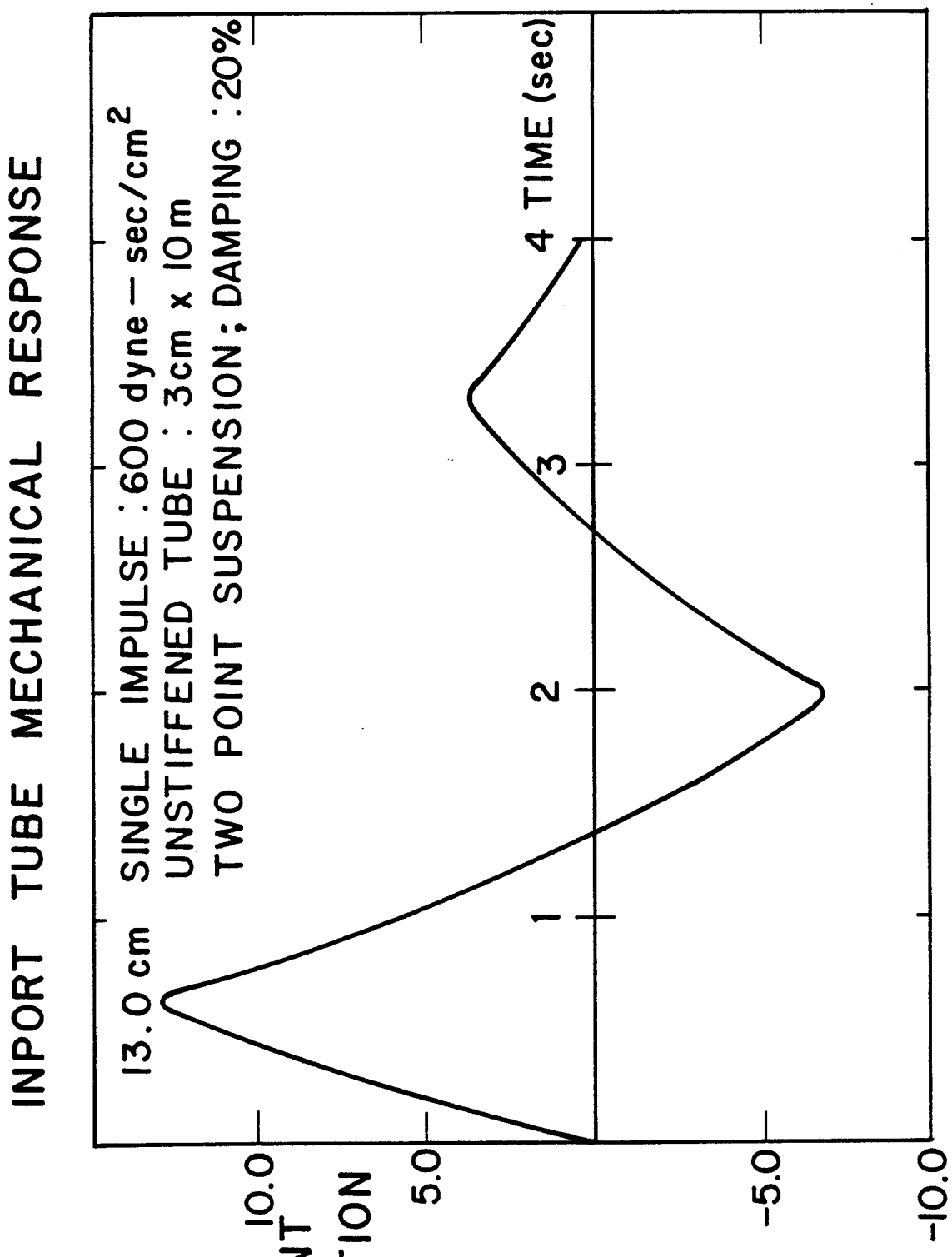
INPORT TUBE MECHANICAL RESPONSE
13.0 cm SINGLE IMPULSE :600 dyne – sec/cm²
UNSTIFFENED TUBE : 3cm x 10m
TWO POINT SUSPENSION; DAMPING :20%
MIDPOINT DEFLECTION (cm)
10.0
5.0
-5.0
-10.0
1
2
3
4 TIME (sec)

Fig. VI.2-15

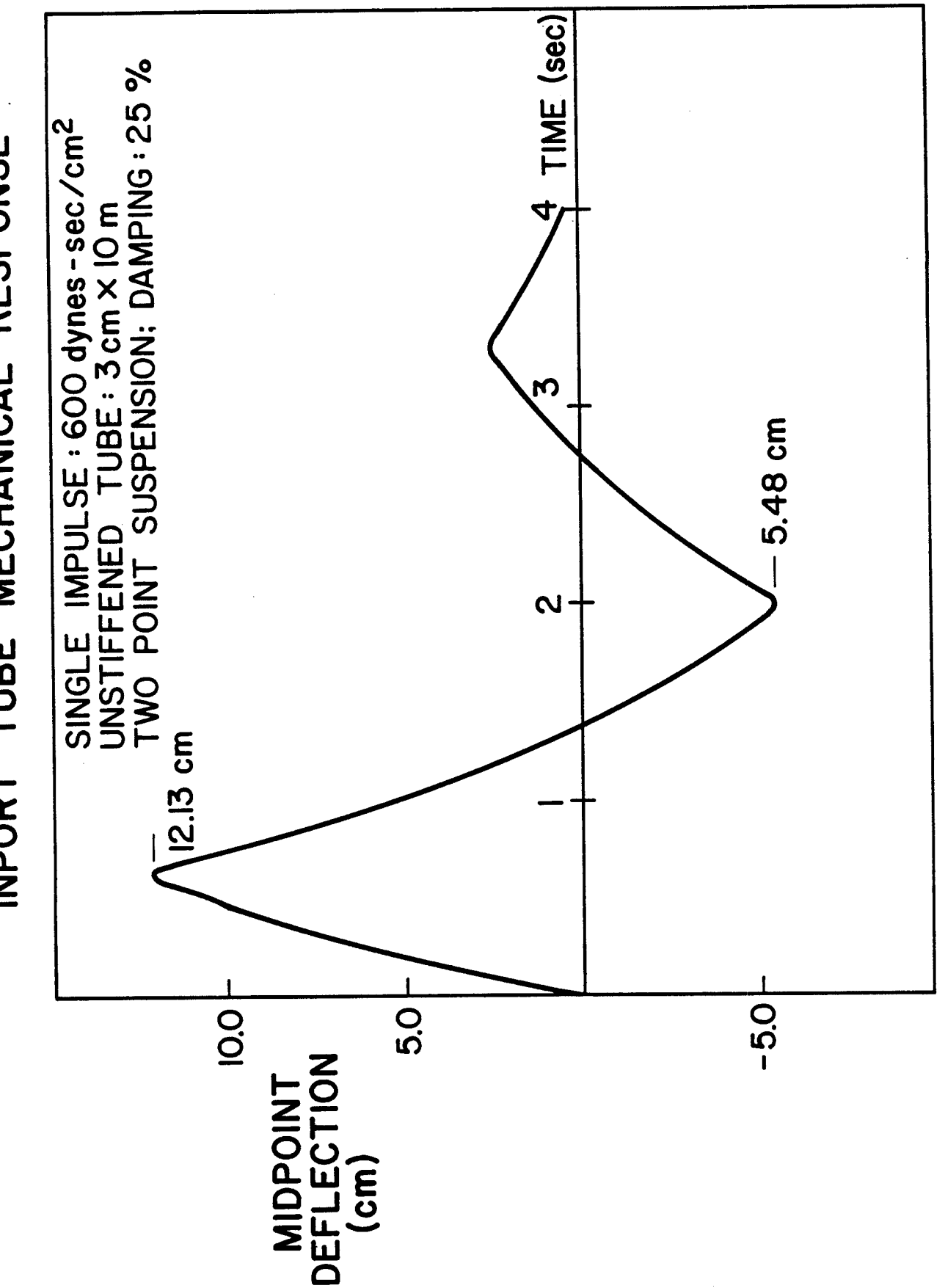
INPORT TUBE MECHANICAL RESPONSE
SINGLE IMPULSE : 600 dynes-sec/cm²
UNSTIFFENED TUBE : 3 cm × 10 m
TWO POINT SUSPENSION; DAMPING : 25 %
12.13 cm
5.48 cm
MIDPOINT DEFLECTION (cm)
10.0
5.0
-5.0
1
2
3
4 TIME (sec)

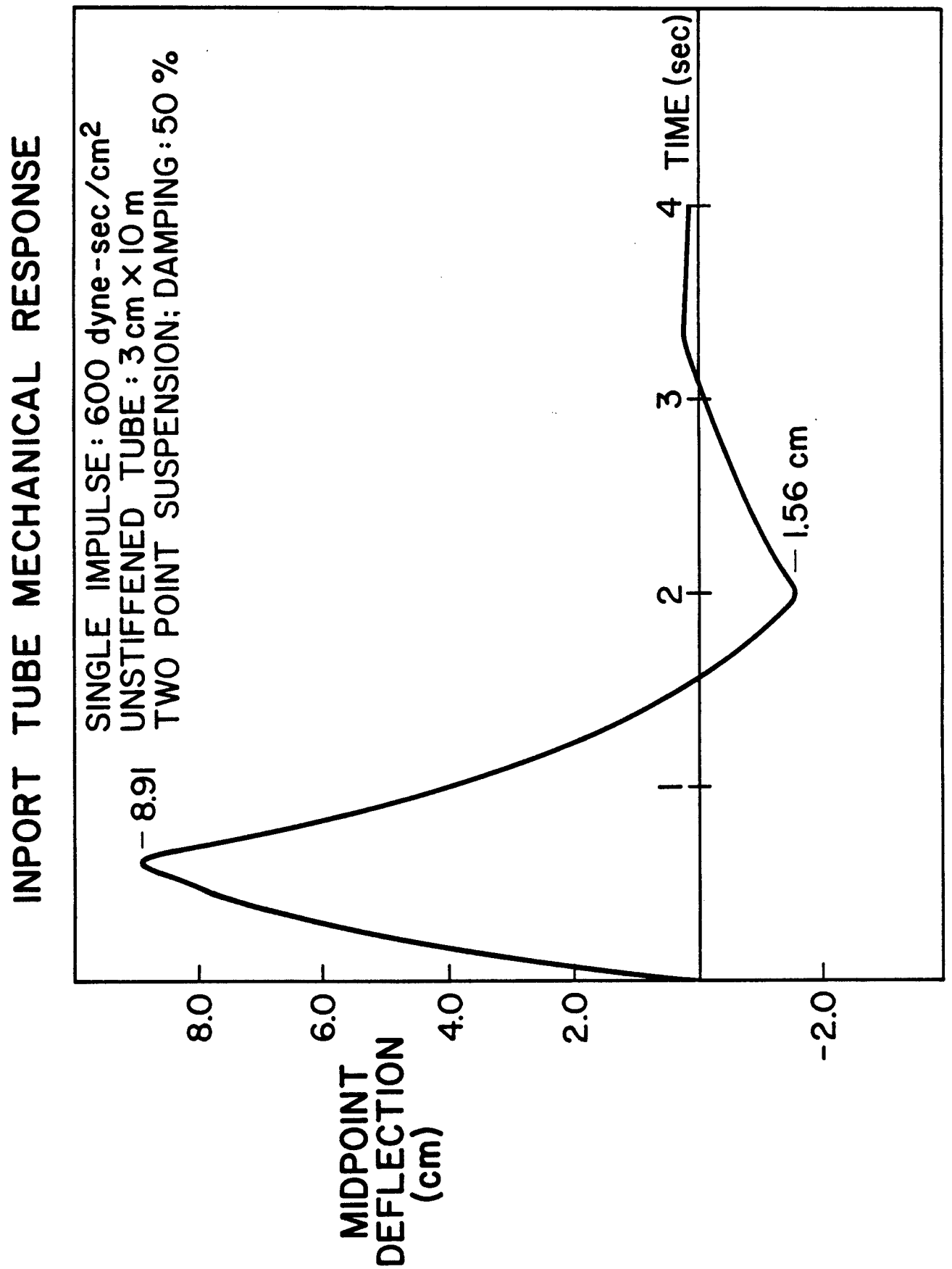
INPORT TUBE MECHANICAL RESPONSE
SINGLE IMPULSE: 600 dyne-sec/cm²
UNSTIFFENED TUBE: 3 cm × 10 m
TWO POINT SUSPENSION; DAMPING: 50 %
8.91
1.56 cm
MIDPOINT DEFLECTION (cm)
8.0
6.0
4.0
2.0
-2.0
1
2
3
4
TIME (sec)

Fig. VI.2-16

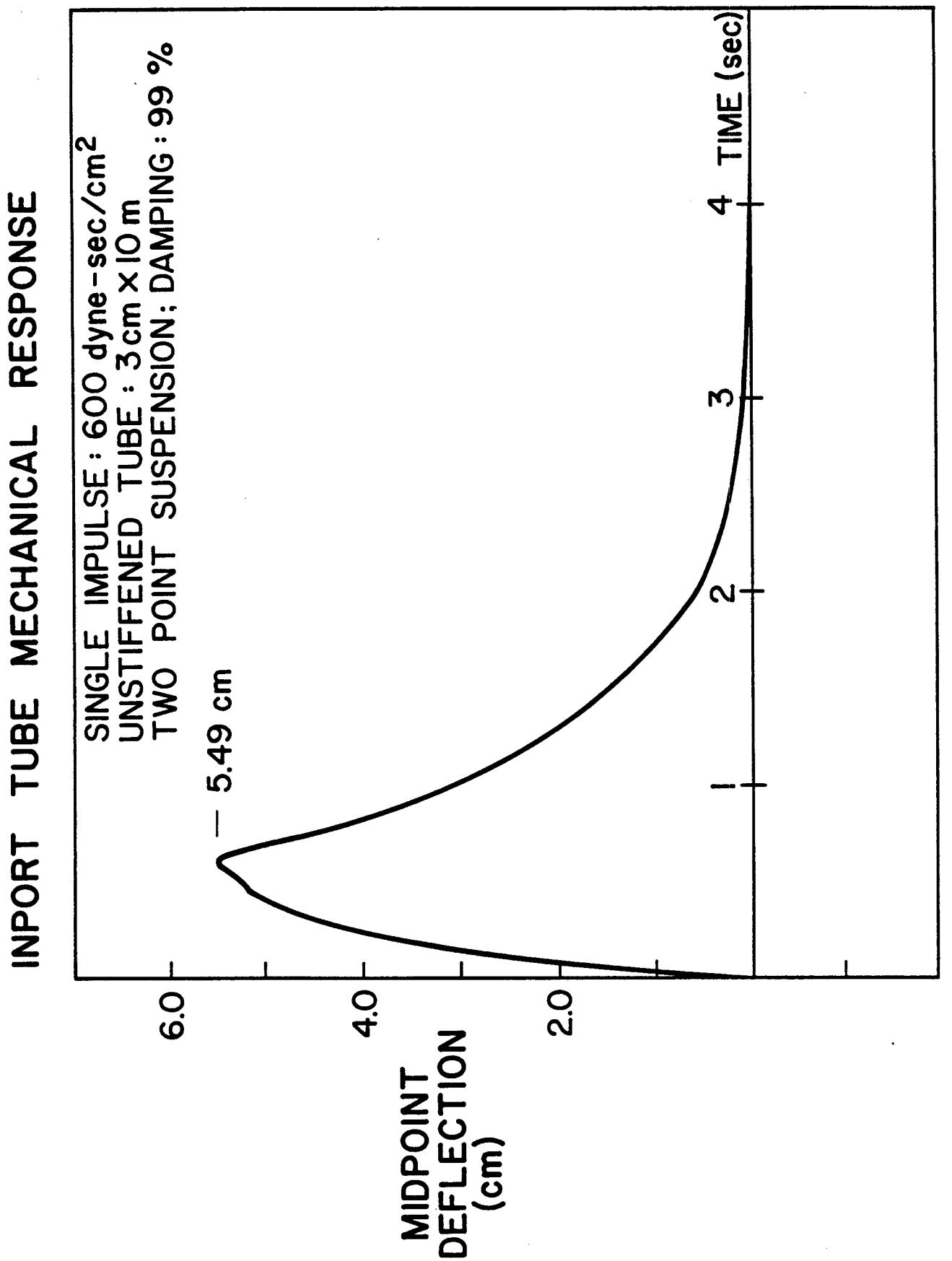
INPORT TUBE MECHANICAL RESPONSE
SINGLE IMPULSE : 600 dyne-sec/cm²
UNSTIFFENED TUBE : 3cm × 10 m
TWO POINT SUSPENSION; DAMPING : 99 %
— 5.49 cm
MIDPOINT DEFLECTION (cm)
6.0
4.0
2.0
1
2
3
4 TIME (sec)

Fig. VI.2-17

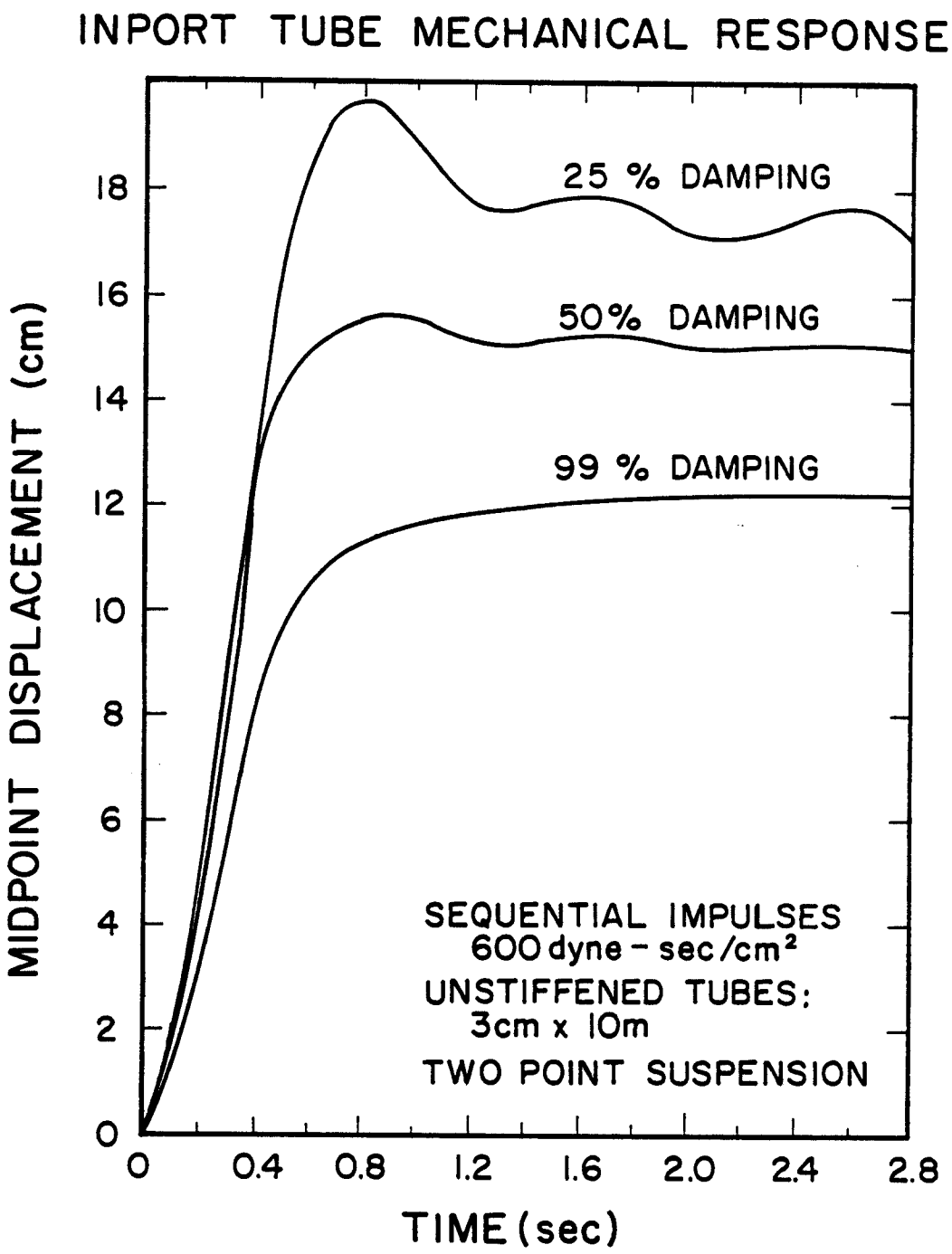
INPORT TUBE MECHANICAL RESPONSE
MIDPOINT DISPLACEMENT (cm)
TIME (sec)
25 % DAMPING
50% DAMPING
99 % DAMPING
SEQUENTIAL IMPULSES
600 dyne - sec/cm²
UNSTIFFENED TUBES:
3cm x 10m
TWO POINT SUSPENSION
0
2
4
6
8
10
12
14
16
18
0
0.4
0.8
1.2
1.6
2.0
2.4
2.8

Fig. VI.2-18

and displacement functions are evaluated and used as starting conditions with another uniform impulsive pressure. The process is repeated and carried out for fifty shots. These curves are for the first fifteen firings and show a small amount of overshoot with eventual stabilization about steady state mean values. On a relative basis the steady state mean amplitudes are moderate, e.g., less than 2% of the length. The limiting case of zero damping is shown for comparison in Fig. VI.2-19 along with the 20% value. The latter is recommended as a conservative estimate for such units. While theoretical and experimental values for metallic reactor components are much smaller single digit percentages, here the tube has a significant natural damping capacity from the woven soft construction and the ever present PbLi in liquid form. A level of 20% is a representative design figure for long span electrical conductors and transmission lines and is typical of experimental measurements (Ref 2).

Finally the response was determined following shutdown. Typical results are shown in Fig. VI.2-20 in which the load sequence was stopped after fifty shots. While the displacement history is very smooth, characteristic of a single mode, it should be noted that this result involves the contributions of the first eight modes in the series. Such results confirm expectations that no unusual characteristics develop for this scenario.

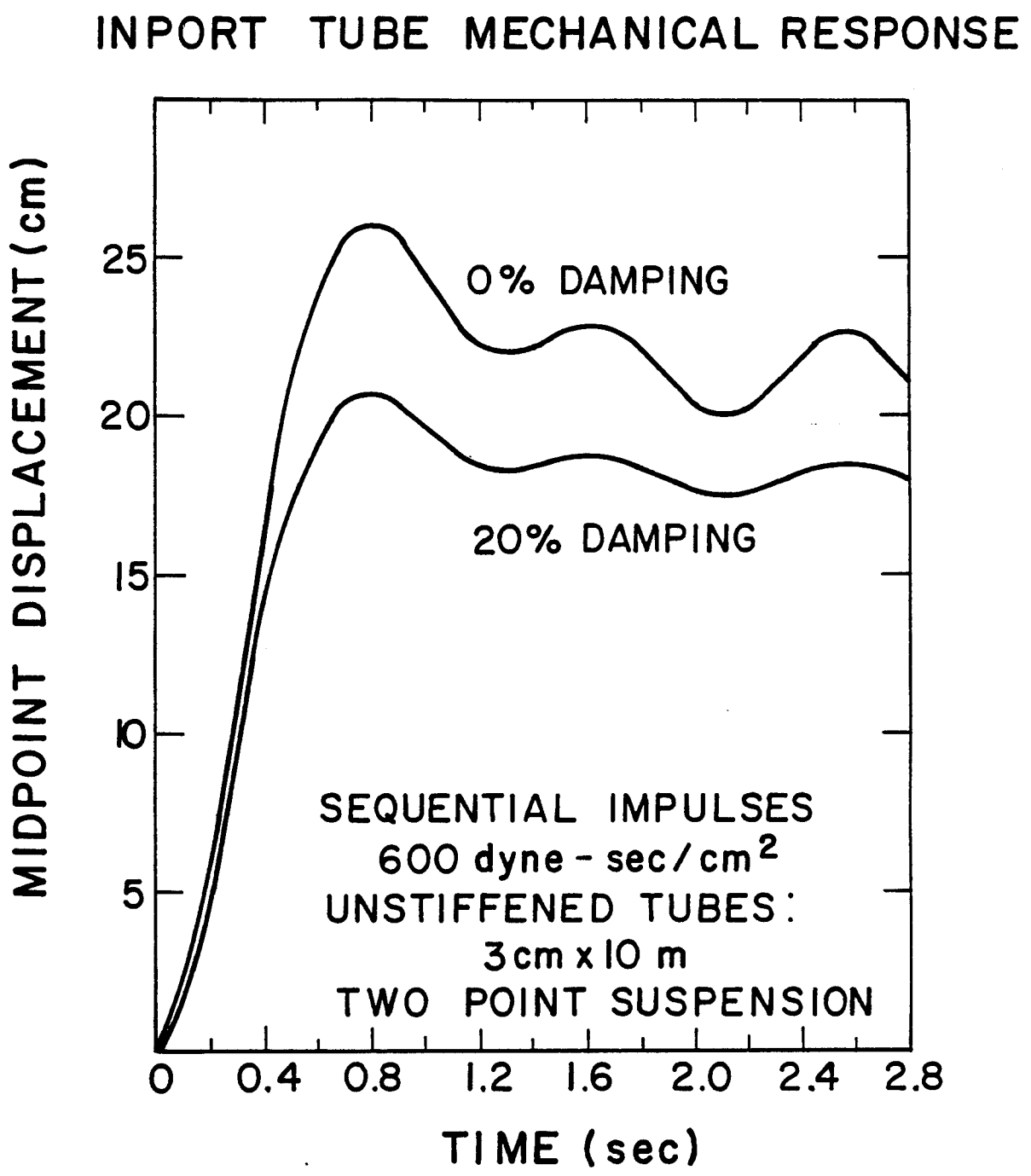
INPORT TUBE MECHANICAL RESPONSE
MIDPOINT DISPLACEMENT (cm)
25
20
15
10
5
0% DAMPING
20% DAMPING
SEQUENTIAL IMPULSES
600 dyne - sec / cm²
UNSTIFFENED TUBES:
3 cm x 10 m
TWO POINT SUSPENSION
0
0.4
0.8
1.2
1.6
2.0
2.4
2.8
TIME (sec)

Fig. VI.2-19

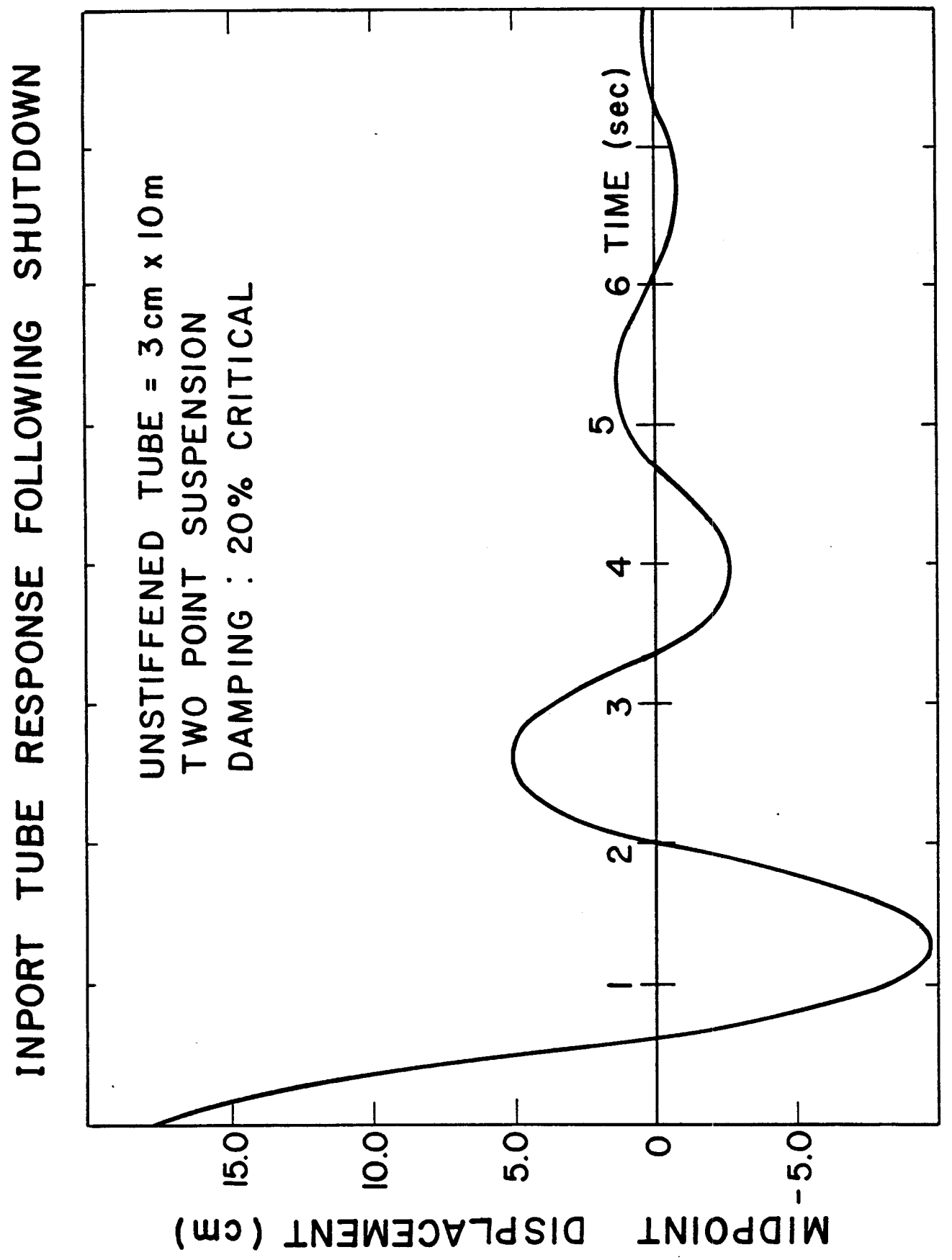
INPORT TUBE RESPONSE FOLLOWING SHUTDOWN
UNSTIFFENED TUBE = 3 cm x 10 m
TWO POINT SUSPENSION
DAMPING : 20% CRITICAL
MIDPOINT DISPLACEMENT (cm)
15.0
10.0
5.0
0
-5.0
1
2
3
4
5
6 TIME (sec)

Fig. VI.2-20

References for Section VI.2

1. R.L. Engelstad and E.G. Lovel,"First Wall Mechanical Design for Light Ion Beam Fusion Reactors," University of Wisconsin Report UWFDM-322, Dec. 1979.

2. Y-K. Wen, "Dynamic Response of Transmission Line System to Wind Load," Engineering Science Research Report BLWT-9-68, University of Western Ontario, London, Ontario, April 1968.

VI.3 Neutronics and Photonics

VI.3.1 Introduction

The neutronics and photonics analysis for HIBALL is presented in this section. A one-dimensional spherical geometry analysis was performed to determine the optimum blanket design which gives the highest possible energy multiplication with adequate breeding ratio. The blanket consisting of the INPORT tubes is also required to protect the ferritic steel structure from radiation damage. The biological shield is also designed. The actual cylindrical cavity is modelled in a detailed three-dimensional neutronics and photonics analysis. All cavity geometrical details are included in this analysis. A time-dependent neutronics analysis is also presented to account properly for the pulsed nature of the neutron source. This analysis yields time-dependent radiation damage rates which form an important input to microstructure evolution calculations. Finally, the calculations of blanket and shield radioactivity and afterheat are given.

VI.3.2 One-Dimensional Time Integrated Studies

VI.3.2.1 Introduction

Neutronics and photonics calculations are required to determine important reactor parameters such as tritium breeding, nuclear heating, and radiation damage. In an inertial confinement fusion reactor, the DT fuel is heated and compressed to extremely high densities before it ignites. Neutron fuel interactions result in spectrum softening, neutron multiplication, and gamma production. In this section, a consistent coupled target-blanket neutronics and photonics study of HIBALL is given. The neutron and gamma source for blanket calculations was obtained from the target neutronics and photonics results given in section III.1.

The HIBALL blanket is required to breed tritium and convert the kinetic energy of the fusion reaction into heat. Furthermore, the INPORT tubes are required to protect the vacuum wall and HT-9 structure in the reflector from radiation damage. One-dimensional steady state calculations are performed to determine the optimum blanket thickness which yields the largest possible energy multiplication with adequate tritium breeding ratio and first wall protection. The thickness of biological shield required to reduce the biological dose to permissible levels is also determined.

VI.3.2.2 Blanket and Shield Model

The HIBALL fusion reactor power plant design incorporates four cylindrical cavities each having a radius of 7 m and a height of 10 m. The blanket region consists of an array of porous tubes (INPORT tubes) made of braided SiC through which the $Li_{17}Pb_{83}$ liquid metal eutectic flows. These tubes are placed inside the reactor cavity. Besides serving as the coolant and tritium breeder, the $Li_{17}Pb_{83}$ coolant is utilized for first wall protection. The tubes occupy 33% of the 2 m thick blanket region yielding an effective blanket thickness of 66 cm. The LiPb coolant occupies 98% of the tube volume with the SiC occupying the remaining 2%. SiC and $Li_{17}Pb_{83}$ have nominal densities of 3.17 and 9.4 g/cm^3, respectively. The first wall is made of ferritic steel (HT-9) which is an alloy composed of 85.25 wt% iron and 11.5 wt% chromium. The first wall has a thickness of 1 cm and a density of 7.8 g/cm^3. A 0.4 m thick reflector composed of 90 v/o ferritic steel structure and 10 v/o $Li_{17}Pb_{83}$ coolant is used. The reactor utilizes a 3.5 m thick concrete shield. The shield consists of 95% ordinary concrete and 5% H_2O coolant. A schematic of the blanket, first wall, reflector, and shield configuration for the HIBALL reactor is given in Fig. VI.3-1.

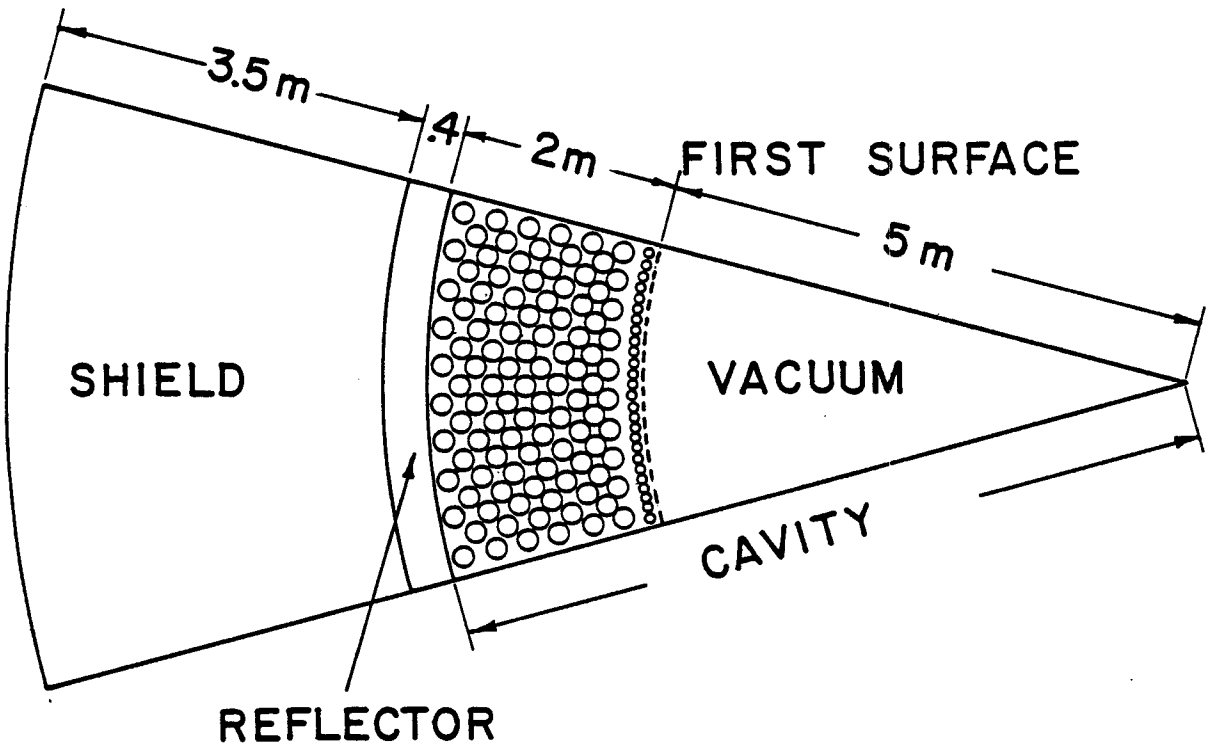

Fig. VI.3-1 HIBALL reactor cavity model.

VI.3.2.3 Calculational Method and Nuclear Data

The one-dimensional discrete ordinates code ANISN[1] was used to perform neutronics and photonics calculations yielding average time integrated results. A P3-S4 approximation was used. Spherical geometry was used in the calculations and hence the results represent the conditions at the central plane of the reactor. The results give conservatively high damage rates and low tritium breeding ratios. The neutron and gamma spectra obtained from the target calculations are used to represent the source for the blanket neutronics and photonics calculations. The source is considered to be an isotropic point source at the center of the cavity. The calculations account for neutron spectrum softening, neutron multiplication, and gamma production in the target. The one-dimensional finite element code ONETRAN[2] implemented at Karlsruhe Nuclear Laboratory was also used to perform the calculations for the final blanket design and the results are compared to the results from ANISN. A coupled 25 neutron-21 gamma group cross section library was used. The library consists of the RSIC DLC-41B/VITAMIN-C data library[3] and the DLC-60/MACKLIB-IV response data library.[4] This data library is based on ENDF/B-IV. The nuclide densities used in the calculations are given in Table VI.3-1. The results presented here are based on a DT yield of 400 MJ and a repetition rate of 5 Hz yielding 7.1×10^{20} fusion neutrons per second.

Neutron and gamma cross section requirements for the neutronic analysis of the HIBALL system are similar to those of fast fission reactor systems. Neutron data are required up to the fusion neutron energy of 14.1 MeV. Presently available neutron cross section libraries like ENDF/B[5] and KEDAK[6] cover this energy range. Although data in these libraries show a lower level of confidence above a few MeV than in the keV and thermal energy range, and some improvement in data, e.g., energy distribution of secondary neutrons is

Table VI.3-1

Nuclide Densities Used in Neutronics Analysis of HIBALL Fusion Reactor

Region	Constituent Elements	Nuclide Density (nuclei/b cm)
Blanket	^{6}Li	0.00040
[98 v/o $Li_{17}Pb_{83}$	^{7}Li	0.00505
+ 2 v/o SiC]	Si	0.00095
(.33 density factor)	C	0.00095
	Pb	0.02661
Ferritic Steel	Fe	0.07174
First Wall	Cr	0.01725
(1.0 density factor)	Ni	0.00066
	Mo	0.00081
	V	0.00046
	Si	0.00069
	Mn	0.00071
	C	0.00130
	W	0.00022
Reflector	Fe	0.06456
[90 v/o ferritic	Cr	0.01553
steel + 10 v/o $Li_{17}Pb_{83}$]	Ni	0.00060
(1.0 density factor)	Mo	0.00073
	V	0.00041
	Si	0.00063
	Mn	0.00064
	C	0.00117
	W	0.00020
	^{6}Li	0.00004
	^{7}Li	0.00051
	Pb	0.00272

conceivable, the quality of the data as stored in ENDF/B-IV is considered, with exceptions given below, to be adequate at this stage of the study.

One major parameter to be determined in the neutronic calculation is the tritium breeding ratio. Tritium is produced by the reactions

$$^{7}Li(n,n'\alpha)T \qquad \text{and} \qquad ^{6}Li(n,\alpha)T \ .$$

The division of the tritium breeding between these two processes is essentially design dependent. Strong doubts about the validity of the $^{7}Li(n,n'\alpha)T$ cross section in ENDF/B-IV have been expressed.[7-10] Lowering the cross section by 15-20% has been suggested.[8] Results of new differential measurements (Fig. VI.3-2) from different laboratories suggest reducing the ENDF/B-IV cross section by about 10%. Some of these results are still of a preliminary nature.

In the HIBALL blanket design, due to the presence of a large amount of lead, neutrons are rapidly slowed down below the threshold of the $^{7}Li(n,n'\alpha)T$ reaction. The contribution of this reaction to the tritium production is only about 2%. Thus ENDF/B-IV cross sections for this process can be used without introducing significant error in the tritium breeding ratio.

The other reaction responsible for tritium breeding; $^{6}Li(n,\alpha)T$ is used in neutron data measurements as a standard. Recently Hale[11] has re-evaluated this cross section below 1 MeV for the ENDF/B-V standard file. He made a thorough analysis of the ^{7}Li compound nucleus system including charged particle reactions. His result (Fig. II.3-3) gives a lower $^{6}Li(n,\alpha)T$ cross section for the 252 keV resonance and for lower energies. For ^{6}Li, group cross sections were generated using the ENDF/B-V Data and used to investigate the effect on HIBALL overall tritium breeding ratio.

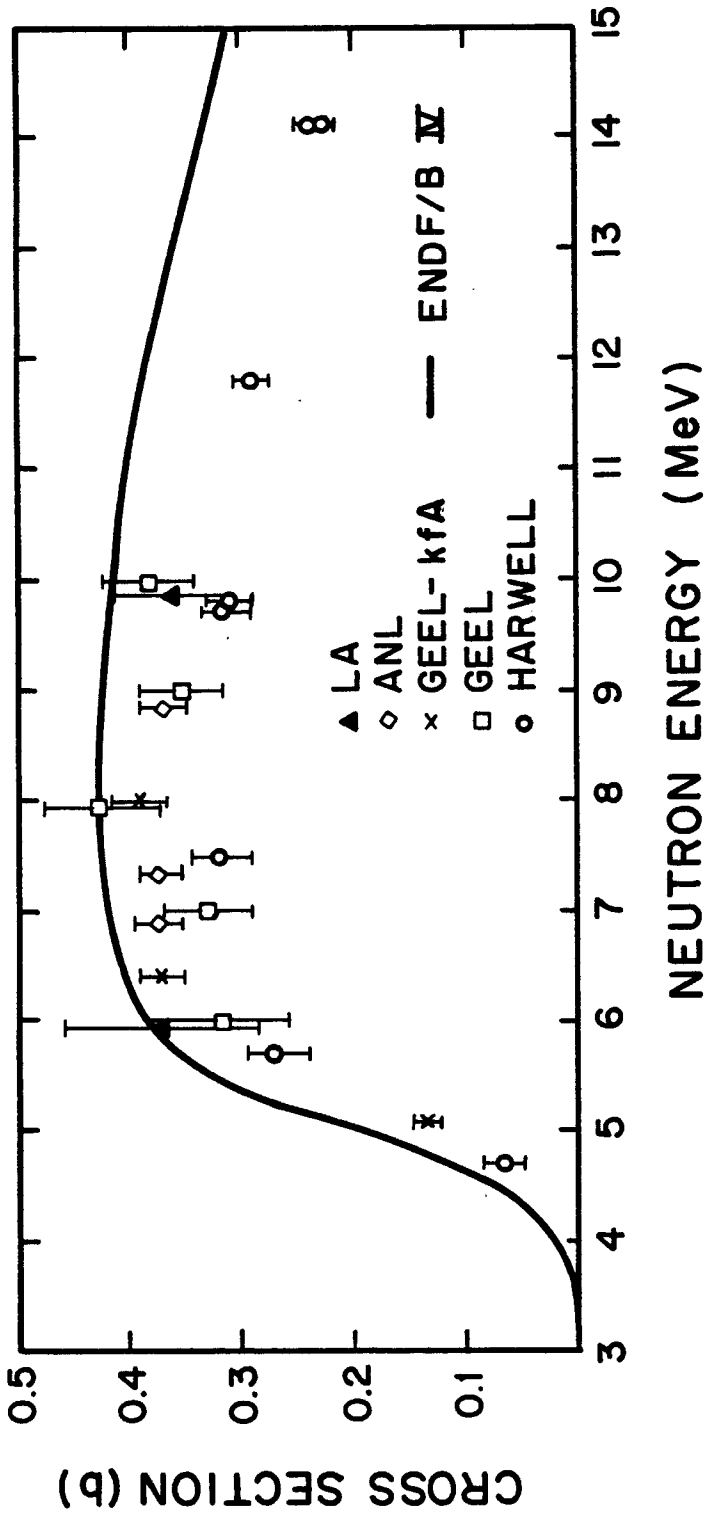

Fig. VI.3-2 Measurements of $^{7}Li(n,n'\alpha)T$ cross section.

Figure VI.3-3

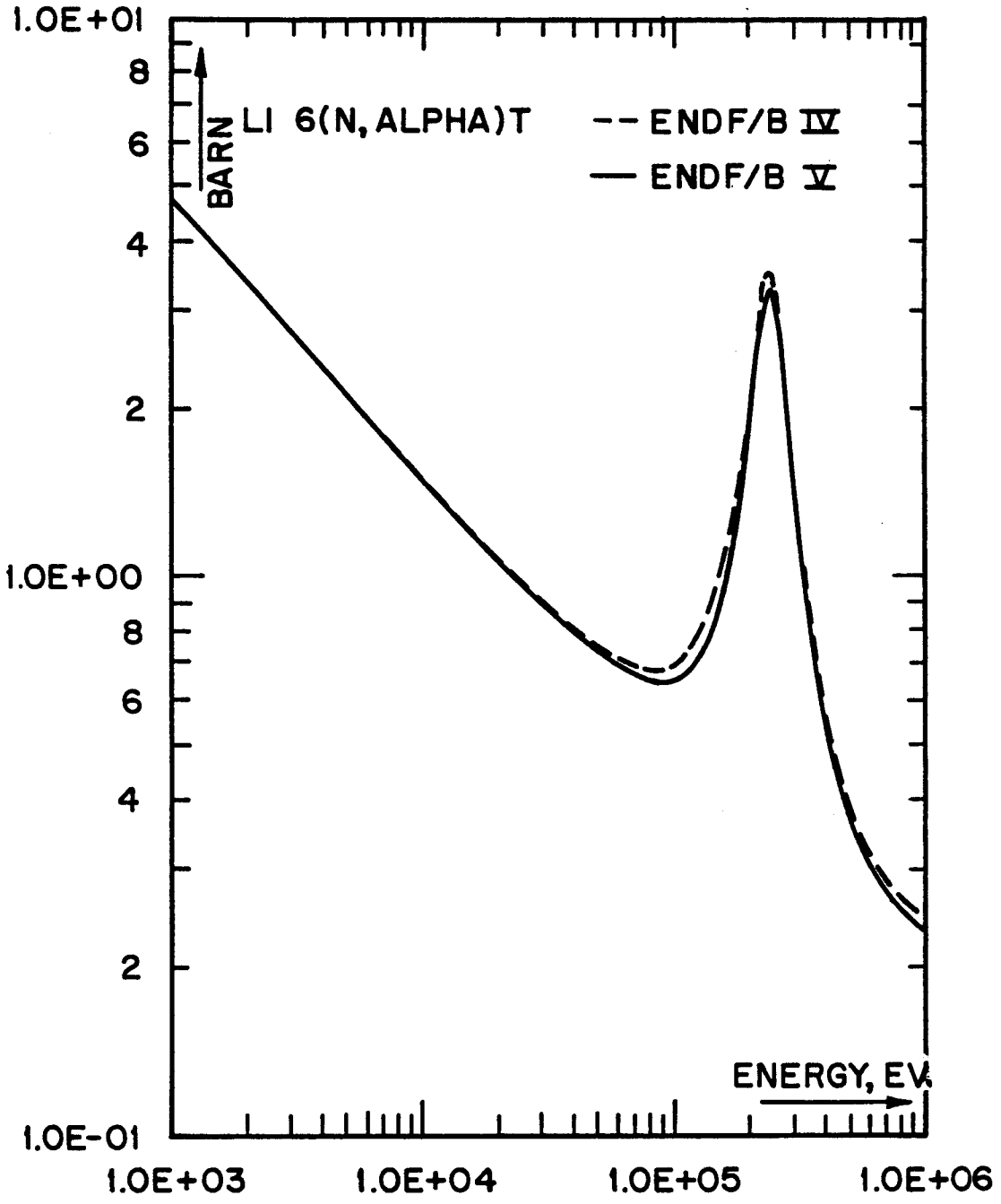

$^{6}Li(n,\alpha)T$ Cross Sections from ENDF/B IV and V

VI.3.2.4 Blanket Optimization

A series of one-dimensional neutronics and photonics calculations was made in which the packing fraction for the INPORT tubes was varied with the blanket region thickness fixed at 2 m. The effect of the tube packing fraction or the effective blanket thickness on radiation damage, tritium breeding and nuclear heating was investigated. The design criterion used in the optimization was that the energy deposition should be as high as possible with a tritium breeding ratio $\gtrsim$ 1.1 in the approximate one-dimensional calculation.

Table VI.3-2 gives the effect of packing fraction on tritium production. It is clear that tritium production in the blanket increases as the thickness increases. On the other hand, tritium production in the reflector region decreases as the effective blanket thickness increases. The net effect is that the overall breeding ratio increases nearly linearly with the effective blanket thickness.

Figure VI.3-4 gives the spatial distribution of tritium production in the blanket and reflector for a packing fraction of 0.33. The contributions to tritium production from $^{7}Li(n,n'\alpha)$ and $^{6}Li(n,\alpha)$ reactions are shown. The contribution from ^{7}Li, which is a high energy reaction (threshold energy = 2.86 MeV), decreases sharply as one moves into the blanket away from the source because of the increased softening of the spectrum. Table VI.3-3 gives a comparison between the results of ANISN and ONETRAN. The effect of using the ENDF/B-V data for the $^{6}Li(n,\alpha)T$ cross section is also given. Using the $^{6}Li(n,\alpha)T$ cross section from ENDF/B-V results in a 2% reduction in the calculated tritium breeding ratio.

Table VI.3-4 gives the neutron, gamma, and total energy deposition in the different regions for different values of the packing fraction. Notice that

Table VI.3-2 Effect of Tube Packing Fraction on Tritium Breeding

Packing Fraction	0	.30	.33	.35	.40
Blanket	0	1.094	1.177	1.226	1.331
Reflector	0.043	0.022	0.018	0.016	0.012
System Total	0.043	1.116	1.195	1.242	1.343

Table VI.3-3 Comparison Between Results for Tritium Production

Tritium Production (Tritons/Fusion)				
Region	Element	ANISN with ENDF/B-IV $^{6}Li(n,\alpha)T$	ONETRAN with ENDF/B-IV $^{6}Li(n,\alpha)T$	ONETRAN with ENDF/B-V $^{6}Li(n,\alpha)T$
Blanket	^{6}Li	1.1500	1.1558	1.1327
	^{7}Li	0.0270	0.0271	0.0271
	Total	1.1770	1.1829	1.1598
First Wall	Total	0.0	0.0	0.0
Reflector	^{6}Li	0.0180	0.0180	0.0175
	^{7}Li	0.0	0.0	0.0
	Total	0.0180	0.0180	0.0175
Tritium Breeding Ratio		1.1950	1.2009	1.1773

Table VI.3-4 Effect of INPORT Tube Packing Fraction on Nuclear Energy Deposition (MeV/Fusion)

Packing Fraction		0	.30	.33	.35	.40
Blanket	Neutrons	---	7.026	7.467	7.729	8.278
	Gamma	---	6.663	6.687	6.697	6.705
	Total	---	13.689	14.154	14.426	14.983
First Wall	Neutrons	0.407	0.020	0.016	0.014	0.009
	Gamma	1.141	0.208	0.180	0.163	0.125
	Total	1.548	0.228	0.196	0.177	0.134
Reflector	Neutrons	2.626	0.287	0.232	0.202	0.142
	Gamma	14.402	4.013	3.367	2.985	2.185
	Total	17.028	4.300	3.599	3.187	2.327
System Total		18.576	18.217	17.949	17.790	17.444
Overall Energy Multiplication		1.326	1.300	1.281	1.269	1.245

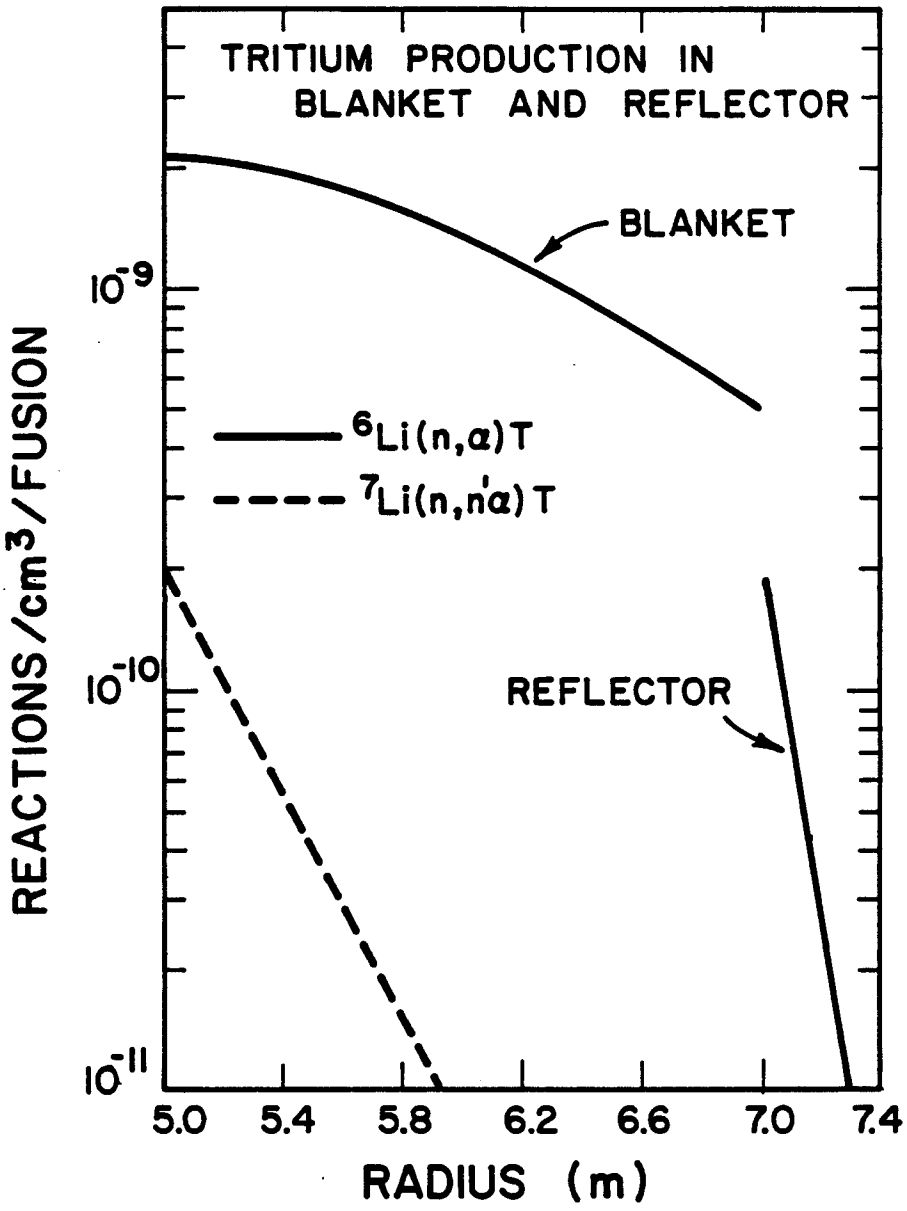

Figure VI.3-4 Tritium production in the blanket and reflector.

more than 50% of energy deposited comes from gamma-ray heating because of neutron reactions in the HT-9 structure. The contribution from gamma heating decreases as the INPORT tube region thickness increases. As the blanket thickness increases, the total energy deposited in it increases with a larger fraction of this energy being deposited by neutrons. The larger energy deposition results from the larger number of neutron and gamma interactions taking place in the thicker blanket. The relative gamma contribution to the heating decreases as the thickness increases because a smaller portion of the blanket will be adjacent to the first wall where large gamma production occurs. The neutron and gamma heating in the first wall and reflector decrease as the blanket thickness increases because of the increased neutron attenuation in the blanket. The total energy deposited in the system is found to decrease as the blanket thickness increases. This results because of the decreased gamma production in ferritic steel due to the lower neutron flux in the first wall and reflector. A neutron absorbed in ^{6}Li releases ~ 4.8 MeV while if it is absorbed in the structure ~ 7 MeV is released. The energy multiplication is also included in Table VI.3-4. This factor is defined as the total energy deposited in the system, including the energy deposited by X-rays and target debris at the first surface of the blanket, divided by the fusion reaction yield of 17.6 MeV.

The spatial variation of the total power density in the blanket for a packing fraction of 0.33 is given in Fig. VI.3-5. The power density decreases as one moves away from the source inside the blanket because of the increased neutron and gamma attenuation. The large gamma production in HT-9 causes the gamma heating to increase sharply as one approaches the first wall. This is the reason for the existance of a minimum in the power density at ~ 30 cm from the first wall.

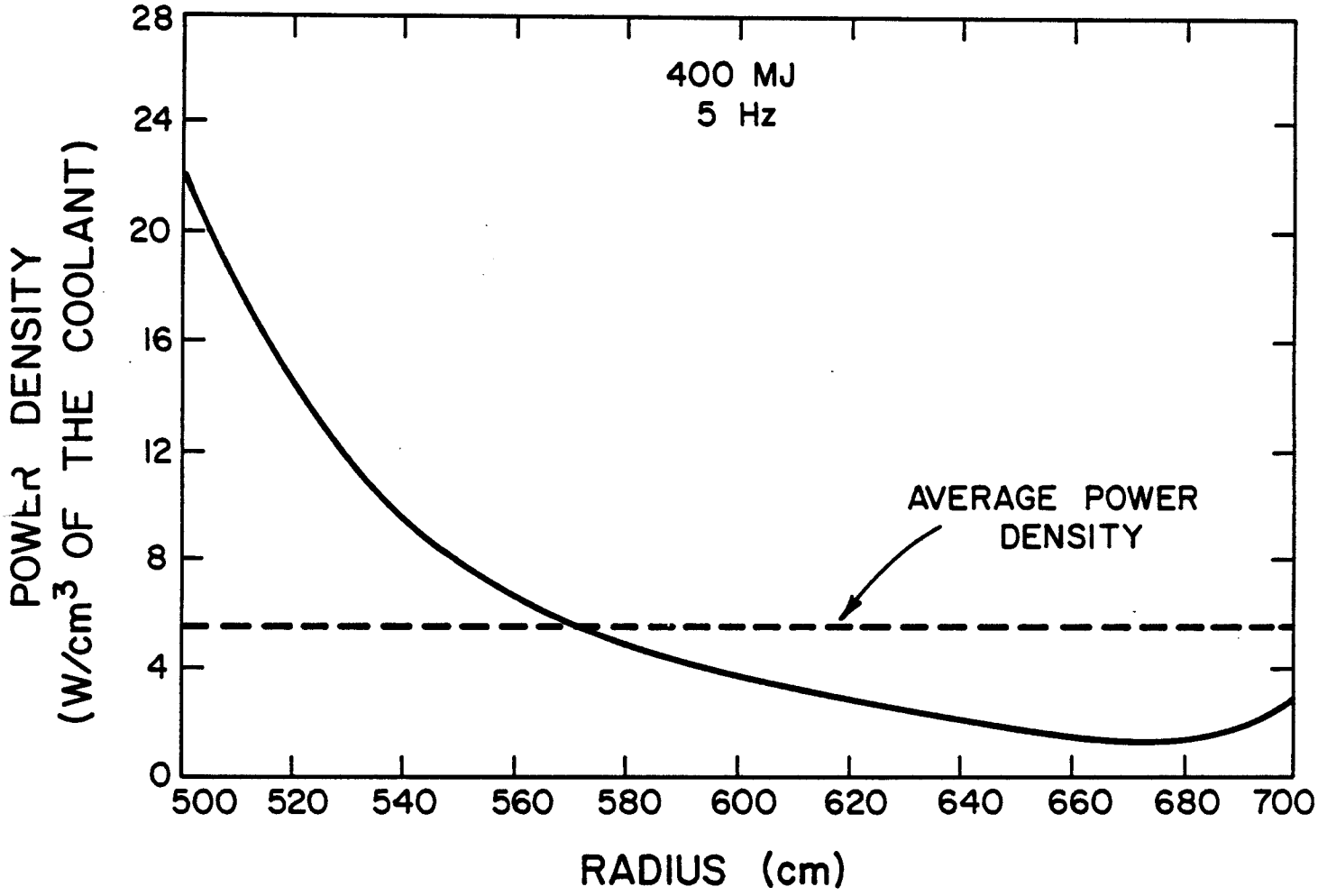

Figure VI.3-5 Spatial variation of power density in the blanket.

It is clear from the previous results that increasing the INPORT tube packing fraction results in increasing the tritium breeding ratio at the expense of power production. Since energy production is the primary goal of a fusion power reactor, a packing fraction of 0.33 is chosen. This yields an energy multiplication of 1.28 and a breeding ratio of 1.195. A relatively high breeding ratio is chosen here because of expected reduction in tritium production when one includes the penetrations and various structural support materials in the detailed three-dimensional cylindrical geometry. The breeding ratio should also be greater than one to account for uncertainties in data and calculational methods.

VI.3.2.5 Neutron and Gamma Spectra

Using the neutron and gamma spectra from the target calculations to represent the source for the blanket neutronics and photonics calculations, the neutron and gamma spectra were calculated at different positions in the blanket, first wall and reflector. The neutron spectra are given in Fig. VI.3-6. In the innermost part of the blanket the spectrum has a pronounced peak at 14.1 MeV with the lower energy part of the spectrum resulting from neutron target interactions and neutron slowing down in the blanket itself. In the first wall and reflector the spectrum is considerably softened primarily because of slowing down in the blanket - reflector system. In Fig. VI.3-7 the gamma spectra in the first wall and the center of the blanket are compared. The gamma photon density in the first wall is larger than that in the blanket because of the large gamma production in iron.

VI.3.2.6 Radiation Damage to Structural Materials

The effect of blanket thickness on the maximum number of atomic displacements (dpa) per full power year in the SiC INPORT tubes and the HT-9 first wall is given in Table VI.3-5. The average dpa rate in the SiC tubes

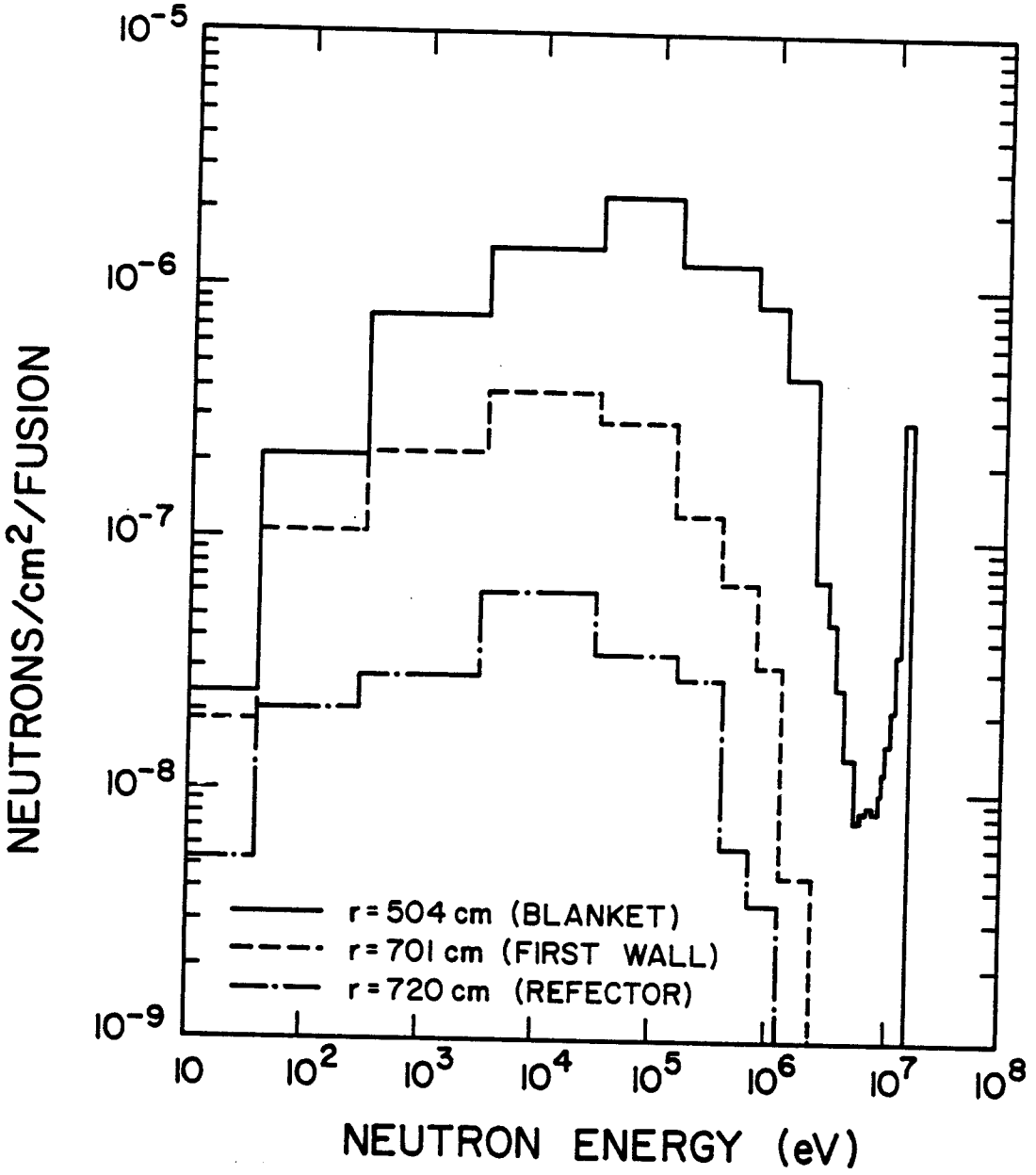

Figure VI.3-6 Neutron spectrum in the blanket, first wall, and reflector.

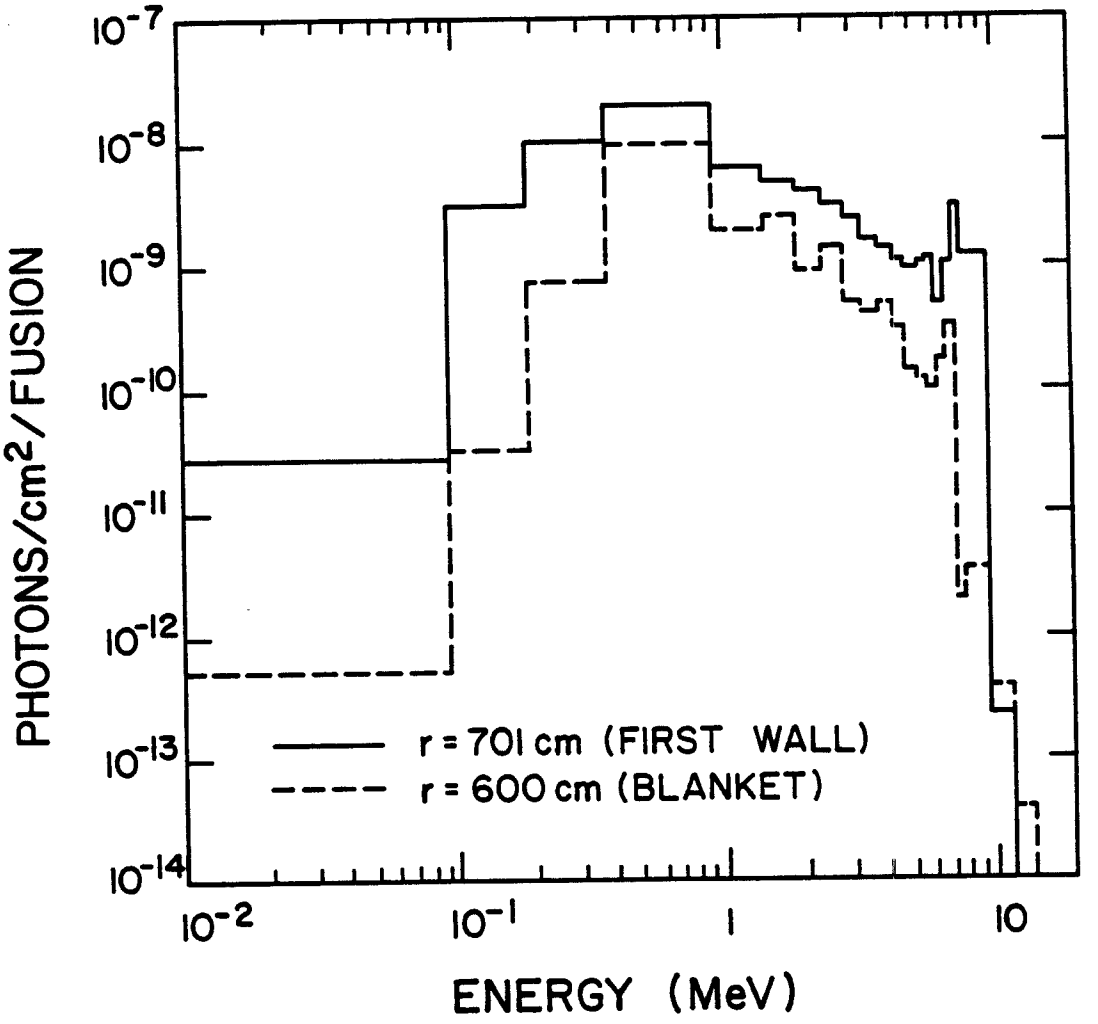

Figure VI.3-7 Gamma spectrum in the blanket and first wall.

Table VI.3-5 Effect of Blanket Thickness on Maximum DPA Rate (dpa/FPY)

Effective Blanket Thickness (cm)	0	60	66	70	80
SiC INPORT Tubes	---	116	118	119	121
HT-9 First Wall	25.360	3.411	2.688	2.289	1.525

increases slightly as the blanket thickness increases while the dpa rate in the ferritic steel first wall decreases as the blanket thickness increases. The reason is that the dpa cross section for iron peaks at 14.1 MeV and has a threshold energy of ~ 1 keV with the total dpa in iron decreasing as the spectrum becomes softer. On the other hand, the dpa cross section for ^{12}C peaks at ~ 3.5 MeV and has a lower threshold energy of ~ 0.2 keV resulting in an increase in the total dpa in C as the spectrum softens.

The helium and hydrogen gas production rates in the HT-9 first wall are given in Table VI.3-6 for different effective blanket thicknesses. The average gas production rate is found to decrease as the blanket thickness increases. The reason is that the hydrogen and helium production cross sections peak at 14.1 MeV. Furthermore, the reactions resulting in helium and hydrogen production are of a threshold nature with threshold energies in the low MeV energy range. The effect on gas production is more pronounced than the effect on dpa because of the lower dpa threshold energy. It is clear from the results that using INPORT tubes with an effective thickness of 66 cm reduces displacement damage and gas production in the HT-9 first wall considerably, allowing it to last for the whole reactor lifetime.

Table VI.3-6 Effect of Blanket Thickness on Gas Production Rate in First Wall (appm/FPY)

Effective Blanket Thickness (cm)	0	60	66	70	80
Helium	229.1	0.659	0.364	0.245	0.090
Hydrogen	736.9	2.451	1.380	0.942	0.362

Because of the large difference between the threshold energies for helium and dpa reactions, the helium to dpa ratio, which is an important parameter in microstructure calculations, decreases with spectrum softening. Figure VI.3-8 shows the effect of effective INPORT tube region thickness on dpa, helium production, and helium to dpa ratio in the HT-9 first wall. It is clear that the wall protection has a more pronounced effect on helium production. Consequently, the helium to dpa ratio decreases from a value of 9 for the unprotected wall to a value of 0.135 when an effective thickness of 66 cm is used. The helium to dpa ratio was also found to decrease as one moves inside the reflector. Figure VI.3-9 shows the spatial variation of dpa, helium production and helium to dpa ratio in the HIBALL reflector. The helium to dpa ratio decreases from 0.135 at the first wall to 0.019 at the back of the reflector.

A comparison between the results for the HT-9 first wall radiation damage obtained using the ANISN code and the results obtained using the ONETRAN code implemented at KfK, is given in Table VI.3-7. The differences obtained are attributed to the different methods used in the codes. ANISN treats the

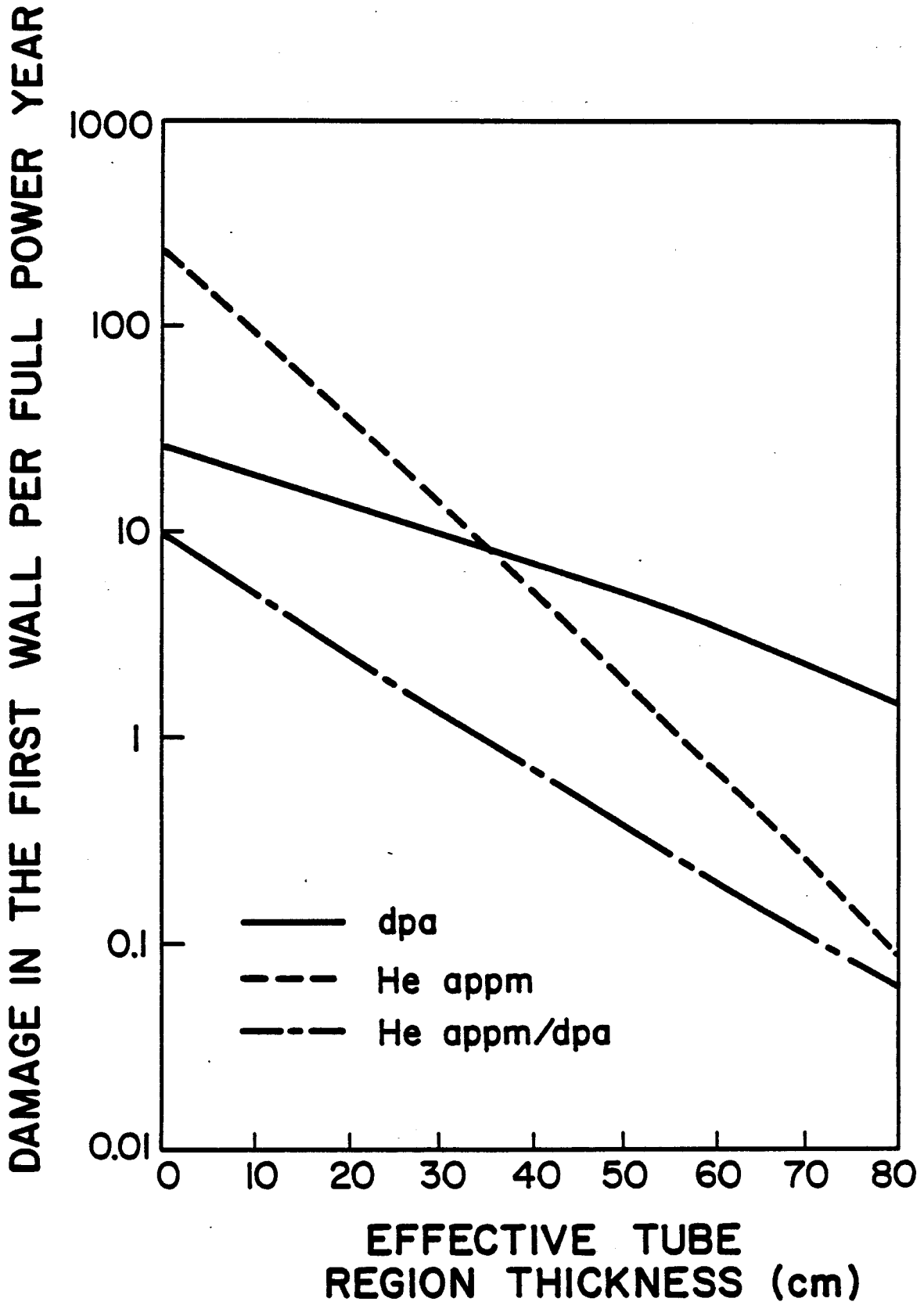

Figure VI.3-8 Effect of INPORT tubes on Damage in HT-9 first wall.

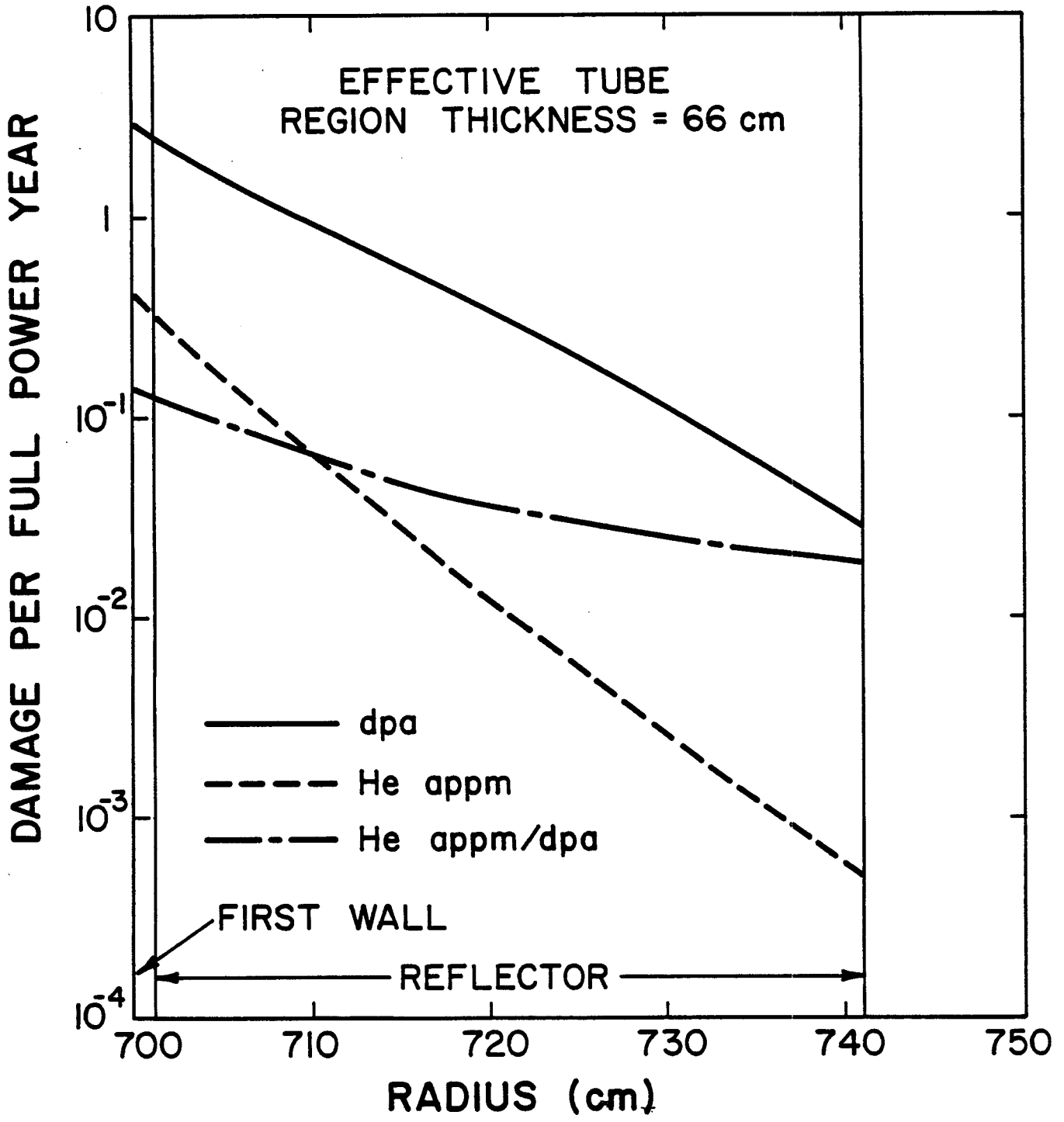

Figure VI.3-9 Spatial variation of damage in HT-9 structure in HIBALL reflector.

Table VI.3-7 Comparison Between First Wall Damage Results of ANISN and ONETRAN

	dpa/FPY	He appm/FPY	H appm/FPY
ANISN	2.688	0.364	1.380
ONETRAN	2.700	0.319	1.230

spatial variable in a finite difference form, while ONETRAN uses a finite element technique.

VI.3.2.7 Shield Design

Shielding of the reactor cavity does not pose special problems because of the simple geometrics involved as compared to shielding of the final focusing magnets discussed in section V.6. The reactor cavity shield is designed such that the biological dose rates outside the shield do not exceed ~ 5 mrem/hr during reactor operation. This design criterion has been set in order to allow hands-on maintenance of auxiliary components outside the reactor during operation. The shield for HIBALL consists of 95 v/o ordinary concrete (Type 3 concrete from reference 12) and 5 v/o water coolant. Ordinary concrete was considered because of its relatively low cost and the absence of materials which can cause high activation. The concrete used has a density of 2.3 g/cm^3 and the composition shown in Table VI.3-8.

A series of one-dimensional neutronics and photonics calculations was made to determine the flux attenuation as a function of shield thickness. Since a spherical geometry was used in the transport calculations, the results

Table VI.3-8 Concrete Composition

Element	Weight %
Calcium	24.33
Silicon	20.24
Oxygen	46.70
Carbon	4.92
Hydrogen	3.81

correspond to the conditions at the reactor midplane where the dose is expected to be greatest. Figure VI.3-10 shows the variation of neutron and gamma energy fluxes, at the shield outer surface, with shield thickness. It is clear that the neutron flux attenuates in the shield faster than does the gamma flux. This is due to the lack of high Z materials, which are more effective in attenuating gamma rays.

The neutron and gamma fluxes at the outer surface of the shield were used to determine the corresponding biological dose values for different shield thicknesses. The tissue composition used in these calculations is given in Table VI.3-9. The variation of the anticipated dose rate with shield thickness is shown in Fig. VI.3-11. A shield thickness of 3.5 m results in a dose rate of 2.64 mrem/hr which is less than the design limit of 5 mrem/hr set in this work. Almost all of the contribution to the dose comes from gamma radiation. The shielding effectiveness can be improved by using high Z materials such as lead to attenuate the gammas. Boron which has a high thermal neutron absorption cross section with only a soft 0.48 MeV gamma being produced can

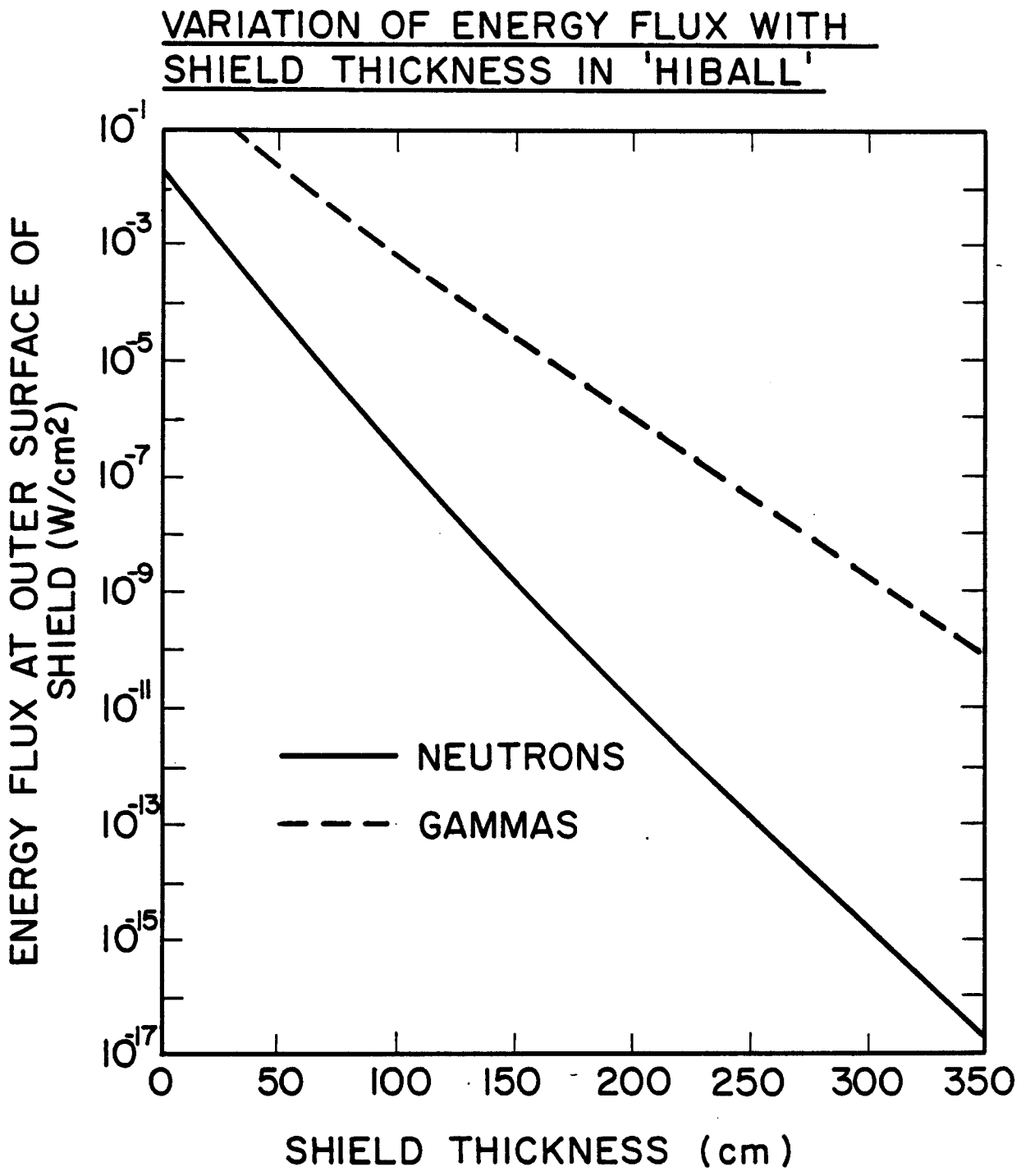

Figure VI.3-10 Variation of energy flux with shield thickness.

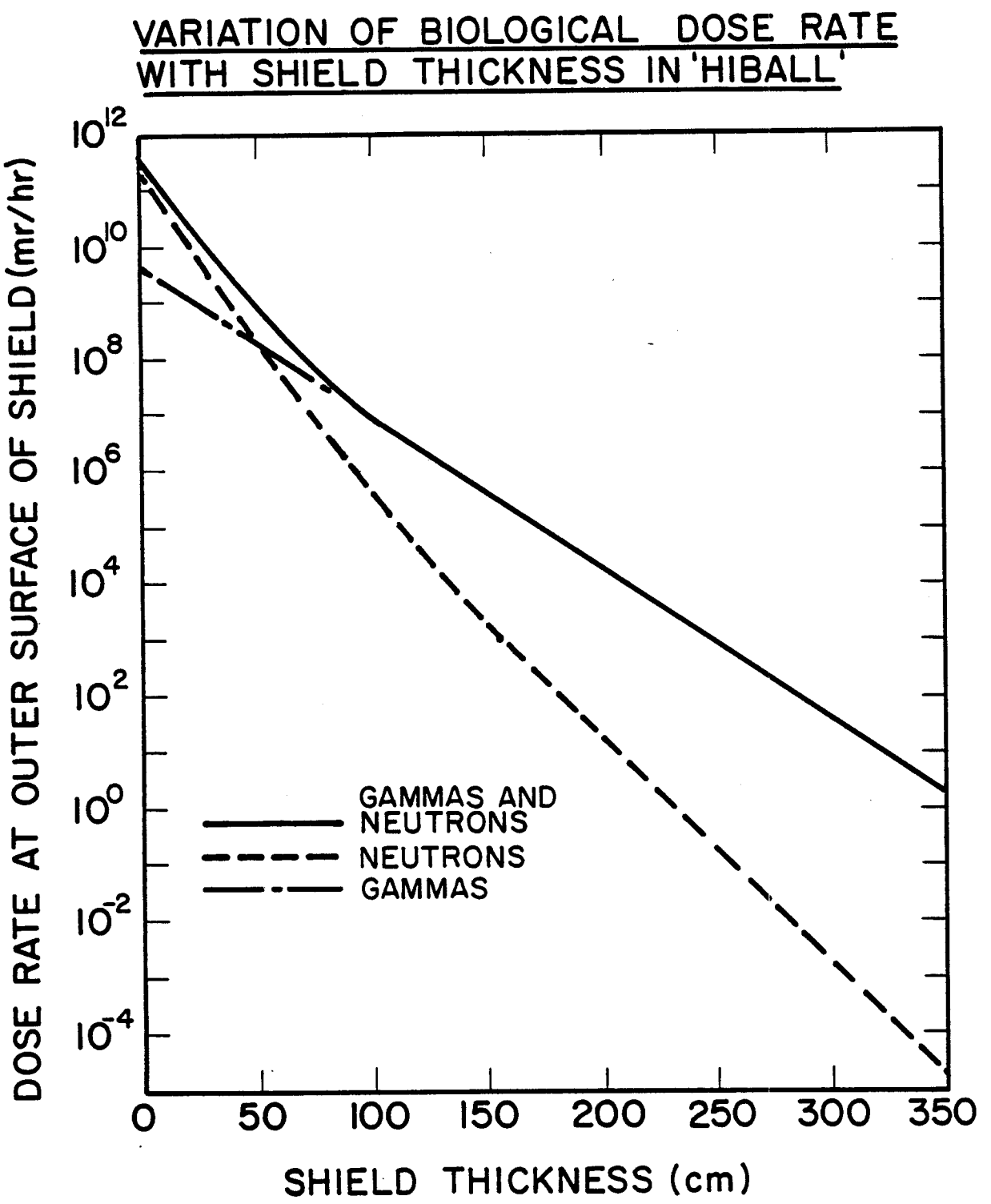

Figure VI.3-11 Variation of biological dose rate with shield thickness.

Table VI.3-9 Tissue Composition

Composition	Weight %
Oxygen	76.2
Carbon	11.1
Hydrogen	10.1
Nitrogen	2.6

also be used. However, cost considerations become an important factor if ordinary concrete is to be replaced by a more effective shield. A 3.5 m thick concrete shield is used in HIBALL, resulting in an extremely low dose rate of 2.64 mrem/hr outside the shield during reactor operation.

Figures VI.3-12 and VI.3-13 show the neutron and gamma spectra at different positions in the shield at the reactor midplane. It is clear that significant neutron and gamma spectrum softening occurs in the first 0.5 m of the shield. At this point most of the neutrons are in the thermal group. The neutron flux attenuates as one moves deep in the shield with the spectrum shape remaining nearly the same. The gamma spectrum assumes a nearly fixed shape peaking at ~ 0.2 MeV at 0.5 m inside the shield. No further significant spectrum softening occurs as one moves deep in the shield. Again, the gamma flux does not attenuate as fast as does the neutron flux because of the gamma production following neutron capture and the lack of high Z materials.

Figure VI.3-14 shows the spatial variation of power density in the reactor midplane. The contributions from neutron and gamma heating are also shown. The peak power density in the shield is 0.045 W/cm^3. The average

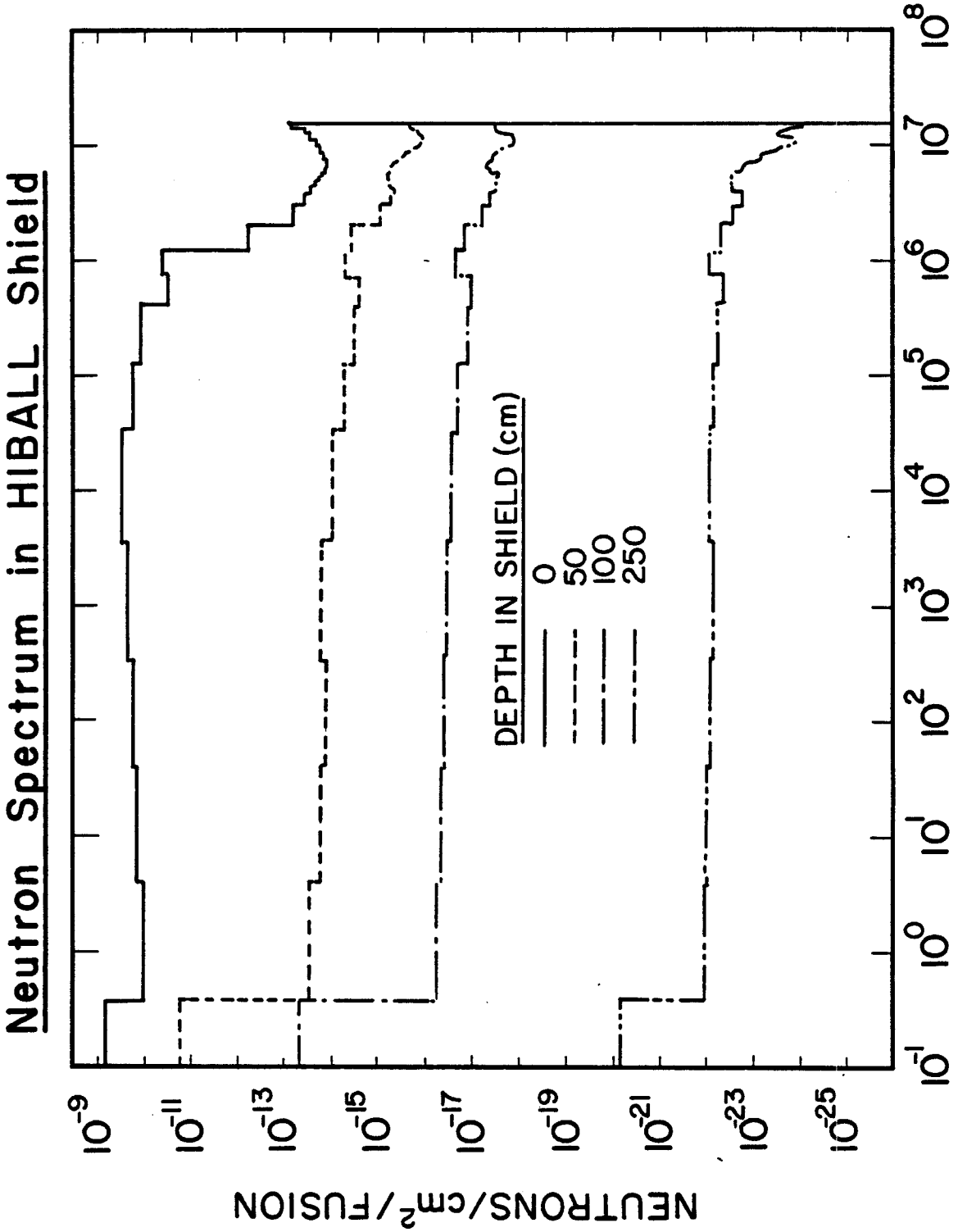

Figure VI.3-12 Neutron spectrum in HIBALL shield.

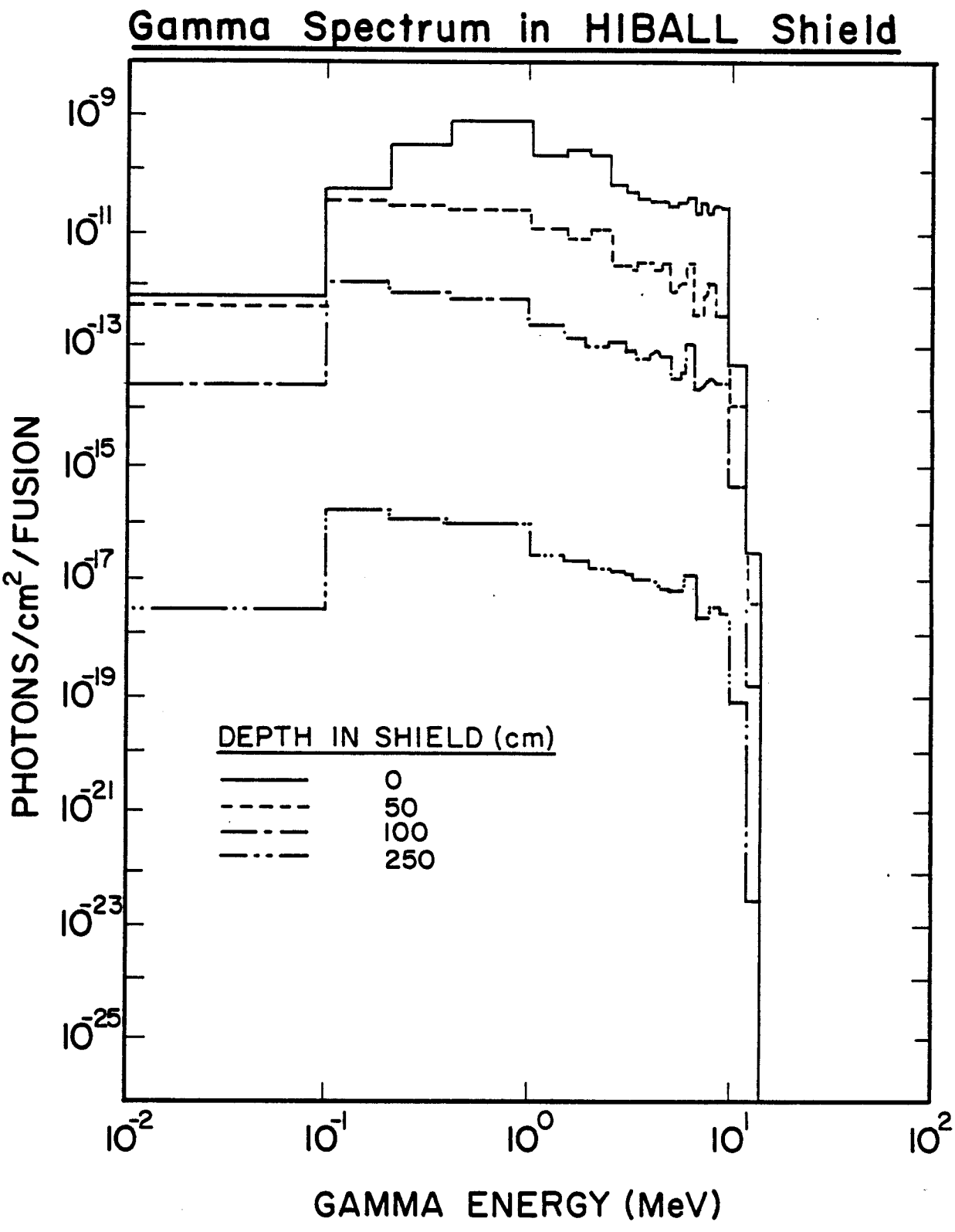

Figure VI.3-13 Gamma spectrum in HIBALL shield.

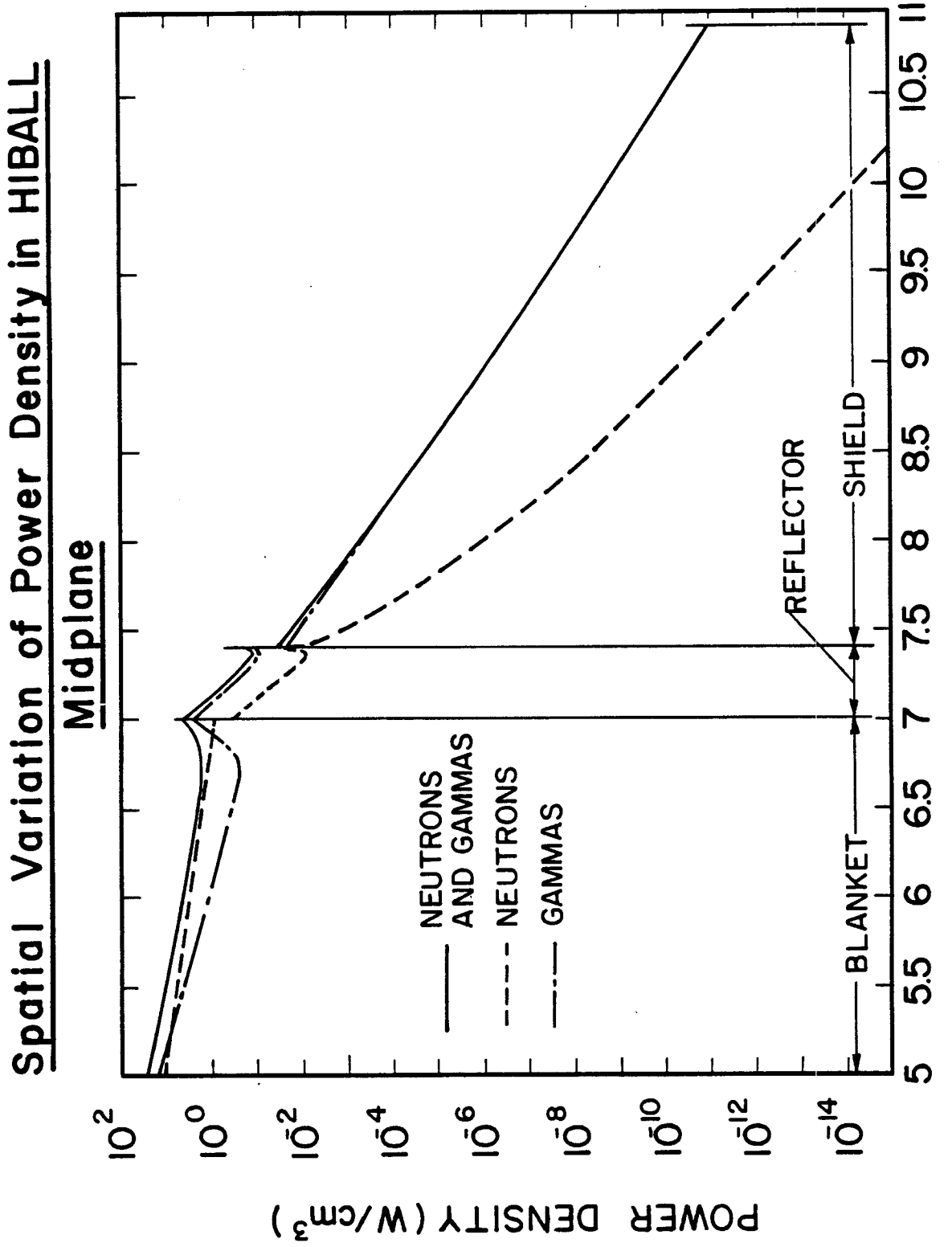

Figure VI.3-14 Spatial variation of power density at HIBALL midplane.

power density in the shield at the reactor midplane is found to be 1.83×10^{-3} W/cm^3.

VI.3.2.8 Summary

A one-dimensional spherical geometry neutronics and photonics analysis was performed to design the blanket and shield for HIBALL. The results show that by increasing the INPORT tube packing fraction, the tritium breeding ratio increases at the expense of energy multiplication. An effective tube region thickness of 66 cm was chosen resulting in an overall energy multiplication of 1.28 and a breeding ratio of 1.195. The INPORT tubes reduce radiation damage in the HT-9 first wall considerably allowing it to last for the whole reactor lifetime. A 3.5 m thick concrete shield was chosen resulting in an extremely low dose rate of 2.64 mrem/hr outside the shield during reactor operation.

VI.3.3 Three-Dimensional Time Integrated Studies

VI.3.3.1 Introduction

The one-dimensional spherical geometry calculations presented in section VI.3.2 are useful for survey studies and predicting conditions at the reactor midplane. However, the one-dimensional calculations are not capable of adequately modeling the HIBALL reactor in which a point source is at the the center of the reactor cavity which has a cylindrical shape with a conically shaped blanket at the top and a $Li_{17}Pb_{83}$ pool at the bottom. Furthermore, the HIBALL blanket/shield system is required to accommodate large penetrations for vacuum pumping which cannot be modeled in a one-dimensional analysis. These geometrical effects are expected to have an impact on the system's overall tritium breeding and energy multiplication. In this section, a three-dimensional neutronics and photonics analysis is presented which adequately models the HIBALL reactor cavity.

The neutronics and photonics problem for an inertial confinement fusion reactor is basically a time-dependent problem. However, the concern here is only with time-integrated quantities such as the tritium breeding ratio and the total nuclear heating which can be obtained using steady state transport calculations. In this work, neutron multiplication, spectrum softening, and gamma production in the target is accounted for by using the results of the target neutronics and photonics calculations presented in section III.1 as a source for the blanket and shield calculations.

VI.3.3.2 Reactor Geometrical Model and Method of Calculation

Figure VI.3-15 gives the blanket and shield configuration for HIBALL. The INPORT tube region has a thickness of 2 m and a height of 10 m. The INPORT tubes have a packing fraction of 0.33 with $Li_{17}Pb_{83}$ occupying 98 v/o of the tubes and the remaining 2 v/o occupied by SiC. The tube support structure is made of HT-9 and occupies 0.7 v/o of the tube region. A one meter deep $Li_{17}Pb_{83}$ pool exists at the bottom of the reactor cavity. The upper blanket consists of 30 segments. The design of an upper blanket segment is shown in Fig. VI.3-16. The upper blanket consists of 97 v/o $Li_{17}Pb_{83}$, 1 v/o HT-9, and 2 v/o SiC and is 50 cm thick. The $Li_{17}Pb_{83}$ in the region connecting the top blanket with the INPORT tubes helps protecting the HT-9 structure between the vacuum ducts. Thirty vacuum pumps are used to maintain the cavity pressure at 10^{-4} Torr. Each vacuum duct is 1 m wide and 0.6 m high. The first wall is 1 cm thick and is made of HT-9. The side wall is 12 m high. The top liner is 7 and 6 m above the midplane at reactor centerline and side wall, respectively. A 40 cm thick reflector consisting of 90 v/o HT-9 and 10 v/o $Li_{17}Pb_{83}$ is used. A 40 cm thick splash plate is used at the bottom of the reactor and is referred to as the bottom reflector in the following analysis. A 3.5 m thick biological shield made of 95 v/o ordinary concrete and 5 v/o H_2O coolant

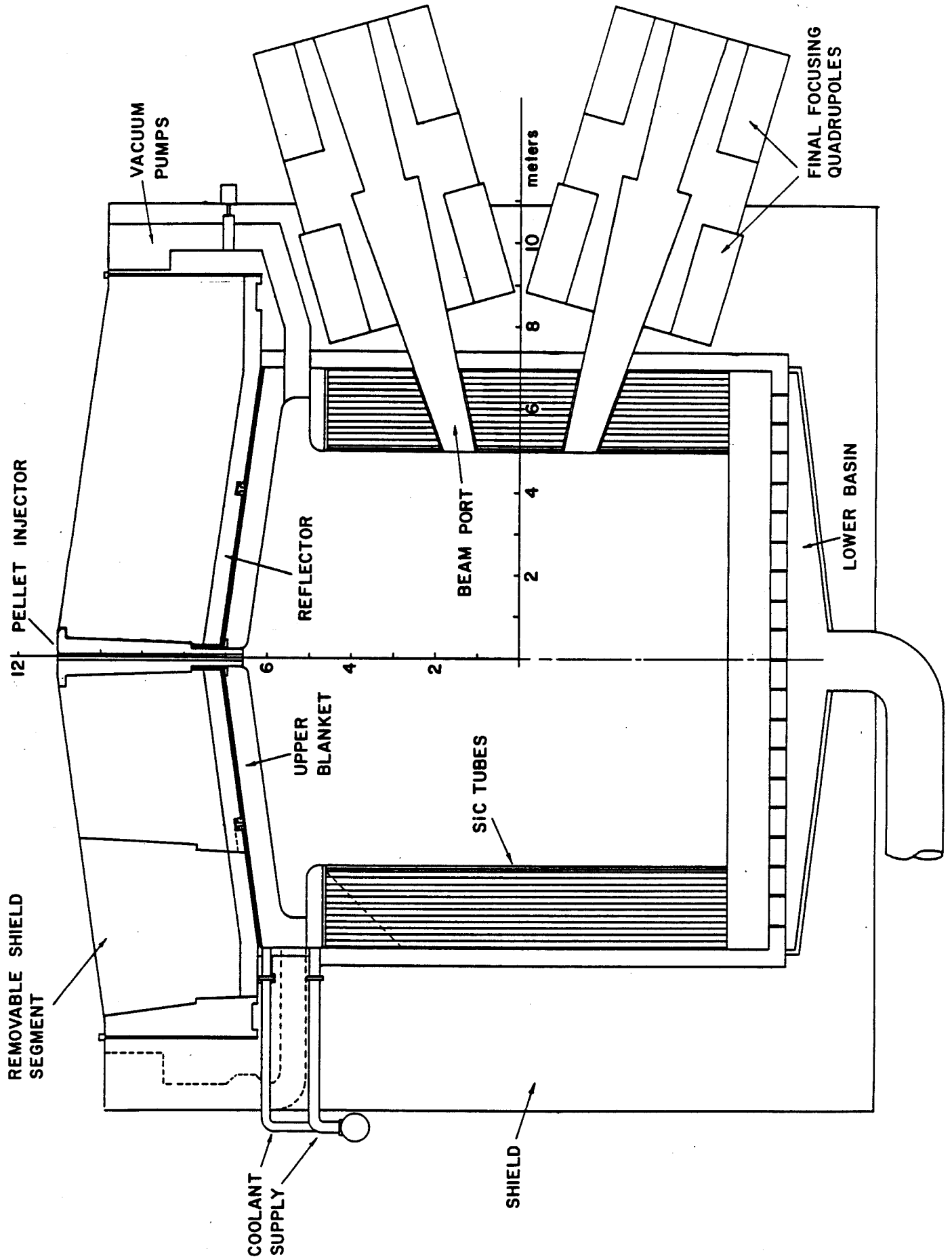

Figure VI.3-15 Blanket and shield configuration for HIBALL.

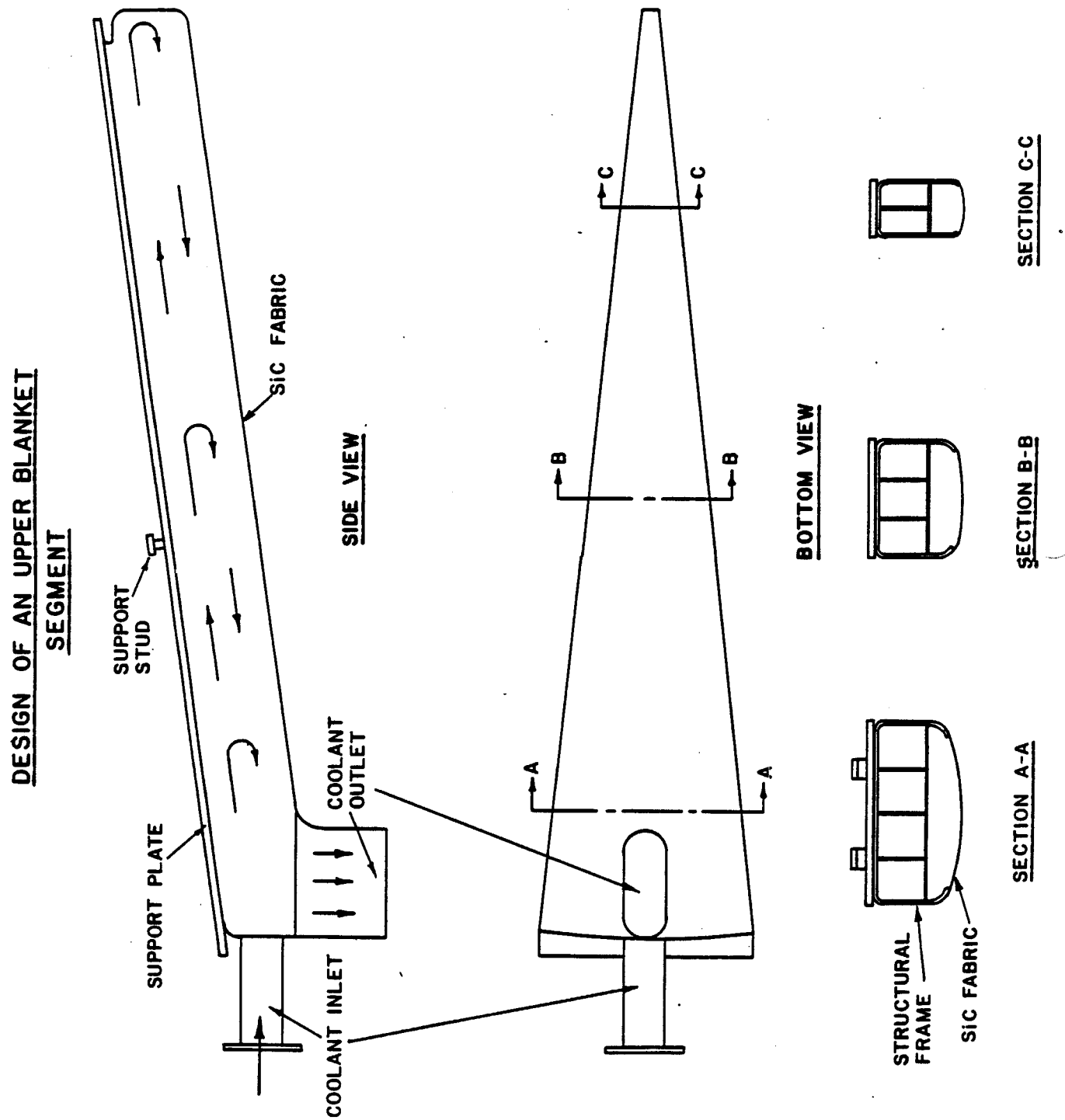

Figure VI.3-16 The design of an upper blanket segment.

surrounds the reactor. The penetration for target injection in the chamber top is very small and is not considered in this analysis. The total area of the 20 beam line penetrations in the INPORT tube region is 3.6 m^2 implying that these penetrations occupy only ~ 1% of the blanket volume. This is smaller than the statistical uncertainty in the results obtained in the Monte Carlo calculations used in this analysis. Furthermore, the geometrical effects of these penetrations have negligible effects on the tritium breeding ratio and the energy multiplication. Hence, the beam line penetrations are not modelled in the present analysis. Detailed radiation shielding analysis for the final focusing magnets is given in section V.6.

The neutronics and photonics calculations were performed using the multigroup three-dimensional Monte Carlo code MORSE.[13] A coupled 25 neutron-21 gamma group cross section library was used. The library consists of the RSIC DLC-41B/VITAMIN-C data library[3] and the DLC-60/MACKLIB-IV response data library.[4] The combinatorial geometry capability of the MORSE code was used to model the problem geometry. Volume detectors were used to estimate the quantities of interest in the different reactor zones. The results presented here are based on a DT yield of 400 MJ and a repetition rate of 5 Hz yielding 7.1×10^{20} fusion neutrons per second. A point isotropic source was used at the center of the reactor cavity with neutron and gamma spectra obtained from the target neutronics and photonics calculations. 4000 histories were used in the Monte Carlo calculations yielding less than 2% statistical uncertainties in the estimates for the tritium breeding ratio and the energy multiplication.

Because of symmetry, only 1/60 of the reactor was modeled with reflecting albedo boundaries used at the planes of symmetry. This corresponds to a "pie slice" with an azimuthal angle of 6°. The geometry for the computational model used is given in Fig. VI.3-17. To quantify nuclear heating in the

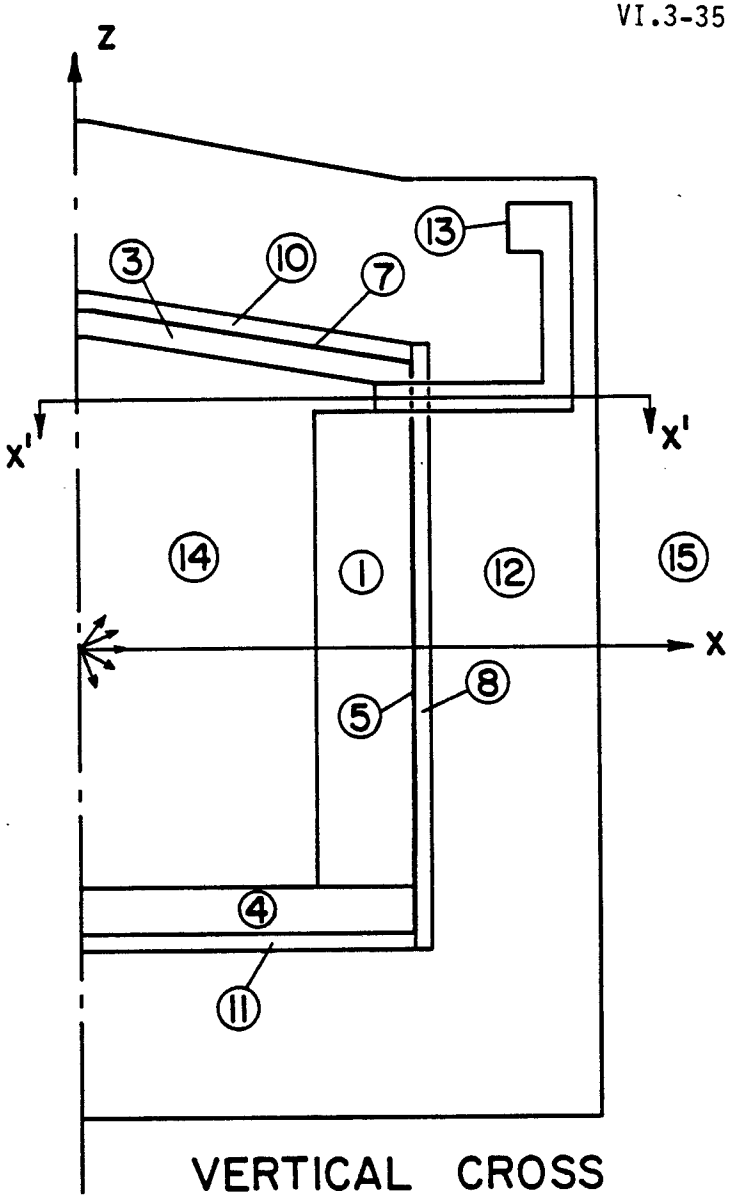

VERTICAL CROSS SECTION AT PLANE y=0

ZONE	DESCRIPTION
1	INPORT TUBES
2	BLANKET REGION AT VACUUM DUCT
3	TOP BLANKET
4	BOTTOM LiPb POOL
5	SIDE WALL
6	WALL AT DUCT
7	TOP LINER
8	SIDE REFLECTOR
9	REFLECTOR AT DUCT
10	TOP REFLECTOR
11	BOTTOM REFLECTOR
12	BIOLOGICAL SHIELD
13	VACUUM PUMP

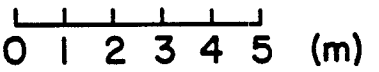

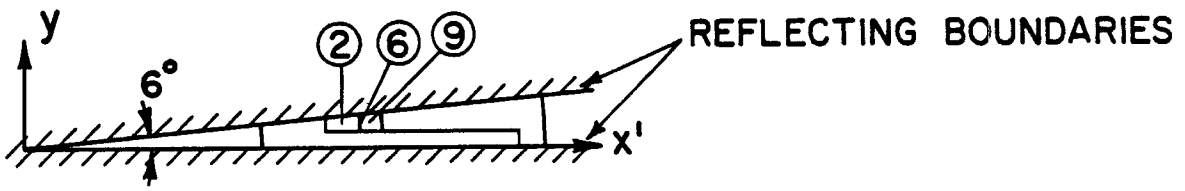

CROSS SECTION x'x'

Figure VI.3-17 HIBALL geometry for Monte Carlo calculations.

vacuum pump, a 2 cm thick region consisting of 50 v/o 316 SS and 50 v/o Cu is designated as zone 13 to simulate the cryo-panels. Zones 14 and 15 represent inner and outer vacuum regions, respectively.

VI.3.3.3 Scalar Flux

Table VI.3-10 gives the average neutron and gamma scalar fluxes in the different zones. The fractional standard deviation based on a 68% confidence interval is also included. It is clear from the results that the fractional standard deviation is very small in the breeding blanket zones and is relatively large in the optically thin regions such as the first wall. The results show that while the gamma flux is about two orders of magnitude less than the neutron flux in the breeding blanket zones, it is only one order of magnitude less than the neutron flux in the reflector zones. This results from the large gamma production following neutron capture in the HT-9 structure.

VI.3.3.4 Tritium Production

Table VI.3-11 shows the results for tritium production per DT fusion reaction in the different reactor zones. The contributions from $^{6}Li(n,\alpha)$ and $^{7}Li(n,n'\alpha)$ reactions are shown separately. It is clear that the contribution from ^{7}Li represents $\sim$ 2% of the total tritium production in the breeding blanket region. The reason is that the number of Pb(n,2n) reactions occurring in the $Li_{17}Pb_{83}$ blanket is much larger than that of $^{7}Li(n,n'\alpha)$ reactions. The resulting (n,2n) neutrons are well below the threshold energy for $^{7}Li(n,n'\alpha)$ reaction and hence can produce tritium only through the $^{6}Li(n,\alpha)$ reaction. In the reflector region the ^{7}Li contribution to tritium production is very small because of the neutron spectrum softening in the breeding blanket.

We notice that as much tritium production occurs in the top blanket as in the bottom $Li_{17}Pb_{83}$ pool, even though the top blanket is only half as thick as

Table VI.3-10 Average Scalar Flux (Particles/cm^2/Fusion)

Region	Zone Number	Neutrons	Gammas
Breeding Blanket	1	3.191(-6) [.015]*	3.237(-8) [.026]
	2	1.691(-6) [.071]	4.453(-9) [.349]
	3	2.937(-6) [.023]	2.448(-8) [.056]
	4	1.708(-6) [.043]	1.108(-8) [.068]
First Wall	5	8.302(-7) [.041]	2.529(-8) [.118]
	6	9.282(-7) [.181]	1.124(-8) [.600]
	7	1.340(-6) [.047]	4.328(-8) [.164]
Reflector	8	2.384(-7) [.034]	1.274(-8) [.048]
	9	4.470(-7) [.153]	3.213(-8) [.245]
	10	3.789(-7) [.044]	2.230(-8) [.070]
	11	8.354(-8) [.126]	3.739(-9) [.132]

*Fractional Standard Deviation

Table VI.3-11 Tritium Production (Tritons/Fusion)

Region	Zone Number	$^{6}Li(n,\alpha)T$	$^{7}Li(n,n'\alpha)T$
Breeding Blanket	1	0.729	0.018
	2	0.014	0.00001
	3	0.212	0.004
	4	0.235	0.004
	Region Total	1.190	0.026
Reflector	8	0.022	0.000002
	9	0.001	0.0000001
	10	0.009	0.000002
	11	0.002	0.0000001
	Region Total	0.034	0.000004
System Total		1.224	0.026

the bottom pool and includes 1 v/o HT-9 structure. The reason in that the 2 v/o SiC present in the top blanket enhances neutron slowing down and hence increases the tritium breeding effectiveness. In fact, our results show that the breeding capability of $Li_{17}Pb_{83}$ can be improved considerably by enriching Li and/or using moderators in the blanket. The improvement in systems using $Li_{17}Pb_{83}$ is much more pronounced than that in systems using other breeding materials because most of the contribution to breeding in $Li_{17}Pb_{83}$ case comes from the $^{6}Li(n,\alpha)$ reaction which has a 1/v cross section in the low energy region.

The overall tritium breeding ratio is found to be 1.25. The confidence interval for the estimated breeding ratio is 0.025 which is 2% of the obtained estimate. The overall tritium breeding ratio obtained here with the actual reactor cavity cylindrical geometry is larger than that obtained from the one-dimensional spherical geometry calculations (1.195). The reason is that in the spherical geometry case, all source neutrons are incident on the blanket perpendicularly to its inner surface and hence will see the same blanket thickness. On the other hand, the source neutrons emitted isotropically at the center of the cylindrical cavity impinge on the inner surface of the blanket at different angles and hence will see larger blanket thicknesses. In other words, the neutron source is surrounded by a larger volume of breeding material in the actual cylindrical case as compared to the case of an equivalent spherical blanket.

VI.3.3.5 Nuclear Heating

Table VI.3-12 shows the nuclear energy deposition for neutrons and gammas in the different zones. The average power density is also included. It is clear that the contributions from neutron and gamma heating are nearly the same in the breeding blanket while the gamma contribution in the first wall and reflector is about an order of magnitude higher than the neutron contribution. This results from gamma generation in the HT-9 structure. About 60% of the total reactor thermal power comes from gamma heating. The energy deposited in the biological shield is 0.06 MeV/fusion which corresponds to a power of 6.82 MW. This represents only 0.27% of the total reactor thermal power. Only the energy deposited in the blanket, first wall, and reflector are considered as recoverable energy. The total recoverable neutron and gamma energy in the reactor per DT fusion is 17.553 ± .292 MeV which is slightly less than that obtained for an equivalent spherical reactor (17.95 MeV). The

Table VI.3-12 Nuclear Heating

Region	Zone Number	Energy Deposition (MeV/fusion)		Average Power Density (W/cm^3)
		Neutrons	Gammas	
Breeding Blanket	1	4.806	4.839	4.409
	2	0.074	0.017	3.911
	3	1.339	1.147	3.515
	4	1.430	1.007	1.800
	Region Total	7.649	7.010	4.409
First Wall	5	0.004	0.050	1.222
	6	0.0001	0.0004	2.010
	7	0.003	0.039	3.068
	Region Total	0.007	0.089	1.653
Reflector	8	0.155	1.628	0.939
	9	0.007	0.066	1.020
	10	0.070	0.733	1.465
	11	0.013	0.126	0.257
	Region Total	0.245	2.553	0.941
System Total		7.901	9.652	3.345

reason is that more tritium production is obtained in the cylindrical case with less neutrons being captured in the HT-9 structure. A neutron absorbed in ^{6}Li releases ~ 4.8 MeV while if it is captured in the HT-9 structure ~ 7 MeV is released.

In order to get a statistically adequate estimate of nuclear heating in the vacuum pump with a reasonable number of histories, a Monte Carlo calculation with an angular source biasing was performed. In this run, 4000 histories were used. A volumetric nuclear heating rate of 6×10^{-11} W/cm^3 was obtained in the vacuum pump (zone 13). The fractional standard deviation was 0.25. Because the vacuum ducts do not see direct line-of-sight source neutrons and they are bent twice, neutron streaming through the ducts was found to not cause any serious problem to the vacuum pump.

The energy flow for the HIBALL fusion reactor design is illustrated in Fig. VI.3-18. The values given for the power correspond to one reactor cavity. Therefore, these values need to be multiplied by 4 to calculate the power from the whole power plant. This corresponds to a total power plant thermal power of 10,193 MW(th). The overall energy multiplication defined as the total energy deposited in the system, including the energy deposited by X-rays and target debris at the first surface of the blanket, divided by the fusion reaction yield of 17.6 MeV, is found to be 1.274.

VI.3.3.6 Summary

A three-dimensional Monte Carlo neutronics and photonics analysis was performed for the HIBALL reactor cavity. An overall tritium breeding ratio of 1.25 and an overall energy multiplication of 1.274 were obtained. The tritium breeding ratio is higher than that for the equivalent spherical reactor cavity. Nuclear heating in the vacuum pump was found to be very small. The power

Figure VI.3-18

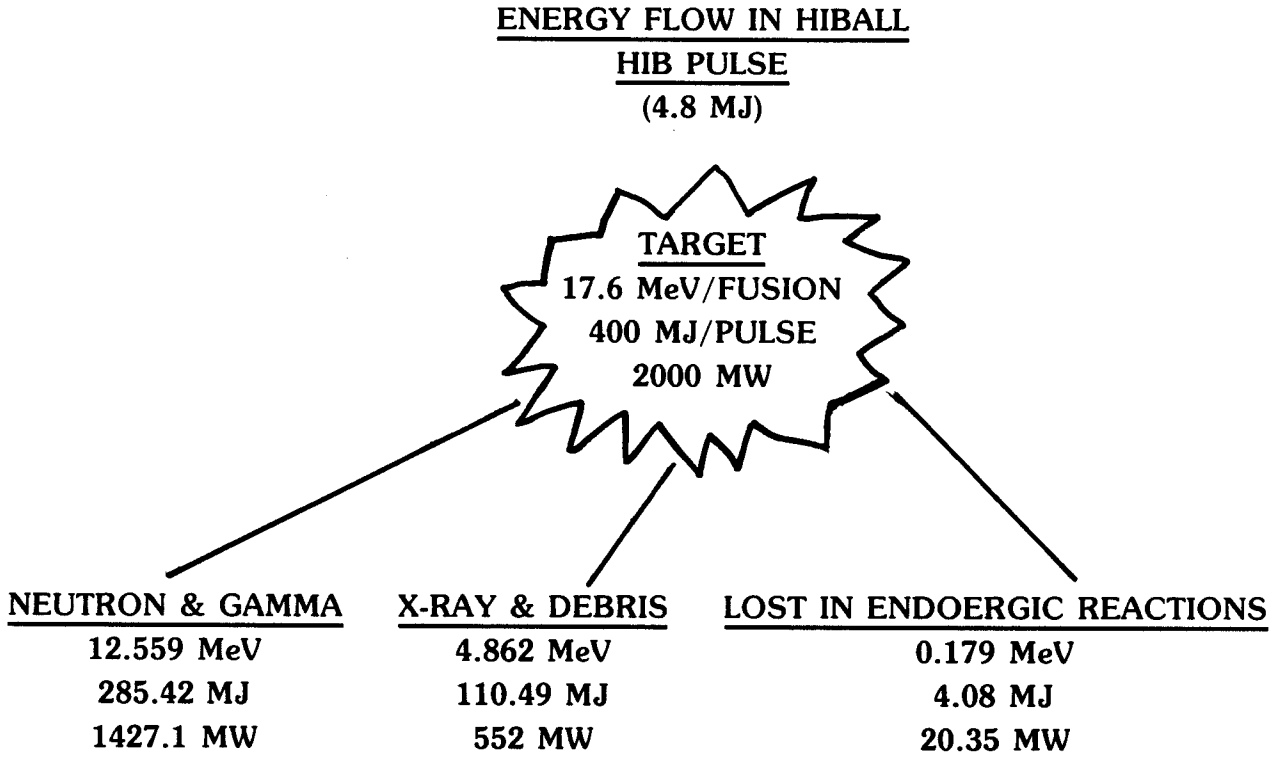

	NEUTRON & GAMMA	X-RAY & DEBRIS	TOTAL	
BREEDING BLANKET	14.659 MeV 333.16 MJ 1667.5 MW	4.862 MeV 110.49 MJ 552 MW	19.521 MeV 443.65 MJ 2219.5 MW (87.05%)	
WALL	0.096 MeV 2.24 MJ 10.8 MW		0.096 MeV 2.24 MJ 10.8 MW (0.42%)	22.415 MeV 509.39 MJ 2548.3 MW
REFLECTOR	2.798 MeV 63.5 MJ 318.0 MW		2.798 MeV 63.5 MJ 318.0 MW (12.53%)	

OVERALL ENERGY MULTIPLICATION = 1.274

in the biological concrete shield represents only 0.27% of the total reactor thermal power. The thermal power for the HIBALL power plant is 10,193 MW(th).

VI.3.4 Time-Dependent Neutronics and Photonics

VI.3.4.1 Introduction

In an inertial confinement fusion reactor the neutron source has a pulsed nature because of the very short burn time over which the fusion reactions occur (10-100 ps). Furthermore, the neutron pulse does not reach the first surface of the blanket until ~ 100 ns after the burn and the neutron slowing down time in the blanket is much greater than the duration of the neutron source. Significant softening of the energy spectrum of neutrons escaping from the target results from neutron interaction with the dense ($\sim 10^{25}/cm^3$) fuel and surrounding tamper material. This leads to a considerable time of flight spread as neutrons reach the first surface. Therefore, time dependent neutronics studies are essential for the proper analysis of inertial confinement fusion reactors.

As a result of the pulsed nature of the neutron source, high instantaneous damage rates are present in an inertial confinement fusion reactor wall and structure. This can lead to significant changes in the microstructure[14] of the first wall material. It has also been found that high instantaneous dpa rates result in higher recombination rates with the void growth being inhibited and swelling decreased.[15] Accurate instantaneous damage rates can be calculated by performing time-dependent neutronics studies. Previous time dependent neutronics studies have been used to calculate the instantaneous dpa rate in the first wall of a laser fusion reactor[16] and an electron beam fusion reactor.[17] No correction for the time of flight spread of neutrons within each energy group was made in these studies.

A modified version of the time dependent discrete ordinates code TDA[18] has been used to perform time-dependent neutronics analysis for HIBALL. The effects of the INPORT first wall protection concept on the peak instantaneous and average dpa and gas production rates in the ferritic steel first wall have been investigated. The steady state discrete ordinates ANISN[1] code was used to determine the average time integrated radiation damage rates.

Energy deposition in the porous tubes and first wall of the HIBALL fusion reactor is important in the determination of their structural integrity. The temporal and spatial dependence of energy deposition is also required for stress analysis studies. The energy deposition rate integrated over the volume of the blanket of a laser fusion reactor was calculated in a previous study.[19] However, no detailed time dependent fluxes or energy deposition rates at different points were given. In this work, the instantaneous energy deposition rates at different positions in the blanket and first wall are calculated.

VI.3.4.2 Heavy Ion Beam Reactor Computational Model

A schematic of the blanket, first wall, reflector, and shield configuration for the HIBALL fusion reactor is given in Fig. VI.3-1. The nuclide densities used in the calculations are given in Table VI.3-1 The results presented here for the damage and energy deposition rates are based on a DT yield of 400 MJ which corresponds to 1.42×10^{20} source neutrons per pulse. A repetition rate of 5 Hz is used to determine the total dpa and helium production in the first wall per full power year (FPY).

The steady state discrete ordinates code ANISN was used to perform detailed neutronics and photonics calculations within the target, giving the time integrated energy spectrum of neutrons escaping from the target as explained in section III.1. This spectrum was used as a source for the time

dependent blanket neutronics analysis performed using the time dependent multi-group discrete ordinates code TDA. ANISN was used to calculate the time integrated reaction rates. Since the particle transport codes used are one-dimensional, spherical geometry was used in the blanket calculations and hence the results represent the worst conditions at the central plane of the cylindrical reactor. A P3-S8 approximation was used in the transport calculations. A coupled 25 neutron-21 gamma group cross section library has been used. This library consists of the RSIC DLC-41B/VITAMIN-C data library[3] and the DLC-60/MACKLIB-IV response data library.[4]

VI.3.4.3 Neutron Source

The target, though absolutely very small, is an extremely dense medium composed primarily of light elements. This results in a substantial collision probability for fusion neutrons created within it. The 14.1 MeV fusion neutrons are degraded in energy as a result of elastic collisions with the fuel (DT) and inelastic collisions with the high Z materials (Pb). Neutron multiplication also results from (n,2n) and (n,3n) reactions with the constituent elements of the target. Since the neutrons escaping from the target represent the neutron source for the blanket neutronics calculations, it is essential to perform detailed neutronics calculations for the target to account accurately for spectrum softening and neutron multiplication.

Since the burn time of the target (10-100 ps) is much greater than the slowing down time of fusion neutrons in the extremely dense target ($\sim$ 0.1 ps), steady state calculations yield useful information. Furthermore, since the burn time is much smaller than the time neutrons take to reach the first surface of the blanket including the time of flight spread, neutrons are assumed to be emitted in a pulse with zero time duration ($\delta(t)$). This implies that the time integrated spectrum of the neutrons leaking from the target as calcu-

lated by the steady state code ANISN gives the correct neutron source spectrum. In other words, if $n_L(E,t)$ is the exact spectrum of neutrons leaking from the target at time t within the burn, the time integrated spectrum calculated by ANISN is given by

$$n_L(E) = \int_{t_B} n_L(E,t)dt \ , \qquad \text{(VI.3-1)}$$

where t_B is the burn time. Since the burn time is very small, all neutrons leaking at different times during the burn are assumed to be emitted at t=0 and the source for the blanket calculations is given by

$$S(E,t) = n_L(E)\ \delta(t) \ . \qquad \text{(VI.3-2)}$$

Since the target has a very small radius compared to the radius of the reactor cavity, the neutron source is represented by a point source at the center of the reactor. Furthermore, neutrons are emitted isotropically from the target and the complete representation of the neutron source is given by

$$S(\mu,r,E,t) = n_L(E)\ \delta(r)\ \delta(t)\ \delta(\mu-1) \ . \qquad \text{(VI.3-3)}$$

Detailed neutronics and photonics calculations have been performed for the HIBALL target as discussed in Section III.1. The results show that a target neutron multiplication of 1.046 is obtained. This results mainly from (n,2n) reactions in the dense DT fuel core and LiPb pusher. The average energy of neutrons leaking from the target is 11.98 MeV implying that 71.2% of the fusion energy is carried by the emerging neutrons. The spectrum of neutrons leaking from the target, $n_L(E)$, is given in Fig. VI.3-19.

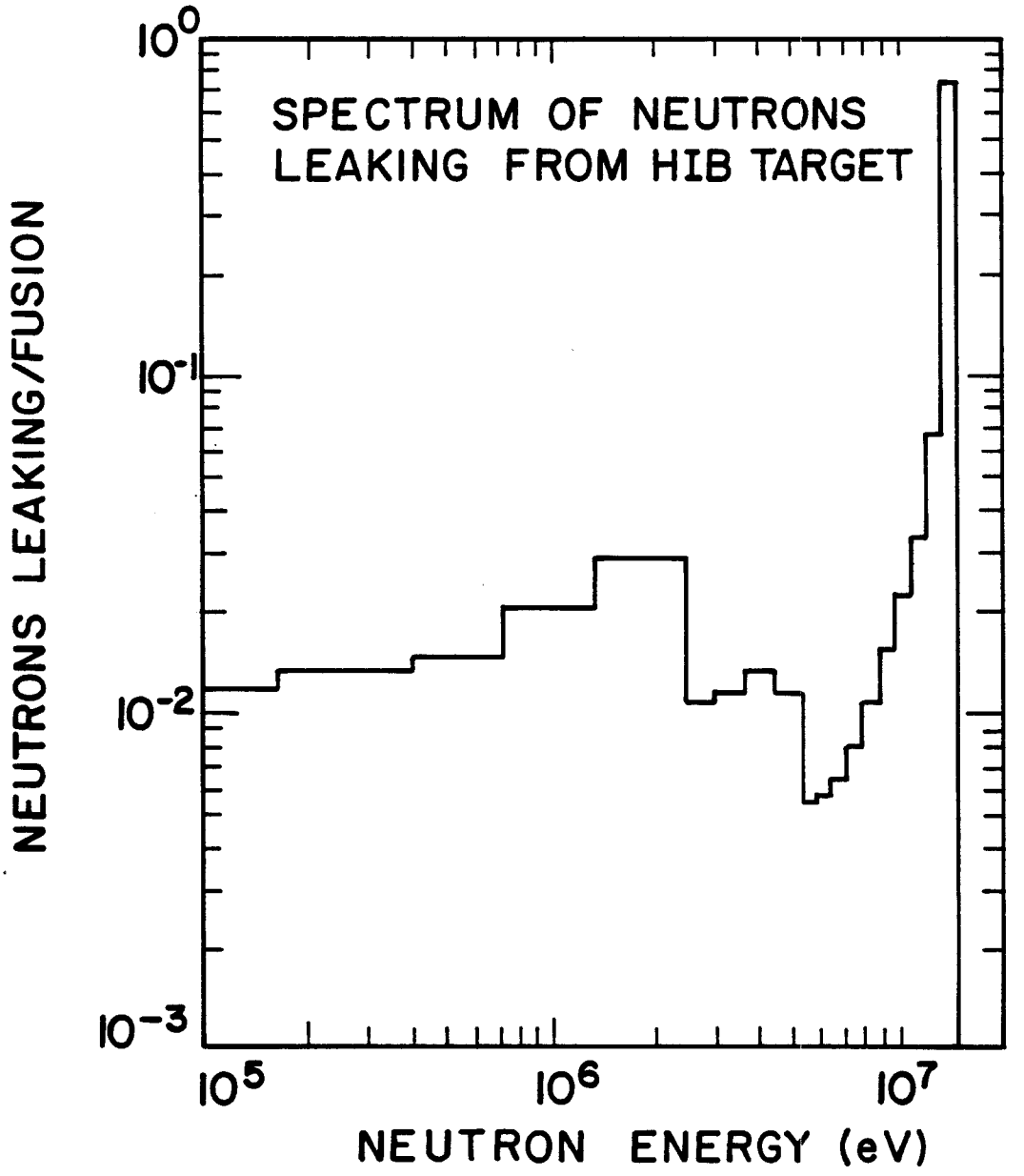

Fig. VI.3-19 Spectrum of neutrons leaking from the pellet.

As neutrons travel from the target to the first surface of the blanket considerable time of flight spreading occurs because of the broad energy distribution of these neutrons. The arrival time spectrum at the first surface located 5 m from the neutron source is shown in Fig. VI.3-20. The numbers at the bottom of the graph indicate the energy groups associated with the various times. Since all neutrons in a specified energy group are forced by the multigroup treatment of the neutronics code to travel at the same velocity corresponding to the average group energy, these neutrons will arrive at the first surface simultaneously and no time of flight spread corresponding to the energy group width will be observed. In order to preserve the correct arrival time spectrum at the first surface, source neutrons are given artificial birth times associated with their energies within the group. If the time of flight spread corresponding to the gth energy group width is Δ_g, the modified neutron source for group g is represented by a rectangular pulse with a time duration of Δ_g. This necessary correction for time of flight spread of neutrons within each energy group was not made in the previous time dependent neutronics analysis of inertial confinement fusion reactors.

VI.3.4.4 Time Dependent Neutron Spectrum in the HT-9 First Wall

A version of the time dependent multigroup discrete ordinates code TDA, modified to facilitate its use for the analysis of inertial confinement fusion reactors[20], has been used to perform time dependent neutronics and photonics calculations for the HIBALL blanket and reflector model illustrated in Fig. VI.3-1. For comparison, calculations have been also made for the case of an unprotected wall.

The source for the problem involves Dirac delta functions which are quite difficult to represent with standard finite difference methods. To circumvent this difficulty the uncollided flux is determined analytically and an analytic

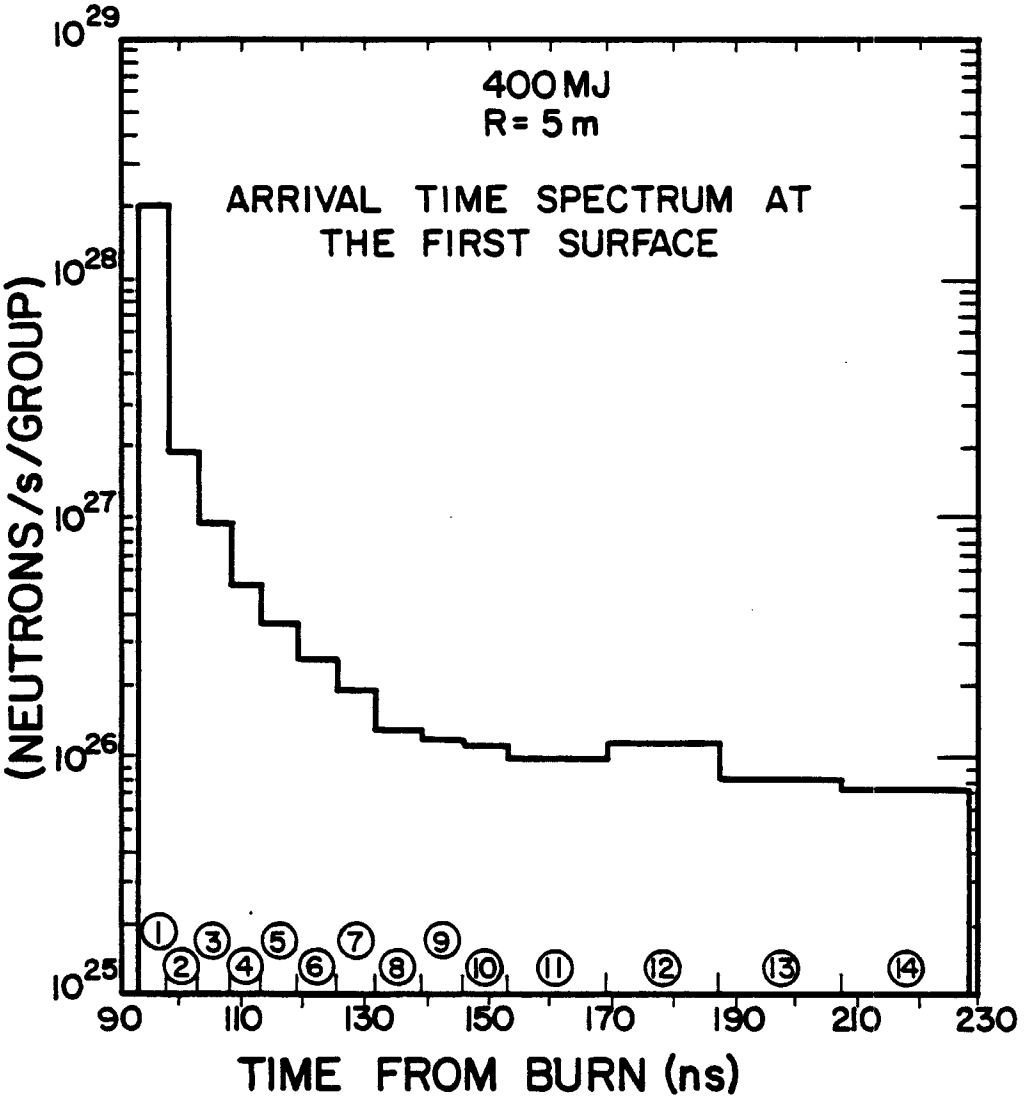

Figure VI.3-20 Arrival time spectrum at the first surface of the blanket.

first collision source is used by the code to determine the collided part of the flux.

The neutron spectrum in the protected ferritic steel first wall is illustrated in Fig. VI.3-21. The results are shown at 10 ns and 70 ns after the uncollided neutrons of the highest energy strike the wall. The neutron spectra in the unprotected wall at different times following the arrival of the leading edge of the pulse at the wall are given in Fig. VI.3-22. Comparing the results in Figs. VI.3-21 and VI.3-22, we notice that significant neutron attenuation occurs in the INPORT tubes.

Neutrons slowed down in the inner blanket region take a relatively long time to reach the first wall. This time depends on the slowing down time of neutrons in the blanket, the speed of slowed down neutrons, and the position within the blanket at which the slowing down interaction occurs. At early times, following the arrival of the fastest uncollided neutrons at the first wall, most of the neutrons in the first wall are in the high energy groups. Only neutrons which have been slowed down in the porous tubes close to the first wall are able to arrive at the wall by this time. Neutrons slowed down in the wall itself result in the relatively low peak at $\sim$ 1 MeV in Fig. VI.3-21. At 60 ns later, most of the high energy neutrons have already passed the first wall while neutrons slowed down in the blanket are still arriving at the first wall primarily because of the relatively long slowing down time of neutrons in the blanket. Therefore, the time dependent spectrum and consequently the instantaneous damage rates in the first wall are governed by two factors; the time of flight spread and the slowing down time spread in the blanket. In lead, which is the main constituent of the blanket, the slowing down time from 14.1 MeV to the inelastic threshold energy of 0.57 MeV is about 1 μs. At energies below 0.57 MeV, slowing down is due to elastic scattering

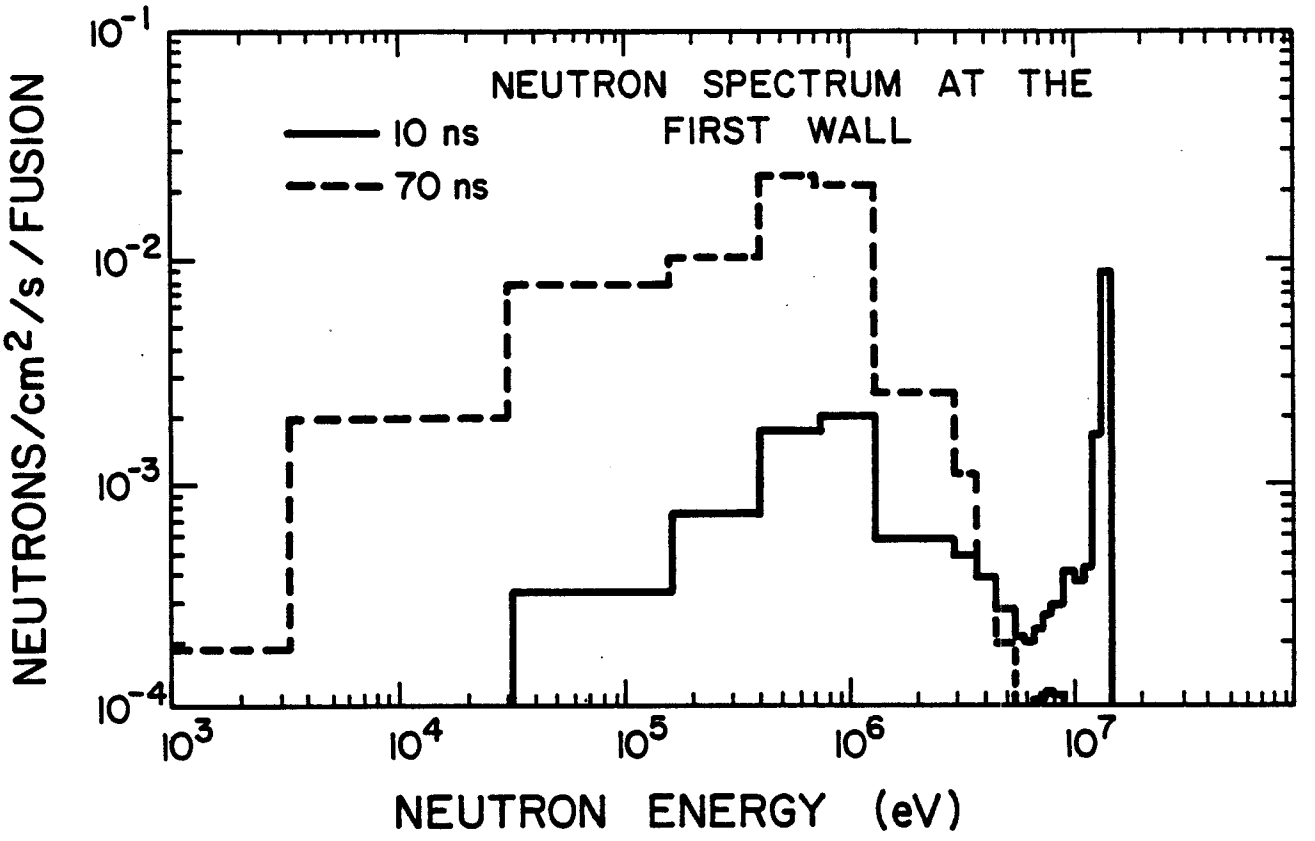

Figure VI.3-21 Neutron spectrum in HIBALL first wall.

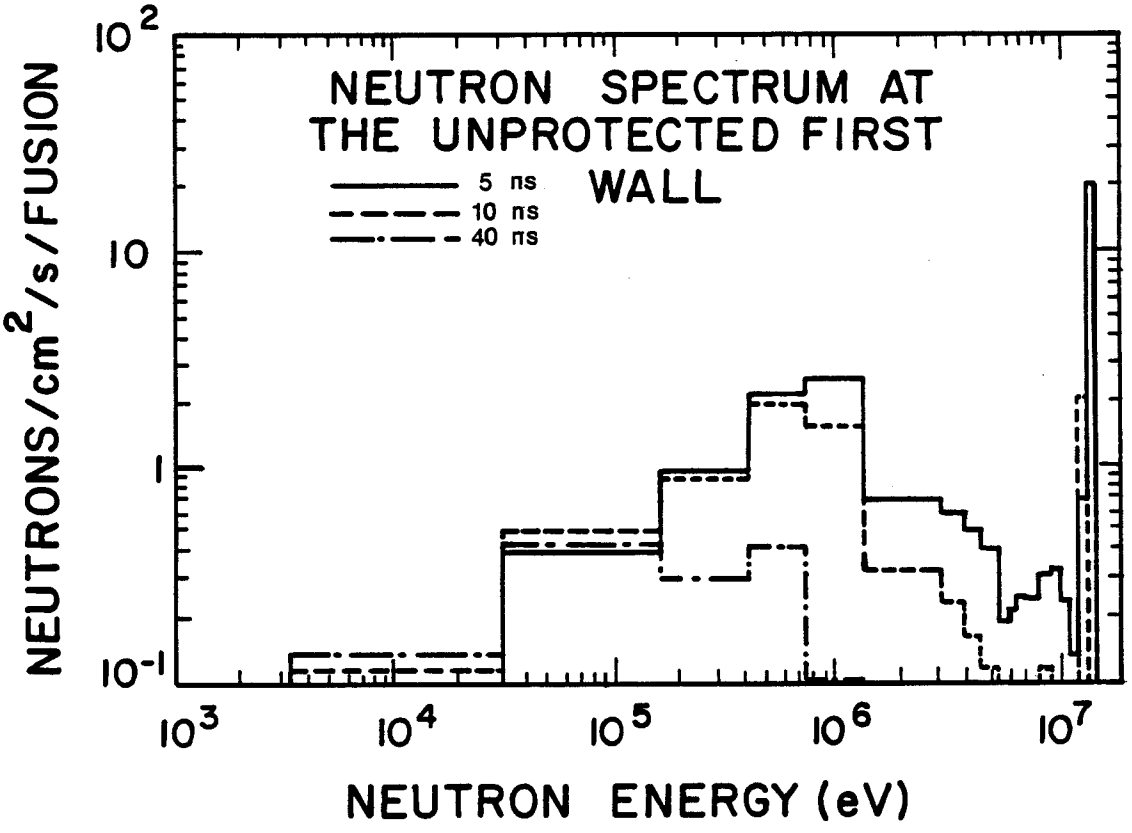

Figure VI.3-22 Neutron spectrum in the unprotected first wall.

with a very small energy loss per collision resulting in much longer slowing down times. Therefore, the time spread of the spectrum in the first wall of our system is determined primarily by the slowing down time in the blanket.

On the other hand, the time of flight spread is the dominant factor in the case of the unprotected wall because of the absence of the "inner" slowing down region. The spectrum at 5 ns after the arrival of the leading edge of the neutron pulse consists mainly of first group neutrons coming directly from the source. The soft part of the spectrum shown in Fig. VI.3-22 is due to backward scattering of 14.1 MeV neutrons in the reflector region and neutron slowing down in the wall itself. As time elapses, lower energy source neutrons arrive at the first wall. The effect of neutron slowing down in the reflector is not as pronounced here as compared to the effect of neutron slowing down in the inner blanket for the case of protected wall. The reason is that the probability of backscattering of high energy neutrons is small compared to the probability of forward scattering. Therefore, the time-dependent damage rate in the unprotected wall is affected primarily by the time of flight spread.

VI.3.4.5 Atomic Displacement Rate

The instantaneous damage rates in the first wall have been calculated using the time dependent neutron spectrum in the wall and the appropriate reaction cross sections. The instantaneous dpa rate in the protected ferritic steel first wall is given in Fig. VI.3-23. The results correspond to a 400 MJ fusion yield. The cumulative dpa is illustrated in Fig. VI.3-24. It is clear that the damage occurs over a relatively long time resulting in a peak instantaneous dpa rate of 0.009 dpa/s at 140 ns after burn. This peak corresponds to the 14 MeV source neutrons arriving without collision. A broad peak at ~ 270 ns corresponds to neutrons emitted in (n,2n) reactions with lead in the

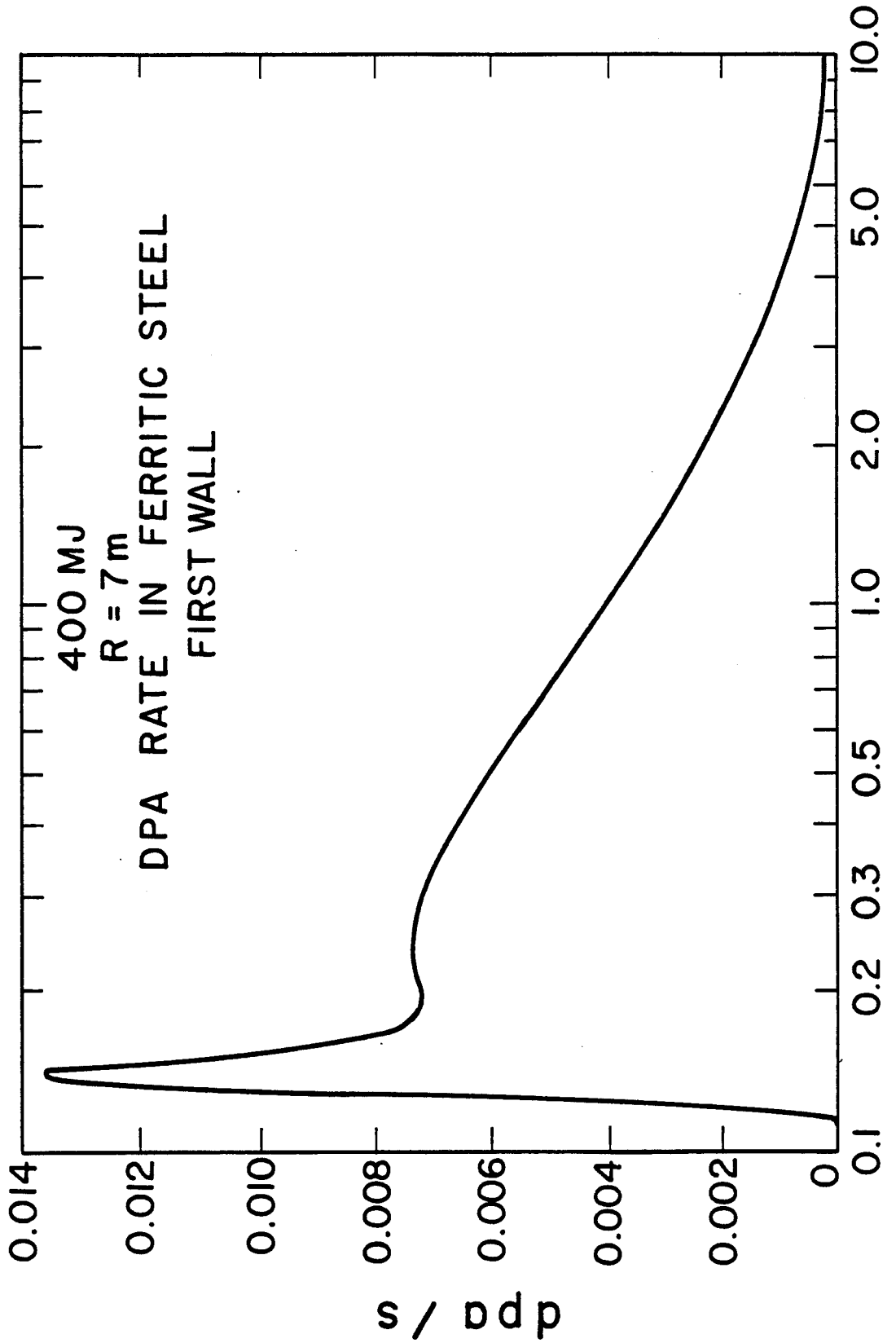

Figure VI.3-23 DPA rate in the protected first wall.

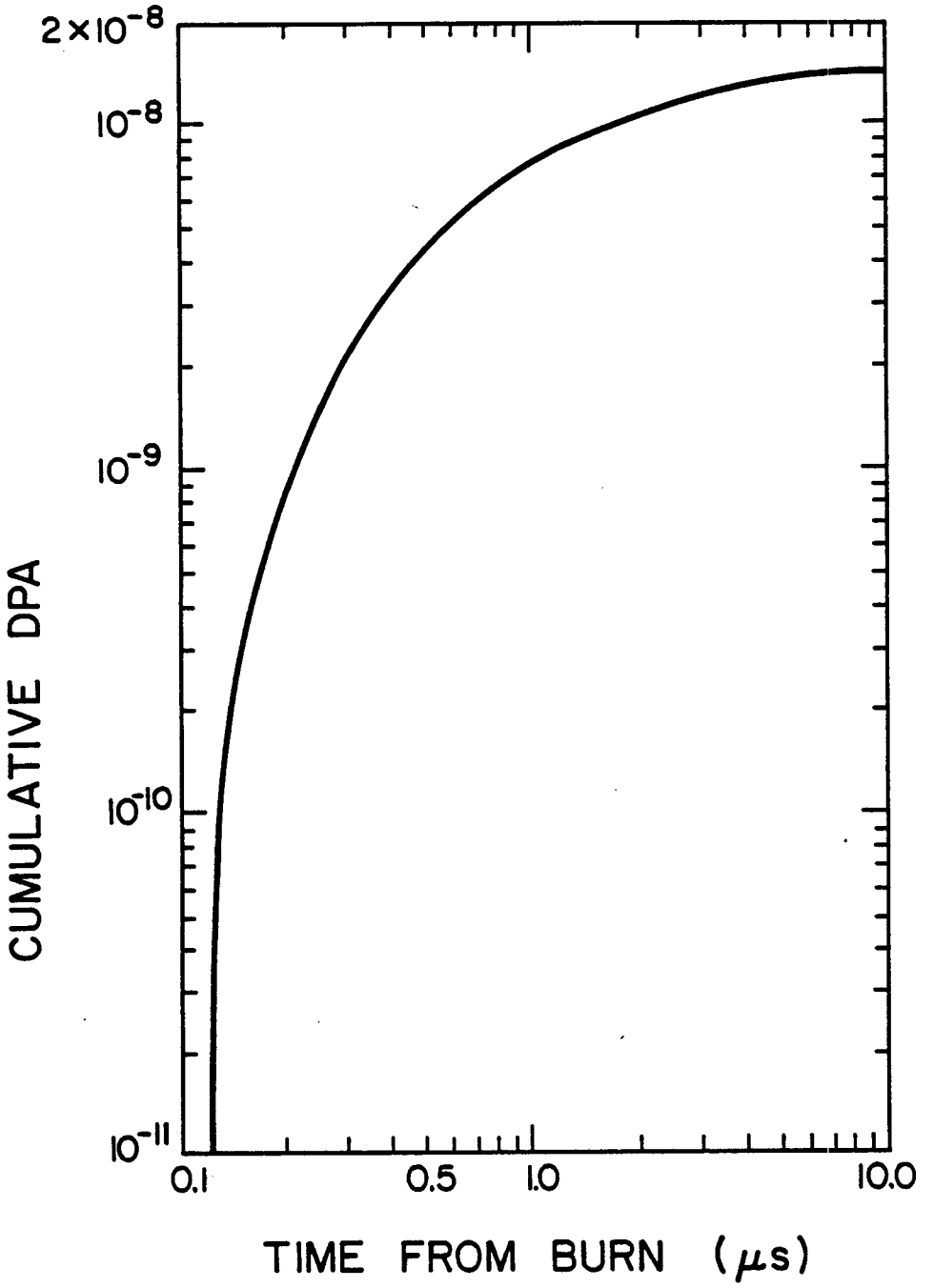

Figure VI.3-24 Cumulative DPA in the protected first wall.

INPORT tubes. This considerable time spread results from the relatively long slowing down time in the blanket allowing neutrons of energies greater than the dpa threshold energy of iron (~ 1 keV) to exist in the first wall over a long period of time.

The instantaneous dpa rate in an unprotected wall is shown in Fig. VI.3-25. The time spread is very small compared to the case of the protected wall. The time spread is determined here by the time of flight spread of neutrons as they travel from the source to the wall. The effect of the INPORT tube protection, used in HIBALL, on the atomic displacement in the first wall is given in Table VI.3-13. The total dpa per full power year (FPY) was determined using the steady state code ANISN with a repetition rate of 5 Hz.

The wall protection is found to decrease the total cumulative dpa and the peak instantaneous dpa rate by factors of 9.4 and 1190, respectively. The larger reduction in the peak instantaneous dpa rate results from time spread FWHM increasing from 5 to 980 ns. The reduction in dpa achieved here is much larger than that achieved in a 316 SS first wall protected by 0.5 m of liquid Li,[17] typical of the HYLIFE concept.[21] In this case the average rate was found to decrease by a factor of 3.6 and the peak instantaneous rate to decrease by a factor of 13. Larger reduction is obtained in our case because Pb is more effective than Li in slowing down high energy neutrons and C is more effective than Li in slowing down low energy neutrons. If we assume that the life of the wall will approach 10 Mw-y/m^2 (the target for the U.S. fusion materials program), and 1 MW-y/m^2 = 11 dpa, then only 4.9 MW-y/m^2 will be accumulated with the INPORT units and 46 MW-y/m^2 without them. This implies that the wall protection concept used in HIBALL will be very effective in reducing damage to the first wall, allowing it to last for the lifetime of the reactor (20 full power years).

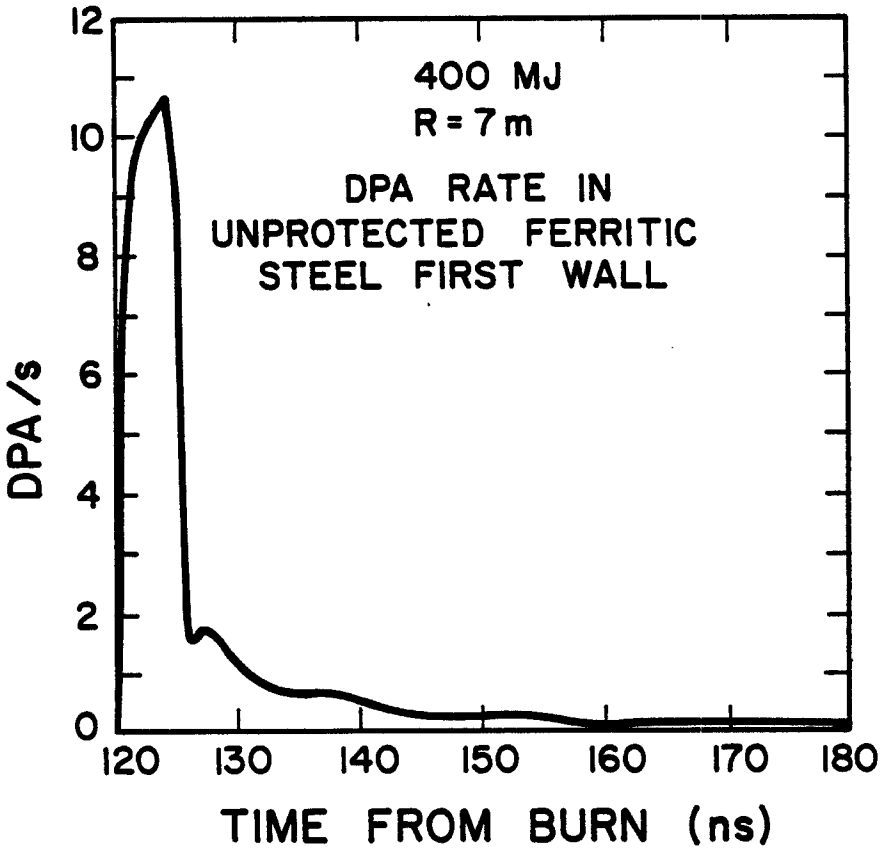

Figure VI.3-25 DPA rate in the unprotected first wall.

Table VI.3-13

Effect of First Wall Protection on Atomic Displacement

	Peak Instantaneous dpa rate (dpa/s)	Time Spread fwhm (ns)	Total dpa (dpa/FPY)
Protected Wall	0.009	980	2.7
Unprotected Wall	10.7	5	25.4

VI.3.4.6 Helium Production Rate

The instantaneous helium production rate in the protected ferritic steel first wall is given in Fig. VI.3-26. A peak instantaneous helium production rate of 0.11 appm/s occurs about 15 ns after the leading edge of the pulse arrives at the wall. The cumulative helium production is given in Fig. VI.3-27. It is clear that the time spread here is much smaller than that for the dpa. The reason is that the (n,α) reaction in iron has a threshold energy of $\sim$ 2.7 MeV and neutrons at energies greater than this energy exist in the first wall over a relatively short period. Only one peak occurs because the (n,2n) neutrons do not contribute to helium production. The instantaneous helium production rate in an unprotected wall is given in Fig. VI.3-28. Again the time spread in this case is determined primarily by the time of flight spread of source neutrons.

The effect of the INPORT first wall protection on the helium production is given in Table VI.3-14. The total helium production in a full power year is found to decrease by a factor of 630 while the peak instantaneous helium production rate is found to decrease by a larger factor of 1627. Since the helium production reaction is a high energy reaction, neutron slowing down in

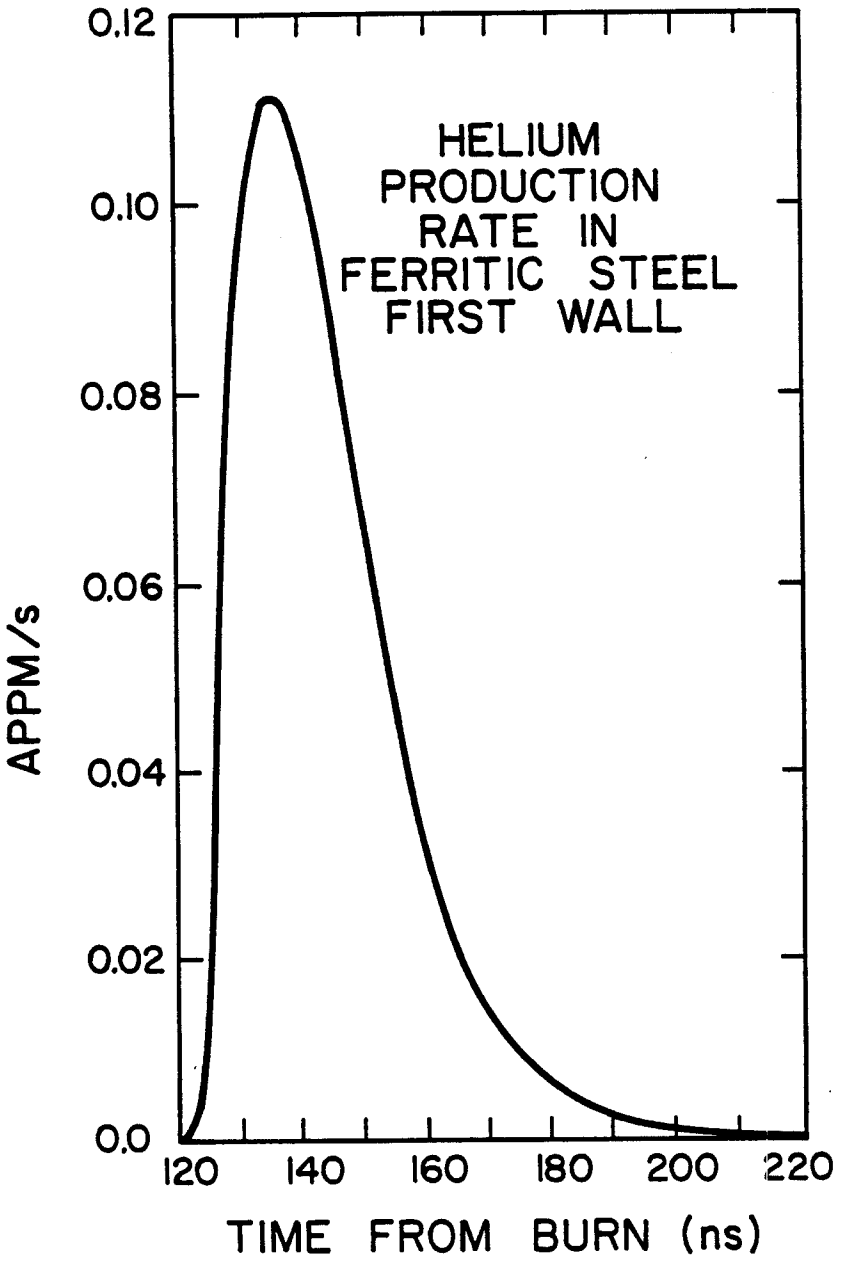

Figure VI.3-26 Helium production rate in the protected first wall.

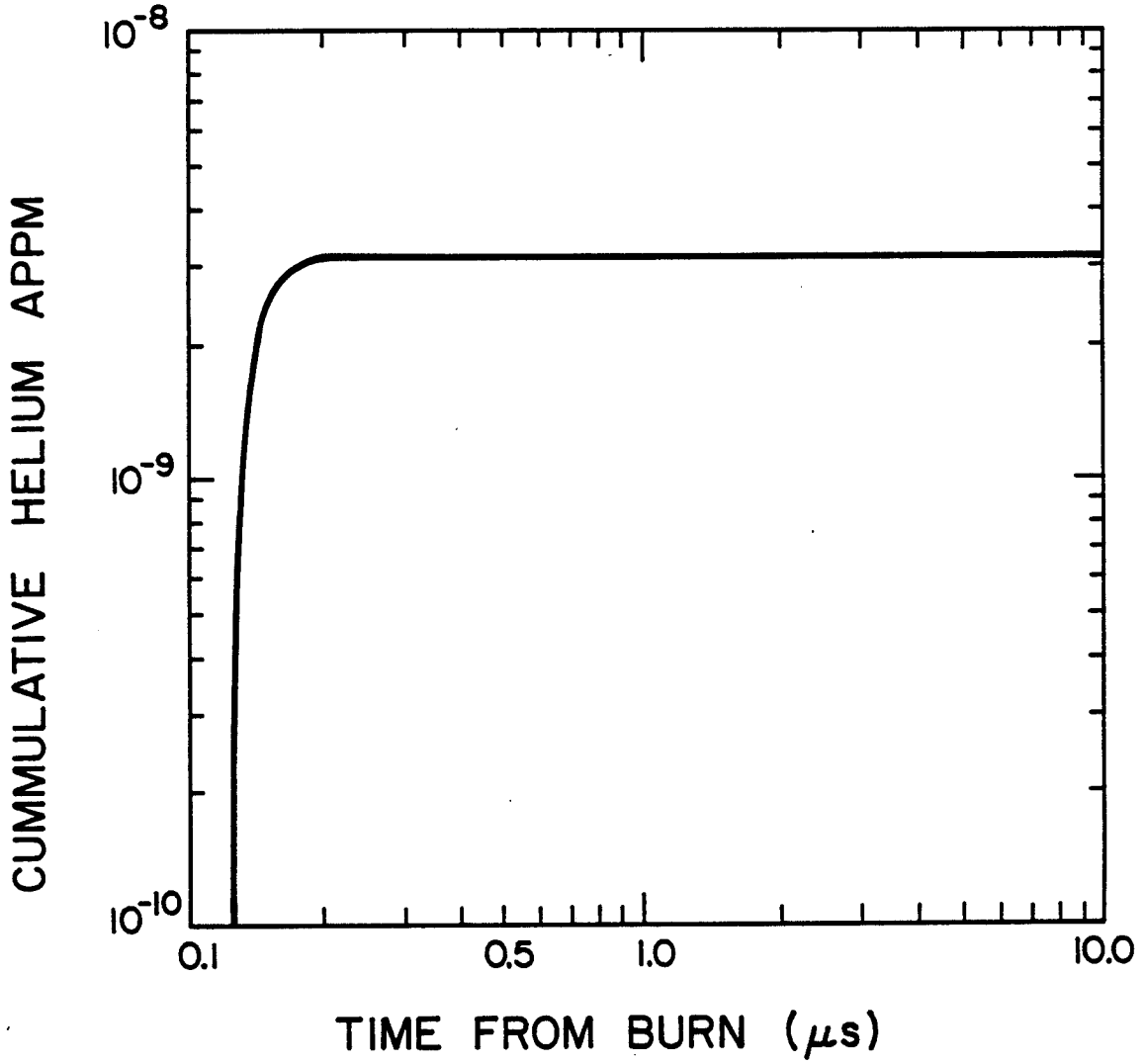

Figure VI.3-27 Cumulative helium production in the protected first wall.

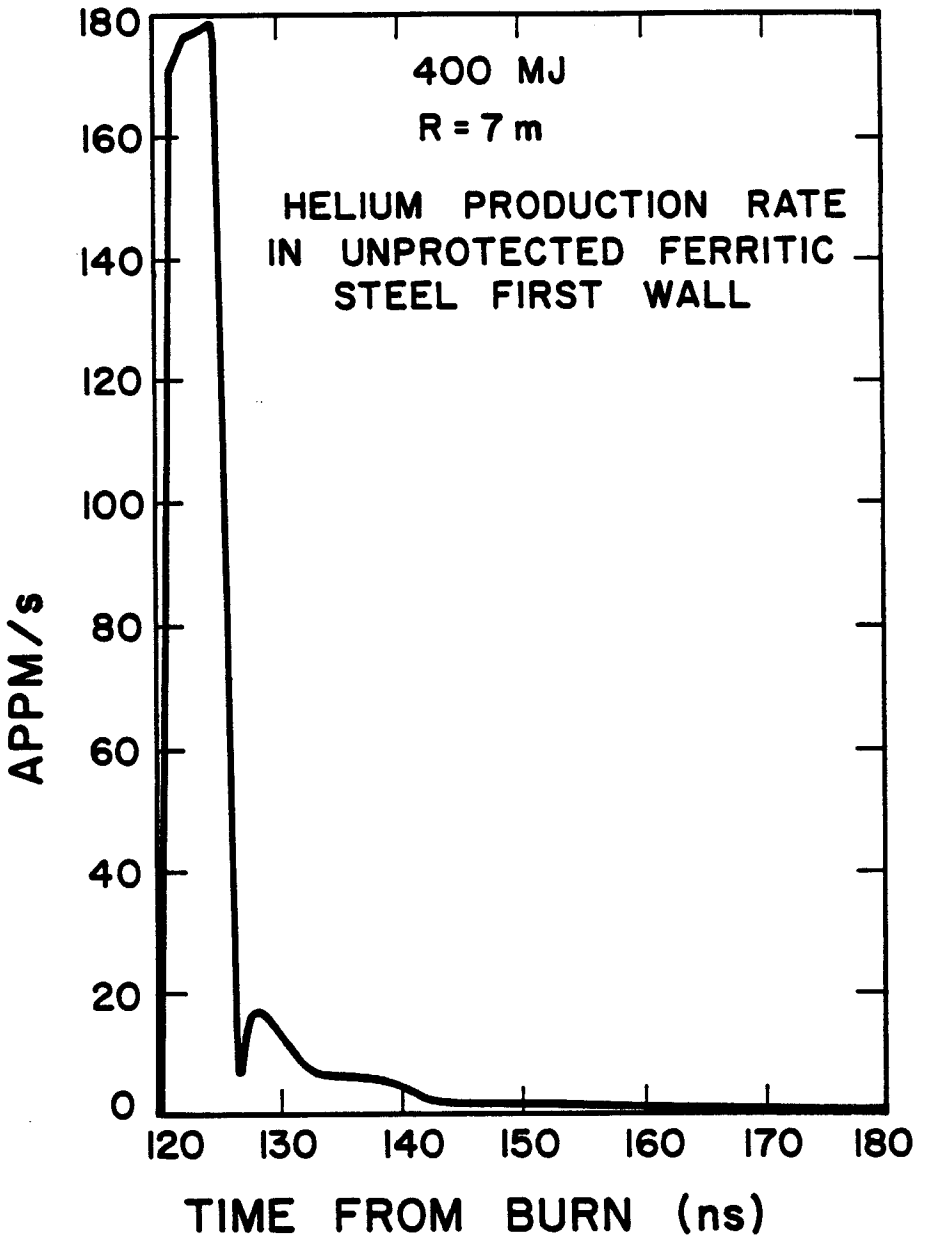

Figure VI.3-28 Helium production rate in the unprotected first wall.

Table VI.3-14

Effect of First Wall Protection on Helium Production

	Peak Instantaneous Helium Production Rate (appm/s)	Time Spread FWHM (ns)	Total Helium Production (appm/FPY)
Protected Wall	0.11	26	0.364
Unprotected Wall	179	5	737

the blanket is found to have a pronounced effect on helium production in the wall.

VI.3.4.7 Energy Deposition Rate

The time-dependent neutron and gamma fluxes are used together with the appropriate kerma factors for neutron and gamma energy deposition to calculate the energy deposition rate in the blanket and first wall. The results are given in Fig. VI.3-29 at the blanket first surface, the center of the blanket, and the first wall. The time distribution is very narrow at the first surface and broadens as one moves towards the first wall. While the time spread at the first surface is determined by the time of flight spread, the spread at the first wall is determined by the slowing down time in the inner blanket. For a 400 MJ fusion yield the peak instantaneous power densities in the blanket and the first wall are found to be 1.82×10^8 and 2.73×10^5 W/cm^3, respectively. This corresponds to peak to average temporal power density ratios of 8.48×10^6 and 1.65×10^5, respectively. The results in Fig. VI.3-30 give the instantaneous energy deposition rate in the unprotected first wall. The distribution is very narrow with a peak power density of 3.3×10^8

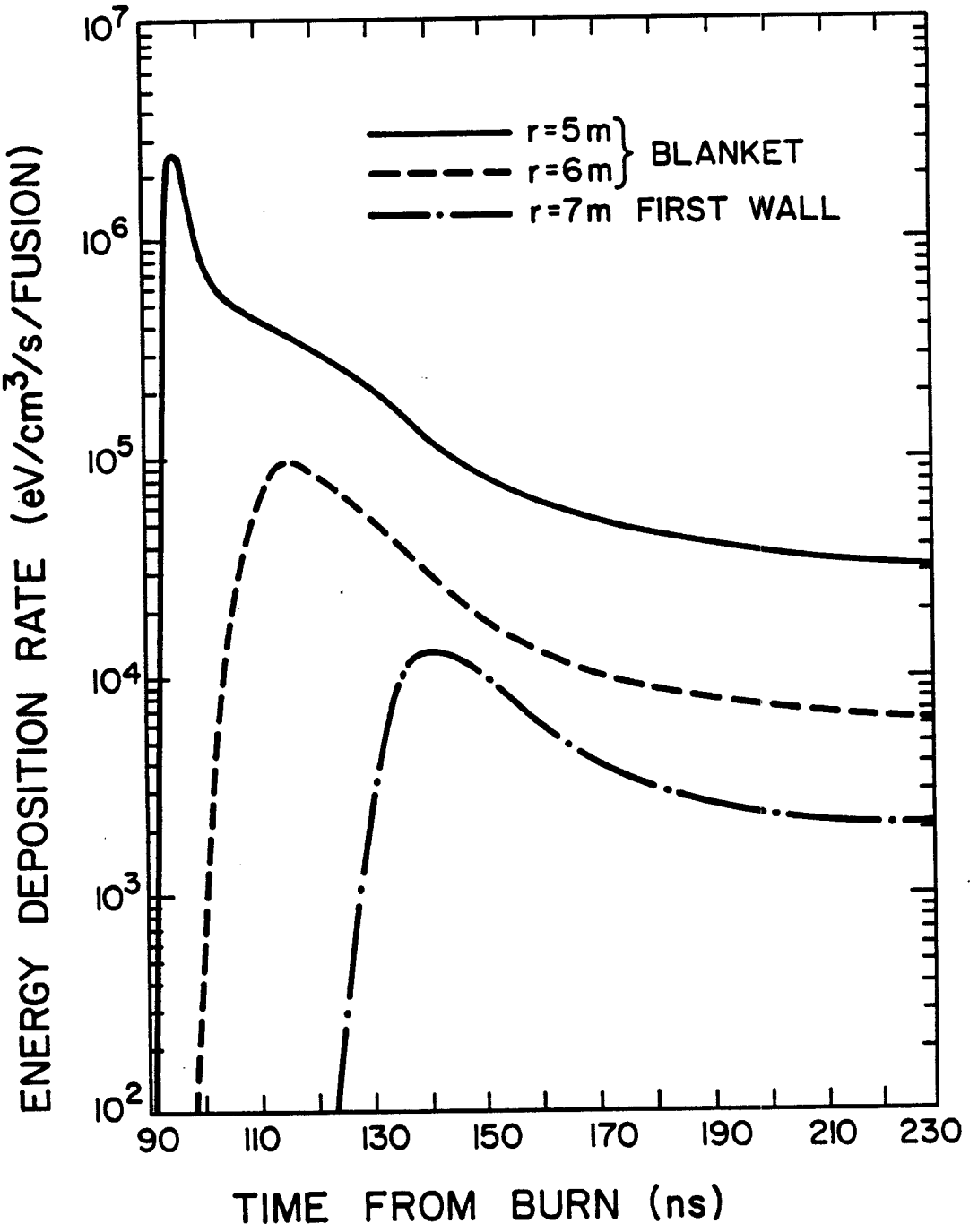

Figure VI.3-29 Energy deposition rate in HIBALL blanket and first wall.

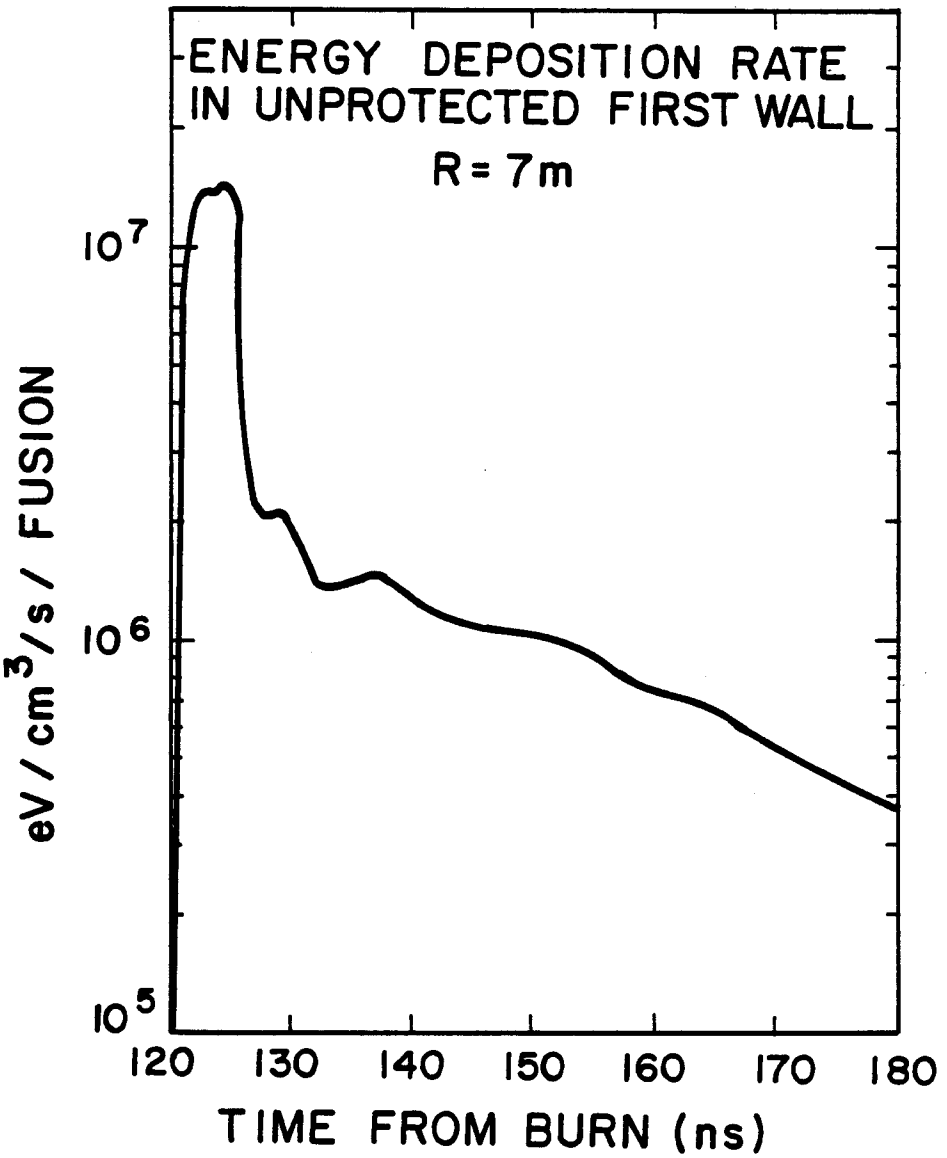

Figure VI.3-30 Energy deposition rate in the unprotected first wall.

W/cm^3 for a 400 MJ fusion yield. The peak to average temporal power density ratio in the wall is found to be 1.1×10^7. The INPORT concept is found to decrease the peak instantaneous power density in the wall by a factor of ~ 1210 and the total nuclear heating in the wall by a factor of ~ 18. These results are useful for stress analysis studies.

VI.3.4.8 Summary and Concluding Remarks

Time dependent neutronics analysis for the ferritic steel first wall of the HIBALL fusion reactor design has been performed. The analysis accounts for neutron interactions in the target resulting in neutron multiplication and significant spectrum softening. The time dependence of the neutron source is modified in such a way that the multigroup treatment adopted in the time dependent transport code predicts the correct time of flight spread of neutrons in each group as they travel from the source to the first surface of the blanket. A modified version of the time dependent discrete ordinates code TDA has been used.

Neutron slowing down in the INPORT first wall protection system is found to have a significant effect on the time dependent spectrum and damage in the first wall. The time over which the damage occurs is found to be determined primarily by the slowing down time in the blanket. In the case of an unprotected wall, where no slowing down occurs in front of the wall, the spread is determined primarily by the time of flight spread.

Using the INPORT first wall protection concept results in significant reductions in peak instantaneous and total dpa and helium production rates allowing the first wall to last for the reactor lifetime (~ 20 FPY). Our results also show that the peak power density in the first wall resulting from nuclear heating decreases considerably when the porous tube concept is used to protect the wall.

VI.3.5 Radioactivity and Afterheat

Radioactivity will be induced in the coolant and structure of the HIBALL reactor through activation by the fusion neutrons. To treat the problem exactly energy dependent neutron fluxes must be calculated for each point in the cavity. Since the ability to perform these calculations with reasonable cost and effort does not exist at this time a simplified approach was taken. Specifically the reactor was modeled in spherical geometry with materials and dimension consistent with a cut through the midplane of the reactor. The multigroup neutron flux used in the activation calculations was taken from the one-dimensional ANISN calculations described in section VI.3.1. For the purpose of the calculation the reactor was broken up into 37 intervals and the average flux in each interval was used. The size and compositions of the various regions is shown in Fig. VI.3-31. The DKR code[22] was used to calculate the radioactivity parameters -- activity, afterheat, and biological hazard potential (BHP).

The activities were calculated for an operating time of two years. Previous calculations on other fusion reactor designs show that the buildup of radioactivity is quite rapid, becoming significant after only a few hours of operation. By the end of two years all short-lived isotopes saturate and the buildup continues at a slower rate. Thus the activity at times after shutdown of much less than two years is relatively independent of operating time while the activity at times very much longer than two years after shutdown is approximately proportional to operating time.

The total activity per unit of thermal power for the cavity region, first material wall and reflector is shown in Fig. VI.3-32. The level at shutdown is 0.62 Ci/watt. this value is somewhat larger than might be expected considering that the bulk of the activity is due to the steel which is shielded

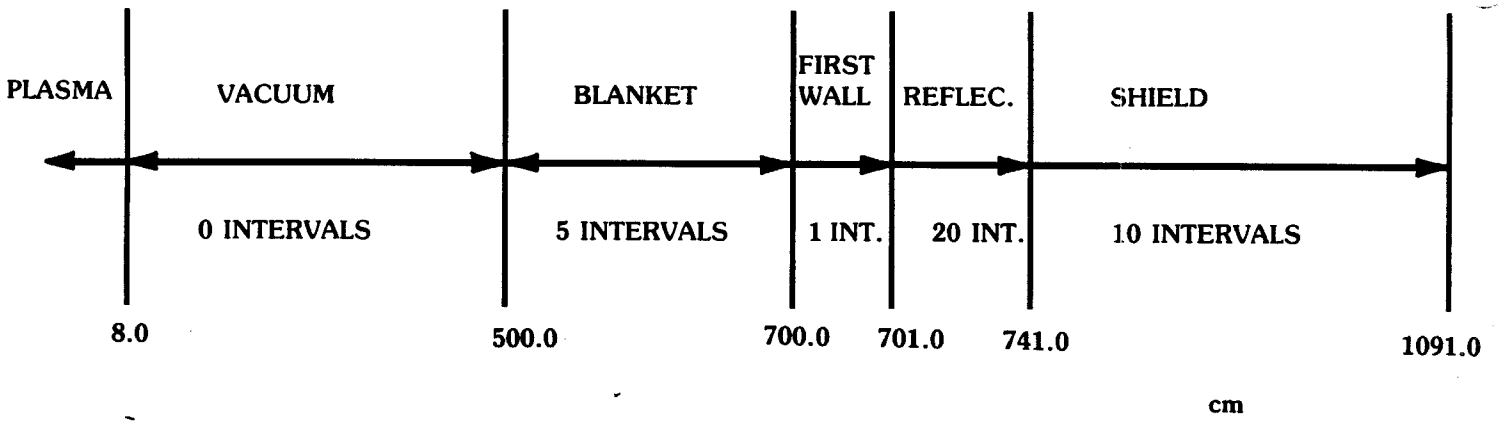

COMPOSITIONS

BLANKET	FIRST WALL	REFLECTOR	SHIELD
99.3 w/o $Li_{17}Pb_{83}$	100% HT-9	88 w/o HT-9	13 w/o Fe
0.7 w/o SiC		12 w/o $Li_{17}Pb_{83}$	28 w/o Si
			.5 w/o H
			44 w/o O
			7 w/o Ca
			4 w/o Al
			3.5 w/o Others

DENSITIES

LiPb: 9.4 g/cm^3
SiC: 3.17 g/cm^3
HT-9: 7.8 g/cm^3

Figure VI.3-31

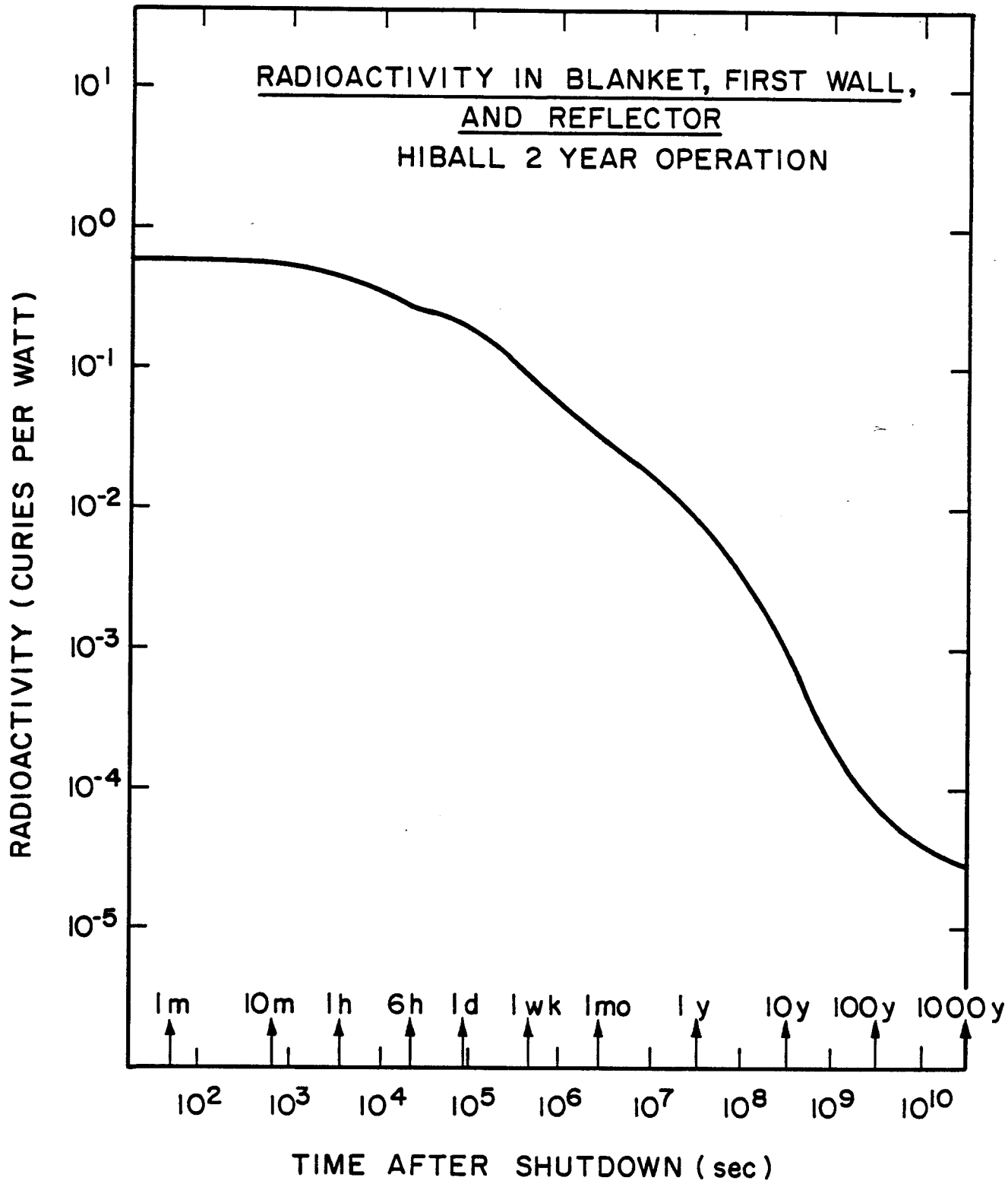

Figure VI.3-32

from the neutron source by the Pb-Li INPORT region. However, the neutron multiplying effects of the Pb in the INPORT region results in the flux in the reflector region remaining relatively high and this feature combined with the large amount of steel in the reflector produces the high activity level. As is typical with steel systems the activity falls off rather slowly with time after shutdown requiring approximately three weeks to be reduced by a factor of 10 and two years to be reduced by a factor of 100. The relative contributions of individual isotopes is shown in Fig. VI.3-33. The initial activity is dominated by the contributions of ^{56}Mn and ^{203}Pb. ^{56}Mn ($T_{1/2}$ = 2.58 hr) decays away first followed by ^{203}Pb ($T_{1/2}$ = 52 hr). Note that unless flow were maintained, the ^{203} Pb activity would not be present in the reactor itself but would be associated with the coolant storage facility. The next major decrease in activity is due to the decay of ^{51}Cr ($T_{1/2}$ = 27.7 days). It is followed by the decay of ^{55}Fe ($T_{1/2}$ = 2.7 yr) which produces the large activity drop between 1 and 100 years. The long term activity is due to ^{93}Mo and ^{93}Nb originating in the small amount of Mo in the steel (HT-9).

The afterheat is shown in Fig. VI.3-34. The value at shutdown is 0.66% of the operating power. For the same reasons as the radioactivity this value is somewhat higher than expected, but is consistent with the activity level. Since the decay energies of the various isotopes are different the afterheat curve has a shape which differs from that of the activity. It falls off much more rapidly, by a factor of 10 in about two days and a factor of 100 in two weeks. The relative contributions of the various isotopes are shown in Fig. VI.3-35. At shutdown ^{56}Mn is the dominating isotope. The decay of this isotope plus the relatively rapid decay of ^{203}Pb account for the order of magnitude drop in two days. ^{51}Cr, which contributes significantly to the activity in the one week to one month period, contributes very little to the afterheat,

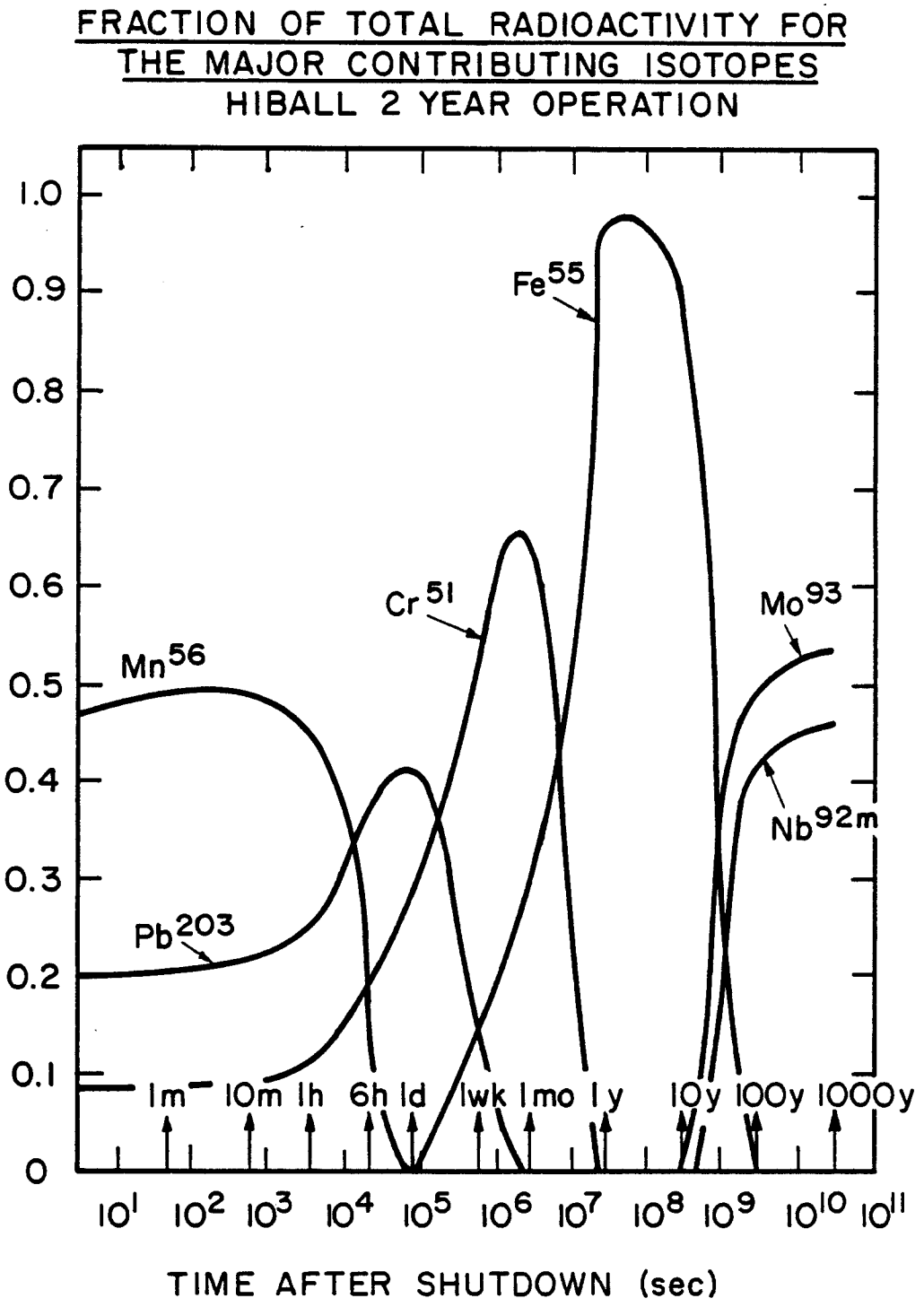

Figure VI.3-33

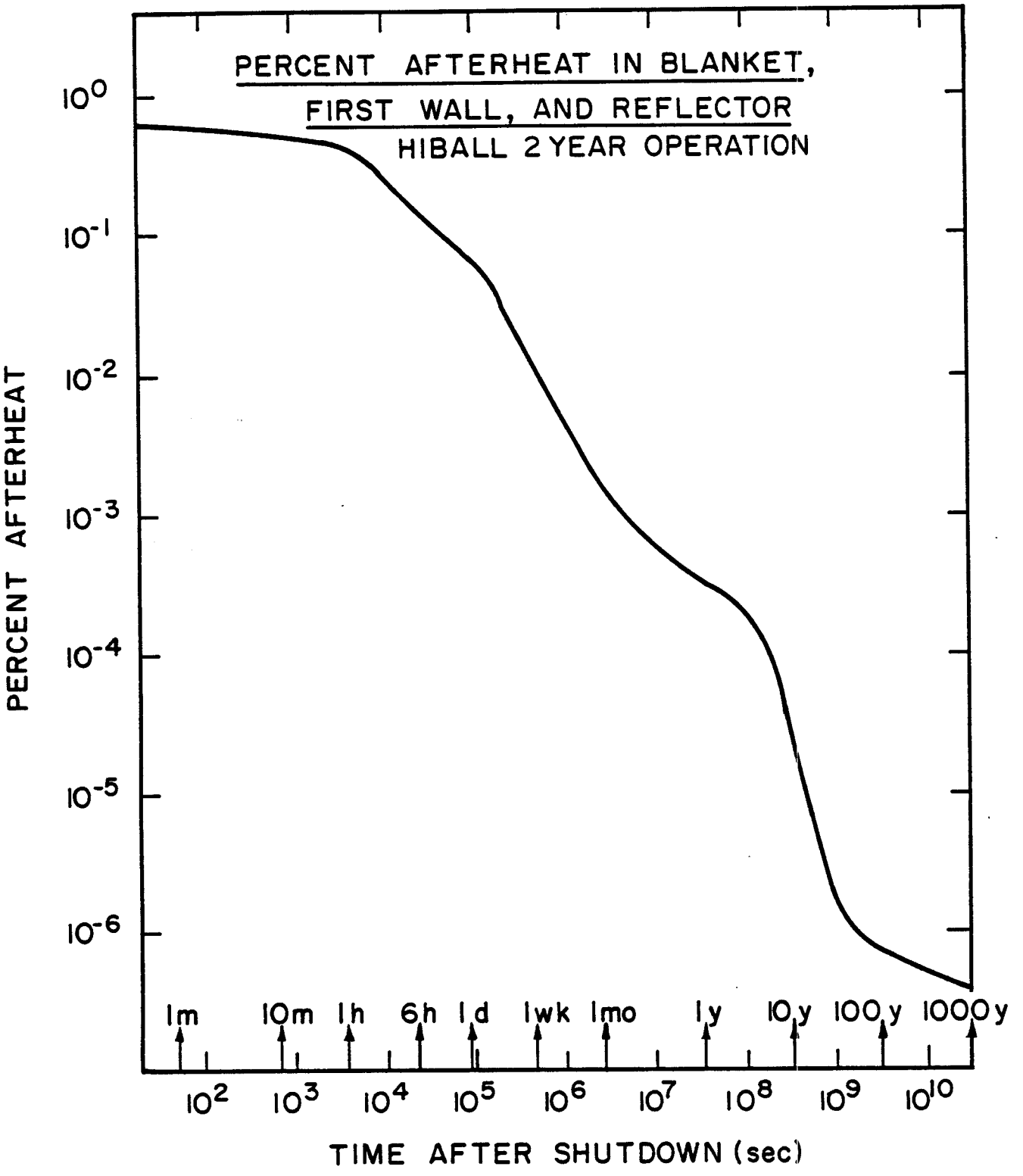

Figure VI.3-34

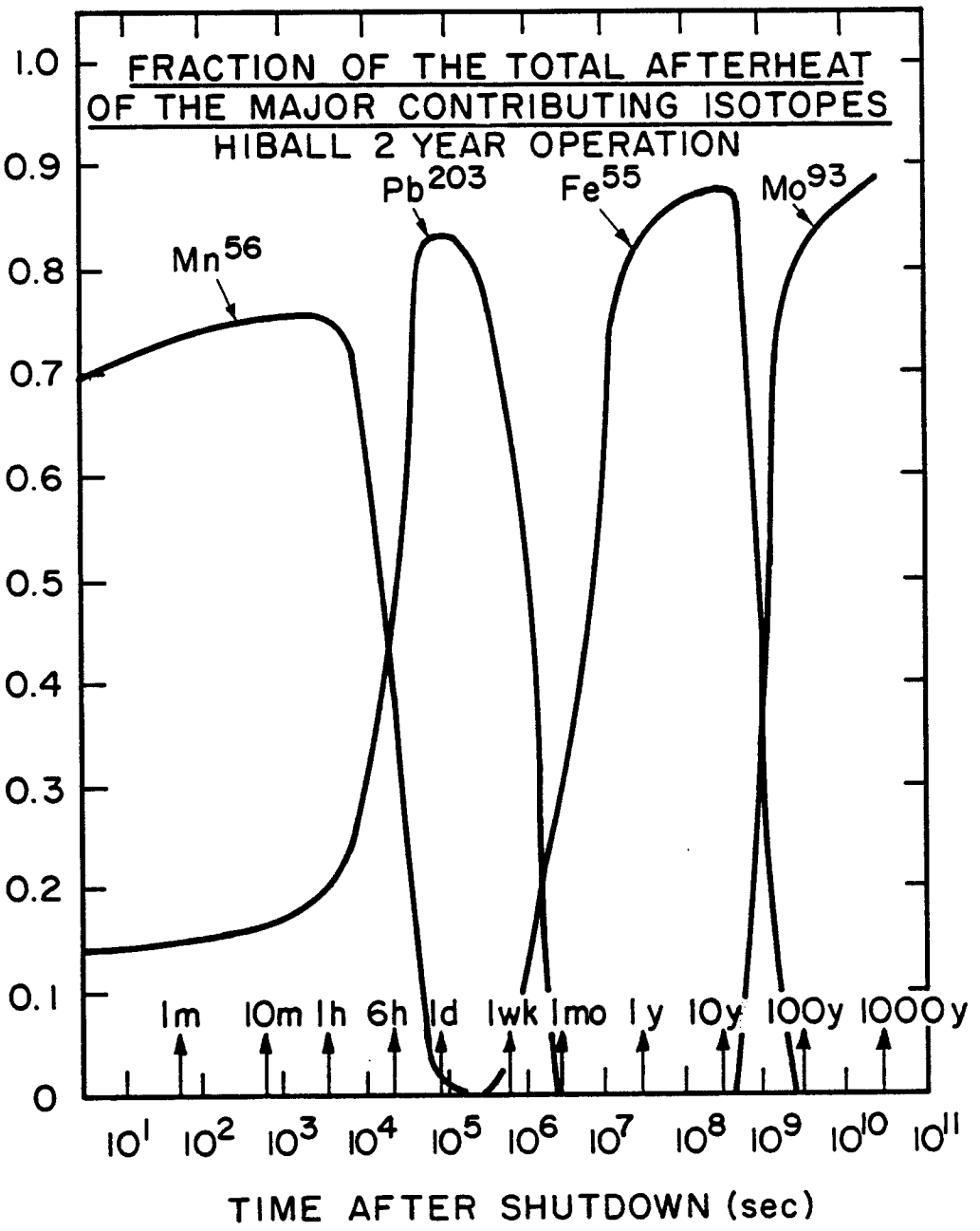

Figure VI.3-35

thus the afterheat in this period is governed primarily by the decay of ^{203}Pb. The decay energy of ^{55}Fe is also low as is the decay energy of the remaining isotopes which leads to the rather low residual afterheat subsequent to about 100 years.

The Biological Hazard Potential (BHP) is shown in Fig. VI.3-36. BHP is defined as the ratio of the activity present in the system per unit of power to the level of activity allowed per unit volume of air in the U.S. Nuclear Regulatory Commission Regulations (10 CFR 20). Thus it is a measure of the potential hazard of a radioactive material. The BHP of the coolant first wall and reflector is shown in Fig. VI.3-36. The units are cubic kilometers of air per kilowatt of thermal power. The shape of the curve is similar to the shape of the activity curve being 26.0 at shutdown and requiring almost one month to be down by a factor of ten and with a long term reduction of only three orders of magnitude.

The activity, afterheat and BHP of the shield are shown in Figs. VI.3-37, VI.3-38, and VI.3-39. The neutronics calculations for the shield were performed for a concrete with no reinforcing material. For the purpose of obtaining a better estimate of the radioactivity related parameters of the shield the fluxes from the above calculations were used with a concrete having reinforcing material and with composition typical of the sacrificial shield of a BWR.[23] It is this composition which was shown in Fig. VI.3-31. The activity in the shield is significantly lower than the activity in the reflector, but the value of 6.3×10^{-3} Ci/watt is still significant. The time behavior of the activity is dominated after the first day by the activity of ^{55}Fe which continues to be the major contributor until times greater than 100 years. The afterheat at shutdown is 7.7×10^{-2}% of the operating power which while relatively small, will still require some residual heat removal capacity.

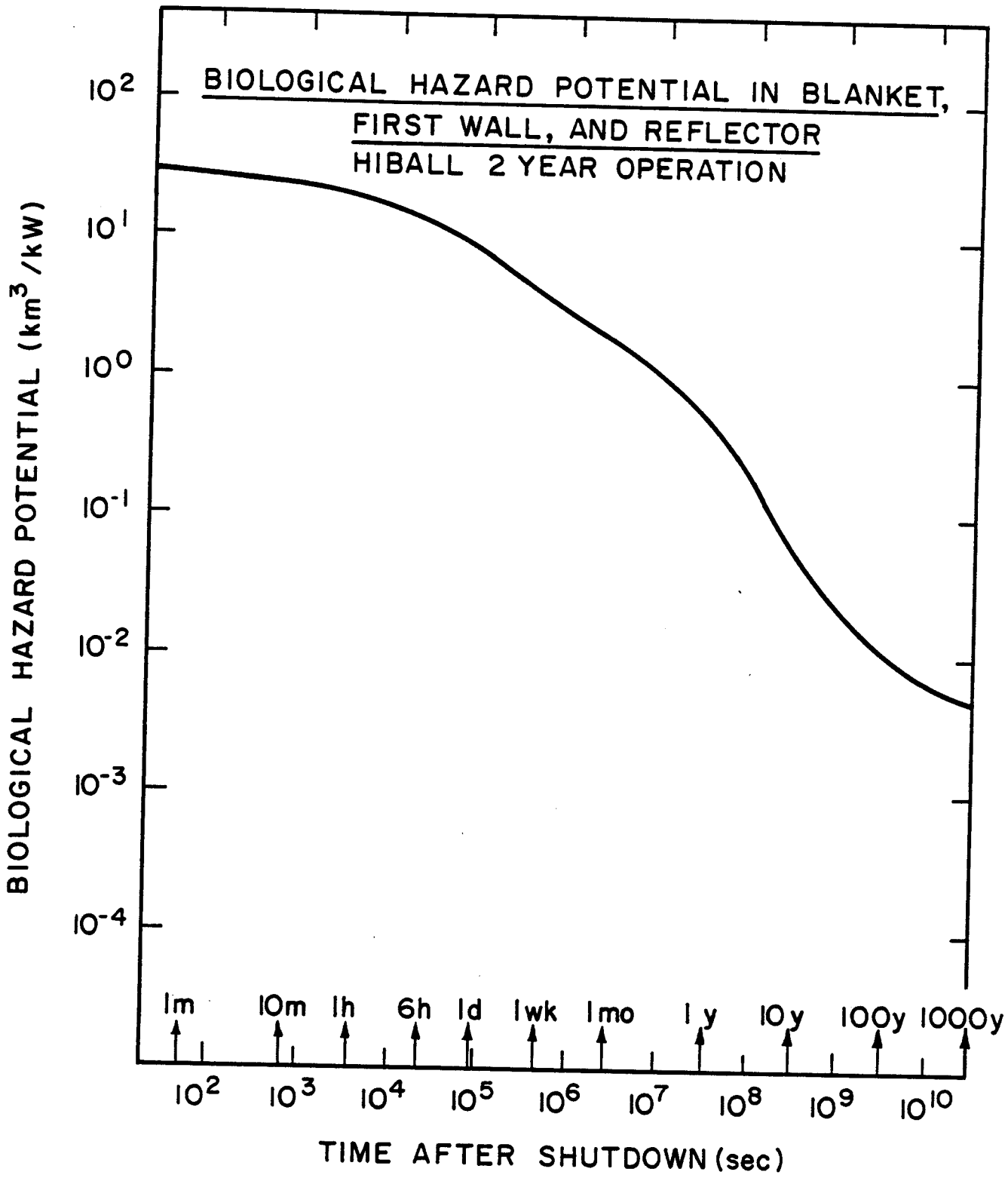

Figure VI.3-36

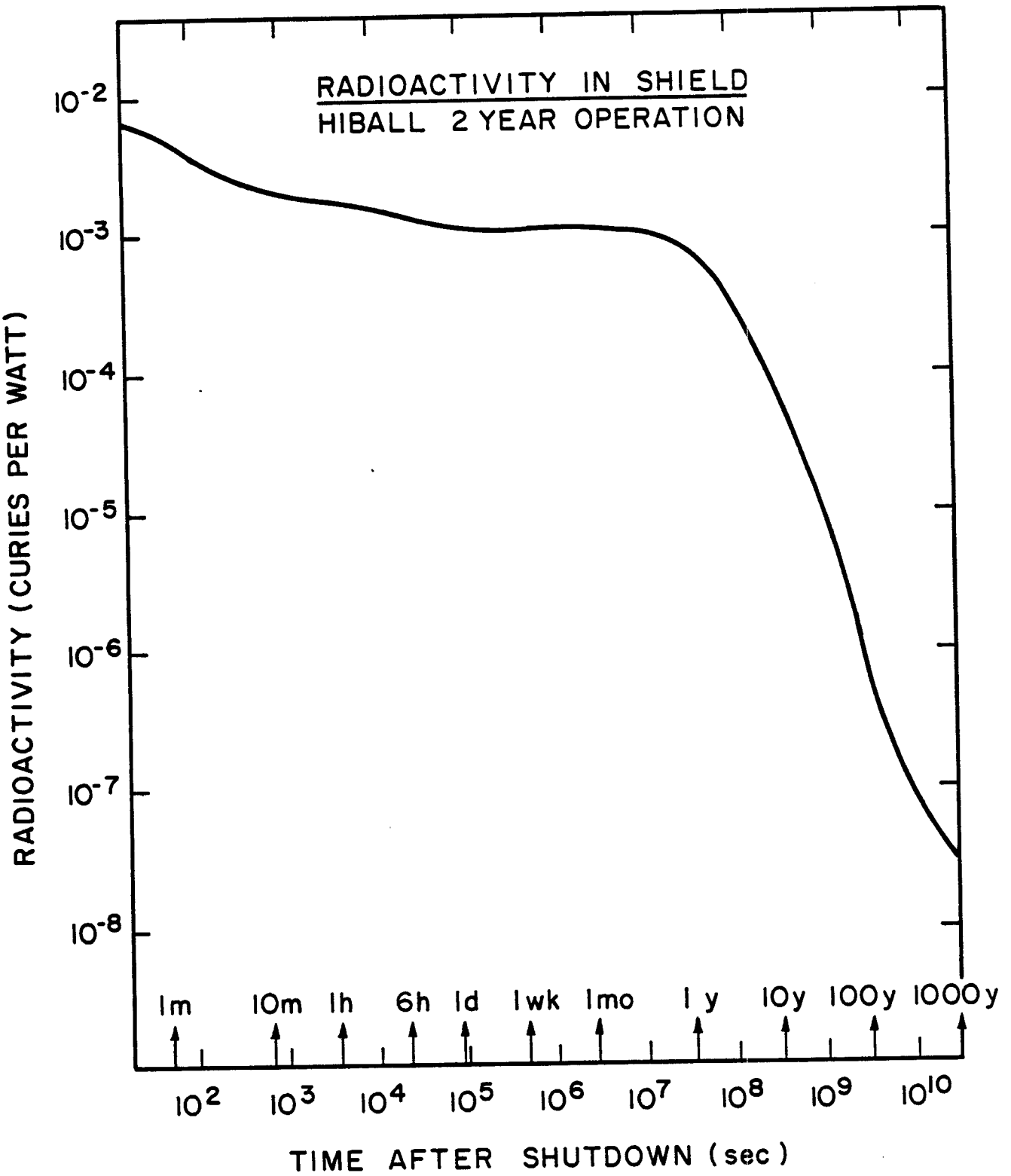

Figure VI.3-37

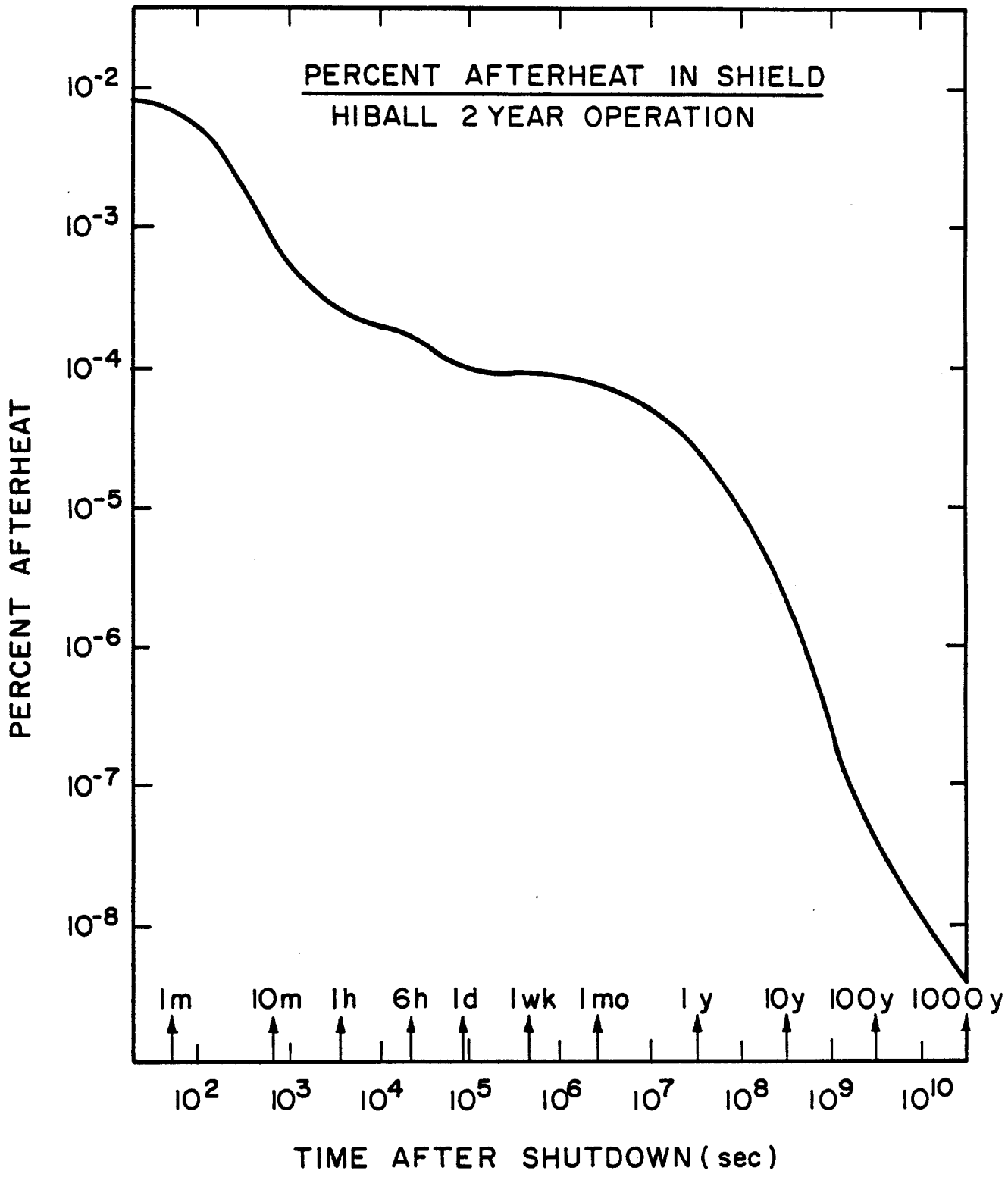

Figure VI.3-38

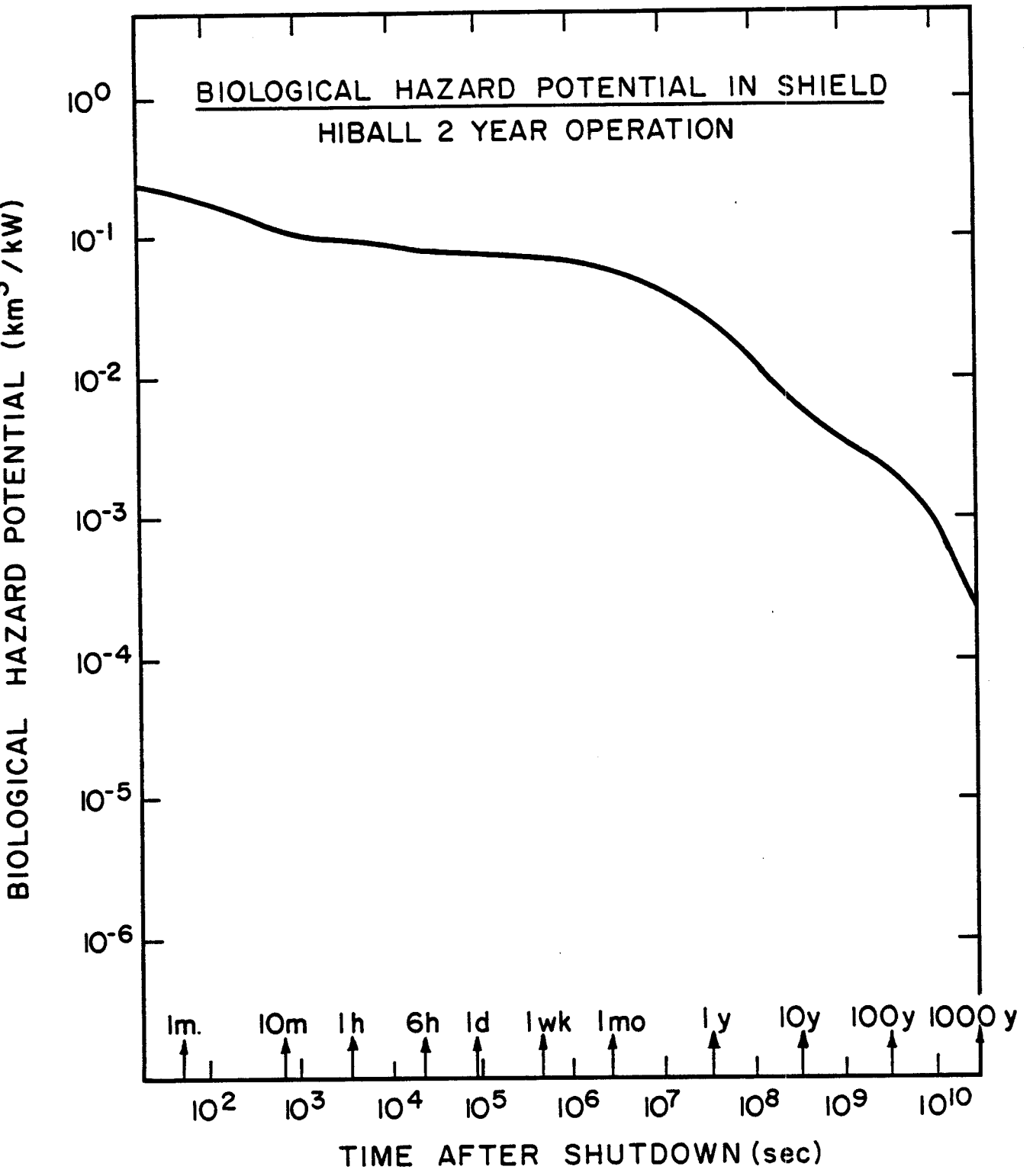

Figure VI.3-39

The afterheat drops off faster with time than does the activity primarily because of the low decay energy of ^{55}Fe. The BHP is also relatively low and falls off slowly, again because of the hazard characteristics of nuclei involved. To get a somewhat different appreciation of the magnitude of the activities in the shield the above values at shutdown correspond to an average activity of 3.4×10^{-3} Ci/cm^3, an afterheat of 4.1×10^{-5} W/cm^3, and a BHP of 6.7×10^{-11} km^3/cm^3.

The calculated neutron and gamma doses outside the shield have been presented in section VI.3.2. An additional component is the dose due to activation products. This component is present during operation and shutdown periods. To calculate this dose the activities calculated above have been used along with a one-dimensional gamma transport program. The results of this calculation indicated that the dose outside the shield from activation of the reflector and materials in the shield is quite low, 4.7×10^{-5} mrem/hr at shutdown.

These low values plus the consideration that the neutronics and prompt gamma calculations were done with no high Z materials in the shield, reinforce the idea that the shield is somewhat overdesigned and that a more realistic choice of shield composition would lead to a thinner shield using less materials while still showing acceptable dose levels outside the chamber.

These calculations must be used with a certain amount of care. First the geometric modeling of the system is very simple. It would have been much more satisfactory to have three-dimensional fluxes for the actual geometry. Furthermore no account has been taken of some of the special features of the system. For example, activation and shielding of the vacuum system has been ignored. The activation of the tube support structure in the INPORT region has been omitted. Also no calculations have been performed to get activities in the

beam transport system. The omission of these details do not invalidate the calculations presented but do require that they be used with care.

The calculations are also only as good as the cross section data used in them. While the data set used in DKR[24] was compiled with care using the best available data either experimental or calculational, it is likely that some reactions have been omitted. For example it is known that if lead is exposed to a neutron flux, an isomeric state at 0.91 MeV in ^{204}Pb, is excited ($T_{1/2}$ = 66.9 min). However, the cross section for this reaction is not known and therefore has not been included.

As a final point the effect of impurities has not been accounted for in the LiPb. Bismuth, for example, is a common impurity in commercial lead. the reaction $^{209}Bi + n \rightarrow {}^{210}Bi \xrightarrow{\beta^-} {}^{210}Po$ is then possible and of concern because ^{210}Po is alpha emitting and volatile. This problem was considered in the NUWMAK[25] study. A Bismuth concentration of 42 appm was used as a basis for the calculation. This value was taken from the assay of a relatively high purity lead purchased for a slowing down time spectrometer. Assuming Bismuth has an 1/v absorption cross section the ^{210}Po content was calculated to be 0.26 Ci/tonne of Pb. There is approximately 2300 tonnes of Pb/cavity in HIBALL. If the previous ratios were correct the corresponding amount of ^{210}Po would be ~ 600 Ci. This amount of activity, while significant, is very much less than the activity of the rest of the material in the system should present no special problem. Also, since the half-life of ^{210}Po is short (138.4 days) it presents no long term storage problem.

References for Section VI.3

1. RSIC Code Package CCC-254, "ANISN-ORNL," Radiation Shielding Information Center, ORNL.

2. T.R. Hill, "ONETRAN: A Discrete Ordinates Finite Element Code for the Solution of the One-Dimensional Multigroup Transport Equation," LA-5990-MS, Los Alamos Scientific Laboratory (1975).

3. RSIC Data Library Collection, "VITAMIN-C, 171 Neutron, 36 Gamma-Ray Group Cross Sections Library in AMPX Interface Format for Fusion Neutronics Studies," DLC-41, ORNL.

4. RSIC Data Library Collection, "MACKLIB-IV, 171 Neutron, 36 Gamma-Ray Group Kerma Factor Library," DLC-60, ORNL.

5. D. Garber (Comp.), ENDF/B Summary Documentation BNL 17541 (ENDF 201) Brookhaven National Laboratory, Upton, NY (Oct. 1975).

6. B. Goel, B. Krieg, "Status of the Nuclear Data Library KEDAK-3," KfK 2386/I, Kernforschungszentrum Karlsruhe, July 1979.

7. R. Herzing, L. Kuijpers, P. Cloth, D. Filges, R. Hecker, and N. Kirch, Nucl. Science and Eng., 60, 169 (1976).

8. H. Bachmann, U. Fritscher, F.W. Kappler, D. Rusch, H. Werle, and H.W. Wiese, Nucl. Science and Eng., 67, 74 (1978).

9. A. Hemmendinger, E.E. Ragan, E.R. Shunk, A.N. Ellis, J.M. Anaya, and J.M. Wallace, Nucl. Science and Eng., 70, 274 (1979).

10. W.A. Reupke and D.W. Muir, Trans. Am. Nucl. Soc., 23, 21 (1976).

11. G.M. Hale, Proc. Internat. Specialists Symposium on Neutron Standard and Applications, Gaithersburg (1977).

12. D.K. Trubey and M.B. Emmett, "Some Calculations of the Fast-Neutron Distribution in Ordinary Concrete from Point and Plane Isotropic Fission Sources," ORNL-RSIC-4, Oak Ridge National Laboratory (1965).

13. RSIC Code Package CCC-203, "MORSE-CG," Radiation Shielding Information Center, ORNL.

14. N. Packen et al., J. Nucl. Mater., 78, 143 (1978).

15. N.M. Ghoniem and G.L. Kulcinski, Nucl. Engr. Design, 52, 111 (1979).

16. F. Beranek and R.W. Conn, "Neutron Moderation in ICF Pellets and Effects on Damage and Radioactive Inventory," University of Wisconsin Fusion Design Memo UWFDM-310, (May 1979).

17. M.M. Ragheb and G.L. Kulcinski, Trans. Am. Nucl. Soc., 34, 644 (1980).

18. RSIC Code Package CCC-180, "TDA," Radiation Shielding Information Center, ORNL.

19. G.E. Bosler and T.G. Frank, Trans. Am. Nucl. Soc., 21, 16 (1975).

20. M. Sawan and G. Moses, "The TDA and TIMEX Codes for Time-Dependent Neutronics and Photonics Analysis of ICF Reactors," University of Wisconsin Fusion Design Memo UWFDM-399, (January 1981).

21. M. Monsler et al., "Electric Power from Laser Fusion: The HYLIFE Concept," proc. IECEC Conf., San Diego, CA, August 1978.

22. T.Y. Sung and W.F. Vogelsang, "DKR: A Radioactivity Calculation Code for Fusion Reactors," University of Wisconsin Fusion Design Memo UWFDM-170, (Sept. 1976).

23. H.D. Oak, G.M. Holter, W.G. Kennedy, Jr., and G.J. Konzek, Technology, Safety and Costs of Decommissioning a Reference Boiling Water Reactor Power Station, NUREG/CR-0672, Appendix E. Prepared by Pacific Northwest Laboratories for the U.S. Nuclear Regulatory Commission, June 1980.

24. T.Y. Sung and W.F. Vogelsang, "Decay Chain Data Library for Radioactivity Calculations," UWFDM-171 (September 1976).

25. B. Badger et al., "NUWMAK, A Tokamak Reactor Design Study," University of Wisconsin Fusion Design Memo UWFDM-330, (March 1979).

VI.4 Behavior of Pb-Li Vapor

A unique engineering problem for ICF reactors is the design of a first surface which can carry away the steady-state average surface heat and at the same time survive the transient temperature increase generated by X-ray and ion debris from the target explosion. In HIBALL, the INPORT tubes serve this purpose. The INPORT tubes, filled with flowing $Pb_{83}Li_{17}$ coolant, protect the first structural wall from excessive neutron damage. The SiC tubes themselves are protected from the short range X-ray and ion debris by a thin layer of PbLi that flows down the outside of the porous tube.

After a target explosion, the X-ray energy is deposited within 10^{-3} cm of the first surface. The temperature of a thin layer of $Li_{17}Pb_{83}$ exceeds its boiling temperature, and is vaporized. This ablated material flows toward the center of the cavity and intercepts the ions generated by the explosion. The energy associated with the ions is absorbed by the $Li_{17}Pb_{83}$ gas and does not directly impinge on the first surface. The gas heats up to a very high temperature and starts to release its energy by thermal radiation toward the cool first surface. The liquid surface temperature increases upon receiving energy from this thermal radiation and condensation of the vapor. The higher surface temperature increases the vapor pressure and consequently increases the vaporization rate. The cavity pressure is very high after the initial X-ray deposition, and varies by the combined effects of evaporation and condensation. It is of critical importance to beam transport and, to a lesser degree, vacuum pumping to calculate the pressure history after an explosion. One important factor determining repetition rate is that the vacuum condition in the cavity be low enough to allow beam transport.

In this section, the behavior of the Pb-Li vapor is discussed. In section VI.4.1 the deposition of target generated X-rays and the subsequent

vaporization of the Pb-Li is described. Section VI.4.2 deals with the stopping of target generated ions in the vapor, the flow of Pb-Li into the reactor chamber and the radiation of photon energy from the vapor back onto the tubes. Section VI.4.3 contains a description of the vaporization and condensation of the Pb-Li vapor. The pressure history of the cavity is thus established. Different X-ray spectrums result in different masses of evaporated material and this is also investigated.

VI.4.1 X-ray Energy Deposition and the Resulting Evaporation

Target generated X-rays will deposit their energy over a short range in Pb-Li and will heat this thin layer to high temperatures. The X-ray deposition and the energy densities of the Pb-Li after deposition are computed. This leads to a simple heat balance method of calculating the mass of vaporized Pb-Li.

The energy deposition from X-rays can be described by exponential attenuation inside the material. The photo-electric cross sections are those given by Biggs.(1) Determination of the energy deposited from a given spectrum must also account for transport of any scattered photons. If, however, the primary interaction is the photo-electric effect, the scattering can be ignored and an exponential deposition profile can be assumed. The photo-electric effect comprises 90% of the interactions for photon energies up to 10 keV, 30 keV and 70 keV for carbon, iron and molybdenum, respectively.(2) Since lead is of yet higher Z, the photo-electric effect is dominant to even higher photon energy.

The volumetric energy deposition for a monoenergetic spectrum can be represented by

$$q_\nu = \mu_\nu F_{o\nu} e^{-\mu_\nu x}$$

where q_ν = energy/unit volume/unit frequency

$F_{o\nu}$ = incident intensity, energy/unit area/unit frequency

μ_ν = absorption cross section at energy $h\nu$.

The total energy deposited per unit volume is obtained by integration over the X-ray spectrum.

Figure VI.4-1 shows the X-ray energy spectrum obtained from the target calculations[3] discussed in section III.1. The spectrum is peaked around 3 keV and extends up to 300 keV. Since most of the photons have energies well below 100 keV, we have used the Biggs data.

Figure VI.4-2 shows the volumetric energy deposition in Pb using the spectrum given in Fig. VI.4-1. The A*THERMAL[4] code was used in this calculation. Note that 88 MJ or 22% of the target yield is in the form of X-rays.

The amount of mass vaporized due to the X-ray energy deposition is computed using a simple model. We calculate the total energy per unit volume required to vaporize the lead, 8.7×10^3 J/cm^3. From the X-ray energy deposition calculation the depth of the material that will be vaporized can be determined. This adiabatic model becomes more accurate for very short X-ray deposition times, i.e. instantaneous.

We simply balance heat in the following manner.

$$\text{Heat of vaporization of lead} = 8.7 \times 10^5 \text{ J/kg} \simeq 8.7 \times 10^3 \text{ J/cm}^3$$

$$C_p(T_b - T_o) = C_p\ (1750°C - 400°C) \simeq 1944 \text{ J/cm}^3$$

$$\text{Total (J/cm}^3\text{) for vaporization} = 1.06 \times 10^4 \text{ J/cm}^3.$$

From the X-ray energy deposition curve (Fig. VI.4-2) this corresponds to a thickness of approximately 2.5 microns. To account for energy deposition above $C_p(T_b - T_o)$ in the region between the saturated liquid and the sensible

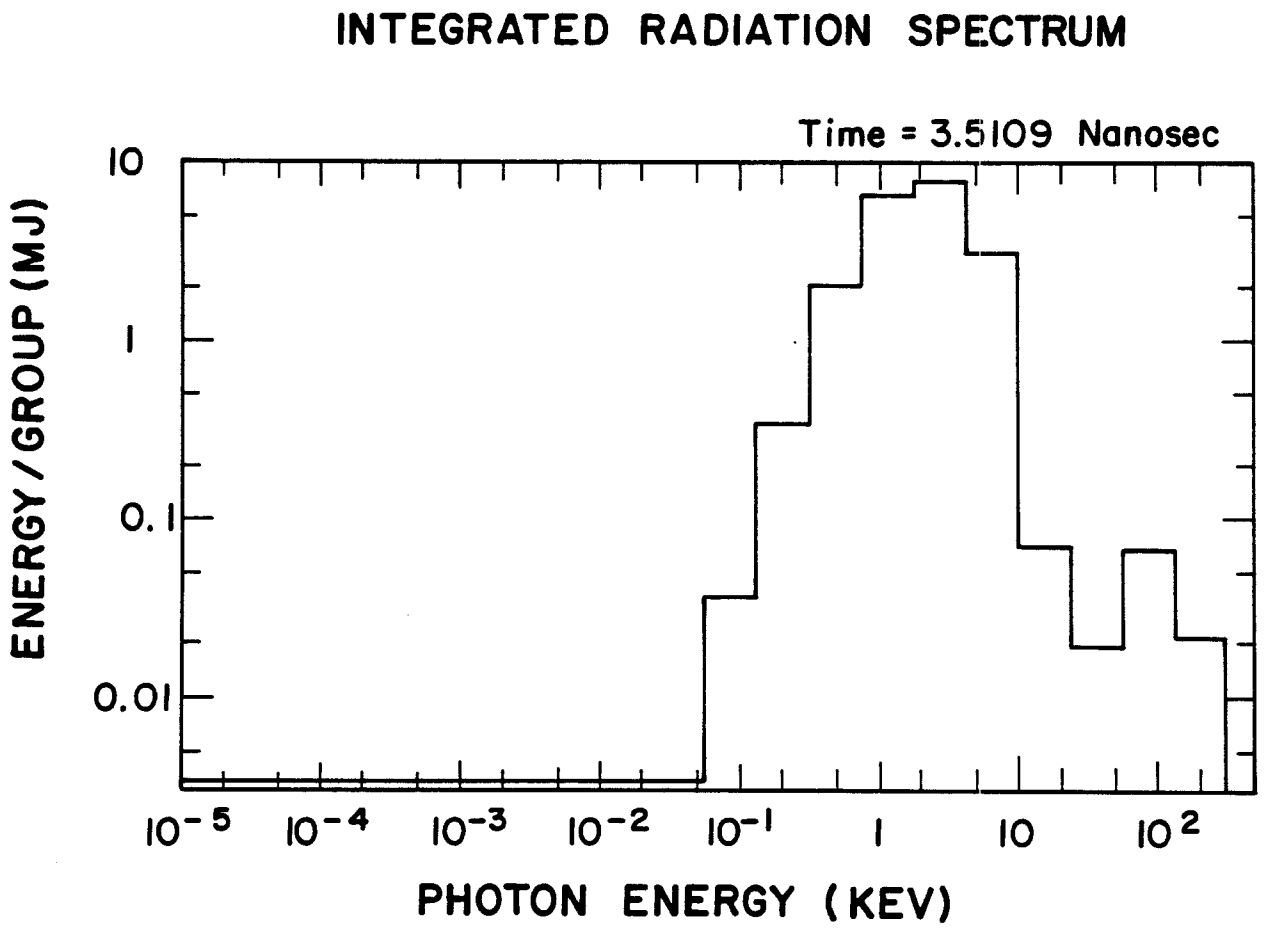

Fig. VI.4-1 X-Ray energy spectrum resulting from pellet burn.

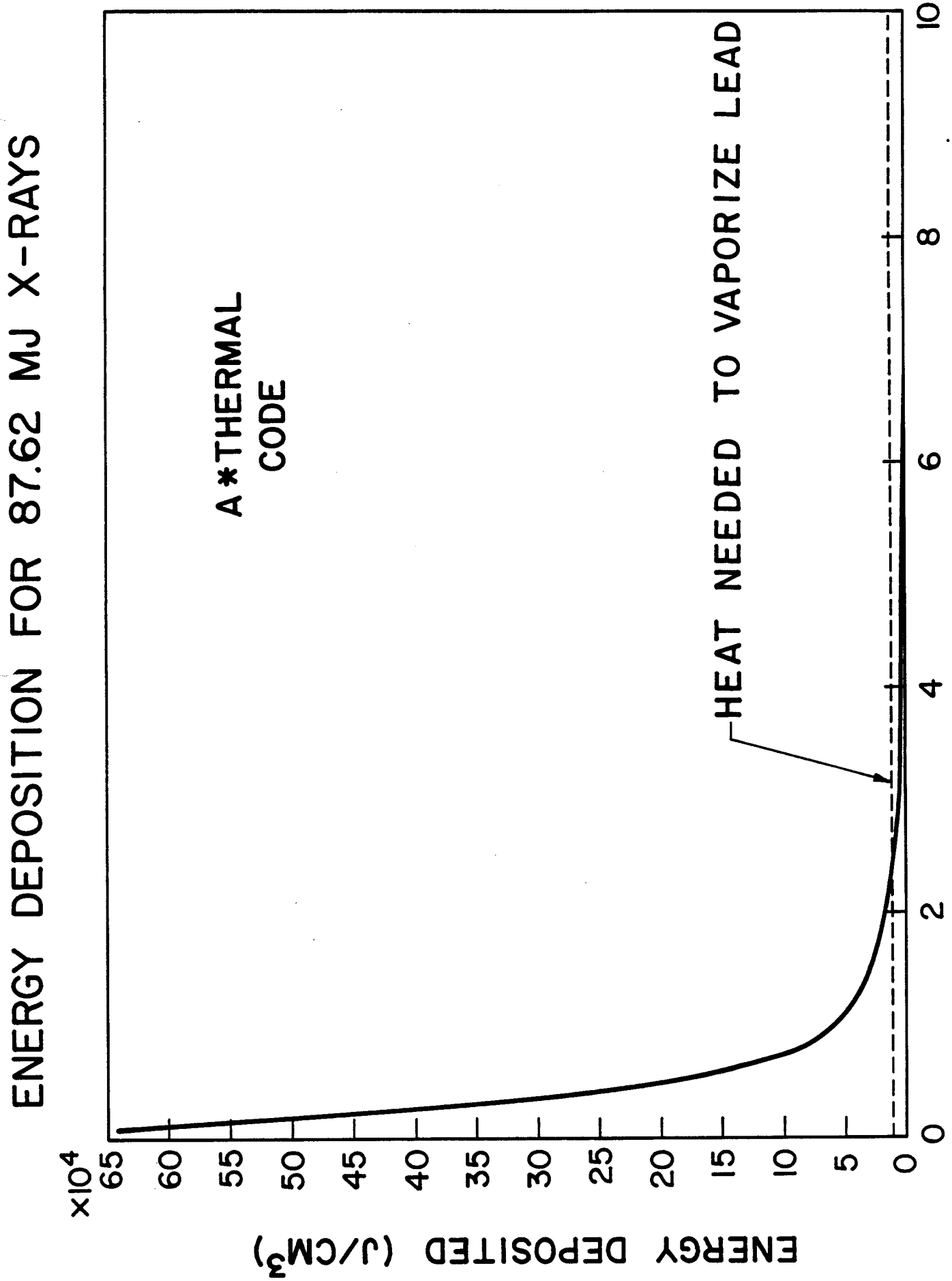

Fig. VI.4-2 X-Ray volumetric energy deposition in liquid lead.

heat, we have assumed that there is some additional vaporization. This additional vaporization accounts for the additional energy deposition above $C_p(T_b - T_o)$ as is shown schematically in Fig. VI.4-3. This gives an additional thickness of the vaporized layer of about 1.8 microns. Therefore the total thickness of material vaporized ≃ 4.3 microns.

We now can calculate the mass of vaporized Pb-Li,

$$M_o \cong \rho 4\pi R^2 \delta$$

where ρ = density of lead

R = radius of the cavity

δ = thickness of material vaporized

Substituting, we get $M_o \simeq 13$ kg/shot.

These calculations were repeated using cylindrical geometry and the results did not differ by very much. This is because the geometry is almost a square cylinder.

An example of how the X-ray spectrum affects the mass of material vaporized is shown in Fig. VI.4-4. Three different blackbody spectrums were used. In this example, the total energy contained in X-rays is 33.6 MJ. The softer spectrum of 0.5 keV has a very short range. The harder the spectrum, the more it penetrates through the material. We conclude that the mass of material vaporized will be determined by the X-ray spectrum and X-ray yield. This is determined by the specific target design.

VI.4.2 Pb-Li Gas Dynamics and Radiation

As discussed in the preceding section, target generated X-rays vaporize several kilograms of Pb-Li off of the INPORT tubes. The resulting gas absorbs the target generated ions, reaches a temperature of about 1 eV and becomes

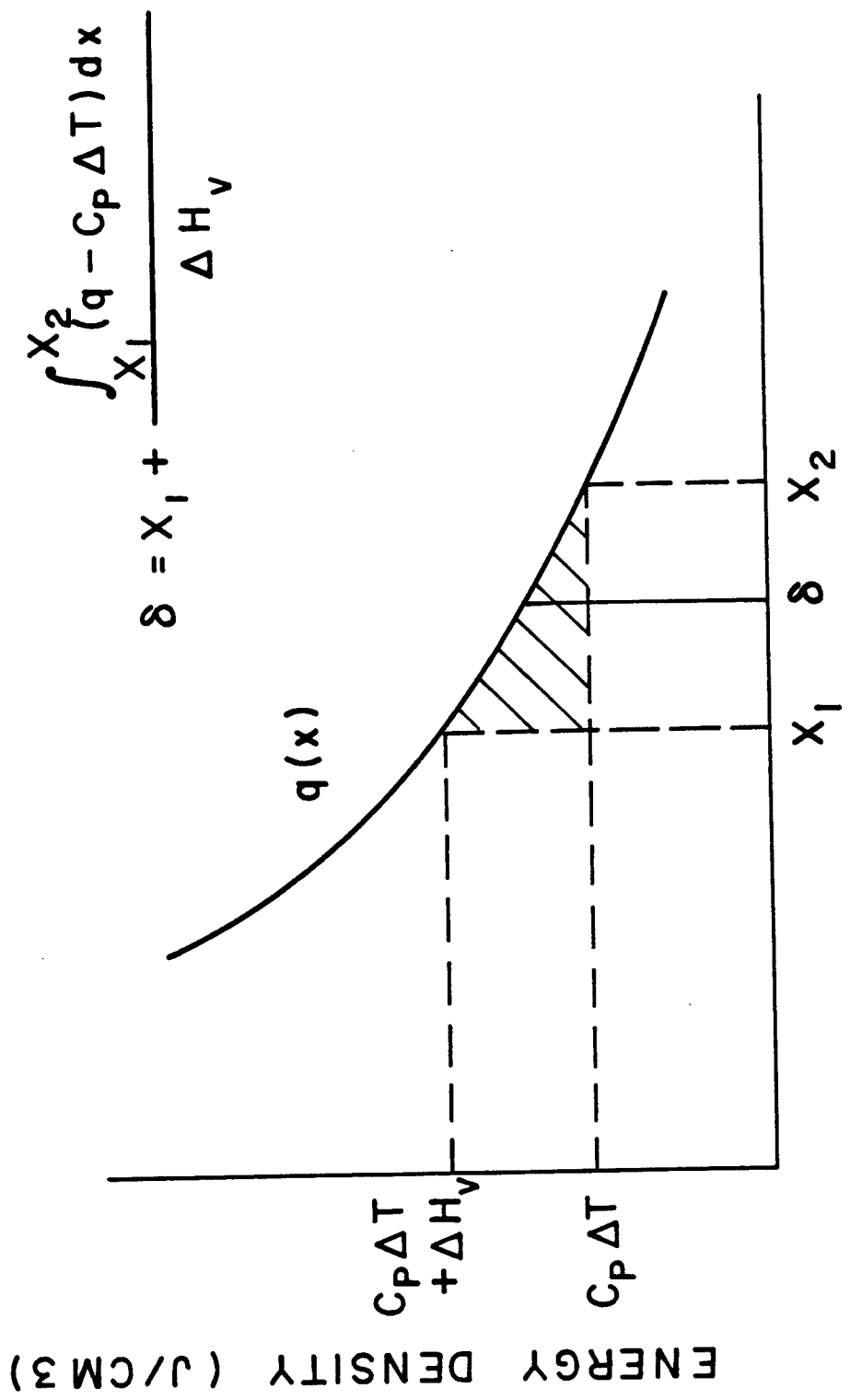

Fig. VI.4-3 Conceptual representation of Pb-Li vaporization.

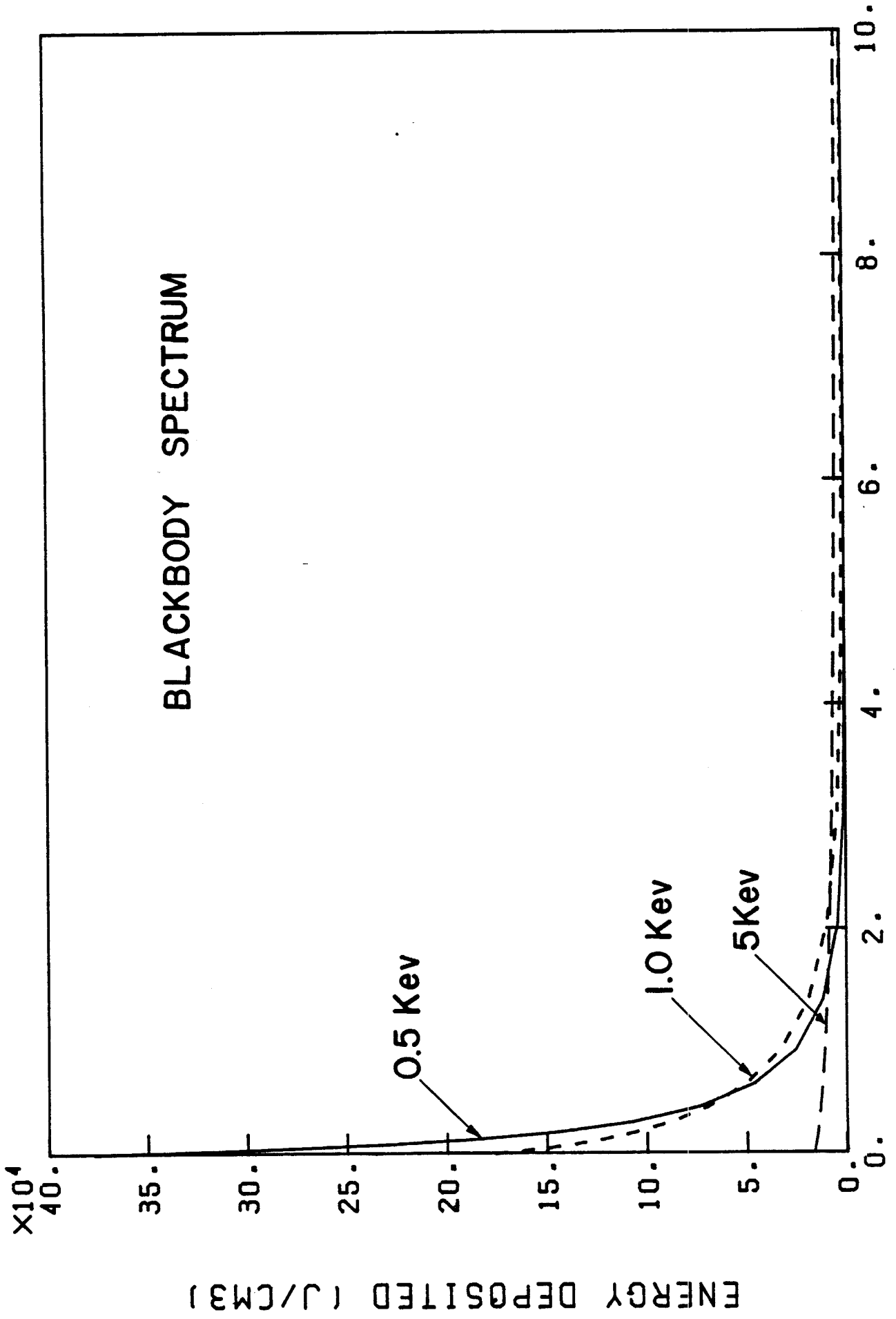

Fig. VI.4-4 X-Ray energy deposition for different blackbody spectra.

partially ionized. As this gas spreads from the tubes into the center of the reactor cavities, it radiates photons which put a heat flux back onto the tubes. Eventually, the gas uniformly fills the cavity and cools enough that the heat flux on the tubes is insignificant. Before this happens, though, there may be some additional vaporization of Pb-Li due to the heat flux. As the gas radiates, it also cools, affecting the rate of recondensation. For these reasons, it is important to consider the behavior of this gas between the time of vaporization and recondensation.

To study this problem, it is necessary to know the equation-of-state and optical data for gaseous Pb-Li. We describe an atomic physics calculation providing this information in section VI.4.2.1.

Once the atomic physics of the gas is understood, the motion and radiation of the gas can be studied. In section VI.4.2.2 we discuss a computer simulation of the gas behavior which uses the results of the atomic physics calculations in section VI.4.2.1.

With this computer model, we can predict what heat fluxes the INPORT tubes might experience from gas radiation and we investigate the sensitivity of such radiation to the total mass of the Pb-Li vaporized. In section VI.4.2.2 we present heat fluxes and average gas temperatures versus time for various Pb-Li masses.

Finally, in section VI.4.2.3 we state our conclusion that the gas behavior is fairly sensitive to the mass of the gas and comment on the significance of these results.

VI.4.2.1 Equation of State and Opacity of Gaseous Pb-Li

The atomic physics of gaseous Pb-Li is studied with the MIXER[5,6] computer code. This code has been developed at the University of Wisconsin to

provide data tables of internal energy density, ionization state, heat capacity and radiation opacities of gas mixtures. This is done as functions of gas temperature, gas density and radiation temperature. Ionization is assumed to occur in either the Saha[7] or the Coronal[8] model and radiative processes to follow a semi-classical formalism.[9] In a mixture of gases the electron density is calculated self-consistently and the interaction of radiation is considered with the 20 lowest excited states of the six most common ionization states for each gas species.

Some results of calculations with this code for $Pb_{83}Li_{17}$ are shown in Figs. VI.4-5 and VI.4-6. Figure VI.4-5 is a plot of the ionization state of $Pb_{83}Li_{17}$ over the plane of gas temperature and density. One can see on this plot where the Saha model is used by remembering the fact that Saha ionization can be a function of density while Coronal ionization cannot. The boundary between the two regions follows the criterion

$$n_e = 10^{16} (k_B T_{gas})^{7/2} \text{ cm}^{-3}$$

where $k_B T_{gas}$ is in eV.[8] Saha ionization is used at high density and low gas temperature. It is also important to note that the dependence of the ionization on the gas temperature makes the equation-of-state rather non-ideal.

Figure VI.4-6 shows the Planck averaged mean free path plotted over the gas temperature - radiation temperature plane for a given density. Notable features of this are the transparency of cool gas to low temperature radiation and the extreme variability of this parameter. This variability can make radiation transport very sensitive to the changes in the conditions in a gas.

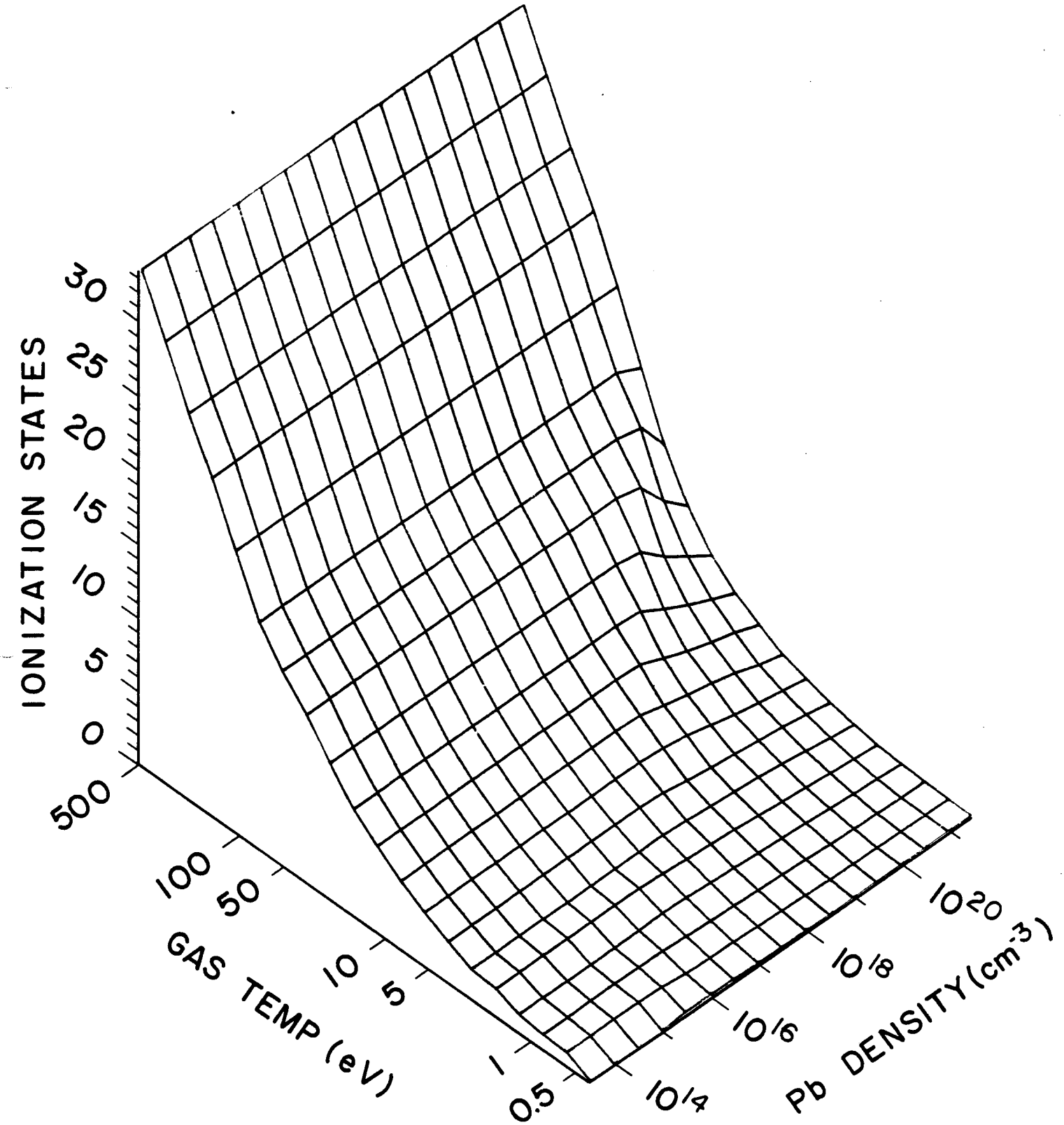

$Pb_{83}Li_{17}$
CHARGE STATE

Fig. VI.4-5

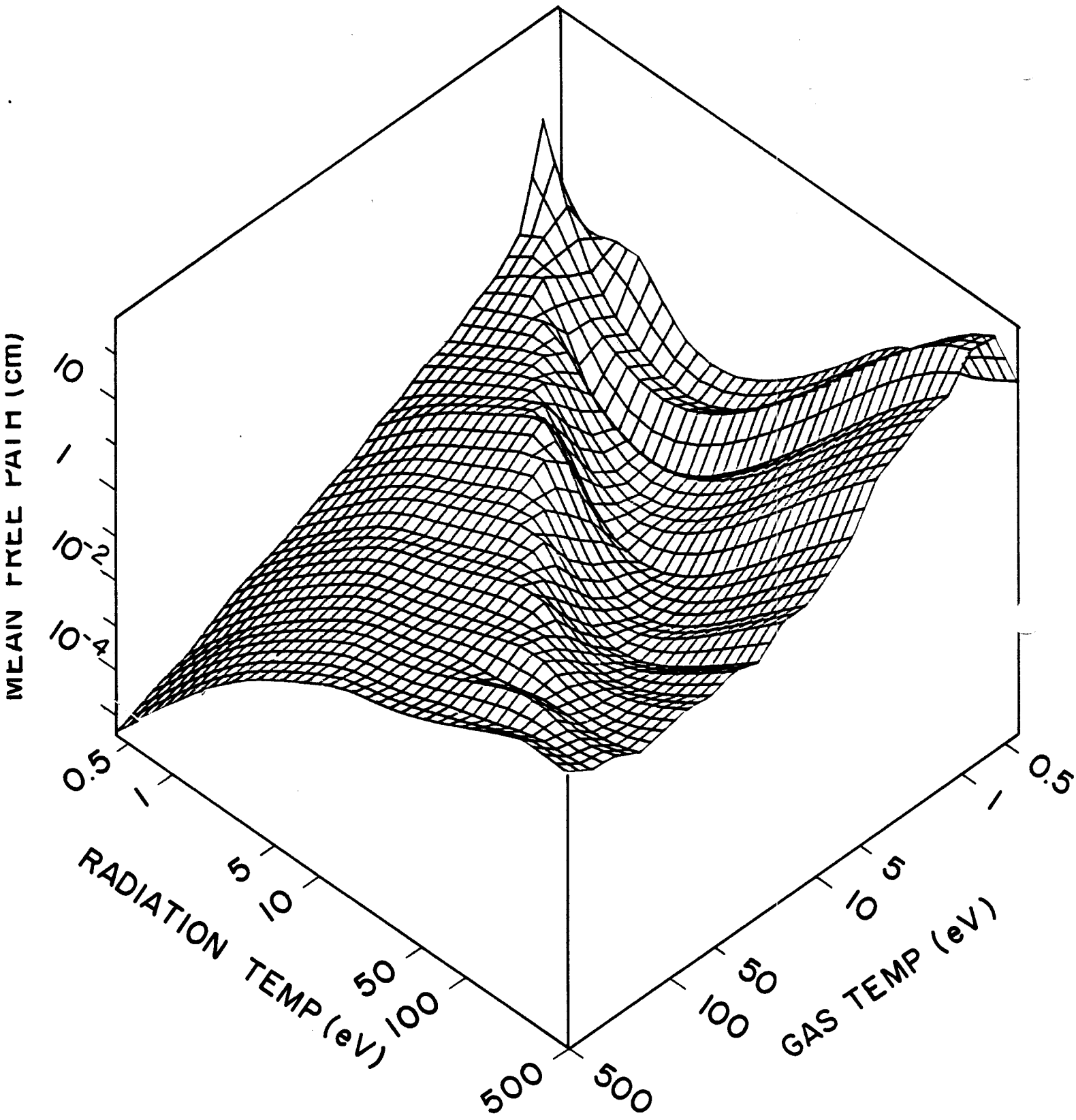

$Pb_{83}Li_{17}$

PLANCK MEAN FREE PATH

Pb DENSITY = $2.7 \times 10^{18}\ cm^{-3}$

Fig. VI.4-6

VI.4.2.2 Radiation - Hydrodynamics in Pb-Li

We have modeled the behavior of the Pb-Li gas with the 1-D Lagrangian radiation-hydrodynamics computer code, FIRE.[10] This code has explicit hydrodynamics and implicit energy transport where heat is conducted through two fluids - the gas at a local temperature of T_{gas} and the radiation fluid at a temperature of $T_{radiation}$. In these calculations, conduction through the radiation field dominates the thermal transport. Transport coefficients and equation-of-state information is obtained from a table of data provided by a calculation with MIXER.

FIRE cannot accurately model the behavior of fluid which is as dense as a liquid. Thus, we must analytically calculate the dynamics from the time when the Pb-Li is at liquid density until the time that the density is low enough for FIRE calculations to be appropriate. We assume that the gas obeys an isothermal blow-off formalism where the temperature of the gas is that due to the deposited target generated X-ray energy minus the energy of vaporization and the energy of ionization. We arbitrarily assume that the energy from target generated ions is uniformly deposited in the gas at 1.5×10^{-4} seconds after vaporization and that FIRE can be used any time after this. Thus, at this time we start the computer calculations with the gas density profile being the Gaussian shape predicted by the blow-off model and the total energy in the gas being the target generated X-ray and ion energy minus the vaporization and ionization energy.

The FIRE calculation simulates the gas dynamics until the time the gas reaches the center of the cavities. Figure VI.4-7 shows the positions of the Lagrangian zone boundaries for a typical calculation during this period. Upon reaching the center, the gas begins to convert its bulk kinetic energy into heat, but FIRE, being a one-dimensional code, predicts that the gas will

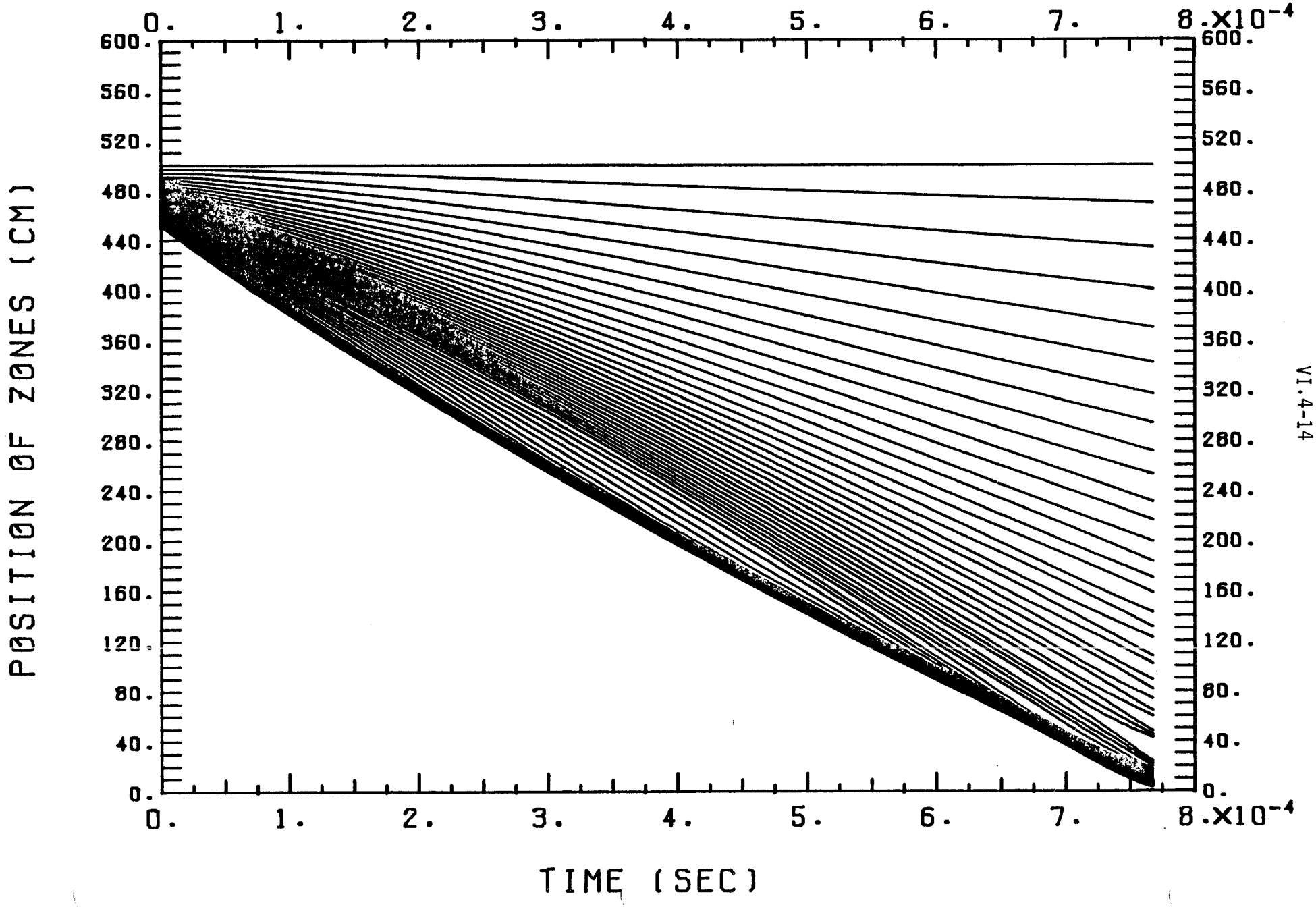
POSITION OF ZONES (CM)
TIME (SEC)
0.
1.
2.
3.
4.
5.
6.
7.
8.X10^-4
600.
560.
520.
480.
440.
400.
360.
320.
280.
240.
200.
160.
120.
80.
40.
0.

Fig. VI.4-7

reflect off the center and propagate back towards the tubes. This is not physical because the system does not have the symmetry needed for such reflections. For this reason we stop this first simulation calculation at the time when the gas reaches the center, typically about 1 millisecond after vaporization.

To simulate the behavior past this time we assume that the gas has a uniform temperature and density and has no bulk kinetic energy immediately after the gas collapses in the center. We find the temperature that will give the proper amount of energy,

$$E_{gas} = E_{x\text{-}ray} + E_{ion} - E_{vaporization} - E_{ionization} - E_{radiation} ,$$

where $E_{radiation}$ is the energy radiated back into the tubes by this time. We then use FIRE again with this new initial condition and with the gas constrained not to move. By combining both uses of FIRE, we calculate the heat flux on the tubes due to radiation and the average temperature of the gas versus time.

To test the sensitivity of the gas behavior to the total mass of Pb-Li vaporized, we have completed calculations for three different total masses; 6.7 kg, 13.3 kg and 26.6 kg. In Figs. VI.4-8 through VI.4-10 the heat fluxes on the surfaces of the tubes are shown for total masses of 6.7 kg, 13.3 kg and 26.6 kg, respectively.

The average temperatures are shown in Figs. VI.4-11 through VI.4-13. Notice that there is in each case a large pulse of heat reaching the surface immediately after the gas collapses in the center. This is an effect of the conversion of bulk kinetic energy into heat. As is seen in Figs. VI.4-11 through VI.4-13, there is also a pulse in the average temperature of the gas

Fig. VI.4-8

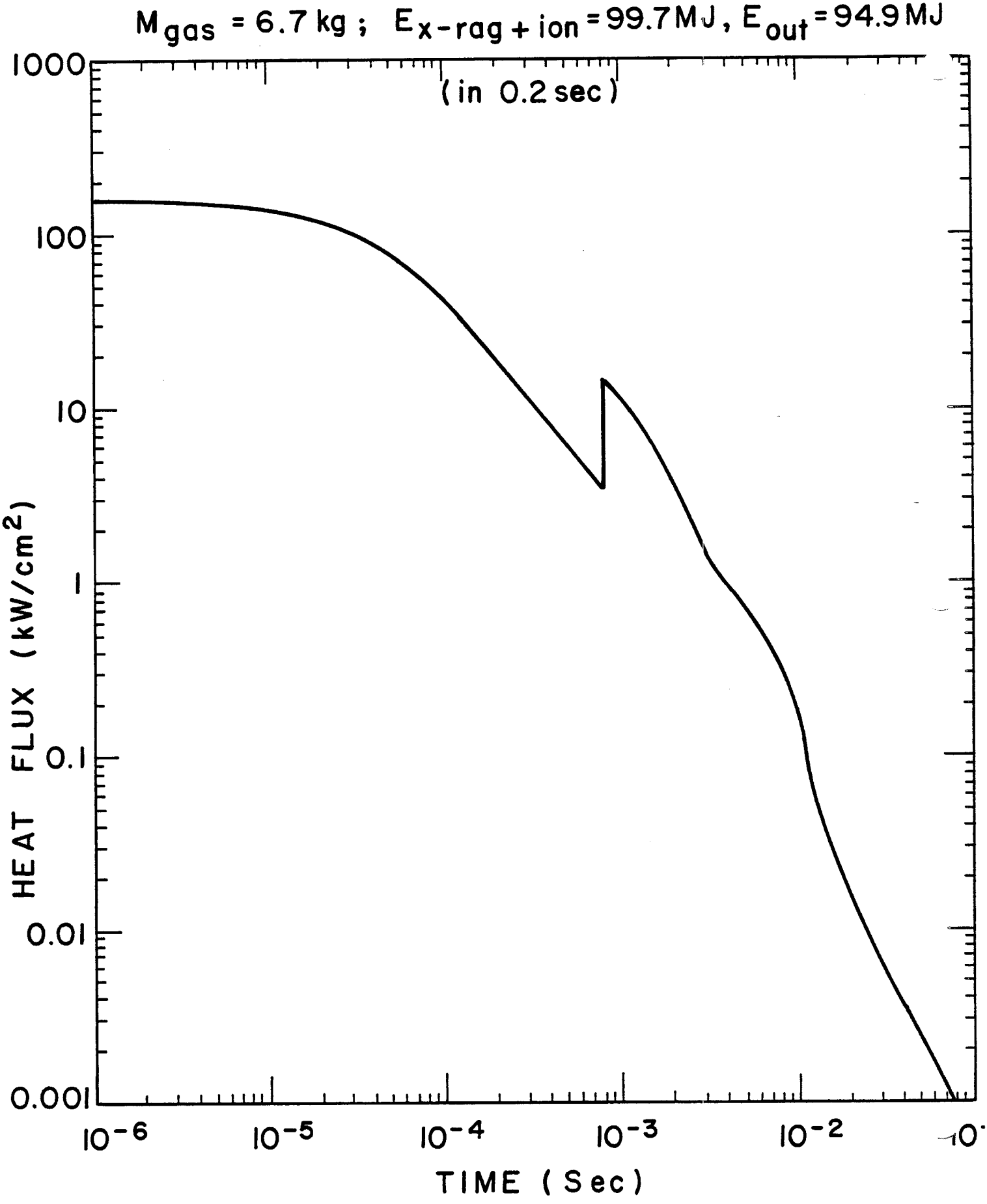
M_{gas} = 6.7 kg ; $E_{x\text{-}rag + ion}$ = 99.7 MJ, E_{out} = 94.9 MJ
(in 0.2 sec)
1000
100
10
1
0.1
0.01
0.001
HEAT FLUX (kW/cm²)
10^{-6}
10^{-5}
10^{-4}
10^{-3}
10^{-2}
TIME (Sec)

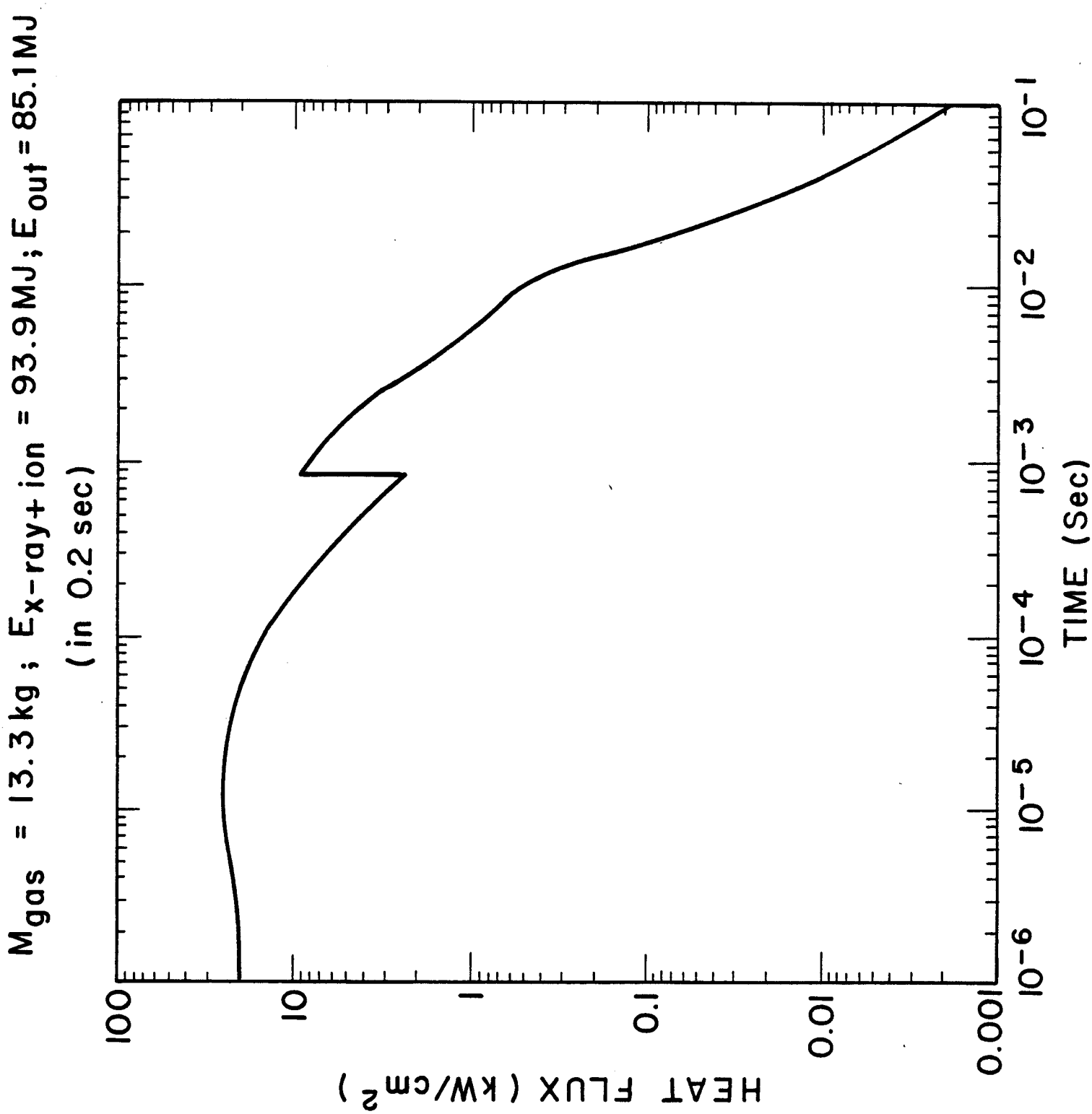
M_{gas} = 13.3 kg ; $E_{x-ray+ion}$ = 93.9 MJ; E_{out} = 85.1 MJ
(in 0.2 sec)
HEAT FLUX (kW/cm²)
100
10
1
0.1
0.01
0.001
10⁻¹
10⁻²
10⁻³
10⁻⁴
10⁻⁵
10⁻⁶
TIME (Sec)

Fig /I.4-9

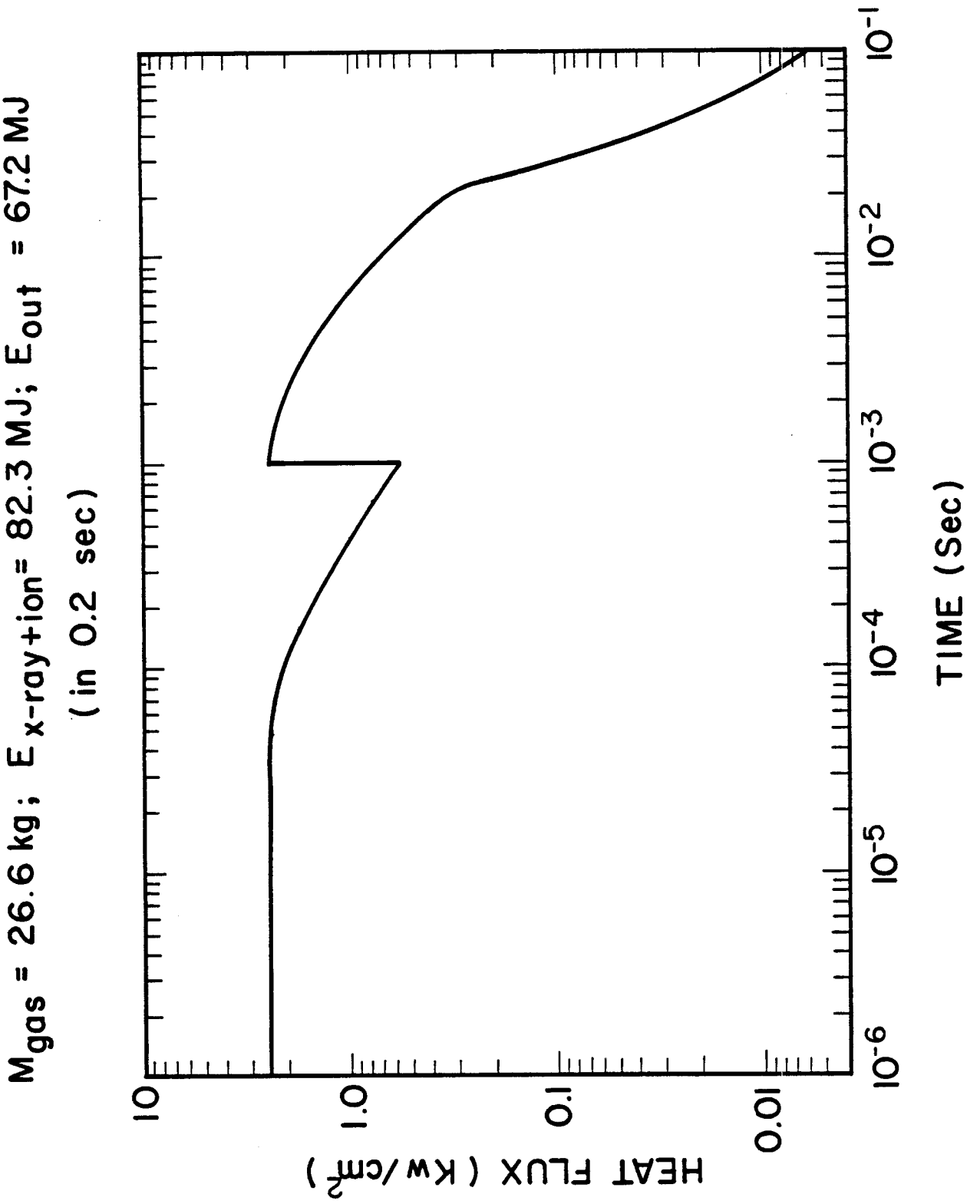
M_{gas} = 26.6 kg; $E_{x\text{-}ray+ion}$ = 82.3 MJ; E_{out} = 67.2 MJ
(in 0.2 sec)
HEAT FLUX (kw/cm²)
10
1.0
0.1
0.01
TIME (Sec)
10^{-6}
10^{-5}
10^{-4}
10^{-3}
10^{-2}
10^{-1}

Fig. VI.4-10

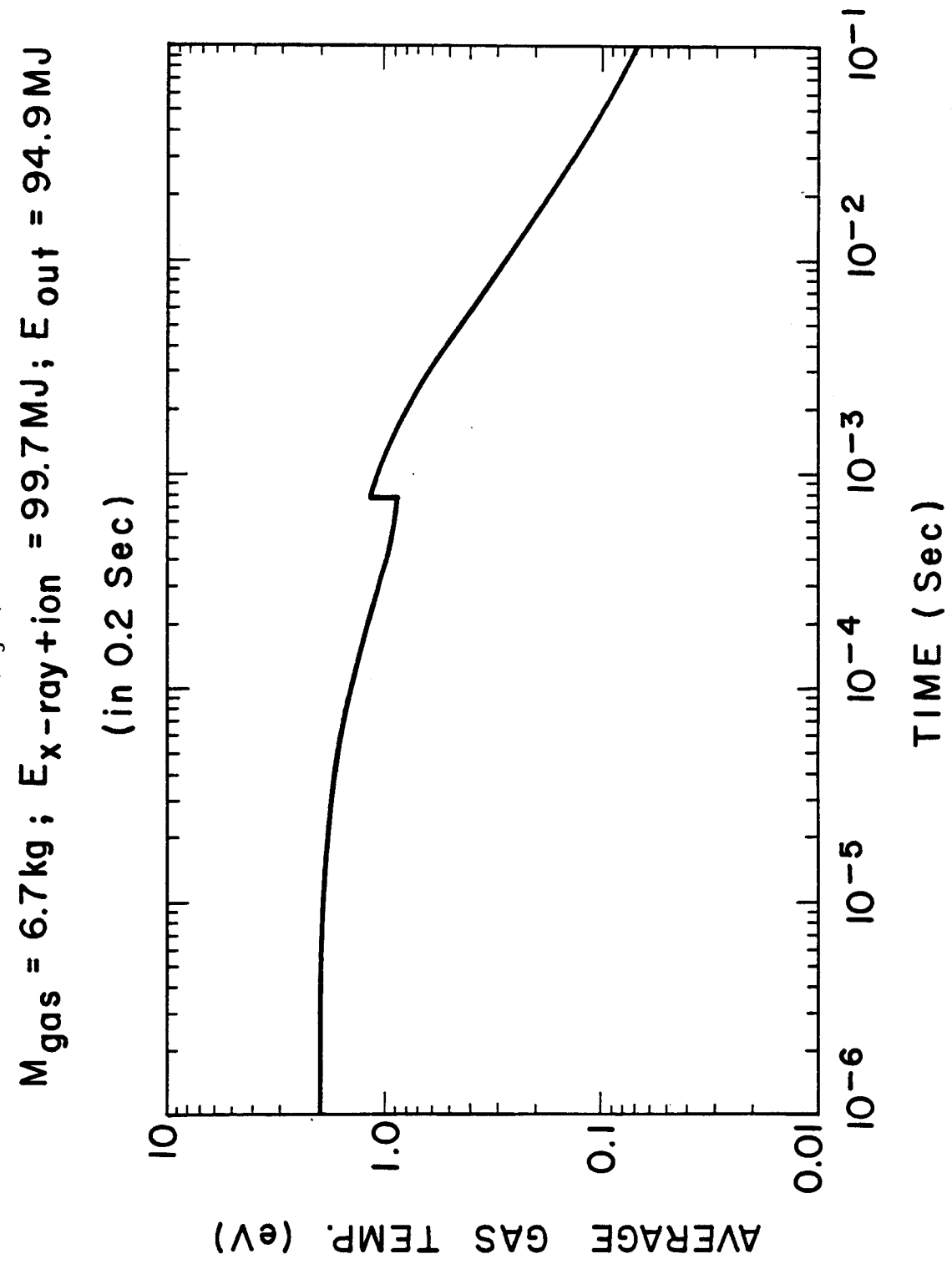
M_{gas} = 6.7kg ; $E_{x-ray+ion}$ = 99.7MJ ; E_{out} = 94.9MJ
(in 0.2 Sec)
AVERAGE GAS TEMP. (eV)
10
1.0
0.1
0.01
10^{-6}
10^{-5}
10^{-4}
10^{-3}
10^{-2}
10^{-1}
TIME (Sec)

Fig. VI.4-11

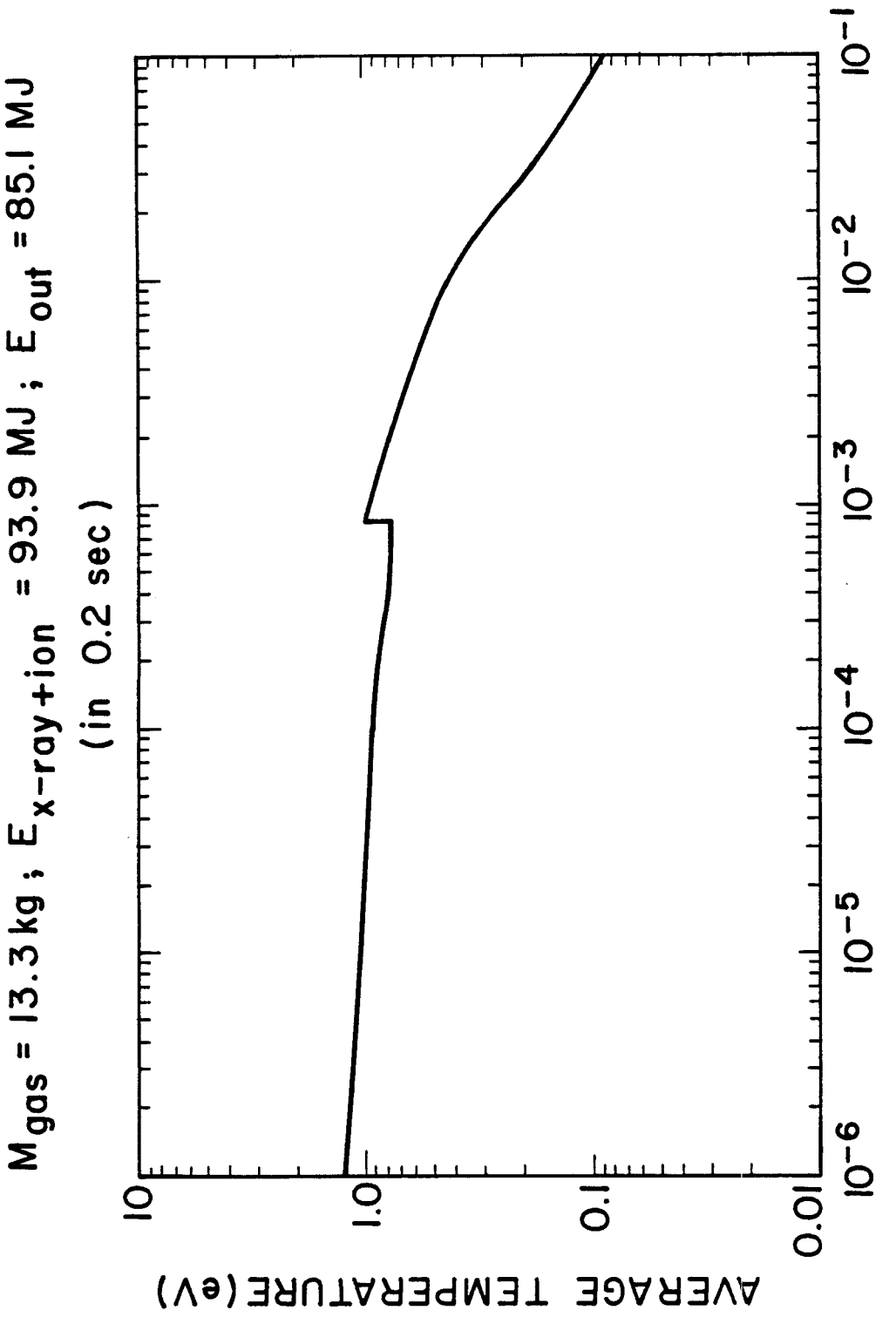
M_{gas} = 13.3 kg ; $E_{x\text{-}ray+ion}$ = 93.9 MJ ; E_{out} = 85.1 MJ
(in 0.2 sec)
AVERAGE TEMPERATURE (eV)
10
1.0
0.1
0.01
10^{-6}
10^{-5}
10^{-4}
10^{-3}
10^{-2}
10^{-1}
TIME (Sec)

Fig. VI.4-12

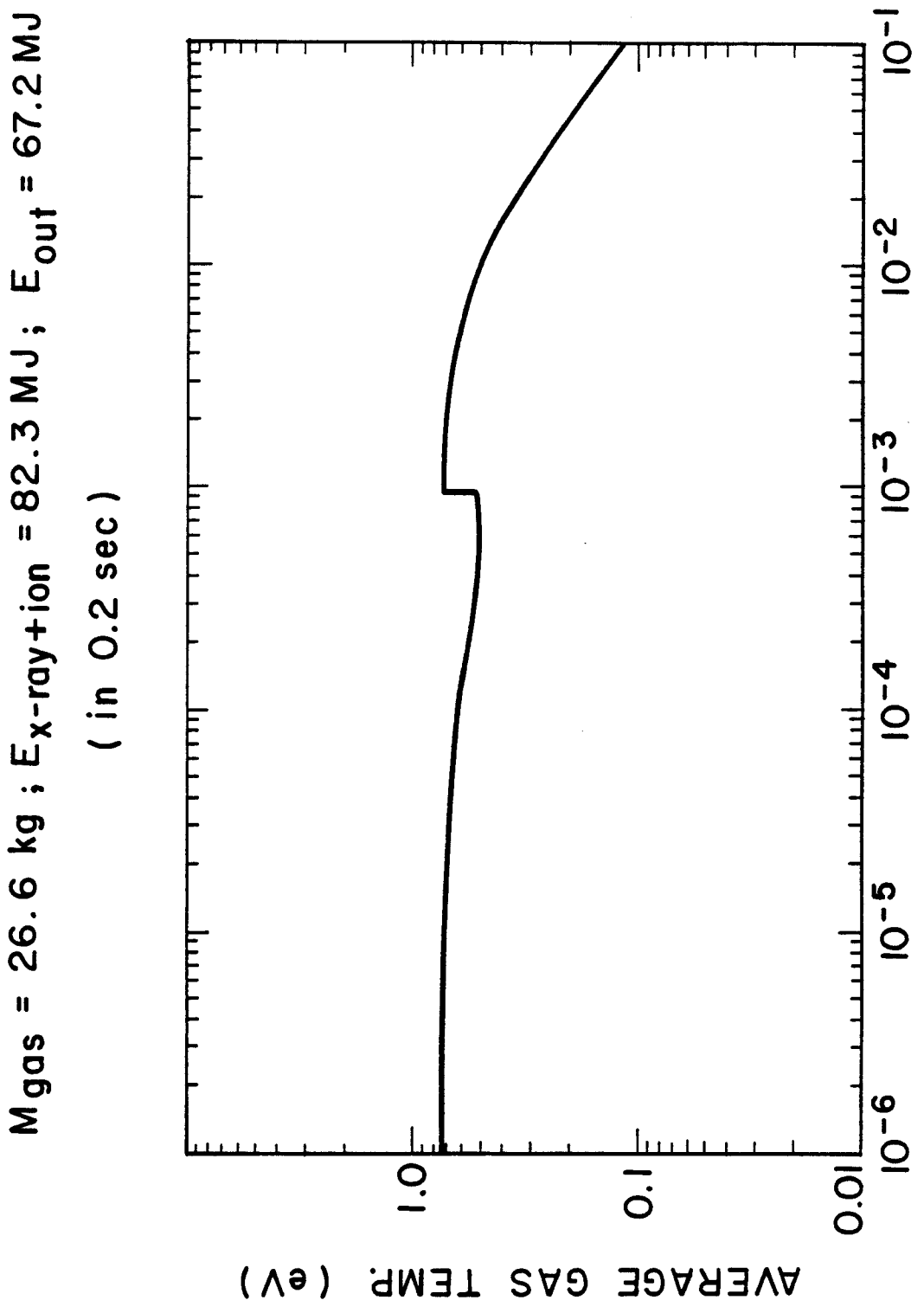
M_{gas} = 26.6 kg ; $E_{x\text{-}ray+ion}$ = 82.3 MJ ; E_{out} = 67.2 MJ
(in 0.2 sec)
AVERAGE GAS TEMP. (eV)
1.0
0.1
0.01
10^{-6}
10^{-5}
10^{-4}
10^{-3}
10^{-2}
10^{-1}
TIME (Sec)

Fig. VI.4-13

which is due to this conversion of kinetic energy into heat and which causes the increase in heat flux. The same process has been seen in imploding wire experiments.

VI.4.2.3 Conclusions

Comparison of Figs. VI.4-8 through VI.4-10 shows that the heat flux can vary by two orders of magnitude when the total mass is changed by a factor of four. At low gas mass the temperature must be high because the internal energy density is high. Also, the radiation passes through less dense gas more easily. Thus, the heat fluxes are higher for low total gas mass. As the mass of the gas is increased, both of these trends are reversed and the gas radiates energy more slowly back to the tubes.

VI.4.3 Evaporation/Condensation Calculations

Once the radiation heat flux and the temperature of the gas is known, the behavior of the gas density in the cavity over time can be investigated. The rate that gas leaves the cavities is governed by geometry of the cavities and the gas temperature. The rate that gas is added to the cavity through evaporation off of the tubes is determined by the temperature of the Pb-Li film on the tubes. This temperature can be found through a temperature diffusion calculation in this film for the surface heat fluxes calculated in section VI.4.2.

In section VI.4.3.1 we describe the methods used in the temperature diffusion calculation, in the condensation and in the evaporation. In section VI.4.3.2 we present and discuss results. Conclusions of a general nature are made in section VI.4.3.2.

VI.4.3.1 Calculation Procedure

The governing equations for heat transfer, condensation and evaporation are:

$$K \frac{\partial^2 T}{\partial \chi^2} = \rho c_p \frac{\partial T}{\partial t} \qquad \text{(VI.4-1)}$$

$$m_{cond.} = 3.64\ P_g\ (M/RT_g)^{1/2} \qquad \text{(VI.4-2)}$$

$$m_{vap.} = P_s\ (\frac{M}{RT_s})^{1/2} \qquad \text{(VI.4-3)}$$

in which:

K	is thermal conductivity of $Li_{17}Pb_{83}$
ρ	is density, g/cm^3
C_p	is specific heat, J/g K
T	is temperature, K
χ	is distance from first surface, cm
t	is time, sec
$m_{cond.}$	is condensation rate, g/sec - cm^2
P_g	is pressure of the gas, Torr
M	is molecular weight
T_g	is temperature of the gas, K
$m_{evp.}$	is evaporation rate, g/sec - cm^2
P_s	is saturation vapor pressure of first surface
T_s	is the temperature of the first surface, K.

The initial conditions are:

$$T = 1150\ K \quad 0 < \chi < 10^{-4}\ cm$$

$$T = T(\chi) \quad \chi > 10^{-4}\ cm$$

$$P_g = 108\ Torr$$

$$T_g = 14500\ K$$

The boundary conditions for Eq. VI.4-1 are:

$$- K \frac{dT}{d\chi} = q_{tot} \text{ at } \chi = 0$$

$$K \frac{dT}{d\chi} = h\ (T - T_c) \text{ at } \chi = \chi_o$$

in which $q_{tot} = q_r + q_c - q_v$. We have used the following definitions:

q_r is energy deposited due to radiation

q_c is energy deposited due to condensation

q_v is energy loss due to evaporation

h is heat transfer coefficient

T_c is temperature of the coolant.

$T(\chi)$ is the temperature profile in the coolant tube wall. This temperature is unknown at the beginning of the calculation and has to be estimated. However, after a few cycles, a quasi-steady-state will be established and $T(\chi)$ can be calculated.

Equation VI.4-1 cannot be solved exactly due to the complicated initial and boundary conditions. Therefore, the following finite difference form is used:

$$T_i' = T_i + \sum_j \frac{cond_{ji}}{[v\rho c_p]_i} (T_j - T_i)\ \Delta\theta \qquad \text{(VI.4-4)}$$

in which $\Delta\theta$ is time step and is $\leq \frac{[v\rho c_p]_i}{\sum_j cond_{ji}}$, T_i is temperature of zone i

before time step $\Delta\theta$, $cond_{ji}$ is the conductance $(\frac{KA}{X})$ between zones j and i, $[v\rho c_p]_i$ is the thermal inertia of zone i and T_i' is new temperature of zone i after $\Delta\theta$.

By using Eqs. VI.4-2, VI.4-3, and VI.4-4, and starting from the initial condition, all the information in the cavity can be calculated step by step.

VI.4.3.2 Results and Conclusions

We have calculated heat transfer in the Pb-Li film, evaporation and condensation with the following assumptions:

a. The cavity is spherical with R = 5 m.

b. The gas zone has a uniform temperature and pressure.

c. The condensation and evaporation are by Pb only.

d. The material properties are independent of temperature.

e. The first surface forms a spherical enclosure over the cavity.

f. The thickness of the tube wall is 1.5 mm.

g. The coolant temperature is 324°C and has a heat transfer coefficient of 12 W/cm^2-°C.

The results of a series of calculations for 13 kg of vaporized Pb-Li are summarized from Fig. VI.4-14 to Fig. VI.4-20. Figure VI.4-14 shows the temperature of the first surface as a function of time. An examination of this curve shows that the temperature history is not the same for the first two shots. Figure VI.4-15 shows the temperature of the wall as a function of distance from first surface just before the first three explosions. It can be seen that temperature has almost converged to a quasi-steady-state after 3 shots. Figure VI.4-16 shows the condensation and evaporation rates. Note that for a vaporized mass of 13 kg, evaporation is not important. Figure VI.4-17 shows the total condensation and evaporation and the mass in the cavity as a function of time. At times after 0.1 sec, the mass of gas in the

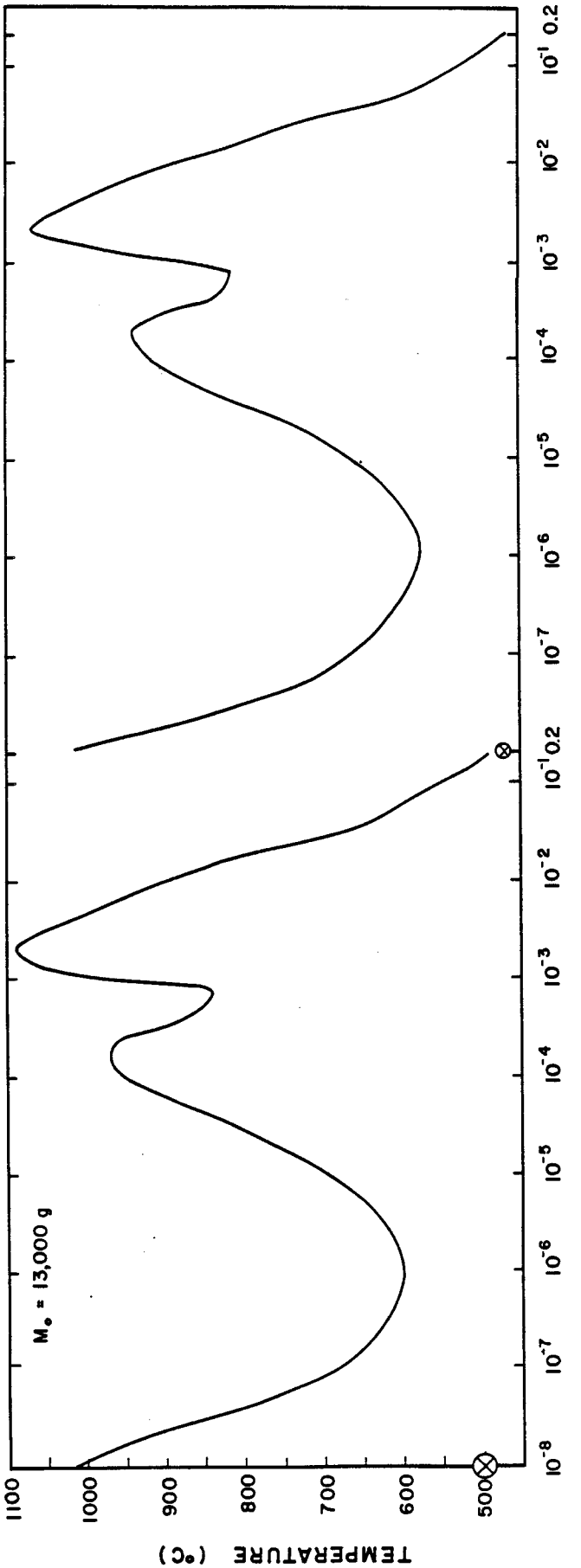

Fig. VI.4-14 Temperature of the first surface during the first two shots.
Mass of vaporized gas = 13000 g.

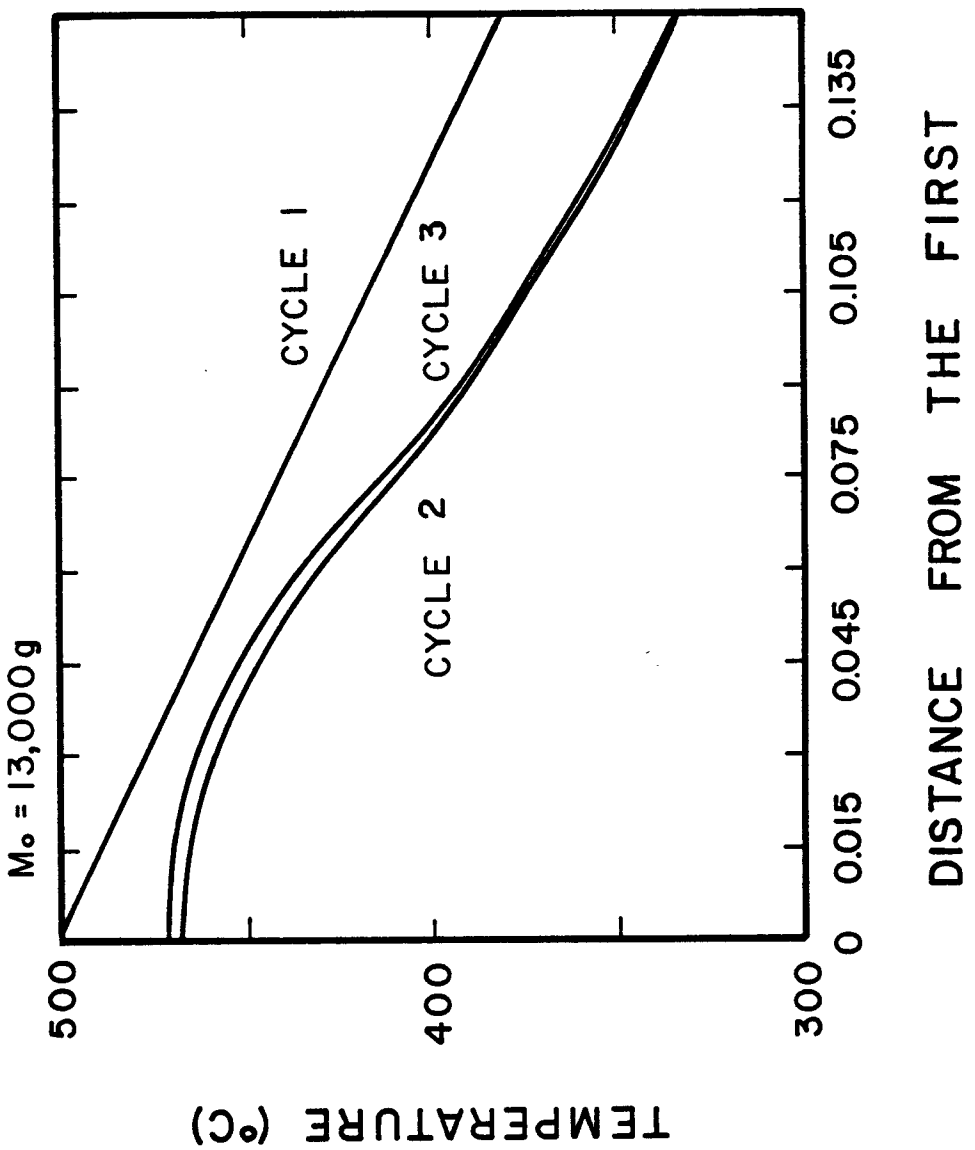

Fig. VI.4-15 Temperature of the PbLi at the start of the first three cycles. Mass of vaporized gas = 13000 g.

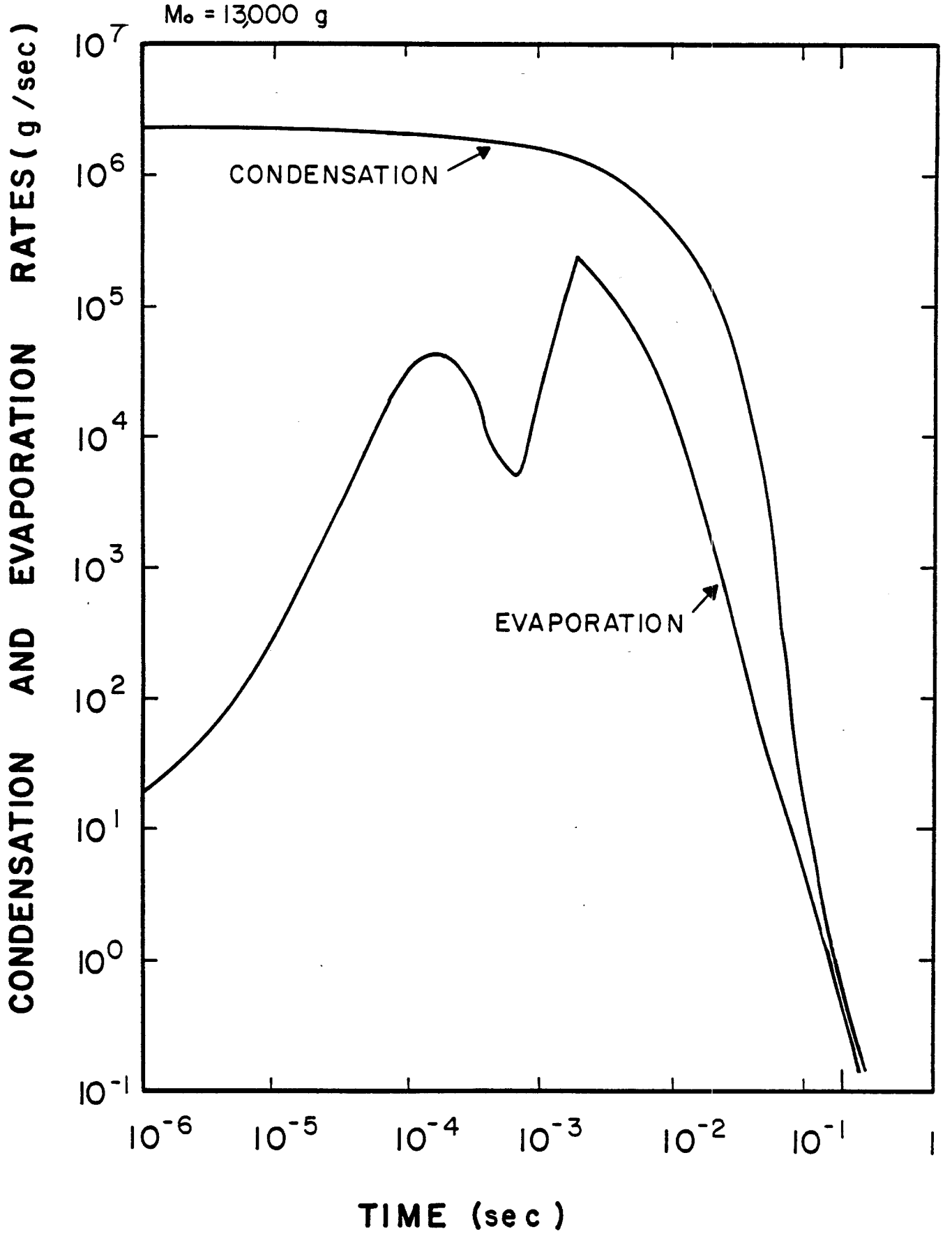

Fig. VI.4-16 Condensation and evaporation rates on first surface for mass of vaporized gas = 13000 g.

Fig. VI.4-17 Total condensation, evaporation and mass in cavity for mass vaporized = 13000 g.

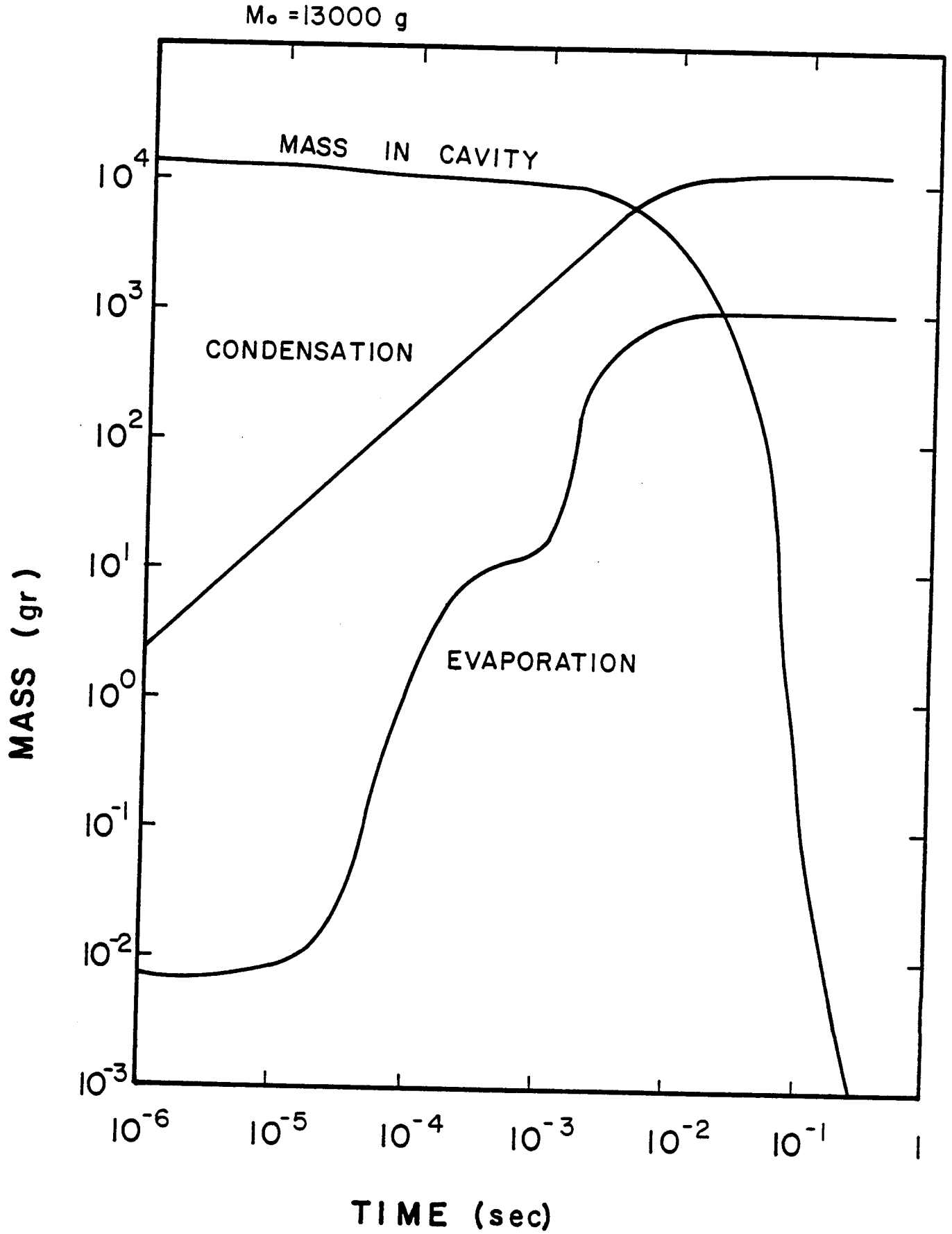

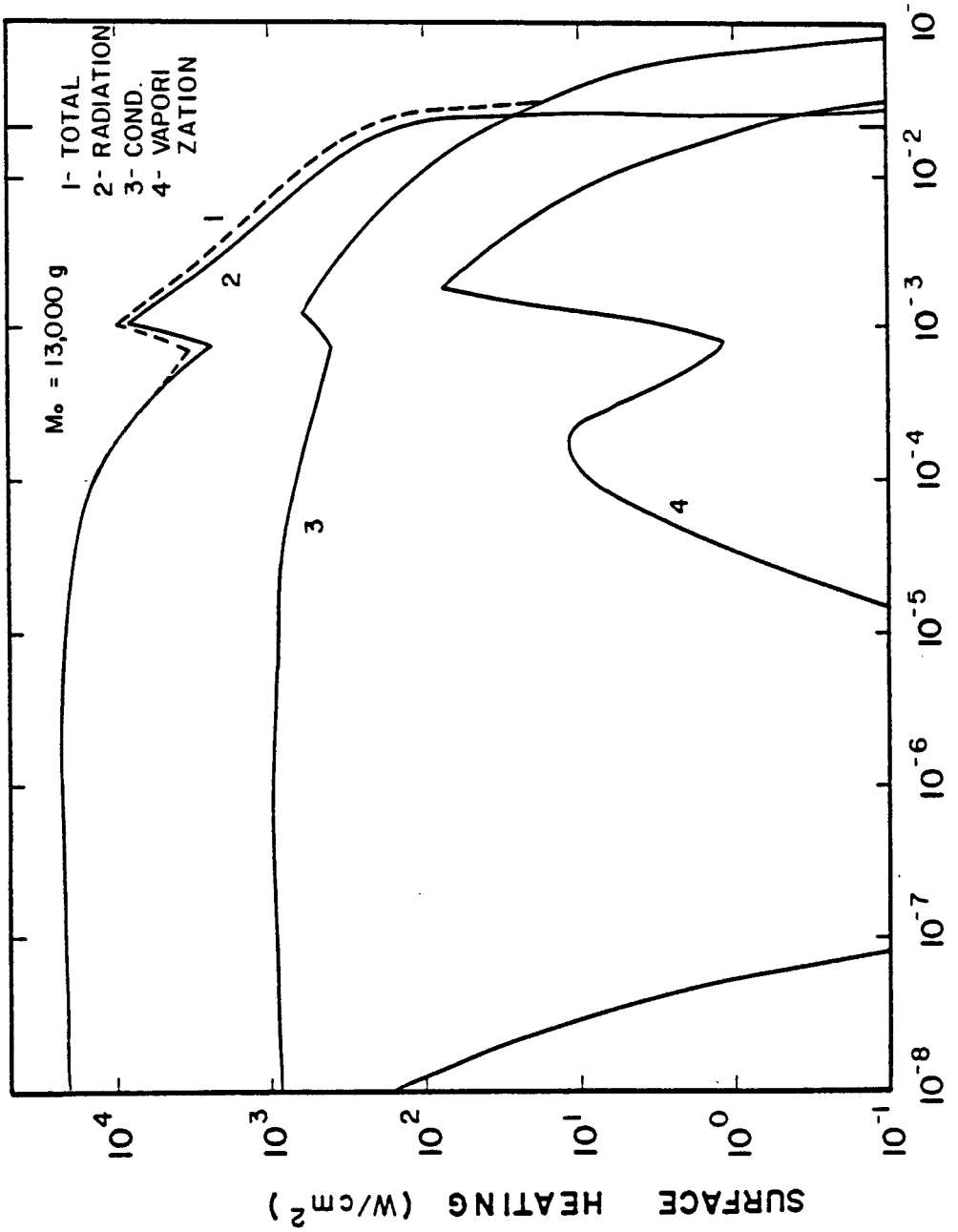

Fig. VI.4-18 First surface heat flux. Mass of vaporized gas = 13000 g.

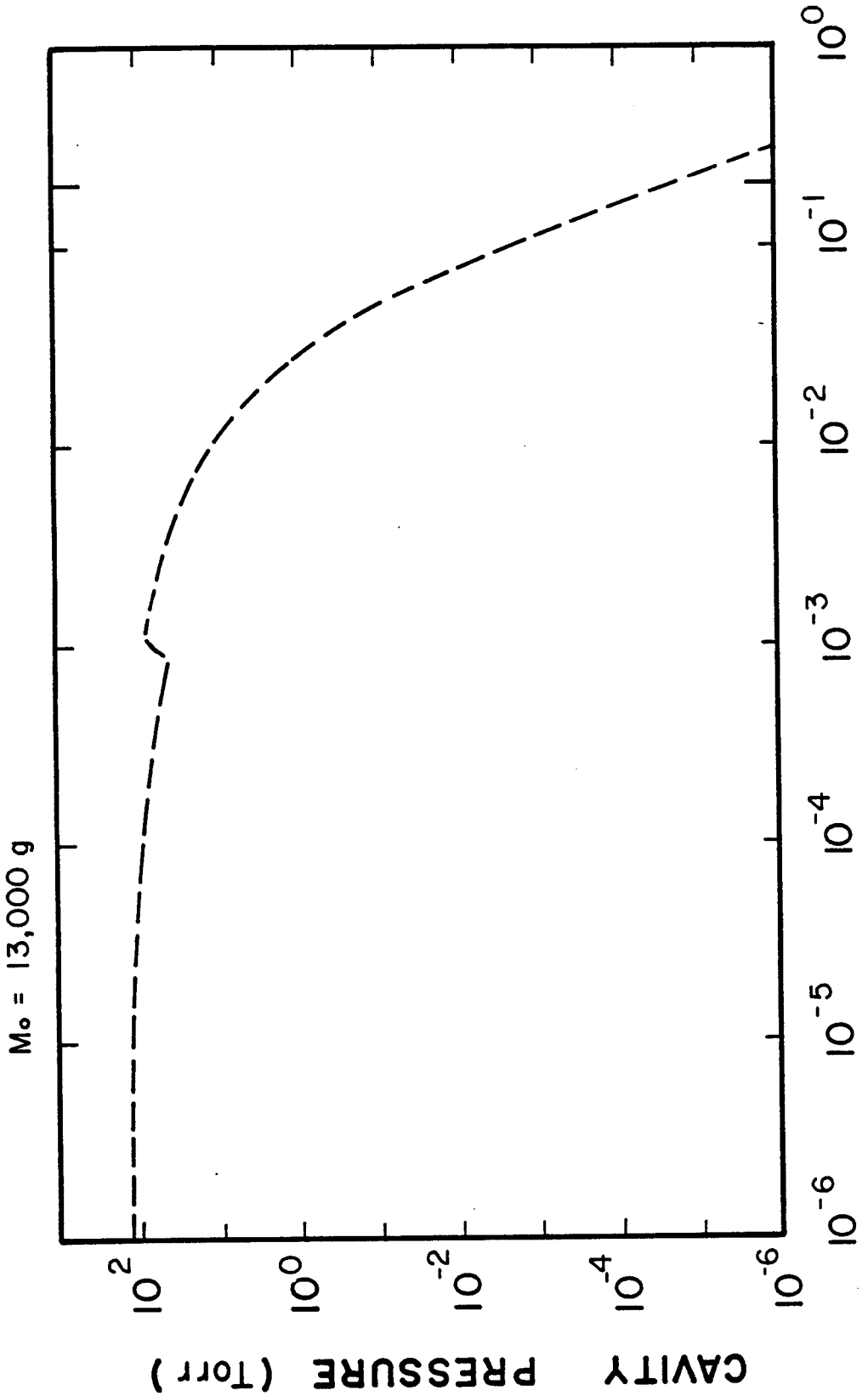

Fig. VI.4-19 Cavity pressure versus time. Mass of vaporized gas =13000 g.

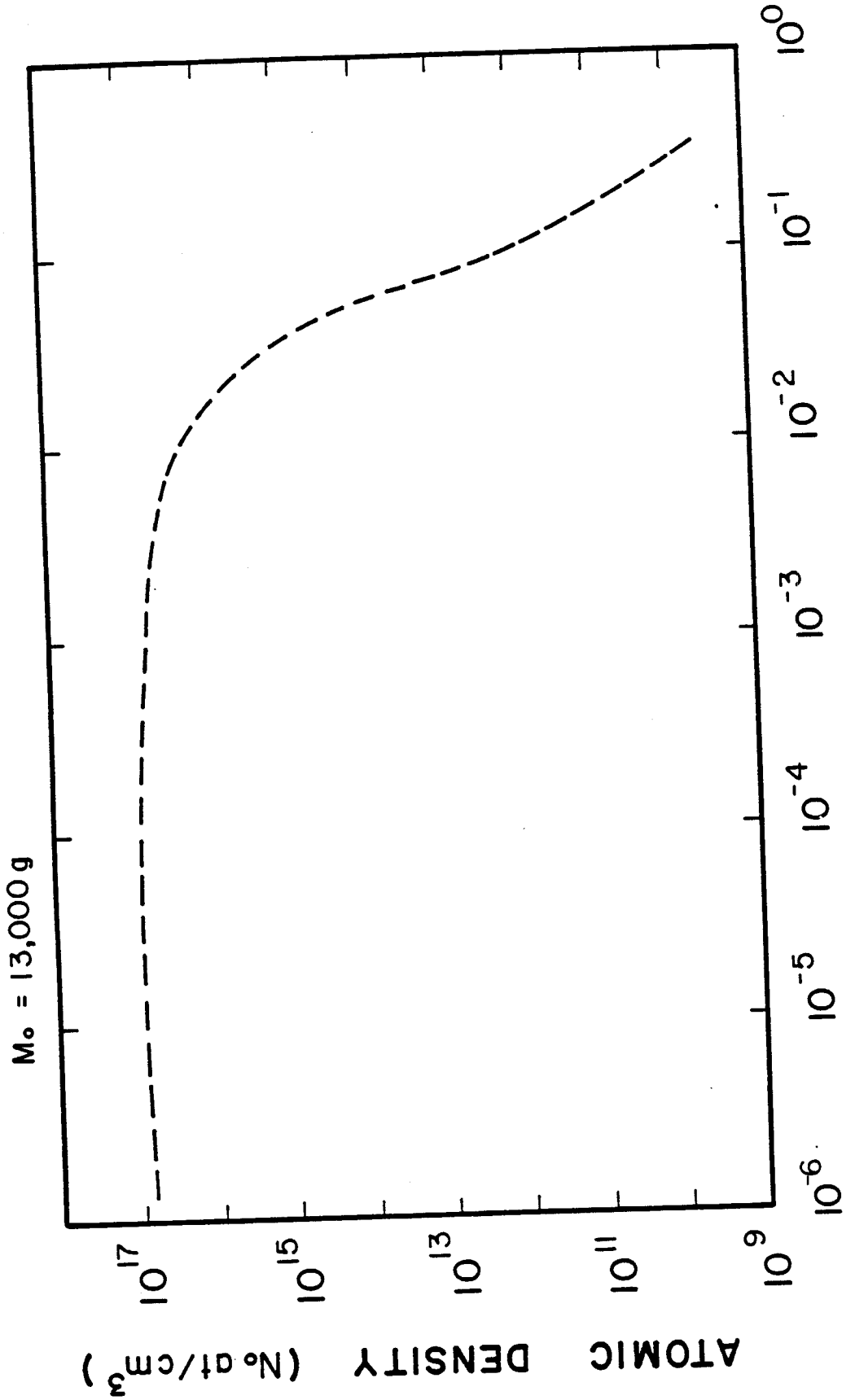

Fig. VI.4-20 Atomic density in cavity versus time. Mass of vaporized gas = 13000 g.

cavities is a small number which is the difference of two larger numbers, M_0 and the condensed mass. Figure VI.4-18 shows the surface heating rate due to radiation, condensation and evaporation, the summation of which is the heating on the first surface. Notice that the heat from radiation is dominant for much of the time. Figure VI.4-19 shows the pressure and Fig. VI.4-20 shows particle density in the cavity as a function of time.

The vacuum pressure at time = 0.2 second should be low enough to allow beam propagation. The particle density at this time is 4×10^{10} cm^{-3}. The calculation of the beam stripping cross section will show that this pressure is acceptable. It must be noted, however, that the total mass in the cavity is only 7×10^{-3} g. This is obtained by subtracting the condensation mass from the sum of initial mass and evaporation mass, both of which are large and very close. The total condensation mass is 1.5×10^{4} gm. Therefore, the uncertainty of the total mass in the cavity at t = 0.2 second is very large. A change of assumptions may lead to a significant variation on the final particle density.

A change of the target design may change the energy associated with the X-rays and/or the spectrum of the X-rays. This will change the initial mass evaporated by the X-ray deposition. To study the effect of different X-ray energy or spectra, a different initial mass is assumed. Two additional computer calculations are performed with M_0 = 26 kg and 6.5 kg. The larger mass reduces the initial gas temperature and also the radiation heat flux to the first surface. Consequently, the thermal energy deposited on the first surface is spread over a longer period of time, as can be seen on Fig. VI.4-21. The lower gas temperature also reduces the condensation rate, as can be seen in Eq. VI.4-2. Smaller initial mass, on the other hand, increases the initial gas temperature. The high gas temperature results in a large heat flux to the

first surface and, consequently, causes a large evaporation rate. Thus, the effect of evaporation dominates cavity mass transfer. Figure VI.4-22 shows the surface temperature of the three cases. As expected, the surface temperature increases drastically if the mass of vaporized gas is reduced. This occurs because the heat flux shown in Fig. VI.4-21 is so much higher at low mass. This leads to a higher evaporation rate in the low mass (6.7 kg) case shown in Fig. VI.4-23. Here the evaporation rate is shown to be, at times, much larger than the condensation rate. This leads to the increases in cavity pressure, mass and atomic density with time at low mass shown in Figs. VI.4-24, VI.4-25, and VI.4-26, respectively. Fig. VI.4-27 shows the atomic density at 0.2 second for the three cases of initial mass. There is a sharp minimum at M_0 = 13 kg which is due to the gas temperature being high enough for quick condensation and the heat flux being low enough for insignificant evaporation. When M_0 = 26.6 kg the gas temperature is too low and recondensation is slow. When M_0 = 6.7 kg, the radiation heat flux is high enough that evaporation is a problem.

In summary, we have considered the vaporization, gas dynamics and condensation of Pb-Li from the film on the INPORT tubes. The mass of the gas vaporized by the target generated X-rays is 13.3 kg and the gas density in the cavity 0.2 seconds after the target explosion is low enough for ion beam propagation. The gas density at 0.2 seconds has been found to be sensitive to the mass of vaporized Pb-Li and thus, sensitive to changes in the target X-ray spectrum.

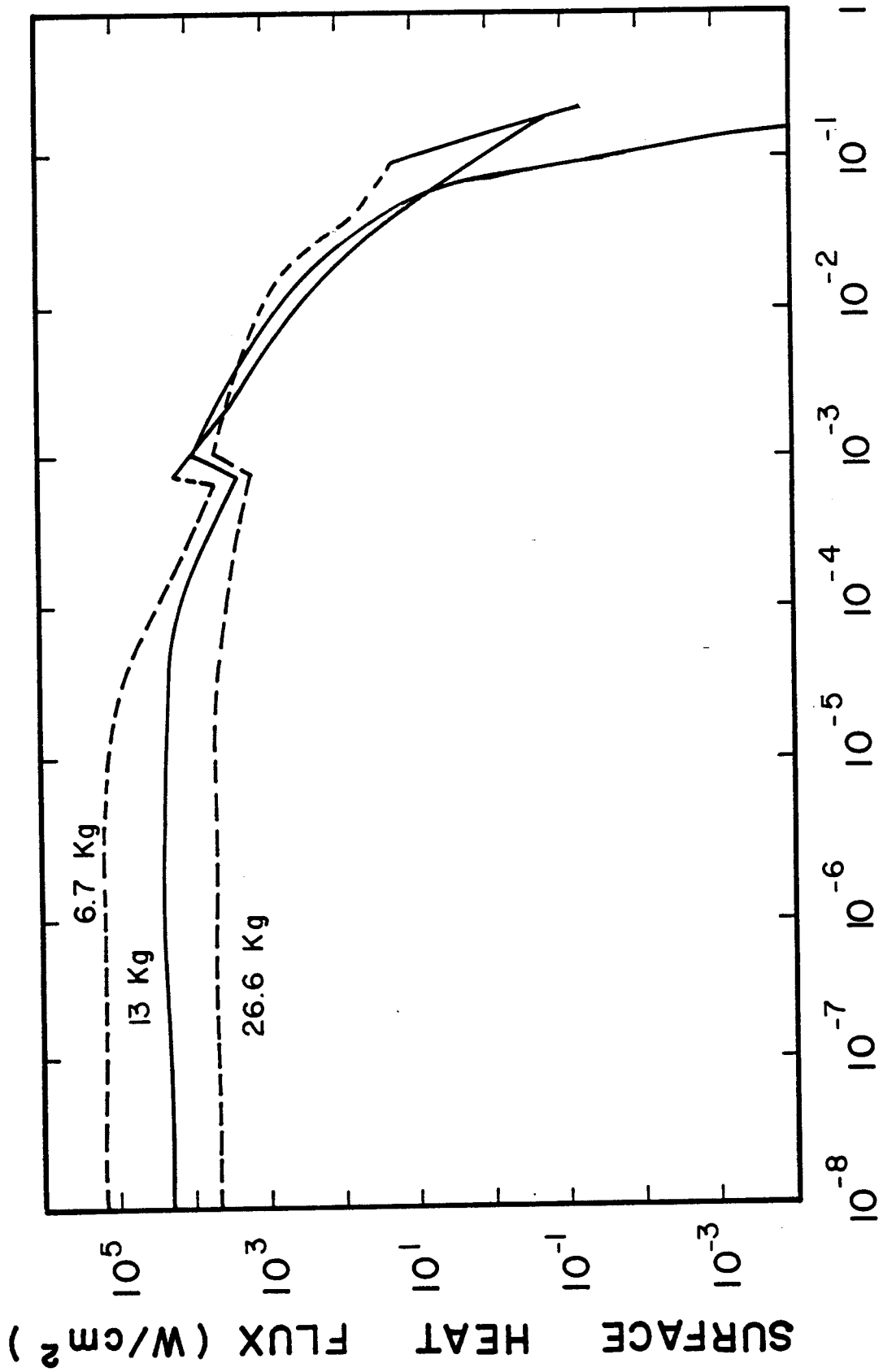

Fig. VI.4-21 Total surface heat flux for different vaporized masses.

Fig. VI.4-22 Temperature of the first surface versus time for different initial cavity gas masses.

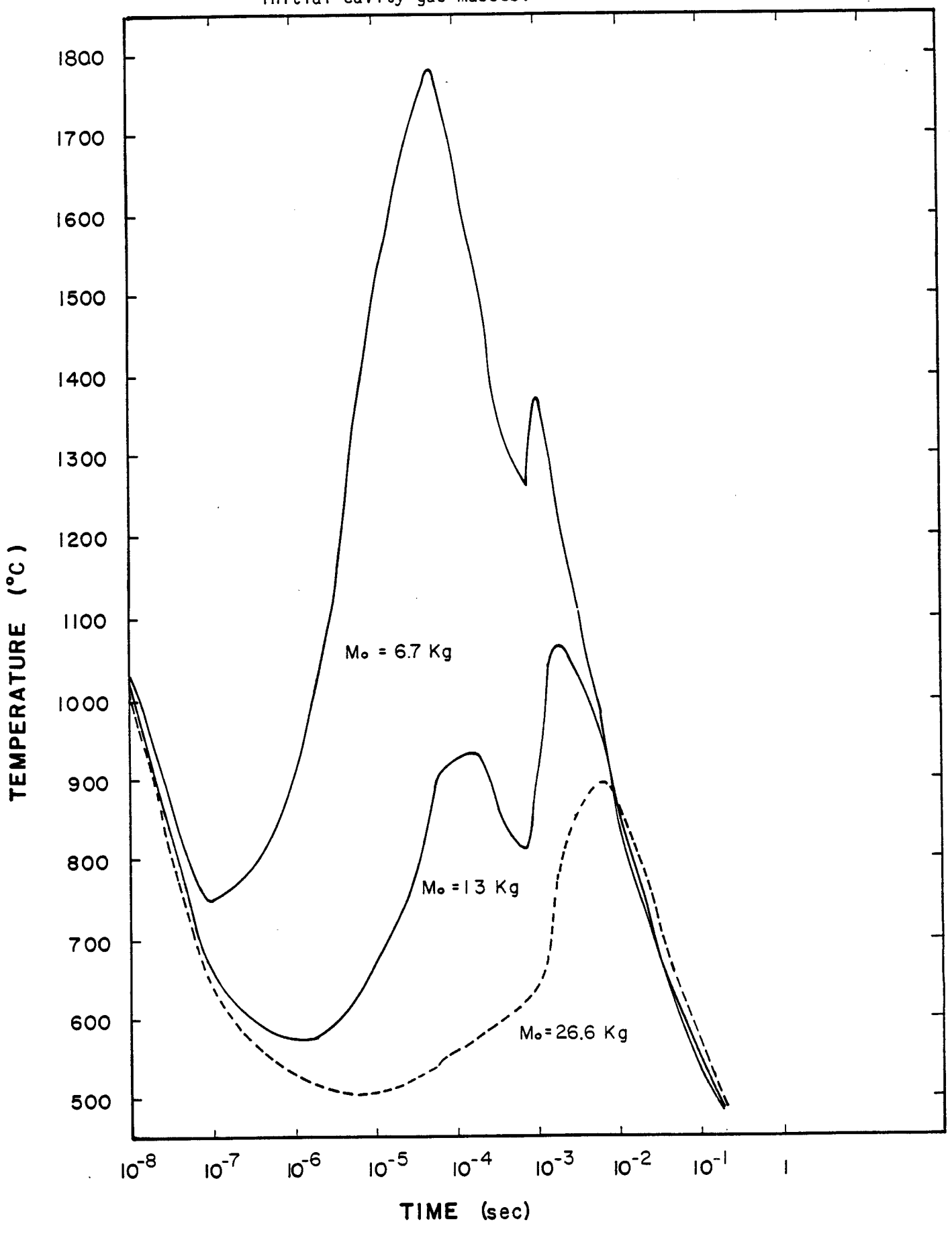

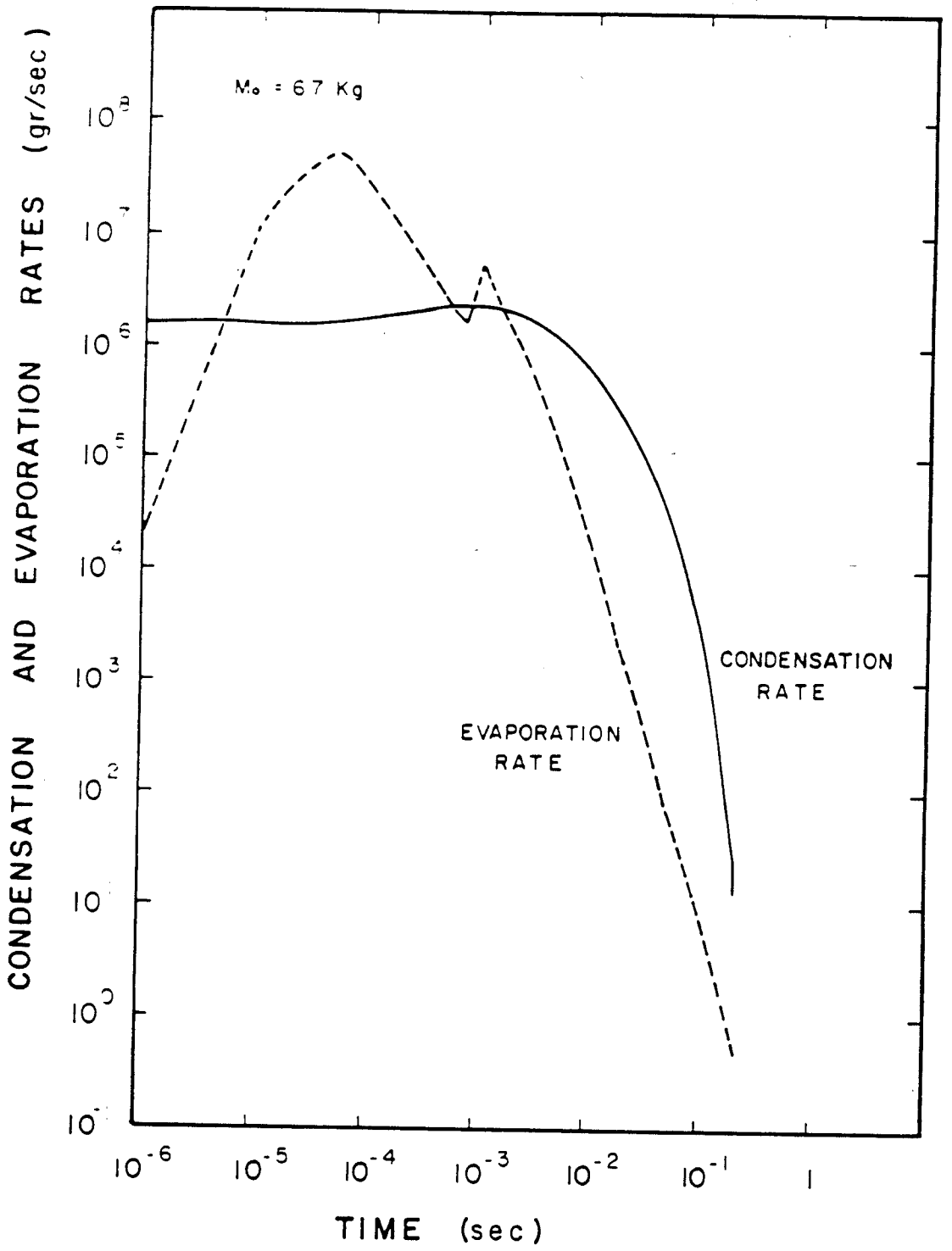

Fig. VI.4-23 Condensation and evaporization rates for mass of vaporized gas = 6700 g.

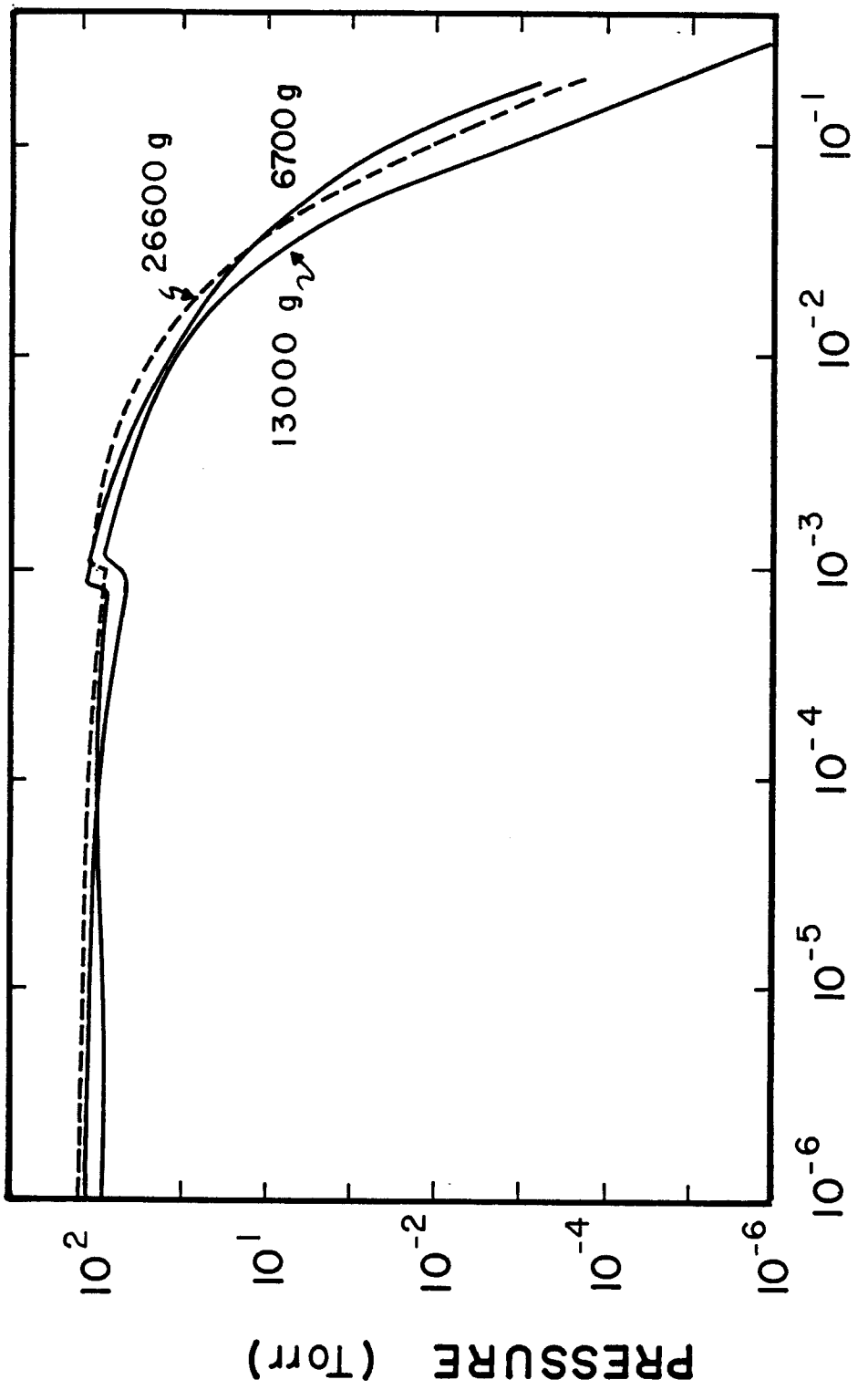

Fig. VI.4-24 Cavity pressure versus time for different masses of vaporized gas.

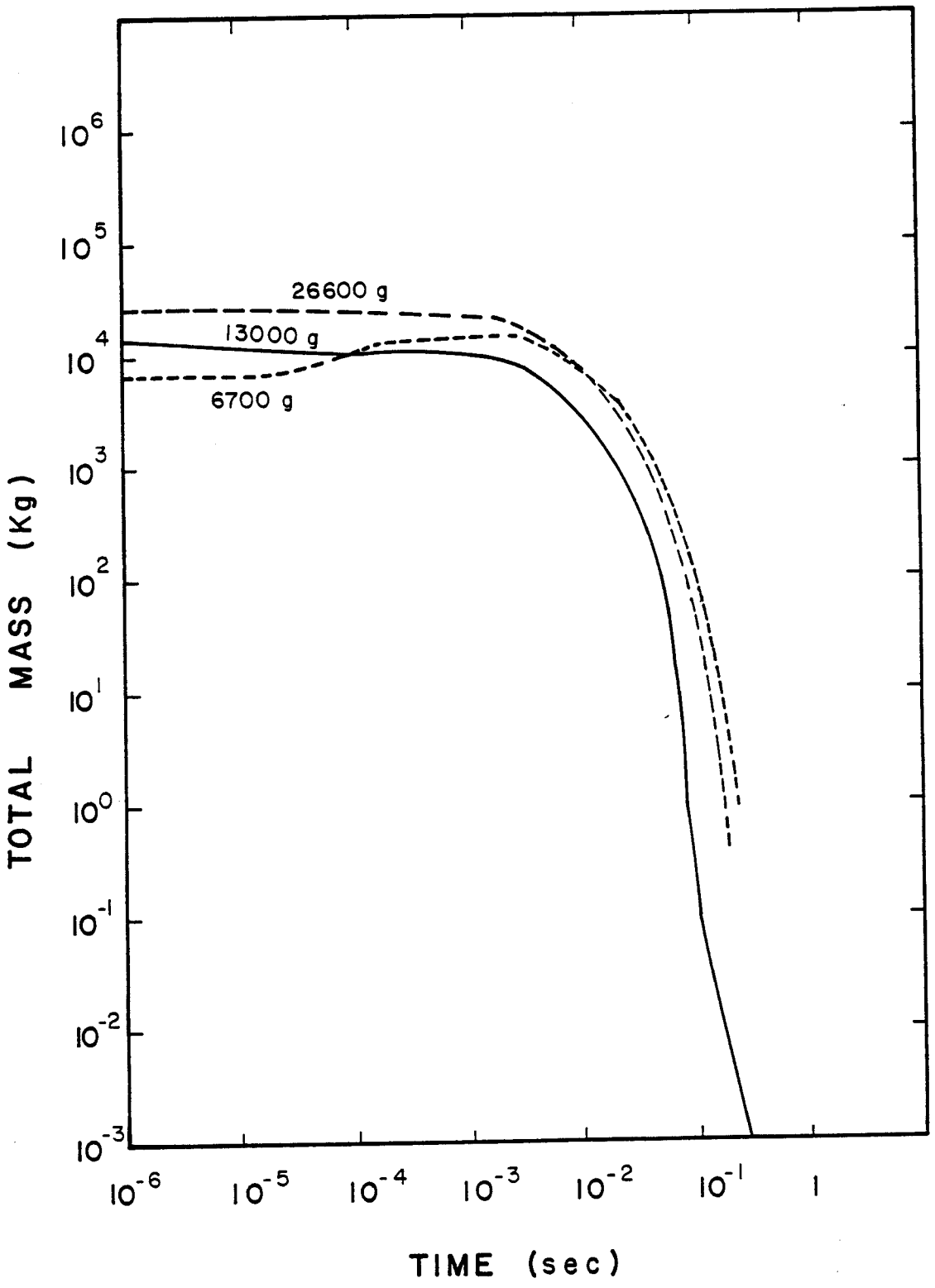

Fig. VI.4-25 Total mass in cavity versus time for diffent masses of vaporized gas.

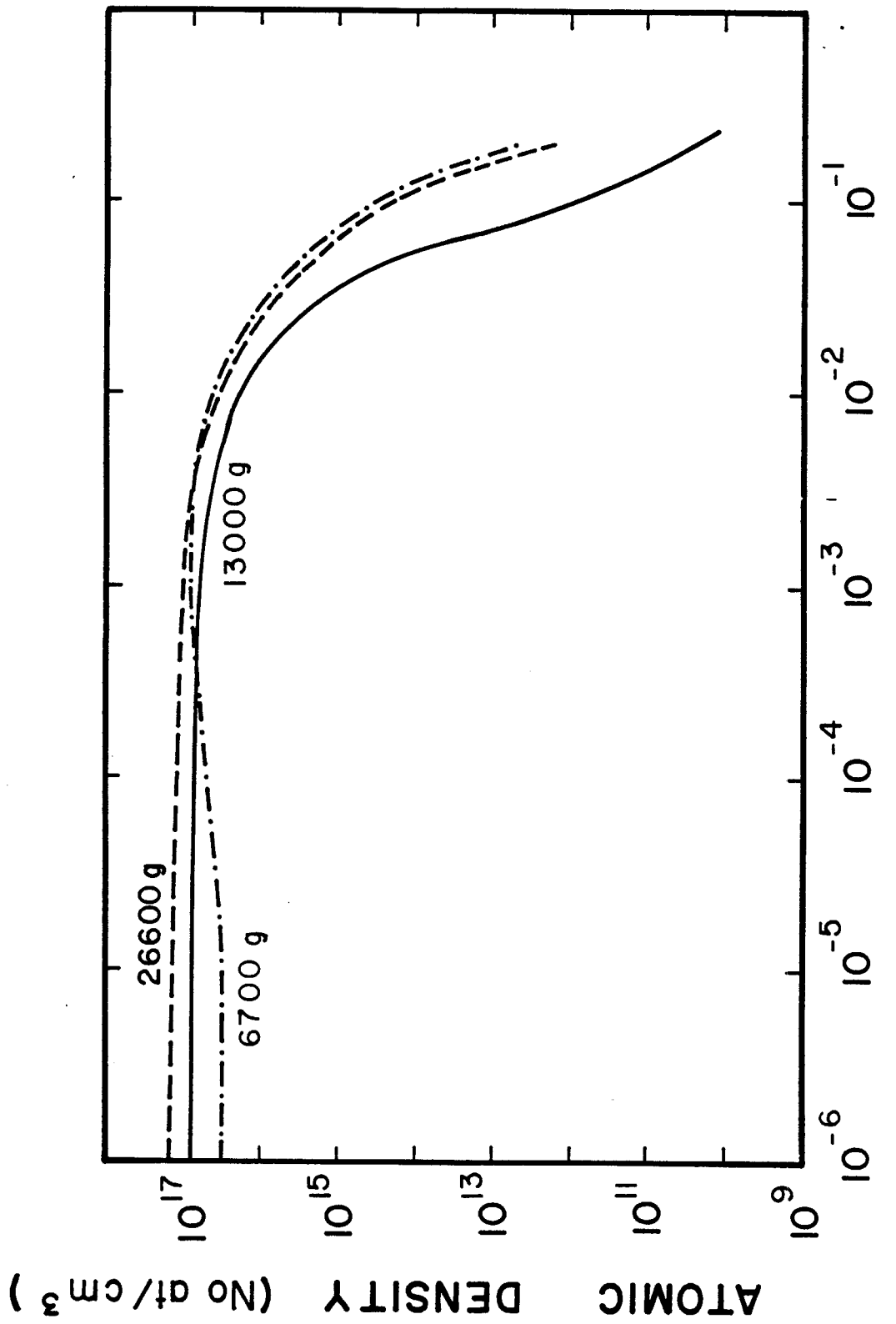

Fig. VI.4-26 Atomic density versus time for different masses of vaporized gas.

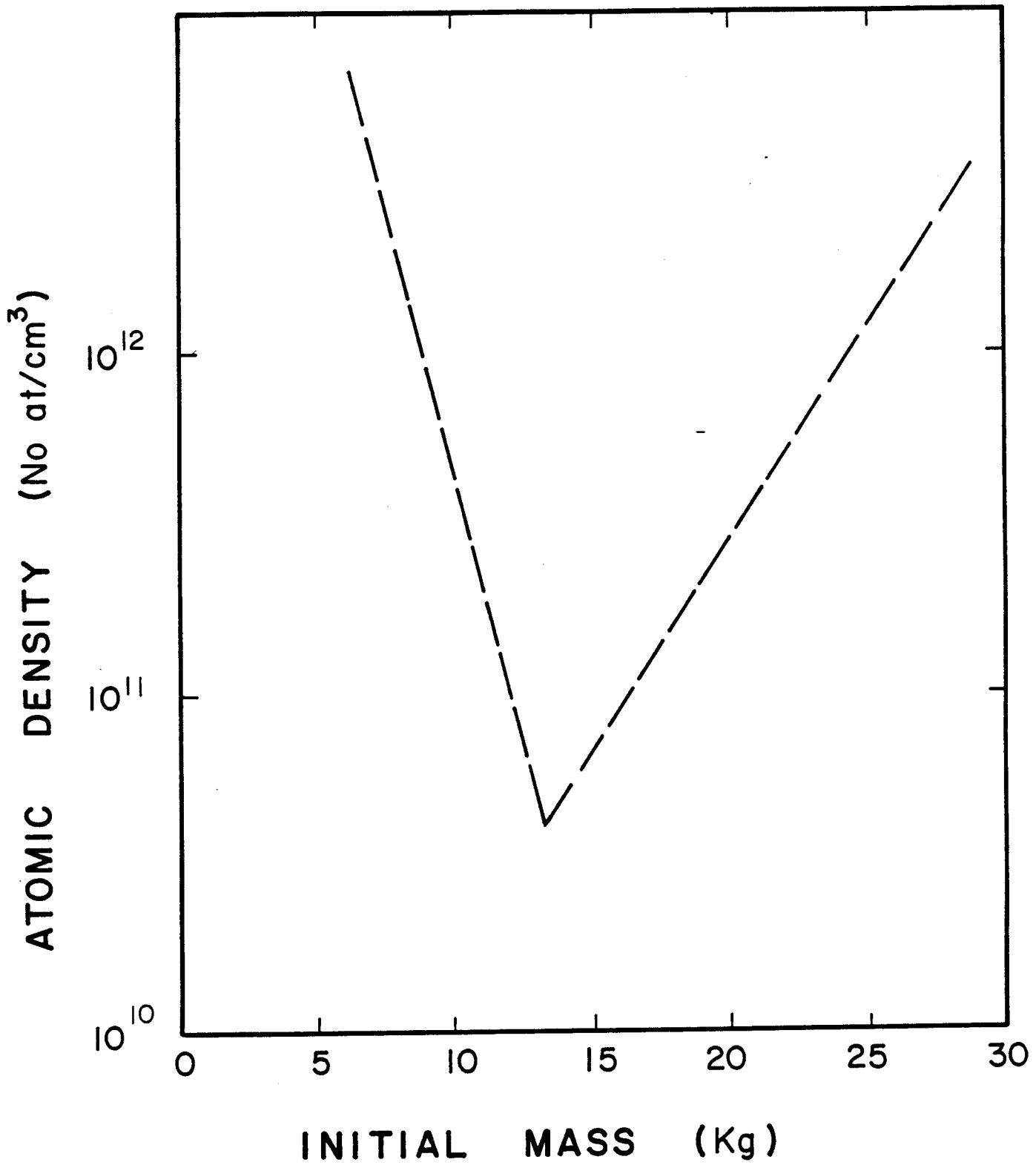

Fig. VI.4-27 Final atomic density in the cavity versus mass of PbLi vaporized.

References for Section VI.4

1. F. Biggs and R. Lighthill, Analytical Approximation for X-ray Cross Sections II, SC-PR-71-0507, Sandia Laboratory, Albuquerque, NM, December 1971.

2. T.O. Hunter and G.L. Kulcinski, "Description of the Response of Reactor First Walls to Pulsed Thermonuclear Radiation (Part I)," University of Wisconsin Fusion Engineering Program Report UWFDM-196, (March 1977).

3. G. Moses, et al., "High Gain Target Spectra and Energy Partitioning for Ion Beam Fusion Reactor Design Studies", University of Wisconsin Fusion Engineering Program Report UWFDM-396, (November 1980).

4. A.M. Hassanein and G.L. Kulcinski, to be published.

5. R.R. Peterson and G.A. Moses, "MFP - A Code for Calculating Equation-of-State and Optical Data for Noble Gases", Computer Physics Communications 20, 353 (1980).

6. R.R. Peterson and G.A. Moses, "MIXER - A Multi-Species Optical Data and Equation-of-State Computer Code", University of Wisconsin Fusion Engineering Program Report UWFDM-372, (Sept. 1980).

7. D. Mihalas, Stellar Atmospheres (W.H. Freeman and Co., San Francisco, 1978).

8. D. Mosher, NRL Memorandum Report 2563 (March 1973).

9. Ya. B. Zel'dovich and Yu. P. Raizer, Physics of Shock Waves and High Temperature Hydrodynamic Phenomena (Academic Press, New York, 1967), Chapter III.

10. G.A. Moses and R.R. Peterson, "FIRE - A Computer Code to Simulate Cavity Gas Response to Inertial Confinement Target Explosions", University of Wisconsin Fusion Engineering Program Report UWFDM-336 (January 1980).

VI.5 Vacuum System

VI.5.1 General Description

The previous section described the behaviour of the PbLi vapor in the cavity after each shot. It was found that the vapor pressure of PbLi falls below 10^{-4} torr in the order of 200 ms after the shot. In the present section we will deal with the non-condensable fraction of the gas load within the cavity, namely D_2, T_2 and He. We will attempt to access the effect of the PbLi vapor on the vacuum systems for the cavity and the beam lines.

The cavity atmosphere is primarily dictated by the requirements needed to propagate the beams to the target with minimal losses due to stripping and charge exchange. These issues have been addressed in Chapter V. Similarly, the equilibrium pressure of the non-condensable fraction has to be maintained reasonably low, although their effect on beam propagation is not as great as PbLi at the same number density, simply because of the difference in mass. Furthermore, the noncondensable partial pressure has to be kept low because it constitutes a continuous source of molecules migrating into the beam lines where the pressure must be kept at $\sim 10^{-7}$ torr.

The source of hydrogen in the cavity is from the unburned fuel in the target, the newly bred T released within the cavity and the deuterium gas load from the target injector. Helium comes primarily from the DT reaction and T_2 breeding, with a minor contribution from T_2 decay. At pressures on the order of 10^{-4} torr, outgassing does not dominate and will be neglected. Outgassing is a serious problem in the beam lines where the pressure must be three orders of magnitude lower.

Immediately after a shot, the walls of the INPORT tubes as well as other cavity surfaces act as condensers for the PbLi vapors. Although the pressure reaches $\sim$ 100 torr, because of the sticking coefficient of unity for PbLi, no

boundary layer develops on the cavity surfaces. For this reason the gas behaves more as in molecular flow rather than viscous flow. The behaviour of the non-condensable species within the vacuum ducts will thus be treated with molecular flow theory rather than viscous flow.

Most of the recent fusion reactor design studies have utilized compound cryopumps for pumping hydrogen and helium. In these pumps, hydrogen species are condensed on chevrons cooled to ~ 15 K while the helium is cryotrapped on molecular sieves applied to panels which are at 4.2 K. Typically these pumps have speeds of ~ 5 ℓ/s cm^2 for D_2, T_2 and ~ 2 ℓ/s cm^2 for He. A major disadvantage of any cryopump is the need for periodic regeneration. This is done by valving the pump off and warming up the cryosurfaces. Although regeneration may only take ~ 20-30 min., during this time the pump is not available for operation. Some designs have resorted to providing twice as many pumps as needed, such that only half are on line at any one time. This is not space efficient, particularly where there are space limitations. In several past designs[1,2] the UW group has proposed the use of back to back cryopumps such as that shown in Fig. VI.5-1. Two sets of cryopanels, with integral baffles and chevron shields, are provided back to back. While the front panel is in use, the rear panel is being regenerated and the pump body itself constitutes the shut-off valve. Although some development work will be needed to perfect the seals for such a pump, we feel that it holds the promise for substantially increasing the pumping capacity in systems which are space limited. We are proposing such pumps for the present study.

In the HIBALL design, vacuum ports have been provided at the junction between the upper blanket modules and the top of the INPORT tubes. The spaces between the headers which connect the two blanket systems together are devoted to vacuum ports. There are 30 ports 65 cm high and 120 cm wide, connected to

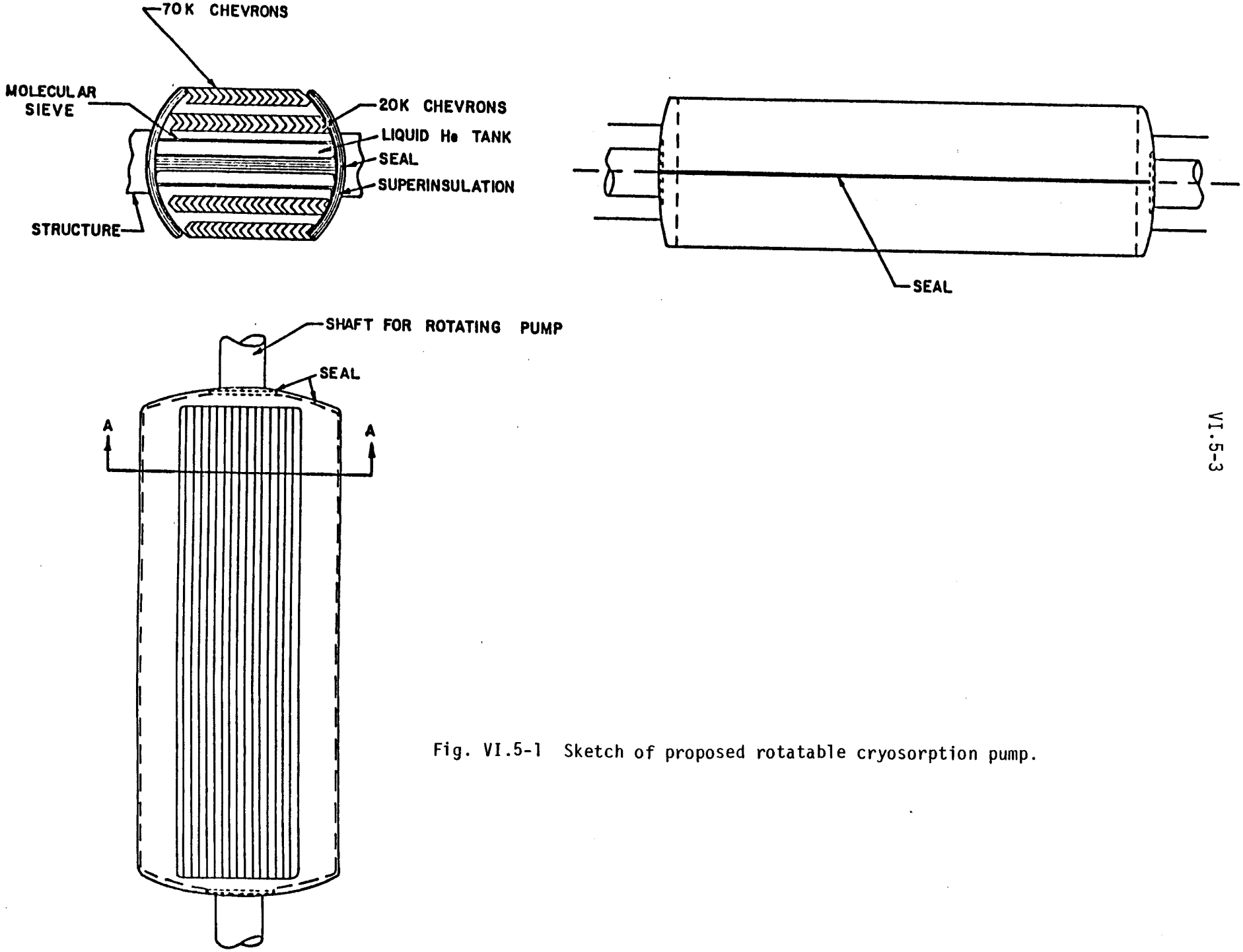

Fig. VI.5-1 Sketch of proposed rotatable cryosorption pump.

rectangular ducts of the same dimensions, leading to cryopumps located in the upper corners of the cavity as shown in Fig. VI.5-2. These pumps are well out of the radiation field and Monte Carlo analysis has shown that the effect of neutron streaming on them is negligible.

VI.5.2 Pumping of Non-Condensable Species

Table VI.5-1 gives the source and species of the non-condensable gas load.

At the initial gas temperature in the cavity (1 eV) of ~ 10,000 K, the non-condensables constitute a gas load of:

D_2 = 320 torr. ℓ/shot

T_2 = 265 torr. ℓ/shot

He = 326 torr. ℓ/shot

The vacuum ducts are assumed to be about 400°C in order to condense any PbLi vapor that they admit. At this temperature the throughput becomes:

D_2 = 108 torr. ℓ/sec.

T_2 = 89 torr. ℓ/sec.

He = 110 torr. ℓ/sec.

The conductance of a short duct (L < 25 r) for molecular flow is given by the relationship:[3]

$$\frac{1}{C_{duct}} = \left(\frac{3}{16}\frac{LU}{A^2} + \frac{1}{A}\right)\sqrt{\frac{2\pi M}{RT}}\ \frac{sec}{cm^3}$$

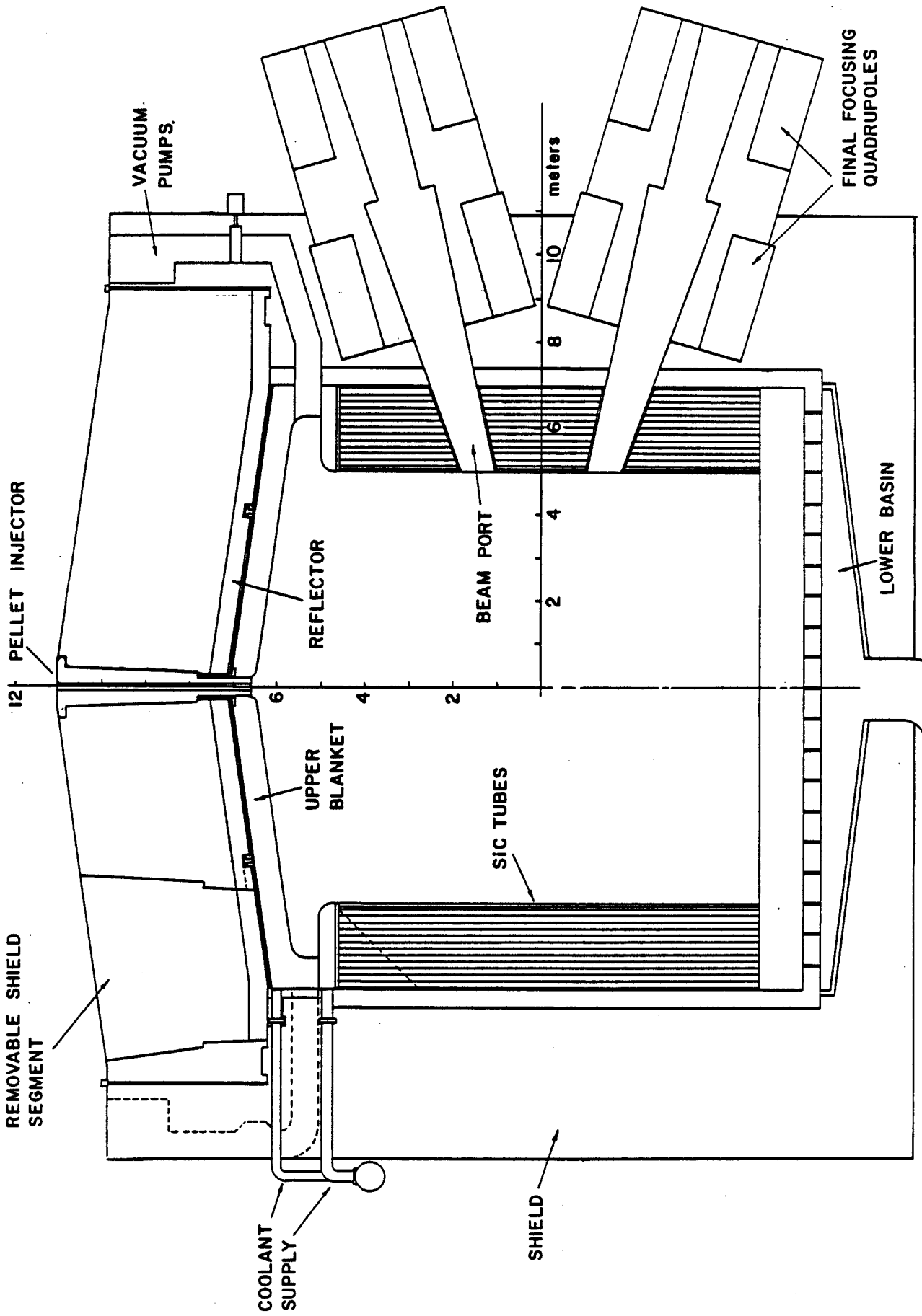

Fig. VI.5-2 Cross section of cavity showing the pump location.

Table VI.5-1

Source	Species	Atoms/Shot	Total (atoms/shot)
Target Injector	D	2.83×10^{20}	
Unburned Fuel	D	3.4×10^{20}	6.23×10^{20}
Unburned Fuel	T	3.4×10^{20}	
Newly Bred	T	1.76×10^{20}	5.16×10^{20}
DT Reaction	He	1.4×10^{20}	
T_2 Breeding	He	1.76×10^{20}	
T_2 Decay	He	1.9×10^{11}	3.16×10^{20}

where C_{duct} is the conductance of the duct in cm^3/sec, L the length in cm, A the cross-sectional area in cm^2, U the perimeter in cm, M the molecular weight in gms., R the gas constant (8.3×10^7 ergs/mole) and T the temperature in degrees Kelvin.

For the given duct area of 65×120 cm^2, L = 450 cm, M = 5 for D_2T_2 and taking T = 673 K we get:

$$C_{duct} = 6.6 \times 10^7 \text{ cm}^3/\text{sec} = 6.6 \times 10^4 \text{ ℓ/s} .$$

For 30 ducts the conductance is:

$$C_{D_2T_2} = 2 \times 10^6 \text{ ℓ/s}$$

$$C_{He} = 2.2 \times 10^6 \text{ ℓ/s} .$$

The area available for locating the cryopumps is ~ 85 m^2 and the utilization factor for back to back pumps is ~ 85%. The total pumping speeds (using 5 ℓ/s cm^2 for D_2, T_2 and 2 ℓ/s cm^2 for He) are then:

$$S_{D_2T_2} = 3.6 \times 10^6 \text{ ℓ/s}$$

$$S_{He} = 1.44 \times 10^6 \text{ ℓ/s} .$$

The effective pumping speed is obtained from:

$$\frac{1}{S_{eff.}} = \frac{1}{S_p} + \frac{1}{C_{duct}}$$

where S_p is the pump speed and C_{duct} the conductance of the ducts. The effective pumping speed is then:

$$S_{eff.\ D_2\ T_2} = 1.3 \times 10^6 \text{ ℓ/s}$$

$$S_{eff.\ He} = 8.7 \times 10^5 \text{ ℓ/s} .$$

Using the throughputs obtained earlier, the equilibrium pressures of the non-condensable species in the cavity at 400°C are:

$$P_{D_2T_2} = \frac{(108+89) \text{ torr ℓ/s}}{1.3 \times 10^6 \text{ ℓ/s}} = 1.5 \times 10^{-4} \text{ torr}$$

$$P_{He} = \frac{110 \text{ torr ℓ/s}}{8.7 \times 10^5 \text{ ℓ/s}} = 1.3 \times 10^{-4} \text{ torr} .$$

The equivalent pressure rise/shot at 400°C consistent with a cavity volume of 900 m^3 is 4.4 x 10^{-5} torr for D_2T_2 and 2.5 x 10^{-5} torr for He. The time needed to evacuate the chamber to the equilibrium pressure is given by:

$$t = \frac{V}{S_{eff.}} \text{Ln} \frac{P_1}{P_2}$$

where t is the time, V the cavity volume, $S_{eff.}$ the effective pumping speed, P_1 the pressure in the cavity after a shot and P_2 the equilibrium pressure. For both D_2, T_2 and He, it is found that the time needed to reach equilibrium pressure is less than 200 msec. Thus, from the standpoint of reconditioning the chamber with respect to the non-condensable species, a repetition rate of 5 Hz is reasonable.

VI.5.3 Effect of PbLi Vapor on the Vacuum Ducts

It was mentioned earlier that the walls of the vacuum ducts will be maintained at 400°C. At this temperature, the surfaces are essentially black to PbLi vapor, and will condense it immediately upon contact. There will not be a boundary layer developed and the vapor will obey molecular flow conditions. For this reason we feel that all the PbLi vapor which enters the vacuum ducts will be condensed before it reaches the cryopumps. Since it will be maintained molten, the PbLi will be returned to the cavity and will rejoin the bulk of the breeding material. The surfaces in the vicinity of the cryopumps will be cooled to ~ 70 K with liquid N_2 and they will certainly cryotrap any itinerant PbLi molecules before they can contaminate the hydrogen and helium pumping surfaces. Since we feel this quantity of frozen PbLi will be very small, a periodic regeneration, perhaps every 6 months, will be adequate to prevent excessive buildup.

VI.5.4 Effect of Cavity Atmosphere on the Beam Lines

The beam lines' interface with the reactor cavity presents some unique problems to the beam line vacuum system. Because the pressure in the cavity during operation never gets below 10^{-4} torr, it represents a continuous gas load which is admitted into the beam lines. Beam stripping and charge exchange problems require that the beam line pressure be on the order of 10^{-7} torr. The storage rings themselves operate at vacuum on the order of 10^{-10} torr.

In the early stages of the study we had proposed rotating shutters in the beam ports in order to minimize the influx of PbLi vapor into the beam lines. The chief concerns were the accumulation of PbLi on the beam ducts amounting to ~ 30 tonnes/day for the 20 beams, and the migration of the vapor deep into the beam line system due to viscous effects. We have been reassessing this problem all along and have concluded that shutters may not be needed. There are two complimentary developments which have led to this conclusion; they are:

1. If the beam duct wall temperature can be carefully controlled such that the condensed vapor runs off in liquid form and is returned to the cavity, then accumulation ceases to be a problem.
2. With a sticking coefficient of unity on the beam duct walls, the vapor does not develop a boundary layer and there are no viscous effects from the walls. By using molecular flow theory, it is evident that the expanding vapor which enters the beam port is immediately condensed on the walls. It can be shown that the pressure can fall two orders of magnitude per meter of beam line if the narrow dimension of the line is < 40 cm.

Although the problem of PbLi vapor in the beam line needs a more rigorous analysis before it can be put to rest, for the present we will assume that the rotating shutters will not be needed.

The non-condensable species, however, will not condense on the beam line walls but will proceed further into the beam lines. The conductance of a beam line for D_2, T_2 and He at 673 K is estimated at $\sim 2.8 \times 10^3$ ℓ/s which gives rise to a throughput of $\sim 2.8 \times 10^{-1}$ torr ℓ/s. For this gas load to be pumped at 10^{-6} torr requires a cryopump system with a capacity of 2.8×10^5 ℓ/s, namely ~ 5.6 m^2 of cryosurface for each beam line. Differential pumping downstream from the main beam line pumping station will quickly reduce the pressure to the prescribed value of 10^{-7} torr and lower.

The main beam line pumping station will be located between the second and third focusing quadrupoles, where a distance of 2 m was allowed for this purpose. We envisage the same kind of back to back cryopumps proposed for the cavity vacuum system to be used in the beam lines as well.

References for Section VI.5

1. B. Badger et al., "NUWMAK - A Tokamak Reactor Design Study," UWFDM-330, Fusion Engineering Program, Nuclear Engineering Dept., University of Wisconsin, Madison, March 1979.

2. B. Badger et al., "WITAMIR-I, A University of Wisconsin Tandem Mirror Reactor Design," UWFDM-400, Fusion Engineering Program, Nuclear Engineering Dept., University of Wisconsin, Madison, Sept. 1980.

3. H.A. Steinherz, "Handbook of High Vacuum Engineering," Reinhold Publishing Corporation, New York, 1963.

VI.6 Flow Characteristics

The coolant and breeding material in HIBALL is $Li_{17}Pb_{83}$. This material is chosen for its high breeding potential, low tritium inventory and inertness with water.(1) The coolant in HIBALL also serves a unique function, that of protection of the first structural surface from X-ray bombardment. It is critical, therefore, that $Li_{17}Pb_{83}$ will form a continuous layer of film outside the coolant tubes. One of the reasons for using braided SiC coolant tubes is that there is enough open space in between the SiC fibers so that $Li_{17}Pb_{83}$ can weep out to form this protection layer. This protection layer has to be regenerated after each shot. Since this layer is directly exposed to the cavity, the maximum allowable temperature is determined by the allowable vapor pressure in the cavity.

The heat transfer problem for the coolant tubes directly exposed to the plasma is completely different from those in the back. The front tubes are subjected to a large surface heat load and, therefore, require a large heat transfer coefficient. Therefore, a high velocity is required. The back tubes are only subjected to energy deposited by neutrons and, therefore, the heat is deposited in the coolant. A low velocity is preferred here to increase the coolant temperature rise and thus reduce the coolant mass flow rate. One of the major objectives of the INPORT tubes is to reduce the flow rate so that the coolant pumping power can be reduced.

The coolant flow pattern, the heat transfer considerations and the stress effect due to the sudden neutron deposition is discussed in this section. The first wall protection from the X-ray deposition, the condensation, and re-evaporation of the protection layer is discussed in section VI.4. The important thermal-hydraulic parameters for HIBALL are summarized in Table VI.6-1.

Table VI.6-1 Thermal Hydraulic Parameters for HIBALL

(For One Cavity)

Structural Material	HT-9, SiC
Coolant and Breeding Material	$Li_{17}Pb_{83}$
Total Thermal Power	2538 MW
Coolant Inlet Temperature	338°C
Coolant Exit Temperature	500°C
Maximum First Surface Temperature	500°C
Maximum First Surface Coolant Temperature	400°C
Maximum Structural Temperature	530°C
Maximum Coolant Velocity	7.5 m/sec
Coolant Flow Rate	3.38×10^8 kg/hr
Total Coolant Pressure Drop	2.0 MPa
Coolant Pumping Dower Required	19 MW
Maximum Blanket Coolant Pressure	.07 MPa
Shield Coolant	Water
Coolant Temperature	45 ~ 60°C
Coolant Flow Rate	3.6×10^5 kg/hr
Maximum Shield Temperature	60°C
Estimated Steam Generator Surface Area	1.3×10^4 m^2
Estimated Steam Condition	
Temperature	482°C
Pressure	15.5 MPa
Flow Rate	4.5×10^6 kg/hr
Gross Thermal Efficiency	.42

VI.6.1 Coolant Flow Pattern

The coolant flow pattern is shown in Fig. VI.6-1 with the upper blanket design shown in Fig. VI.6-2. The coolant enters the reactor at 330°C. A fraction of the coolant will cool the top blanket and exit from the top blanket at 400°C. This coolant will enter the back section of the tube region

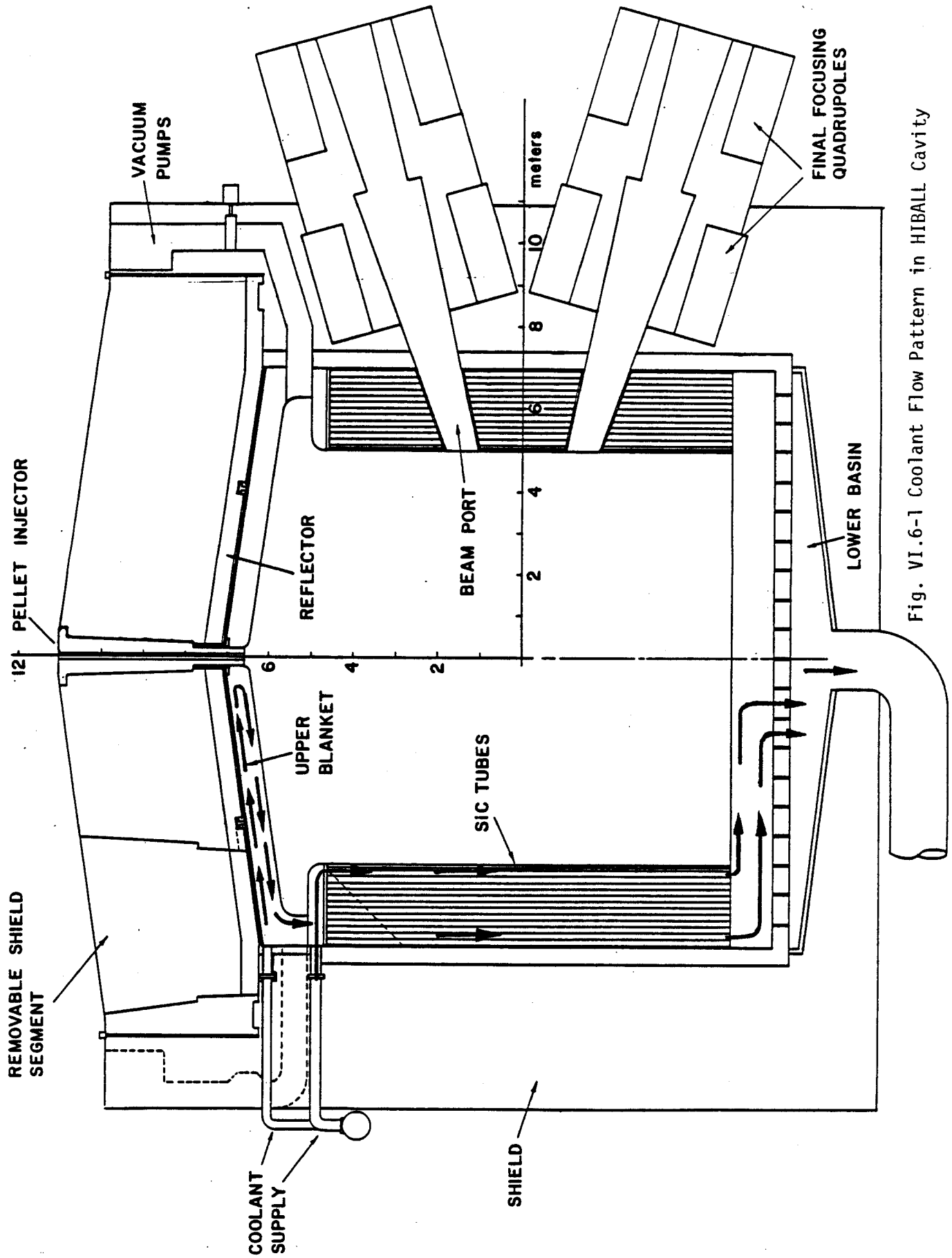

Fig. VI.6-1 Coolant Flow Pattern in HIBALL Cavity

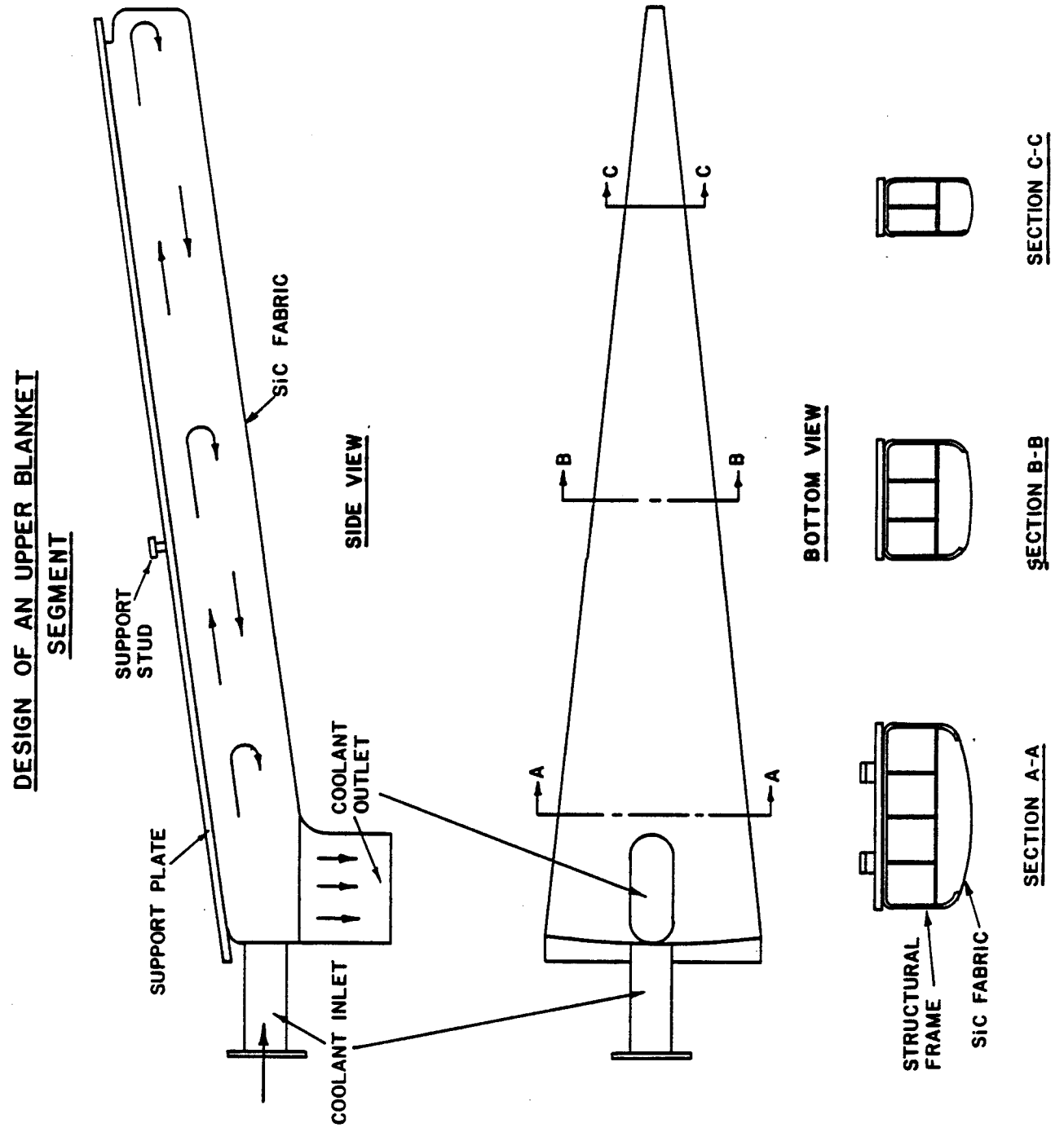
DESIGN OF AN UPPER BLANKET SEGMENT
SUPPORT STUD
SiC FABRIC
SIDE VIEW
SUPPORT PLATE
COOLANT OUTLET
COOLANT INLET
A
A
B
B
C
C
BOTTOM VIEW
SECTION C-C
SECTION B-B
SECTION A-A
STRUCTURAL FRAME
SiC FABRIC

Fig. VI.6-2

and exit from the tube region with a temperature of 500°C. Another fraction of the coolant will cool the row of tubes facing the plasma, then exit from the tube region with a temperature of 400°C. This coolant will be heating the bottom part of the cavity and exit from the reactor also at 500°C. The maximum coolant temperature at the first surface is 400°C.

The basic design philosophy in the coolant flow pattern is to insure a uniform coolant exit temperature. The maximum allowable structural temperature is estimated to be 530°C, and the coolant exit temperature should be as close to this temperature as possible so that a high thermal conversion efficiency can be insured. The coolant entrance temperature is a compromise between the power cycle requirement and the coolant freezing temperature consideration. The 170°C coolant temperature rise is large enough to insure a reasonable coolant flow rate.

VI.6.2 First Surface Heat Transfer Considerations

The first surface of a D-T fusion reactor receives ~ 20% of the total energy in various forms. This heat is deposited in the form of surface energy. A severe heat transfer problem exists in this area. In an inertially confined system, the surface energy will be deposited in a pulsed form and may cause excessive ablation problems. The non-uniform heat deposition on the first surface and its associated problems are discussed in section VI.4. In this section, the heat transfer problem on a time average basis is discussed.

The restrictions and conditions of the first surface of HIBALL are:

1. The maximum time average surface heating load is 172 W/cm^2.
2. Maximum temperature on the surface of the coolant tubes is 500°C due to vapor pressure considerations.
3. Maximum coolant velocity is 7.5 m/sec due to erosion considerations.

The exit coolant temperature has to be maximized under these limitations.

The energy deposited on the first coolant tubes can be divided into two categories, that of volumetric heating and surface heating. The volumetric energy deposition is caused by neutrons, while the surface energy deposition is caused by X-rays, debris and alpha particles. Because of the cylindrical geometry, the energy deposition is a function of distance from the center and is shown in Fig. VI.6-3. The maximum surface heating is 172 W/cm^2, which is very large. This surface heating rate will cause temperature drops across the protection layer, the tube wall and coolant boundary layer. The sum of these temperature drops has to be small enough to keep $T_{max} \leq 500^0C$.

The velocity required in the first tubes can be calculatd by an energy balance as shown in Fig. VI.6-4. To ensure good heat transfer and a minimum degradation of coolant temperature, it is necessary to keep the diameter of the first tubes as small as possible. The required coolant velocity, however, increases with decreasing coolant tube size and coolant temperature rise. To keep a velocity $\leq$ 7.5 m/sec, a coolant tube ID of 3 cm and a coolant temperature rise of 70°C are required.

The surface temperature of the first coolant tube can be calculated as a function of combined thickness of $Li_{17}Pb_{83}$ film and coolant tube wall. The maximum allowable temperature on the surface is 500°C. The calculated results are shown in Fig. VI.6-5. The maximum temperature occurs at the middle point of the cylinder due to the maximum surface heat deposition, as shown in Fig. VI.6-5. It is clear that the total wall thickness has to be $\leq$ 1.5 mm without exceeding the maximum allowable surface temperature. This calculation defines the first tube coolant parameters, as listed in Table VI.6-2.

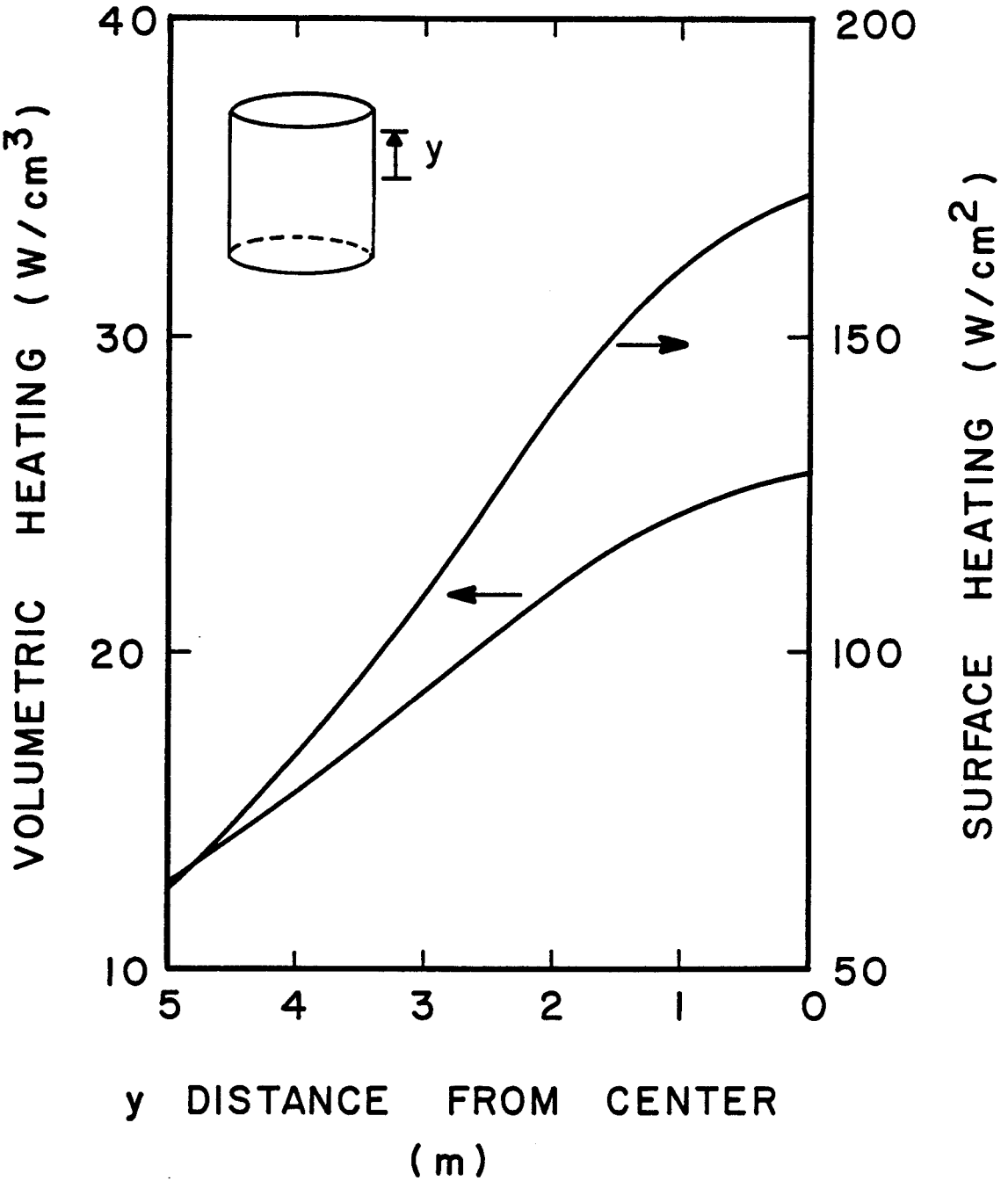

Fig. VI.6-3 Energy Deposition Along the First Coolant Tube

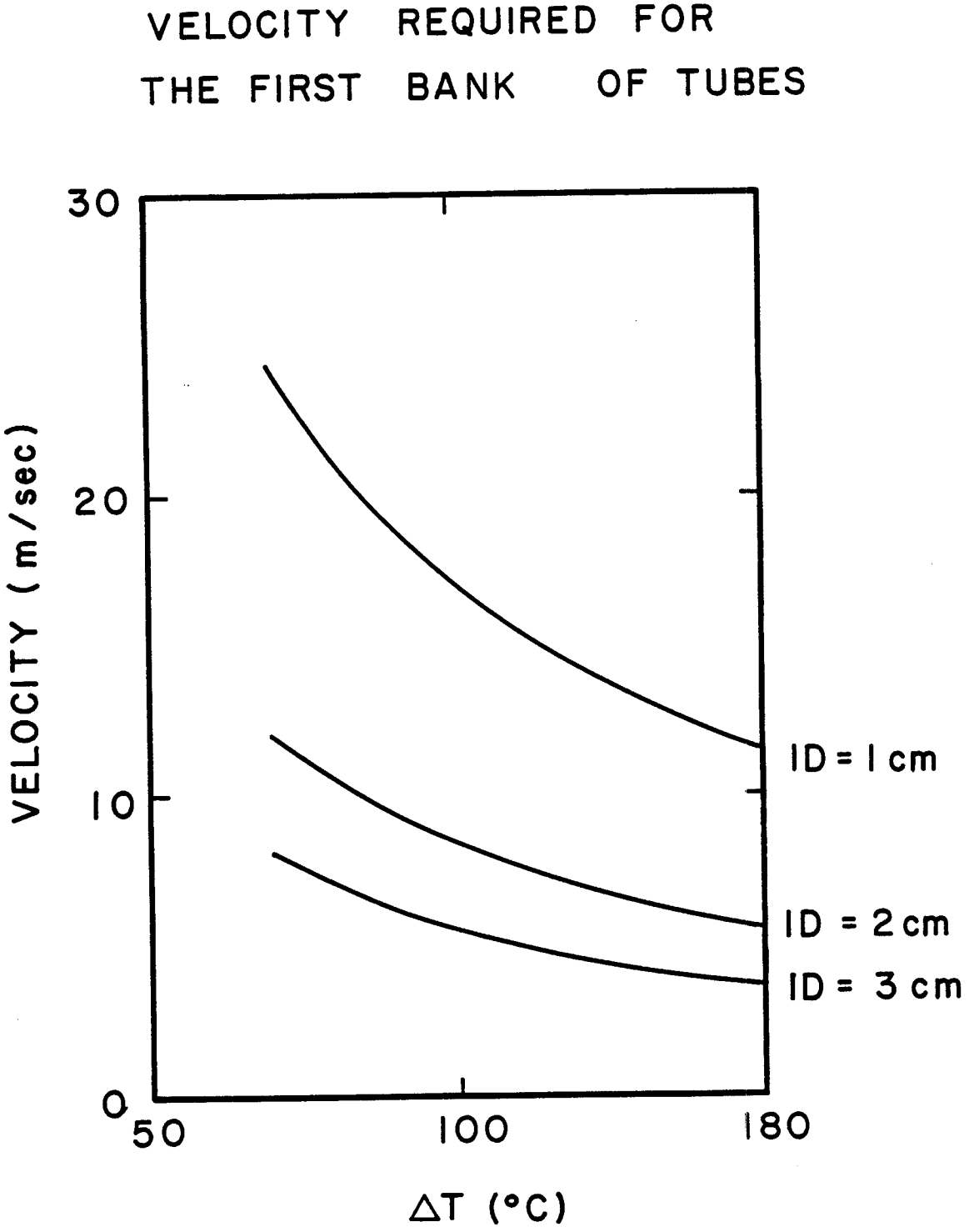
VELOCITY REQUIRED FOR
THE FIRST BANK OF TUBES
30
20
10
0
VELOCITY (m/sec)
50
100
180
ΔT (°C)
ID = 1 cm
ID = 2 cm
ID = 3 cm

Fig. VI.6-4

Fig. VI.6-5 First Surface Temperature as a Function of First Surface Thickness and Coolant Temperature Rise

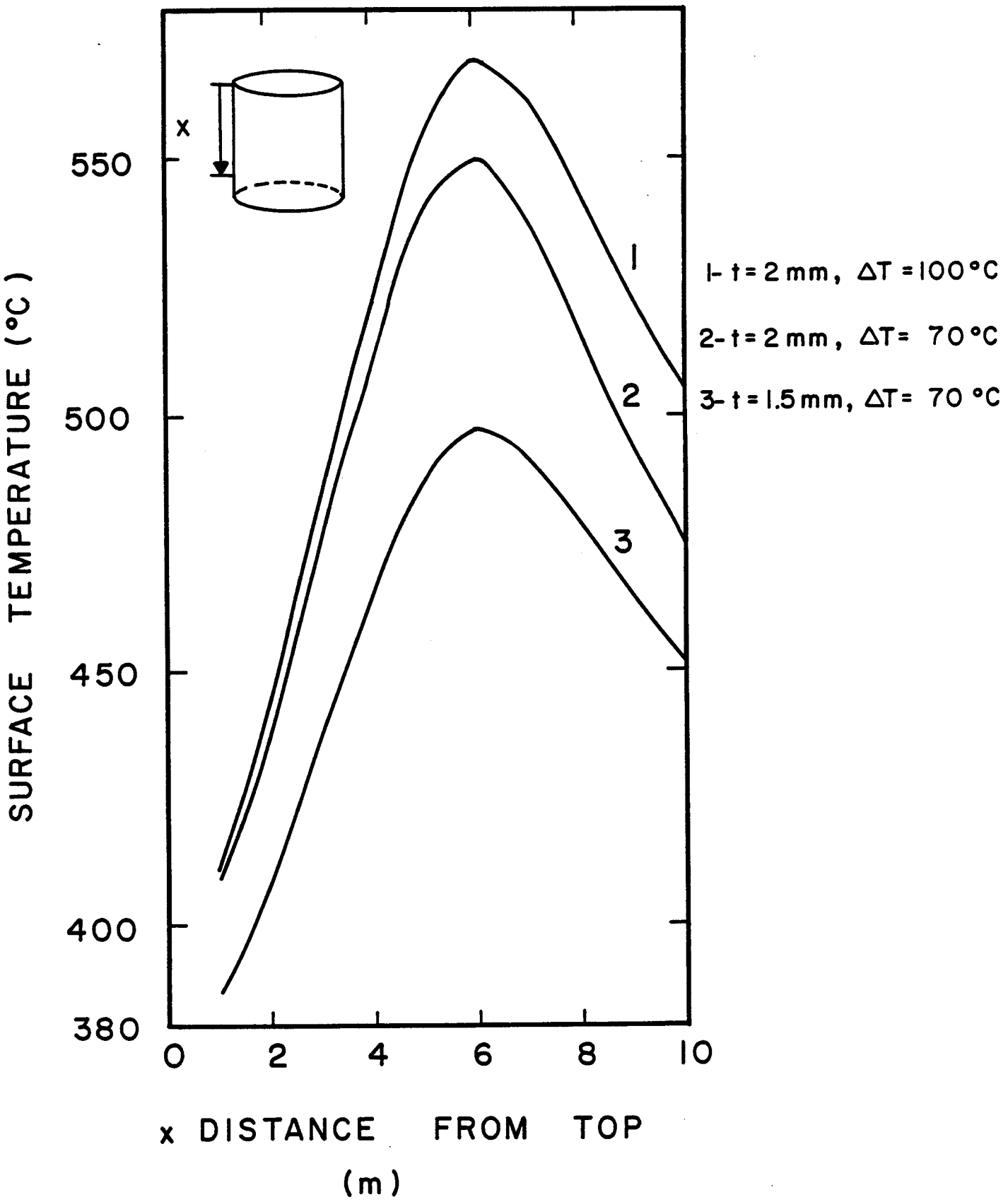

Table VI.2-2

System Parameters for First Flow of Coolant Tubes

Tube I.D.	3 cm
Total Tube Wall Thickness (including $Li_{17}Pb_{83}$ layer)	1.5 mm
Maximum Surface Heat Flux	17.2 W/cm^2
Maximum Volumetric Heat Deposition	25 W/cm^3
Coolant Tube I.D.	3 cm
Coolant Tube Thickness (including $Li_{17}Pb_{83}$ layer)	1.5 mm
Coolant Velocity	7.5 m/sec
Maximum Surface Temperature	500°C
Minimum Surface Temperature	380°C
Maximum Vapor Pressure of $Li_{17}Pb_{83}$	10^{-5} Torr

VI.6.3 Effect of Expansion Due to Sudden Nuclear Energy Deposition

A unique phenomena in an inertially confined system is caused by the sudden deposition of energy. The rapid thermal expansion caused by the temperature rise will send a shock wave outward. If a tube with a radius of r is subjected to a temperature rise of ΔT, the radius change can be written as

$$dr = r\beta\Delta T/2$$

in which β is the linear thermal expansion coefficient or

$$v = \frac{dr}{dt} = r\beta\Delta T/(2\ dt)$$

in which dt is the time for energy deposition.

For the first tubes in HIBALL

$$\Delta T = q_{max}/5\rho c_p$$
$$= 3.4^0C/shot$$
$$dt = 10^{-6} \text{ sec}$$
$$\beta = 7.4 \times 10^{-5}/^0C$$
$$r = 1.5 \text{ cm} .$$

Therefore,

$$dr = 2 \times 10^{-4} \text{ cm}$$
$$v = 200 \text{ cm/sec} .$$

The pressure on the coolant tube caused by this sudden outward expansion can be calculated by

$$p = \frac{\rho}{2g} v^2$$

in which ρ is the density of the material.

The pressure calculated for the INPORT tubes is only 3 psi and is readily acceptable. However, similar calculations show that under different conditions, such as those in HYLIFE,[2] the sudden deposition of neutron energy can have a large impact on the reactor design. This is caused by a large coefficient of expansion for lithium and a larger ΔT/shot due to the lower repetition rate.

References for Section VI.6

1. D.K. Sze, R.G. Clemmer and E.T. Cheng, "LiPb, A Novel Material for Fusion Applications", the Fourth Topical Meeting on the Technology of Controlled Nuclear Fusion.

2. J. Maniscalco, et al., "A Laser Fusion Power Plant Based on a Fluid Wall Reactor Concept", The Third Topical Meeting on the Technology of Controlled Nuclear Fusion, May 1978, Santa Fe, NM.

VI.7 Support Mechanism and Stress Considerations

VI.7.1 General Description

The SiC tubes are designed to be suspended from the top such that they hang freely. They are attached to an upper support plate which also is the coolant distribution manifold. Restraint against lateral motion is provided by a support plate on the bottom which also contains the flow control nozzles.

The cylindrical blanket zone is divided into 30 modules, each subtended by 12° of cavity circumference. Each module consists of the upper distribution manifold and tube support plate, the tubes themselves and the bottom support plate. Ten of the 30 modules fall in line with the cavity beam ports. These modules will have beam tubes built in as part of the units.

The first two rows which are 4 cm apart consist of tubes which are 3 cm in diameter spaced at ~ 5.1 cm center to center. There are 41 such tubes in each module. The remaining tubes which are 10 cm in diameter follow behind. These tubes are arranged on a 12.5 cm triangular pitch in between support struts as shown in Fig. VI.7-1. There are 102 such tubes in each module.

Several schemes for attaching the tubes to the upper support plate were considered, two of which are shown in Fig. VI.7-2(a) and Fig. VI.7-2(b). In Fig. VI.7-2(a) a bead is woven into the tube at the end. This bead is then captured between a threaded conical flange and the upper plate. Figure VI.7-2(b) shows several plies of the braided fabric encircling a conical restraining ring. The tube is simply inserted from the top through the hole and is held in place by the conical ring.

The upper tube support plate is welded to struts which anchor into the 40 cm thick reflector wall. The sections at the end of each strut slide into milled slots in the reflector. Pulling up on the upper manifold which is part of the tube support plate disengages the module from the reflector. This

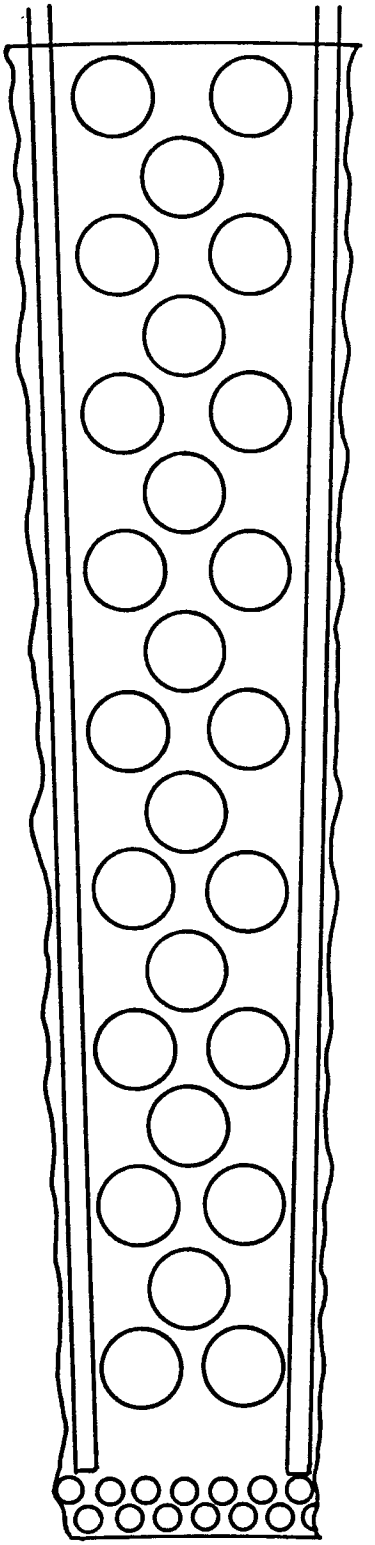

Fig. VI.2-1 Distribution of INPORT tubes between support struts.

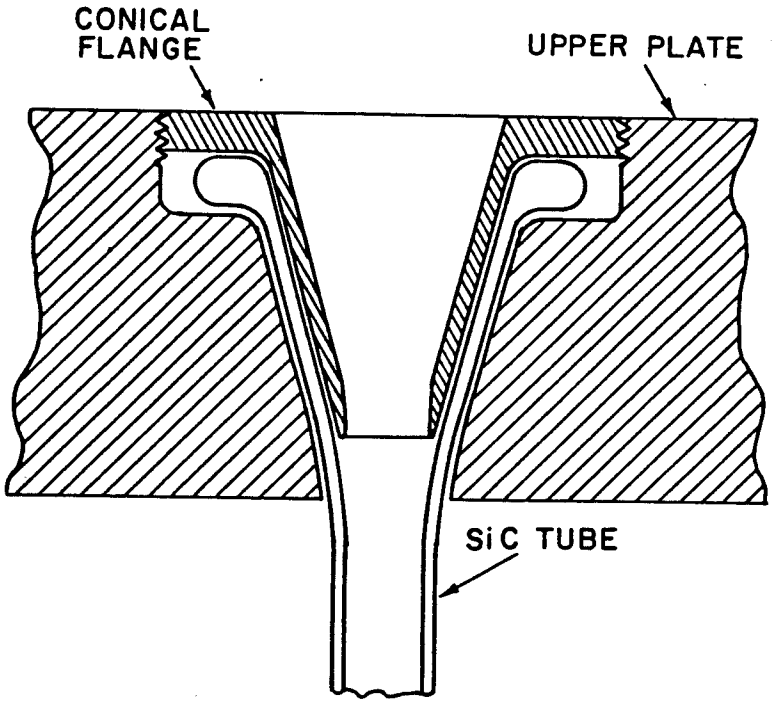

Fig. VI.2-2a

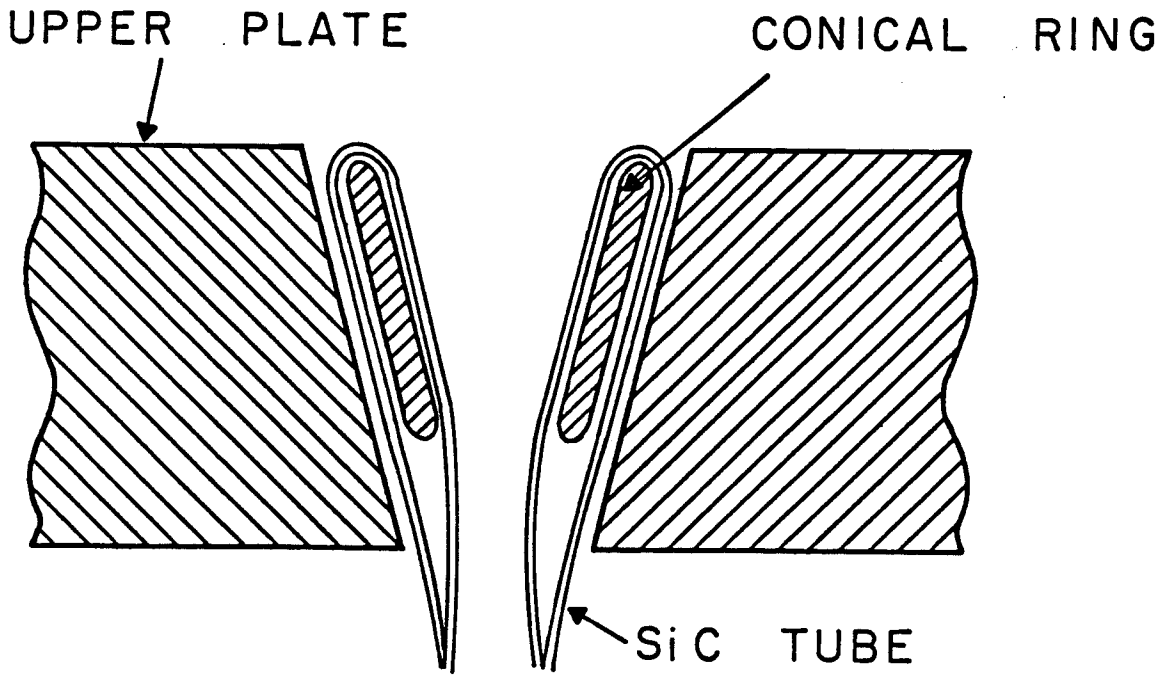

Fig. VI.2-2b

Two methods for attaching INPORT tubes.

attachment scheme is needed for maintaining the blanket modules and will be discussed in a later section.

VI.7.2 INPORT Tube Stresses

The stresses in the SiC tubes can be divided into two parts, the longitudinal and the circumferential stresses. Circumferential stresses are from the pressure of the coolant and vary linearly from the top to the bottom as a function of the supported head. The longitudinal stresses consist of two components, the pressure component and the dead weight (weight of the coolant) component. The former component is small at the top and builds up linearly to the bottom while the latter component is maximum at the top and falls off linearly to zero at the bottom.

A reliable value for allowable stress is not known for braided SiC tube construction. However, estimates can be made based on experience with other composite materials. Various sources give SiC fiber strength of 2450-3720 MPa (355-540 ksi). Strength depends on fiber diameter and when braided into a tube, the fiber strength is reduced substantially. Experience with graphite material systems indicates that the strength for orthogonal layup could be ~ 276 MPa (40 ksi) considering each principal stress individually. Ceramic materials typically have a wide variation in strength due to their extreme sensitivity to minute flaws. Because of this sensitivity a safety factor of two was taken and thus the maximum allowable stress is 139 MPa (20 ksi).

In this design the wall thickness for the 10 cm diameter tubes is 2.25 mm and in the 3 cm diameter tubes it is 0.9 mm. This means that there will be 5 plies and 2 plies in the 10 cm and 3 cm diameter tubes respectively (the thickness per ply is 0.45 mm). The fibers in the orthogonal layup are oriented at 45° and cover 50% of the available surface area. The fibers themselves are made up of filaments with a density factor of 75%.

In calculating the stresses, it was assumed that the incoming coolant had an initial presure of 0.1 MPa (~ 15 psi). At the bottom of the tubes the added head produces a pressure of 1.04 MPa (150 psi). The masses supported by the tubes are 700 kg and 61.3 kg for the 10 cm and 3 cm diameter tubes, respectively. Stress distribution as a function of tube distance from the top is given in Fig. VI.7-3 and Fig. VI.7-4 and numerically in Table VI.7-1. The principal circumferential and longitudinal stresses are amplified by a factor of 1.4 because of the 45° orientation of the fibers in the orthogonal layup.

The total stress represents the sum of all the stress components. It can be seen that the maximum stress occurs at the bottom of the tubes and is 130 MPa (18.9 ksi) for the 10 cm tubes and 97 MPa (14 ksi) for the 3 cm tubes. The thickness of the wall in the front (3 cm) tubes is dictated by thermal hydraulic considerations. The 25% lower stress in these tubes is desirable because they will be subjected to impact loading from their reaction to the target implosion, as discussed in section VI.2.

Table VI.7-1

Stresses in INPORT (SiC) Tubes

Stress	TOP (MPa)		BOTTOM (MPa)	
	10 cm	3 cm	10 cm	3 cm
Longitudinal (Dead Weight)	36.2	26.2	0	0
Longitudinal (Pressure)	4.17	3.1	43.4	32.3
Circumferential (Pressure)	8.34	6.22	86.8	64.7
TOTAL (MPa)	48.71	35.52	130.2	97.0
(psi)	(7,060)	(5,147)	(18,870)	(14,060)

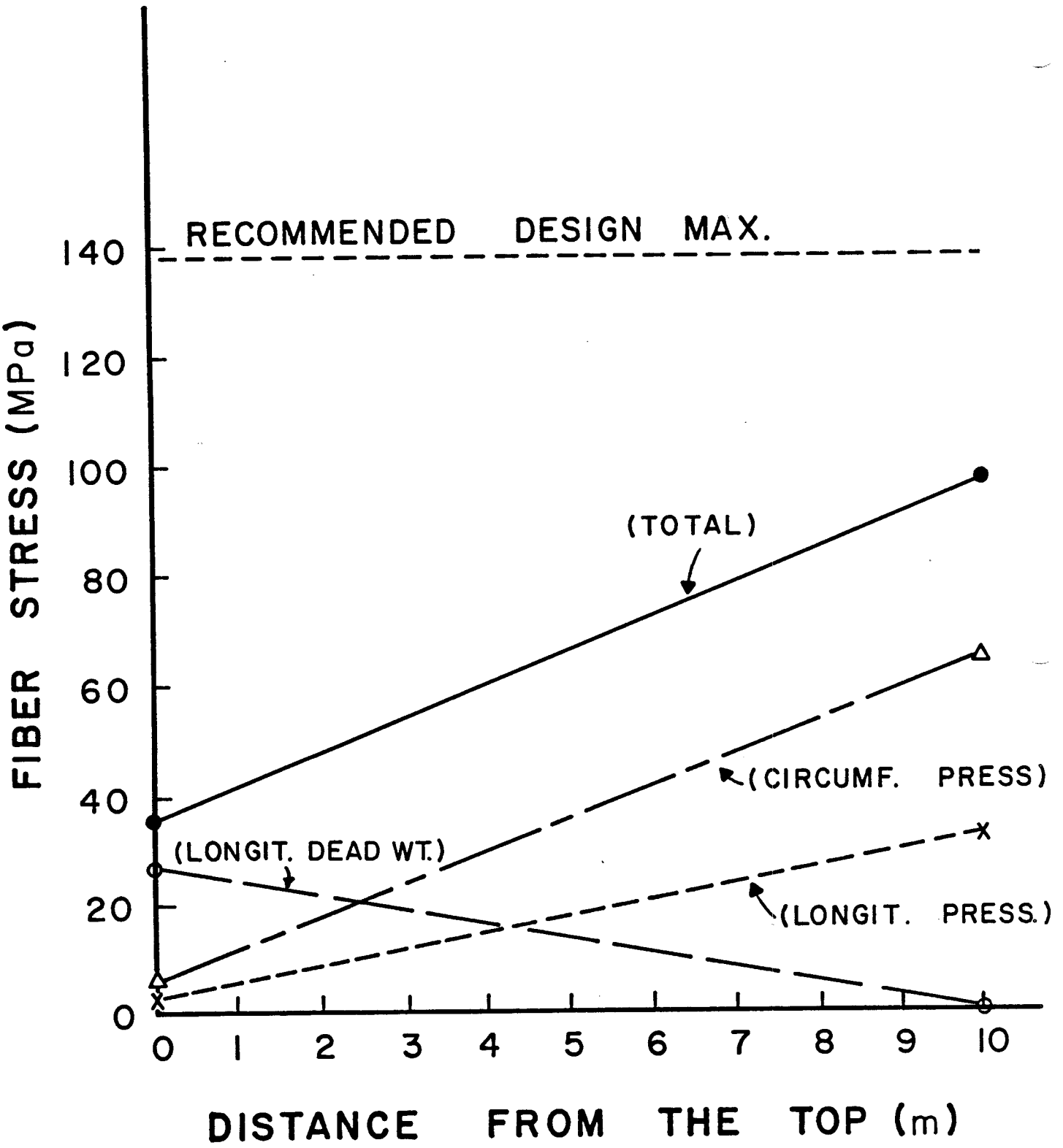

Fig. VI.2-3 Stresses in 10 cm diameter INPORT tubes.

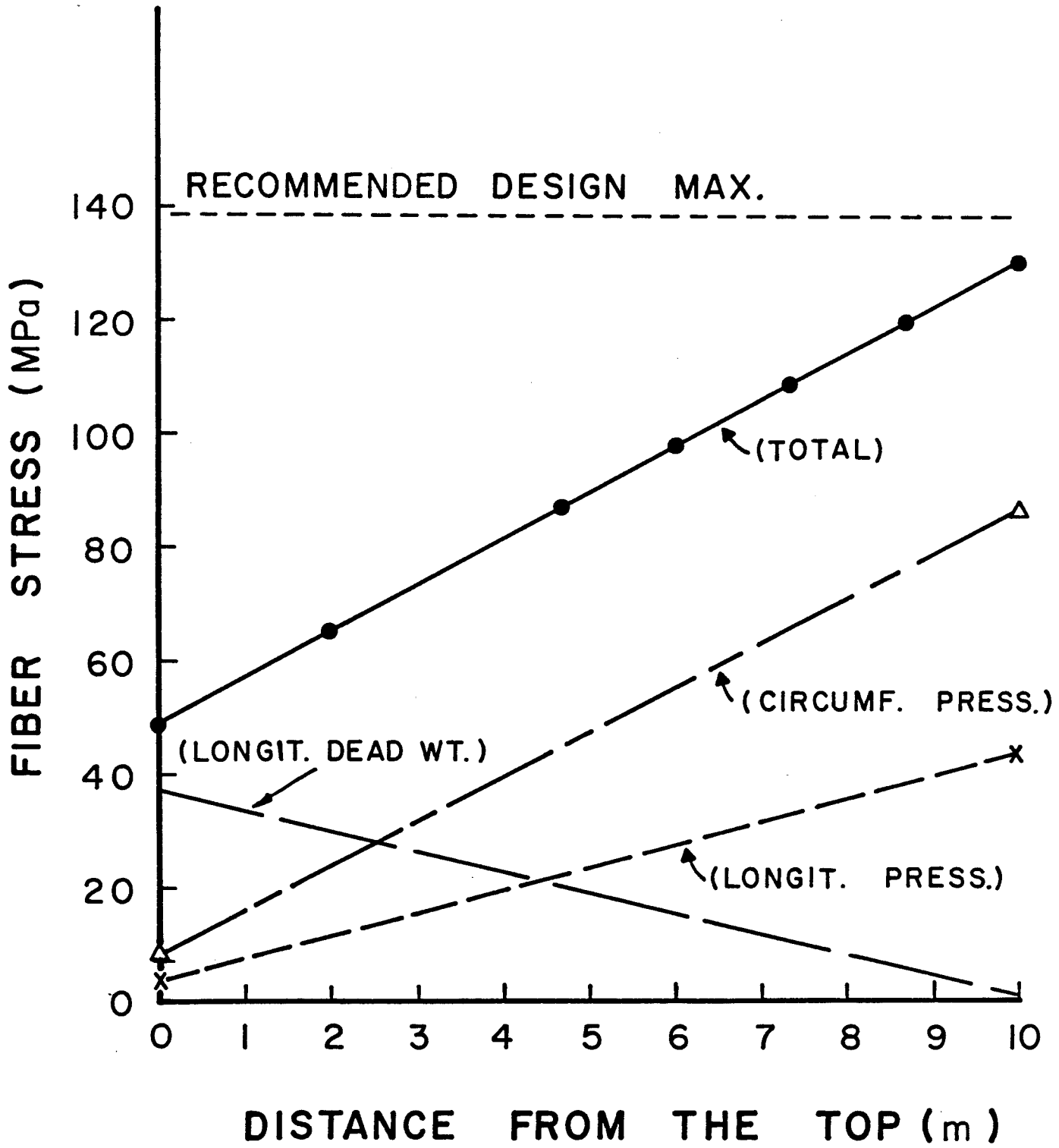

Fig. VI.2-4 Stresses in 3 cm diameter INPORT tubes.

VI.7.3 Tube Support

The tube support scheme has to be analyzed in two parts:

a) Analysis of the upper support plate

b) Analysis of the support struts

Figure VI.7-5 shows a top view and a side view of a single module support structure. It consists of an upper plate (the holes have been omited for simplicity) and struts which terminate in a tee section. These tee sections fit into slots milled in the cavity reflector. Thus, a module with integral tubes and bottom plate can be taken out by simply lifting on the assembly to disengage the tee sections from the reflector. The struts will have cooling passages such that $Li_{17}Pb_{83}$ will flow through them. After traversing the struts, the coolant then flows down the reflector side to the bottom pool.

It was decided to use four struts to support each module. The tube distribution between two struts is shown in Fig. V.7-6(a) and the loading on the plate in Fig. V.7-6(b). The upper support plate was modelled as a statistically indeterminate beam of varying cross sections and concentrated loads. The stress in the plate is then:

$$\sigma(x) = K \frac{M(x)C}{I(x)}$$

where K is a stress concentration factor taken as 2, M(x) the local moment, C is one-half of the plate thickness and I(x) the local moment of inertia. Using a maximum design stress of 70 MPa (10 ksi) for HT-9, we calculate a plate thickness of 3 cm.

Similarly, the struts were analyzed as cantilevered beams of varying cross section and a variable loading as shown in Fig. VI.7-7. The weight of the tubes is reacted by a moment on the tee sections and an upward force

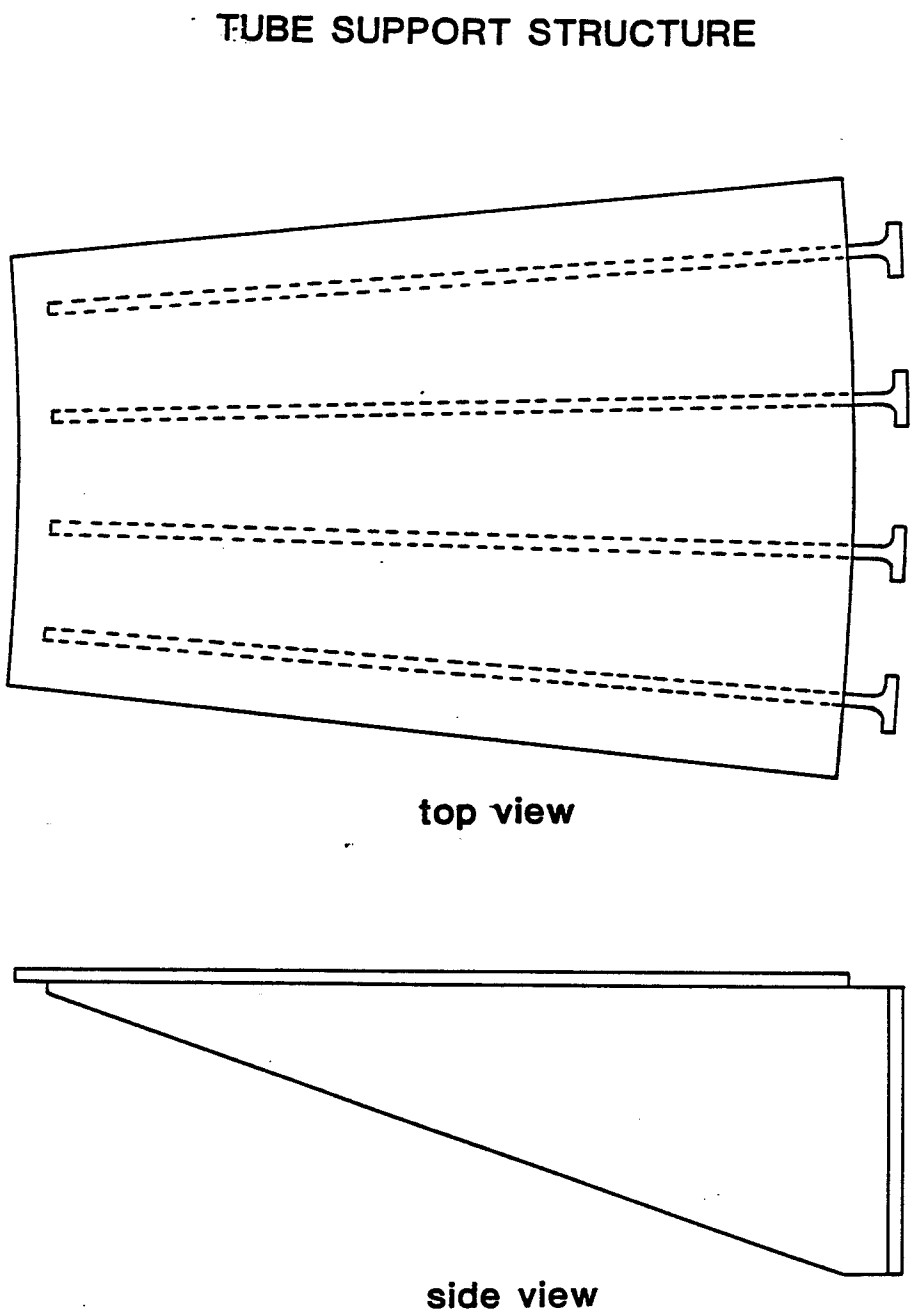

Fig. VI.2-5 Top and side views of upper support plate.

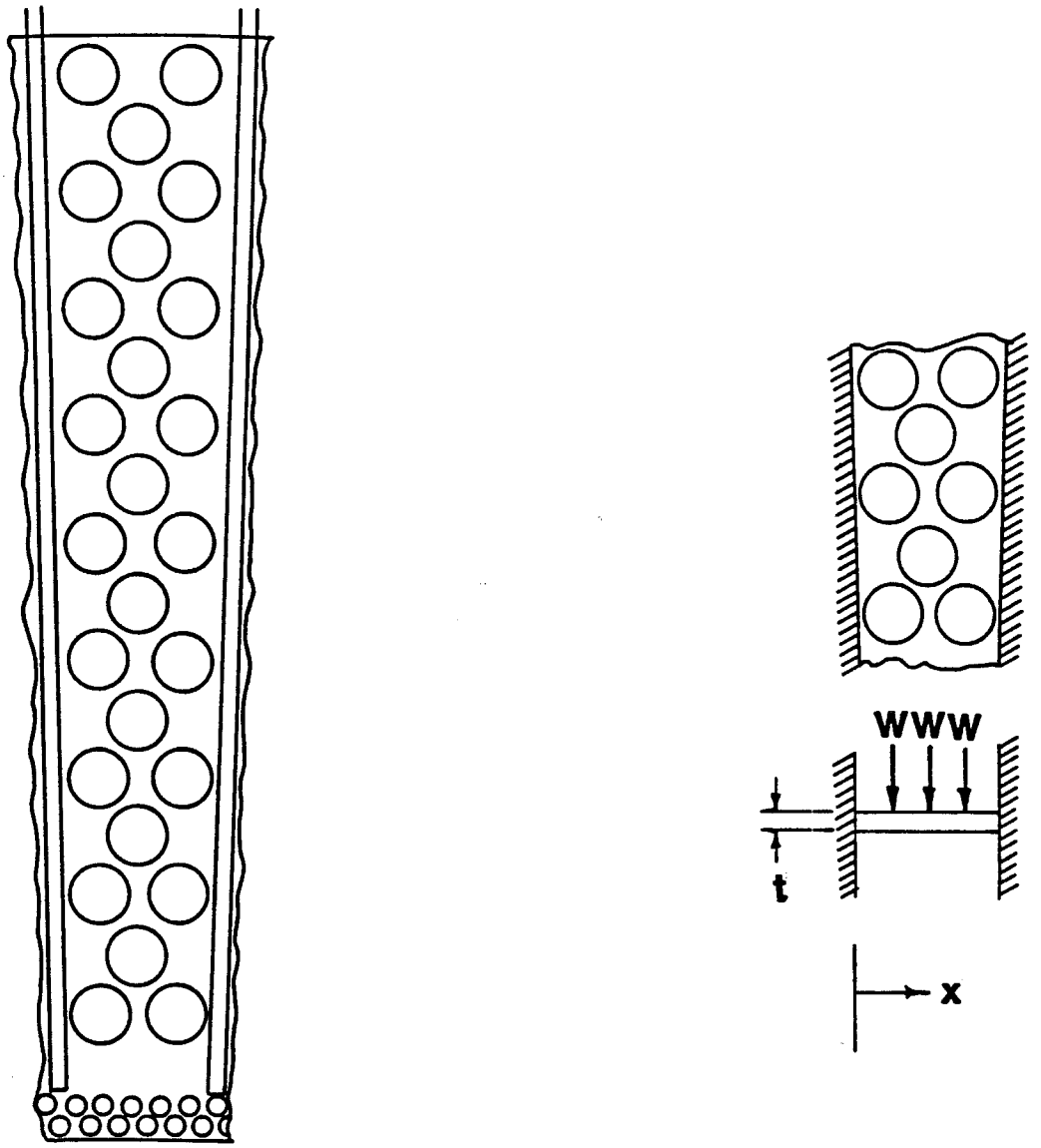

(a) (b)

Fig. VI.2-6 (a) Tube distribution between support struts.
(b) Loads on upper support plate.

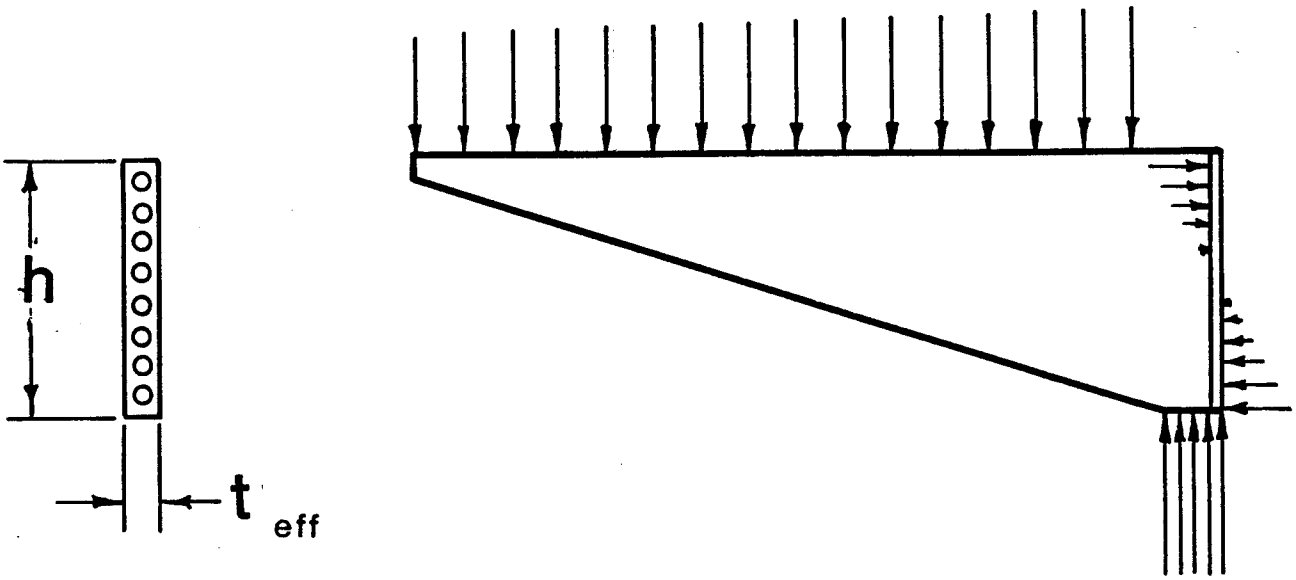

Fig. VI.2-7 Loading and reactions on support strut.

exerted by the reflector. The stress equation reduces to:

$$t_{eff.}\, h^2 = \frac{3wL^2}{\sigma_{max.}}$$

where t_{eff} is the strut effective thickness, h the depth of the strut in the back, w the loading per unit length and L = 180 cm. Substituting values we get

$$t_{eff.}\, h^2 \approx 14{,}700\ cm^3$$

and for h = 70 cm, the effective thickness of the strut is 3 cm. The maximum stress in the strut is at the point of attachment into the reflector. Table VI.7-2 summarizes the tube support parameters.

Table VI.7-2

Summary of Tube Support Parameters

Number of 3 cm tubes/module	41
Number of 10 cm tubes/module	102
Total mass/module (tonnes)	74
Max. allowable stress (MPa)	70
Number of struts/module	4
Effective strut thickness (cm)	3
Strut depth in back (cm)	70
Upper support plate thickness (cm)	3

VII Tritium

VII.1 Introduction and Overview

HIBALL is a heavy ion beam reactor composed of 4 chambers which produce a total power of 10,152 MW_t and a net electrical output of 3309 MW_e by focusing high energy Bi^{+2} ions on a cryogenic DT target. The cavity has a "wetted wall" design in which liquid metal flows down woven SiC INPORT tubes and "weeps" through the weaving, forming a layer of liquid on the tube surface. The liquid metal chosen, $Li_{17}Pb_{83}$, protects the INPORT tubes from the target explosion and serves as the coolant and breeding material. This section describes the tritium systems of HIBALL -- the tritium pathways are summarized in Fig. VII.1-1 and the inventories in the various reactor components are given in Table VII.1-1.

The reactor cavities are fueled with multilayer targets containing 4.0 mg DT, which are fired at a rate of 5 sec^{-1} per cavity. A one day fuel supply consists of 2.8 kg D and 4.1 kg T. The fraction of fuel burned is 0.29, thus 1.9 kg/d of deuterium and 2.9 kg/d of tritium are handled by the exhaust system. In addition, 2.8 kg/d of D_2, used to propel the target, and 1.5 kg/d of tritium bred by the $Li_{17}Pb_{83}$ will enter the exhaust processing system. The details of how the targets will be manufactured are unspecified, but recommendations are made on minimizing the tritium handling in target manufacture.

The chamber exhaust is pumped by compound cryopumps with on-line times of 2 hours and a tritium inventory of 0.37 kg. The pumps are regenerated so that helium is released first, then the hydrogen isotopes are released and sent to the fuel cleanup unit. The purpose of the fuel cleanup unit (T_{INV} = 0.041 kg) is to remove impurities from the hydrogen isotopes before sending them to the cryogenic distillation unit. (The distillation system consists of 4 columns (T_{INV} = 0.083) which separate the isotopes into an H stream which is vented, a

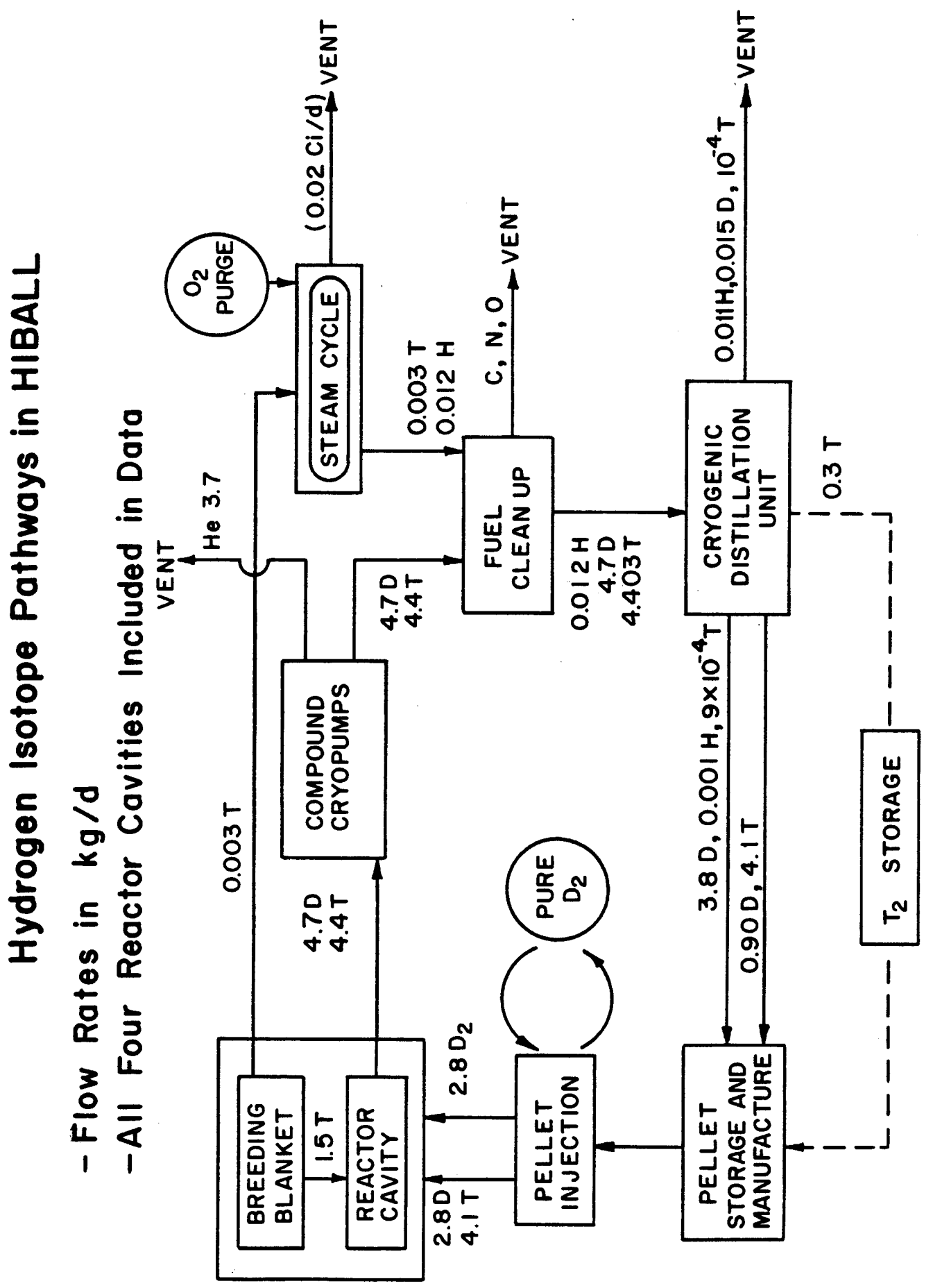
Hydrogen Isotope Pathways in HIBALL
- Flow Rates in kg/d
- All Four Reactor Cavities Included in Data
BREEDING BLANKET
1.5 T
REACTOR CAVITY
2.8 D
4.1 T
2.8 D_2
PELLET INJECTION
PURE D_2
PELLET STORAGE AND MANUFACTURE
3.8 D, 0.001 H, 9×10^{-4} T
0.90 D, 4.1 T
CRYOGENIC DISTILLATION UNIT
0.011H, 0.015 D, 10^{-4} T
VENT
0.3 T
T_2 STORAGE
0.003 T
4.7 D
4.4 T
COMPOUND CRYOPUMPS
VENT
He 3.7
4.7 D
4.4 T
FUEL CLEAN UP
0.012 H
4.7 D
4.403 T
C, N, O
VENT
0.003 T
0.012 H
STEAM CYCLE
(0.02 Ci/d) VENT
O_2 PURGE

Fig. VII.1-1

Table VII.1-1 HIBALL Tritium Inventory

Fuel cycle (kg):		
Cryopumps	0.37	
Fuel cleanup	0.041	
Isotopic separation	0.083	
Subtotal		0.494
Blanket (kg):		
$Li_{17}Pb_{83}$ (cavity and reflector)	0.013	
SiC tubes	0.012	
Subtotal		0.025
Target manufacture (kg):	4.1	4.1
Storage (kg):		
Targets	4.1	
Uranium beds	4.1	
Subtotal		8.2
TOTAL INVENTORY (kg)		12.819
TOTAL ACTIVE INVENTORY (kg)		0.519

pure D_2 stream for the target injector, and a pure DT stream for the target factory and storage.

In the blanket system a low solubility of 7×10^{-2} wppm T in alloy/torr$^{1/2}$ results in an inventory of 0.013 kg T in the $Li_{17}Pb_{83}$ (1.9×10^7 kg). Tritium is bred at a rate of 4.4×10^{-6} kg/sec and extracted from the reactor chamber by pumping at pressures less than or equal to the vapor pressure of tritium above the eutectic (10^{-4} torr). The inventory in the silicon carbide tubes (1.6×10^4 kg) at 500°C is unknown, but has been approximated as 0.012 kg. Only very minimal amounts of silanes and hydrocarbons will form as the liquid metal protects the silicon carbide from interacting with hydrogen atoms.

The liquid metal is circulated into the heat exchange cycle. The tritium pressure above the eutectic is 10^{-4} torr, which causes a tritium containment problem in the steam cycle. The permeation of tritium through clean HT-9 results in a loss of 33.3 g T_2/day to the steam cycle. Oxide coatings or other tritium barriers can be used to reduce the permeation by factors of 10 to 100. With a design goal to limit tritium losses to 10 Ci/day, the steam generator is designed with double walled tubes purged with an oxygen atmosphere. This provides a very effective barrier limiting losses to less than 1 Ci/day. the tritiated water from the sweep gas is condensed and eventually merged with the reactor exhaust for reprocessing.

VII.2 Fuel Cycle

The HIBALL reactor is an inertial confinement fusion (ICF) device where the fusion reaction occurs by implosion of a cryogenic D-T target with 10 GeV Bi^{+2} ion beams. There are four reactor cavities with 20 bismuth ion beam ports per cavity. The target yield is 400 MJ at a gain of 83, with a repetition rate of 5 sec^{-1} per cavity and a total energy per fusion event of 17.6 MeV. This results in a total thermal power of 10,152 MW_t and a net electrical output of 3309 MW_e. The energy production in HIBALL is about three times higher than the energy produced from previous laser driven ICF reactor designs.(1) The fractional burnup (f_b) of the target is given by $f_b = T_b/(T_b + T_p)$, where T_b is the amount of tritium burned per day and T_p is the unburned tritium fuel that must be pumped out of the chamber per day. In the HIBALL reactor the fractional burnup is 29% which is comparable to other ICF reactor systems (20-40%).(1) At this point there has been no consideration of the possibility of misfirings.

Each reaction chamber is equipped with a target injection system and cryopumps. Exhaust from regeneration of the cryopumps from the four chambers is combined and sent into the fuel cleanup and processing system. The daily D-T fueling and exhaust characteristics of HIBALL are given in Table VII.2-1.

VII.2.1 Fueling

The HIBALL reactor is fueled by injection of a cryogenic DT target. The target consists of three shells: the equimolar DT fuel, a Li-Pb ablator (Li:Pb mole ratio 18.1:1), and a lead outer shell as the high-Z component. The target composition is given in Fig. VII.2-1. The targets are injected at a velocity of 200 m/sec with a target injection gun (section III.5) that also releases 1.6 mg of D_2 propulsion gas into the chamber per shot. The target is loaded into a plastic 2-piece carrier called a sabot. During injection,

PELLET COMPOSITION

Layer	Materials	Weight (mg)	Atoms x 10^{20}	Density g/cm^3	Thickness mm
3	Pb	288	8.34	11.3	0.245
2	Li Pb	26 41	22 1.2	1.26	0.739
1	D T	1.6 2.4	4.8 4.8	0.21	0.477

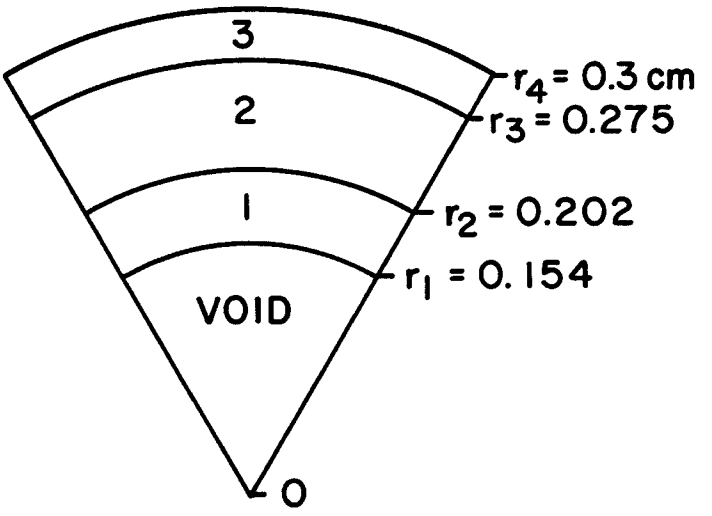

Fig. VII.2-1

Table VII.2-1 Daily Fueling and Exhaust Characteristics*

	Deuterium	Tritium
Fraction burned (%)	29	29
Fuel injected (kg/d)	2.8	4.1
Fuel burned (kg/d)	.80	1.2
Fuel exhaust pumped (kg/d) (from D-T reaction)	2.0	2.9

*For all four reactor cavities

the sabot is shed into a buffer cavity and does not enter the reactor. Deuterium propulsion gas in the buffer cavity which does not reach the reaction chamber (139.4 mg/shot) will be recycled periodically with the hydrogen isotopes.

The choice of lithium and lead for target materials is favorable because they are compatible with the $Li_{17}Pb_{83}$ liquid wall. Debris from the target shells will dissolve in the liquid wall. In Table VII.2-2 the change in blanket composition with time is shown. Since the ratio of Li:Pb in the target is greater than in the eutectic (17:83 atom%), the ratio of Li:Pb in the blanket slowly increases with time. Therefore, quantities of lead will have to be added and properly mixed to maintain the eutectic composition.

The target injection rate is 5 sec^{-1} per cavity, requiring 4.32×10^5 targets/day, corresponding to 4.1 kg T/day and 2.8 kg D/day. The details of how the targets will be manufactured have not been developed at this time in the reactor study. However, the effects of target manufacture on the tritium inventory are discussed in section VII.2.6.

Table VII.2-2 Change in $Li_{17}Pb_{83}$ Composition with Time

	Mass Changes			
	^{+}Pb (target) (kg)	^{+}Li (target) (kg)	^{-}Li Li(n,α)T (kg)	^{+}Li (total) (kg)
1 shot	3.29×10^{-4}	2.65×10^{-5}	2.03×10^{-6}	2.45×10^{-5}
1 day	142	11.4	.877	10.5
1 year	5.18×10^{4}	4.16×10^{3}	320	3.84×10^{3}

	Composition Changes		
	Original blanket	1 year operation	% change
Mass Li (kg)	3.26×10^{4}	3.64×10^{4}	11.8
Mass Pb (kg)	4.74×10^{6}	4.79×10^{6}	1.09
Ratio Li:Pb	0.205	0.228	
Formula	$Li_{17}Pb_{83}$	$(Li_{18.9}Pb_{83})$	

VII.2.2 Exhaust

Each fusion event will cause a pressure rise in the chamber as Li-Pb debris is ablated from the walls and gases from the D-T reaction and unburned fuel are released. The major components present in the exhaust are given in Table VII.2-3. Between fusion events, the chamber must be pumped to at least 10^{-4} torr, as higher pressures will cause interference and scattering of the ion beams. The vaporized liquid metal will recondense on the liquid wall. Any Li-Pb vapor or debris that enters the vacuum or beam ports is assumed to condense on the cold duct surfaces and will not contaminate the cryopumps.

Table VII.2-3 Exhaust Gas Composition

	mg/shot	kg/d[a]
Deuterium target (unburned)	1.1	1.9
Tritium target (unburned)	1.7	2.9
Helium (DT fusion)	.93	1.6
Helium (breeder)	1.2	2.1
Tritium (breeder)	.87	1.5
Li-Pb vapor[b]	0	0
D_2 target injection	1.6	2.8
TOTAL GASES	7.4	12.8
TOTAL TRITIUM	2.57	4.4

[a] All four cavities.

[b] Lithium and lead vapor will condense on cold surfaces before reaching cryopumps.

The amount of lithium and lead in the gas phase in the chamber that results from the equilibrium vapor pressure of lithium and lead above $Li_{17}Pb_{83}$[2,3] is given in Table VII.2-4. The vapor pressure is less than the 10^{-4} torr pressure limit at the operating temperature. The bismuth from the ion beam, is similar to lead and will dissolve completely in the wetted wall and will not be emitted in the exhaust gas. The concentration of bismuth in the chamber with time is given in Table VII.2-5. After 20 years of operation the bismuth concentration in the liquid metal is still less than 1 wppm.

Table VII.2-4 Vapor Pressure of $Li_{17}Pb_{83}$ at 500°C

	Li	Pb
Activity	1.3×10^{-4}	0.81
Pressure (pure)	2.86×10^{-3}	1.69×10^{-5}
Pressure (above eutectic)	3.7×10^{-7}	1.4×10^{-5}

Table VII.2-5 Bismuth Concentration in $Li_{17}Pb_{83}$

Time	Bi dissolved (kg)	wppm Bi in $Li_{17}Pb_{83}$
1 shot	1×10^{-9}	2.1×10^{-10}
1 day	4.3×10^{-4}	9.0×10^{-5}
1 year	1.6×10^{-1}	0.033
10 years	1.6	0.33
20 years	3.2	0.66

VIII.2.3 Cryopumps

The reactor chambers are pumped with compound cryopumps, capable of pumping both the hydrogen isotopes and helium at the high volumetric flow rates required. The separation of hydrogen isotopes from helium on the cryosorption panels is extremely sharp.(4) By controlled heating, the helium panel is regenerated first, then the hydrogen isotopes are removed and sent to the fuel cleanup unit. The on-line time for the pumps is two hours and the tritium inventory in the pumps is 0.37 kg.

VII.2.4 Fuel Cleanup

The exhaust from the cryopumps enters the fuel cleanup unit where hydrogen isotopes are separated from hydrocarbons, water, ammonia or any other impurities. The fuel cleanup unit is patterned after the Tritium Systems Test Assembly (TSTA) designs.(5) Impurities are first absorbed onto molecular sieve beds at 75°K while hydrogen isotopes flow into the distillation unit. These impurities are then recovered from the sieves and catalytically oxidized to form tritiated water and tritium free compounds. The tritiated water is condensed and electrolyzed to recover the tritium. For a 500 mole T flow rate TSTA has estimated an inventory in the fuel cleanup unit of 14 g.(6) In HIBALL the exhaust contains 1467 moles T/day giving an inventory of 41 g.

VII.2.5 Isotopic Separation Unit

Hydrogen isotopes from the fuel cleanup unit enter the crogenic distillation system in the mole ratio 12 H:2350 D:1467 T. (A stream of the deuterium from the target injection gun that does not enter the cavity will also be purified.) The goals of the separation system are to separate and vent hydrogen, to form a purified D-T stream for the target manufacturing system and storage, and to form a pure D_2 stream for the target injection

system. The separation scheme, patterned from the literature[6,7] is shown in Fig. VII.2-2. The inventory in the separation system is estimated as 83.4 g.

VII.2.6 Tritium Considerations in Target Manufacture

The details of the target manufacturing system have not been addressed at this time, thus the tritium inventory in the target manufacturing process and the inventory that must be kept in storage as targets to insure production in case of a malfunction are unknown. This inventory will be dependent on:

(1) the number of targets produced per day;

(2) the time required to make a day's quantity of targets;

(3) the process used - batch or continuous; and

(4) the amount of tritium that must enter the recycling system due to rejection of targets that do not conform to specifications.

The fusion targets for HIBALL must be produced economically at a rate of 4.32×10^5/day. Three possible pathways for target production are outlined in Fig. VII.2-3. After selected steps in the manufacturing process, the product is examined to insure it meets certain specifications,[8] and at this point a number of targets will be rejected. If the rejected targets contain D-T, the fuel must be recovered and reprocessed. To minimize the tritium handling, the filling of the targets with DT fuel should come as late in the manufacturing process as possible or at least following steps with large rejection rates.

To minimize the tritium storage for the target manufacturing system, the time required to fill the targets with DT should be as short as possible. If the DT fuel is diffused into a hollow shell, the targets will be produced in a batch process and the fill-time will be dependent on the permeation rate of DT through the shell at temperatures below the shell melting point. In SOLASE[9] two target designs were examined. Plastic targets required a 1 day fill-time resulting in a one day fuel storage, while glass targets required a five day

HIBALL Isotope Separation Unit

Flow Rates in g/d
T = Tritium Inventory (g)

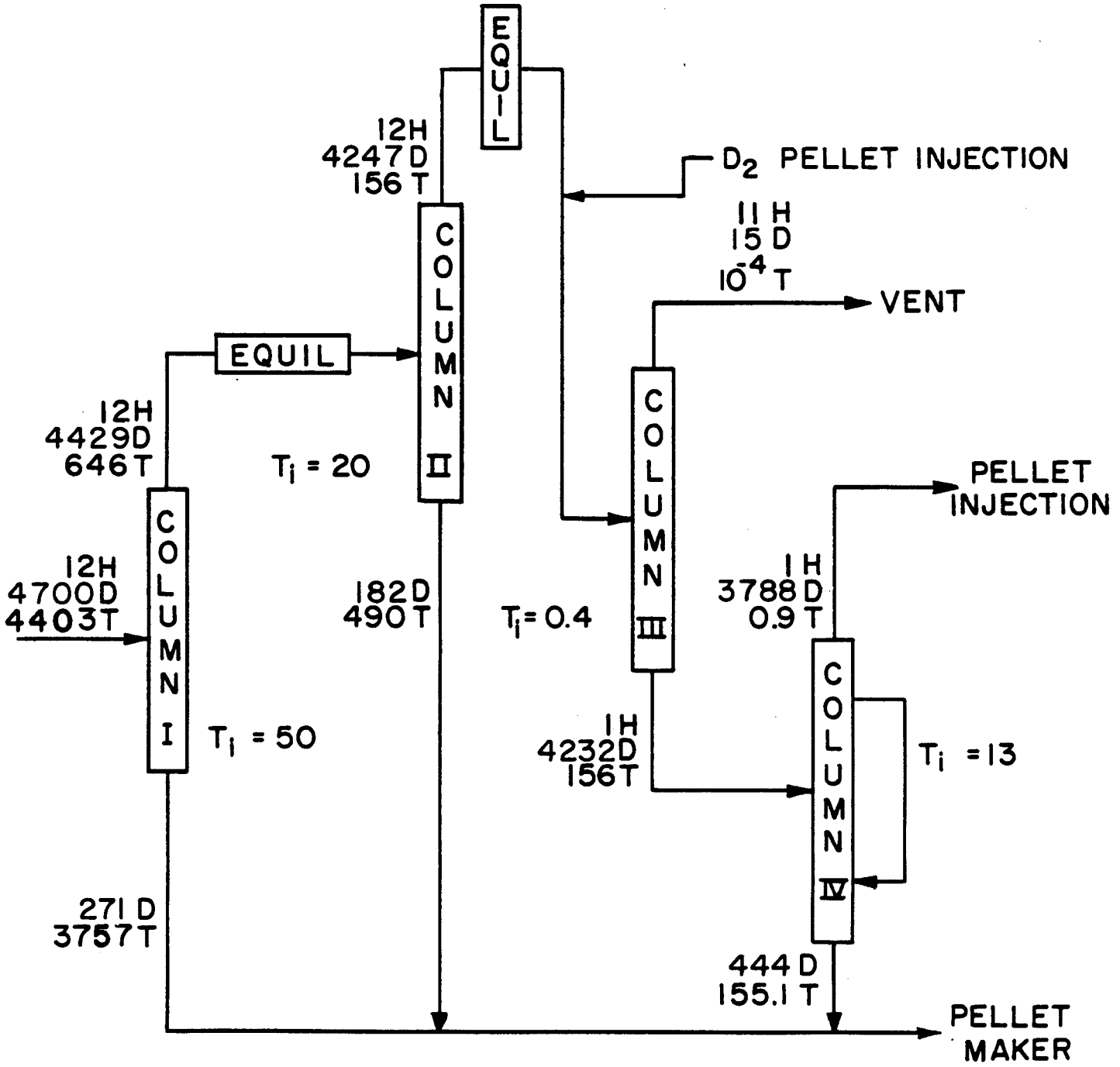

Fig. VII.2-2

POSSIBLE PELLET MANUFACTURING SCHEMES

STEP	PROCESS	TRITIUM RECYCLE?	
1	FORMATION OF Li-Pb SHELL	NO	
2	DT FILL		PATH I
	(a) BATCH GAS DIFFUSION	YES	
	(b) CONTINUOUS DRILL, FILL & SEAL	YES	
3	Pb COATING	YES	
4	CRYOGENIC PROCESS		
1	FORMATION OF CRYO. DT SHELL	YES	
2	Li — Pb COATING	YES	PATH II
3	Pb COATING	YES	
1	FORMATION OF Li-Pb SHELL	NO	
2	Pb COATING	NO	PATH III
3	DT FILL		
	(a) BATCH GAS DIFFUSION	YES	
4	CRYOGENIC PROCESS		

Fig. VII.2-3

full-time and a five day inventory in storage. Therefore, Path III in Fig. VII.2-3 is probably unreasonable because it would require diffusion of DT through two layers at fairly low temperatures (mp. Pb = 327°C; mp. $Li_{18.1}Pb \approx 450°C$), resulting in a large storage inventory.

While microdrilling of laser targets and parts has been successfully tried,[10] the filling and sealing process has not been demonstrated. Although the drill-and-fill process is continuous, requiring less tritium storage than batch processes, the high symmetry requirements of the target would probably result in a high rejection rate of improperly sealed shells and a significant amount of tritium recycle and recovery. Therefore, until this option is proven to be practical, target production by diffusion methods seems more reasonable.

In Path I the first step is the preparation and analysis of the ablation shell. Hollow glass and hydrogen shells have been prepared by introducing a stream of gas bubbles into a controlled jet producing uniform spheres.[11] The DT is then diffused into the shell. The permeability of DT through this layer of Li-Pb is unknown, so the time to fill this shell and the required DT storage are unknown. The Li-Pb shell is then coated with lead. There are four major processes that have been developed for producing metallic coatings onto microspheres[12]: magnetic sputtering, electroplating, electroless plating, and chemical vapor pyrolysis. At present the sputtering technique seems to have the most general applicability. After the coatings are applied initial cooling of the target freezes the DT non-uniformly. By vaporizing the inner coating of fuel with a laser or heat pulse and quickly refreezing the DT, a uniform layer can be produced.[13,14]

Hendricks et al. proposed a process in which cryogenic spheres are transported past sputtering guns which apply consecutive layers onto the sphere.[8]

A cold helium gas jet[15] can be used to keep the targets frozen and levitate the targets as they pass the sputtering guns and quality control apparatus. This process is outlined in Path II. This method has the disadvantage of handling tritium throughout the process; however, there is no batch diffusion step requiring a large storage inventory. While the tritium reprocessing of imperfect D-T spheres would be minimal, the processing after the coatings are applied would require more sophistication. From a comparative standpoint, Path II is probably the superior method from tritium considerations, assuming the coatings can be applied to high standards requiring minimal tritium recycling.

Until the details of the target manufacturing system are known it will be assumed that one day's fueling supply (4.1 kg) will be stored as cryogenic targets and another day's supply will be tied up in the target manufacturing system.

VII.2.7 Storage

The storage requirements for HIBALL include a one day supply of targets to fuel the reactor (4.1 kg T) and a one day supply kept on uranium beds to feed into the target manufacturing system. (This storage inventory will depend on the target manufacturing process as discussed in the preceding section.) The storage inventory of 8.2 kg T, represents a large fraction of the total inventory.

References for Section VII.2

1. M.S. Ortman, E.M. Larsen, S.I. Abdel-Khalik, "A Study of the Tritium Handling Systems in Magnetic and Inertal Confinement Fusion Reactors With and Without Tritium Breeding," Nuclear Technology/Fusion 1, 255-274 (April 1981).

2. J.L. Ballif, D.W. Jeppson, W.W. Yuan, and B.E. Chou, "Lithium Literature Review: Lithium's Properties and Interactions," (TC-1000, Hanford Engineering Developmental Laboratory (January 1978).

3. D.H. Shiu and Z.A. Munir, "The Heat of Vaporization and Vapor Pressure or Liquid Lead," Met. Trans. 2, 2953-2955 (1971).

4. J.L. Anderson, "Design and Construction of the Tritium Systems Test Assembly," Proceedings Tritium Technology in Fission, Fusion and Isotropic Applications, Dayton, Ohio, April 29 - May 1, 1980, CONF-800427, American Nuclear Society (1980), 341-346.

5. E.C. Kerr, J.R. Bartlit and R.H. Shermon, "Fuel Cleanup System for the Tritium Systems Test Assembly: Design and Experiments," Proceedings Tritium Technology in Fission, Fusion and Isotropic Applications, Dayton, Ohio, April 29 - May 1, 1980, CONF-800427, American Nuclear Society (1980), 115-118.

6. J.L. Anderson and R.H. Sherman, "Tritium Systems Test Assembly Design for Major Device Fabrication Review," LA-6855-P, Los Alamos Sci. Lab (June 1977).

7. B. Badger et al., "WITAMIR-I - A Tandem Mirror Reactor Study," University of Wisconsin Fusion Design Memo UWFDM-400, Chapter XI, (Dec. 1979).

8. C.D. Hendricks, W.L. Johnson, "Power Production of Inertial Confinement Fusion Targets," Lawrence Livermore Laboratory, UCRL-52539, February 15, 1979.

9. R.W. Conn et al., "SOLASE, A Laser Fusion Reactor Study," University of Wisconsin Fusion Design Program Memo UWFDM-220, Chapter IV, (1977).

10. B.W. Weinstein, C.D. Hendericks, J.T. Weir, "Laser Microdrilling in the Fabrication of Laser Fusion Targets," Lawrence Livermore Laboratory, UCRL-77406, October 15, 1975.

11. C.D. Hendricks, "Fabrication of Targets for Laser Fusion," Lawrence Livermore Laboratory, UCRL-76380, January 20, 1975.

12. S.F. Meyer, "Metallic Coating of Microspheres," Lawrence Livermore Laboratory, UCRL-84463, August 15, 1980.

13. R.L. Woerner and C.D. Hendricks, "Fabrication of Cryogenic Laser Fusion Targets," Lawrence Livermore Laboratory, UCRL-79442, September 27, 1977.

14. K. Kim and H. Rieger, "Fabrication and Characterization of Cryogenic Targets for Inertial Confinement Fusion," Dept. of Electrical Engineering, University of Illinois, Urbana, Report 1979, UCRL-15113 (1980).

15. W.L. Johnson, S.A. Letts, D.W. Myers, J.K. Crane, J.D. Illige, and C.W. Hatcher, "Plasma Processed Coating of Laser Fusion Targets," Lawrence Livermore Laboratory, UCRL-83000, September 19, 1979.

VII.3 Blanket System

The breeding material is the liquid lithium-lead eutectic, $Li_{17}Pb_{83}$ (.68 Li:99.32 Pb wt%). This material flows through woven SiC fixtures at the top and woven SiC tubes at the sides of the reactor providing a protective coating on the SiC surfaces and forming a pool at the bottom of the reactor. The cavity reflector also contains $Li_{17}Pb_{83}$. The liquid alloy serves as the heat exchange material and is circulated through the steam cycle. The properties of the blanket system and the tritium extraction scheme are discussed in this section.

VII.3.1 Solubility of Tritium in $Li_{17}Pb_{83}$

In order to determine the tritium inventory in the breeding material and the method of extraction, the solubility of tritium in $Li_{17}Pb_{83}$ at the reactor temperatures (300-500°C) must be known. Ihle et al.[1] has determined the deuterium solubility in Li-Pb alloys at 677 and 767°C, much higher temperatures than the reactor conditions. In NUWMAK,[2] $Li_{62}Pb_{38}$ was used as the breeding material, and a model was proposed for determining the solubility of hydrogen isotopes in lithium-lead alloys versus temperature. This model[3] assumes that the Sievert's constant for the solubility of tritium in the lithium-lead alloy ($K_{S(alloy)}$) is related to the Sievert's constant for tritium in pure lithium ($K_{S(Li)}$) by the expression:

$$K_{S(alloy)} = K_{S(Li)} \cdot \gamma_{Li(alloy)} \cdot N_{Li(alloy)} = K_{S(Li)} a_{Li(alloy)}$$

where: $a_{Li(alloy)}$ = activity of lithium in lithium-lead

$\gamma_{Li(alloy)}$ = activity coefficient for lithium in lithium-lead

$N_{Li(alloy)}$ = mole fraction of lithium in the alloy.

The Sievert's constant for hydrogen isotopes in pure lithium[4-8] (Fig.

VII.3-1) and the activity of lithium in lithium-lead[1,9-11] (Fig. VII.3-2) are well-known quantities.

The major assumptions in this model are:

(1) The manner in which tritium dissolves in the alloy is by association with the lithium only. Any lead-tritium interaction is assumed to be negligible. This behavior is expected from periodic trends[12]; lithium is capable of forming hydride bonds while lead-hydrogen interactions are weak. A comparison of the hydrogen solubility in lithium and lead to that in other metals,[4,5,14-16] (Fig. VII.3-3) shows that lithium has one of the highest hydrogen solubilities of any known metal while lead has one of the lowest hydrogen solubilities.

(2) The manner in which lead enters into the lead-lithium-tritium equilibrium is to chemically bond the lithium making it less available to interact with the tritium. The degree to which the lithium is available for bonding is related to the activity coefficient for lithium in lithium lead.

(3) The lithium activity is unaffected by ppm quantities of tritium.

A plot of the theoretical solubility constant for deuterium in lithium-lead alloys is shown in Fig. VII.3-4. This figure also contains the experimental solubility data of Ihle et al.[1] and the data for deuterium solubility in pure lithium[4,7,8] and hydrogen solubility in pure lead[13,17]. (Note in Fig. VII.3-4 the data is plotted such that the Sievert's constant is directly proportional to the solubility, rather than inversely as in Ihle's paper. Also, there is no attempt to plot the theoretical solubility in regions where solid phases occur.) If the assumptions in the theoretical model are reasonable two important conclusions can be drawn:

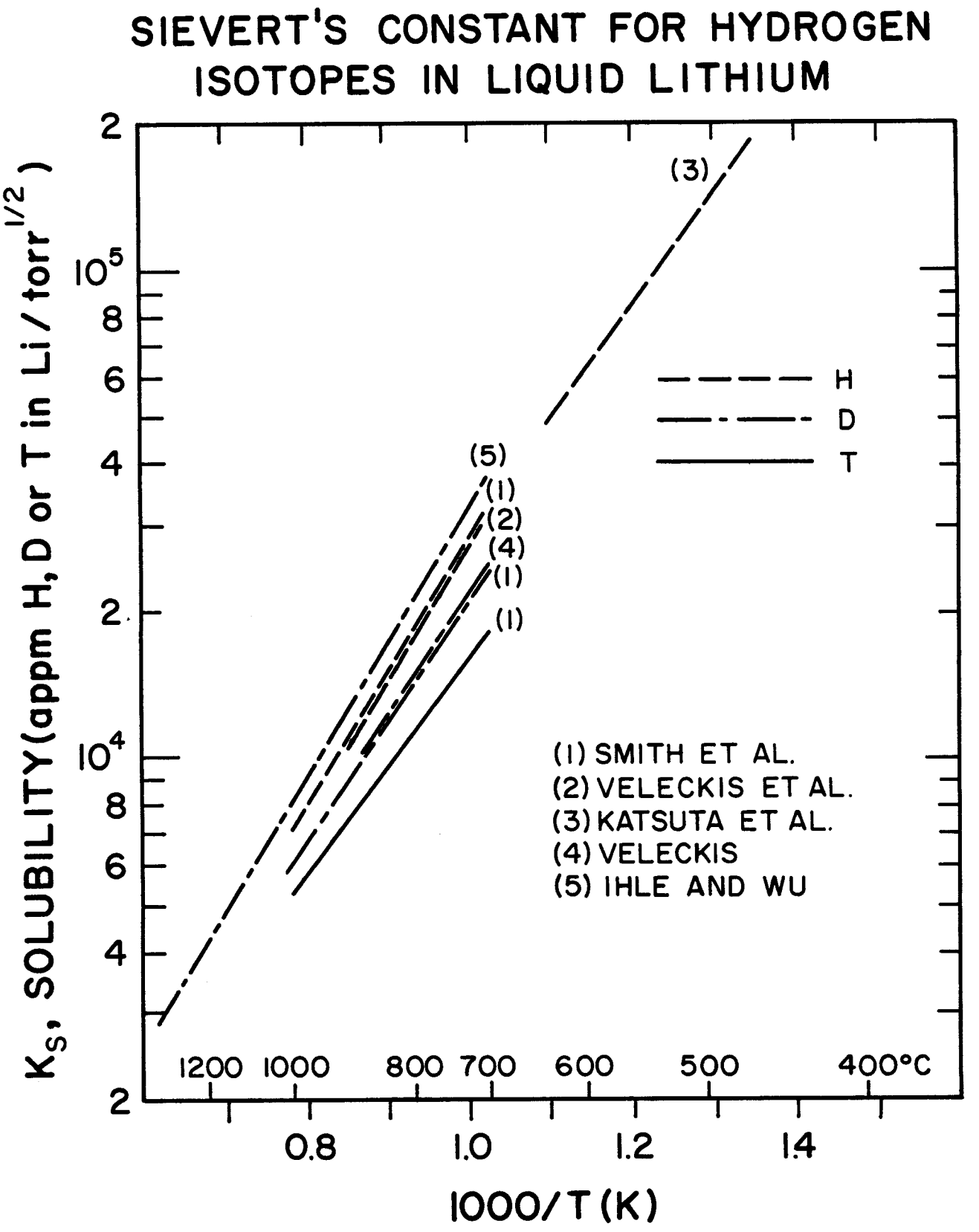
SIEVERT'S CONSTANT FOR HYDROGEN ISOTOPES IN LIQUID LITHIUM
K_S, SOLUBILITY (appm H, D or T in Li / torr$^{1/2}$)
2
10^5
8
6
4
2
10^4
8
6
4
2
(3)
(5)
(1)
(2)
(4)
(1)
(1)
H
D
T
(1) SMITH ET AL.
(2) VELECKIS ET AL.
(3) KATSUTA ET AL.
(4) VELECKIS
(5) IHLE AND WU
1200 1000 800 700 600 500 400°C
0.8 1.0 1.2 1.4
1000/T (K)

Fig. VII.3-1

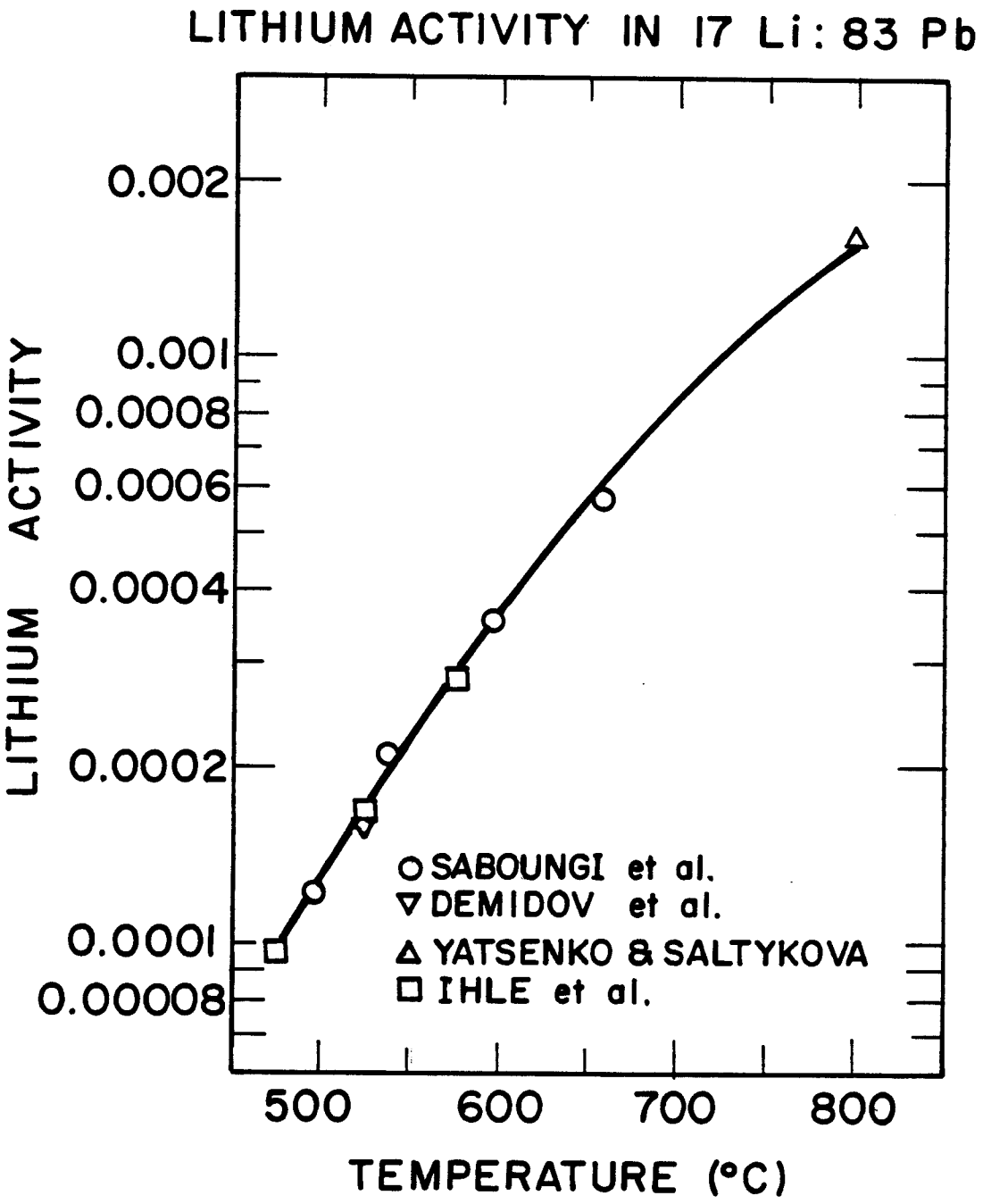
LITHIUM ACTIVITY IN 17 Li : 83 Pb
LITHIUM ACTIVITY
0.002
0.001
0.0008
0.0006
0.0004
0.0002
0.0001
0.00008
500
600
700
800
TEMPERATURE (°C)
SABOUNGI et al.
DEMIDOV et al.
YATSENKO & SALTYKOVA
IHLE et al.

Fig. VII.3-2

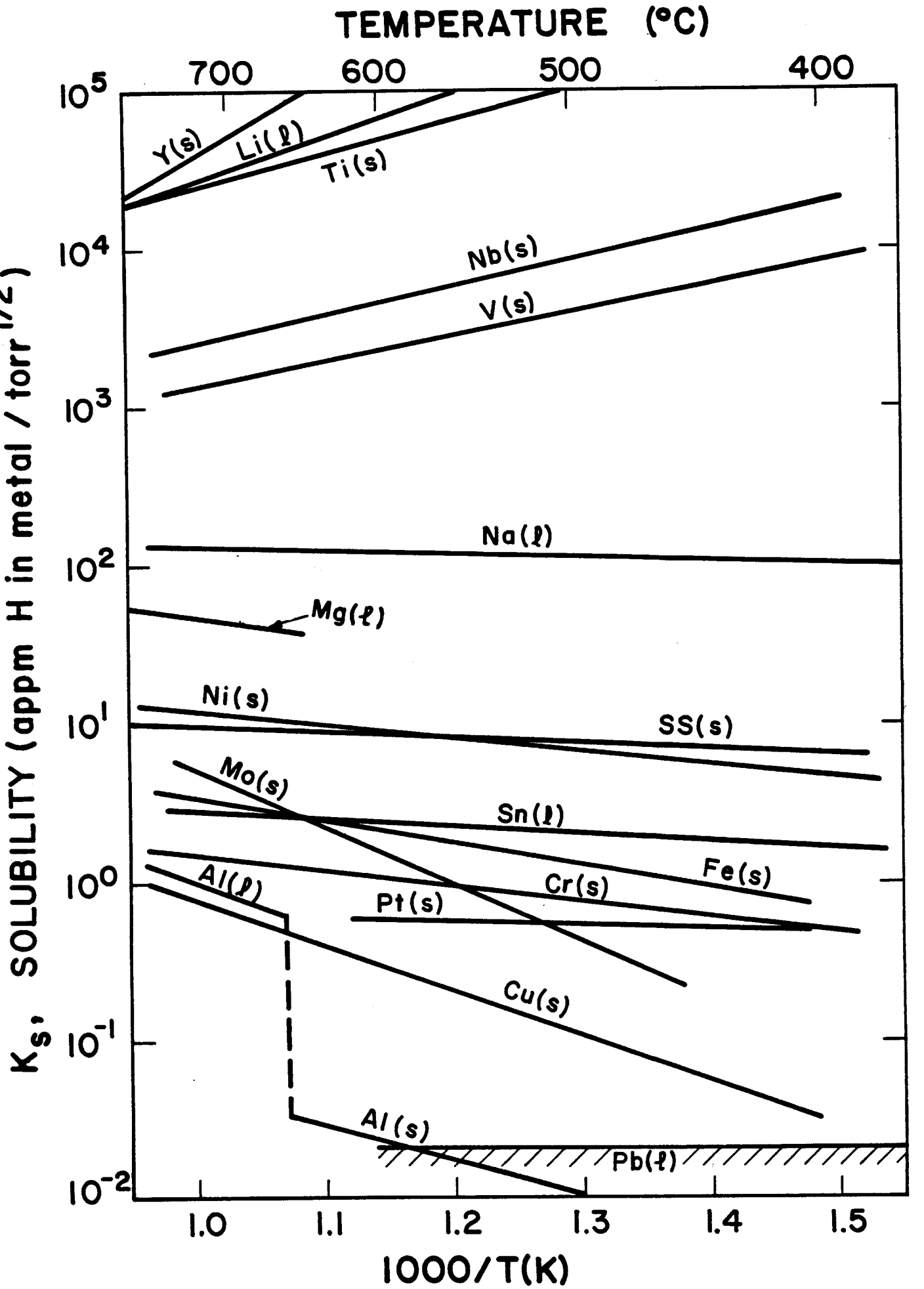

Fig. VII.3-3 Comparison of solubilities of various metals.

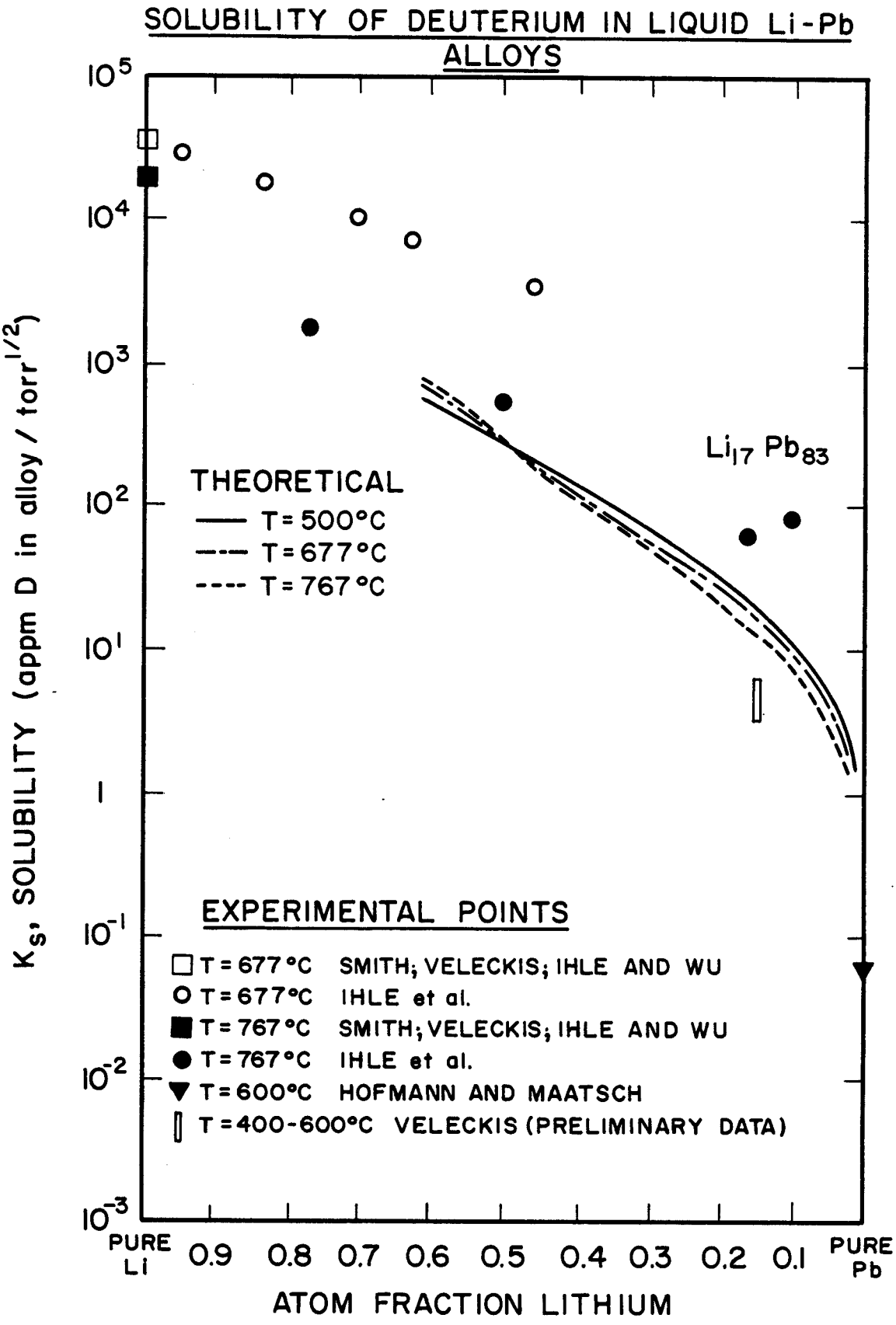
SOLUBILITY OF DEUTERIUM IN LIQUID Li-Pb ALLOYS
K_s, SOLUBILITY (appm D in alloy / torr$^{1/2}$)
10^5
10^4
10^3
10^2
10^1
1
10^{-1}
10^{-2}
10^{-3}
THEORETICAL
T = 500°C
T = 677°C
T = 767°C
$Li_{17}Pb_{83}$
EXPERIMENTAL POINTS
T = 677°C SMITH; VELECKIS; IHLE AND WU
T = 677°C IHLE et al.
T = 767°C SMITH; VELECKIS; IHLE AND WU
T = 767°C IHLE et al.
T = 600°C HOFMANN AND MAATSCH
T = 400-600°C VELECKIS (PRELIMINARY DATA)
PURE Li
0.9
0.8
0.7
0.6
0.5
0.4
0.3
0.2
0.1
PURE Pb
ATOM FRACTION LITHIUM

Fig. VII.3-4

(1) The theoretical model predicts only a slight temperature dependence. This behavior is expected from examination of Fig. VII.3-3 which shows that lithium dissolves hydrogen exothermically while metals with low hydrogen solubilities (such as lead) generally dissolve hydrogen endothermically. This probably leaves Li-Pb alloys in an intermediate category showing little temperature dependence. The temperature dependence observed in the work by Ihle et al. is greater than has been observed for any other metal or alloy system and does not agree with the model predictions.

(2) The theoretical model predicts lower solubilities than those determined by Ihle et al.

Preliminary experiments conducted by E. Veleckis[18] at Argonne National Laboratory indicate deuterium solubilities that are fairly temperature independent and lower than both the data found by Ihle et al. and the model predictions. The Sievert's constant used in this design for tritium solubility in $Li_{17}Pb_{83}$ at 500°C (based on preliminary Argonne results) is 4 appm $H/torr^{1/2}$ or 7×10^{-2} wppm $T/torr^{1/2}$ which at 10^{-4} torr gives a tritium concentration of 7×10^{-4} wppm in $Li_{17}Pb_{83}$. The mass of $Li_{17}Pb_{83}$ in the four chambers and the reflectors is 1.91×10^{7} kg, resulting in a low tritium inventory of 0.013 kg.

VII.3.2 Tritium Breeding and Recovery

The breeding ratio of $Li_{17}Pb_{83}$ is 1.25 resulting in a breeding rate of 4.4×10^{-6} kg T/sec in each chamber. The $Li_{17}Pb_{83}$ alloy (4.8×10^{6} kg/chamber) serves both as breeder and coolant and is circulated through the power cycle at a rate of 3.38×10^{8} kg/hr. Assuming the tritium solubility is 7×10^{-4} wppm, the flow rate of tritium in one reactor chamber is 6.6×10^{-5} kg T/sec.

In order to recover tritium at the breeding rate, 6.7% of the tritium must be extracted during each pass of $Li_{17}Pb_{83}$ through a chamber. The pressure of tritium above $Li_{17}Pb_{83}$ is 10^{-4} torr; therefore, the pressure that must be maintained in the reactor to allow the tritium to be released from the liquid metal is less than or equal to 10^{-4} torr.[19] The quantity of tritium that must be extracted is 7.4×10^{-4} mole T_2/sec. This is a volumetric flow rate of 3.7×10^5 ℓ/sec at 700°K and 10^{-4} torr. The high pumping rate necessary to remove the exhaust between shots, ($\sim 4 \times 10^6$ ℓ/sec at 10^{-4} torr and 700°K) is sufficient to remove the tritium at the breeding rate and a separate extraction unit will not be needed. The breeder and coolant characteristics are summarized in Table VII.3-1. Although the diffusion of tritium in $Li_{17}Pb_{83}$ is unknown, the high surface area of the flowing liquid metal in the chamber should allow easy release of tritium from the eutectic into the chamber.

Table VII.3-1 Breeder and Coolant Characteristics

Blanket temperature (°C)	
Inlet	330
Outlet	500
Tritium concentration (wppm)	7×10^{-4}
Inventory (kg)	
Tritium	.013
$Li_{17}Pb_{83}$	1.9×10^7
Tritium Breeding	
Ratio	1.25
Rate (kg/sec)	4.4×10^{-6}
Flow Rate (kg/sec)	
Tritium	6.6×10^{-5}
$Li_{17}Pb_{83}$	9.4×10^4

VII.3.3 Silicon Carbide Interactions with Hydrogen Isotopes

The silicon carbide tubes are surrounded with the alloy containing 7×10^{-4} wppm tritium at 10^{-4} torr and 500°C, resulting in some of the tritium dissolving into the silicon carbide reaching an equilibrium concentration. Experiments on deuterium solubility in SiC at 1000 to 1400°C[21] are shown in Fig. VII.3-5. The solubility is very temperature dependent; decreasing as the temperature increases. This dependence is thought to be due to chemical bond formaton between hydrogen atoms and the lattice atoms. The presence of Si-H and C-H bonds have been observed.[22] The pressure dependence on the solubility was determined to be to the 0.61 power, indicating that the hydrogen dissolves monatomically. It also can be observed that the temperature dependence differs substantially for vapor deposited β-SiC and powdered α-SiC.

Due to the large exothermicity of the dissolving process, extrapolations to lower temperatures result in large tritium inventories. At 500°C and 10^{-4} torr, the data for β-SiC extrapolates to 0.017 atoms D/atom Si or ~ 800 wppm. This seems quite unlikely. The last data point measured for β-SiC was at 1000°C, resulting in 0.05 wppm for 10^{-4} torr. It is impossible to predict where the solubility curve will begin to level off. It is also impossible to predict if the woven β-SiC will behave similarly to vapor deposited β-SiC. If it is assumed that the data can only be extrapolated for a few hundred degrees (to 800°C) before leveling off, for β-SiC a solubility of 0.76 wppm at 10^{-4} torr is obtained. This results in an inventory of 0.012 kg T in 1.6×10^4 kg SiC.

Silicon carbide can react with hydrogen to produce hydrocarbons and silanes. The thermodynamics[20] for the interactions of hydrogen atoms and hydrogen molecules with SiC are given in Table VII.3-2. Hydrogen molecule reactions are unfavorable, while hydrogen atom reactions have negative free

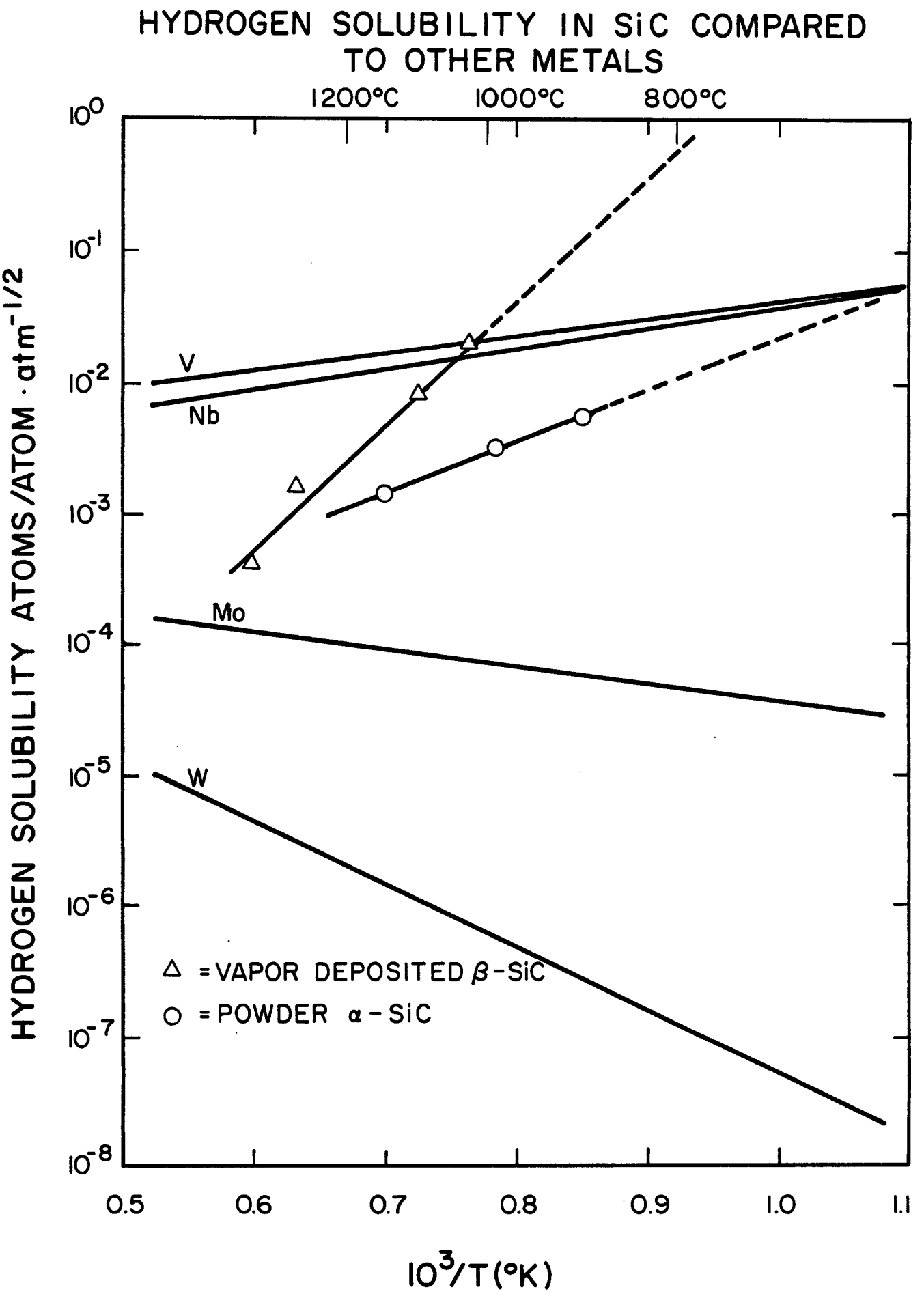
HYDROGEN SOLUBILITY IN SiC COMPARED TO OTHER METALS
1200°C
1000°C
800°C
HYDROGEN SOLUBILITY ATOMS/ATOM · atm^-1/2
10^0
10^-1
10^-2
10^-3
10^-4
10^-5
10^-6
10^-7
10^-8
V
Nb
Mo
W
△ = VAPOR DEPOSITED β-SiC
○ = POWDER α-SiC
0.5
0.6
0.7
0.8
0.9
1.0
1.1
10^3/T(°K)

Fig. VII.3-5

energies. The SiC tubes are coated with a protecting layer of liquid metal which should absorb the hydrogen atom debris. Therefore, production of hydrocarbons and silanes should be minimal.

Table VII.3-2 Thermodynamics for Hydrogen-Silicon Carbide Interactions

Free Energy (kcal/mole)

H_2 Interactions	600°K	700°K	800°K
α-SiC(s) + 2 H_2(g) → Si(s) + CH_4(g)	10.45	12.70	15.03
α-SiC(s) + 1/2 H_2(g) → Si(s) + 1/2 C_2H_2(g)	38.85	37.98	37.13
α-SiC(s) + 2 H_2(g) → SiH_4(g) + C(s)	35.41	37.51	39.65
H Interactions			
α-SiC(s) + 4H(g) → Si(s) + CH_4(g)	-168.9	-161.5	-153.9
α-SiC(s) + 1 H(g) → Si(s) + 1/2 C_2H_2(g)	- 6.00	- 5.58	- 5.11
α-SiC(s) + 4 H(g) → SiH_4(g) + C(s)	-144.0	-136.7	-129.3

References for Section VII.3

1. H.R. Ihle, A. Neubert and C.H. Wu, "The Activity of Lithium, and the Solubility of Deuterium, in Lithium-Lead Alloys," Proc. Tenth Symp. Fusion, Padova, Italy, September 4-9, 1978, Pergamon Press, New York, 639-644 (1979).

2. B. Badger et al., "NUWMAK - A Tokamak Reactor Design Study," University of Wisconsin Fusion Design Memo UWFDM-330, March 1979.

3. E.M. Larsen, M.S. Ortman, K.E. Plute, "Comments on the Hydrogen Solubility Data for Liquid Lead, Lithium and Lithium-Lead Alloys and Review of a Tritium Solubility Model for Lithium-Lead Alloys," University of Wisconsin Fusion Design Memo UWFDM-415, to be published.

4. F.J. Smith, A.M. Batistoni, G.M. Begun, J.F. Land, "Solubility of Hydrogen Isotopes in Lithium," Report 1976, Conf. 760631-1.

5. E. Veleckis, E.H. Van Deventer and M. Blander, "The Lithium-Lithium Hydride System" J. Phys. Chem. 78, 1933-1940 (1974).

6. H. Katsuta, T. Ishigai and K. Furukawa, "Equilibrium Pressure and Solubility of Hydrogen in Liquid Lithium," Nucl. Tech. 32, 297-303 (1977).

7. E. Veleckis, "Thermodynamics of the Lithium-Lithium Deuteride System," J. Phys. Chem. 81, 526-531 (1977).

8. H.R. Ihle and C.H. Wu, "The Solubility of Deuterium In and Its Separation From Liquid Lithium by Distillation," Hydrogen in Metals, Vol. 1, Proceedings of the 2nd International Congress, Paris, France, June 6-10, 1977, Pergamon Press, New York (1977).

9. M.L. Saboungi, J. Marr, and M. Blander, "Thermodynamic Properties of a Quasi-Ionic Alloy from Electromotive Force Measurements - The Li-Pb System," J. Chem. Phys. 68, 1375-1384 (1978).

10. A.I. Demidov, A.G. Morachevskii, and L.N. Gerasimenko, "Thermodynamic Properties of Liquid Lithium-Lead Alloys," Sov. Electrochem. 9, 813-814 (1973).

11. S.P. Yatsenko and E.A. Saltykova, "Thermodynamic Properties of Liquid Lithium-Lead Alloys," Russ. J. Phys. Chem. 50, 1278 (1976).

12. F.G.A. Stone, "Hydrogen Compounds of the Group IV Elements," Prentice Hall Inc., New Jersey, 1962.

13. (a) H. Cerjak and F. Erdmann-Jesnitzer, "Increasing the Creep Strength Through Reaction Products Formed in the Melt. I. Lead-Lithium-Hydrogen Alloys," Metall. 22, 113-123 (1968), as sited by Ref. 5b.
(b) F. Erdmann-Jesnitzer, A.P. Van Peteghem and R. De Wilde, "Untersuchungen zur Verbesserung des Kriechverhaltens von Blei-Lithium-Legierungen durch Wasserstoff," Metall. 28, 449-455 (1974).

14. M. Hansen, Constitution of Binary Alloys, Second Edition, McGraw-Hill Book Co., Inc., New York, 789-790 (1958).

15. V.A. Maroni and E.H. Van Deventer, "Materials Considerations in Tritium Handling Systems," J. Nucl. Mater. 85 & 86, 257-269 (1979).

16. S.D. Clinton and J.S. Watson, "The Solubility of Tritium in Yttrium at Temperatures from 250 to 400°C," J. Less-Common Met. 66, 51-57 (1979).

17. W. Hofmann and J. Maatsch, "Loslichkeit von Wasserstoff in Aluminum, Blei-und Zinkschmelzen," Z. Metallkunde 47, 89-95 (1956).

18. E. Velekis, Argonne, Private Communication.

19. K. Ruttiger, "Vacuum Degassing in the Liquid State," Vacuum Metallurgy, O. Winkler and R. Bakish (eds.), Elsevier Publishing Company, New York (1971), 337-463.

20. JANAF Thermochemical Tables, D.R. Sull et al., The DOW Chemical Company, Midland, Michigan.

21. R.A. Causey, J.D. Fowler, C. Ravanbakht, T.S. Elleman and K. Eghese, "Hydrogen Diffusion and Solubility in Silicon Carbide," J. Amer. Cer. Soc. 61, No. 5-6, 221-225 (1975).

22. R.B. Wright, R. Varma, D.M. Gruen, "Raman Scattering and SEM Studies of Graphite and Silicon Carbide Surfaces Bombarded with Energetic Protons, Deuterons and Helium Ions," J. Nucl. Mater. 63, 415-421 (1976).

VII.4 Tritium Containment Systems

The active tritium inventory in the HIBALL reactor is 0.52 kg or 5.0×10^6 Ci, with an additional inventory of 12.3 kg or 1.2×10^8 Ci in storage and target manufacture. Tritium is being processed at a rate of 4.4×10^7 Ci/day (2.9×10^7 Ci from the exhaust and 1.5×10^7 Ci from the breeder). The losses of tritium to the environment must be limited to ~ 10 Ci/day. Using containment schemes similar to those found in the TSTA[1] design and in a previous reactor design,[2] losses are expected to be less than 10 Ci/day.

VII.4.1 Permeability of Tritium into Steam Cycle*

The primary containment problem which is the most difficult to control is the permeation of tritium from the $Li_{17}Pb_{83}$ breeder/coolant through the walls of the steam generator. Once in the steam cycle the tritium is generally considered lost to the environment because the tritium exchanges with protium forming HTO. Separation of HTO from the bulk of the steam is technically difficult and expensive.[3]

The steam generator composition is HT-9. Permeation data for HT-9 and chromium ferritic steels has been reviewed in WITAMIR.[2] By assuming that, Permeability = Solubility x Diffusivity, and comparing the available data, the "best fit" line in the WITAMIR study resulted in a tritium permeation through clean HT-9 of:

$$P = \frac{1.8 \times 10^3}{\sqrt{3}} \exp\left(\frac{-11100}{RT}\right) \frac{\text{mole } T_2 \cdot \text{mm}}{\text{d} \cdot \text{m}^2 \cdot \text{atm}^{1/2}} \cdot$$

For HIBALL:

Tube thickness = 1 mm

Pressure above coolant = 10^{-4} torr

*Based on WITAMIR[2] steam cycle. The steam generator system has not been designed in HIBALL-I.

Area = 5.2×10^4 m^2 Temperature range = 315-490°C

In order to calculate the total loss to the steam cycle, the area of the tubing is assumed to have a linear relationship with temperature, and the permeation, in units of g $T_2 \cdot d^{-1} \cdot m^{-2}$, is plotted against area (m^2) as seen in Fig. VII.4-1. The area under the curve represents the total loss of tritium through clean HT-9; this is a permeation rate of 33 g T_2/day. Losses of this magnitude are unacceptable and must be minimized.

One factor that will reduce the permeability is the fact that the liquid metal side of the steam tubing will have clean surfaces, while the steam side will form an oxide layer. In situ formed oxide coatings are effective in reducing tritium permeability[4] as shown in Table VII.4-1. For ferritic steels at 660°C, permeabilities are reduced by factors of 100 or more due to the oxide coating. At lower temepratures (315-490°C) the ability to maintain an effective oxide coating decreases.[6] For HIBALL the permeability through HT-9 is assumed to be decreased by about a factor of 10 due to the oxide layer on the steam generator side of the tubing.

Another method of achieving lower losses of tritium to the steam cycle include formation of a permeation resistant nickel-alumide layer[6] on the liquid metal side of the tubing. This is accomplished by addition of aluminum to the liquid-metal coolant, which forms an aluminum layer on nickel alloy surfaces, reducing the permeation by a factor greater than 100 for 304 SS at 550°C. The HT-9 alloy, however, is low in nickel and thus would not be adaptable to this scheme. Using a different material in the steam cycle from the reactor material may cause enhanced corrosion through mass transfer mechanisms.

Work has been done on the development of multilayered metal composites and impurity coated refractory metals as tritium barriers.[7] Reductions of a

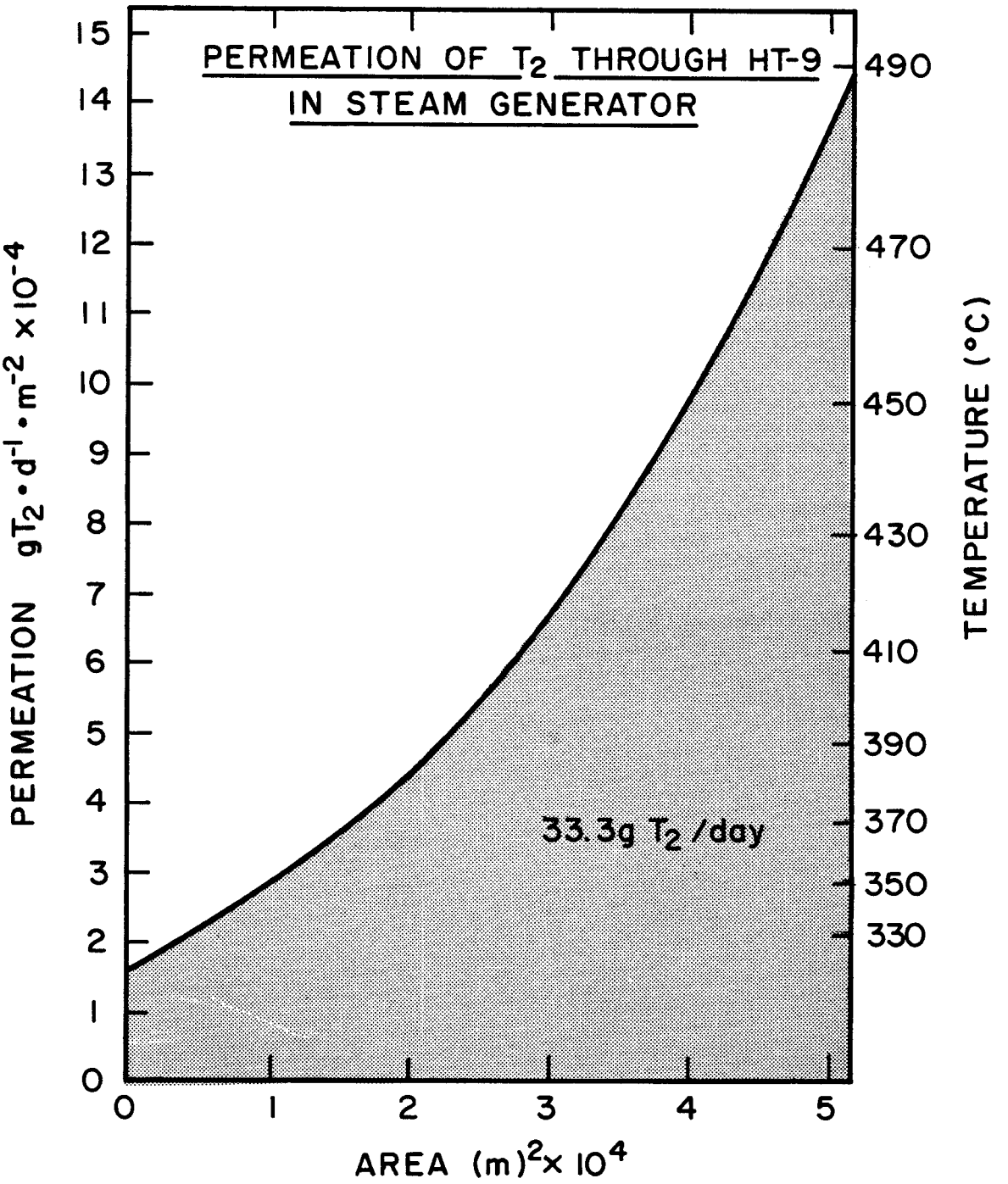
PERMEATION OF T_2 THROUGH HT-9
IN STEAM GENERATOR
PERMEATION $gT_2 \cdot d^{-1} \cdot m^{-2} \times 10^{-4}$
TEMPERATURE (°C)
AREA $(m)^2 \times 10^4$
33.3g T_2/day
0
1
2
3
4
5
6
7
8
9
10
11
12
13
14
15
330
350
370
390
410
430
450
470
490

Fig. VII.4-1

factor of 50 have been demonstrated for stainless steel structures containing an intermediate layer of Cu-Al-Fe alloy at 600°C. Metallic coatings with low hydrgen permeability coefficients would also present a barrier to the tritium. At present, the HIBALL design will utilize an oxide coating barrier, however, future designs will try to employ more effective tritum barriers.

Table VII.4-1 Permeation Barrier Factors of Ferritic and Austenitic Steels Produced by Steam Oxidation of the Downstream Side

	Ferritic	Ferritic	Austenitic
	Fe-2-1/4 Cr-1 Mo	SS 406	SS 316
Reference	5	4	4
Temperature (°C)	472	660	660
Steam Pressure (atm)	2	0.94	0.94
Factors by Which Permeabilities are Reduced			
0.33 d	10	13	---
1 d	25	72	1.6
6 d	100	144	2.8
24 d	170	291	3.8
40 d		434	4.3

VII.4.2 Containment in Steam Cycle

Assuming a factor of 10 reduction in permeation due to the oxide coating results in 3.3 g T_2/day lost to the steam cycle. In order to further reduce this quantity, the tubes in the steam generator will have a double-walled

construction, with a purge gas containing a low partial pressure of O_2 sweeping the tubing gap. Although double-walled tubing is expensive and difficult to produce,[3] this concept provides an effective tritium containment scheme. The oxygen in the purge gas helps to maintain a good oxide layer and it also converts tritium to HTO by combining it with the hydrogen that diffuses through the steamside. This significantly reduces the free tritium partial pressure, and thus reduces the diffusion driving force to the steam side.

If the oxygen partial pressure in the purge gas is assumed to be 1 torr and the maximum HTO pressure allowed in the gap is 0.1 torr, then the volumetric flow rate of the purge gas is 5.3 ℓ/sec. The HT pressure in the gap is about 10^{-16} torr, resulting in $\sim 10^{-2}$ Ci/day loss to the steam generator. The parameters for the steam cycle are given in Table VII.4-2.

The HTO that is formed in the purge flow is condensed and sent to a fuel cleanup unit where tritiated water is electrolyzed and hydrogen isotopes are then sent to the cryogenic distillation system for separation.

Secondary and tertiary containment schemes have not been addressed in detail at this time for HIBALL. However, the designs for containment in the TSTA facility will be tested in the near future, providing essential information to the fusion community on the aspects of tritium handling and containment.

Table VII.4-2 Parameters in Steam System

Tritium diffusion to LiPb side	3.3 g/day
Steam generator surface area	5.2×10^4 m^2
Tritium diffusion rate	1.5×10^{10} atoms T/cm^2 sec
O_2 pressure in purge gas	1 torr
Maximum HTO pressure	0.1 torr
Temperature range	315-490°C
Required purge gas flow rate	5.3 ℓ/sec
HT partial pressure in gap	1×10^{-16} torr
Total tritium loss to water	0.02 Ci/d

References for Section VII.4

1. R.V. Carlson and R.A. Jalbert, "Preliminary Analysis of the Safety and Environmental Impact of the Tritium System Test Assembly," Proceedings Tritium Technology in Fission, Fusion and Isotropic Applications, Dayton, Ohio, April 29 - May 1, 1980, CONF-800427, American Nuclear Society (1980), 347-352.

2. B. Badger et al., "WITAMIR-I - A Tandem Mirror Reactor Study," University of Wisconsin Fusion Design Memo UWFDM-400, Chapter XI, (Dec. 1979).

3. A.B. Johnson, Jr. and T.J. Kabele, "Tritium Containment in Fusion Reactors," Topical Meeting on Technology of Controoled Nuclear Fusion, Richland, Washington, Sept. 21, 1976, 1319-1328, CONF-760935.

4. J.T. Bell, J.D. Redman and H.F. Bittner, "Tritium Permeability of Structural Materials and Surface Effects on Permeation Rates," Proceedings Tritium Technology in Fission, Fusion and Isotropic Applications, Dayton, Ohio, April 29 - May 1, 1980, CONF-800427, American Nuclear Society (1980), 48-53.

5. T.A. Renner and D.J. Rave, "Tritium Permeation Through Fe-2-1/4 Cr-1 Mo Steam Generator Material," Nucl. Technol. 47, 312-319 (1979).

6. J.C. McGuire, "Hydrogen Permeation Resistant Layers for Liquid Metal Reactors," Proceedings Tritium Technology in Fission, Fusion and Isotropic Applications, Dayton, Ohio, April 29 - May 1, 1980, CONF-800427, American Nuclear Society (1980), 64-68.

7. V.A. Maroni, E.H. Van Deventer, T.A. Renner, R.H. Pelto, and C.J. Wierdak, "Experimental Studies of Tritium Barrier Concepts for Fusion Reactors," Proceedings Radiation Effects and Tritium Technology for Fusion Reactors, Gatlinburg, Tennessee, October 1-3, 1975, CONF-750989 Vol. IV, 329-361.

VIII Materials

VIII.1 Introduction

The materials problems in HIBALL can be categorized according to placement in the reactor and material type as shown in outline form.

1. Inside Reactor Cavity
   a. SiC
   b. HT-9 Structure
2. Reflector Region
   a. HT-9 Structure
3. Reactor Vessel Shield
   a. HT-9 Structure
   b. Pb
   c. Boron Carbide
4. Final Focussing Magnets
   a. NbTi Superconductor
   b. Cu Stabilizer
   c. Electrical Insulation

By far the most severe problems occur in the SiC INPORT units and the HT-9 structure of the reflector region and we will concentrate on these areas here. The analysis of each of these materials will be made in the following sequence:

1. Environment
   a. Thermal, Chemical, Stress
   b. Radiation
2. Comparison With Existing Data and Prediction of Expected Life in HIBALL

Obviously, a great deal of extrapolation will be necessary to arrive at meaningful lifetime predictions. The readers should recognize that we are breaking new ground in this area and the results should be viewed accordingly.

VIII.2 Materials Problems Inside Reactor Cavity

VIII.2.1 Silicon Carbide INPORT Units

VIII.2.1.1 Environment

VIII.2.1.1.1 General

The SiC woven structures are expected to operate in intimate contact with the $Pb_{83}Li_{17}$ coolant over a temperature range of 300-500°C. There is a possibility of some erosion due to the high (5 m/s) velocity of the coolant in the inner tubes. However, due to a relatively short lifetime (to be demonstrated later) of 1 to 2 years, and a capacity factor of ~ 70%, the total exposure time at temperature will be 6000 to 12,000 hours.

The stresses in the SiC tubes come from drag exerted by the flowing PbLi and amount to maximum static stresses of 130 MPa in the inner (smaller) tubes and 97 MPa in the outer (larger) tubes. The pulsed loads due to neutron heating amount to less than 1 MPa. Finally, the maximum pulsed stresses due to ablation of the front surface amount to 60 MPa-seconds at a 5 Hz rate.

VIII.2.1.1.2 Radiation Environment

It is assumed that all surfaces on the INPORT units facing the plasma are entirely covered by a liquid $Pb_{83}Li_{17}$ film which is at least 1 mm thick. The consequences of "dry" spots will be examined later. The SiC is mainly subjected to neutron damage because the target debris and most of the X-rays will be absorbed in the liquid film.

The neutron spectrum at the inner ring of tubes is shown in Fig. VIII.2-1 and the variation in displacement damage rate in the SiC is given in Fig. VIII.2-2. Figure VIII.2-3 gives the transmutation rate into gaseous elements throughout the $Pb_{83}Li_{17}$-SiC zone. The peak dpa rate in the SiC tubes is 118 per FPY and it drops to 10 dpa per FPY in the back (17th) row of INPORT units. Similarly, the peak helium and hydrogen production rate is 3705 and 1408 appm

Fig. VIII.2-1

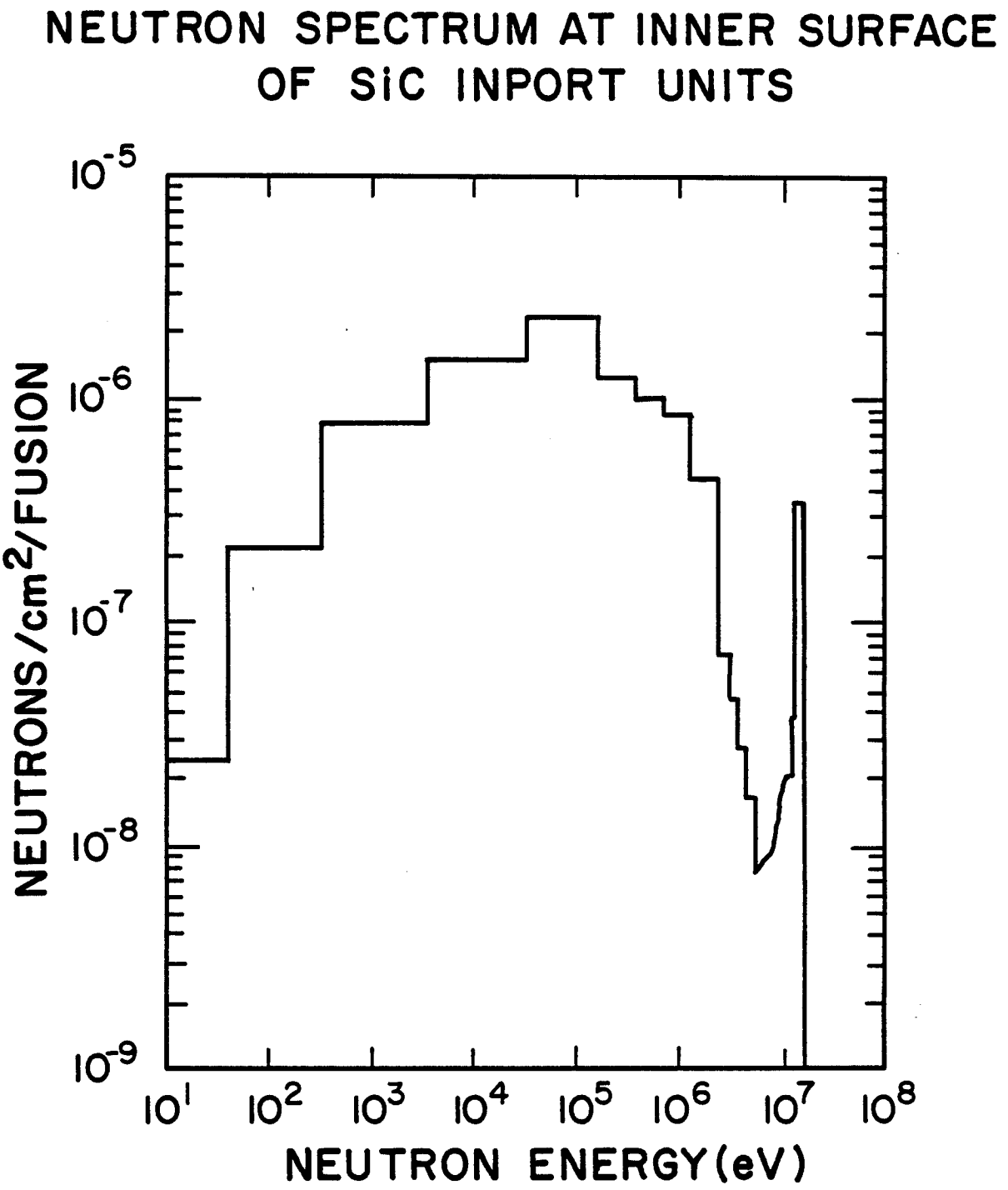
NEUTRON SPECTRUM AT INNER SURFACE OF SiC INPORT UNITS
NEUTRONS/cm2/FUSION
10-5
10-6
10-7
10-8
10-9
10¹
10²
10³
10⁴
10⁵
10⁶
10⁷
10⁸
NEUTRON ENERGY(eV)

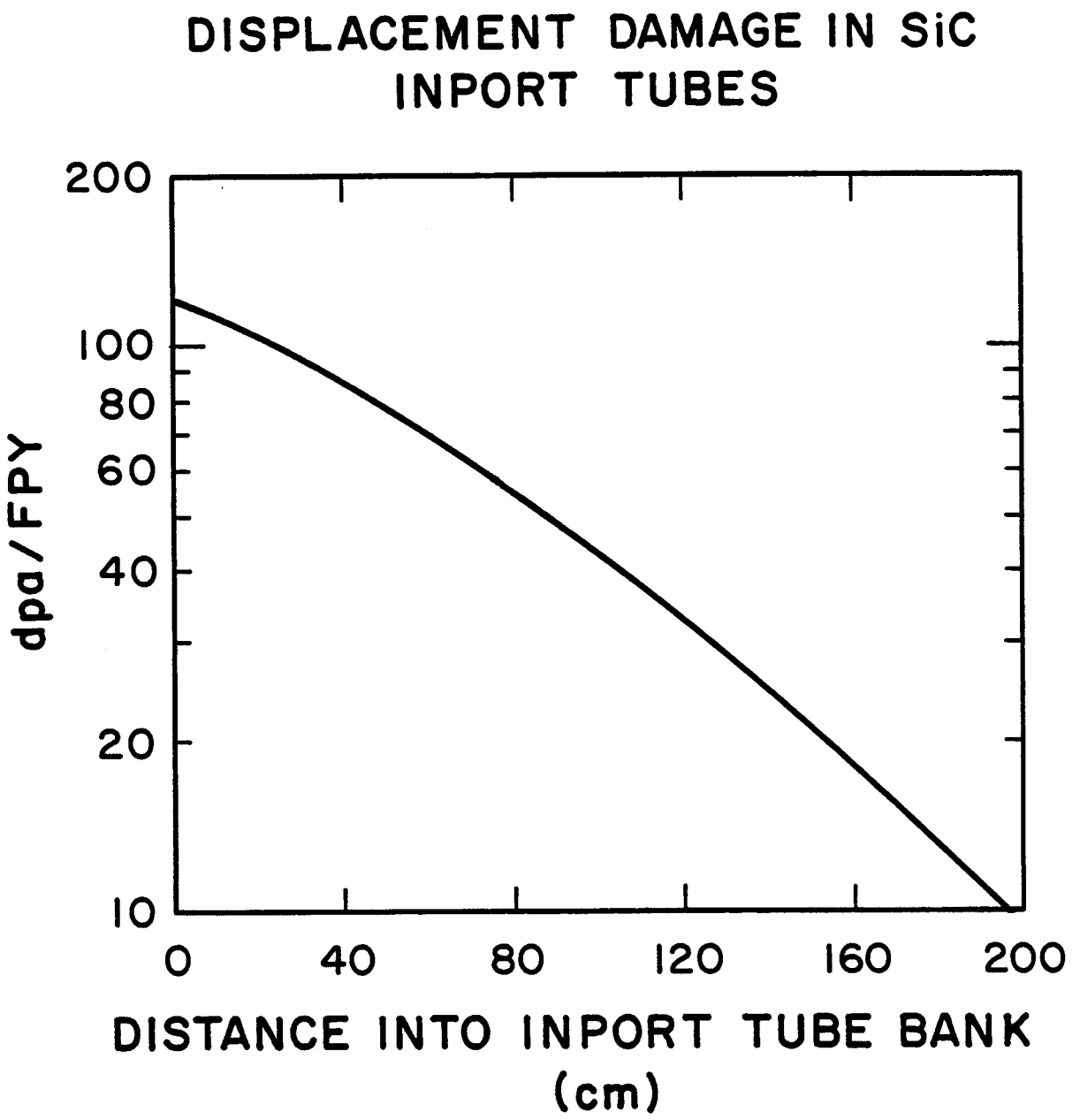
DISPLACEMENT DAMAGE IN SiC
INPORT TUBES
200
100
80
60
40
20
10
dpa/FPY
0
40
80
120
160
200
DISTANCE INTO INPORT TUBE BANK
(cm)

Fig. VIII.2-2

Figure VIII.2-3

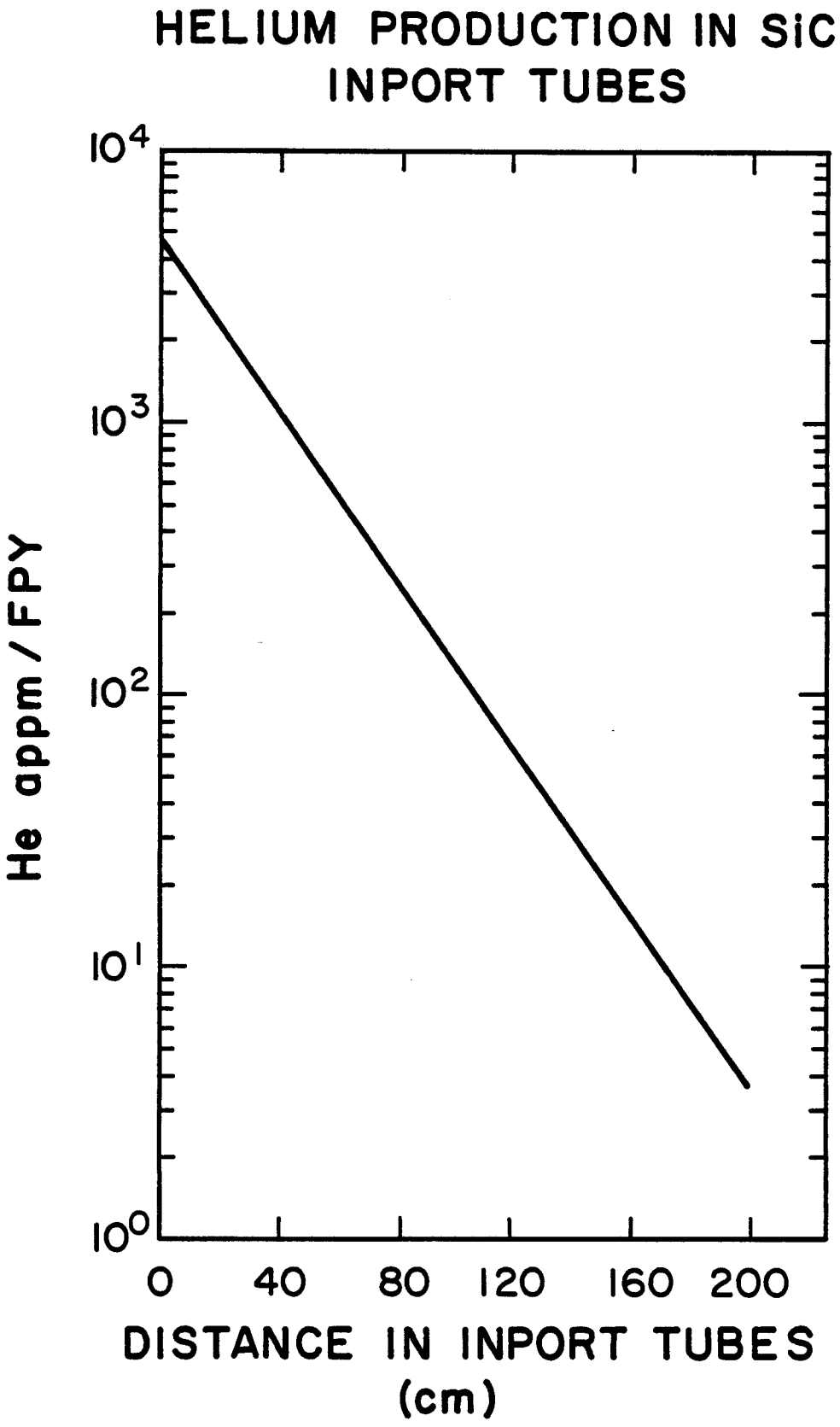

per FPY respectively and this drops to 4 appm and 1.7 appm per FPY respectively in the back row of tubes.

If the tubes become uncovered, for any reason, the SiC would be exposed to high intensity X-ray and particle debris fluxes. The X-ray flux (see Chapter III) results in a 27.9 J/cm^2 exposure to the SiC spread over 10 ns. The target debris (see Chapter III) will impact on the unexposed surface with an additional 6.6 J/cm^2 flux spread over 10 microseconds.

VIII.2.1.2 Previous Experience with SiC in Environment Typical of HIBALL

VIII.2.1.2.1 Mechanical Properties

As shown in section VI.2, the strength of SiC is entirely adequate in the 300-500°C range. However, essentially nothing is known about the effect of long term exposure to Pb or Li with respect to the tensile properties.

VIII.2.1.2.2 Chemical Compatibility of SiC with $Pb_{83}Li_{17}$

An extensive literature search revealed only one experimental reference to the compatibility of SiC with Li. W.H. Cook[1] determined that after 100 hours at 816°C, the corrosion resistance of SiC to Li was "bad". This particular rating was given to a material which suffered any one of the following physical changes:

1) a depth of attack of more than 0.076 mm,
2) more than a 6% weight change, or
3) more than a 3% dimensional change.

Obviously the testing conditions are far more severe than HIBALL conditions, but there is no reasonable way to extrapolate this experimental point to the 300-500°C operating regime at this time; therefore, continued experimental research into this topic is strongly recommended for the HIBALL conditions.

In view of the lack of pertinent experimental data, we chose to investigate the thermodynamics of Li interaction with SiC. Thermodynamic data[2] on

the formation of $Li_2C_2(s)$ as a corrosion product is given in Table VIII.2-1. Formation of lithium carbide from lithium interactions with silicon carbide is not favorable, however, there is no thermodynamic data on formation of known or other silicides or higher carbides which may be responsible for the incompatibility at higher (~ 1100°K) temperatures. Extrapolating the information for pure lithium and lead to the alloy system is difficult and more experimental work must be done. If it is assumed that the corrosive action occurs only from lithium, then because of the low percentage of lithium in the alloy (0.68 wt%) and the low activity of lithium in $Li_{17}Pb_{83}$ (~ 10^{-4} at 500°C) the compatibility should fall in the fair to good range.

Table VIII.2-1 Thermodynamic Formation of Lithium Carbide from Lithium and Various Ceramic Materials

Reaction	Free Energy (kcal/mole) 600°K	700°K	800°K
$Li(l) + C(s) \rightarrow 1/2\ Li_2C_2(s)$	-6.18	-5.96	-5.75
$Li(l) + \alpha\text{-}SiC(s) \rightarrow 1/2\ Li_2C_2(s) + Si(s)$	9.76	9.79	9.81
$Li(l) + \beta\text{-}SiC(s) \rightarrow 1/2\ Li_2C_2(s) - Si(s)$	10.13	10.18	10.21
$Li(l) + B_4C(s) \rightarrow 1/2\ Li_2C_2(s) + 4\ B(s)$	2.85	3.04	3.19
$Li(l) + TiC(s) \rightarrow 1/2\ Li_2C_2(s) + Ti(s)$	36.13	36.11	36.07
$Li(l) + ZrC(s) \rightarrow 1/2\ Li_2C_2(s) + Zr(s)$	39.31	39.33	39.35

VIII.2.1.2.3 Radiation Effects on SiC

The amount of fission neutron irradiation data on SiC is very limited[3-6] and, of course, there is no information on 14 MeV neutron effects at the present time. What data is available is entirely from solid SiC samples and there is no information on woven structures. However, there is some data on woven grahite fibers[7] which indicates successful operation up to ~ 10 dpa at ~ 500°C.

Traditional lifetime analyses for fusion reactor first walls cannot be used for the woven SiC INPORT units. Dimensional changes (due to voids, linear growth, etc.) can be easily accommodated, crack propagation has little meaning in a structure made up of thousands of individual strands, and thermal stress has little significance when the fibers are only microns in diameter. Ductility changes will be important and could give some indication of when the tubes (at least in the front rows) might begin to break apart under the periodic motion associated with the target debris. However, no meaningful measurements of the ductility of irradiated fibers has been conducted as of now. Ductility is notoriously sensitive to small amounts of He in metals, but helium effects in ceramics like C or SiC are far less documented. In fact, at high enough temperatures, helium is known to migrate out of carbon.[8]

What then, is a reasonable set of criteria by which to judge the lifetime of the SiC INPORT units? Because of the sparcity of data we will examine the following information

	HIBALL Limit
Linear Expansion	< 10%
Fracture Strength	> 180 MPa
Burnup of SiC	< 1%

VIII.2.1.2.3.1 Linear Length Changes in Irradiated SiC

Early work by Price[3] revealed that the linear expansion of SiC saturated at relatively low levels of irradiation (less than 3 x 10^{20} n/cm^2 which is ~ 0.3 dpa). Price found that this saturation level of expansion was inversely proportional to temperature as indicated in Fig. VIII.2-4. Such information would suggest that saturation levels of ~ 0.5% might be reasonable.

Later work by Sheldon[4] to 5 x 10^{22} n/cm^2 (~ 50 dpa) at 550°C also confirmed the saturation effect and projected that "acceptable" linear expansion could be tolerated up to 100 dpa (~ 10^{23} n/cm^2).

Even more recent work by Corelli et al.[5], Fig. VIII.2-5, showed that at $\lesssim$ 200°C, the swelling saturated at roughly 3 to 4% by 10^{22} n/cm^2 (~ 10 dpa). This corresponds to a linear expansion of ~ 1%, very close to the data of Price (Fig. VIII.2-4).

In summary, it appears that linear expansions of 0.5 to 1% might be observed after ~ 1 month of operation in HIBALL. After that time, we might expect very little additional expansion and therefore irradiation induced growth would not appear to be a life limiting feature.

This conclusion is supported by studies at BNWL where graphite clothes were irradiated to 4, 7, and 10 dpa at 470°C.[7] The dimensional changes ranged from +33% to -27%, far in excess of those observed in SiC. Despite these large dimensional changes, the two-dimensional cloth remained essentially unchanged. Such results give us more confidence in the ability of the SiC cloth structure to withstand neutron irradiation.

VIII.2.1.2.3.2 Fracture Strength of Irradiated SiC

There are two studies of significance in this area: one by Mathney et al in 1979[6] and the other by Corelli et al.[5] in 1981. Both studies used a

Figure VIII.2-4

THE NEUTRON-INDUCED EXPANSION OF SILICON CARBIDE [AFTER PRICE]

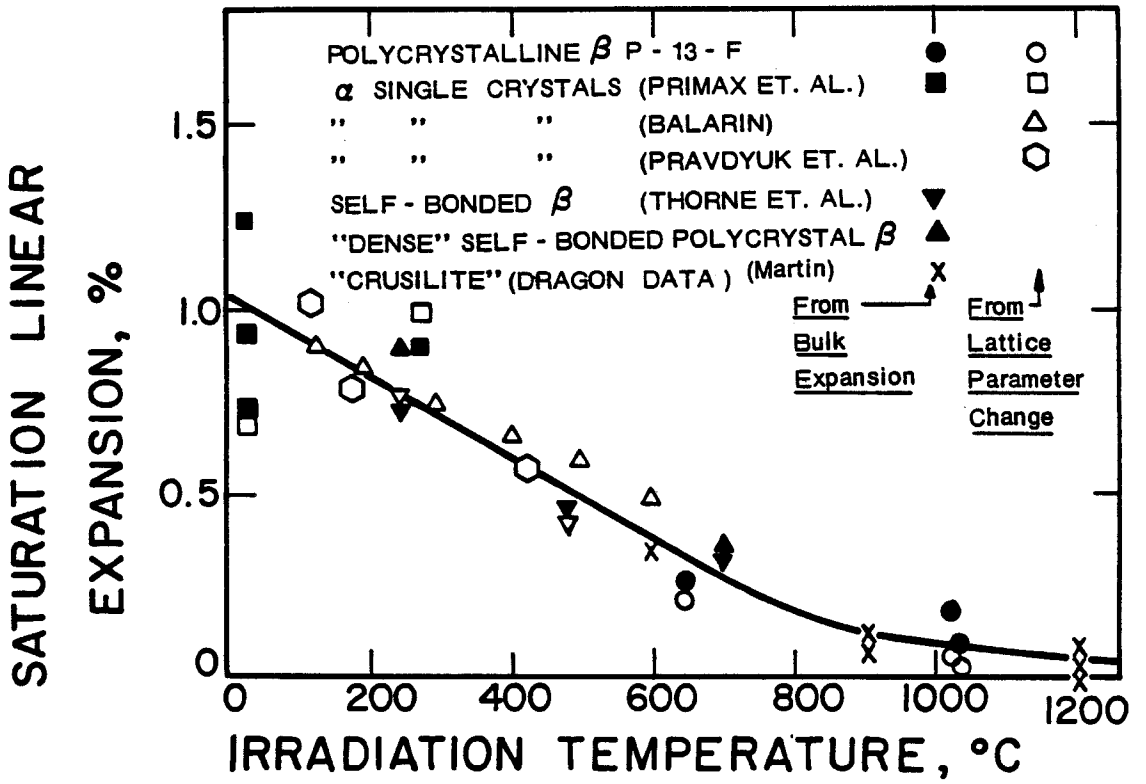

Figure VIII.2-5

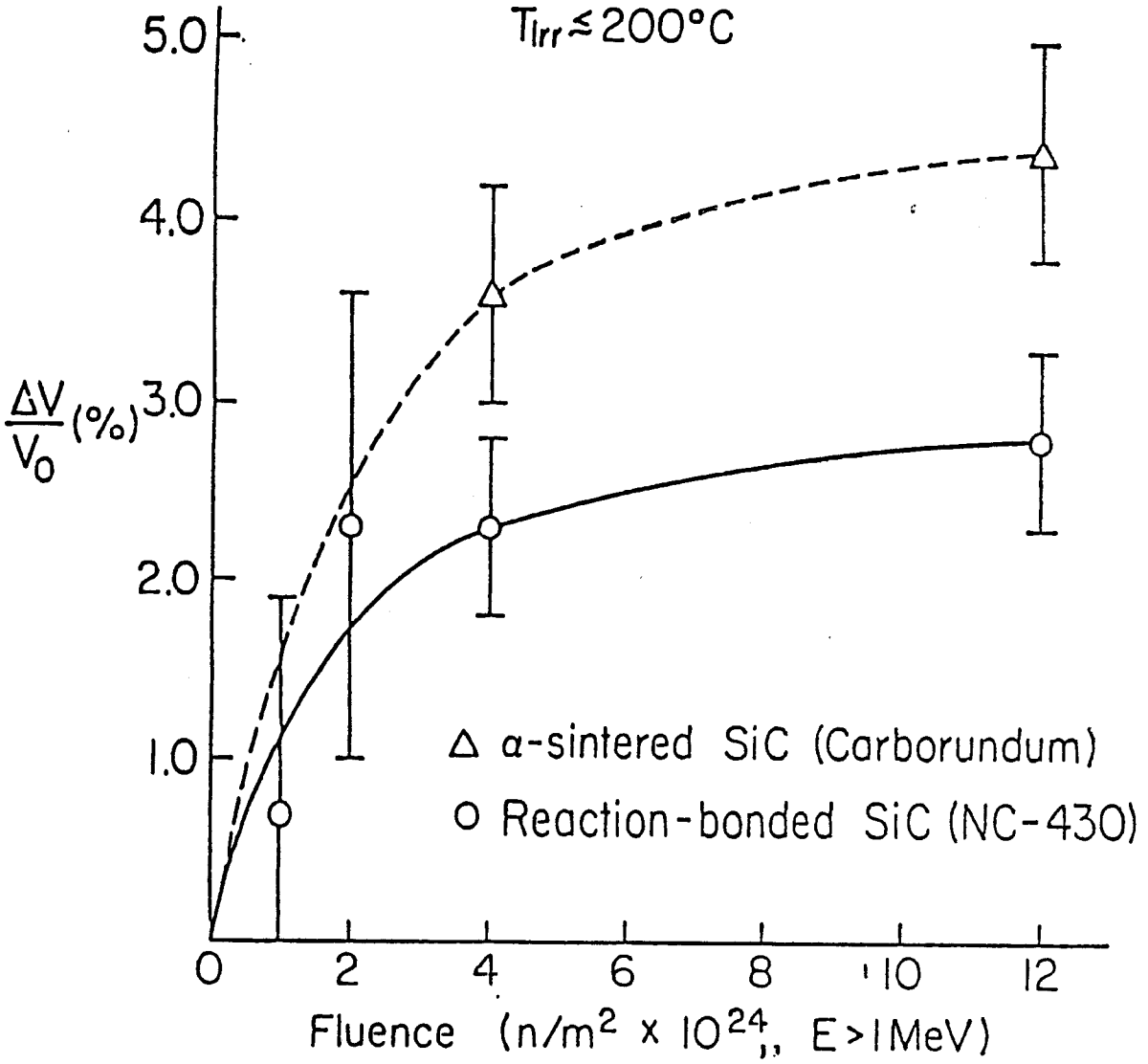

Swelling $\Delta V/V_0$, vs. fluence for NC-430 SiC and sintered α-SiC.

material labelled NC-430 which is 88.5% SiC, silicon metal of 8-10%, and minor impurities such as Fe (0.4%), Al (0.1%), and Boron (0.005%). The initial fracture strength was 230 to 270 MPa. After irradiation up to ~ 1 dpa at $\leq$ 200°C the fracture strength remained unchanged when tested at 1200°C (Fig. VIII.2-6).

Irradiation of sintered α-SiC revealed much more sensitivity to irradiation. The fracture strengths of the α-SiC dropped to ~ 120 MPa at 1200°C after ~ 1 dpa damage at 200°C (Fig. VIII.2-7).

In summary, low fluence (~ 1 dpa) irradiation at < 200°C seems to have little effect on the fracture strength of NC-430 but it can reduce the fracture strength of α-SiC by a factor of 3. There is no higher fluence data on which to extrapolate to the 100 dpa level at this time.

VIII.2.1.2.3.3 Effect on Thermal Conductivity

It is well known that neutron irradiation will reduce the thermal conductivity of carbon and SiC. Recent work by Corelli et al.[5] shows that the thermal conductivity is reduced by a factor of 3 in the first dpa of damage and seems to saturate at that level (Fig. VIII.2-8). Since the majority of the heat conduction in the INPORT units is done by the Pb-Li alloy, such a drastic change has little effect on the liquid surface temperature. Therefore, we do not view such a degradation as a serious problem.

VIII.2.1.2.3.4 Burnup of SiC Atoms

The neutron spectral difference between fission and fusion systems is quite dramatic. For example, the damage rate per full power year in HIBALL is 118 dpa/FPY. At a maximum neutron wall loading of ~ 5 MW/m^2 on the tubes this translates into 24 dpa per MW-y/m^2. In a fission reactor the damage rate is ~ 10 dpa per 10^{22} n/cm^2 (E > 0.1 MeV).

Figure VIII.2-6

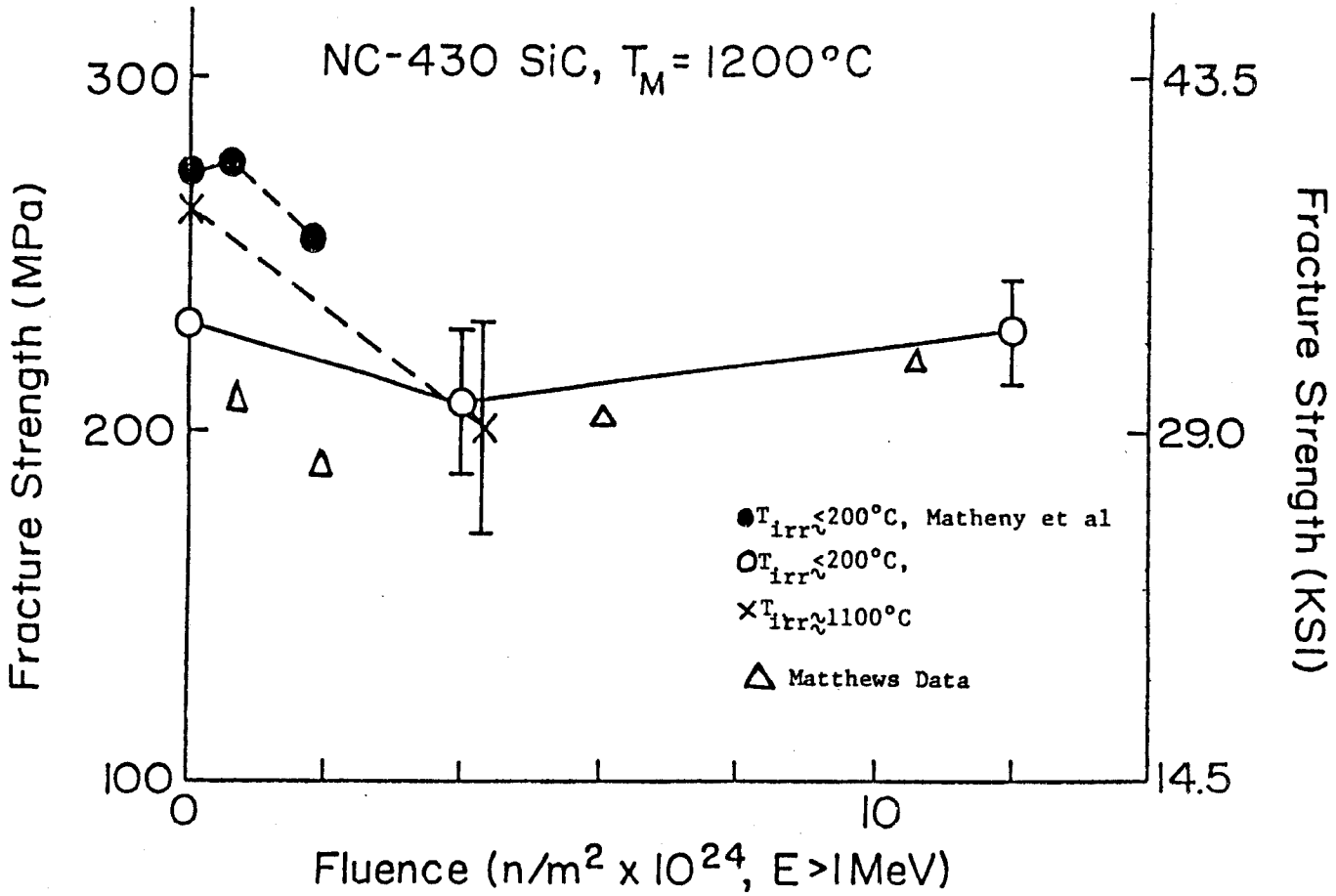

Mean fracture strength vs. fluence of NC-430 SiC at 1200°C.

Figure VIII.2-7

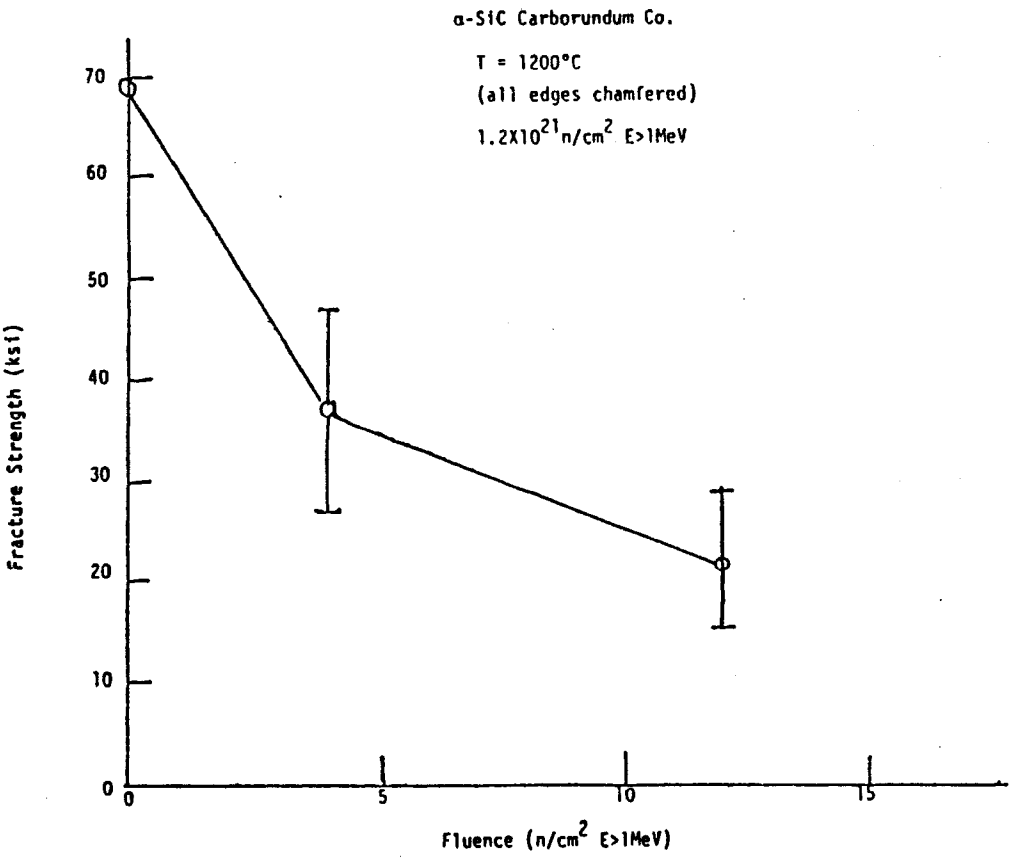

Mean fracture strength vs. fluence of sintered α-SiC at 1200 ^{o}C.

Figure VIII.2-8

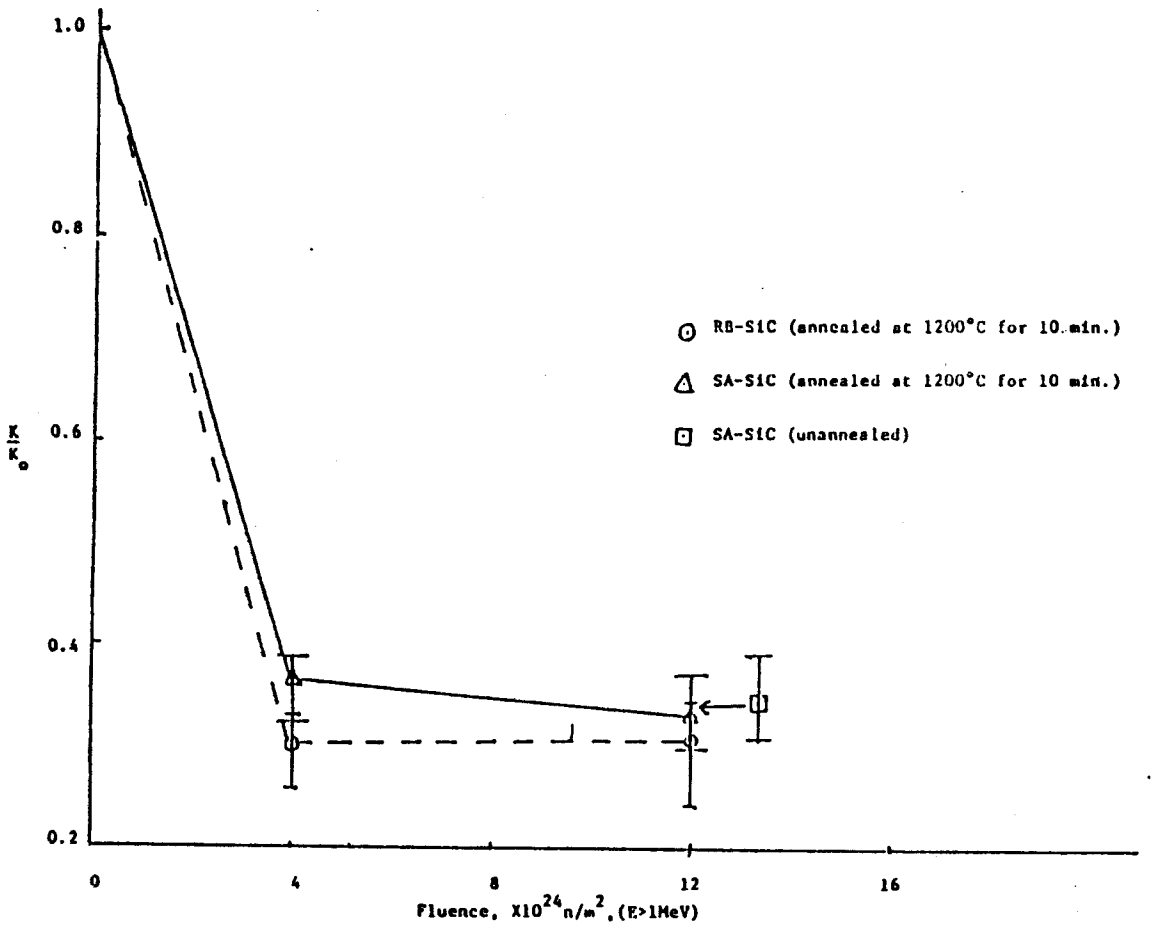

Relative thermal conductivity, K/K_o (measured at $T \approx 23\ ^oC$), vs. fluence for NC-430 SiC and sintered α-SiC.

The production of helium is ~ 740 appm He per MW-y/m^2 in HIBALL but only ~ 14 appm per 10^{22} n/cm^2 in a fission reactor. Similarly the production of hydrogen is ~ 280 appm per MW-y/m^2 in HIBALL but ~ 11 appm per 10^{22} n/cm^2. A comparison of the appropriate values for fission and fusion reactors is given in Table VIII.2-2.

From the information in Table VIII.2-2 we find that roughly 0.5% of the SiC molecules lose one of its atoms per FPY. While there is no firm rule of thumb as to how much burnup can be tolerated, we think the value of 1% is reasonable. On this basis, we would limit the INPORT unit lifetime to 2 FPY in the inner units. The burnup drops off rapidly in the outer tubes such that the limit is not reached for 10 FPY in the 10th row and the last (17th) row of tubes never reaches the 1% limit in 20 FPY's.

Table VIII.2-2 Comparison of Radiation Damage Parameters in SiC

	HIBALL	HFBR[a]
Displacement damage		
dpa per MW-y/m^2	24	---
dpa per 10^{22} n/cm^2 (b)	---	10
dpa/FPY	118	16
Helium production		
appm He per MW-y/m^2	740	---
appm He per 10^{22} n/cm^2 (b)	---	14
appm He/FPY	3705	22
Hydrogen production		
appm H per MW-y/m^2	280	---
appm H per 10^{22} n/cm^2 (b)	---	10
appm H/FPY	1408	16

(a) High flux beam reactor[5].
(b) (E > 0.1 MeV).

References for Section VIII.2

1. W.H. Cook, "Corrosion Resistance of Various Ceramics and Cermets to Liquid Metals," Oak Ridge National Laboratory, June 15, 1960, ORNL-2391.

2. D.R. Sull et al., JANAF Thermochemical Tables, The DOW Chemical Company, Midland, Michigan.

3. R.J. Price, J. Nucl. Mat. 33, 17 (1969).

4. B.E. Sheldon, UKAEA-Harwell, AERE-R8025, August 1975.

5. J.C. Corelli et al., Chapter 8 in "Ceramic Materials for Fusion Reactors," EPRI-AP-1702, February 1981.

6. R.M. Matheny, J.C. Corelli, and G.G. Trantina, J. Nucl. Mat. 83, 313 (1979).

7. W.J. Gray, Battelle Northwest Laboratory, BNWL-2390, August 1977.

8. J. B. Holt et al., "Helium Generation and Diffusion in Graphite," Lawrence Livermore Laboratory Report, April 1976.

VIII.3 HIBALL Reflector Region

VIII.3.1 HT-9 Structural Material

VIII.3.1.1 General Environment

The reflector is cooled by a Pb-Li alloy which ranges in temperature from 300 to 500°C. The flow velocity is 1 m/s and the coolant pressure is 2 MPa. A relatively high vacuum ($< 10^{-5}$ torr) normally exists on the chamber-side of the reflector region, but the first wall of the reflector region is periodically covered with Pb vapor at 500°C or higher. The hydrogen partial pressure is 10^{-4} torr at 500°C.

VIII.3.1.2 Radiation Environment for HT-9

The two key measures of radiation damage, the displacement damage and amount of He produced per FPY are plotted in Fig. VIII.3-1 as a function of effective INPORT unit thickness. Because of the protection afforded by the inport units the maximum damage in the HT-9 side wall is 2.7 dpa per FPY and this drops by a factor of 100 over the 41 cm thickness (Fig. VII.3-2). Similarly, the maximum helium production is 0.4 appm He per FPY and this drops by a factor of 1000 across the reflector. The appm He/dpa ranges from 0.1 to 0.02.

The damage rate of the neutrons behind the INPORT units is given in Fig. VIII.3-3. The peak damage rate is 0.009 dpa per second and the damage rate stays above 10^{-3} dpa per second for ~ 5 microseconds and above 10^{-4} dpa sec^{-1} for 10 microseconds.

VIII.3.2 Previous Experiments Under HIBALL-Type Conditions

VIII.3.2.1 Compatibility of HT-9 with Pb-Li Alloys

As might be expected, there is no data concerning the $Pb_{83}Li_{17}$ eutectic alloy on HT-9 at temperatures of 350-500°C. There is a small amount of information on low alloy, high strength steels in pure lead[1-5], and some data on

Fig. VIII.3-1 Variation in damage parameters for HT-9 in the reflector region of HIBALL.

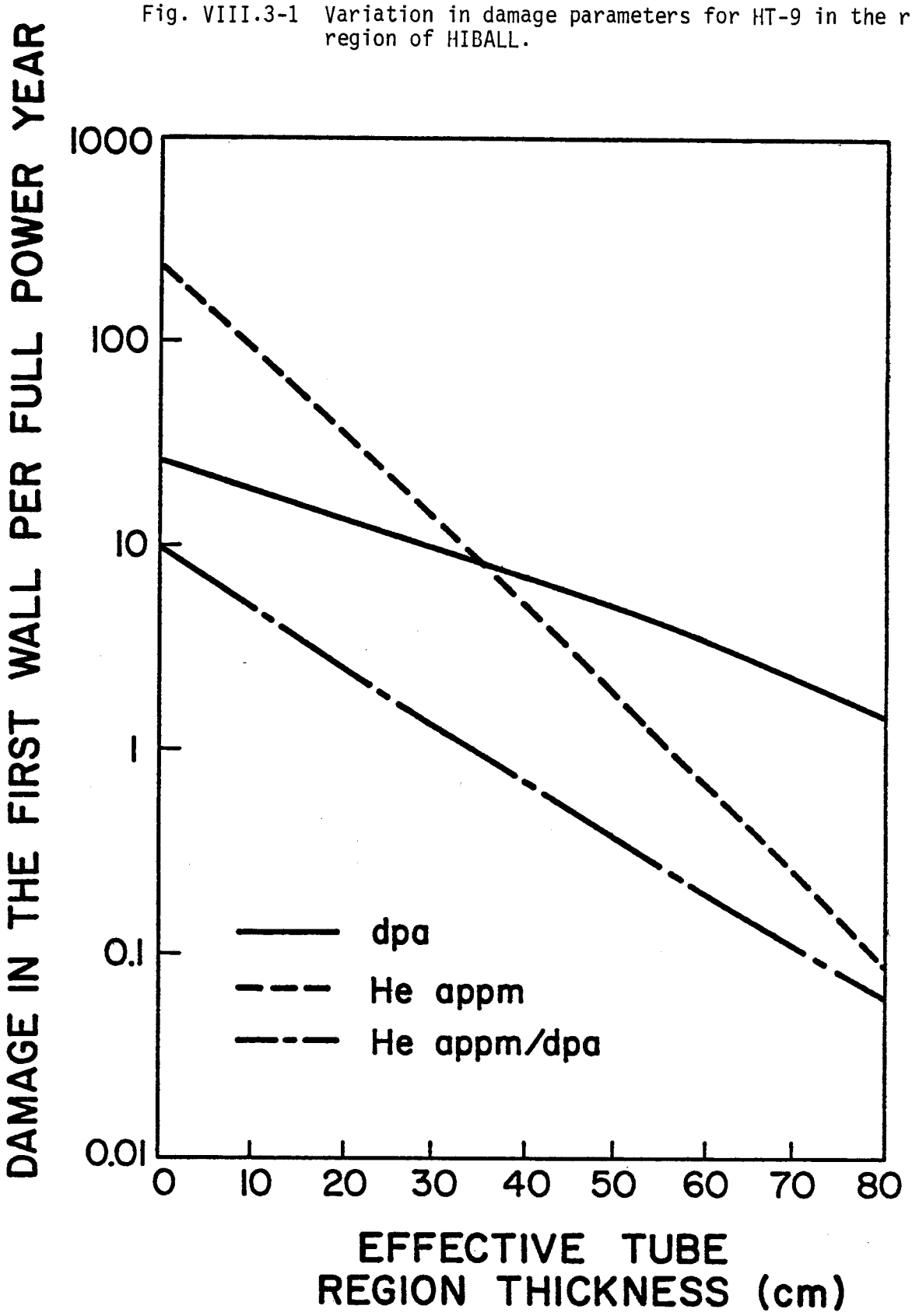

Figure VIII.3-2

Spatial variation of radiation damage in HT-9 structure of HIBALL reflector region.

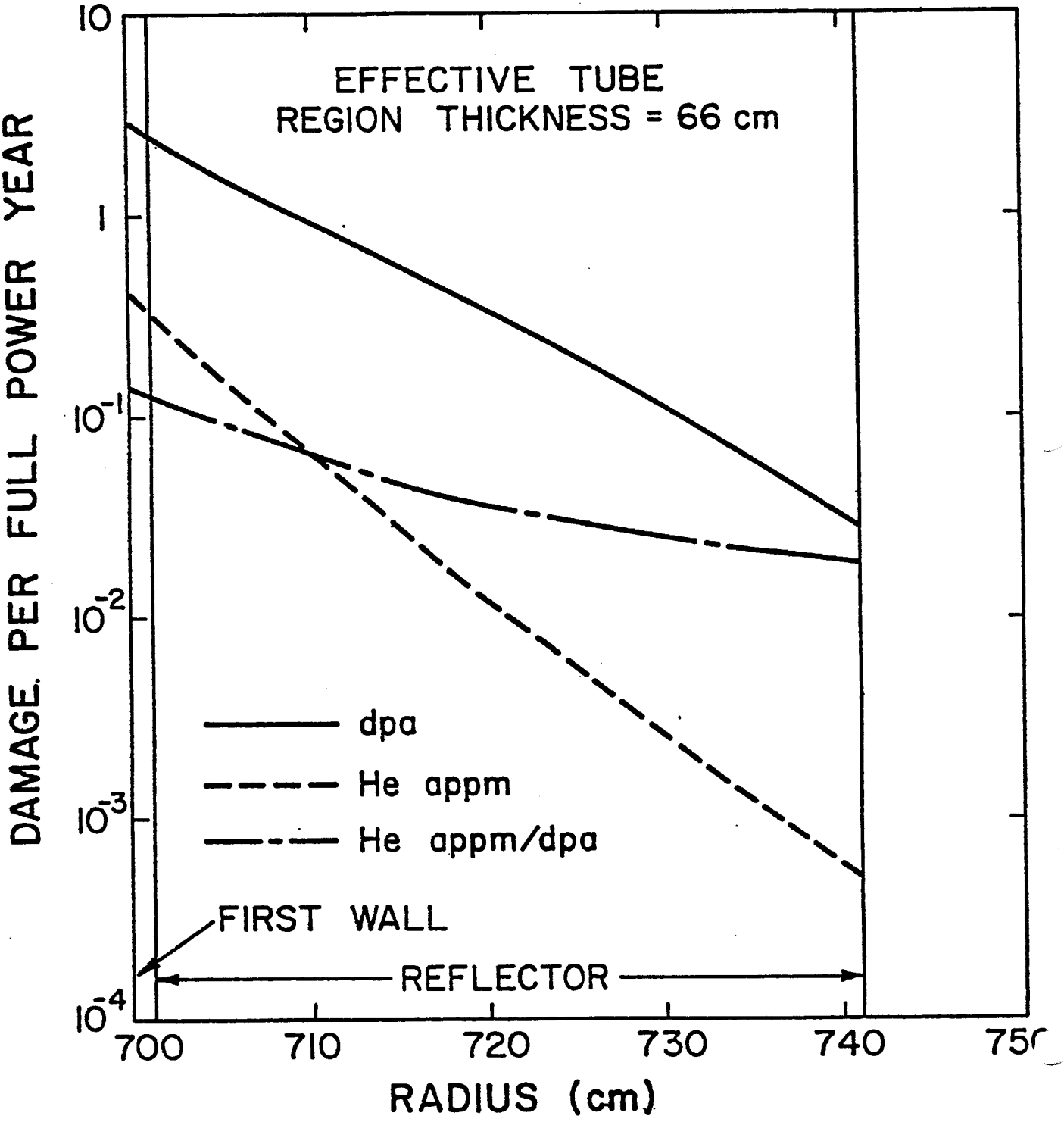

Figure VIII.3-3

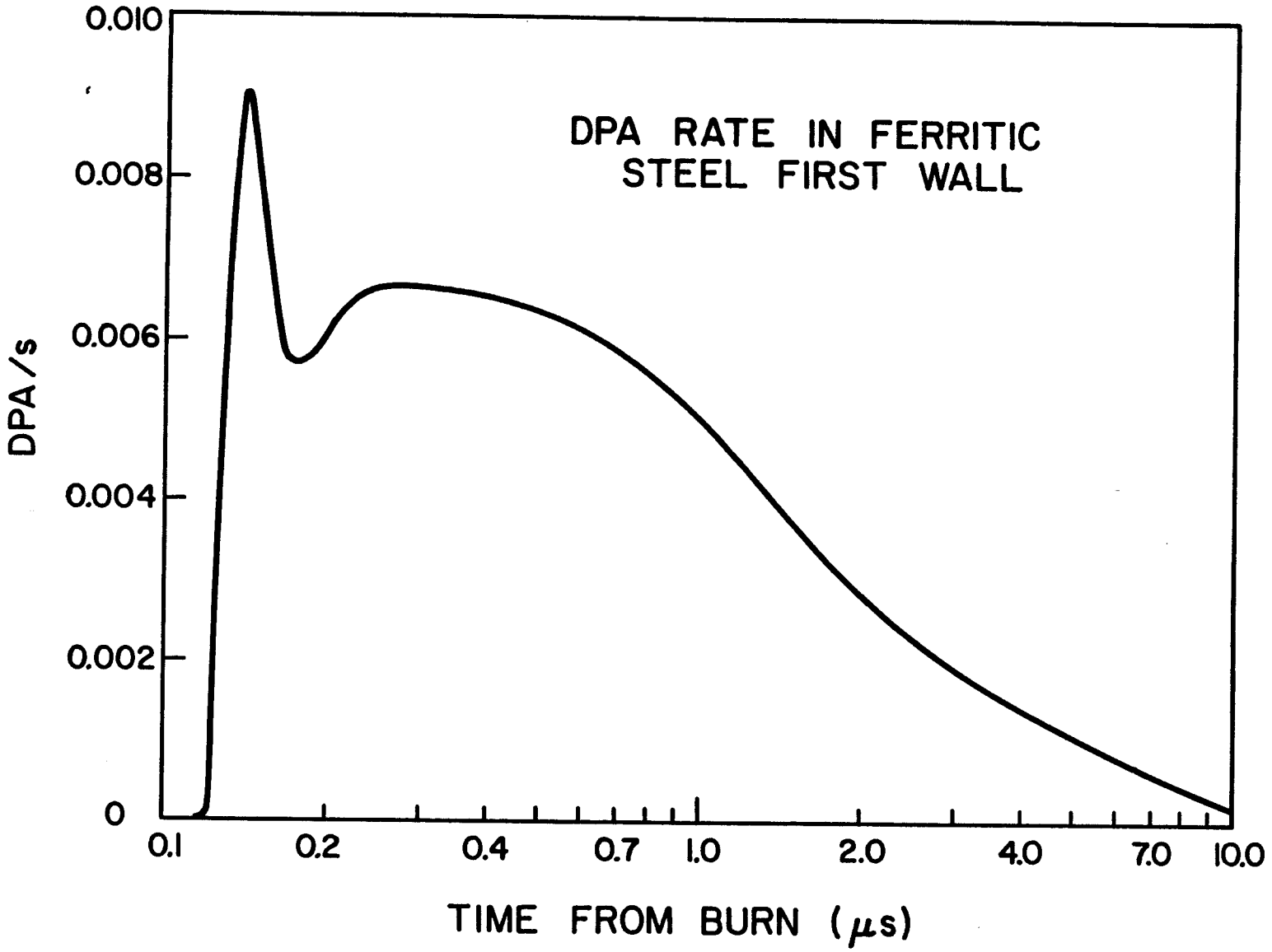

2-1/4 Cr-1 Mo alloys with a $Li_{99}Pb_1$ system at 500°C.[6] The only information on liquid metals and HT-9 is a recent study at ANL in pure lithium and lithium contaminated with nitrogen at 482°C.[7]

Despite claims in earlier studies that low alloy steels were not embrittled by pure lead, recent results showed embrittlement could occur near the melting point of the lead (327°C).[4,5] The embrittlement of the high strength 4100 series steels started at ~ 200°C and reached a maximum (lowest ductility) at ~ 320°C. Above ~ 370°C there was degradation in the ductility (see Fig. VIII.3-4). The addition of Sn increased the width of the embrittling zone.

At higher temperatures, 700°C, 2-1/4 Cr-1 Mo alloy suffered a severe attack after 300 hours of exposure to lead.[3] However, the addition of Ti to the Pb completely eliminated the corrosion under the same conditions. It has been known for a long time that the addition of Ti or Zr to Pb would inhibit corrosion by forming tightly adherring TiC and ZrC films on the steel surface.

On the other end of the spectrum, a $Li_{99}Pb_1$ alloy was shown to attack Fe_3C and Mo_2C in the welded zones of a 2-1/4 Cr-1 Mo alloy at 500°C after exposure up to 1600 hours. Figure VIII.3-5, from the paper by Anderson et al.[4], shows that the cementite and Mo_2C are unstable with respect to Li below 500°C while the chromium carbides are stable over a wide range.

Work at Harwell[8] has shown that low alloy steels can be significantly decarborized by exposure to Li even at ~ 200°C. However, higher Cr containing steels such as 2-1/2 Cr-1 Mo, or the 9 Cr-1 Mo alloys showed much greater resistance.[9] Presumably, the higher Cr content of HT-9 would help to protect that alloy from decarborization and hence embrittlement.

A recent study by Chopra and Smith[7] has shown that nitrogen can have a large effect on the fatigue life of HT-9 in flowing Li at 482°C. They found

Figure VIII.3-4

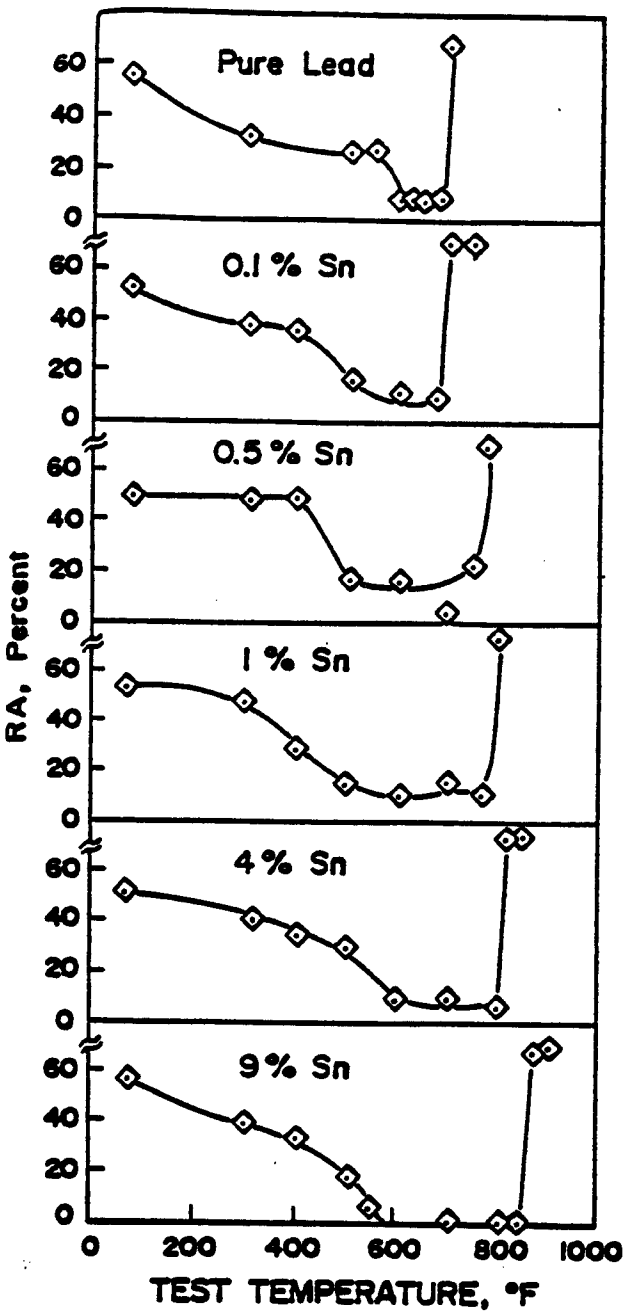

Reduction of area, RA, for 200-ksi (1379-MPa) 4145 steel, surface wetted with various Pb-Sn alloys as a function of test temperature. (4,5)

Figure VIII.3-5

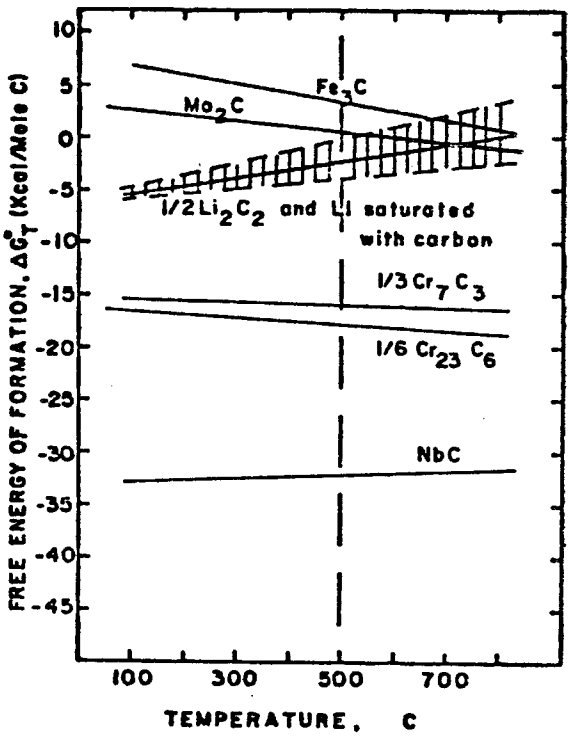

Relative thermodynamic stability of several carbides in carbon saturated lithium. (4)

that in short term fatigue tests, where the nitrogen level was between 80 and 130 ppm, the fatigue life in Li was the same as that obtained in Na. However, when the nitrogen level reached > 1000 ppm of nitrogen, there was a dramatic drop in the fatigue life (Fig. VIII.3-6) by as much as a factor of 5. This strongly suggests that close control of the nitrogen level of the HIBALL coolant will be necessary.

In summary, it appears that pure lead can have an embrittling effect on low chromium containing steels between 200 and 320°C but operation above that temperature and below 700°C should be acceptable. Ti or Zr inhibitors can be added to the Pb-Li alloy to reduce the corrosion. The higher chromium content of the HT-9 is also likely to help the weld zones to resist attack by the lithium.

VIII.3.2.2 Radiation Effects to HT-9

The response of HT-9 to neutron irradiation has been the subject of intense investigation in the LMFBR program. It has been found (by scientists at General Atomic) that HT-9 is resistant to significant void production below 100 dpa which is roughly equivalent to 40 FPY in HIBALL (see Fig. VIII.3-7). Similarly neutron damage to 5 dpa has been shown to have very little effect on the tensile properties and tensile ductility of the HT-9 alloy. However there is a modest upward shift in the ductile to brittle transition temperature (DBTT) of 100°C in 5 dpa (Fig. VIII.3-8). This DBTT shift seems to be saturated above 5 dpa and at 25 dpa it is still only ~ 100°C. Since the melting temperature of $Pb_{83}Li_{17}$ is 254°C, this is still 150°C above the DBTT. Therefore it appears that ferritic steel can last the lifetime of HIBALL without necessarily having to enter the brittle regime.

The effect of high damage rates (Fig. VIII.3-3) on the final damage state can only be a subject for speculation at this time. Theoretical analysis

Figure VIII.3-6

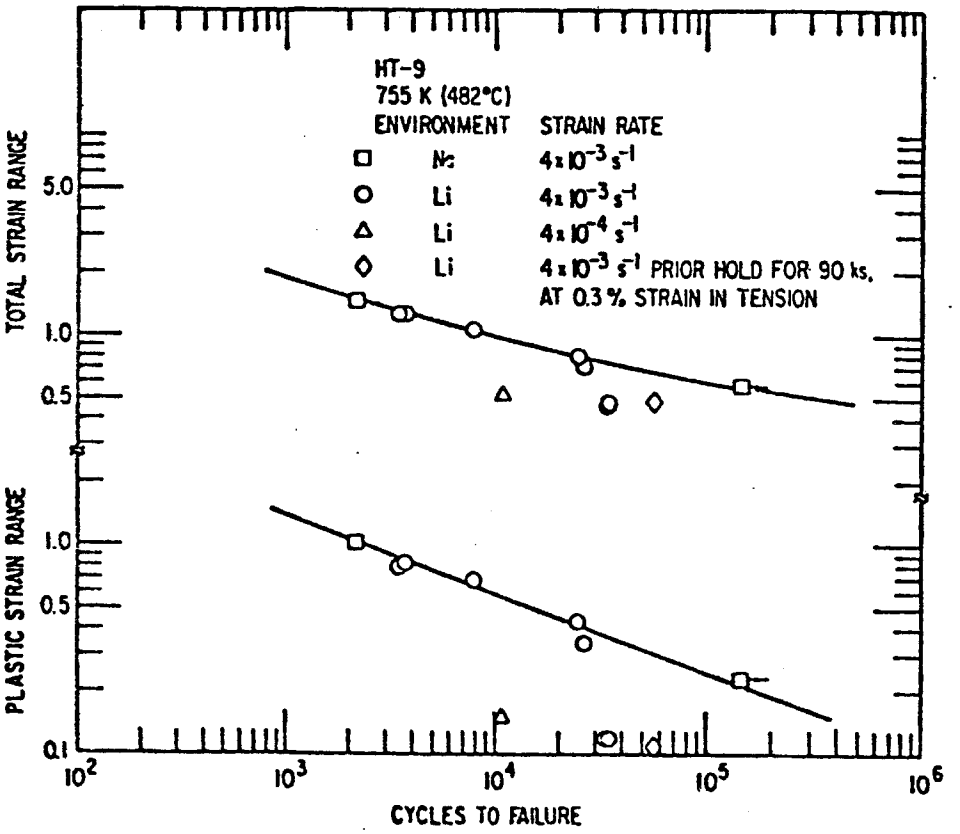

Total and plastic strain range vs. cycles to failure for HT-9 alloy tested in lithium at 755 K.(7)

Figure VIII.3-7
Swelling of candidate CTR materials during neutron irradiation.

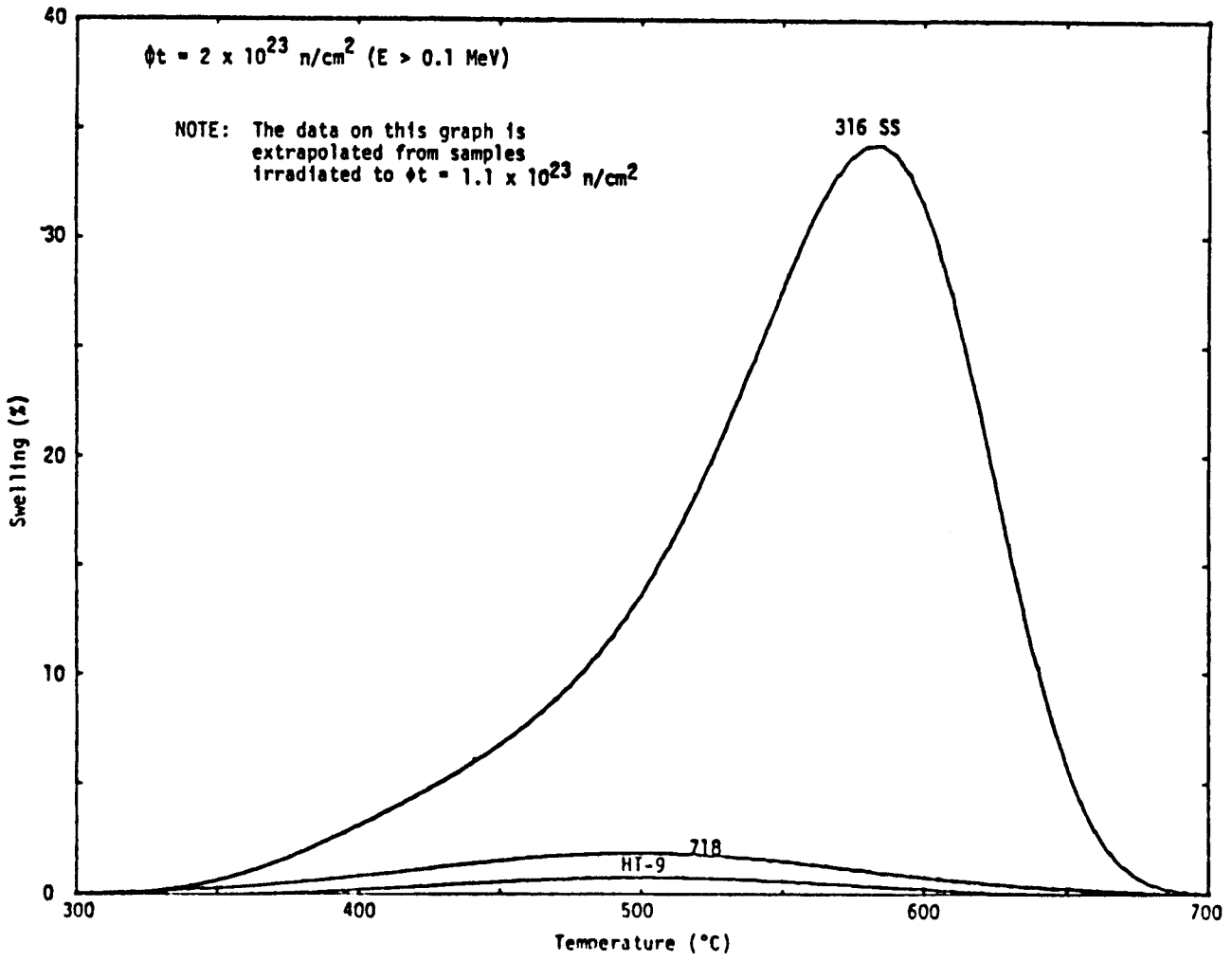

Figure VIII.3-8

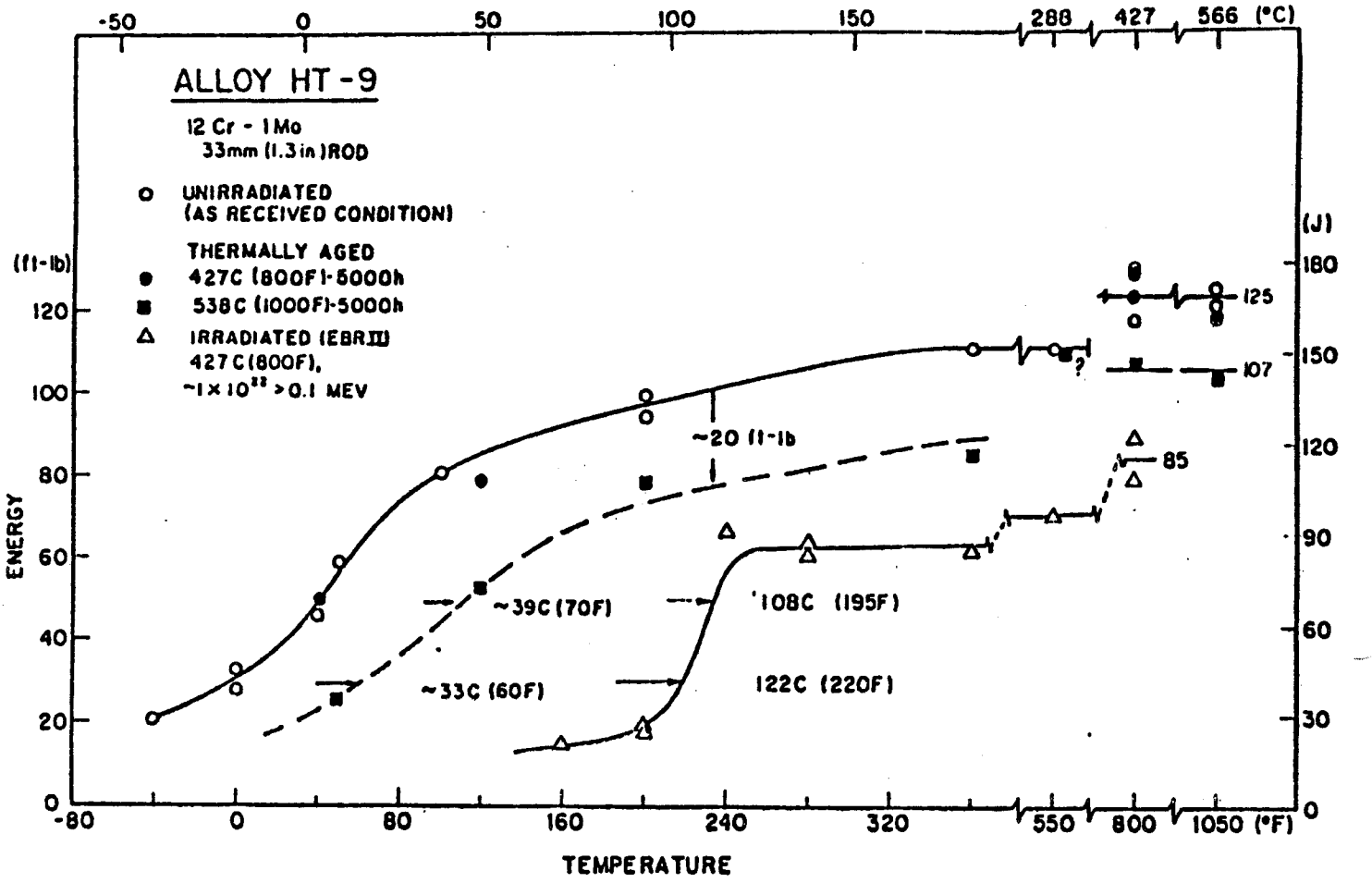

Charpy-V energy values as a function of test temperature for HT-9 in the as-received condition, after 5000 hr aging at 427°C, after 5000 hr aging at 538°C, and after irradiation to a neutron fluence of 1.1 x 10^{22} n/cm^2 (E > 0.1 MeV) at an irradiation temperature of 419°C ± 15°C in the EBR-II reactor. From F. Smidt and scientists at Naval Research Laboratory.

reveals that the high damage rates may promote such a high supersaturation of point defects that enhanced recombination will occur and lower the residual damage. However no experimental data on pulsed data exists at this time and we will have to wait for future clarification in test facilities.

References for Section VIII.3

1. W.R. Warke and M.M. Breyer, "Effect of Steel Composition on Lead Embrittlement," J. of the Iron and Steel Institute, p. 779 (Oct. 1971).

2. C.F. Old, "Liquid Metal Embrittlement of Nuclear Materials," J. Nuclear Materials 92, (1980).

3. R.C. Asher, D. Davis, and S.A. Beethour, "Source Observations on the Compatibility of Structural Materials with Molten Lead," Corrosion Science, 17, 545 (1977).

4. J.C. Lynn, W.R. Warke, and P. Gordon, "Solid Metal-Induced Embrittlement of Steel," Mat. Sci. and Engr. 18, 51 (1975).

5. M.M. Breyer and K.L. Johnson, "Liquid Metal Embrittlement of 4145 Steel by Lead-Tin and Lead-Antimony Alloys," J. of Testing and Evaluation 2, 471 (1974).

6. T.C. Anderson et al., "Intergranular Penetration of 2-1/4 Cr-1 Mo Weldiments by a Lithium-Lead Liquid," to be published, 2nd Int. Conf. on Liquid Metal Technology in Energy Production, April 20, 1980, Richland, WA.

7. O.K. Chopra and D.L. Smith, to be published.

8. C.F. Olds and P. Trevena, AERE-R9505 (1979).

9. J.E. Cordell, in Proc. BMES Conf. on Liquid Alkali Metals, Nottingham, p. 177 (1973).

VIII.4 Helium Behavior in the HIBALL Structural Material

VIII.4.1 Introduction and Background

Fusion reactor first walls are expected to withstand severe operational environments. Aside from the detrimental effects of radiation damage, nuclear reactions produce both solid and gas transmutants in the structural materials. The generation of helium as a result of transmutation reactions arouses concern about its effects on the long-term integrity of the first wall. The presence of helium has been recognized to degrade the high temperature ductility of stainless steel.[1] More recently, void formation and swelling of metals were recognized to be strongly influenced by the presence of helium.[2]

Helium is thermodynamically insoluble in metals and tends to precipitate into bubbles if the temperature is high enough for the helium atoms to migrate. Whereas helium concentrations in steel typical of fission reactor environments are in the range of 1-10 appm,[3] the situation is expected to be much more severe for Magnetic Confinement Fusion Reactors (MCFR's) and Inertial Confinement Fusion Reactors (ICFR's) because the transmutation cross sections for the 14 MeV neutrons are much higher. Generation rates are projected to be considerably greater than fast breeder reactors with up to 644 appm/yr in a Princeton design,[4] 285 appm/yr in UWMAK-I,[5] and ~ 294 appm/yr in the INTOR design.[6] The helium generation rates in HIBALL depend on whether or not the steel is protected by the INPORT units. Components such as the inlet for the target injector or the front part of the struts holding up the INPORT units will experience helium production rates of ~ 230 appm per full power year. On the other hand, the HT-9 first wall behind the INPORT units will only experience helium production rates of ~ 0.4 appm per FPY.

The helium content and the high ratio of helium concentration to displacement damage predicted for fusion reactors has given rise to the

expectation that bubbles rather than voids may exist in many fusion reactor structural materials.[7,8] Furthermore, the synergistic effects of helium and displacement damage have been predicted to have a significant influence on the microstructural evolution.[9,10] The object of this section is to examine only the effects of helium in HIBALL on the dimensional stability of the HT-9 structure.

VIII.4.2 Helium Migration Mechanisms

The migration mechanisms of helium in metals are not well understood. Speculations for these mechanisms include substitutional, interstitial, mutual (interstitial + substitutional) diffusion, momentum transfer, diffusion by di-vacancies and various combinations of the mechanisms. It is not the intent of the present section to discuss the details and supportng evidence of all of these mechanisms. However, selected theoretical and experimental evidence for helium migration by a trapping-detrapping mechanism are briefly discussed.

An interstitial migration mechanism was inferred from computer calculations of minimum energy lattice configurations for a variety of atomic jumps by helium atoms, vacancies, and self-interstitials in face-centered cubic metals.[11] There is strong evidence that helium has a low value for the activation energy for interstitial diffusion and a high interstitial formation energy.[12]. Smidt and Pieper[13] found for stainless steel assuming 25 ppm He, a migration energy of 2.3 eV for the helium atom to reach a bubble. The value is close to the self-diffusion energy of nickel, 2.8 to 2.9 eV. This is consistent with the motion of helium as a substitutional atom to form bubbles.

The model considered in the present study is substantiated by experiments and explains helium migration[12-14] reasonably well. Helium forms in an interstitial position and moves rapidly as an interstitial until it encounters a vacancy, void, or other helium trap, or is lost to the surface. The gas

atom moves to a vacancy and its jump distance is best represented by the distance between available vacancies. The time spent in a vacancy or other trap is large compared with the time the gas atoms spend in an interstitial position. The trap sites fill rapidly because they offer a large sink to diffusing gas atoms. Following this model, Reed[12] gave the following diffusion coefficient

$$D^{He} = \nu_o \frac{\lambda^2}{6} C_v^{-2/3} \exp\{-E^D_{He}/kT\} \qquad \text{(VIII.4-1)}$$

where ν_o is the frequency factor for the detrapping of helium, λ is the jump distance, and E^D_{He} is approximately the detrapping energy of helium in ferritic steel.

VIII.4.3 A Simplified Theory for Helium Swelling

VIII.4.3.1 Assumptions and Equations

Ideally, one would like to formulate a theory in which all possible atomistic interactions are accounted for. However, there are two major difficulties with such a notion. The detailed description of the atomistic processes can be computationally burdensome,[15,16] with a very limited chance of correlating to experiments. On the other hand, basic material parameters such as binding and migration energies of defect complexes are not very well determined. In view of these difficulties, theorists have attempted to envoke convenient approximations. The validity of such approximations can only be tested by detailed and careful correlations with experiments. In this section we develop a simplified conceptual rate theory in which many complicating features have been neglected. Only those details that are believed to play dominant roles are retained. A qualitative description of the present model is given below.

Helium is assumed to migrate by an interstitial mechanism in between vacancy traps. There is no distinction in the theory between interstitial and substitutional helium. Once two helium atoms collide, they form a di-helium gas atom cluster for which vacancies are readily available. Because of the possibilities of thermal dissociation and radiation re-solution, this cluster is unstable. Once a tri-helium gas atom cluster is formed, it can attract few more vacancies and form the critical nucleus size for small gas-filled cavities. Nucleation is therefore dictated by the behavior of gas atoms rather than by vacancies. It has been recently discussed by Meyer et al.[17] that experimental evidence supports this assumption. The nucleation rate of cavities is the rate at which they cross this boundary in size space. The density of cavities will therefore increase as the density of single and di-helium species increase. After a certain irradiation time, it becomes more probable for single helium to collide with larger size cavities than with the small nuclei. Thus a gradual shift from the nucleation stage to the growth stage is achieved. The large size cavities are assumed to start growing from the nucleus site at only one average speed. The size distribution is therefore approximated by a delta function and by keeping track of vacancy, interstitial and helium atom flows in and out of the average cavity, we can determine its size and nature (void or bubble) at any time. Since interstitial loops nucleate rapidly during irradiation[15,16], their number density is assumed to be constant and they are only at a state of growth.

Such a simplified description is obviously not complete but it will provide an order-of-magnitude comparison with the experiment. The roles of vacancy loops, divacancies, precipitates, dislocation dynamics, cavity migration and coal essence, and matrix chemical changes in complex alloys are all neglected. Under these restrictive assumptions, the following rate

equations describe swelling under conditions of simultaneous helium gas and displacement damage production.

$$\frac{dC_{He}}{dt} = P - 2K_{11}C_{He}^2 - k_{12}C_{He}C_{2He} - \bar{k}C_{He}N + 2(2C_{2He})b$$

$$+ mNb - Z_{He}\rho_d D_{He}C_{He} - 6D_{He}\frac{\sqrt{Z_{He}\rho_d}}{d}C_{He} + 2\gamma_h(2)C_{2He} \qquad \text{(VIII.4-2)}$$

$$\frac{dC_{2He}}{dt} = K_{11}C_{He}^2 - K_{12}C_{He}C_{2He} - 2C_{2He}b + 3C_{3He}b - \gamma_h(2)C_{2He} \qquad \text{(VIII.4-3)}$$

$$\frac{dC_{3He}}{dt} = K_{12}C_{He}C_{2He} - K_{13}C_{He}C_{3He} - 3C_{3He} + 4C_{4He}b \qquad \text{(VIII.4-4)}$$

$$\frac{dN}{dt} = K_{12}C_{He}C_{2He} - 3C_{3He}b \qquad \text{(VIII.4-5)}$$

$$\frac{dC_v}{dt} = P_d - Z_v\rho_d D_v C_v - K_{vi}C_vC_i \qquad \text{(VIII.4-6)}$$

$$\frac{dC_i}{dt} = P_d - Z_i\rho_d D_i C_i - K_{vi}C_vC_i \qquad \text{(VIII.4-7)}$$

$$\frac{dm}{dt} = 4\pi R_c D_{He}C_{He} - bm \qquad \text{(VIII.4-8)}$$

$$\frac{dR_c}{dt} = \frac{1}{R_c}\{D_vC_v - D_iC_i - D_vC_v^e\left[\exp\frac{\Omega}{kT}\left(\frac{2\gamma}{R_c} - p\right) - 1\right]\} \qquad \text{(VIII.4-9)}$$

$$\frac{dR_{i\ell}}{dt} = \frac{1}{b}\{Z_iD_iC_i - Z_vD_vC_v + D_vC_v^e \exp\frac{-(\gamma_{sf} + F_{e\ell})b_v^2}{kT}\} \qquad \text{(VIII.4-10)}$$

where the concentrations are expressed in atoms per atom (apa) and the radii are in meters. Some of the terms in the above equations are defined in Table VIII.4-1 and the numerical values used in the present calculations are included in Table VIII.4-2 (ref. 20). The first three equations describe the concentrations of single gas atoms, diatomic clusters and triatomic clusters. The fourth equation describes the total cavity number density.

The vacancy and interstitial concentrations are represented by two coupled rate equations. The last three equations describe the gas atom concentration in a cavity, the average radius of the cavity, and the average interstitial loop radius.[18]

The quantities K_{mn} are defined as follows:

$$K_{mn} = \frac{z_{mn}\Omega D_{He}}{a_o^2} \qquad \text{(VIII.4-11)}$$

where z_{mn} is the combinatorial number, Ω is the atomic volume, a_o is the lattice parameters, and D_{He} is the helium diffusion coefficient given by Eq. VIII.4-1.

The thermal dissociation parameter for di-gas atom clusters[19] is

$$\gamma_h(2) = \frac{D_{He}}{a_o^2} \exp\left(-\frac{E^B_{2He}}{kT}\right) \qquad \text{(VIII.4-12)}$$

where E^B_{2He} is the di-helium binding energy.

The elastic energy of a dislocation loop of radius $R_{i\ell}$ is given by[31]

$$F_{e\ell} = \frac{\mu b_v^2}{(1-\nu)4\pi(R_{i\ell}+b_v)} \ln\left(\frac{R_{i\ell}+b_v}{b_v}\right) \qquad \text{(VIII.4-13)}$$

where π is the shear modulus, ν is the Poisson's ratio, and b_v is Burger's

vector. Details of the derivation of the previous set of equations are given in reference 20.

Table VIII.4-1 Terms and Processes in the Rate Equations

Term/Process	Description
P	Production of helium gas atoms.
$2K_{11}C_{He}^2$	Rate at which helium gas atoms disappear by formation of diatomic clusters (two gas atoms are consumed for each diatomic cluster).
$K_{12}C_{He}C_{2He}$	Rate of formation of triatomic clusters from di-gas atoms and single gas atoms.
$K_{13}C_{He}C_{3He}$	Rate of formation of four-atom clusters from tri-gas atoms and single gas atoms.
$K_{14}C_{He}C_{4He}$	Rate of formation of five-atom clusters from four-gas atoms and single gas atoms.
$2(2C_{2He})b$	Rate at which single atoms are returned to the matrix by resolution of diatomic clusters.
$3C_{3He}b, 4C_{4He}b$	Resolution rates.
$Z_{He}\rho_d D_{He} C_{He}$	Rate of diffusion-controlled absorption of helium gas atoms by dislocations.
$6D_{He}\sqrt{\frac{Z_{He}\rho_d}{d}}\,C_{He}$	Removal rate of helium gas atoms by grain boundaries.
$\gamma_h(2)C_{2He}$	Thermal dissociation rate of diatomic clusters into single gas atoms.
P_d	Production of rate defects.
$Z_{v,i}\rho_d D_{v,i} C_{v,i}$	Rate of diffusion-controlled absorption of vacancies/interstitials by dislocations.
$K_{vi}C_vC_i$	Rate of homogeneous point defect recombination.
$C_v^e \exp\frac{-(\gamma_{sf} + F_{e\ell})b^2}{kT}$	Equilibrium vacancy concentration at the edge of an interstitial dislocaiton loop of radius $R_{i\ell}$ with a stacking fault energy, γ_{sf}.

Table VIII.4-2 Material Parameters used in the Calculations[20]

Parameter	Definition	Numerical Value
a_o	lattice parameter	3.63 Å
k	Boltzmann's constant	8.617×10^{-5} eV/K
b	Burger's vector	2.5668×10^{-8} cm
c_{vi}	recombination combinatorial number	48
c_{11}	combinatorial number for He-He	84
c_{12}	combinatorial number for $He-2He_2$	20
c_{13}	combinatorial number for $He-He_3$	12
d	grain diameter	3.0×10^{-3} cm
ρ_o	initial value of dislocation density	10^8 cm/cm^3
E^B_{2He}	binding energy of di-helium	0.79 eV
E^D_H	detrapping energy of helium	3.16 eV
E^F_i	formation energy of an interstitial	4.08 eV
E^M_i	migration energy of single-interstitial	0.20 eV
E^F_v	formation energy of a vacancy	1.60 eV
E^M_v	migration energy of single vacancy	1.40 eV
γ	surface energy	6.24×10^{14} eV/c,^{2}
Ω	atomic volume	1.1958×10^{-23} cm^3
ν	Poisson's ratio	0.291
$R_c(0)$	initial value of the cavity radius	20 Å
$R^c_{i\ell}$	initial value of the interstitial loop radius	5 Å
γ_{sf}	stacking fault energy	9.2×10^{12} eV/cm^2
π	shear modulus	1.7665×10^{23} eV/cm^3
B	Van der Waal's constant	1.75×10^{-23}
ν_H	helium vibrational frequency	5.0×10^{14}/sec
ν_i	interstitial vibrational frequency	5.0×10^{12}/sec
ν_v	vacancy vibrational frequency	5.0×10^{13}/sec
Z_{He}	bias factor of helium gas atoms	1.00
Z_i	bias factor of interstitials	1.01
Z_v	bias factor of vacancies	1.00

VIII.4.4 The EXPRESS Computer Code

In order to solve the previous set of rate equations (VIII.4-2 to VIII.2-10) for Inertial Confinement Fusion conditions, a special computational technique was developed. The EXPRESS computer code (Integration/EXtrapolation Method for Pulsed Rate Equations of Stiff Systems) solves time dependent rate equations describing the evolution of the space-averaged damage state of an ICFR first wall. As such, it represents an extension of the HEGBUF code[20], developed by M. Takata to describe the damage-state evolution in steady-state and slowly pulsed fusion machines.

The equations describing this system possess the property of stiffness; that is, the time scales characterizing the various elements of the system span a large range of values. The integration of such a system requires the use of specialized numerical techniques. Many of these techniques have been incorporated into a set of subroutines called the GEAR package.[21] When the pulse frequency is high, as in the case of ICFR's, even the methods of GEAR become prohibitively expensive.

To alleviate this difficulty, we have developed an integration/extrapolation method which allows us to obtain the solution of the equations without integrating each pulse. A detailed description of this method is contained in a UCLA report.[22] A flow diagram is shown in Fig. VIII.4-1.

VIII.4.5 Results

In all of our calculations, the displacement and helium production rates were idealized by square waves of definite pulse lengths (T_{on}). The peak displacement damage and helium production rates are determined by conserving the total number of displacements and helium within one pulse. The magnitude of the on-time is determined as the "full width at half maximum (FWHM)" from the nuclear analysis of the wall response. It was also found that under our

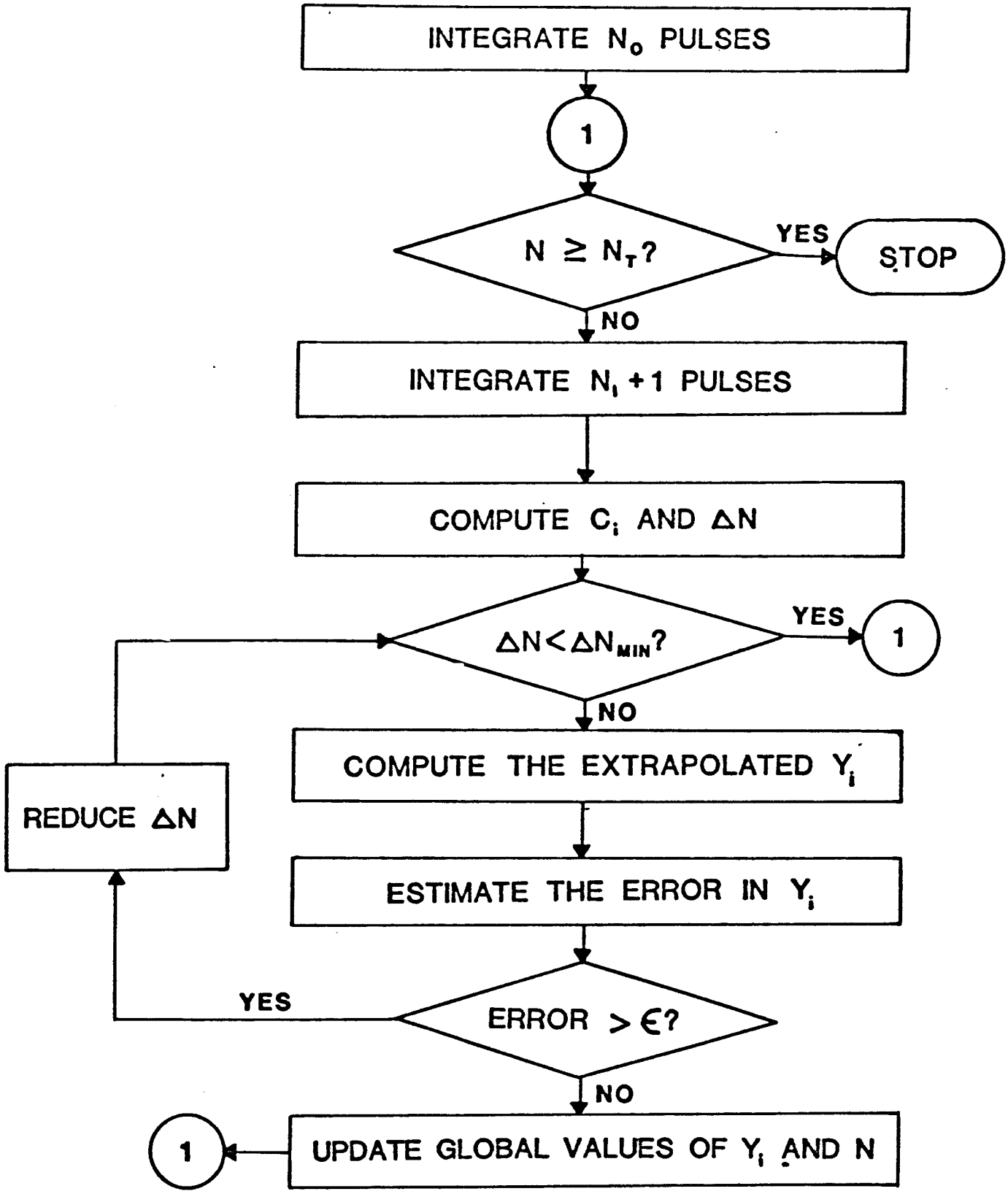

Fig. VIII.4-1 Flow diagram of integration/extrapolation method of solution developed.

specific conditions, the helium mean-lifetime is much longer than the on-time. No helium diffusion is therefore expected during the short on-time, and the helium on-time can be approximated by the displacement damage on-time.

The following conditions apply:

$$\tau_i < T_{on} < \tau_v < \tau_{He} \qquad \text{(VIII.4-14)}$$

and

$$T_{on}(He) \simeq T_{on}(dpa) \qquad \text{(VIII.4-15)}$$

We will here analyze the following two cases.

VIII.4.5.1 Unprotected Ferritic Steel First Wall

Based upon the previous assumptions, and the results of the nuclear analysis, we use as input to the computer code EXPRESS the following:

T_{on} = 5 ns

T_{cycle} = 0.2 s

instantaneous dpa/s = 32.12 dpa/s

instantaneous He/s = 2.89×10^{-4} at/at/s

dpa/FPY = 25.36 dpa/FPY

He/FPY = 227.6 appm/FPY

He/dpa ratio $\hat{=}$ 9 appm/dpa

Figure VIII.4-2 shows the concentration of single helium atoms in the ferritic steel matrix, as a function of irradiation time. The calculations for this case (500°C) were performed up to ~ 80,000 pulses. The helium is mainly trapped in vacancies and has a very little chance for diffusion. The cavity concentration is shown in Fig. VIII.4-3 where the solid lines are for equivalent continuous-irradiation, and the dotted are for the actual pulsed case. By ~ 80,000 pulses, the cavity density in the pulsed case is already

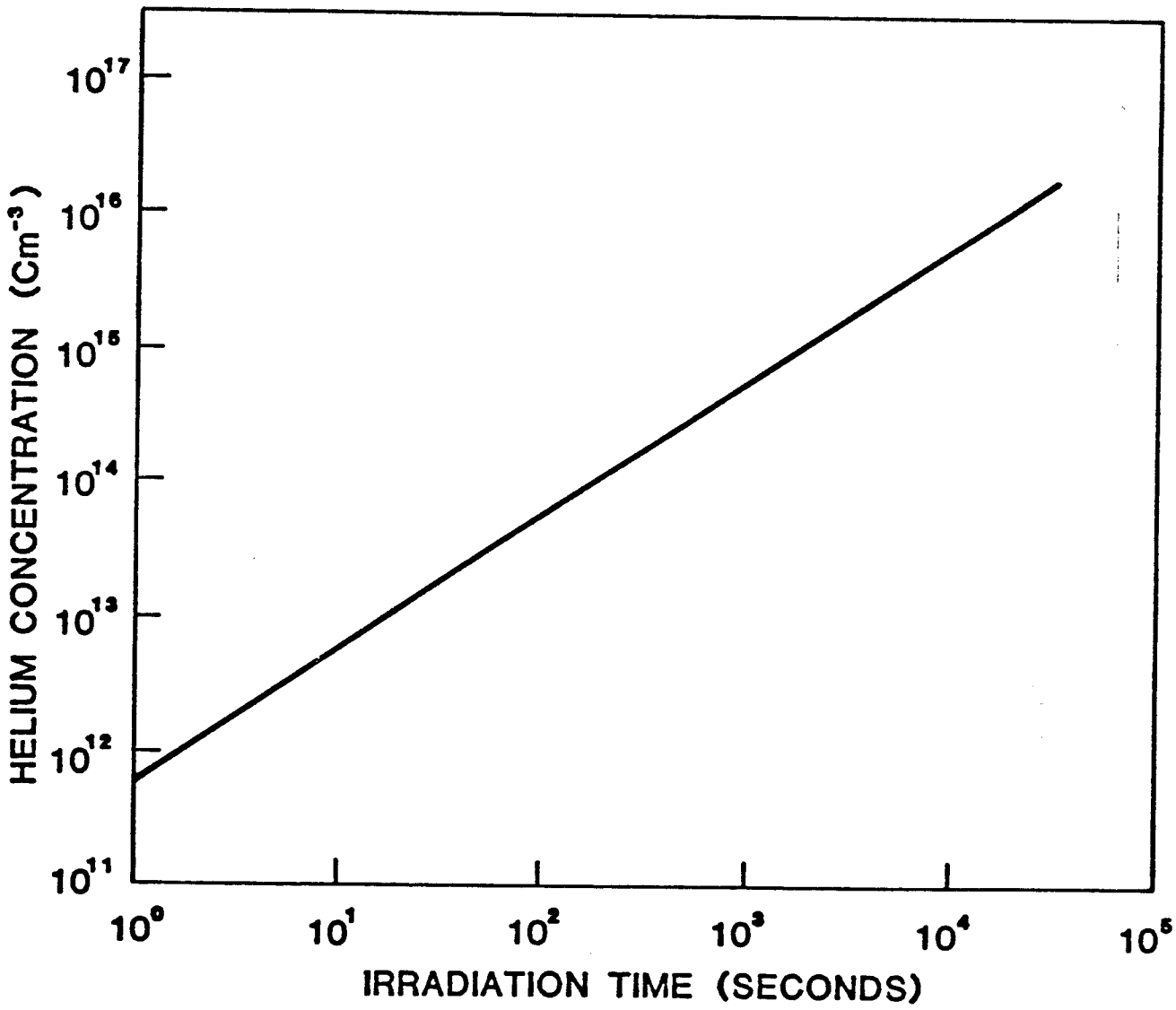

Fig. VIII.4-2 Concentration of single He atoms in ferritic steel matrix, as a function of irradiation time.

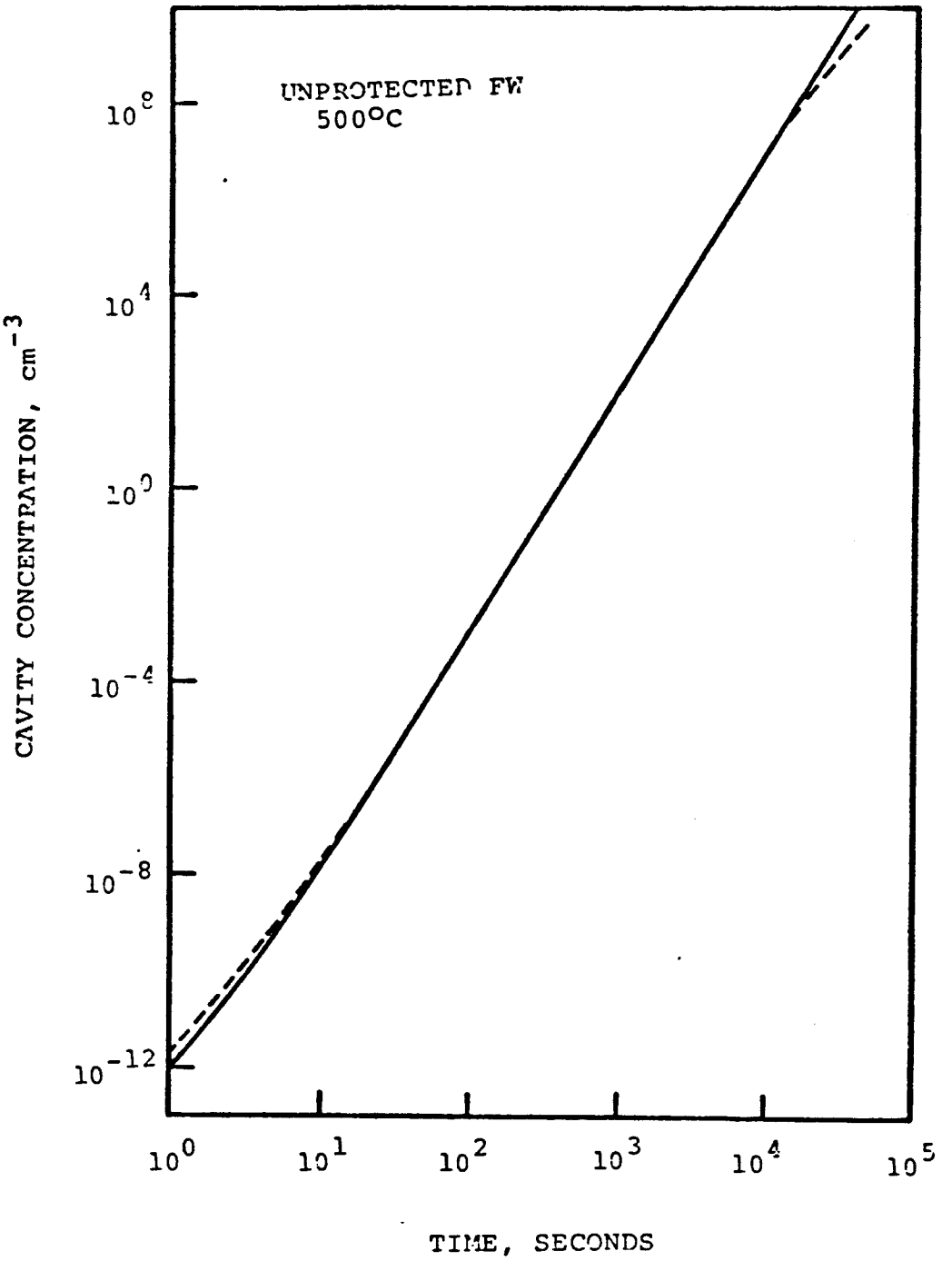

Fig. VIII.4-3 Cavity concentration; solid lines are for equivalent continuous irradiation, dotted are for pulsed case.

smaller than the corresponding continuous irradiation. The concentrations of both vacancies and interstitials for the first 300 pulses are shown on Fig. VIII.4-4 and up to 80,000 pulses on Fig. VIII.4-5. The solid lines are for the continuous irradiation equivalent, while the dotted lines represent the envelope of the fluctuations in these components. The increase in the average radius of the cavity is shown in Fig. VIII.4-6 where it is evident that pulsing of irradiation results in a smaller cavity radius. This is mainly due to the enhanced vacancy-interstitial recombination brought about by the fluctuations shown on the previous figure. It is concluded therefore that under pulsed irradiation, a lower amount of swelling is observed than that observed under the equivalent continuous irradiation. This conclusion is unique to the HIBALL conditions and caution should be used in extrapolating to other conditions.

A comparison of the cost of the new integration/extrapolation method, and the straight numerical integration of the previous equations is shown in Fig. VIII.4-7. A gain of over a factor of 20 in the cost of integration is achieved using our new method. This is extremely important in studies of pulsed effects that include ratcheting (build-up) phenomena.

VIII.4.5.2 Protected Ferritic Steel First Metallic Wall

A summary of radiation damage parameters in the first metallic wall, and in the reflector, is given in Table VIII.4-3 below.

Figure VIII.4-8 shows the concentrations of the primary components of damage: vacancies, interstitials, and helium atoms, during the first pulse and pulse 615. The vacancy and interstitial concentrations are shown to be higher than the helium concentration during the first pulse where the helium is relatively mobile. As damage accumulates, the concentration of helium increases due to its decreased mobility. It is also shown that the self-

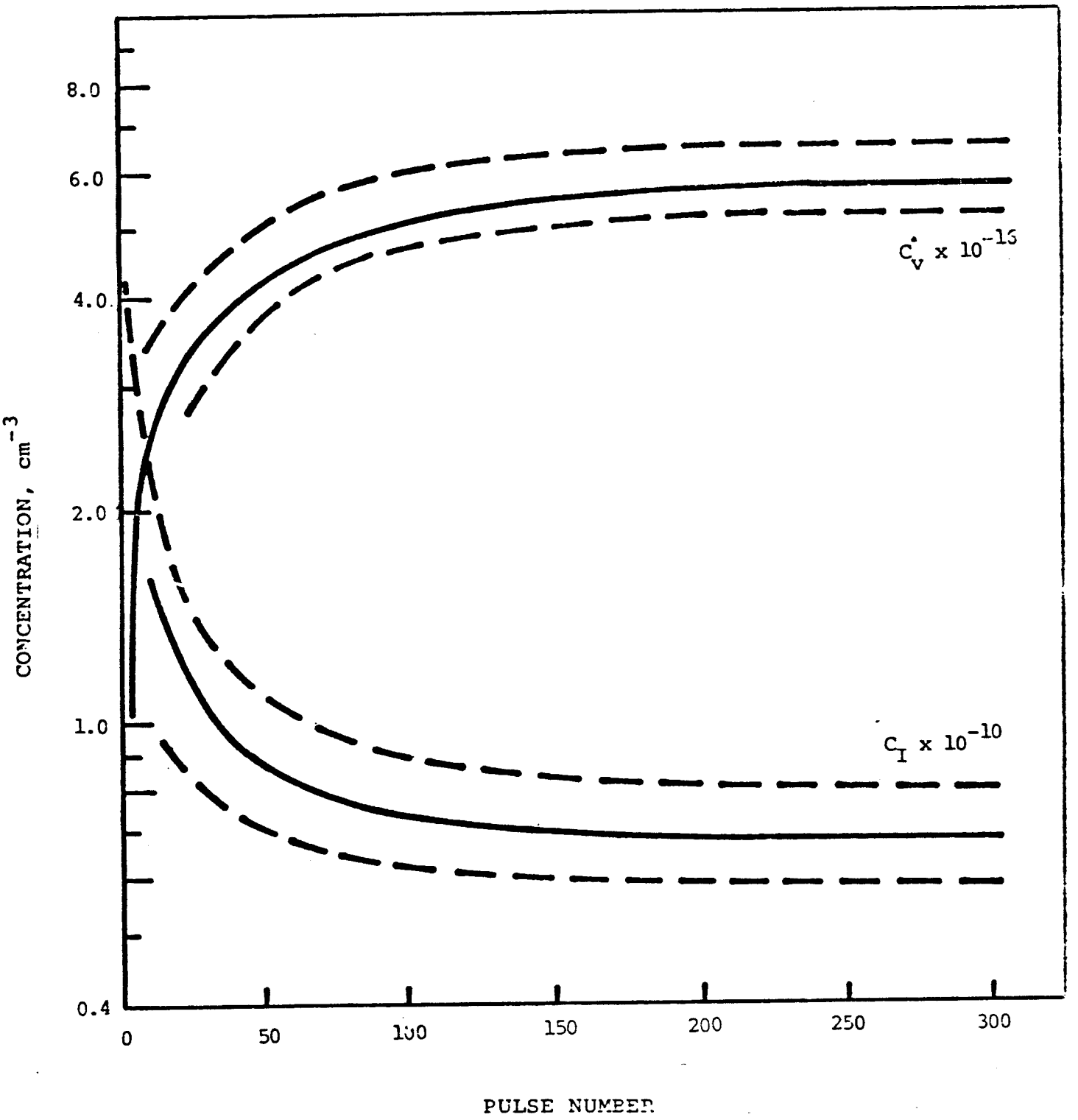

Fig. VIII.4-4 Concentrations of vacancies and interstitials for the first 300 pulses.

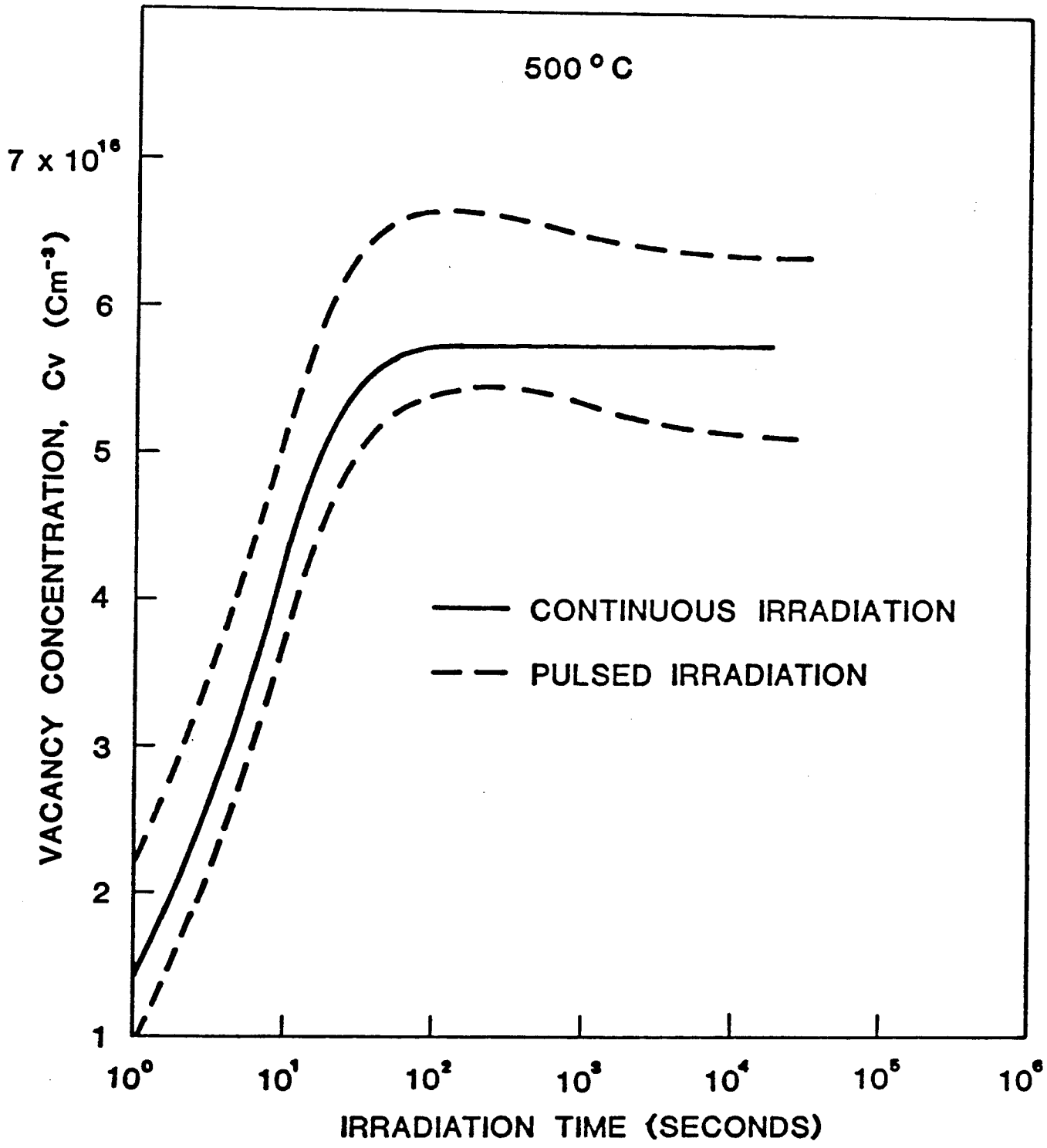

Fig. VIII.4-5 Concentration of vacancies up to 80000 pulses.

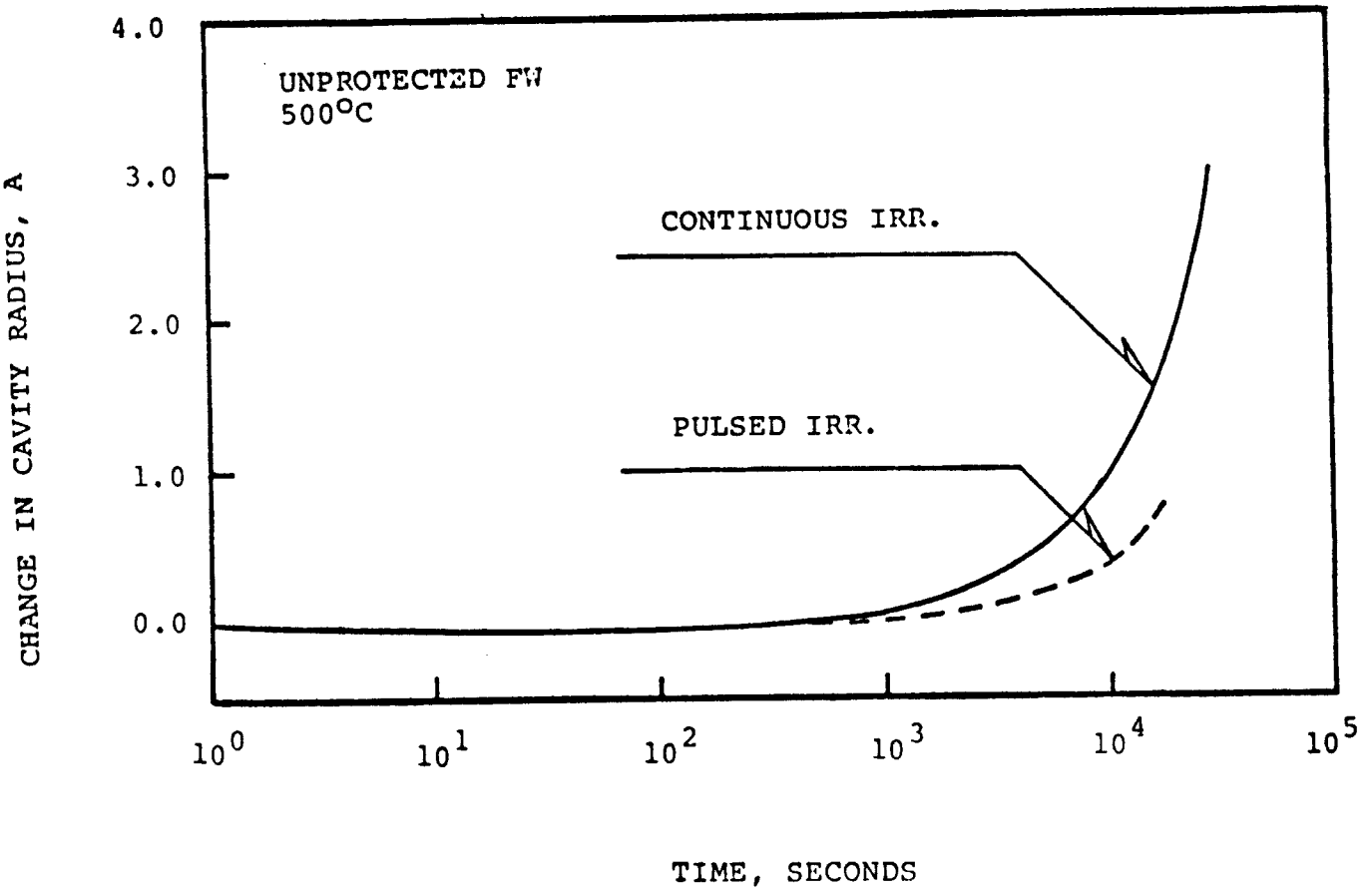

Fig. VIII.4-6 Change in cavity radius vs. time of irradiation.

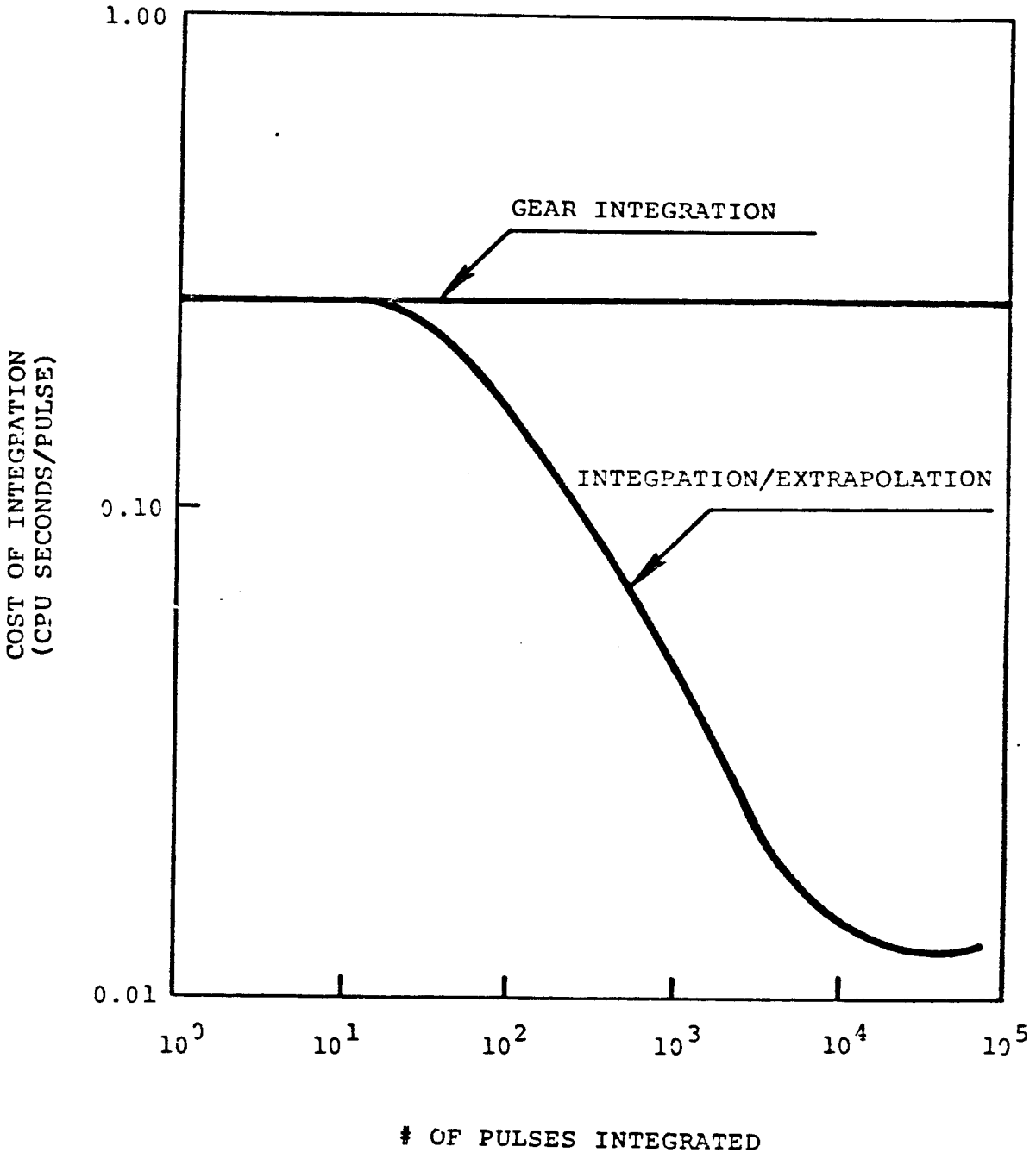

Fig. VIII.4-7 Cost comparison for two computational methods used.

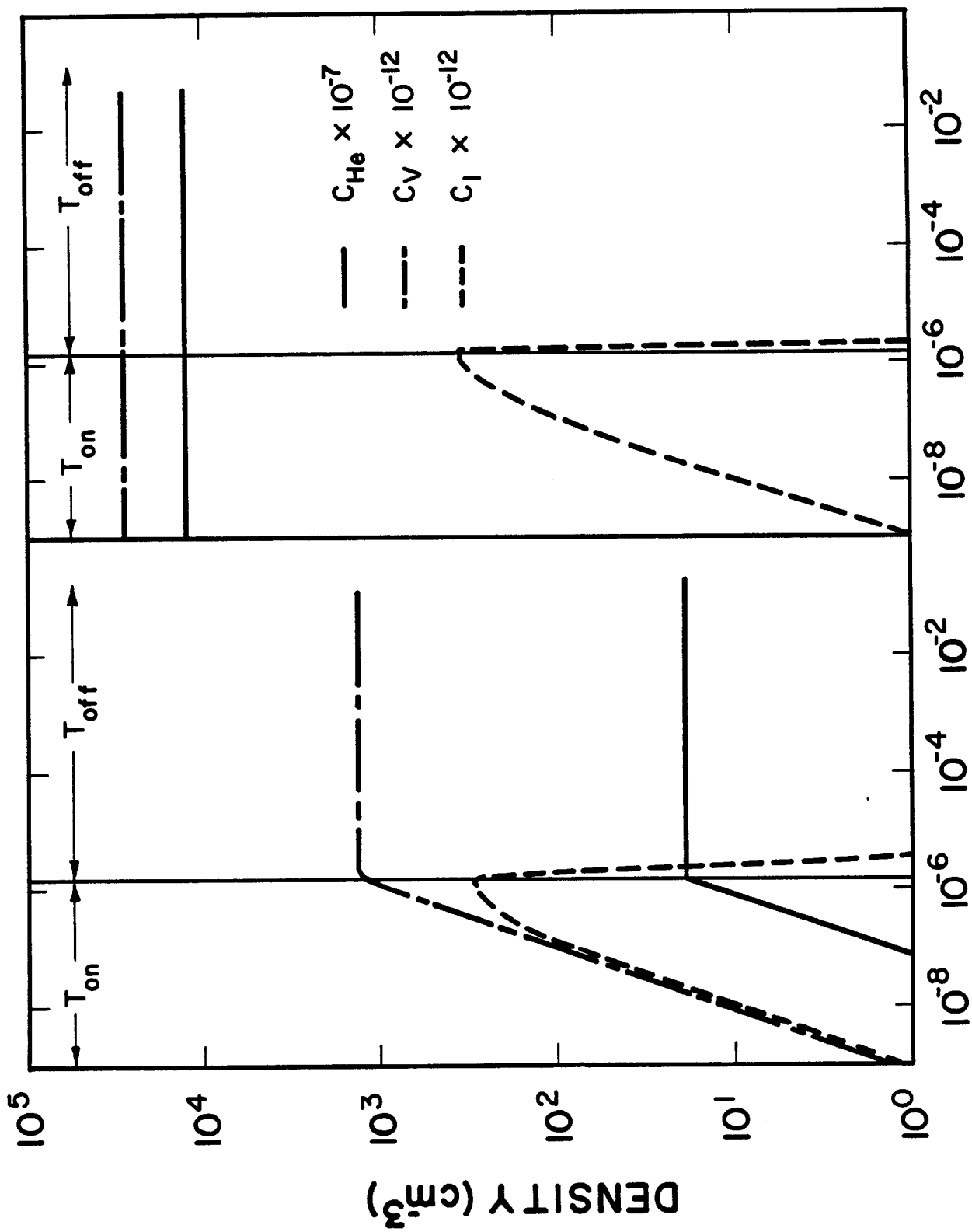

Fig. VIII.4-8 Concentration of vacancies, interstitials, and He atoms, during the first pulse and pulse 615.

Table VIII.4-3 Radiation Damage Parameters for the Protected First Metallic Wall

	First Wall	Half Ref. Thickness	Full Ref. Thickness
T_{on}, πs	1.5	2.0	2.4
T_{cycle}, s	0.2	0.2	0.2
dpa/yr	2.7	0.32	0.028
appm He/yr	0.364	0.0112	5.4×10^{-4}
He/dpa	0.135	0.035	0.019
$dpa/s_{inst.}$	1.14×10^{-2}	1.02×10^{-3}	7.4×10^{-5}
$He/s_{inst.}$	1.54×10^{-9}	3.56×10^{-11}	1.4×10^{-12}

interstitials diffuse significantly during the pulse on-time, while both vacancies and helium remain in the matrix during this short period. The helium diffusion coefficient is shown in Fig. VIII.4-9 as a function of the pulse number.

Equivalent steady state calculations were made for the peak damage position in the first wall. Figure VIII.4-10 shows the results of these calculations where $\frac{\Delta V}{V}$, the cavity average radius, and the concentration are shown as functions of irradiation time. The maximum swelling is shown to be insignificant over the first wall lifetime at 450°C ($< 10^{-3}\%$).

In order to understand this low value of swelling, we developed a simplified model for the partitioning of gas atoms in cavities. The model assumptions are:

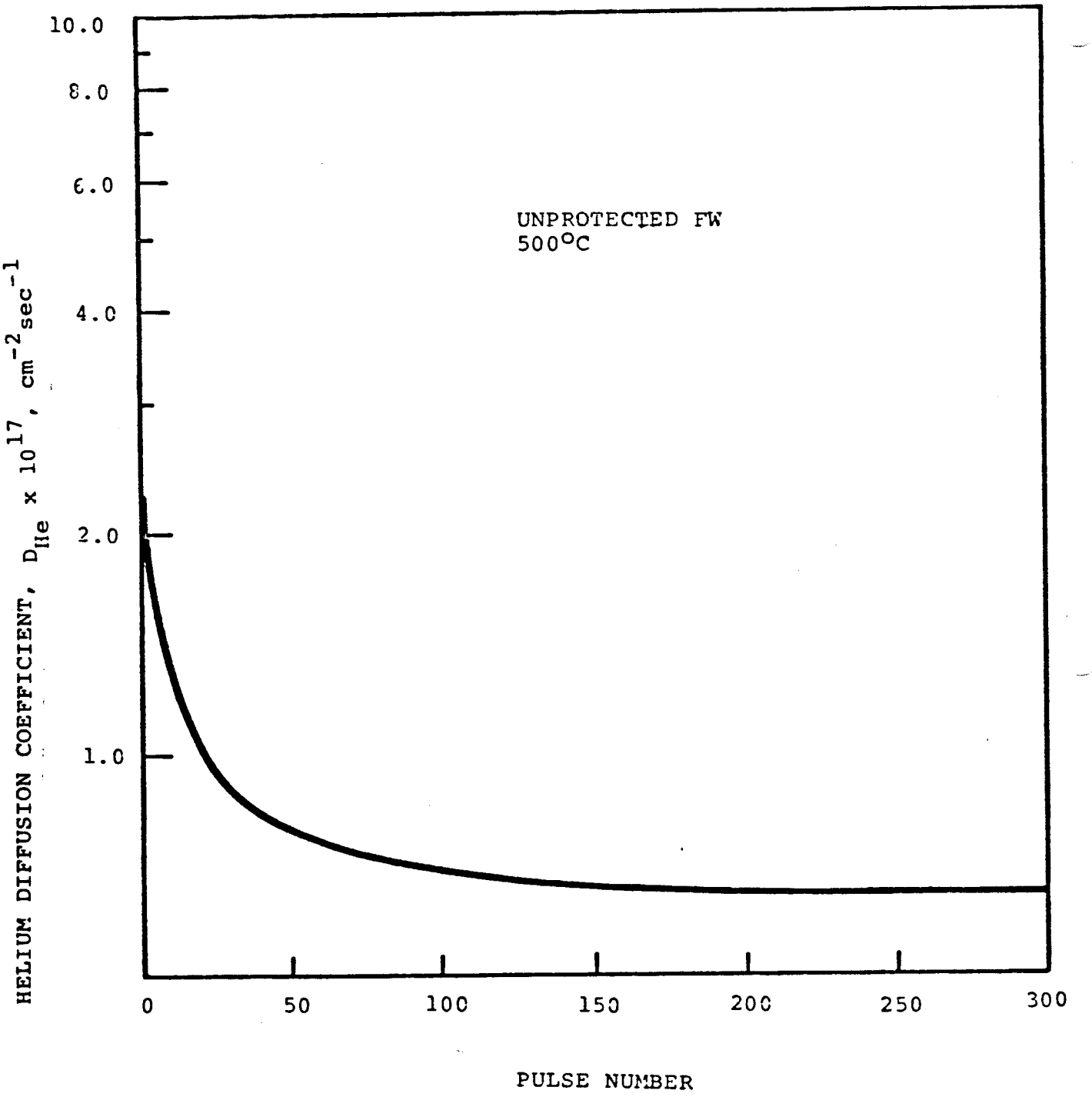

Fig. VIII.4-9 He diffusion coefficient as a function of pulse number.

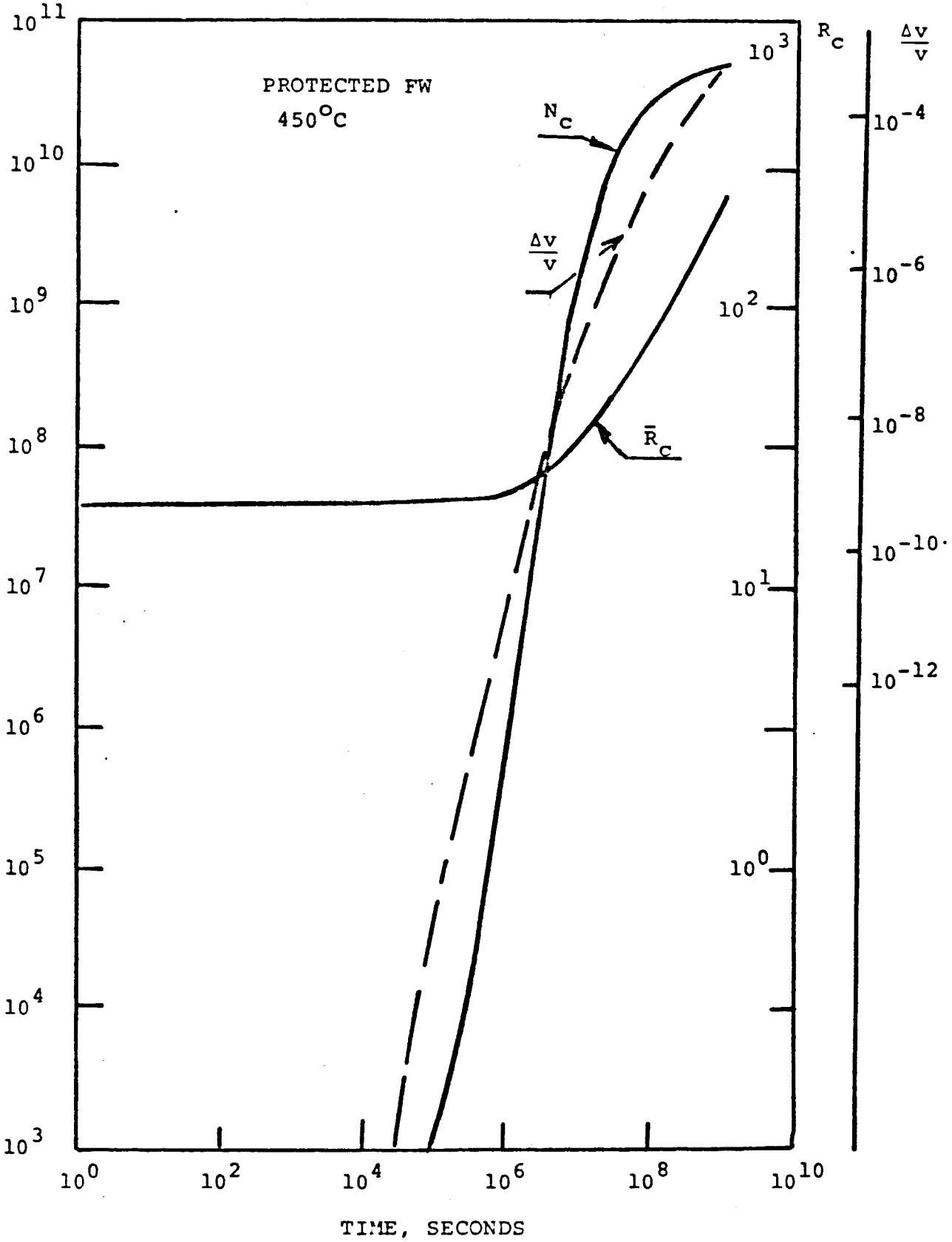

Fig. VIII.4-10 $\Delta v/v$, cavity average radius, and concentration as function of irradiation time.

(1) Continuous irradiation.

(2) HFIR cavity density for 316 SS

$$N_C = 6.642 \times 10^{22} \exp(-0.023\ T(K))$$

(3) Cavities are equilibrium bubbles.

(4) Van der Wall's equation of state.

(5) All gas is in cavities.

The calculated swelling, based on this model is shown in Table VIII.4-4. These simplified calculations indicate that the maximum amount of swelling will again be small over the lifetime of the wall. It is concluded therefore the swelling is not a major design problem, and lifetime will be more limited by other considerations (such as embrittlement at low temperature and creep rupture at high temperature).

Table VIII.4-4 Percent Swelling for the Protected First Wall

T, °C	1 yr	10 yrs	30 yrs
300	0	6.4×10^{-4}	1.93×10^{-3}
400	6.42×10^{-5}	6.6×10^{-4}	1.97×10^{-3}
500	6.6×10^{-5}	3.0×10^{-4}	1.58×10^{-3}
600	3.04×10^{-5}	9.7×10^{-4}	5.0×10^{-3}

VIII.4.6 Conclusions

From our study of helium behavior in the HIBALL design, we conclude the following:

(1) Helium migrates interstitially by a trapping/detrapping mechanism.

(2) The He/dpa ratio is the parameter that significantly affects cavity nucleation.

(3) Maximum nucleation will be in the first wall.

(4) A successful new integration/extrapolation technique has been developed for pulsed systems:

CPU time → down by ~ 20

Error → up by ~ 1-4%

(5) The cavity density in pulsed irradiation is higher than continuous irradiation only before significant helium diffusion occurs.

(6) Fluctuations in point defect concentrations due to pulsing lead to a smaller growth rate of cavities.

(7) Overall swelling due to pulsing will be smaller than corresponding continuous irradiation.

(8) Swelling will not be a life-determining factor for the HIBALL design.

References for Section VIII.4

1. D. Kramer, H.R. Brager, C.G. Rhodes, and H.G. Park, J. Nucl. Mat. 26, 121 (1968).

2. E.E. Bloom, Radiation-Induced Voids in Metals, ed. by J.W. Corbett and L.C. Ianniello, CONF-71061, U.S. Atomic Energy Commission, Washington, D.C., 1972, p. 1.

3. G.L. Kulcinski, D.G. Doran, and M. Abdou, Properties of Reactor Structural Alloys After Neutron or Particle Irradiation, ASTM-STP-570, American Society for Testing and Materials, Philadelphia, PA, 1975, p. 329.

4. R.G. Mills, "A Fusion Power Plant," Princeton University, MATT-1050, 1974, p. 292.

5. B. Badger et al., "UWMAK-I," University of Wisconsin Fusion Design Memo UWFDM-68, Vol. I, (1973).

6. International Tokamak Reactor Zero Phase, R.S. Pease, Chairman, International Atomic Energy Agency, Vienna, available from UNIPUB, new York, 1980, p. 384.

7. G.R. Odette and S.C. Langley, Radiation Effects and Tritium Technology for Fusion Reactors, ed. by J.S. Watson and F.W. Wiffen, Vol. I, CONF-750989, National Technical Information Service, Springfield, VA, 1976, p. 395.

8. F.V. Nolfi, Jr., A. Taylor, D.I. Potter, S.C. Agarwal, and B. Okray Hall, Trans. Am. Nucl. Soc. 26, 190 (1970).

9. F.V. Nolfi, Jr., and Che-Yu Li, Nucl. Technol. 38, 405 (1978).

10. K. Farrell, M.B. Lewis and N.H. Packan, Scripta met. 12, 1121 (1977).

11. W.D. Wilson and C.L. Bisson, Phys. Rev. B1, 3510 (1970).

12. R.J. Reed, Rad. Effects 31, 129 (1977).

13. F.A. Smidt, Jr., and A.G. Pieper, Properties of Reactor Structural Alloys After Neutron or Particle Irradiation, ASTM-STP-570, American Society for Testing and materials, Philadelphia, PA, 1975, p. 352.

14. W.D. Wilson and C.L. Bison, Rad. Effects 19, 53 (1973).

15. M.R. Hayns, J. Nucl. Mat. 59, 195 (1976).

16. N.M. Ghoniem and D.D. Cho, Phys. Stat. Solidi 54, 171 (1979).

17. Mayer et al., to be published, J. Nucl. Mat.

18. N.M. Ghoniem and G.L. Kulcinski, Rad. Effects 39, 47 (1978).

19. D.D. Cho and N.M. Ghoniem, "The Initial Stages of Point Defect Clustering in Fusion Reactor First Wall," Univ. of California-Los Angeles, UCLA-ENG-7935, 1979.

20. N.M. Ghoniem and M.L. Takata, "A Theory for the Interaction of Helium and Displacement Damage in Fusion Reactor Structural Materials," submitted to J. Nucl. Mat.

21. A.C. Hindmarch, Lawrence Livermore Laboratory Report, UCID-3001, (1974) rev. 3.

22. R. Schafer and N.M. Ghoniem, "EXPRESS: A Computer Code for the Integration/Extrapolation of Pulsed Rate Equations for Stiff Systems," UCLA report, 1981.

IX Maintenance

IX.1 Radiation Environment

The calculations presented in section VI.3 showed that the dose outside the shield was acceptable during and following operation. However, the calculations presented in section VI.3.5 indicated that very high levels of activity will be associated with the structure in the INPORT region and the first wall and reflector. In addition, neutron streaming will produce activity in the vacuum lines and pumps, the beam ports, and the beam dump. The activity generated in those parts of the system that are struck by heavy ions must also be considered. The consequences of this for maintenance is that dose levels will be so high that remote maintenance will be required for all major tasks such as replacement of INPORT tubes, service of vacuum systems, coolant lines, magnets, etc. The following sections indicate, at least in a schematic fashion, the features of the design that have been incorporated to carry out these tasks and how they might be performed.

IX.2 Cavity Components

IX.2.1 Introduction and Maintenance Philosophy

A mechanical description of the cavity was given in Section VI.1.2. In this section we will outline the procedures and maintenance philosophy for the internal cavity components.

There are essentially only two kinds of cavity components which will require periodic replacement due to radiation damage; they are the radial blanket modules and the upper blanket modules. These blanket modules were designed with maintainability as a prime consideration.

Figure IX.2-1 shows a cross section of the cavity. The upper blanket covers the top of the cavity and is divided into 30 identical modules. Each module has one supply header connected to it at the upper outer periphery. The coolant circulates through the blanket and exits through a tube which connects with the radial blanket. The coolant from the upper blanket then drains through the back tubes of the radial blanket.

During operation when the upper blanket is filled with $Li_{17}Pb_{83}$, the upper blanket modules are supported on the reflector by means of studs. These studs fit in milled slots in the reflector and are locked to it by means of a latching mechanism. When the upper blanket modules are drained, the latching mechanism can be deactivated and then the reflector and shield is free to rotate about the central axis while the blanket modules remain in place. At this time the modules are supported on the outer edge and on a central hub. Figure IX.2-2 is a view of the upper blanket from inside the reactor cavity showing the coolant drain tubes and the vacuum system ducts. In Fig. IX.2-3 are several views of an upper blanket module. Support studs are shown only at one location but in principle there can be more of them along the length of the module. The cross sections show details of the structural frame and the

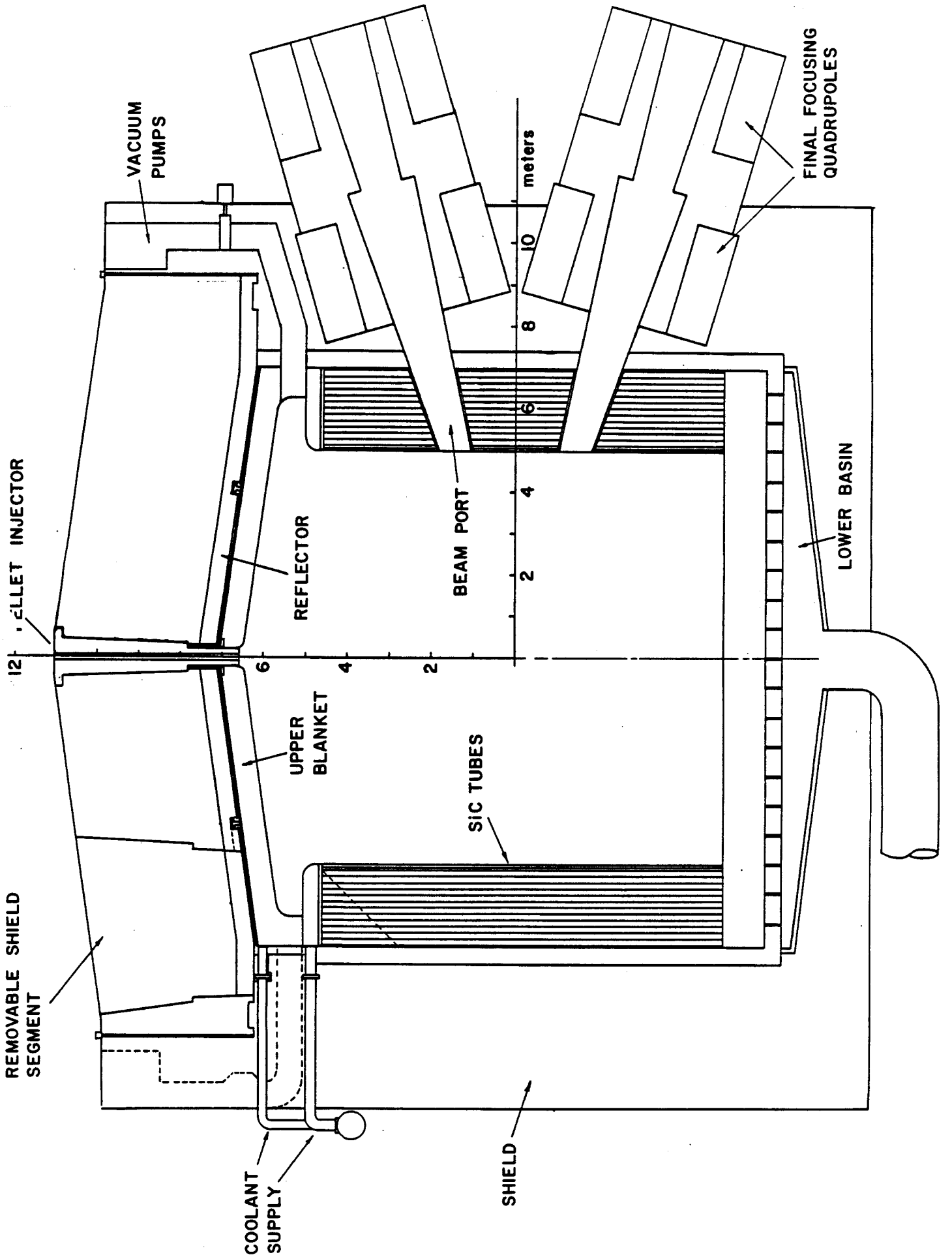

Fig. IX.2-1 Cross section of reactor cavity.

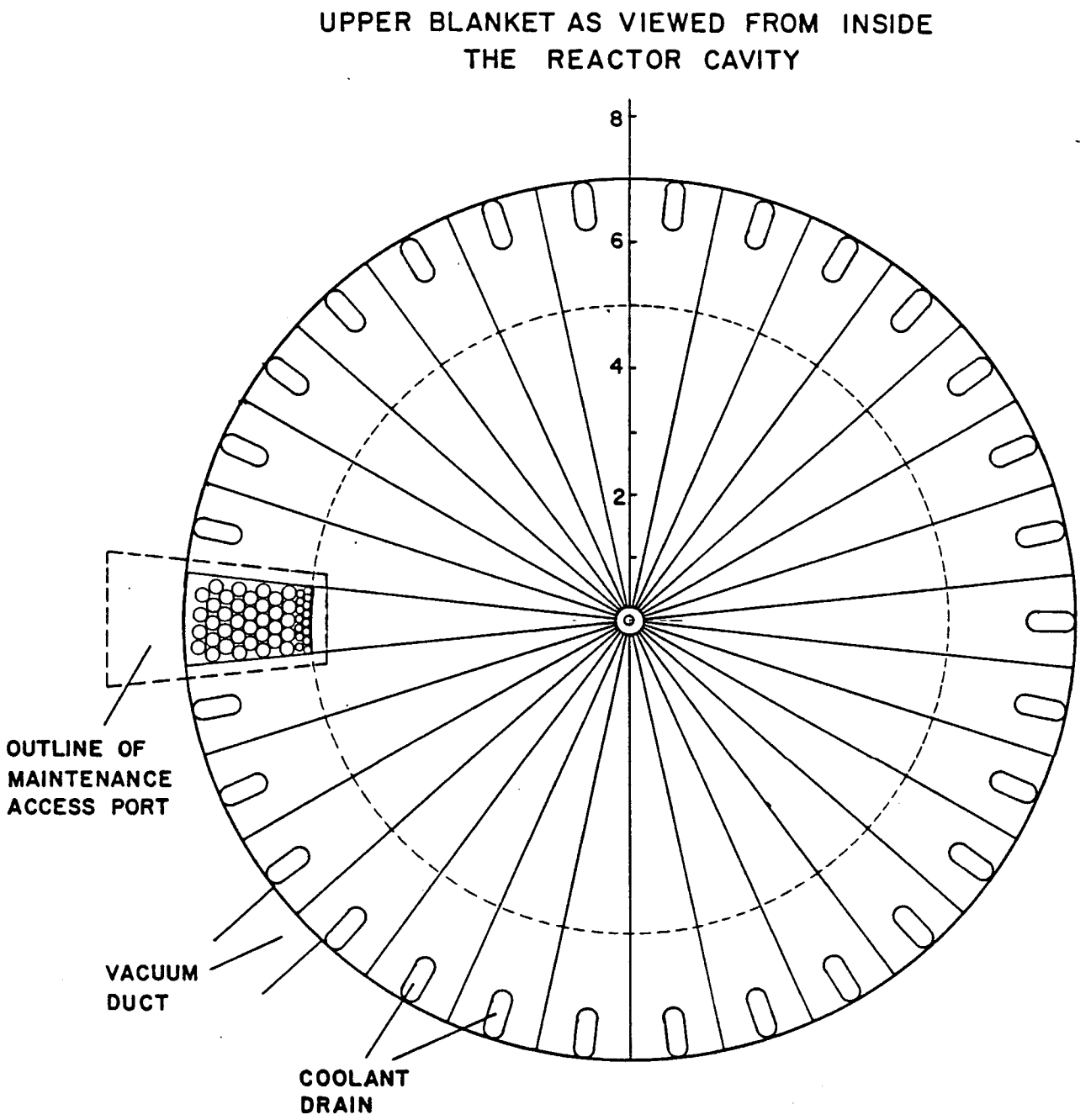

Fig. IX.2-2 Upper blanket as viewed from inside the reactor cavity.

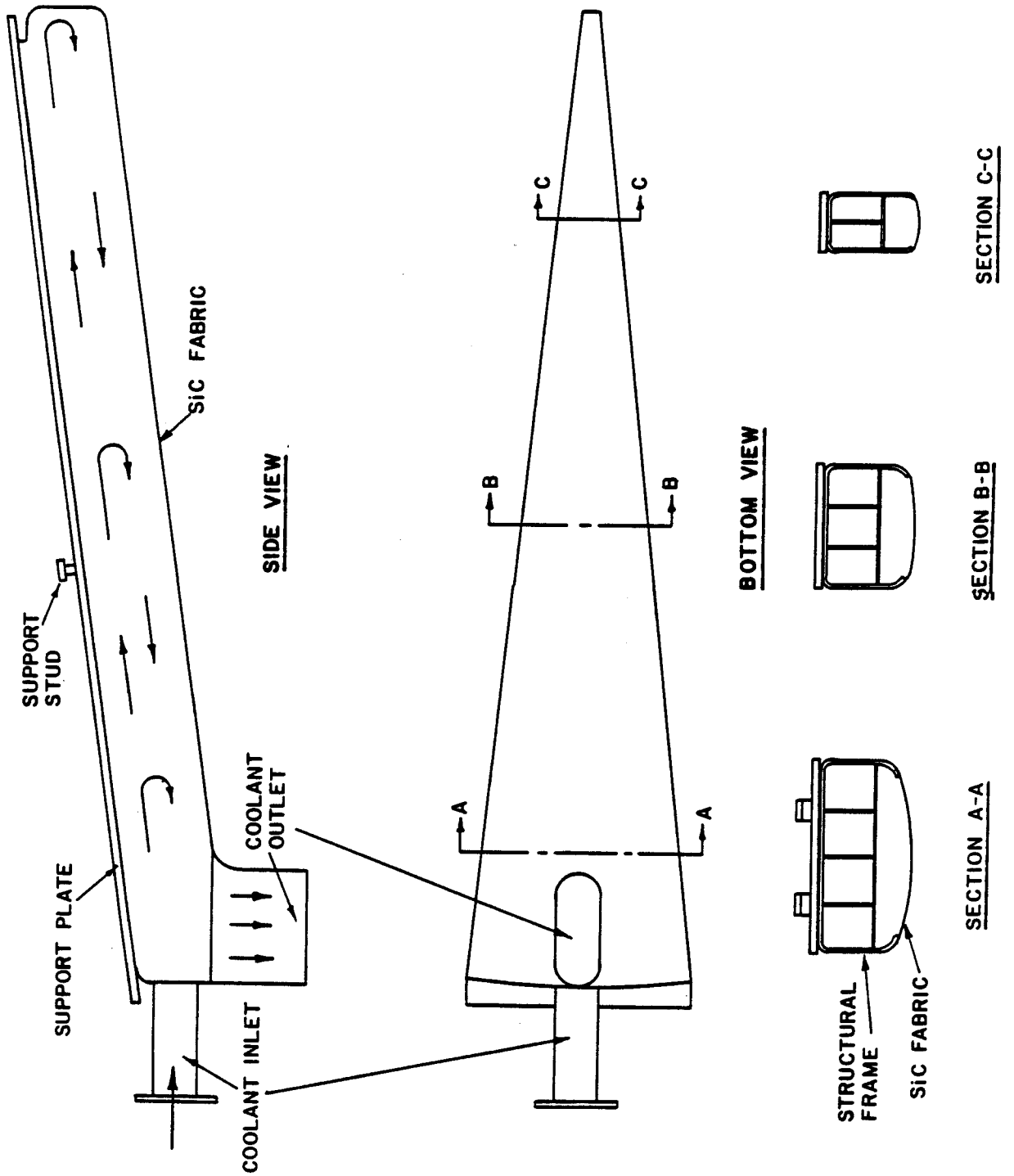

Fig. IX.2-3 Design of an upper blanket module.

SiC fabric which surrounds the frame entirely. Arrows in the side view indicate the direction of coolant flow.

The radial blanket is also divided into 30 equal modules. An outline of a single module and its SiC tubes is superimposed on Fig. IX.2-2 where the dotted line indicates the first surface. Each module consists of a distribution manifold which is a part of the upper tube support plate, the SiC tubes and the lower restraining plate. Ten out of the thirty modules have two beam ports built in. Each module is attached to the 40 cm thick reflector by means of 4 equally distributed struts welded to the HT-9 support plate. The struts have tees machined on the ends which fit into milled slots in the reflector. Pulling up on a module retracts the struts from the slots in the reflector and disengages them.

The maintenance philosophy that has been adopted for the HIBALL cavities depends on five key features. They are:

1. The reactor cavity is built below grade such that the maintenance hall essentially sits on top of it as shown in Fig. IX.2-4.
2. The upper reflector and shield are designed to rotate about the central axis while the upper blanket remains stationary.
3. Upper and radial blanket modules can be removed into the maintenance hall through an access port in the upper shield. A shielded plug is placed in the port during reactor operation.
4. The unprotected central hub of the target injector can be pulled out from the outside for replacement.
5. Remote viewing devices (TV camera, etc.) can be inserted through the central aperture devoted to the target injector. The target injector unit can be removed vertically into the maintenance hall.

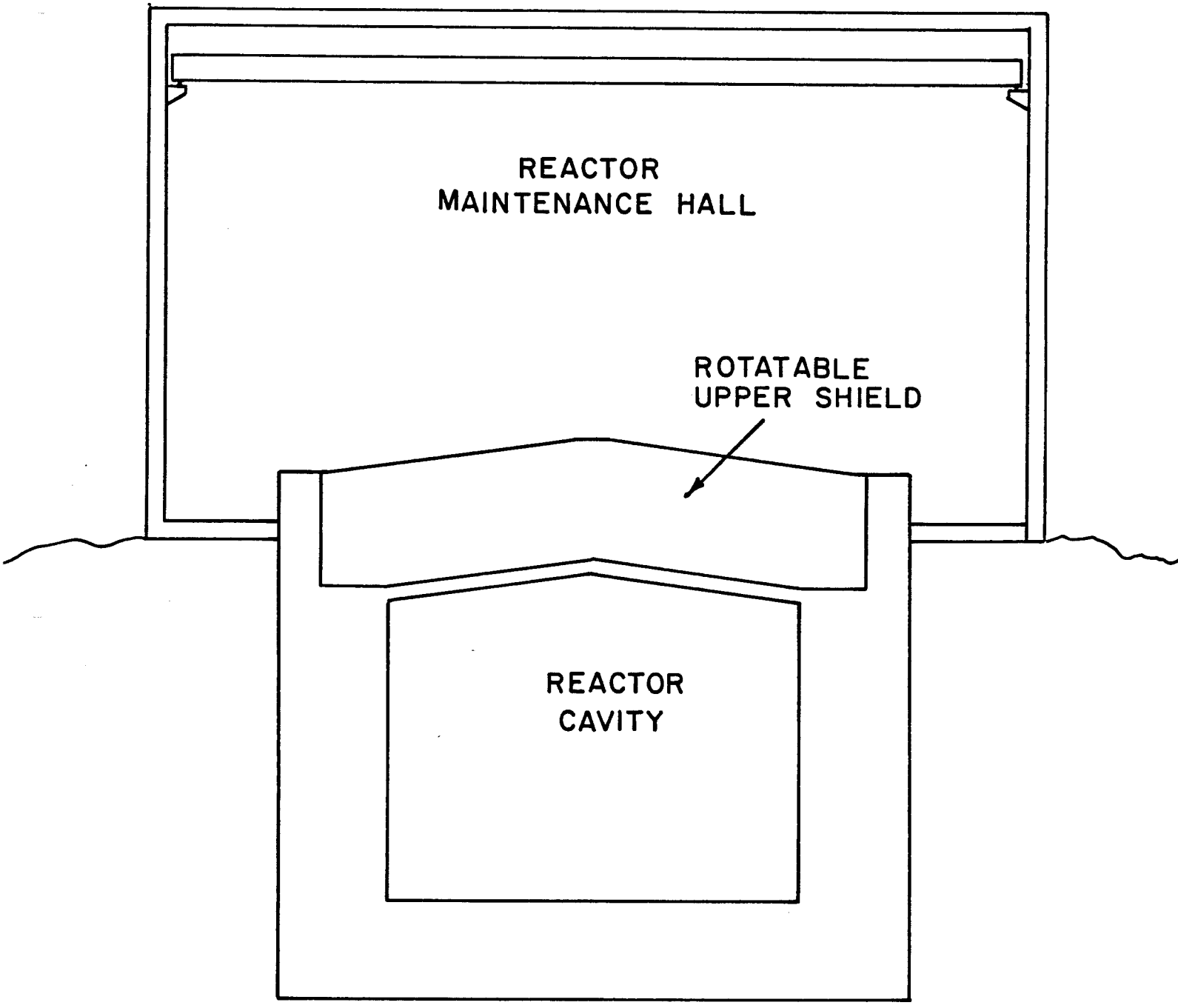

Fig. IX.2-4 Cross section showing reactor cavity below grade with maintenance hall above.

In the following sections we will address specific aspects of blanket maintainability, namely, preparation for blanket replacement, remote disconnection and connection of coolant lines and removal and replacement of blanket modules.

IX.2.2 Preparation for Blanket Maintenance

In preparing the cavity for blanket replacement many preliminary operations have to be carried out. The list below enumerates the key operations that can be performed during a 24 hour period after shutdown while the short lived radio-isotopes, in particular Mn-56, are decaying.

- Vacuum ports are valved off to prevent contamination of the cryopumps with undesirable gasses and the cryosurfaces are warmed up.
- Beam lines are isolated from the cavity by valves.
- The $Li_{17}Pb_{83}$ is drained from the cavity entirely.
- The $Li_{17}Pb_{83}$ coolant is drained from the reflector and the reflector is hooked up to an auxiliary cooling system, perhaps of helium gas. The reflector is cooled sufficiently to maintain its temperature above the ductile-brittle transition level. This will also keep whatever residual $Li_{17}Pb_{83}$ molten and will prevent freezeup of the blanket support systems.
- The cavity is brought up to atmospheric pressure with air.
- The upper shield seal between the rotatable and stationary shield components is disconnected.
- The plug in the upper shield access port is unsealed and removed.
- The target injector is removed and remote viewing devices are inserted in its place.
- The mechanical latch which locks the upper blanket modules to the reflector is deactivated making it possible to rotate the reflector/shield.

IX.2.3 Disconnecting and Connecting Coolant Lines

The breeding/cooling material selected for HIBALL, $Li_{17}Pb_{83}$ is an excellent solder. We feel we should take advantage of this fact in designing the means for connecting and disconnecting the coolant lines. The idea shown in Fig. IX.2-5 is to make a coupling with a wide enough flange such that the $Li_{17}Pb_{83}$ forms a frozen barrier at the outer periphery. A mechanical latch is used to apply pressure between the flanges and provide restraint against displacement. A heater must be provided to melt the connection during disassembly. On the other hand, because of the high temperature surroundings in the vicinity of the joint, it may be necesary to actively cool the edges of the stationary flange. The coolant is turned off to melt the joint. This is truly a remotely maintainable self-healing coupling which is relatively easy to manipulate.

In a practical sense, for this scheme to work entirely automatically, the following sequence must be followed:

Disconnecting a Coolant Joint

- The breeding/cooling material is drained out.
- The heater on the flange is turned on, or alternatively, the coolant on the flange edge is turned off.
- The mechanical latch is deactuated to release the pressure between the flanges.
- The stationary half of the joint is retracted to provide clearance for uncoupling the joint.

Connecting a Coolant Joint

- The flanges are aligned and the conical surfaces are mated. The newly inserted blanket module will have a flange which has been appropriately fluxed.

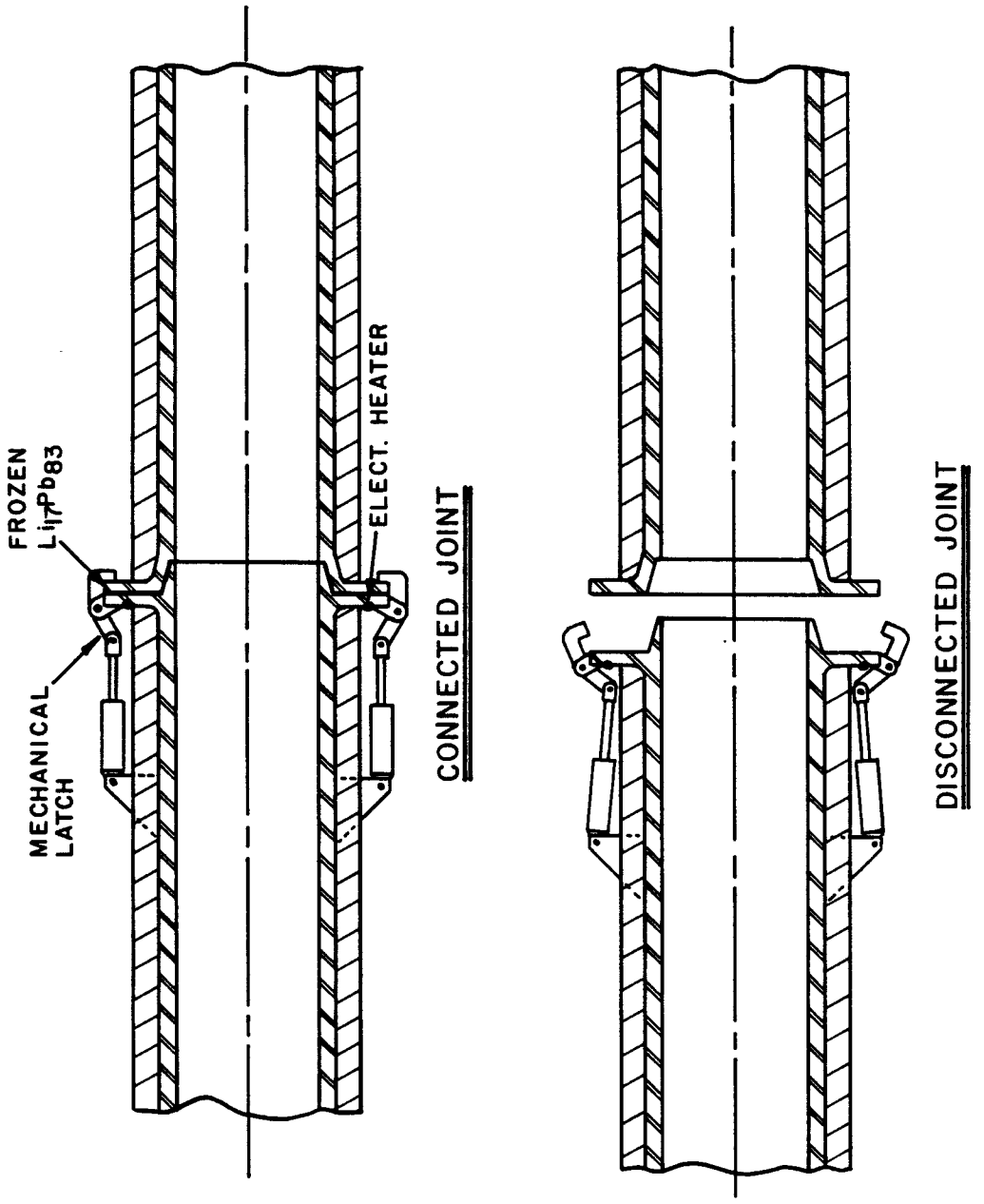

Fig. IX.2-5 Coolant tube remote joining concept.

- The mechanical latch is actuated and the joint is immobilized.
- As the breeding material is admitted into the header it forms a frozen seal on the edge between the flanges.

IX.2.4 Replacing Blanket Modules

Figure IX.2-2 shows the outline of the maintenance access port superimposed on a view of the upper blanket and Fig. IX.2-6 shows an upper blanket module being removed through the access port.

Following the preparation outlined in section XI.2-2, the upper shield/reflector is rotated and made to index onto the blanket module to be replaced. Once the coolant line is disconnected, an overhead crane in the maintenance hall equipped with a special fixture is attached to the upper blanket module. In order to decouple the module from its supports, it has to be lifted up in the back and then pulled radially outwards. When the support studs clear the slots in the reflector, the blanket module is tilted forward as shown in Fig. IX.2-6 and is lifted out of the cavity into the reactor hall.

With an upper blanket module removed, the radial blanket module immediately below it is now visible through the access port. Another special fixture is attached to it and is used to extract it vertically through the access hatch as shown in Fig. IX.2-7. After the coolant line is disconnected, an upward pull on the module disengages the tee sections on the upper support plate struts from the milled slots in the reflector. Once engaged, the whole module is free to be removed from the cavity.

Replacing the spent modules with new ones entails reversing the process outlined above. A new radial blanket module is inserted into the cavity, attached to the reflector and the coolant line. It is followed by a vertical blanket module which is also inserted and the appropriate attachments

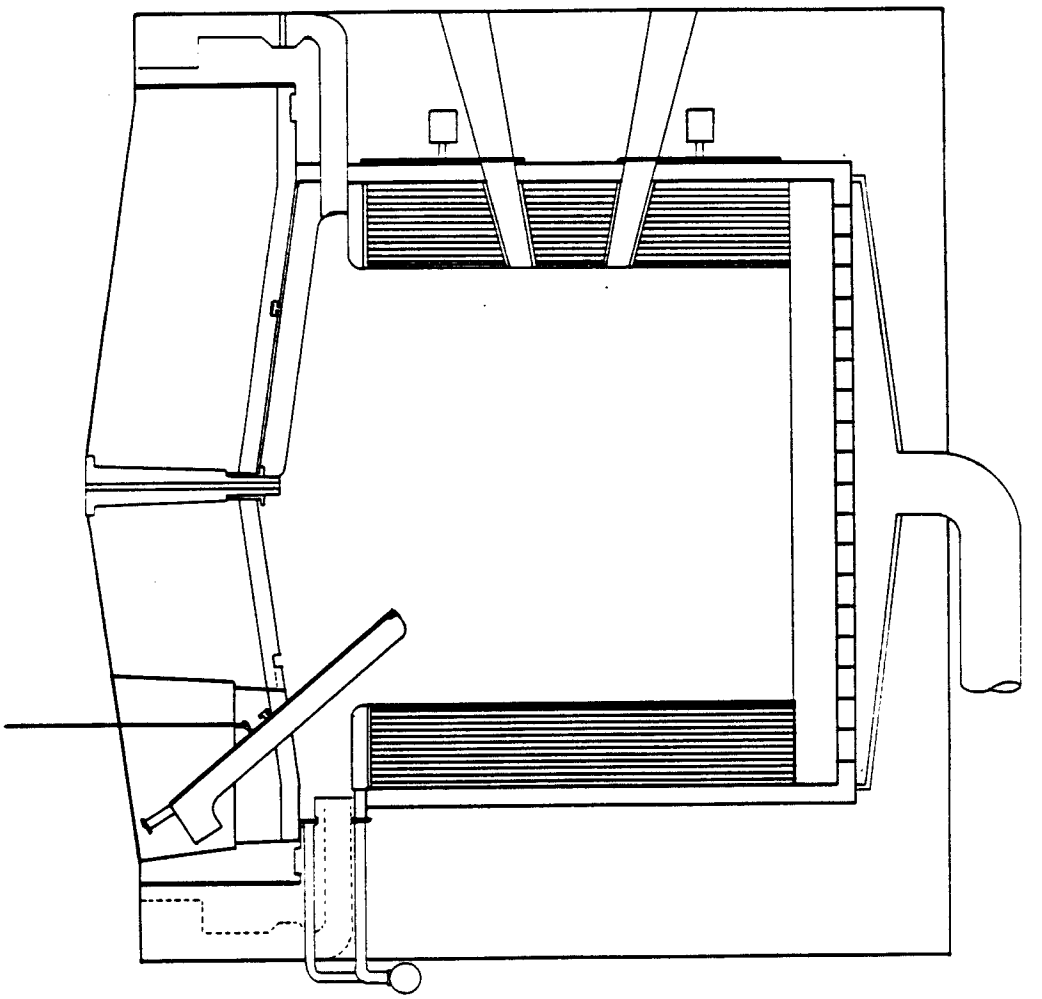

Fig. IX.2-6 Cross section showing removal of an upper blanket module.

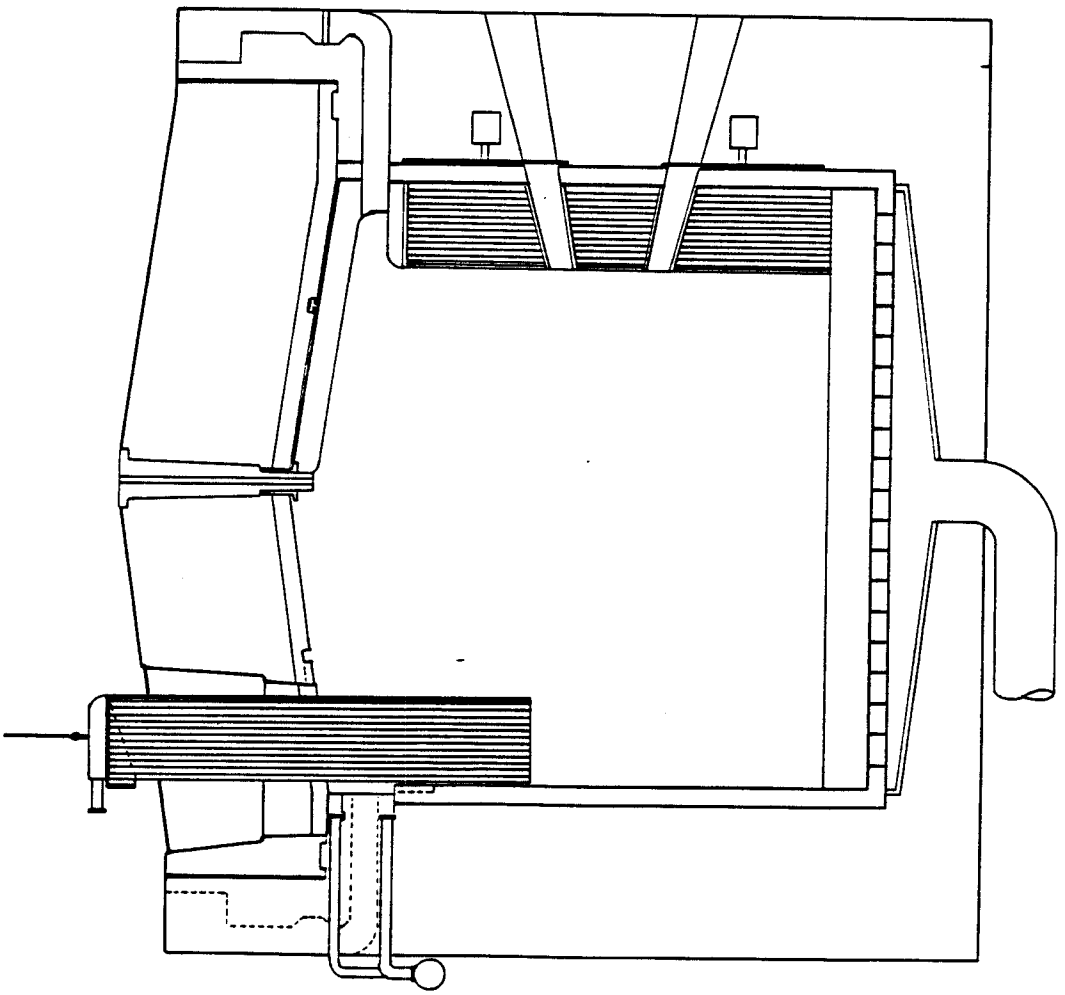

Fig. IX.2-7 Cross section showing removal of a radial blanket module.

performed. The upper reflector/shield is then rotated to the next location and the same procedure repeated.

Although the blanket modules are large and bulky, they are quite light once the breeding material has been drained from them. For example, the mass of an upper blanket module is ~ 1.5 tonnes and a radial module ~ 1.8 tonnes. The mass of the shield plug is ~ 150 tonnes, well within the capacity of the overhead crane in the maintenance hall.

When blanket replacement is completed, the cavity must be returned to operational status. The upper shield is rotated to a designated location, the access port is plugged, the seals are secured and the support mechanism which locks the upper blanket modules to the reflector is actuated. The cavity is now ready for evacuation and initiation of startup procedures.

A summary of the attractive features of this maintenance concept is given below:

Summary

- Preassembled blanket modules with integral support manifolds and beam tubes minimize "in reactor" manipulation.
- Coolant headers, vacuum pumps and ducts remain undisturbed.
- Number of coolant connections is minimized and the designed joints can be disconnected remotely with relative ease.
- Although bulky, the blanket modules are light.
- Operations are limited to simple linear translation and vertical lifting.
- The unprotected central hub of the target injector can be easily removed for servicing.

X Preliminary Cost Estimate

X.1 Basis for Costing

The following list enumerates the basis for the costing:

a. Methodology adopted from the US-DOE "Fusion Reactor Design Studies - Standard Accounts for Cost Estimates," PNL 2648,

b. Unit costs for the cavities taken from the US-INTOR study,

c. Driver and beam transport costs by GSI-Darmstadt,

d. Constant dollars used - no escalation due to inflation, and

e. Cost of target factory amortized over 30 years and accounted for in the target costs.

X.2 Driver and Beam Transport

The cost estimate for the HIBALL driver and beam transport system is of a preliminary nature and in many cases does not include development costs or redundancy of critical elements.

For the driver and beam lines, the most costly items have been derived from current projects which are comparable in size or magnitude. The linac costs are based on the German SNQ project and the superconducting element, on the HERA proposal which relied mainly on magnet fabrication at FNAL. The costs of the induction modules linac were based on available data from the LBL fusion linac study. Assembly and testing has been included for the major cost items but not for the many smaller systems. It should be mentioned that these costs do not reflect any optimization or simplification which may result from more detailed analysis.

Table X.2-1 gives the linac costs and Table X.2-2 the costs of the transfer ring, the five condenser rings, the ten storage rings and all the associated beam lines. These costs were compiled at GSI-Darmstadt (FRG) and are given in DM with the gross values converted to dollars at the present conversion rate of 2.5 DM per U.S. dollar.

Table X.2-1 Linac Costs

in MDM

		($DM \times 10^6$)		($\$ \times 10^6$)
Source and injection	8 x 3.0	24		
RFQ linac	0.2 MDM/m x 160 m	32		
27 MHz Widerøe	0.15 MDM/m x 120 m	18		
54 MHz Widerøe	0.15 MDM/m x 208 m	31		
108 MHz Alvarez	0.1 MDM/m x 320 m	32		
324 MHz Alvarez	0.06 MDM/m x 2500 m	150		
Funnel section	1.2 MDM x 7	8		
Debuncher, energy + emitt. meas., beam dump		5		
			300	
RF < 108 MHz	1.75 MDM/MW x (20 + 26)	81		
RF 108 MHz	1 MDM/MW x (23 + 72)	95		
RF 324 MHz	0.7 MDM/MW x (250 + 653)	632		
			808	
Controls		19		
Software		25		
			44	
Cooling		130		
Air condition		33		
El. power distribution		50		
Safety + communications		8		
			221	
Injection building	200 DM/m^3x60x60x20 m^3	14		
Linac low energy	9 kDM/m x 530 m	5		
Linac high energy	13 kDM/m x 2500 m	33		
Equipment building	130 DM/m^3 x 15x15x3000 m^3	88		
Operation building		28		
Workshop and stores		40		
			208	
			1581	632.4

Table X.2-2 Rings and Beam Transport Costs

		($DM \times 10^6$)		($\$ \times 10^6$)
Length of superconducting elements	31.4 km			
Cost per m incl. vacuum, controls, power supplies, refrigerator	38.5 kDM			
Total beam line and ring cost		1209		
Kickers and septa	1.5 MDM x 42	63		
Switching magnets	0.3 MDM x 36	11		
Beam rotator		4		
Beam combiner		6		
RF syst. in storage rings	5 MDM x 10	50		
Induction linacs		876		
Timing and controls		35		
Correction dipoles	0.7 x 80	56		
Final focusing	3.5 x 80	280		
Remote handling equipment		10		
Cooling plant + distribution		130	2730	
Ring tunnels	10 kDM/m x 14.7 km	147		
Transport tunnels	5 kDM/m x 24 km	120		
Utility buildings for rings	10 MDM x 4	40		
Refrigerator + power supply buildings	3 MDM x 20	60		
Maintenance building		40	407	
			3137	1254.8

X.3 Cavities

In the reactor cavities at the present level of design, the costing procedure consists simply of calculating the masses of materials used in the cavity and applying a unit cost which is based on a completely fabricated product. In places where such a method is impractical, for example in the area of cryopumps or cryogenerators, algorithms are used which relate the cost to the capacity of the system.

The unit costs and cost algorithms used in this study are derived from the guidelines adopted for INTOR. Prices given reflect only the material and fabrication costs. Engineering, assembly and contingency are assessed as a percentage of the direct costs.

Table X.3-1 gives the unit costs used in the cavities and Table X.3-2 summarizes these costs.

Table X.3-1 Unit Costs Used in HIBALL Cavity

		$ (1981)
1. Blanket		
Fabricated SiC		
10 cm diam. INPORT tubes	$/unit	5660
3 cm diam. INPORT tubes	$/unit	865.4
Upper blanket modules	$/kg	1500
Beam ports	$/kg	1500
HT-9 Structure	$/kg	45
$Li_{17}Pb_{83}$	$/kg	4.5
2. Reflector and Liner		
HT-9	$/kg	20
3. Shield		
Structure	$/kg	10
Concrete	$/m^3	250
4. Vacuum System		
Valves	$/unit	70,000
Cryopanels (algorithm used)		
Root blowers (algorithm used)		
5. Pipes and Headers		
36 cm diam. inlet pipes,	$/m	10,000
1.0 m diam. header	$/m	20,000

Table X.3-2 Summary of Cavity Costs

		$ x 10^6 (1981)	$ x 10^6 (1981)
Blanket			
SiC	INPORT tubes	18.384	
	Upper blanket	7.155	
	Beam tubes	2.777	
HT-9	Radial blanket	1.758	
	Upper blanket	1.882	
$Li_{17}Pb_{83}$		20.205	52.161
Reflector and Liner			
HT-9	Reflector	47.438	
	Other liner	1.883	
	Bottom drain	2.400	
	Upper latching mechanism	1.500	53.221
Shield			
Structure		73.000	
Concrete		4.471	77.471
Vacuum System			
Valves (30 + 2 spares)		2.240	
Cryopumps (He)		2.800	
Cryopanels (D_2T_2)		2.880	
Roots blowers		0.800	8.720
Pipes and Headers			
Coolant lines and flanges		2.520	
Headers		2.108	4.628
TOTAL/CAVITY			196.201

X.4 Remaining Direct Costs

The remaining major cost item in the reactor plant is the main heat transfer and transport system. This account is estimated at 560×10^6 and is broken down in the following manner:

Liquid metal pumps	225×10^6
Steam generators	175×10^6
Pipes/dump tanks/cleanup system	160×10^6

In the balance of plant, it was assumed that a 1000 acre site will be required at $5000/acre. The structures and site facilities take into account that the buildings for the linac, rings and beam line tunnels are already included in section X.2.

For the turbine plant equipment, the electric plant equipment and the miscellaneous plant equipment, we have used the guidelines provided by PNL-2987 "Fusion Reactor Design Studies Standard Cost Estimating Rules" prepared for the US DOE by Battelle Northwest. Table X.4-1 lists the direct costs for the reactor plant and the balance of plant.

Table X.4-1 Breakdown of Direct Costs

	$ x 10^6 (1981)	
Reactor Plant		
Reactor cavities (4)	785	
Pellet injectors (4)	12	
Main heat transfer system	560	
RF linac	632	
Transfer ring (1)		
Condenser rings (5)		
Storage rings (10)	1255	
Induction linac (20)		
Beam lines		3244
Balance of Plant		
Land and land rights	5	
Structures and site facilities	280	
Turbine plant and heat rejection	430	
Electric plant equipment	275	
Miscellaneous plant equipment	50	1040
		4284

X.5 Indirect Costs and Interest During Construction

As mentioned in section X.1, the guidelines given in PNL 2648 were used in arriving at the indirect costs.

Since this economic analysis is in constant dollars, the interest during construction is based on a 5% annual deflated cost of capital. An 8 year construction period was used on the assumption that the driver, reactor plant and balance of plant construction could be ongoing simultaneously. With the capital disbursed according to the classical S curve biased to the right, the interest during construction factor is 0.17 (PNL 2648). Table X.5-1 gives the breakdown of the indirect cost and the interest during construction.

Table X.5-1. Indirect Costs and Interest During Construction

		$ x 10^6 (1981)
Total Direct Costs		4284
Indirect Costs		
Construction Facilities (15% of TDC)	642	
Engineering & Cost Management (15% of TDC)	642	
Owners Costs (5% of TDC)	214	1498
Interest During Construction	983	983
5%/Annum Deflated Interest		
8 year Construction Period		
Grand Total Cost		6765

The net electric power output of HIBALL is 3768 MWe. Thus the capital cost is:

$$\text{Capital Cost} = \frac{\$6765 \times 10^6}{3768 \times 10^3 \text{ kW}} = \$1795/\text{kWe} \quad .$$

This can be compared with other recent fusion designs:

STARFIRE	2000
NUWMAK	2227
WITAMIR	2130

X.6 Busbar Costs

X.6.1 Target Costs

The cost of the target factory was amortized in the target costs and thus does not appear as a direct cost. We assumed a $\$200 \times 10^6$ target factory cost which, after the indirect costs and interest during construction were added became $\$316 \times 10^6$. Thus the target cost breakdown is as follows:

	cents/target
30 year amortization of target factory	2.4
Operation and maintenance (2% of capital cost)	1.4
Interest on capital (10% annual)	7.2
Material (D_2, plastic, etc.)	2.0
Profit	2.0
	15.00

At a 70% availability, the number of targets needed for all four cavities is 4.4×10^8/annum. The annual target cost is thus $\$66 \times 10^6$.

X.6.2 Operation and Maintenance

As provided in PNL 2648, the operation and maintenance was taken as 2% of the total capital cost, or $\$135 \times 10^6$.

X.6.3 Component Replacement

A two year lifetime was taken for the INPORT tubes and the upper blanket modules. The annual component replacement cost is thus $\$64 \times 10^6$.

X.6.4 Interest on Capital

A straight 10% annual interest on capital was used. Table X.6-1 gives the busbar cost.

Table X.6-1. HIBALL Busbar Costs

Assumptions: 70% availability

10% interest on capital

3768 MWe net power output = 2.31×10^{10} kWh/yr

$$\text{Busbar Cost} = \$ \frac{(66 \times 10^6 + 135 \times 10^6 + 64 \times 10^6 + 676.5 \times 10^6)\ 1000\ \text{mills/\$}}{2.31 \times 10^{10}\ \text{kWh}}$$

$$= 40.8\ \text{mills/kWh}.$$

Some of the other recently designed fusion power systems have the following busbar costs:

STARFIRE	35.1
NUWMAK	37.5
WITAMIR	36.1

APPENDIX

HIBALL PARAMETER LISTING #6

I. GENERAL PARAMETERS

	4/29/81	5/8/81	6/30/81
Average DT power - 17.6 MeV/fusion (MW)	8000	8000	8000
Target power (MW)	7873.6	7920	7920
Target multiplication	0.984	0.99	0.99
Target yield (MJ)	400	400	396
Ion beam pulse energy (MJ)	4.8	4.8	4.8
Overall accelerator efficiency (%)	26.5	26.5	26.7
Target gain	83	83	83
Fusion gain ηG	18.5	18.5	22
Blanket multiplication	1.27	1.274	1.274
Total nuclear thermal power (MW)	10149	10193	10193
Gross power		10233	10233
Gross thermal efficiency (%)	42	42	42
Gross electrical output (MW)	4168	4278	4298
Recirculating power fraction	0.2	0.2	0.123
Net electrical output (MW)	3309	3309	3768
# of chambers	4	4	4
Chamber repetition rate (Hz)	5	5	5
Chamber geometry	cylindrical	cylindrical	cylindrical
Chamber diameter (m)	14	14	14
Chamber height (m) (at vacuum wall)	10	10	10
Chamber alloy	HT-9	HT-9	HT-9
# of beam ports per chamber	20	20	20
Breeding material	$Pb_{83}Li_{17}$	$Pb_{83}Li_{17}$	$Pb_{83}Li_{17}$
Breeding ratio	1.25	1.25	1.25

II. TARGET PARAMETERS

	4/29/81	5/8/81	6/30/81
Composition			
D (mg)	1.61	1.6	1.6
T (mg)	2.42	2.4	2.4
DT load (mg)	4.0 (2.0)	4.0 (2.0)	4.0 (2.0)
Material #1 (mg)	PbLi 67.1	PbLi 67.1	PbLi 67.1
Material #2 (mg)	Pb 288	Pb 288	Pb 288
Burnup (%)	30 (60)	30 (60)	30 (60)
Total mass (mg)	359	359	359
Configuration (# of shells)	3	3	3
Target diameter (cm)	0.6	0.6	0.6
Absorbed ion energy (MJ)	4.8	4.8	4.8
No burn ignition temperature (keV)	5	5	5
Fuel ρR at ignition (g/cm^2)	2	2	2
Hot spot ρR at ignition (g/cm^2)	0.4	0.4	0.4
Pusher ρR at ignition (g/cm^2)	1	1	1
DT yield (MJ)	400	400	400
Target yield (MJ)	393.67	396	396
Target energy multiplication	0.984	0.99	0.99
Average DT power (MW)	8000	8000	8000
Target power (MW)	7873.6	7920	7920
Target gain	83	83	83
Neutron yield (MJ)	284.8	284.8	284.8
Neutron spectrum, $\bar{E}$ (MeV)	11.98	11.98	11.98
Neutron multiplication	1.046	1.046	1.046
Stopping Power (MeV-cm/mg)			
10 GeV Bi → Pb_{cold}		40	40
Bi → PbLi		65	65
Gamma yield (MJ)	0.6	0.6	0.6

	4/29/81	5/8/81	6/30/81	
Gamma spectrum, $\bar{E}$ (MeV)	1.53	1.53	1.53	
X-ray yield (MJ)	87.6	89.5	89.5	
X-ray spectrum - blackbody (keV)	see histo-gram	see histo-gram	see histo-gram	
Debris yield (MJ)	20.6	21.0	21.0	
Debris spectrum (keV/amu)	0.6	0.6	0.6	
Radioactivity production (Ci/target @ t = 0)	1.2×10^6	1.2×10^6	1.2×10^6	?
Radioactivity production (Ci/target @ t = 0.2 sec)				?
Target injection velocity (m/s)	1000	200	200	
Target injector type	gas gun	gas gun	gas gun	
Target tracking	KfK	KfK	KfK	
Target cost				

III. TARGET MANUFACTURE AND DELIVERY PARAMETERS

	4/29/81	5/8/81	6/30/81
Target manufacture			
Production rate (#/s)			
Material stored within target factory (kg)			
Deuterium			
Tritium			
Material #1			
Material #2			
Cost/target (cents)			
Target storage			
# of targets in storage			
Average target storage time (hr)			
Target delivery			
Longitudinal positioning tolerance (mm)			0.5
Lateral positioning tolerance (mm)			0.7
Target velocity (m/s)			200
Repetition Frequency (Hz)			5
Injection:			
Type			gas gun
Projectile (sabot+target) mass (g)			2
Propellant gas amount (Torr liters/shot)			608
Propellant gas			D_2
Total prop. gas handled (mg/shot)			141
Buffer cavity pressure, min, (Torr)			1
max, (Torr)			2
Buffer cavity volume (m^3)			0.88

	4/29/81	5/8/81	6/30/81
Injection channel diameter (mm)			10
Prop. gas entering reactor cavity (mg/shot)			1.6
Gas gun total efficiency			0.5
Gun barrel diameter (mm)			10
Pressure of prop. gas reservior (Bar)			5
Acceleration distance (m)			2
Acceleration (m/s^2)			10^4
Acceleration time (ms)			20
Total target travel time (ms)			80
Tolerance on total travel time (ms)			±5
Distance muzzle to focus (m)			12
Tracking:			
Lateral tracking			none
Longitudinal tracking, type			light-beam interception
Tracking position 1, distance from focus (m)			5.5
Tracking position 2, distance from focus (m)			3.0
Light beam diameter (mm)			0.2
Precision of arrival time prediction (μs)			±1
Duration of processing tracking results (ms)			1

IV. DRIVER PARAMETERS

	4/29/81	5/8/81	6/30/81
Ion			
Type	Bi	Bi	Bi
Charge state	+2	+2	+2
Energy (GeV)	10	10	10
Velocity v (m/s)	9.25×10^7	9.25×10^7	9.25×10^7
Beta, $\beta = v/c$	0.309	0.30875	0.30875
Gamma, $\gamma = (1 - \beta^2)^{-1/2}$	1.051	1.051	1.051
Magnetic stiffness (Tesla • meters)		105.4	107.7
Mass number	209	209	209
Source	Elsire	"Elsire" (reflex)	"Elsire" (reflex)
Accelerator			
Type	RF	RF Linac	RF Linac
Efficiency (%)	33.5	33.5	33.3
Length (km)	3.0	3.0	3.0
Effective voltage drop, U_Σ (GV)	5	5	5
Beam current during single pulse (mA)	147	155	160
Single pulse length (ms)			
Length of macro pulse train containing 450 single pulses (ms)	7.5	7.5	7.5
Repetition rate of pulse trains (Hz)	20	20	20
RF duty cycle	0.16	0.16	0.16
Momentum width, $\Delta p/p$	$\pm 5 \times 10^{-5}$	$\pm 3 \times 10^{-5}$	5×10^{-5}
Source emittance, normalized, ε_N (m)	2×10^{-7}	2×10^{-7}	2×10^{-7}
Linac emittance, normalized, ε_N (m)	4×10^{-7}	6×10^{-7}	6×10^{-7}
Micro-bunch frequency (MHz)	108.4	108.4	108.4
Pulse length (μs)	700	15	15
bunch spacing (μs)	35	see figure	see figure
gap between bunches (μs)	1	1 (16)	1 (16)

	4/29/81	5/8/81	6/30/81
Transfer Ring			
Injection, radial stacking			
# turns	20	3	3
Maximum dilution factor	5	2	2
Beam emittance			
horizontal (mm-mrad)		12	12
vertical (mm-mrad)		2	2
Average dipole field, $\bar{B}$ (Tesla)	?	0.159	0.159
Average radius (m)	?	663.4	663.4
Circumference (m)	?	4168	4168
Revolution frequency (kHz)	?	22.22	22.22
Revolution time (μs)	35	45	45
Coasting beam current (A)	3.4	0.46	0.46
# lattice periods	?	240 (?)	240 (?)
ν_{Ho}	?	59.85 (?)	59.85 (?)
ν_{Vo}	?	59.85 (?)	59.85 (?)
Beam full width (cm)			
horizontal	?	2.2 (?)	2.2 (?)
vertical	?	0.9 (?)	0.9 (2)
Vacuum pressure (Torr)	$< 10^{-10}$	(10^{-9} ?)	(10^{-9} ?)
Ejection kicker			
Flat top time (μs)	35	45	45
Rise time (μs)	< 1	< 1	< 1
Reset time (μs)		< 15	< 15
Kicking angle (mrad)		2.5	2.5
Stored energy per shot (kJ)	?	0.05	0.05
Average frequency of shots (sec^{-1})		200	200
Power (kW) (η = 0.2)	?	50	50
Beam rotator $\int$ Bdz (Tesla-m)	330	330	330
Condenser rings			
# of rings		5	5

	4/29/81	5/8/81	6/30/81
Injection radial stacking			
# of turns		3	3
Maximum dilution factor		1.67	1.67
Beam emittance			
horizontal (mm-mrad)		10	10
vertical (mm-mrad)		12	12
Average dipole field, $\overline{B}$ (Tesla)		0.477	0.477
Average radius (m)		221.1	221.1
Circumference (m)		1389.4	1389.4
Revolution frequency (kHz)		66.67	66.67
Revolution time (μs)		15	15
Coasting beam current (a)		1.38	1.38
# lattice periods		80 (?)	80 (?)
ν_H		19.85 (?)	19.85 (?)
ν_V		19.85 (?)	19.85 (?)
Beam full width (cm)			
horizontal		2.0 (?)	2.0 (?)
vertical		2.2 (?)	2.2 (?)
Vacuum pressure (Torr)		$< 10^{-10}$	$< 10^{-10}$
Ejection kickers (1 per ring)			
Flat top time (μs)		> 15	> 15
Rise time (μs)		< 1	< 1
Reset time (μs)		< 100	< 100
Kicking angle (mrad)		2.5	2.5
Stored energy per shot (kJ)		0.1	0.1
Average frequency of shots (sec^{-1})		40	40
Power per CR, η = 0.2 (kW)		20	20
Storage rings			
# of rings	10	10	10
Injection, radial stacking			
# of turns	7	3	3
Maximum dilution factor	4	1.5	1.5

	4/29/81	5/8/81	6/30/81
Beam emittance			
horizontal (mm-mrad)		45	45
vertical (mm-mrad)		90	90
Average dipole field, $\bar{B}$ (Tesla)	?	1.431	1.431
Average radius (m)	?	73.7	73.7
Circumference (m)	?	463.1	463.1
Revolution frequency (MHz)	0.2	0.2	0.2
Revolution time (μs)	5	5	5
Coasting beam current (A)	24	21	21
# of lattice periods	?	40 (?)	40 (?)
ν_{Ho}	?	9.85 (?)	9.85 (?)
ν_{Vo}	ν_H	ν_H	nH
Beam full width (cm)			
horizontal	6(or 4)	3.7 (?)	3.7 (?)
vertical	12(or 8)	5.2 (?)	5.2 (?)
Vacuum pressure (Torr)	10^{-10}_	10^{-10}_	10^{-10}_
	10^{-11}	10^{-11}	10^{-11}
Adiabatic compression			
RF (MHz)	0.4	0.4	0.4
Harmonic number	2	2	2
Initial volts per turn (kV)	2	2	2
Final volts per turn (kV)	200	200	200
Rise time (ms)	< 0.1	10	10
Initial $\Delta p/p$	5×10^{-5}	$\pm 3 \times 10^{-5}$	$\pm 3 \times 10^{-5}$
Final $\Delta p/p$	5×10^{-4}	$\pm 5 \times 10^{-4}$	$\pm 5 \times 10^{-4}$
Final $\Delta\Phi$	±15°	±15°	±15°
Final Δt (ns)	±100	±100	±100
Separatrix $\Delta p/p$	$\pm 3 \times 10^{-3}$	$\pm 3 \times 10^{-3}$	$\pm 3 \times 10^{-3}$
Synchrotron freq/revolution freq.	1/350	1/350	1/350
Fast extraction kickers			
# of kickers per ring		2	2

	4/29/81	5/8/81	6/30/81
Kicking angle (mrad)	20	6*	6*
Rise time (μs)	1.5	1.5	1.5
Flat top time (ns)	> 500	> 500	> 500
Stored energy per shot (kJ)		2	2
Average frequency of shots (sec^{-1})		4	4
Power per kicker, η = 0.2 (kW)		40	40
Fast Compression: induction linac (space charge effects included)			
Length (m)	100-200	200	200
Voltage (MV)	160	300	150
Pulse shape	sawtooth	sawtooth	sawtooth
Pulse length (ns)	200	200	200
Focal length (km)	< 1.16	0.8	0.8
Δp/p	$>\pm 8 \times 10^{-3}$	$\pm 5 \times 10^{-3}$	$\pm 5 \times 10^{-3}$
Beam lines			
Total number-long	20	20	20
Length (km) per long beam line	1.2	1.2	1.2
# into each chamber (short)	80	20	20
Length (km)	0.3	0.3	0.3
Total length of all beam lines (km)	48	48	48
Lattice period (m)	?	> 2.8	> 2/8
Phase advance	π/3	π/3	π/3
Beam tube inner diameter (cm)	10	8	8
Beam chamber entry			
Final focusing magnets	triplet	quadrupoles	quadrupoles
Distance from FFM to target (m)	8.5	8.5	8.5
Clearance for cavity-beam line vacuum pump (m)	2	2	2

*For 4 cm hor. beam width (space charge).

		4/29/81	5/8/81	6/30/81
Cavity pump down time between shots (ms)		150	150	150
Beam port dimensions (cm)				
vertical		85	103	103
horizontal		25	34.3	34.3
Distance from beam port to target (m)		7	7.28	7.27
Final Beams				
# of beams	Step 1	---	---	---
	Step 2	20	20	20
Pulse length (ns),	Step 1	---	---	---
	Step 2	20	20	20
Particle Current/beam (kA) (Electric current = 2x particle current)	Step 1	---	---	---
	Step 2	1.2	1.25	1.25
Pulse energy (MJ)		5	4.8	4.8
Maximum power (TW)		250	250	250
Pulse repetition rate (Hz)		20	20	20
Focused spot diameter (mm)		6	6	6
Focused spot area (mm^2)		28.3	28.3	28.3
Unnormalized emittance per beam (mm-mrad)				
vertical		120π	90π	120π
horizontal		30π	45π	30π
Normalized emittance per beam (mm-mrad)				
vertical		58π	29π	
horizontal		17.4π	15π	

V. "CAVITY" REGION PARAMETERS

	4/29/81	5/8/81	6/30/81
Coolant and breeding material	$Pb_{83}Li_{17}$	$Pb_{83}Li_{17}$	$Pb_{83}Li_{17}$
Li-6 enrichment, %	natural	natural	natural
Tube Region			
Inport tube structural material	HT9-0.7	HT9-0.7	HT9-0.7
and v/o	SiC-2	SiC-2	SiC-2
Inport tube coolant v/o	97.3	97.3	97.3
Tube region support structure v/o	HT9-0.7	HT9-0.7	HT9-0.7
First surface radius (m)	5	5	5
Region thickness (m)	2	2	2
Region density factor	0.33	0.33	0.33
Effective coolant thickness (m)	0.66	0.66	0.66
Mass of coolant in tubes/cavity (tonnes)	2295	2295	2295
Tubes			
Length (m)	10	10	10
Diameter (cm)			
First two rows	3	3	3
Wall thickness (mm)		0.8	0.8
Remainder	10	10	10
Wall thickness (mm)		2	2
Number			
First two rows	1230	1230	1230
Remainder	3060	3060	3060
Number of penetrations in region	20	20	20
Total area of beam penetrations at first surface (m^2)	3.6	3.6	3.6
Pb at. density - $x10^{-10}$ atom/cm^3*	4	4	4

*Just before shot.

	4/29/81	5/8/81	6/30/81
Noncondensible at. density @ 500°C - x 10^{-10} atoms/cm^3	0.13	0.13	0.13
Pressure - Torr	< 10^{-4}	< 10^{-4}	< 10^{-4}
Chamber top			
Structural material and v/o	HT-9 1 SiC 2	HT-9 1 SiC 2	HT-9 1 SiC 2
Coolant v/o	97	97	97
Height at chamber centerline (m)	6.5	6.5	6.5
Region thickness (m)	0.5	0.5	0.5
Mass of coolant in top cavity (tonnes)	717	717	717
Number of penetrations in top region	1	1	1
Total area of penetrations at chamber inner surface (m^2)	small	"small"	"small"
Chamber bottom pool			
Structural material and v/o	---	---	---
Coolant v/o	100	100	100
Height at chamber centerline (m)	5	5	5
Region thickness (m)	1.0	1.0	1.0
Mass of coolant in bottom pool/ cavity (tonnes)	1448	1448	1448
Maximum 1st surface neutron energy current - at chamber midplane (MW/m^2)	4.54	4.54	4.54
Neutrons passing through each beam line penetration per shot	8.14×10^{16}	8.14×10^{16}	8.14×10^{16}
Maximum total 1st surface X-ray and debris heat flux (J/cm^2)	34.5	34.5	34.5
DT power per cavity (MW)	2000	2000	2000
Total n & γ power in cavity (MW)	1667.4	1667.4	1667.4
Tube region	1097.1	1097.1	1097.1
Cavity top	293.1	293.1	293.1
Cavity bottom	277.2	277.2	277.2

	4/29/81	5/8/81	6/30/81
Total power in cavity, including X-rays and debris (MW)	2208.7	2208.7	2208.7
Energy multiplication(1)	1.1	1.1	1.1
n & γ energy multiplication(2)	1.17	1.17	1.17
Average power density (W/cm^3)	3.44	3.44	3.44
Tube region	4.41	4.41	4.41
neutron	2.20	2.20	2.20
gamma	2.21	2.21	2.21
Top region	3.51	3.51	3.51
neutron	1.89	1.89	1.89
gamma	1.62	1.62	1.62
Bottom region	1.80	1.80	1.80
neutron	1.06	1.06	1.06
gamma	0.74	0.74	0.74
Peak/average spatial power density in tube region	4.87	4.87	4.87
Impulse on first row of tubes ($dyne\text{-}sec/cm^2$)	600	600	600
Amount of coolant blown off per shot (kg)	13	13	13
Maximum DPA/FPY in SiC			
Tube region	118	118	118
Top region	70	70	70
Bottom region	---	---	---
Average DPA/FPY in SiC			
Tube region	33.5	33.5	33.5
Top region	29.6	29.6	29.6
Bottom region	---	---	---

(1) Total energy deposited in region/Dt yield

(2) Total n & γ energy deposited in region/n & γ energy incident on 1st surface.

	4/29/81	5/8/81	6/30/81
Maximum H production in SiC (appm/FPY)			
Tube region	1408	1408	1408
Top region	833	833	833
Bottom region	---	---	---
Average H production in SiC (appm/FPY)			
Tube region	273	273	273
Top region	216	216	216
Bottom region	---	---	---
Maximum He production in SiC (appm/FPY)			
Tube region	3705	3705	3705
Top region	2192	2192	2192
Bottom region	---	---	---
Average He production in SiC (appm/FPY)			
Tube region	353	353	353
Top region	274	274	274
Bottom region	---	---	---
Tritium breeding ratio	1.216	1.216	1.216
^{6}Li	1.190	1.190	1.190
Tube region	0.729	0.729	0.729
Top region	0.226	0.226	0.226
Bottom region	0.235	0.235	0.235
^{7}Li	0.026	0.026	0.026
Tube region	0.081	0.081	0.081
Top region	0.004	0.004	0.004
Bottom region	0.004	0.004	0.004
Coolant			
Inlet temperature (°C)	330	330	330
Outlet temperature (°C)	500	500	500
Flow rate/cavity (kg/hr)	2.7×10^{8}	2.94×10^{8}	2.94×10^{8}
Maximum velocity within tubes in first two rows (m/s)	5	5	5

	4/29/81	5/8/81	6/30/81
Maximum velocity within tubes not in the first two rows (m/s)	1.3	1.3	1.3
Pressure (MPa)	0.2	0.2	0.2
ΔP for entire loop (MPa)	2.0	2.0	2.0
Pumping power delivered to coolant per cavity (MW)	17.7	17.9	17.9

VI. "NON-CAVITY" REGION PARAMETERS

	4/29/81	5/8/81	6/30/81
A. Vacuum Boundary Wall			
Structural material	HT-9	HT-9	HT-9
Side wall			
Inside diameter (m)	14	14	14
Thickness (m)	0.01	0.01	0.01
Height (m)	12.0	12.0	12.0
Top liner			
Height above midplane (m)			
at centerline	7.0	7.0	7.0
at side wall	6.0	6.0	6.0
Thickness	0.01	0.01	0.01
Maximum neutron wall loading (MW/m^2)			
- side wall at midplane	0.032	0.032	0.032
Average power density (W/cm^3)	1.65	1.65	1.65
Side wall	1.22	1.22	1.22
neutron	0.097	0.097	0.097
gamma	1.13	1.13	1.13
Top liner	3.07	3.07	3.07
neutron	0.20	0.20	0.20
gamma	2.87	2.87	2.87
n & γ energy multiplication	0.008	0.008	0.008
Power deposited in vacuum wall/ cavity (MW)	11.0	11.0	11.0
Side wall	6.2	6.2	6.2
Top liner	4.8	4.8	4.8
Maximum DPA/FPY			
Side wall	2.69	2.69	2.69
Top liner	4.98	4.98	4.98

	4/29/81	5/8/81	6/30/81
Peak instantaneous DPA rate (DPA/s)			
- side wall at midplane	0.009	0.009	0.009
Maximum H production (appm/FPY)			
Side wall	1.38	1.38	1.38
Top liner	3.20	3.20	3.20
Maximum He production (appm/FPY)			
Side wall	0.364	0.364	0.364
Top liner	0.862	0.862	0.862
Peak instantaneous He production rate			
(appm/s) - side wall at midplane	0.11	0.11	0.11
Maximum temperature (°C)	?	1520	1520
Expected lifetime (FPY)	?	20	20
Radioactivity at shutdown (Ci)	?	?	?
B. Reflector			
Structural material	HT-9	HT-9	HT-9
Coolant	$Pb_{83}Li_{17}$	$Pb_{83}Li_{17}$	$Pb_{83}Li_{17}$
Side reflector			
Inside diameter (m)	14.02	14.02	14.02
Thickness (m)	0.4	0.4	0.4
Mass of structure (tonnes)	1530	1530	1530
Mass of coolant (tonnes)	205	205	205
v/o of structure	90	90	90
v/o of coolant	10	10	10
Top reflector			
Thickness (m)	0.4	0.4	0.4
Mass of structure (tonnes)	432	432	432
Mass of coolant (tonnes)	58	58	58
v/o of structure	90	90	90
v/o of coolant	10	10	10
Bottom of reflector (splash plate)			
Thickness (m)	0.4	0.4	0.4
Mass of structure (tonnes)	484	484	484

	4/29/81	5/8/81	6/30/81
Mass of coolant (tonnes)	65	65	65
v/o of structure	90	90	90
v/o of coolant	10	10	10
Total mass of structural material in reflector/cavity (tonnes)	2446	2446	2446
Total mass of coolant in reflector/cavity (tonnes)	328	328	328
n & γ energy multiplication	0.223	0.223	0.223
Average power density (W/cm^3)	0.941	0.941	0.941
Side reflector	0.939	0.939	0.939
neutron	0.082	0.082	0.082
gamma	0.857	0.857	0.857
Top reflector	1.465	1.465	1.465
neutron	0.127	0.127	0.127
gamma	1.338	1.338	1.338
Bottom reflector (splash plate)	0.257	0.257	0.257
neutron	0.023	0.023	0.023
gamma	0.234	0.234	0.234
Peak/average spatial power density - in side reflector	4.577	4.577	4.577
Power deposited in reflector/cavity (MW)	318.3	318.3	318.3
Side	211.1	211.1	211.1
Top	91.4	91.4	91.4
Bottom	15.8	15.8	15.8
Maximum DPA/FPY			
Side reflector	2.43	2.43	2.43
Top reflector	4.50	4.50	4.50
Bottom reflector	1.36	1.36	1.36
Average DPA/FPY			
Side reflector	0.41	0.41	0.41
Top reflector	0.73	0.73	0.73
Bottom reflector	0.125	0.125	0.125

	4/29/81	5/8/81	6/30/81
Maximum H production in structural material (appm/FPY)			
Side reflector	1.15	1.15	1.15
Top reflector	2.68	2.68	2.68
Bottom reflector	0.026	0.026	0.026
Average H production in structural material (appm/FPY)			
Side reflector	0.17	0.17	0.17
Top reflector	0.41	0.41	0.41
Bottom reflector	0.004	0.004	0.004
Maximum He production in structural material (appm/FPY)			
Side reflector	0.300	0.300	0.300
Top reflector	0.715	0.715	0.715
Bottom reflector	0.006	0.006	0.006
Average He production in structural material (appm/FPY)			
Side reflector	0.032	0.032	0.032
Top reflector	0.96	0.96	0.96
Bottom reflector	0.006	0.006	0.006
Tritium breeding ratio	0.034	0.034	0.034
^{6}Li	0.034	0.034	0.034
Side	0.022	0.022	0.022
Top	0.010	0.010	0.010
Bottom	0.002	0.002	0.002
^{7}Li	4×10^{-6}	4×10^{-6}	4×10^{-6}
Side	2×10^{-6}	2×10^{-6}	2×10^{-6}
Top	2×10^{-6}	2×10^{-6}	2×10^{-6}
Bottom	0	0	0
Coolant			
Mass of coolant within reflector per cavity (tonnes)	328	328	328

	4/29/81	5/8/81	6/30/81
Flow rate/cavity (kg/hr)	3.7×10^7	4.4×10^7	4.4×10^7
Inlet temperature (°C)	330	330	330
Outlet temperature (°C)	500	500	500
Maximum coolant velocity (m/s)	1	1	1
Pressure (MPa)	2	2	2
ΔP for entire loop (MPa)	0.7	0.7	0.7
Pumping power delivered to coolant per cavity (MW)	1	1	1
Maximum structure temperature (°C)	550	550	550
C. Shield			
Structural material and v/o	concrete	concrete	concrete
	95	95	95
Coolant and v/o	H_2O 5	H_2O 5	H_2O 5
Side shield			
Inside diameter (m)	14.82	14.82	14.82
Thickness (m)	3.5	3.5	3.5
Top shield			
Height above midplane at centerline (m)	7.41	7.41	7.41
Thickness (m)	3.5	3.5	3.5
Bottom shield			
Height below midplane (m)	6.40	6.40	6.40
Thickness (m)	3.5	3.5	3.5
Maximum power density at midplane (W/cm^3)	0.045	0.045	0.045
Average power density (W/cm^3)	0.0018	0.0018	0.0018
Power deposited in shield/cavity (MW)	6.82	6.82	6.82
Power deposited in neutron & debris dump per beam line (MW)	?	?	?
Energy flux at outer surface of shield at midplane (W/cm^2)			
neutron	1.52×10^{-17}	1.52×10^{17}	1.52×10^{17}

	4/29/81	5/8/81	6/30/81
gamma	2.38×10^{-10}	2.38×10^{-10}	2.38×10^{-10}
Dose rate at outer surface of shield at midplane (mrem/hr)	2.64	2.64	2.64
neutron	1.4×10^{-5}	1.4×10^{-5}	1.4×10^{-5}
gamma	2.64	2.64	2.64
Peak DPA rate in F.F. magnet stabilizer (DPA/FPY)	4.48×10^{-6}	4.48×10^{-6}	4.48×10^{-6}
Peak radiation dose rate in F.F. insulator magnets (Rad/FPY)	7.2×10^{6}	7.2×10^{6}	7.2×10^{6}
Peak power density in F.F. magnets (W/cm^3)	5.35×10^{-7}	5.35×10^{-7}	5.35×10^{-7}
Coolant			
Inlet temperature (°C)	45	45	45
Outlet temperature (°C)	60	60	60
Flow rate per cavity (kg/hr)	3.25×10^{5}	3.6×10^{5}	3.6×10^{5}
Maximum velocity (m/s)	1	1	
Pressure (MPa)	0.5	0.5	0.5
ΔP in entire loop (MPa)	0.2	0.2	0.2
Pumping power delivered to coolant/ cavity (MW)	1.25	1.4	1.4
Peak structure temperature (°C)	60	60	60

VII. BALANCE OF PLANT

	4/29/81	5/8/81	6/30/81
Steam temperature (°C)	482	482	482
Steam pressure (MPa)	15.5	15.5	15.5
Steam flow rate (kg/hr)	1.9×10^7	1.8×10^7	1.8×10^7
Feedwater temperature (°C)	300	300	300
Reheat temperature (°C)	482	482	482
Steam generator surface area (m^2)	5.2×10^4	5.2×10^4	5.2×10^4

VIII. SYSTEM PARAMETERS

	4/29/81	5/8/81	6/30/81
Average DT power per cavity (MW)	2000	2000	2000
Total power recoverable per cavity (MW)	2538.2	2548	2548
System energy multiplication	1.27	1.274	1.274
Total pumping power delivered to coolant per cavity (MW)	20	20	20
Gross power per cavity (MW)	2558.2	2558.2	2558
Gross power per 4 cavities (MW)	10233	10233	10233
Gross thermal efficiency (%)	42	42	42
Gross plant output (MWe)	4298	4298	4298
Recirculating power (MWe)	827	827	530
Driver system	467	467	375
Linac	313	313	300
Storage rings			
Beam handling	154	154	75
Final focusing			
Target manufacture and delivery (MW)	?	?	?
Coolant pumps	160	110	110
Vacuum pumps			5
Plant auxiliaries			40
Net plant output (MWe)	?	?	3768
Net plant efficiency (%)	?	?	36.8

IX. TRITIUM PARAMETERS (FOR 29% BURNUP)

	4/29/81	5/8/81	6/30/81
Material inserted per shot			
D - target (mg)	1.61	1.6	1.6
(# of atoms)	4.856×10^{20}	4.8×10^{20}	4.8×10^{20}
T - target (mg)	2.42	2.4	2.4
(# of atoms)	4.856×10^{20}	4.8×10^{20}	4.8×10^{20}
Li - target (mg)	26.5	26.5	26.5
(# of atoms)	2.30×10^{21}	2.30×10^{21}	2.30×10^{-21}
Pb - target (mg)	329	329	329
(# of atoms)	9.56×10^{20}	9.56×10^{20}	9.56×10^{20}
Bi - ion beam (mg)	1.0×10^{-3}	1.0×10^{-3}	1.0×10^{-3}
(# of atoms)	3.0×10^{15}	3.0×10^{15}	3.0×10^{15}
Li - INPORT (g)	79	79	79
(# of atoms)	6.85×10^{24}	6.85×10^{24}	6.85×10^{24}
Pb - INPORT (g)	13200	13000	13000
(# of atoms)	3.8×10^{25}	3.8×10^{25}	3.8×10^{25}
Nonvolatiles (mg)	1.36×10^{4}	1.4×10^{4}	1.4×10^{4}
(# of atoms)	4.52×10^{25}	4.52×10^{25}	4.52×10^{25}
Total (mg)	1.36×10^{4}	1.36×10^{4}	1.36×10^{4}
Total # of atoms	4.52×10^{25}	4.52×10^{25}	4.52×10^{25}
D_2 (target injector) mg/shot	.940	1.6	1.6
# of atoms	2.83×10^{20}	4.8×10^{20}	4.8×10^{20}
Total D, T, D_2 (mg)	2.888	5.6	5.6
(# of atoms)	7.52×10^{20}	1.44×10^{21}	1.44×10^{21}
Fractional burnup, $f_b = T_b/(T_b + T_p)$	.29	.29	.29
Material pumped per shot			
D - target, unburned (mg)	1.146	1.1	1.1
(# of atoms)	3.44×10^{20}	3.4×10^{20}	3.4×10^{20}
T - target, unburned (mg)	1.719	1.7	1.7

	4/29/81	5/8/81	6/30/81
(# of atoms)	3.44×10^{20}	3.4×10^{20}	3.4×10^{20}
D_2 (target injector) - mg/shot	.940	1.6	1.6
- # atoms	2.83×10^{20}	4.8×10^{20}	4.8×10^{20}
T - lost from coolant (mg)	.877	.88	.88
(# of atoms)	1.76×10^{20}	1.76×10^{20}	1.76×10^{10}
He-DT fusion reaction (mg)	.942	.94	.94
(# of atoms)	1.41×10^{20}	1.4×10^{20}	1.4×10^{20}
He-T decay (mg)	1.3×10^{-9}	1.3×10^{-9}	1.3×10^{-9}
(# of atoms)	1.9×10^{11}	1.9×10^{11}	1.9×10^{11}
He-T production (mg)	1.17	1.17	1.17
(# of atoms)	1.76×10^{20}	1.76×10^{20}	1.76×10^{20}
He - total (mg)	2.11	2.11	2.11
(# of atoms)	3.17×10^{20}	3.17×10^{20}	3.17×10^{20}
Bi - ion beam (mg)	1.0×10^{-3}	1.0×10^{-3}	1.0×10^{-3}
(# of atoms)	3.0×10^{15}	3.0×10^{15}	3.0×10^{15}
Li - not condensed (mg)	0	0	0
(# of atoms)	0	0	0
Pb - not condensed (mg)	0	0	0
(# of atoms)	0	0	0
Nonvolatiles (mg)	0	0	0
(# of atoms)	0	0	0
Total (D, T, He, D_2 Target inj.)	6.79	7.39	7.39
Total # of atoms	1.46×10^{21}	1.65×10^{21}	1.65×10^{21}
# of shots per chamber per second	5	5	5
# of chambers	4	4	4
Total condensibles pump rate/chamber (g/s)	0	0	0
Total noncondensibles pump rate/chamber (g/s)	3.4×10^{-2}	.037	.037
Cavity pressure (Torr @ 0°C)	10^{-4}	10^{-4}	10^{-4}
Coolant breeding region			
Breeding material	$Pb_{83}Li_{17}$	$Pb_{83}Li_{17}$	$Pb_{83}Li_{17}$

	4/29/81	5/8/81	6/30/81
Flow rate for one chamber (kg/hr)	2.7×10^8	3.38×10^8	3.38×10^8
Breeder mass within one chamber (kg)	4.78×10^6	4.46×10^6	4.46×10^6
Total breeder mass for all chambers (kg)	1.91×10^7	1.78×10^7	1.78×10^7
Inlet temperature (°C)	330	330	330
Outlet temperature (°C)	500	500	500
Breeding ratio	1.25	1.25	1.25
Steady state tritium concentration (wppm)	6.1×10^{-4}	6.1×10^{-4}	6.1×10^{-4}
Tritium pressure (Torr @ 0°C)	10^{-4}	10^{-4}	10^{-4}
Weep rate (kg/hr)			
Extractor			
Inlet temperature (°C)			
Outlet temperature (°C)			
Inlet concentration (wppm)			
Outlet concentration (wppm)			
Extraction method	In situ extraction	In situ extraction	In situ extraction
Size of extractor			
Mass of breeding material within extractor (kg)			
% of total breeding material within extractor			
Steam generator			
Material composition		HT-9	HT-9
Wall thickness (mm)		1.0	1.0
Primary inlet temperature (°C)		330	330
Primary outlet temperature (°C)		500	500
Secondary inlet temperature (°C)		315	315
Secondary outlet temperature (°C)		490	490
Secondary pressure (MPa)		15.5	15.5
Surface area (m^2)		5.2×10^4	5.2×10^4

	4/29/81	5/8/81	6/30/81
Tritium permeation rate to H_2O (Ci/s)		.38	.38
Tritum inventory - steady state			
Breeding material - 4 cavities			
Reactor chamber - kg	.011	0.11	0.11
Reflector - kg	7.9×10^{-4}	7.9×10^{-4}	7.9×10^{-4}
Cryopumps (2 hr on-line) - kg	.374	.37	.37
Cryogenic distillation columns (kg)	.157	.16	.16
Fuel cleanup (kg)	.042	.042	.042
Structural material and piping (kg)			
Steam generator piping (kg)			
Storage - 3 days fuel supply (kg)	12.5	12.5	12.5
Total (kg)	13.08	13.1	13.1
Total (Ci)	1.3×10^8	1.3×10^8	1.3×10^8
Containment			
Total building volume (m^3)			
Volume of reactor & auxiliaries (m^3)			
Cleanup volume (m^3)			
Containment pressure (Torr @ 0°C)			
Time for tritium cleanup (hr)			